NEW SILOXANE - NYLON-6 DIBLOCK COPOLYMERS

FOR

EMULSIFICATION AND TOUGHENING OF BLENDS

Cary Alan Veith

B.S.Ch.E., University of Akron (1980)

SUBMITTED TO THE DEPARTMENT OF CHEMICAL ENGINEERING
IN PARTIAL FULFILLMENT OF THE REQUIREMENTS FOR THE DEGREE OF

DOCTOR OF PHILOSOPHY
IN CHEMICAL ENGINEERING

at the

MASSACHUSETTS INSTITUTE OF TECHNOLOGY

June, 1989

Signature of Author: _____
Department of Chemical Engineering

Certified by: _____
Robert E. Cohen
Department of Chemical Engineering
Thesis Co-Advisor

and by: _____
Ali S. Argon
Department of Mechanical Engineering
Thesis Co-Advisor

Accepted by: _____
William M. Deen
Chairperson of the Committee for
Graduate Students

NEW SILOXANE - NYLON-6 DIBLOCK COPOLYMERS FOR EMULSIFICATION AND TOUGHENING OF BLENDS

by

Cary Alan Veith

Submitted to the Department of Chemical Engineering
on April 20, 1989
in Partial Fulfillment of the Requirements
for the Degree of Doctor of Philosophy in Chemical Engineering.

ABSTRACT

Comprehensive kinetic studies of the synthesis of poly(trifluoropropylmethylsiloxane) and poly(dimethylsiloxane) have been undertaken to produce suitable rubber macromonomers for subsequent copolymerization with ϵ-caprolactam. The time scales of the propagation reactions in the two siloxane homopolymerizations have been quantified to determine the optimum time for termination which minimizes unwanted backbiting and cyclization (i.e. depolymerization) reactions. Study of the undesirable depolymerization reactions of these siloxanes in the presence of caprolactam monomer and/or nylon-6 catalyst has led to an optimum set of reaction conditions for productive copolymerization with ϵ-caprolactam. Derivatized $LiAlH_4$ catalysts, utilization of an ultrasonic reactor and changes in polymerization temperature have overcome the destructive siloxane depolymerization reactions during the growth of the nylon-6 block. Solubility studies, morphological and mechanical property characterization in addition to "simulated" block copolymerizations with unreactive polysiloxanes have verified block structure integrity.

The resulting morphologies of blends of one of the copolymers with homopoly(dimethylsiloxane) and homopolyamide-6 have been studied in thin films and in bulk and showed direct evidence of the emulsification of the two homopolymers by the diblock copolymer as observed by transmission electron microscopy. Comparison to existing statistical and microscopic thermodynamic theories for the morphology of crystalline-rubber diblock copolymers in the solid state, solution and the melt has been made. The dry (ca. 2000 ppm water), melt annealed diblock copolymers which are only ca. 20% crystalline, exhibited marked improvements in toughness even with very low rubber content (~3%). Toughness is increased more than 200 % over homopolyamide-6 for dry samples with ca. 25 %w siloxane in the diblock. This reaffirms that incorporation of submicron, rubbery heterogeneities can enhance and activate energy-absorbing mechanisms in semicrystalline polymers. This thesis utilizes a rather well defined crystalline-rubber poly(dimethylsiloxane)-b-polyamide-6 diblock copolymer to systematically explore the phenomena of rubber toughening of nylon-6.

Thesis Advisors: Dr. Robert E. Cohen,
Professor Department of Chemical Engineering
and Dr. Ali S. Argon,
Professor Department of Mechanical Engineering

ACKNOWLEDGEMENTS

The achievement of such a goal is not without great sacrifice and dedication to science. Along the path, there have been many supporters whose help, encouragement and advice has not been forgotten. It is hoped that a few words of thanks will serve to express my deep appreciation for their caring and support.

To my loving and devoted wife, Amanda who has stood by me steadfast and unwavering in her commitment to help me accomplish this goal. Not only through her physical efforts but also through her spirit has she immeasurably comforted me in times of disappointment and frustration in my research (and there have been many). Her unending love and warm smile have made this task so much easier and for her presence in my life, I am grateful.

To my parents, my father who has been an endless source of good ideas to supplement my technical work and my mother who so strongly encouraged me to strive for the very best I can be and go on to graduate school. Both of you, in your own special way were always with me during this time and for your constant involvement even across many miles, I love you and thank you.

To Drs. Andrezj Galeski and Osman Gebizlioglu who have given me so much useful guidance and direction during my education here at M.I.T. To Osman, a special thanks for orienting me upon arrival in the lab and showing me how-to-gamit. And to Andrezj, who is one of those rare, gifted scientists who sees so precisely the most expedient solution to any problem. I am very thankful for having had the opportunity to learn from you and for the many valuable experimental techniques you have taught me.

To Dr. Pao-Lao (Paul) Cheng, for your experience and guidance in the synthesis aspects of my work; I have benefited a great deal from your expertise and still enjoy very much the friendship we began while you were in the lab.

To my friends and classmates, many of whom are now scattered across the country, your friendship and comradery has made for some of the best entertainment in my lifetime while here in Boston.

To my UROP's, Marcelo Fogaca, Linda Yeh and Andrew Yee who have all worked very hard to help me accomplish my research. For your patience, dedication and the ability to work independently, I thank you.

And last but surely not least, to Professors Bob Cohen and Ali Argon from whom I have learned a great deal. Thank you for the financial and intellectual support you have given me during my education and for the opportunity to benefit from your knowledge.

TABLE OF CONTENTS

LIST OF FIGURES

LIST OF TABLES

CHAPTER I. INTRODUCTION

Rubber toughened plastics rapidly are increasing in engineering importance primarily as a result of innovative synthesis and a better understanding of the mechanisms responsible for increased toughness. These "bipolymeric" materials synergistically enhance material properties by combining the tensile strength of thermoplastics with the elongation of rubbers. This provides greater impact strength, strain to fracture and energy absorbed during deformation than either of the corresponding homopolymers. Rubber modified semicrystalline polymers offer additional benefits with the inherent toughness of the crystal structure as well as the interaction of the rubber-thermoplastic interface in producing tough, thermally stable and solvent resistant materials.

The yielding mechanisms in rubber modified crystalline polymers are very complex owing to the complicated morphology and interaction of the three "phases", crystal, glass and rubber. Toughness of crystalline polymers alone can vary by several orders of magnitude depending on morphology, degree of crystallinity, crystallite size, molecular weight, etc. Thus, the understanding of the interrelation between chemical structure, morphology and mechanical properties is essential in studying rubber modified crystalline polymers.

This chemical structure depends on the combination of rubber and thermoplastic which generally can be accomplished either one of two ways. The first is through physical blending, a technique which is simplistic in approach but is not always successful (even when two phase morphology is desired) due to the thermodynamics of mixing. Two different polymer chains are generally incompatible due to a strong positive

enthalpic interaction of the chemically different segments more than offsetting a weak entropy of mixing which is small due to the large molar volume of macromolecules. This precludes simple blending on the micro-scale and the macroscopically phase separated system often leads to poorer mechanical properties than either of the two pure homopolymers.

Alternatively, block and/or graft copolymers can be used to bring into intimate contact these two materials via chemical connectivity. These copolymers are simply long chains (e.g. A) of one type of monomer segment covalently bonded to another chain (e.g. B) of a different type of monomer. If this AB copolymer has one junction it is a diblock, if it contains two junctions or an ABA structure, it is a triblock and so on. Multiple junctions are indicative of alternating block copolymers and/or graft copolymers, the latter possessing a nonlinear, ternary junction. This general class of materials require much more effort in preparation, sometimes necessitating novel and innovative synthesis methods but result in materials with markedly different properties than their corresponding blends. Due to the confinement of the junction in the interphase region, these copolymers exhibit good adhesion between phases, microphase separated domains with domain size correlating directly with the molecular weight of the blocks, and the ability of the copolymer to emulsify blends of the homopolymers A and B.

The industrial importance of nylon-6 and the need to improve its low notched impact resistance combined with the academic incentives of discovering the thermodynamic and kinetic interplay between rubber and semicrystalline phases are major incentives to study the nylon-6/rubber copolymer system. Previous research into nylon-rubber copolymers has

failed to establish a clear, concise relation between well defined chemistry, morphology and mechanics. This is due, in part, to the complexities of nylon-6 (such as multiple crystalline forms, moisture sensitivity, etc) but moreover, to the lack of simplicity in copolymer chemical structure; to date, primarily graft and alternating copolymers, which are more poorly characterized, have been studied comprehensively.

Since the simplest "building block" in the multiple phase system of nylon-6 and rubber is a diblock copolymer, the discovery of a viable pathway to its synthesis is of great importance. This thesis work successfully has developed the novel capability to synthesize a poly-dimethylsiloxane-nylon-6 diblock copolymer of sufficiently high molecular weight to help elucidate the toughening mechanisms in nylon-6-rubber copolymers and blends through well-defined morphology. The chief benefit of the siloxane block in the copolymer structure in this toughening application is its excellent thermal stability that permits melt annealing (i.e. heating of the copolymer above the melting temperature and cooling at a prescribed rate) to form the desired morphology. The siloxane block will be synthesized first, then a special compound, 11-(dimethylchlorosilyl)1-oxo-1-(1'-aza-2'-oxo-cycloheptyl)-n-undecyl (or alternatively, 11-(dimethylchlorosilyl)-n-undecanoyl-1-caprolactam abbreviated DMCSUCL), will be used to terminate the growing siloxane creating the macromonomer. Subsequent polymerization with ϵ-caprolactam gives the poly(dimethylsiloxane-b-ϵ-caprolactam) diblock copolymer which can be used to emulsify addition of homopolyamide-6 and/or homopoly(dimethylsiloxane) to swell the microphase separated domains. After sufficient improvement in the chemistry of the anionic catalyst, good

control over the molecular weights of both blocks was achieved with the synthesis process described here. The simple diblock copolymer structure provided a sound, fundamental approach to tailoring morphology and altering mechanical properties in the poly(dimethylsiloxane)-nylon-6 system.

This thesis is organized roughly into two main parts. Most of Chapter II provides the majority of the theoretical background in amorphous and semicrystalline multiphase polymers. The main topics covered include techniques in copolymerization, thermodynamics of phase equilibria, kinetic control by crystallization and mechanics of deformation. This is primarily a literature review used to lay the groundwork for future discussion. The second half or the remaining chapters mostly contain the experimental results of this thesis and are discussed in detail with respect to specific works, especially those dealing with nylon-6 and its copolymers. Some of the literature covered in the latter chapters has not been discussed in Chapter II to avoid duplication but relevant points are reiterated in view of the experimental findings. Thus, the reader can explore general information about a number of different topics in multiphase copolymers found in Chapter II or can refer to later chapters for specific details and discussions without having to read a lot of introductory literature review.

CHAPTER II. MOTIVATION FOR RESEARCH

Comprehensive examination of well-defined chemistry, morphology and mechanical properties in the nylon-6 / polysiloxane rubber system is the subject of this thesis. To provide a theoretical framework for its discussion, the three areas of general block copolymer synthesis, morphology and material properties are introduced in this chapter (§§A, B, C) followed by a brief discussion of the approach and the applied methodology (§D). Subsequent chapters provide the details of the various research areas and the quantification of results.

A. ADVANCED TECHNIQUES FOR COPOLYMERIZATION

Due to the breadth of copolymerization mechanisms, there is no single reference that covers all aspects of covalently joining two different polymer chains at one or a few specific sites. Because of the variety of monomers, there are many different methods currently in use and new techniques still are being introduced (e.g. group transfer, transformation reactions and new catalysts in metathesis polymerizations). Despite this diversity, well-defined copolymerization methods generally can be grouped into one of three categories,

1. Sequential addition of different monomers
2. Coupling of mutually reactive end groups of two or more polymers
3. End-functionalized prepolymers
   a. Functionalized free radical agents
   b. Difunctional condensable block prepolymers
   c. Macromonomers

The distinction between groups 3b and 3c is somewhat arbitrary but will become clearer after examples of these are presented below with additional discussion to briefly illustrate their application. Intentionally left off this list are older, more random methods of building block structure such as mastication and free radical graft copolymerization which are usually contaminated by significant amounts of homopolymer and poor understanding of molecular architecture.

1. Sequential Addition

As the title implies, this method entails initiation and polymerization of a first monomer whose active site is used to subsequently polymerize a second monomer forming the two blocks of a diblock copolymer. Difunctional initiators can be used to obtain triblock structures as well and the process can be continued with repeated monomer additions if multiblock copolymers are desired. Additional monomer(s) must be capable of reacting with the existing reactive group from the propagation of the preceding monomer under the same conditions, i.e. solvent versus bulk, polar versus nonpolar, etc. Changes in temperature usually can be accommodated between successive block polymerizations but addition and/or removal of large quantities of solvent is more difficult especially if high purity must be maintained. Specific termination with end group functionalization can be used if necessary depending on the propagation mechanism. Without a doubt, this method is preferred when possible because it minimizes preparation of additional solvents, reagents and reactor hardware.

The most well known and classic example of sequential addition is successive anionic copolymerization of styrene with a diene using

sec-BuLi initiator in hexane or benzene as has been prepared extensively in this laboratory [1] and elsewhere [2]. However, many other less well known copolymers have been prepared anionically such as poly(styrene-b-dimethylsiloxane) [3-5] for surface tension analysis and evaluation of the critical micelle concentration (CMC) as well as for thermoplastic elastomer applications. Others include poly(styrene-b-ethylene oxide) [6-8] for analysis of phase equilibria plus morphological investigation in crystalline-amorphous diblock copolymers and poly(ethylene oxide-b--propylene oxide) copolymers for use as oil-aqueous surfactants [9]. Extensive compilation of block copolymers prepared anionically is available in a book by Morton [10].

As simple as this method appears, the order of sequential addition of the monomers in anionic polymerization is extremely important. The carbanion of the first monomer must be of sufficient basicity to be able to initiate the additional monomer yet can not be too reactive to cause unwanted side reactions. This matching of active monomer nucleophilicity to subsequent monomers is very important just as the choice of initiator is also important; the nucleophilicity of the initiator can not be so strong as with cumyl potassium and methyl methacrylate for example, so as to initiate side reactions at the ester carbonyl but must be nucleophilic enough as with fluorenyl sodium to react with the substituted vinyl group avoiding the ester side reaction. This general problem was studied early by Graham et.al. [11] for styrene and methyl methacrylate copolymers and a very good compilation of the order of the nucleophilicity of many anionically polymerizable monomers is available in Rempp

and Merrill's book [12] which should serve as a guide for designing anionic block copolymerizations.

Contrary to accepted reasoning [13], use of the sequential addition is not restricted to monomers that copolymerize by an anionic mechanism, although it is by far the most common. Successive addition can occur in step growth copolymerizations such as in the polymerization of bisphenol-A with excess phosgene (or other diacid chloride) to give polycarbonate (or a derivative) followed by addition of a diamine and reaction with the remaining acid chloride building two polyamide blocks around a central polycarbonate block. This type of block step copolymerization is limited to irreversible condensation reactions such as those of an acid chloride and amine or hydroxyl and isocyanate to ensure that equilibrium lies far to the right (nearly 100%) so that well-defined block structure is obtained. If end groups are used that exhibit reversible reactions (far from equilibrium), such as carboxyl-hydroxyl to form polyesters, then random reaction of unreacted dicarboxylic acid or diol can destroy block structure leading to random copolymers or at best random multiblock copolymers.

2. Coupling

Coupling reactions between preformed functional blocks provide routes to some block copolymers that are incapable of polymerization by a common mechanism, such as the coupling of vinyl and step growth polymer blocks, (e.g. ω-carboxylic polystyrene and terminally hydroxylated polyesters). In theory these reactions are very useful but in practice they are more difficult because of the low reactive group concentrations and the requirement of main chain stability in the melt (i.e. elevated

temperatures) or dissolution of both polymer blocks in a common, unreactive solvent which precludes use of this method with many semicrystalline polymers. It is precisely the incompatibility of many types of polymer blocks that is desired in the final properties of the copolymer which cause phase separation or at least segregation even in solution. Once the reaction has generated a small amount of copolymer however, this material compatibilizes the "solution" speeding up the remaining coupling reactions.

Examples of coupling reactions are hydrosilylation of dimethylhydrosilyl terminated siloxanes to allyl or vinyl terminated poly(ethylene oxide) using platinum catalyst [14] or the formation of "star" block copolymers by coupling multiple preformed styrene-isoprene diblocks through the use of divinylbenzene linking agent [15]. Another innovative technique is to utilize the mutual reactivity of carbanion and carbocation to cross terminate polystyrene and poly(oxolane) (or poly-THF) as done by Berger, et.al. [16] being aware of possible attack by the anion on the polyether linkage as indicated by Vandenberg [17].

3. End Functionalized Prepolymers

a. Functionalized Free Radical Copolymerization

An often overlooked method of copolymerization is the use of free radical initiators and chain transfer agents that carry a functional group which is inert during polymerization but capable of further reaction as in coupling or macromonomer reactions (categories 2 and 3b, respectively). Despite their use, not all chains will necessarily carry one and only one functional group due to chain transfer and termination by coupling or disproportionation. Subsequent selective fractionation

and extraction undoubtedly will be required to give pure copolymer which may be a mixture of block structures. These unwanted reactions can be minimized by limiting the conversion to around 25% or so but this necessitates an extra separation step downstream from the polymerization reactor. Despite these drawbacks, this pathway is important especially for developing copolymers that contain one block which can be polymerized only by a free radical mechanism such as poly(vinyl chloride) for example.

Use of initiators such as 4,4'-azo-bis-(4-cyanopentanoic acid) [18] yielded carboxyl terminated polystyrene which was converted to the acid chloride via treatment with thionyl chloride and then condensed with a poly(acrylonitrile) carrying terminal hydroxyl groups prepared from the 4,4'-azo-bis-(4-cyanopentan-1-ol) initiator. Better yields of monofunctionality are obtained when a chain transfer agent such as mercaptopropionic acid, $HS(CH_2)_2COOH$ that carries the same functionality as the initiator fragment [19] is used in amounts exceeding that necessary to overcome normal chain transfer processes.

b. Difunctional Condensable Prepolymers

This type of copolymerization proceeds almost exclusively by a step growth mechanism and is used predominantly by industry due to ease of preparation and attainment of desired mechanical properties. It involves the prepolymerization of one of the components followed by condensation with the second block component which may or may not have been presynthesized. It is used in the copolymerization of polyesters and polyalkylene oxides such as poly(1,4-dimethylolcyclohexane terephthalate)poly(tetramethylene oxide) [20], the polyamides and polyethers

with a commercial product formerly known as Nyrim^{R} now of the Dutch State Mines Co. [21] or polysulfone-poly(dimethylsiloxane) alternating copolymers [22]. This process is depicted with the synthesis of a polybutadiene-urethane-urea (PBUU) as shown in equation (2-1).

$$\text{HO–PB–OH} \xrightarrow{\text{MDI}} \text{OCN–(R–NHCOO–PB–OCONH)}_{\overline{x}}\text{R–NCO} \xrightarrow{\text{TMDA}}$$

$$\text{H}_2\text{N–(CH}_2)_4\text{–(NHCONH–(R–NHCOO–PB–OCONH)}_{\overline{x}}\text{R–NHCONH–(CH}_2)_4)_{\overline{y}}\text{NH}_2 \qquad (2\text{-}1)$$

In this case the polybutadiene-urethane (PBU) prepolymer is synthesized by chain extending the diol with a diisocyanate such as methylenediphenyldiisocyanate, MDI to give the isocyanate end-capped PBU. This prepolymer is then copolymerized with a diamine such as tetramethylenediamine, TMDA to give the PBUU which has use as a drug delivery material [23].

c. Macromonomers

The synthesis of macromonomers, polymers fitted at the end of the chain with a monomeric functionality, are ideally suited to block copolymerization especially diblock preparation. Macromonomers can be synthesized via a "direct" (one-step) or two-step process. The direct process deactivates the living site of a carbanion for example, with an unsaturation such as methacroyl chloride after reduction of nucleophilicity of the carbanion to an oxanion before addition of the electrophile. This affords a polystyrene for example with a ω-methacrylate monomer functionality. See equation (2-2) with ST = styrene.

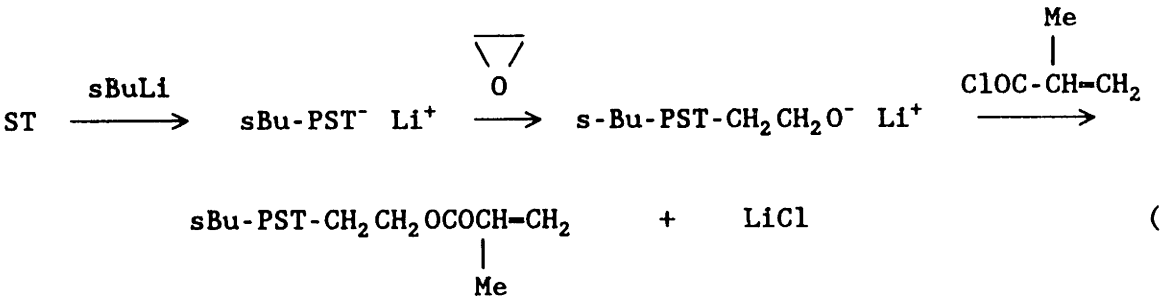

(2-2)

The two-step process is applicable to commodity end-functionalized polymers such as those previously fitted with a hydroxyl or carboxyl end group which is reacted with an antagonist function carrying an electrophile. Functionalization of ω-carboxyl polymers to give the styrenic unsaturation is accomplished through coupling of the terminal polymeric carboxyl and 4-vinylaniline with dicyclohexylcarbodiimide, (DCCI) and 1-hydroxybenzotriazole (HOBT). The HOBT is used to activate the carbonyl through esterification followed by nucleophilic attack of the amine to give a terminal styrene unsaturation capable of anionic or free radical copolymerization [24] as shown in equation (2-3).

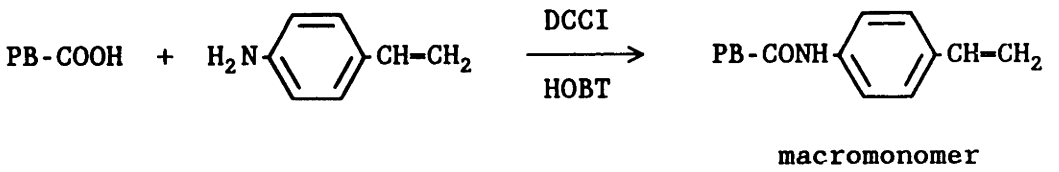

(2-3)

macromonomer

One of the earliest examples of this type of macromonomer was demonstrated by Greber and Reese [25] who equilibrated ω,ω-di-p-vinylphenylsiloxanes with dichlorosilanes or cyclic siloxanes to yield a styrenic unsaturation at both ends of the polysiloxane.

These processes yield good control of the molecular properties of the individual blocks because the macromonomer is usually characterized and quite often separated and purified prior to copolymerization. The synthesis of the siloxane-nylon-6 diblock copolymers in this thesis extensively utilized the macromonomer technique by reacting the anionically polymerized siloxane with a dimethylchlorosilyl function giving a ω-N-acyllactam siloxane to initiate copolymerization of caprolactam. The siloxane was purified and characterized by size exclusion chromatography, proton magnetic resonance and ultraviolet spectroscopy before copolymerization. This gave good control over siloxane and nylon-6 block lengths, branching and polydispersity provided no side reactions occur which will be discussed further in Chapters V and VI.

II. B. THERMODYNAMICS AND KINETICS OF COPOLYMER SYSTEMS

The relation between thermodynamic driving forces towards attainment of equilibrium and the hindrance of this process due to kinetic limitations is of paramount importance in the study of polymers. The long chain lengths and low mobilities of macromolecules in glassy and crystalline regions restrict chain conformations yielding nonequilibrium structures for many polymers like polystyrene as well as polyethylene. This is one type of competition between kinetics and thermodynamics that occurs in polymers when quenched from the melt or analyzed for the glass transition temperature for example, but will not be the subject of this section.

Rather, in multicomponent systems where one of the components is crystallizable and one is not (such as an amorphous-crystalline diblock copolymer or a simple, physical blend), there is a slightly different

competition of controlling forces. Here, the two components try to obey the free energy forces of phase equilibria but sometimes are forced into nonequilibrium structures due to crystallization effects. As will be discussed, there are many factors affecting the balance between phase equilibria and crystallization including casting solvent, degree of incompatibility, block lengths, crystallization rates etc. which all contribute to deciding which phenomenon exerts the greatest control over the final morphology.

To begin, simple polymer-polymer phase equilibria is discussed followed by consideration of the effects of adding copolymers, particularly block copolymers to the system. Phase equilibria of these copolymers and blends in the context of micellar structures is covered followed by extension to copolymer-solvent equilibria. Next a limited discussion of homopolymer crystallization is presented so that the diblock phase equilibria can be compared to copolymer crystallization in a variety of solvents exhibiting different compatibilities for the crystalline and amorphous blocks. This will culminate in a discussion of the controlling phenomenon (phase separation versus cyrstallization) as interpreted through temperature-composition diagrams.

1. Phase Equilibria of Copolymers and Blends

a. Physical Blends

Recent advances have been made in the area of simple physical blending of two or more polymers (see ref 26 for a comprehensive review) with the goal of achieving a unique combination of properties, lowering product cost and/or studying the theory of phase separation. Since the entropy of mixing two distinct polymers is low, miscibility is largely

governed by the enthalpic interactions between the different polymeric segments. For UCST (upper critical solution temperature) systems these energetic interactions can be approximated with good accuracy in nonpolar cases (e.g. the polydienes studied by Cohen and Wilfong [27]) by the Hildebrand [28] solubility parameters of the two polymers expressed as the Flory interaction paramter χ_{AB},

$$\chi_{AB} = (V_r/RT)(\delta_A-\delta_B)^2 \tag{2-4}$$

This term, χ_{AB}, is derived from the mean field Flory-Huggins [29,30] lattice approach to polymer solutions as applied to polymer mixtures by Scott [31] and Tompa [32] and when multiplied by k_BT represents the enthalpic interaction of the two different polymer segments. Strictly speaking, this parameter is only enthalpic in nature for regular solutions, i.e. where only combinatorial entropy terms are present whereas for real mixtures it contains nonideal contributions to the entropy of mixing as well.

Expressing this χ_{AB} in terms of a critical molecular weight for phase separation (assume $M_A=M_B=M$ which implies $M=2\rho/M_{cr}$) gives

$$M_{cr} \doteq 2\ \rho\ RT/(\delta_A-\delta_B)^2 \tag{2-5}$$

As an example, miscibility is attained for molecular weights of (O)~10^5 g/mole for $(\delta_A-\delta_B)$=0.1 $(cal/cm^3)^{1/2}$ at 25°C versus M = (O)~10^3 g/mole for a solubility parameter difference of 1.0 $(cal/cm^3)^{1/2}$ also at 25°C. This indicates that the monomeric segments must have very similar cohesive energy densities especially at higher, practical molecular weights to be

compatible. It also demonstrates that miscibility is the exception and not the rule in polymeric blends. Some commercial examples of miscible blends are polystyrene and poly(phenylene oxide) (commonly known as Noryl^{R}, a product of General Electric) or poly(vinylidene fluoride) (PVF_2) and poly(methyl methacrylate) (PMMA), a semi-crystalline-amorphous "miscible" blend (accounting for the additional crystalline phase which is present if the PVF_2 concentration exceeds 50 % wt [33]; note however, thermodynamic equilibrium is still maintained between the amorphous phases).

However, not all polymer phase behavior can be described by the simplistic solubility parameter approach. Modifications for polar compounds have been introduced by Van Arkel [34], Hansen [35] and others which are summarized in Van Krevelen's book [36]. These modifications incorporate dispersive, polar and hydrogen bonding contributions to the cohesive energy density in geometric mean form. These improvements have been updated and tabulated by Hoy [37] whose values are used in some "order of magnitude" calculations in this thesis.

For some polymer-polymer systems (and polymer-solvent systems as well) the Flory-Huggins lattice approach is not satisfactory and theoreticians are forced to resort to the conformal solution theory to adequately describe phase behavior. This is prevalent with LCST (lower critical solution temperature) systems which generally exhibit an exothermic enthalpy of mixing. A blend of polystyrene-poly(vinylmethylether) is the classical example of a LCST system and its phase equilibria (binodal and spinodal curves) is best described by the equation of state

theory as originally put forth by Prigogine [38] and later adapted by Flory [39].

Due to this "likeness" restriction for miscibility or near-equality of solubility parameters between polymers, most blends are immiscible and display phase separation on the order of > 0.5 – 1 μm domain size. This is not always detrimental, as exemplified by a class of materials known as thermoplastic elastomers (TPE's) which can be prepared by physical blending of immiscible polymers such as AB (acrylonitrile-butadiene) and PVC (poly(vinyl chloride)) with a PVC plasticizer [40], EPDM with polypropylene for automotive applications [41-43] or poly(dimethyl siloxane) and polyethylene [44]. This last material is a lightly crosslinked siloxane network interpenetrated by the continuous polyolefin phase (IPN).

b. Copolymers as Compatibilizers

For most applications with immiscible polymers, a copolymer is added to aid in compatibilizing the two phases. This generally results in smaller domain sizes and an enhancement of material properties. Within the class of the aforementioned TPE's, SBR-BR blends (styrene-butadiene rubber blended with butadiene rubber) is one example extensively used in the rubber tire industry. These multiphase materials retain the T_g's of their respective phases (−57°C and −105°C, respectively) and blends of different amounts of BR for example can vary the tire wet cornering coefficient on smooth pebbles as determined by Veith [45].

Another common example of the use of a copolymer as a compatibilizer is in commercial high impact polystyrene or HIPS. Low impact strengths are seen in pure blends of polybutadiene (PB) and polystyrene

(PS) but the introduction of a graft copolymer as found in HIPS, dramatically increases the energy absorbed during deformation [46]. A thorough review of the benefits of copolymers as compatibilizers for rubber toughening applications can be found in Bucknall's book [47]. Countless other examples of the use of copolymers to compatibilize and stabilize blends abound in the literature and an exhaustive summary is beyond the scope of this chapter (see ref 26). Suffice it to say that the use of copolymers as interfacial agents to reduce the interfacial energy, improve the interfacial adhesion and permit a finer phase dispersion has been well established and documented. Further discussion of this topic as it pertains to compatibilization by block copolymers (specifically diblocks) is given in the next section.

c. Phase Equilibria of Block Copolymers and Blends

Polymer-polymer or polymer-copolymer blends mentioned in the previous sections often contain a large variance in domain size (0.5 μm to 100 μm) due to the variability of the physical blending process or the presence of random, graft or alternating type copolymers. Simpler copolymer structures such as di- and triblock copolymers with immiscible blocks usually give better defined morphology which is more amenable to ascertaining deformation and phase equilibria effects. Due to a minimum of junctions (one to just a few) in block copolymers, the size of the microdomains scales to the radius of gyration of the individual chains (for monodisperse polymers) leading to regular arrays of regions on the order of 10 to 10^4 Å in size. These dimensions of the microdomains have significant impact in the ultimate properties of the copolymer such as permeation of gases through block copolymers [48] as well as permitting

the interfacial region (which is on the order of 20-30 Å [49,50] to contribute significantly to the thermodynamic properties as stressed theoretically by Leary and Williams [51].

1. Diblock Copolymer Phase Behavior

The precise shape of equilibrium microdomains and the transition point between changes in shape for amorphous blocks can be predicted by thermodynamic theories and is a direct function of the length of the blocks [52,53,54]. Helfand [52] has even included a Fortran computer program to facilitate use of his theory which calculates the optimum domain size and shape and corresponding transitions based on statistical thermodynamics. For spherical inclusions, the equilibrium values of domain size as a function of chain length calculated by Helfand and Wasserman [39] were higher than those experimentally determined by Hashimoto, et.al. [49b] and Cohen, et.al. [81] via small angle neutron scattering due to nonequilibrium morphology from solvent cast samples.

Only one theory [55] at present exists in predicting the domain size of an AB diblock where the A block is crystalline and the B block is amorphous and it is restricted to lamellar morphology. The validity of the theory is limited by the lack of confirming experimental data on equilibrium crystalline-amorphous diblock morphology. However, it is not known universally how the lengths of the crystalline and amorphous blocks affect the morphology due to kinetic limitations but as will be seen in this thesis work, not all crystal-amorphous diblock morphology is lamellar despite experimental attempts to approach equilibrium. Hopefully, this work will contribute somewhat to a better understanding of

this newly emerging area of polymer thermodynamics for semicrystalline diblock copolymers.

Thermodynamic approaches to the problem of predicting phase equilibria, microdomain size and shape and interfacial properties in diblock copolymers can generally be divided into two categories; the first being a statistical thermodynamics approach as introduced by Meier [54] and expanded by Helfand et.al. [56,57] and later modified by Noolandi et.al. [58-60]. Helfand and his coworkers point out that their theory which embodies the conformational probability density distribution as the nucleus, contains the necessary terms to describe the free energy of the microdomain system without having to decide a priori which terms should be included. This theory correctly considers the entropy loss of the chain in the micro-separated domain, for example, when it is forced to turn back into the domain after contact with the energetically unfavorable interface. The previous theories of Meier [54] and Leary and Williams [51] and some of the current ones, such as those by Noolandi, "build up" the total free energy by adding appropriate terms based on learned intuition and/or experimental observations. This latter approach is, however, much less cumbersome mathematically and has given satisfactory results.

The second approach applies macroscopic thermodynamic principles based on the Flory-Huggins theory (despite the entropy calculated from a statistical configuration of segments) including additional terms to account for contributions to the free energy. This treatment has been applied by Krause [61] and Bianchi et.al. [62] but omits the loss of conformational entropy when the chain is forced to turn back into its

microdomain after "walking" to the interface. Despite some deficiencies inherent with the Flory-Huggins approach, these theories are simple to apply and Krause [61] has included a contribution that accounts for dissolution of copolymer molecules into the supposedly segregated A or B domains. In her formulation, she predicts a lower free energy for the "dissolved" case indicating that within her framework there should be dissolved copolymer in the microdomains (greater dissolution at higher temperature).

To get an idea of the thermodynamic forces at work during phase separation, the individual contributions to the total free energy will be discussed. First, phase separation occurs through a nucleation process where a second phase is generated within the metastable mother phase (i.e. at a point in composition and temperature located between the binodal and spinodal). This nucleation and the subsequent formation of a new phase requires an increase in free energy, i.e. work is expended to form the surface offset by the free energy gained by creating the interior bulk of the new phase. Locally, near the nucleus, the concentration is lower than in the bulk mother phase which "feeds" the nucleus [63] and allows for ripening. Now the separation develops, driven by the lower <u>total</u> free energy of the two phase structure. This lower ΔG_M is comprised of two opposing terms: the enthalpy of mixing which is negative (i.e. demixing reduces the free energy) and a decrease in entropy of mixing due to segregation (which increases ΔG_M). In polymers, the entropic contribution is minimal due to the large molecular weights and so the enthalpic contribution to the free energy often governs phase behavior.

The formation of a separate phase always involves work to form the new surface which is a positive contribution to the free energy. To minimize this work, the system will strive to minimize the created phase surface/volume ratio which implies the domain size will grow till opposed by other restraints. In contrast to mixtures of homopolymers, these restraints for copolymers are very strong because of two factors, joint localization and the requirement of constant, uniform density.

Because the enthalpy favors phase separation, the joint of the block copolymer is localized in the interfacial region at the expense of some entropy loss. If it were not located there, however, some A segments would be "dragged" into the B domain which would create a positive enthalpic contribution to ΔG_M and hence this conformation would be rejected. If the joint were fixed at a given plane, this would result in a minimization of enthalpy but at the expense of a large decrease in conformational entropy which is also undesirable. An estimate of the magnitude of ΔS_{conf} comes from Helfand [52] where the probability (or percentage) of placement of the joint within the interfacial region is simply $k_B \ln[a_I/(d/2)]$ where a_I = the interfacial thickness, d = the domain periodicity and k_B is the Boltzmann constant. Thus, a compromise is reached between these two factors and recent experiments have confirmed that the interfacial region has substantial width ((0)~20 Å). Obviously, for block segments with a large segmental free energy of interaction, $k_B T\chi_{AB}$ the interfacial region will be narrower and vice versa. To see this mathematically, if a chain of Z segments of A wander into the B domain, they experience a total energy of interaction of $k_B T\chi_{AB} Z$. If this were a random fluctuation, it would have

energy $O(k_BT)$ thus yielding $Z \sim 1/\chi_{AB}$. Assuming random walk statistics, the penetration depth scales as $b_K Z^{1/2}$ or the interfacial thickness, $a_I \sim b_K/\chi_{AB}^{1/2}$. Thus, greater immiscibility between blocks is due to an increase in χ_{AB} and thus, the interfacial thickness diminishes.

This simple covalent bond is the main reason why the critical molecular weight for phase separation is higher for a diblock than a physical blend at the same composition and temperature. Because of this junction, less energy is required to homogenize a diblock versus a blend and the order-disorder transition temperature (the point at which the diblock microdomains disappear) lies below the UCST of a blend at a given composition and molecular weight. The order-disorder transition, also called the microphase separation temperature (MST) will be discussed more fully below.

Leibler [64] has developed a theory based on statistical thermodynamics and the random phase approximation that predicts that the ratio M^c_{di}/M^c_{bl} (critical molecular weight of diblock to blend) equals 5.25. This is deduced via the critical condition for phase separation in blends which is $\chi_{AB}N = 2$ versus $\chi_{AB}N = 10.5$ for diblock copolymers assuming equivalent enthalpy of interactions for both systems. This ratio has also been calculated by Meier [54] using a statistical thermodynamic theory and found to lie between 2.5 – 5.0 despite the fact that he used incorrectly $\Delta G_M=0$ as the criteria for phase separation of the blend. Regardless of the numerical value of this ratio, it is clear that diblock copolymers have greater potential for one phase behavior due to the restriction of the covalent junction than corresponding blends. For asymmetrical diblock copolymers (i.e. disparity in block lengths) and

blends with $M_A \neq M_B$, the critical molecular weights for incipient phase separation increase implying that it is easier to homogenize both a diblock and a blend with one block shorter than the other.

The second factor which opposes total macroscopic phase separation in diblock copolymers is dictated by the physics of these macromolecules, i.e. the requirement that the density be maintained constant at the bulk value. This implies that there must be some preferred weighting of conformations that cause the block macromolecule to "reach" or "walk" away from the interface towards the center of the domain in an effort to maintain constant segment density. This necessarily results in a lowering of conformational entropy and favors smaller domains so that excluded volume effects which cause perturbations in ideal, Gaussian chain conformations are kept to a minimum. Thus, this covalent bonding places a severe restriction on the size of the microdomains.

In summary, the surface free energy drives the system toward larger domains which is countered by the constraint of uniform density and joint localization restricting the size of the domains. The dimension of the interface is an optimization of the entropy lost on locating the joint along a plane versus the enthalpy gained in letting the joints "wander" into the bulk phases. And the loss of conformational entropy sustained by phase separation (restriction of the chains to their respective domains) including that of turning the chain away from the interface is balanced by the decrease (i.e. negative gain) in enthalpy of segregating A and B chains from each other (demixing). These terms combine to yield the free energy for the phase separated material which can be minimized to predict equilibrium domain size and shape, inter-

facial thickness and separation parameters such as temperature and molecular weight.

2. Blend of Diblock and Homopolymers

When the diblock copolymer is mixed with its respective homopolymers, it can either dissolve into the respective regions of the homopolymers locating at the interface in which case it lowers the surface tension of the mixture or it can phase separate into its respective micellar domain. In either case, the total free energy of the system expressed as the sum of the enthalpic, entropic and interfacial free energies, is minimized. Note that $\Delta G_M < 0$ is a necessary but not sufficient condition for phase separation in a multicomponent system. With the former case (surfactant effect), location of the copolymer at the interface causes a decrease in conformational entropy but this is compensated by the negative gain in enthalpy from orienting the compatible segments in their respective domains (i.e. A blocks of the copolymer with homopolymer A and likewise for B segments). The interfacial thickness is determined at equilibrium through minimization of the total free energy of mixing including a term to account for the contribution of the interfacial tension. The reduction of interfacial tension becomes greater with increasing molecular weight of the blocks due to a lessening of the restrictions on the conformations of the segments in the molecule as a whole. This is why homopolymers with molecular weights less than the corresponding blocks are compatibilized by copolymers because the interfacial energy can be significantly lowered. However, this extension of block molecular weights with the concomitant reduction in interfacial free energy can not proceed unimpeded; theoretically an eventual upper

critical molecular weight is reached where the energetics of the system can be lowered further by micellization of the pure copolymer and the complete phase separation of the homopolymers into regions of A and B plus micelles of AB block copolymer [65]. This phenomenon will be treated in the next section.

Theoretical treatment of a blend of copolymer with its respective homopolymers has been extended by Noolandi et.al. [58-60,65] and Meier [66] over their diblock theories and by others [67,68] for spherical and lamellar domains. Noolandi [65] has made extensive phase diagram predictions of order-disorder transitions (mesophase to homogeneous phase) in polybutadiene-styrene diblock / homopolybutadiene systems as homo-PB is added using the temperature dependent χ_{AB} of Roe and Zin [69]. Leibler [68a] using the random phase approximation introduced by de Gennes [70] has analyzed the interfacial effects and compatibility of diblock copolymer-homopolymer blends when the $\chi_{AB}N$ is ~ 2, i.e. near the miscibility point. He found that only at high copolymer concentrations did the diblock chains orient themselves at the interface with a significant fraction dissolved within the A and B domains. His theory predicts a growing interfacial zone as the copolymer concentration increases near the critical point in contrast to some experimental results cited below.

The experimental observations of emulsification of homopolymer blends were systematically explored initially by Molau [71] using graft copolymers to emulsify oil-in-oil (polyacrylate and polystyrene) emulsions. Since this early postulate of interfacial activity of copolymers, a substantial amount of experimental work has been done too numerous for

a comprehensive listing. Instead, the key works will be discussed briefly with respect to emulsification of polyblends and determination of microdomain characteristics such as interfacial thickness, domain size and interparticle spacing via X-ray and neutron scattering.

Early demonstration and explanation of the emulsification of homopolymers by a block copolymer was given by Riess et.al. [72] for polystyrene-polyisoprene polymers. This was subsequently verified [73] by fluorescence microscopy which allowed UV determination of the location of the block junction since some styrene-9-phenyl-10-anthracene was incorporated into the chain at the crossover point to the isoprene block. This experiment determined that copolymer was located primarily at the interface as well as some located in the homopolymer phase that has a lower molecular weight than the corresponding block molecular weight.

Hashimoto, Kawaii and coworkers [74-76] have done extensive work in this area of copolymer emulsification with the same type of polystyrene-polyisoprene system as Riess, et.al. They found that if the homopolymer molecular weight was less than or equal to the corresponding block molecular weight, emulsification was achieved and the homopolymer(s) were able to dissolve into the respective domains. This coarsening effect was more pronounced for longer block lengths of the dispersed phase component due to a faster reduction in interfacial area (and hence its contribution to ΔG_M). The interfacial thicknesses for the copolymer blended with varying amounts of homopolymers and cast from several different solvents were determined using Porod's law [77] assuming a Gaussian smoothing function. The values ranged from 17Å to 20Å, being slightly larger for

the ternary blends. In addition, they also verified experimentally, the change in microdomain shape from lamellae to cylinders to spheres as the block length of the dispersed component was reduced.

Cohen et.al. [78,79] have used a similar methodology as that of Kawaii et.al. to study phase behavior with a poly-1,4-butadiene-b-1,4-isoprene diblock copolymer/PB,PI homopolymers system that possesses greater compatibility than previous investigators (e.g. PS-PI). They found that the copolymer was soluble for butadiene/isoprene ratios from 0.5 to 2.0 while corresponding blends were heterogeneous for all compositions confirming theoretical predictions that the critical molecular weight for diblock phase separation is greater than the corresponding blend molecular weight. Similar results were found by Cohen and Wilfong [27] for poly-1,2-butadiene-b-1,4-butadiene diblocks and blends where the ratio of critical molecular weight of block to blend was determined to be 5 – 6 in excellent agreement with Leibler. Cohen [80] extended the two-dimensional concept of M^c_{di}/M^c_{bl} versus composition of one of the blocks (as either in the diblock or in the blend) with a three-dimensional plot, the third axis being the fraction of diblock in the blend. He showed the same basic behavior was retained as a function of the copolymer composition.

Previous studies by Cohen et.al. [81] on more immiscible diblock systems of polystyrene-butadiene have confirmed domain size and interfacial thickness measurements of Hashimoto's PS-PI ternary system. Interfacial thicknesses were found to be ~ 20-23 Å, slightly higher than Hashimoto's. Cohen's results for mean sphere radius were found to be greater than Hashimoto's at equal $\bar{M}_n$ but both sets of data lie below the

size predicted by Helfand's theory [57]. This was attributed to nonequilibrium effects caused by solvent casting. Depending on the solvent, precipitation at the CMC (critical micelle concentration) produces a nonequilibrium morphology different from the bulk equilibrated structure since chains can not diffuse from the micelles to other domains to lower the system free energy because of the strong incompatible enthalpic interaction.

Most block copolymers by their very two-phase nature, offer unique opportunities to study the thermodynamics of phase equilibria. The study of the order-disorder transition (i.e. from a ordered mesophase such as paracrystalline spheres in a bcc packing to a disordered phase) of styrene-butadiene diblock copolymer blended with homopolystyrene has been extensively conducted by Roe et.al. [82-84] using high temperature SAXS and light scattering. These investigators found that at temperatures moderately above the T_g of polystyrene (~120-140C) the intensity of the interdomain scattering peak decreased substantially indicating that the electron density contrast between the phases was decreasing probably due to interpenetration of each domain by other block copolymer molecules. However, no gradual thickening of the interfacial region occurred during the order-disorder transition as measured by the intercept from regression of SAXS high Q data points, suggesting that the interface acted as a "membrane" passing diffusing copolymer molecules from one domain to the other until the long range order had been destroyed. This seems plausible at short disorder times, i.e. soon after the temperature is raised above T_r, the order-disorder transition temperature but at longer times, the interface must grow in width until a homogeneous density distribution

results as predicted by Leibler [68a]. Clearly, more experimentation is needed.

Hashimoto, et.al. [85,86] have studied the time-dependent order-disorder transition using a T-jump SAXS experiment and determined effective diffusivities (because A-B energetic interactions influence the diffusivity and necessitate use of D_{eff}) from plots of relative intensity versus time at various temperatures and concentrations. They found an Arrhenius temperature dependence on D_{eff} and an inverse relation to polymer concentration of PS-PB diblocks in C_{14} solvent ($D_{eff} \sim 10^{-14}$ cm^2/s). Somewhat surprisingly, $D_{eff} \sim c^{-1.75}$ (c = polymer weight fraction) which is in close agreement with the theoretical scaling prediction for semi-dilute solution (see ref 70).

In addition to the order-disorder transition, Roe and Zin [84] also have determined binodal phase diagrams via light scattering and found that the theory of Meier [66] predicted homopolymer solubility in the ordered block copolymer domains an order of magnitude too low due to neglecting the fact that homopolymer will be solubilised into the dispersed microdomain thereby increasing the conformational entropy of the copolymer chains (i.e. the A-B chains are less stretched). Thus, emulsification of homopolymer into the microdomains is thermodynamically favored (gain in entropy) as long as its molecular weight does not exceed the critical point which would cause a loss of conformational freedom as compared to its ΔS_{conf} in the phase separated state.

Micellar Organization in Diblock Copolymers

The emulsification of homopolymers by diblock copolymers can be viewed from a slightly different perspective because the amphipathic

behavior of diblock copolymers at interfaces parallels other surfactant applications in detergency and colloidal science. Due to the covalent bond linking the two immiscible blocks, diblock copolymers naturally undergo microphase separation into aggregates of molecular dimensions at concentrations greater than or equal to the critical micelle concentration (CMC). This CMC or the transition concentration where copolymer molecules (whether in solution or melt and with or without homopolymers) organize from a homogeneous phase to an ordered micellar phase (mesophase) is reflected in the change of a variety of physical properties such as conductivity, refractive index, density or X-ray scattering intensity for example. It also plays an important role in determining the phase behavior in these systems.

Phase equilibria of block copolymer/homopolymer solutions (A, B, A-B, S) must consider <u>two</u> possible critical points one due to micellization, the other corresponding to liquid-liquid phase equilibria and which point is reached first upon removal of solvent. This is important in the casting of films because the "evaporation path" on the phase diagram can markedly influence the morphology and hence material properties. In order to understand the various interrelationships in these complex ternary or quaternary systems, phase equilibria of a comparatively simpler, binary amorphous diblock copolymer-solvent system will be discussed first. This will be undertaken in the context of the phase diagrams presented by Hong and Noolandi [60] rearranged into a slightly different format (T-ϕ_C vs their $\chi_{AB}Z_C$-ϕ_C diagrams) for easier discussion and understanding.

3. Diblock Copolymer-Solvent Phase Equilibria

Since diblock copolymers have the two immiscible blocks covalently bonded, phase separation can be manifested by liquid-liquid phase equilibria where one liquid phase may be a mesophase [60] or as micellization in the case of more asymmetric blocks with different solvent compatibilities. Consider first the case of a symmetrical diblock in nonselective solvents which range from "very poor" to "very good" as shown in Figure 2-1. Here, the two blocks are of equal length, $Z_{CA} = Z_{CB}$, where A, B represent the two immiscible blocks and C stands for copolymer; note also that ϕ_C = volume fraction of copolymer and that χ_{AS} and χ_{BS} represent the solvent-block interaction parameters with χ_{AB} = the polymer-polymer interaction parameter. The phase diagram consists of the various one-phase (H, M) and two-phase (HH, HM) regions as indicated. These classifications are consistent with the interpretation of the phase rule which considers a diblock copolymer to be a single phase and a single component due to its nonequilibrium nature and mechanical inseparability of the microdomains. This is explained by Krause [87] for diblock copolymer / solvent systems in terms of the phase rule. Similar reasoning will be followed with semicrystalline-amorphous systems described in the next section where a crystalline phase with excluded solvent will be considered as one phase even though it contains large portions of amorphous material.

Returning to Figure 2-1, as the "goodness" of the solvent increases or χ_{AS} decreases, the temperature of demixing and the critical block copolymer concentration for mesophase formation both decrease. The latter quantity, ϕ_C^*, represents the lowest concentration of block

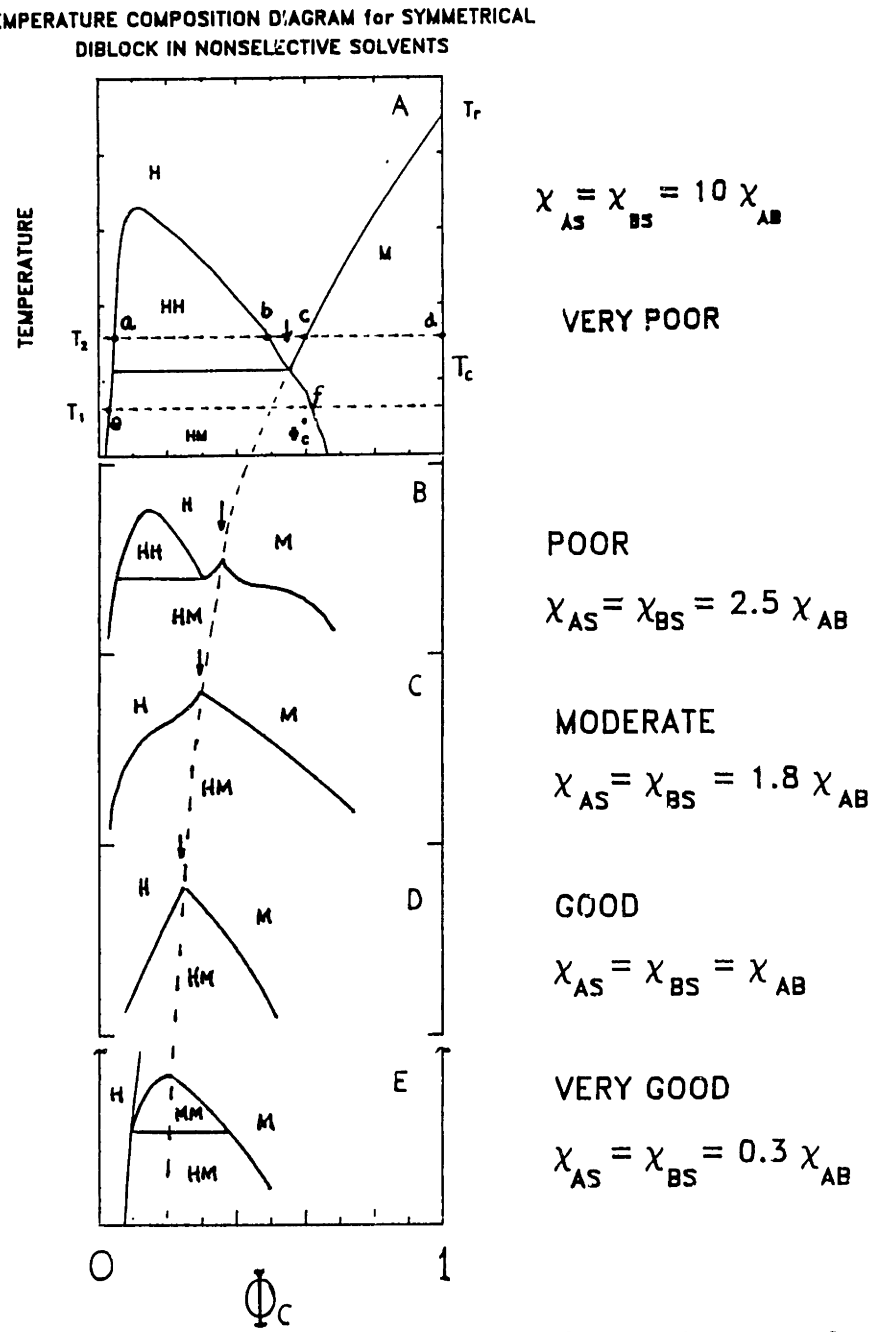

Figure 2-1. Schematic temperature-composition phase diagrams for a symmetrical diblock copolymer in progressively better nonselective solvents; H-homogeneous phase, M-mesophase, HH-liquid-liquid equilibria, HM-liquid-mesophase equilibria; after Noolandi, et.al. [60].

copolymer to yield mesophase formation and is determined by the intersection of the mesophase and binary phase spinodals (at ↓) as depicted by the solid lines. The mesophase spinodal represents the equilibrium "melting curve" of the ordered domains or their transition from an ordered to a disordered phase. For pure copolymer, this occurs at a temperature (in actuality it probably occurs over a small range in temperature due to polydispersity and kinetic effects) known as the order-disorder transition temperature denoted T_r. This is the subject of much recent investigation both theoretically [57,64] and experimentally [85-89].

The fact that two critical points exist in cases of poorer solvents suggests competition between types of phase separation as solvent is removed at constant temperature. Consider pure solvent at T_2 in the "very poor" solvent case and slowly add copolymer. Only an infinitesimal amount of copolymer (exaggerated for clarity) can be solubilised before two liquid phases are formed at 'a', one deplete in copolymer and one enriched in copolymer ($\phi_c \approx 0.5$), point 'b'. At this temperature, liquid-liquid phase separation predominates over liquid-mesophase separation and the enriched homogeneous phase grows in size as more copolymer is added. Then, when the copolymer volume fraction exceeds ~ 0.5, a homogeneous phase is formed. Further addition of copolymer eventually results in incipient mesophase formation at 'c' and additional removal of solvent culminates in consolidation of the mesophasic solid at 'd'. Alternately, if this process is conducted at T_1, the formation of the mesophase will occur earlier near point 'e', (depending on what composition between the HM binodal and spinodal phase separation actually

occurs) resulting in a homogeneous phase rich in solvent and a swollen mesophase at point 'f'. Here, the microdomains are formed much earlier in the casting process and further removal of solvent consolidates the mesophase. From the phase diagram it can not be ascertained if this morphology will be significantly different than that formed at T_2. Note that both paths produce a mesophase at $\phi_c \approx 0.60\text{-}0.65$. Theoretically, the final mesophase morphology will only depend on the temperature of the cast and its effect on the minimization of the free energy (through γ or χ_{AB} for example) to give the equilibrium shape as computed by Helfand [52] or Meier [66] for example. However, kinetic effects may induce variations from equilibrium and some difference in mesophase appearance (i.e. cylinders versus spheres, etc.) may be seen as a result. Thus, casting above the critical point, T_c will cause liquid-liquid phase separation to occur prior to microdomain formation whereas temperatures below T_c yield mesophase structures without undergoing any liquid-liquid transition(s). However, it is unknown how and to what degree kinetic effects may alter the morphology from the two different "paths".

For highly incompatible solvents, the liquid-liquid (HH) phase region lies at very high temperature and reduces in size as the solvent compatibility improves. Moderate to good solvents do not even show HH behavior because the copolymer-solvent system can further reduce its free energy at these lower temperatures by undergoing mesophase formation which liberates large enthalpy in the coalescence of like blocks into their respective microdomains. Only high temperatures favor two liquid phase behavior preventing the formation of the mesophase except at higher copolymer concentrations. This sequence of phase diagrams also points

out that very good solvents (i.e. those that exhibit greater affinity for both blocks than the blocks for themselves or χ_{A-S}, $\chi_{B-S} < \chi_{A-B}$) can cause formation of two different mesophases represented by region MM in the bottom case, panel E of Figure 2-1.

In reality, there are not many nonselective solvents (toluene with PS-PB is close to nonselectivity) for both blocks so that many block copolymers are preferentially solvated. This gives rise to different phase behavior because the phenomenon of micellization occurs in preference to liquid-liquid phase separation. Since micellization is not a strict first order thermodynamic transition, the T-ϕ_C behavior at low ϕ_C must be interpreted as a locus of CMC's. All the theories in the literature to date, which describe micellization of copolymers (these will be discussed next) in terms of microscopic thermodynamics, do not directly interpret the CMC as a function of temperature; only for various compatibilities, $\chi_{BS}N_B$ does temperature (indirectly) affect the predicted value of the CMC. Thus, combining the CMC transition with other thermodynamic transitions in a T-ϕ_C diagram presents real challenges to theoreticians because at least two different theories (maybe more for excluded volume effects at dilute polymer concentrations, for example) must be invoked to explain the phase behavior across the entire region. No published work yet has begun to unravel the complications of predicting the superposition of these different transitions within a unified phase diagram. Since the case of a nonselective solvent prevails in many real systems, it is worthwhile to discuss it briefly, in semi-quantitative terms using general trends developed above. But before that is done, some background on the CMC transition is necessary.

Micelle Theory

Discussion of micelle theory pertains to the transition of a diblock copolymer from a homogeneous solution into a micellar dispersion when it is mixed with either its homopolymers or a selective solvent. In this transition there is no additional equilibrium liquid phase formed due to the selectivity of the solvent. To date, most of the theories and experimental data have pertained to copolymer/homopolymer systems and only recently has a theory emerged dealing with micellization of a diblock copolymer in solution. These will be discussed below. Regardless, the developments and ramifications of micelle theory apply to both solvent and homopolymer diluents for a diblock copolymer.

The first comprehensive treatment of micelle formation in diblock copolymer-homopolymer mixtures was advanced by Leibler, Orland and Wheeler [90] (hereafter referred to as the LOW theory). This was a microscopic thermodynamic mean field model that assumed spherical micelles with complete immiscibility of block segments, a symmetric copolymer (N_A=N_B) and segmental interaction described by χ_{AB}. The LOW theory correctly predicts that as the degree of incompatibility of A-B segments or degree of copolymer polymerization increases, the CMC decreases and that the micelles are bigger (less free copolymer chains) and more stretched. Thus, the core blocks are predicted to be actually under tension for large incompatibility between segments. The theory also correctly predicts that at the CMC transition, rapid continuous variations in properties (such as the entropy) occur rather than a discontinuous change, the latter being indicative of a first order

transition. Thus, micellization theoretically is not a rigorous first order transition and experimental data confirm this.

The LOW theory has been extended by Roe [91] (now referred to as the LOW-Roe theory) by recasting the equations so as to allow for some finite solubility of the homopolymer A into the previously exclusive B core which will occur at higher temperatures for a UCST system; (recall complete immiscibility or low temperatures were presumed in the LOW model). In addition, LOW-Roe allows for unsymmetrical block lengths in the copolymer and uses the root mean square (rms) value for chain statistics versus the concept of segment length times the degree of polymerization for less ambiguity in definition. However, despite these modifications, the LOW-Roe theory is still unable to give a completely accurate comparison with experimental data [92] such as CMC or radius of gyration as a function of temperature. The swelling of the styrene-block core due to the solubilization of butadiene is the most severely underestimated of the two parameters and calls for further theoretical modifications for higher temperature applications. This may include adding terms to the free energy expression to account for entropy loss due to joint localization at the interface or as discussed below, a more accurate functional representation of χ_{AB} with respect to temperature, molecular weight and composition.

Recently, Kinning et.al. [93] compared experimental results of a styrene-butadiene diblock/homo-PS system with the LOW-Roe theory. They found that these systems micellize at concentrations 1 to 2 orders of magnitude above the theoretical CMC suggesting that reductions in the segmental interaction density, A_{AB} ($=\chi_{AB}RT/V_r$) can account for this

discrepancy. However, for some of the blends, the necessary changes in Λ_{AB} to give agreement were clearly outside the experimental margin of error. In addition, their experiments demonstrated that the amount of free copolymer in the matrix increased with overall copolymer composition and was greater than that predicted by the theory. The amount of free copolymer in the matrix at a given temperature corresponded theoretically to the amount for a much higher temperature (115°C actual vs 300°C theoretically for SB 40kg/mole / 10kg/mole diblock in 17 kg/mole PS matrix). This suggests that additional work is needed to describe block copolymer micellization in homopolymer blends.

The trend of increasing copolymer concentration in the matrix as the overall copolymer composition is increased also is correctly predicted by the micelle theory of Noolandi et.al. [59,65,95]. This theory justifiably accounts for the loss of entropy due to joint localization and for solubilization of the matrix homopolymer A into the core consisting of predominantly B blocks. The theory correctly incorporates the asymmetric case of block lengths and gives excellent agreement of micelle size and scaling exponents with experiment [95]. However, the theory does not make any comparison with experiments on the amount of solubilized matrix polymer A in the core of block B only noting that it is nearly negligible. Thus, this theory like the others, failed to account for this fact which must be accommodated as by Roe, in future treatments.

Noolandi [95] also found that the corona was swelled by dissolved homopolymer if the molecular weight of the homopolymer was less than the corona block molecular weight. This is partially substantiated by Cheng et.al. [96] who found (via SANS) that homopolymer of comparable or

greater molecular weight than the corresponding block of the copolymer was excluded to the interstitial regions of the micellar domains thus leaving the corona essentially unperturbed.

Extending the LOW theory to diblock copolymer/solvent systems (A-B, S) and small head groups (low N_B) has been done by Munch and Gast [97]. They considered spherical micelles (due to the small head group) that excluded solvent from the core but also included calculations that predicted when the transition from spherical to lamellar micelles would occur as a function of solvent size, B (or core) block length and compatibility between the B block and solvent, S. The solvent is athermal for the A block (corona) of the copolymer. These calculations show that even for large solvent sizes and incompatibility which both favor lamellar micelles, if the B block length is small enough, then spherical micelles will result. This also can be interpreted as the result of the balance between stretching entropic potential versus interfacial free energy in the core to determine its size; the interfacial term is minimized for a spherical shape but the least perturbation of the conformations of the core chains is realized by lamellar micelles. Thus, the balance depends on which term dominates and in the case of small lyophobic blocks, the larger (negative) gain in the interfacial free energy is not offset by the smaller decrease in conformational entropy due to distortion of the chains in spheres rather than lamellae.

Munch and Gast also determined that the corona thickness is increased by the incompatibility between the solvent and the core block B, (the A block is in the corona, B block in the core). With their theory,

the corona dimension dependence is attributed to the fact that the CMC decreases as the incompatibility increases causing a dilution of free copolymer chains due to aggregation (or micellization). This must cause a relaxation or expansion in the corona to match the decrease in osmotic pressure (π) in the free solution at equilibrium; (recall $\pi/c=RT/M$ for ideal sclutions where M is the solute molecular weight). Thus, for high $\chi_{BS}N_B$ the polymer concentration in solution is less and both the corona and core blocks extend beyond their random coil conformations in to match the lower π.

Hypothetical Phase Diagrams for Micellized Copolymers

Returning to the phase diagram of a diblock copolymer in a selective solvent, certain semi-quantitative predictions can be made concerning the CMC and related transitions based on the above theories. At low copolymer concentrations (ϕ_C) in a selective solvent, the "phase diagram" consists of the loci of the critical micelle concentrations as a function of temperature as shown by the solid curves in Figure 2-2. For illustration, consider a symmetric copolymer ($N_A = N_B$) in a solvent good for the A block and poor for the B block, or $\chi_{AB} \approx \chi_{BS} >> \chi_{AS} \approx 0$. Because a strong preference exists for the A block, no liquid-liquid equilibria occurs with these systems and a micellar structure with core B blocks surrounded by a corona of A blocks and solvent results (point 'a') as the copolymer concentration is increased from pure solvent at T_1. At higher temperatures, T_2, the CMC or micelle formation occurs at higher ϕ_C, i.e. $\phi_C^a(T_1) < \phi_C^b(T_2)$. Now consider an asymmetric copolymer where $N_A > N_B$ with N ($= N_A + N_B$) remaining the same. The effect of the molecular weight of the core block at constant temperature T_1 is shown at point 'c'

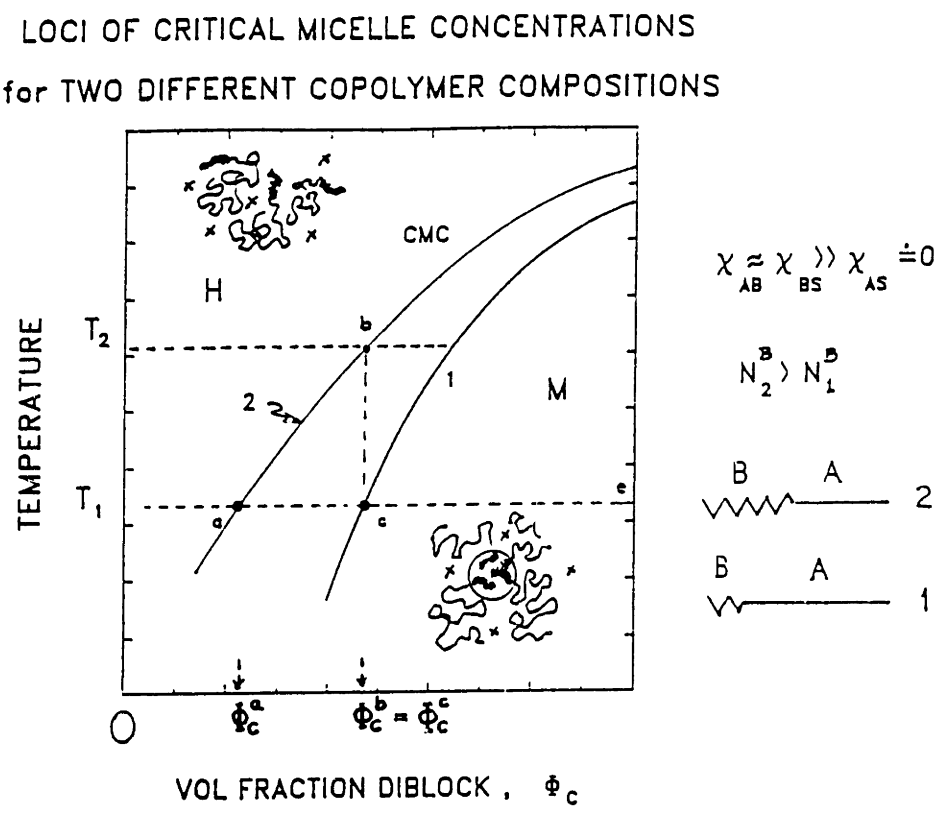

Figure 2-2. Loci of critical micelle concentrations as a function of temperature for two different copolymer compositions; $N_{B,2} > N_{B,1}$; H = homogeneous phase, M = micellar phase. Schematic depicts conceptualized morphology.

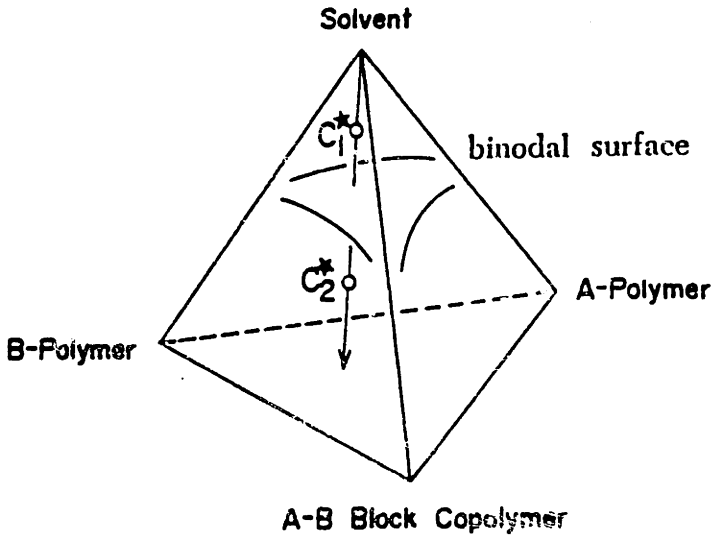

Figure 2-3. Four component composition diagram at constant temperature. AB = diblock, A, B = homopolymers and S = solvent; C_1^* = critical micelle concentration; C_2^* = spinodal limit of one phase behavior; after Incue [74].

where curve #1 represents a shorter core block length and shows that a higher CMC will result, $\phi_C^a(T_1) < \phi_C^c(T_1)$. At points 'a', 'b' or 'c', micelles are formed consisting of the copolymer swollen with solvent in a solution of free copolymer and solvent. Solvent penetration into the core is dependent on χ_{BS}. Thus, the description 'M' is used to denote this micellar structure (see sketch on Figure 2-2) which according to the guidelines established earlier for phase requirements, constitutes a one-phase system. At a composition of pure copolymer, the criteria for the order-disorder transition temperature is given as $\chi_{AB}N = 10.5$ for the symmetric copolymer and $\chi_{AB}N > 10.5$ for the asymmetric one. This leads directly to a higher order-disorder transition temperature, T_r for the symmetric copolymer than for the shorter B block copolymer. As more copolymer is added to the system beyond the CMC, i.e. moving from points 'a' or 'c' towards the right hand ordinate in Figure 2-2, the background concentration of free copolymer in solution increases slightly which is a clear contradiction to the laws of thermodynamics for a first-order phase transition. This is more notable for strongly incompatible systems and suggests that the copolymer composition within the micelles repartitions with the background solution to maintain equilibrium. Other variables such as the number of micelles, mean number of chains per micelle and size of the micelles also may change as the overall copolymer concentration increases. The right hand region, beyond the CMC in copolymer concentration was left intentionally blank due to an incomplete understanding of the phase equilibria which occurs after micellization. There are no theories for guidance in this region and it is unknown at this

time whether transitions from the micellar solution to another type of mesophase exist.

Diblock Copolymer / Homopolymer(s) / Solvent Systems

If homopolymer(s) are added to the diblock-solvent system creating a ternary or quaternary mixture (i.e. A-B, A, (B), S), the resulting morphology will depend on the order of occurrence of the two processes just discussed, micellization versus macrophase separation. As shown by Inoue et.al. [74] in Figure 2-3, a schematic pyramidal phase diagram can be used to understand the interaction of the four components at constant temperature where solvent removal is indicated by traversing from the top apex downwards. If the CMC is reached prior to the binodal surface then an oil-in-oil emulsion is created, the homopolymers being emulsified by the copolymer at the interface (if their molecular weights are approximately less than or equal to the copolymer block weights). This is represented by C_1^*. Note that Inoue et.al. [74] should have stated that if micellization occurs prior to the spinodal surface, then microphase separation will occur because the spinodal represents the limit of stability. On the other hand, if the limit of stability is reached before the CMC, i.e. the CMC is inside the spinodal surface (or C_2^*), then the homopolymer and copolymer solutions macrophase separate and the copolymer forms its own inherent domain structure (maybe micellized) without inclusion of the homopolymers.

Inoue et.al. [74] have developed a preliminary theory to describe this phenomenon based on the Flory-Huggins theory but it is inadequate for two reasons: first, the F-H theory due to its mean-field approximations works much better on polymer-polymer than polymer-solvent mixtures

and second, their theory does not incorporate the free energy of the micelle into its model which only calculates the critical point of phase separation using the spinodal criteria ($\partial\Delta\mu/\partial\phi$, $\partial^2\Delta\mu/\partial\phi^2 = 0$). The CMC for their treatment must be determined experimentally and compared to the theoretical critical polymer concentration for phase separation.

If the solvent is highly selective, i.e. very lyophilic towards one of the blocks, the CMC will be extremely low as discussed above and the copolymer will preferentially form micelles. This is often the case because many copolymer blocks are highly incompatible and do not have a nonselective solvent. Whether the unfavored homopolymer (lyophobic towards the selective solvent) will become emulsified within the corresponding domains in solution versus complete phase separation can not be answered today from a theoretical point of view; this quaternary system is very complex mathematically. Experimental observations during this thesis indicate that emulsification in a selective solvent does occur at low homopolymer concentrations (~10 %w) forming a stable oil-in-oil emulsion and will be discussed further in Chapter VIII. Also missing in the theoretical context is a development for spherical micelles that incorporates a crystallizable block and its subsequent chain folding during precipitation from solution for the simple case of a copolymer/solvent. As will be seen in Chapter VIII, this type of morphology exists in siloxane-nylon-6 diblock copolymers and in other diblock systems with disparate block lengths and will be discussed shortly.

Semicrystalline - Amorphous Diblock Copolymers

Significantly greater attention in the literature has been given to the amorphous diblock copolymers, both experimentally and theoretically because these materials are much more readily available (comparatively easier synthesis requirements) and usually exhibit simpler morphologies as compared to crystalline-amorphous materials (such as Nyrim^R of the Dutch State Mines Co., for example). Semicrystalline - amorphous diblock copolymers have the added complication (over wholly amorphous ones) of the crystalline "phase", or more accurately "domain" as it relates to the morphology. The fact that homopolymer crystallization is really a metastable, kinetically driven phenomenon, makes the task of predicting domain size, shape, number of folds per chain, etc. very difficult from a thermodynamic or equilibrium point of view. This is because it is not known with certainty what effect the amorphous block will have on the crystallization process. DiMarzio et.al. [98] have proposed that chain folding occurs as a consequence of <u>equilibrium</u> in an amorphous-crystalline diblock copolymer that exhibits a lamellar morphology. Here the opposing driving forces are the maximization of the entropy of mixing of the amorphous segments (to approach a random coil conformation) versus extended crystallization of the chains to minimize the fold energy ($E_{fold}=2A_o\sigma_e$) by reducing the number of folds per chain which in the limit, reaches an extended chain state. Their theory leads to expressions where the amorphous thickness, ℓ_a, scales with $N_a^{2/3}$ where N_a = the amorphous block degree of polymerization. This scale makes sense because it is between the random coil, which scales as $N^{1/2}$ and the fully extended chain which scales as N. The crystalline length, ℓ_c scales as

N_c which seems correct because the length of the chain does not affect the folding free energy balance.

Whitmore and Noolandi [55] used this chain folding model to develop a statistical thermodynamic theory to predict lamellar thickness, number of folds per chain and the distance between cilia or junction points of the crystalline and amorphous blocks along the lamella-amorphous phase boundary. They only considered lamellar morphology and did not attempt to predict where transitions to other morphologies would occur probably due to a lack of experimental evidence for any other type of crystalline habit in a multiphase system and the degree of complexity in determining the associated chain folded structure. Their theory determined that the lamella thickness was dominated by the free energy balance between the fold energy and the conformational entropy associated with stretching the amorphous blocks out of their random-coil conformations.

Application of the theory is limited, however, for two reasons; first, there is a lack of equilibrium experimental data on lamellar structure crystalline-amorphous diblocks and secondly, the theory is more applicable to near-equivalent block lengths ($N_A \approx N_B$) so that kinetic effects during crystallization are minimized. Despite these two shortcomings, there is encouraging agreement between theory and experiment. For PEO-PS block copolymers with 61 w% PEO ($N_{PEO} \approx 3.7N_{PS}$), the experimentally determined number of folds (from TEM and SAXS) [99,6-8] was n_f = 8 at T_c = 10C and n_f = 5 at T_c = 43C versus theoretical prediction of n_f = 2 to 3. The moderate disagreement goes to show that disparate block lengths can cause discrepancies between theory and experiment (maybe due to kinetic effects) and that the problem of domain prediction in semi-

crystalline-amorphous block copolymers is more difficult than expected due to the uncertainty in the fold energy and the unaccountability of the uncrystallized portions of the chains. Noolandi's theory corrects for the uncrystallized chains only by a degree of crystallinity factor to the heat of crystallization not taking into account loose cilia, crystal lattice defects or tie molecules. The theory correctly confirmed experimental observations that the number of folds per chain correlated solely as a function of amorphous block length for copolymers with less than 50 w% PEO, and as a function of both amorphous and crystalline block lengths for compositions greater than 50 w%.

Even more interesting is that experimentally the morphology is always found to be lamellar regardless of the ratio of block lengths, even for ~28 w% styrene in the poly(ethylene oxide-b-stryene) or PEO-PS copolymer. This was also found for poly(caprolactone-b-styrene) copolymers as well. Thus, in contrast to the theories for domain size and shape in amorphous-amorphous diblock copolymers, the transition between alternate morphologies (e.g. lamellar to cylindrical) may not be universal for all crystalline-amorphous diblocks and may depend on a number of parameters (e.g. the casting solvent and temperature which define the evaporation "path", diblock composition, etc.) as well as the kinetic control that is exerted during this process. This topic is discussed further in section B.3 of this chapter after a brief introduction to homopolymer crystallization.

2. Homopolymer Crystallization Kinetics

Crystallization kinetics play a critical role in forming polymer morphology and affecting molecular and material properties. This nonequilibrium process makes polymers unique as compared to monomeric molecules such as metals which usually achieve equilibrium during crystallization. Polymer "crystals" are not fully crystalline because the organization of a long polymer molecule with a contour length $O(10^3)$ Å into a much thinner ribbon or lamella O(50-100) Å in thickness is governed by metastable chain folding yielding uncrystallized loops, free ends or cilia and point defects. Growth (in most cases) is governed by nucleation and subsequent chain folding onto the lowest free energy surface, this thin dimension being determined by the inverse undercooling, i.e. $1/(T_m^o - T_c)$ and maintained due to minimization of the interfacial area and prohibitive growth from the high free energy surface. Refer to Figure 2-4 for a detailed description of lamellar and spherulitic structures that will be elaborated on below. The noncrystalline fraction is the result of imperfect crystallites within the lamellae, interlamellar tie chains (i.e. molecules that fold into two different, neighboring lamellae) and cilia or chain ends.

These lamellae are arranged into a greater superstructure in most crystalline polymers. Although there are many crystalline structures such as dendrites, hedrites, sheaf-like fibrils, etc. as examined in detail by Wunderlich [100], most crystalline polymers crystallize from the melt and also frequently (but not always) from solution in spherulites (or sometimes as axialites although the distinction is minor and discussed thoroughly in Chapter VIII). A schematic of the organizational

A)

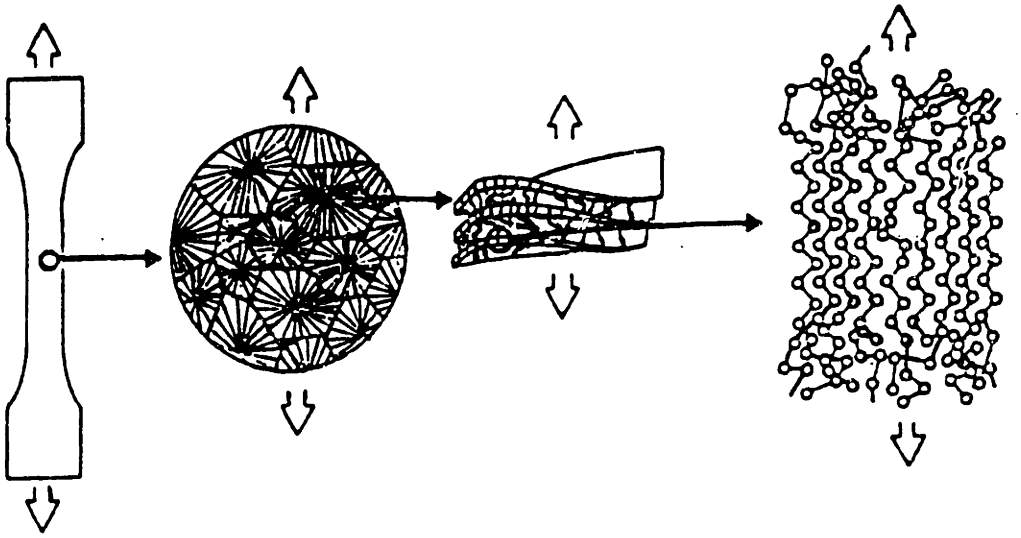

tensile bar | spherulite | lamellae | chain-folded crystal

B)

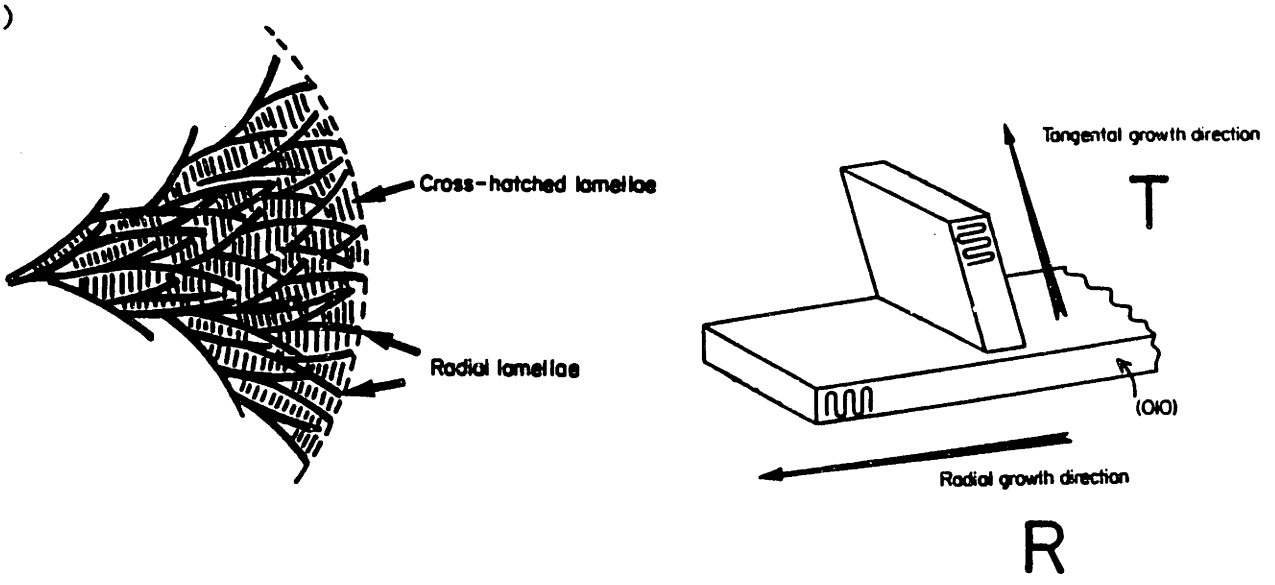

Figure 2-4. a) Hierarchical breakdown of spherulitic morphology ranging from super-spherulitic to molecular organization; after Schultz [128]; b) model of tangential growth found in some spherulites; after Norton and Keller [105].

structure of polymer spherulites is seen in Figure 2-4a which shows the various hierarchical levels from bulk spherulite (ca. 20 μm diameter) down to the bundles of lamellae (ca. 50 - 100 Å thick each) that make up the radiating fibrils. Further detail schematically shows the interrelation of chain folding and amorphous tie/cilia molecules trapped between the lamellae. The chain folded surface has a higher surface free energy, σ_e than the lateral surfaces ($\sigma_e \simeq 4\text{-}6\ \sigma_s$, where σ_s is the lateral or side surface tension) which prohibits growth normal to this surface. Not only is the nucleation barrier height greater (see Appendix 1 for further explanation) but the growth rate would be much slower from the high free energy surface due to a lower probability of critical nucleus formation (the $\exp[-\Delta F^*/kT]$ term). Thus, growth is limited to the radial and sometimes tangential directions normal to the lateral surfaces which possess lower free energies. Tangential growth is usually found with secondary nucleation and yields cross-hatched spherulitic structure which is characterized by banded spherulites in the polarizing optical light microscope (see e.g. ref 101). This tangential nucleation and growth is depicted schematically in Figure 2-4b.

The spherulitic morphology is evident with nylon-6 polymers as shown in Figure 2-5. This is a transmission electron micrograph of a blend of nylon-6 homopolymer ($\bar{M}_n$ = 21.7 kg/mole) and poly(dimethylsiloxane-b-methylvinylsiloxane-b-ϵ-caprolactam) triblock copolymer ($\bar{M}_n$ = 103 kg/mole) synthesized in the course of this thesis research and stained

---

Figure 2-5. (see next page) Spherulite of blend (43/57 %w) of nylon-6 homopolymer ($\bar{M}_n$ = 21.7 kg/mole) and poly(dimethylsiloxane-b-methylvinylsiloxane-b-ϵ-caprolactam) triblock copolymer ($\bar{M}_n$ = 103 kg/mole, 3 %w siloxane); stained with 1% OsO_4 and 2% PTA.

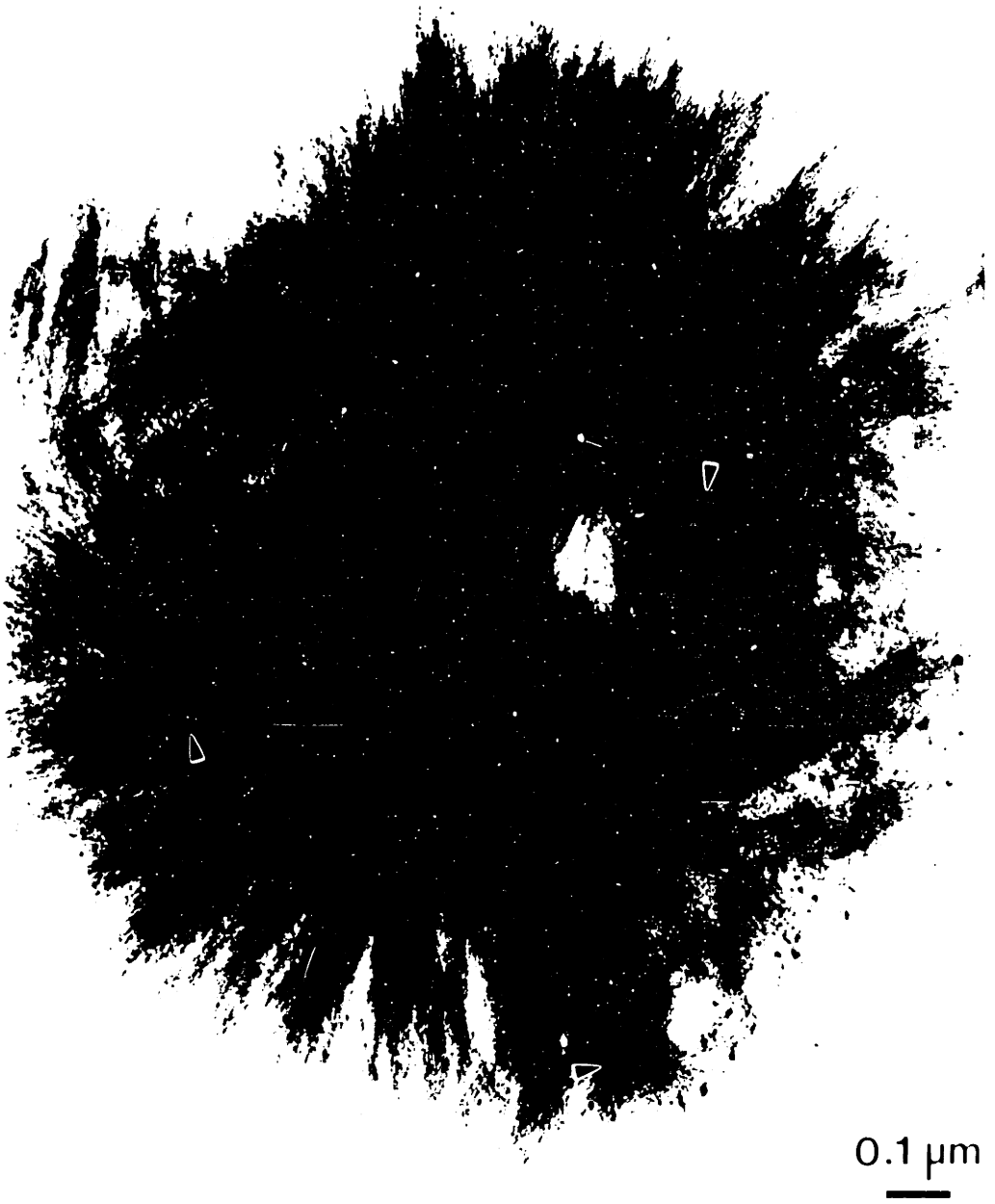

Fig. 2-5
p. 63

with OsO_4 and phosphotungstic acid solutions. The amorphous regions are stained dark due to penetration of both staining agents leaving the crystalline regions relatively unstained and lighter in contrast except at the center of the spherulite which is over stained. This accounts for the high degree of contrast in this micrograph due to complexation of the OsO_4 with the unsaturation of the methylvinylsiloxane and the PTA with the amorphous regions of the nylon-6. The radiating lamellae can be seen emanating from the center nucleus, fanning outward and undergoing splaying (arrows) which is believed to be caused by pressure from molecular portions of uncrystallized cilia in the interlamellar regions [102,103]. Other noncrystallographic branching mechanisms may also be operative. These lamellae can be estimated from Figure 2-5 to be ~ O(1) μm in length and approximately 50 to 80 Å in thickness if it is presumed that the lamellae are being viewed edge-on. The fact that there exist alternating dark/light regions representing the amorphous interlamellar regions sandwiched by the crystallites supports this observation. The central region of this spherulite does not possess true spherical symmetry due to the presence of the double circle or leaf-like structure as observed recently in TEM replicas of isotactic polypropylene [104] and isotactic polystyrene [105].

The small, darker, circular regions near the outer boundary of the spherulite are believed to be the higher molecular weight rubbery regions of the copolymer which contain a small concentration of vinyl groups for complexation with the OsO_4 stain giving a dark phase contrast. This copolymer has been rejected by the growing crystal front probably due to the fact that it contains a long rubbery chain covalently linked to the

crystallizable nylon-6 block. Thus, it can not be accommodated into the growing crystal lamellae as well as the homopolymer without significant free energy penalty (i.e. loss in conformational entropy of the amorphous block in the interlamellar regions plus the positive enthalpy of mixing siloxane and amorphous nylon-6). In other words, the amorphous phase density in between the lamellae would be exceedingly high if the copolymer entered the lamellae, chain folded and left the rubbery chain confined to the interlamellar region. Thus the copolymer with the long rubbery chains attached are not preferred in the early-to-middle stages of the spherulitic growth process and only enter the spherulite structure near the completion of the crystallization process (i.e. near the domain boundary). Here the large enthalpic driving force of crystallization more than offsets the lesser loss in conformational entropy of confining the rubbery blocks to the interlamellar or interspherulitic domains because of space filling requirements. Near the center, the crystallizable volume is smaller and at a greater premium because of a smaller radius whereas near the boundary, the volume is greater and the interspherulitic regions can accommodate the rubbery chains with more ease.

It is clear from this introduction of polymer morphology resulting from crystallization that spherulites are unique and very complex in structure generating complicated relationships between their components. These dependences give rise to many interesting properties which are addressed in Chapters VII through IX. Before addressing the issue of crystallization in rubbery-crystalline systems (block copolymers and

blends), some basic fundamental relationships of homopolymer crystallization will be introduced.

a. Introduction to Kinetic Expressions

Most of the details of homopolymer crystallization are derived in Appendix I and only the general results will be quoted here. Generally homopolymer crystallization kinetics are controlled by two competing terms; one relating to the thermodynamics of forming a stable nucleus of critical size at the melt-crystal interface (as in secondary nucleation) and the second governing the rate at which macromolecules diffuse to the growing surface and become incorporated into the growing crystal. This is expressed by equation (2-6) for the steady growth rate as a function of temperature.

$$\dot{G} = \dot{G}_o \exp \left[- \frac{\Delta F^*}{kT} - \frac{\Delta F_\eta}{kT} \right] \qquad (2\text{-}6)$$

Here $\dot{G}_o$ is a pre-exponential factor being a weak function (linear) of T, ΔF^* is the thermodynamic free energy for nucleus formation, ΔF_η corresponds to the transport barrier height for bringing a macromolecule to the interface and k = Boltzmann's constant, (1.3806×10^{-16} ergs $^oK^{-1}$ molecule^{-1}).

However, there are several types of nucleation such as primary, secondary and molecular nucleation [106], any one of which may be the rate controlling process during crystallization. For all polymers, isothermal crystallization nearer to T_m^o (the equilibrium melting temperature of the perfect polymer crystal) will cause the thermodynamic term ΔF^*, to govern the rate of growth through nucleation of the polymer chain

onto the substrate whereas at temperatures approaching the glass transition temperature, the transport or diffusion term ΔF_η, will control the observed rate. These two terms have opposite temperature coefficients, the thermodynamic term has a negative coefficient versus a positive $d\dot{G}/dT$ for the transport term. This competition leads to the classic bell curve of polymer crystallization rate versus temperature and has a maximum where

$$kT_{max} = T_{max}^2 \left[\frac{\partial(\Delta F^*/T)}{dT} + \frac{\partial(\Delta F_\eta/T)}{dT} \right] \qquad (2\text{-}7)$$

$$= - [\Delta H^*(T) + \Delta H_\eta(T)]$$

i.e. at the point where the negative of the sum of the enthalpies of nucleus formation and transport is proportional to the maximum characteristic fluctuation energy of the system, kT_{max}. Note that both enthalpic terms are functions of temperature and are inherently negative. Thus, at some temperature, T_{max}, the polymer crystal growth process is the best compromise of the two growth terms ($d\dot{G}/dT$) of opposite sign and the crystals attain their maximum growth rate.

Depending on the degree of the undercooling ($T_m^o - T_c$), where T_c = the crystallization temperature, the rate of chain folding may not keep pace with nucleation events. Previously, it was tacitly assumed that once a chain nucleated onto the substrate, the chain folding occurred quickly and completely following more or less an adjacent reentry model finishing the folding well ahead of the next nucleation event. Thus, nucleation was rate controlling. This type of growth is called "Regime I" crystal-

lization and the growth rate is proportional to the nucleation rate. If however, several nucleation events occur before a chain completely folds onto the substrate, then "Regime II" crystallization dominates. This latter type is more likely to prevail at higher undercoolings and represents growth proportional to the square root of the nucleation rate introducing a factor of 1/2 into the analysis of $\sigma_e\sigma_s$. Lauritzen [107] has introduced a dimensionless parameter, Z to determine which is the corresponding crystallization regime. It scales as $10^3(L/2a)^2e^{-K/T\Delta T}$ for modest undercoolings where L is the lamellar width, a = the width of a single chain, $\Delta T = T_m^o - T$ and $K = Nb\sigma_e\sigma_s T_m^o/k\Delta H_f$ with N=4 for Regime I and N=2 for Regime II. Thus if $Z \lesssim 0.01$ than Regime I governs whereas if $Z \sim 1.0$, than Regime II dominates. Extensive analysis and publication of homopolymer crystallization kinetics has been done by Hoffman et.al. [108-112] who have invoked modifications for more complex cases such as surface roughness and varying molecular weights of the crystallizing chains.

Extension of this treatment of growth rates which are commonly determined by polarizing microscopy to data obtained by DSC (differential scanning calorimetry) is straightforward and entails substituting the expression for the growth rate into the Avrami analysis (see Appendix I) and calculating the Avrami constant, K which when plotted versus $T_m^o/T\Delta T$ yields estimates of the surface free energy product, $\sigma_e\sigma_s$ if heterogenous nucleation controls. This presumes that the functional form of the Avrami analysis is consistent with the mode of nucleation whether it is heterogeneous or homogeneous and thermally activated (spontaneous) or athermal (instantaneous). However, this can not be ascertained a

priori and at best, the Avrami analysis only provides a phenomenological framework to analyze crystallization data. Despite its obvious shortcomings, it has been widely used in the literature and will be invoked in this thesis not to calculate absolute values, but rather to explain trends in crystallization of nylon-6 homopolymer and the copolymers. This is done despite objections [109] that the accepted functionality of the transport term as shown in Appendix I, is not obeyed with impurities rejected at the crystallizing front, such as amorphous blocks and noncrystallizable homopolymers in blends.

Considerable energy is required to orient a polymer chain at the crystal-melt interface which accounts for the high end surface free energy, σ_e of polymer chain folded crystals. At the interface, high chain density restricts possible conformations and causes the chain to minimize the work of orientation by folding back into the crystal. This folding and reentry into the crystal represents the minimal increase in free energy (or expended work due to unfavorable gauche conformations of the folds) as compared to bundle-like or switchboard models. The latter two types of morphology are not favored due to the presence of diffuse phase boundaries (i.e. an entropy gradient stretching over large molecular dimensions, ca. 20 Å) which require substantial work to form. Thus, chain-folded crystallites minimize the thickness of the interfacial region and require the least amount of work to create it.

The presence of a second component in the melt not only affects the bulk free energy but changes the interface density which affects σ_e. Regardless of the type of crystallization (homogeneous, heterogeneous, thermal or athermal), this value of σ_e dictates nuclei shape and the

thermodynamic activation barrier height and thus, the rate of nucleation and growth. Depending on the phase equilibrium of the second component, it can either promote nucleation and growth by phase incompatibility with the crystallizing material or it can hinder growth by increasing the diffusional resistance in transporting the crystallizable macromolecules to the interface. The phase behavior of this foreign material and its interaction during crystallization is discussed next.

3. Competitive Driving Forces in Multiphase Materials: Kinetics vs Thermodynamics

Multiphase semicrystalline materials combine the complexities of phase equilibria covered in section B.1 of this chapter and the competing driving force of crystallization which was discussed previously, section B.2. These two processes sometimes interact cooperatively such as the known behavior of elastomers acting as nucleating agents in crystallizable blends increasing the spherulite density [113] or antagonistically where the amorphous phase retards the diffusion of the crystallizable species to the crystal front, impeding the growth process [114]. For compatible crystalline and amorphous blends, the expression for the free energy of nucleus formation must be modified [114] and the change in growth rate is directly related to the ratio of the glass transition temperatures; for an amorphous T_g greater than the T_g of the crystal, the free energy barrier to transport of the crystalline material to the interface increases and the growth rate drops. Opposite effects are seen when the ratio of T_g's is reversed.

In this thesis, only incompatible crystal-amorphous systems will be considered which inevitably lead to a reduction in the growth rate due to

occlusion, rejection and deformation of the immiscible, amorphous "phase" by the growing crystal front. To accurately represent the crystallization process in the presence of the immiscible component, modifications to the growth equations have to be made. It is not the purpose of this section to discuss the kinetics of the growth process as modified by the presence of the rubber, but rather to focus on which process is preferred when the two phenomena, crystallization and phase separation compete during solvent evaporation or cooling from a homogeneous melt. The effects of the phase separated domains on the crystal growth rate are discussed further in Chapter VII, §A and semi-quantitatively in Chapter VIII, §C with regards to the observed morphology.

To acquire an understanding of the interplay between the two processes one must first consider the phase diagrams for the competing phenomena. This was first done by Hashimoto and Kawaii et.al. [115] for crystalline-amorphous di- and triblock copolymers of PEO-PI. This is a convenient system to study because the melting point of PEO is well below the boiling point of many solvents and it is soluble in a variety of both good and poor solvents. In addition, the isoprene block is well suited for staining purposes in the electron microscope. They considered a three-dimensional phase diagram consisting of a triangular base for the three components, PEO, PI and S (solvent) plus the third vertical dimension being temperature thus constructing a prism. See Figure 2-6a. At a given temperature, a ternary diagram or horizontal plane of the prism is used to describe the phase regions as shown in Figures 2-6b,c.

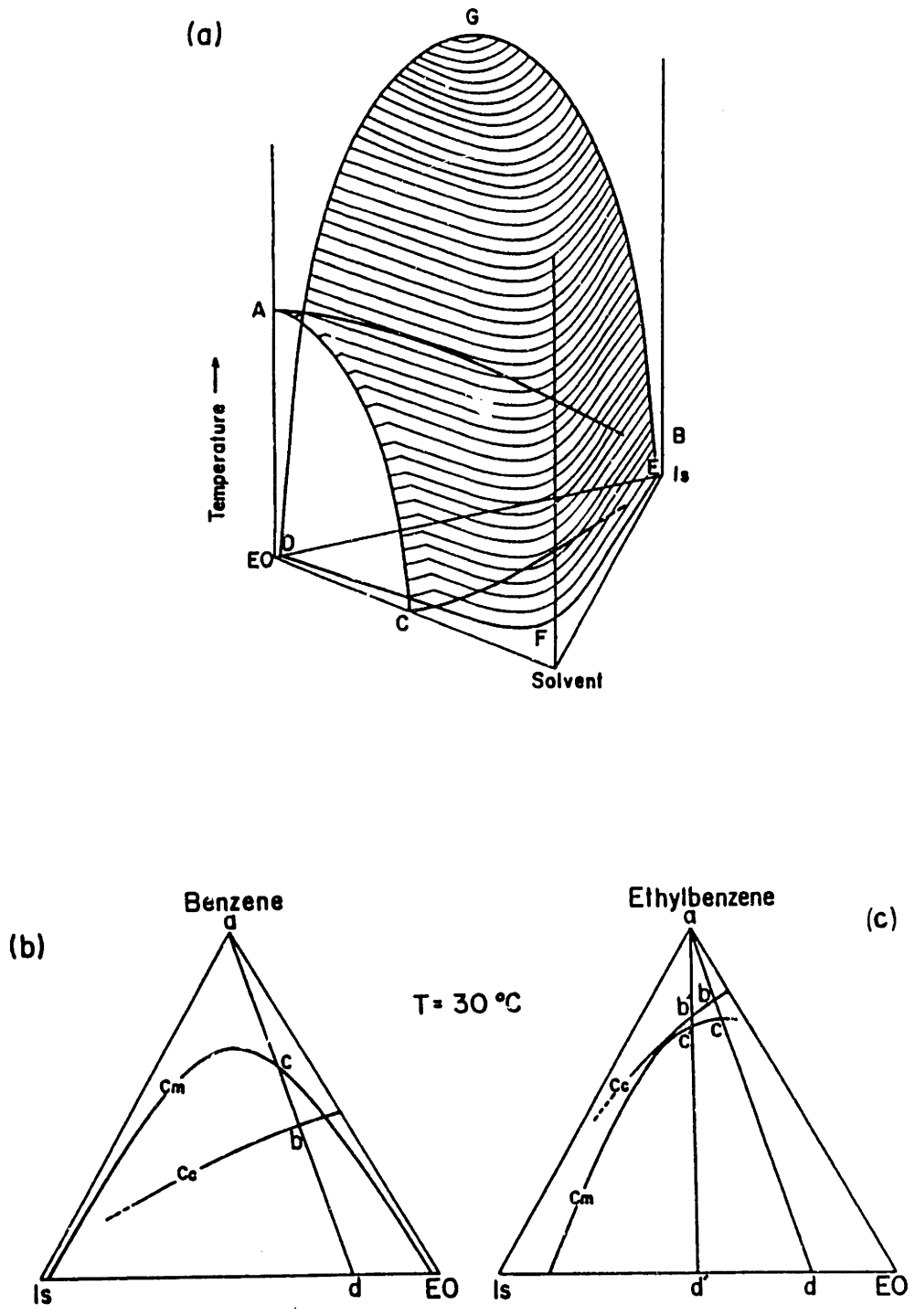

Figure 2-6. a) Two-component diblock/solvent composition diagram as a function of block fraction and temperature; b), c) Constant temperature ternary diagrams indicating controlling phenomenon: crystallization (C_c) versus micellization (C_m); after Hashimoto and Kawaii [115].

These diagrams indicate that if the solvent is good for the crystallizable block, then micelle formation will occur prior to crystallization upon solvent removal and this is represented by point 'c' in Figure 2-6b. Given the three-dimensional structure of the phase diagram, Figure 2-6a, this behavior also will occur at higher temperatures closer to T_m of the pure diblock (ca. 62°C) as well because the crystal-liquidus curve moves to lower solvent concentrations at approximately the same rate as the locus of the solution-micelle transition. In other words, both curves move to higher copolymer concentration (lower in the triangular diagram) at approximately equal rates as the temperature is raised so no crossover from phase equilibria dominating to crystallization controlling occurs. Thus, for the PEO-PI diblock in a good solvent for both blocks, (such as benzene), micellization occurs prior to crystallization for almost all temperatures and compositions. Obviously for copolymer concentrations extremely rich in isoprene, at the edge of the diagram, crystallization may occur and this should be considered in the limit of highly disparate block lengths. Hashimoto and Kawaii et.al. were able to show via transmission electron microscopy that these microphase domains disrupted the crystallization process causing less order in the spherulitic structures for copolymers with greater than 50-60% PEO.

On the other hand, suppose the solvent is poor for the crystalline block, such as ethylbenzene but good for the amorphous block. This causes the crystal-liquidus curve to be much lower in copolymer concentration causing crystallization to occur earlier in the solvent evaporation process. The solution-micelle transition is now greater than the concentration where crystallization occurs as shown in Figure 2-6c,

*points 'b' vs 'c'. Here crystallization dominates and the structure appears as multilayer platelets containing regions of sandwiched amorphous material similar to morphologies of PEO-PS obtained by Kovacs et.al. [99] and by Kawaii et.al. [116] for PEO-αMePS. From these previous studies, the morphology is lamellar with each layer of the platelets consisting of one crystal lamella and one amorphous lamella. This is a drastically different morphology than the disrupted spherulitic structure obtained when phase separation dominates.

The preceding discussion of phase diagrams (from Hashimoto and Kawaii et.al. [115]) qualitatively considered phase transitions of copolymers with various composition as a function of temperature. To simplify this into the context previously described for micellization as shown in Figure 2-2, T-ϕ diagrams will be discussed next, showing crystallization competing with micellization for a single copolymer composition.

The crystal-liquidus (c-ℓ) line is depicted in Figure 2-7 for a fixed diblock copolymer composition with known melting point, T_m in a good, high boiling solvent for the crystallizable block, B; as an example see Flory, ref [117,118] and Richards [119]. The locus of critical micelle concentrations as a function of temperature is also shown and denoted by the abbreviation 'CMC'. For the case of a good solvent for the A block ($\chi_{AS} \approx 0$) and a moderate to poor one for the amorphous block B ($\chi_{AB} \approx \chi_{BS} >> \chi_{AS}$), microphase separation will occur prior to crystallization at point 'a' as solvent is evaporated at a given temperature T_1. This will result in a small concentration of free copolymer chains in equilibrium with micelles. Existing theories should

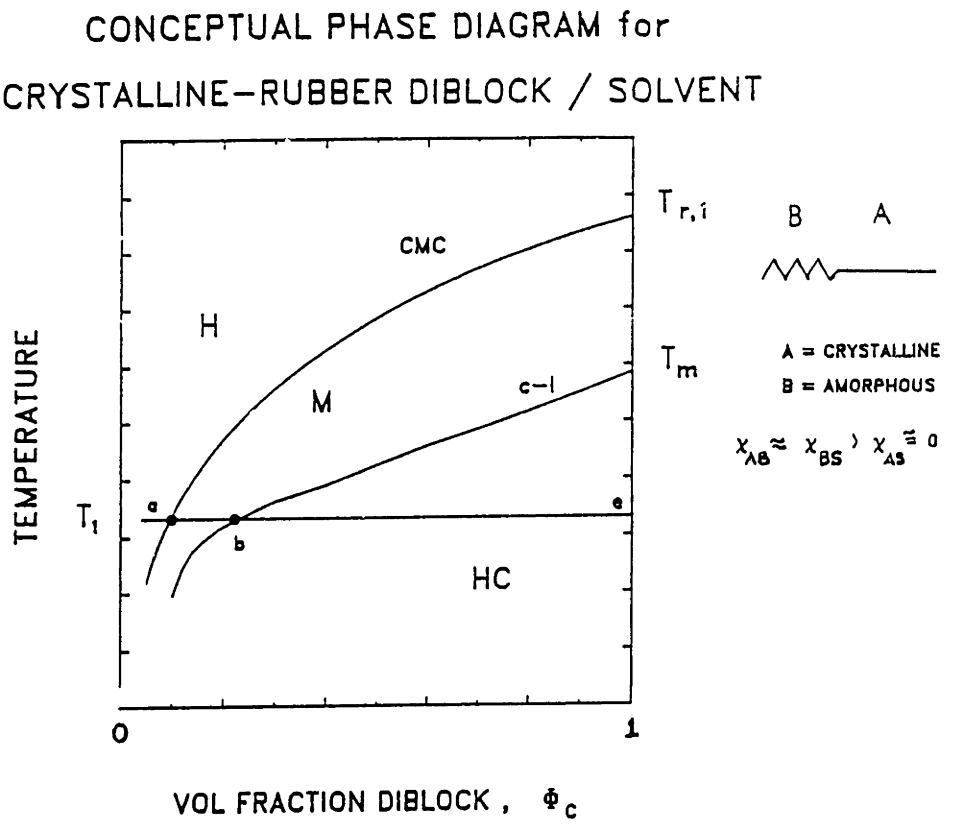

Figure 2-7. Conceptual phase diagram for competition between crystallization and phase separation; crystal-liquid (c-ℓ) solubility curve and loci of critical micelle concentrations (CMC). Isothermal casting process from 'a' to 'e'.

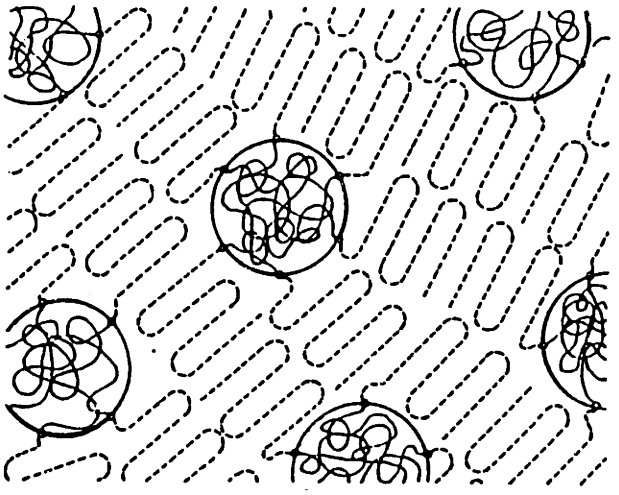

Figure 2-8. Schematic of resulting morphology from casting process as above where phase separation controls the morphology; after Kawaii [90].

be able to predict (within their limitations) this concentration, number of micelles, free copolymer concentration, etc. As additional solvent is removed, the M or micellar region is traversed until the c-ℓ binodal is reached (point 'b') where crystallization commences in the interstitial regions around the microdomains yielding a semicrystalline interstitial phase.

For these transitions as shown in Figure 2-7, the controlling phenomenon will be microphase separation regardless of the temperature of casting the diblock film between T_1 and T_m (and even below T_1 as well). This is because the $\chi_{BS}N_B$ is so high that micellization is highly favored and crystallization will always follow the juxtaposition established by the micellar structure. Once the solvent is removed at T_1 for example, the temperature can be raised above T_m (vertical movement on the right-hand ordinate at 100% copolymer in Fig. 2-7) and the morphology may be reformed depending on miscibility in the melt. If the degradation temperature is above the order-disorder temperature the copolymer can be heated to a homogeneous fluid above T_r. Upon cooling from the homogeneous melt, mesophase formation will occur at T_r and crystallization will then commence in situ forming the interstitial crystalline domains. Experimental work in this thesis suggests that for longer amorphous blocks within the limit for spheres, both "paths" will yield the same morphology consisting of spheres of siloxane in a semicrystalline nylon-6 matrix because of similarity between χ_{AB} and χ_{BS}. This is represented schematically in Figure 2-8 and will be discussed further in Chapter VIII.

Now consider the case where the solvent is poor for the crystalline block but good for the amorphous block. This case is much more complicated because the interaction of the amorphous phase equilibria of the crystalline component with the CMC must be considered. For purely crystalline polymers in poor solvents, the phase diagram is as shown in Figure 2-9, after Richards, [119]. Practically no theoretical work has been attempted in predicting phase behavior of crystalline-amorphous diblock / solvent systems in a selective solvent poor for the crystalline block and good for the amorphous component. The experimental use of this type of system also is limited, see ref [115] for example. Nonetheless, a hypothetical phase diagram will be constructed based on intuition and prior discussion.

With a good solvent for the amorphous block, the locus of CMC's will be at a higher copolymer volume fraction than the c-ℓ line for temperatures like T_1 which are below the solubility curve as shown in Figure 2-10. As the solvent is removed at T_1, the strong B-S interactions ($\chi_{BS} \ll 1$) delay microphase separation so that crystallization of the A block occurs first at 'a' because of its incompatibility with the solvent. The morphology would be expected to be highly nonequilibrium due to the solvated amorphous block interfering with the ordering of the crystal and it could lead to a pseudo-lamellar type organization. If given sufficient time to perfect the crystal structure, the resulting morphology could appear as depicted schematically in Figure 2-11 and observed experimentally by Kawaii et.al. [115,116] and Lotz, et.al. [99]. A shift towards a lamellar morphology was observed in this thesis work as well when diblock films were cast from a selective solvent for the rubber

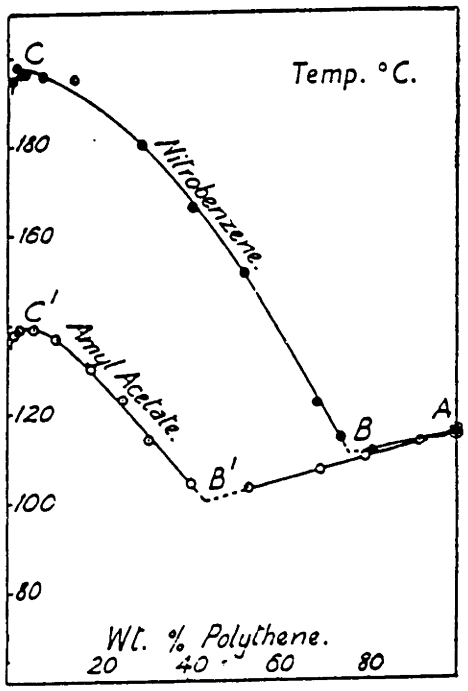

Figure 2-9. Phase equilibria and solubility curve for polyethylene in poor solvents; $\chi_{AS} > 1$; after Richards [119].

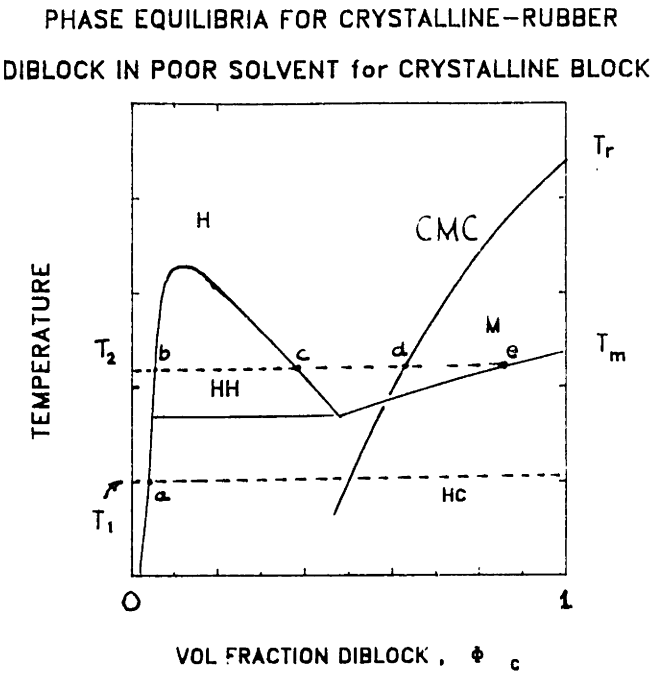

Figure 2-10. Phase equilibria and solubility curve for diblock with an immiscible, noncrystalline block in a poor solvent for the crystalline block but good for the amorphous block; $\chi_{AS} \approx \chi_{AB} >> \chi_{BS}$.

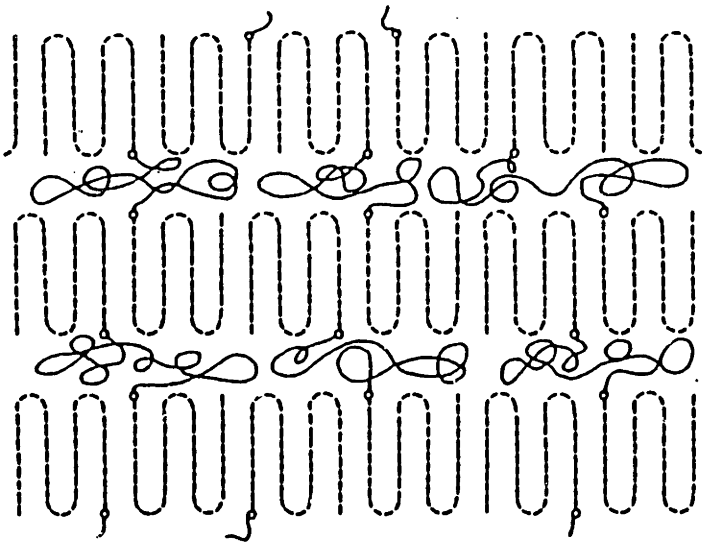

Figure 2-11. Schematic of resulting morphology when crystallization precedes phase separation; crystalline block is chain folded and amorphous block is between lamellae; after Kawaii [90].

block. Experimental evidence of this morphological change depending on casting solvent will be presented in Chapter VIII for PDMS-Nylon-6 diblock copolymers cast from toluene/trifluoroethanol (2/1 v/v). This solvent is presumed to be a selective solvent for the PDMS block versus trifluoroethanol, a good, selective solvent for the nylon-6 block. For temperatures like T_2 above the c-ℓ solubility curve, liquid-liquid phase separation occurs first as the copolymer content is increased (see point 'b'). This may or may not (depending on the exact location of the CMC) be followed by homogenization ('c') which precedes micellization ('d'). Here, micellization is believed to occur before crystallization (at 'e') because the high casting temperature (and thus, the low supercooling) effectively increases the nucleation barrier to permit mesophase formation to compete more favorably with crystallization. Although this last schematic, Figure 2-10 is rather conjectural, the basic tenants are believed to be correct; at low temperatures, crystallization will precede phase separation due to the high $\chi_{AS}N_A$ and at higher temperatures, liquid-liquid phase equilibria will compete with micellization. The exact position of the CMC locus will depend on many factors such as amorphous block length, degree of incompatibility with the solvent, temperature, etc. This discussion also demonstrates that considerable work (both experimental and theoretical) is needed to better understand the competing phenomena in poorer solvents for the crystalline block in amorphous-crystalline diblock copolymers.

As can be seen from the previous discussion, the morphology resulting from the complex interrelation between phase equilibria and crystallization can be very different depending on which process is control-

ling. In the most general sense, very little is known about phase behavior of amorphous diblock copolymers in solution and there is a lack of experimental data to compare with the few existing theories. More data has become available recently on amorphous diblock / homopolymer blends via the use of X-ray scattering techniques and work is underway in this laboratory in these areas but agreement with theoretical predictions to date is moderate, at best. Even less perhaps is known about the phase behavior of crystalline-amorphous diblock copolymers in solution or blended with other homopolymers from either a theoretical or experimental basis. It is hoped that the synthesis, characterization and initial morphological investigation of the emulsification behavior of a PDMS-Nylon-6 diblock copolymer from this thesis may provide a starting point for further exploration into these areas.

II. C. DEFORMATION IN THERMOPLASTICS

Overview

There are many different competing mechanisms that govern deformation in polymers depending on the chemical structure and molecular architecture. Glassy homopolymers as well as rubber-modified amorphous copolymer systems deform primarily by shear banding or crazing which are both localized, orientation and birefringence-producing mechanisms. Shear deformation occurs at essentially constant density and is due to the deviatoric components of the applied stress tensor. It is favored under plane stress conditions (i.e. in thin samples) in amorphous polymers designated as type II such as polycarbonate (PC), polyphenylene oxide (PPO) and amorphous poly(ethylene terephthalate) (a-PET) which have flexible heteroatom linkages in the main chain.

Crazing on the other hand produces significant dilatation through the formation of cavities resembling oblate spheroids bridged by fibrils and is more prevalent in plane strain, physically aged samples. Crazes can be initiated by surface flaws or microheterogeneities within the bulk and are more prevalent in type I glasses such as polystyrene (PS) and poly(methyl methacrylate) (PMMA). These polymers possess bulky side groups and craze from temperatures just below T_g all the way down to liquid nitrogen temperature. Crazing also occurs in type II polymers defined above but usually in a more limited temperature range [120] and often in competition with shear yielding [121]. Propagation of crazes in glasses can be described by a meniscus instability model [122] or various other models such as the lens craze model which utilizes the meniscus instability and the wedge disclination craze tip models or the crack tip

model, all of which are detailed in the doctoral thesis of Hawkins [123].

Deformation processes in semicrystalline polymers are more complicated than their amorphous counterparts due to the anisotropic effects of the crystalline phase on the initiation and propagation of crazes and shear bands. Crazing has been found in isotactic polypropylene (i-PP), polyethylene (PE) and isotactic polystyrene (i-PS) but generally has not been observed in all semicrystalline polymers. Shear bands are more notable in compression where dilatation is suppressed. In addition, the high ductility of some semicrystalline polymers results from other mechanisms known as micronecking and/or microfibrillation which transform spherulitic microstructure into highly oriented microfibrils through formation of a stabilized neck in the gauge section during extension. This drastic change in microstructure consumes much energy (hence the renowned toughness) and involves molecular processes that are still not completely understood. As a result of competing mechanisms, multiple crystal lattices and material anisotropy, semicrystalline polymer deformation clearly requires more investigation both theoretically and experimentally.

The practice of incorporating rubbery particles into glassy polymers to enhance ductility is widespread. As a result of both industrial and academic incentives to achieve a better understanding of this phenomenon, rubber-toughened glasses such as high impact polystyrene [124,125] or (HIPS), acrylonitrile-butadiene-styrene (ABS) [126] polymers or comparable systems have received much attention. A great deal has been learned through microscopic investigation of these multiphase polymers such as

how the rubber particles exert forces on the matrix polymer to initiate massive crazing or shear yielding which lower the flow stress of the material and significantly increase the energy absorbed during deformation. Mechanical models based on microscopic observations have led to a more unified understanding of this type of deformation. Unfortunately, much less is known about semicrystalline-rubber systems because of the morphological complexities in studying their microstructures as a direct result of less well-defined synthesis routes to these types of copolymers. This section provides an overview of the deformation processes in semicrystalline homopolymers followed by a brief description of rubber-toughened amorphous polymers for background into the relatively unexplored area of rubber-modified semicrystalline polymers.

1. Semicrystalline Homopolymer Deformation

Semicrystalline polymers consist of diverse microstructures containing crystalline and amorphous regions configured mostly by the prior thermal history of the material. In many crystalline polymers including nylon 6, these microstructures are spherulites formed when the polymer is cooled from the melt or precipitated from solution. They are highly anisotropic on the microscopic scale $O(\sim 10^3)$ Å and contain radiating fibrils or bundles of lamellae emanating from point nuclei. Spherulites usually grow radially until impingement occurs creating a space filling morphology (except in the case of low crystallinity polymers like i-PS, for example) which can be seen in a polarizing optical light microscope (see Figure 8-2, Chapter 8 of this thesis for the micrograph). Spherulites were discussed initially in Chapter II § 2.2 and will be covered in more detail in Chapter VIII, Morphological Characterization when the

microstructure of nylon-6 and its copolymers/blends is considered. Thus, bulk spherulitic polymers really are composite materials because the radiating lamellae are comprised of crystallites sandwiched by amorphous layers (refer back to the schematic in Figure 2-4), although they have much less anisotropy than many typical composites such as graphite-resin layups for example. It is the interaction between the two inseparable domains of crystal and glass that give semicrystalline polymers extraordinary properties such as increased impact strength and ductility; however, this also complicates the study of their deformation.

Spherulites and semicrystalline polymers in general, deform by a number of different and often competing mechanisms such as a multitude of slip modes (interspherulitic, interlamellar and transverse and chain direction slip within the crystallites) and to a lesser extent by twinning (paired rotation of crystallographic lattices) and martensitic transformations (stress-induced phase change of crystalline unit cell) [127]. Because the radiating fibrils grow in all directions due to spherical symmetry and often twist about the radial axis, there is no primary orientation to the applied load and thus, a variety of these deformation mechanisms may be operable all within the same spherulite. In addition, the response of spherulites to both plastic and elastic deformation is highly nonuniform and the various components have different characteristic relaxation times associated with the deformation. This complexity of the various microstructures (crystallite, fibril, amorphous tie layer, etc.) within a spherulite virtually prohibits development of an universal, predictive model of the deformation. Nonetheless, variables such as loading temperature, specific thermal

history which controls domain size, crystallinity and crystallite size as well as molecular weight will often favor one type of mechanism over another and generalized phenomenological statements about the deformation can be made.

a. Phenomenological Observations on Deformation

All semicrystalline polymers under stress undergo competition between plastic deformation and fracture processes [128]. Obviously, to obtain high ductility the crystals must deform plastically before cracks develop. This can be accomplished by increasing the amorphous fraction via higher molecular weights, lowering the crystallization temperature and/or incorporating chain defects to facilitate easier deformation in the interior and improve general deformability. The effects of these and other variables on yield, fracture and elastic modulus that are at the experimenter's control in the manipulation of semicrystalline polymer morphology are discussed below.

Molecular Weight / Tie Chains

For low molecular weights, the local yield stress at the interface between crystal and amorphous is less due to lower tie chain density. Thus for temperatures below T_g the critical stress for fracture is reduced as a result of fewer, low energy intercrystallite cleavage sites. [128]. Above T_g an opposite trend is possible because modest reductions in tie chain density (from that at very high molecular weight) can increase toughness due to a decrease in the intraspherulitic yield stress which brings intraspherulitic yielding into competition with interspherulitic failure. This trend should not be carried too far

because obviously, large reductions in molecular weight drastically reduce entanglements in the amorphous interlamellar and interspherulitic regions causing premature intraspherulitic and/or grain boundary failure. This must have been the case with coarse i-PP spherulites studied by Friedrich and Hornbogen [129] which have a tendency to segregate more material to the interspherulitic regions. These investigators found that under impact, low molecular weight material failed brittly at the grain boundaries whereas high molecular weight i-PP promoted ductile, tufty drawing of the interspherulitic regions. Unfortunately no values were given for the molecular weights to assess where this reduction begins to become detrimental. This study also demonstrates that embedded in the above discussion of molecular weight effects are other effects such as deformation rate (which is usually high in impact) and spherulite size which will be discussed shortly.

The molecular weight is directly related to the tie chain density which determines the continuity of the system and thereby controls the level of the elastic modulus [128]; higher molecular weights would in principle, generate more connectivity between crystal and amorphous regions increasing their parallel interaction to give higher moduli. Recall that in series, the amorphous-crystal composite is only as strong as the weakest component whereas in parallel the moduli combine as $1/E = 1/E_a + 1/E_c$. See also reference [129] for explanation of orientation effects on the modulus. However, molecular weight effects on the elastic modulus are harder to isolate because of many secondary effects such as crystallinity and crystallite size, for example.

Crystallinity / Crystallite Size / Crystallization Temperature

As the crystallization temperature, T_c is reduced, more lower molecular weight, defective chains can be accommodated into the crystal and will be segregated away from the amorphous interspherulitic grain boundaries thereby strengthening these regions which are often paths of least resistance for fast fracture processes. Decreasing T_c also reduces crystallite size or lamellar thickness which lowers the modulus of the amorphous-crystalline composite [130] so that plastic yielding can occur at a lower stress. It is believed that thinner lamellae permit easier interlamellar shear slip but no conclusive evidence exists due to simultaneous changes of other morphological variables. The lamellar thickness also can be increased by post-crystallization annealing at temperatures close to the melting point; this thickening is enhanced with higher molecular weights. Crystallization after annealing also increases the crystallinity content which is usually lower for longer chains. Thus, annealing increases both lamellae thickness and the degree of crystallinity but these two properties scale oppositely with molecular weight.

Spherulite Size

This is one of the most over-correlated physical parameters in the literature on deformation of semicrystalline polymers. Often, nucleating agents are used such as monomeric crystals [131] or other crystalline polymers in a polyblend [132] to vary the spherulite size but without consideration of other sub-spherulitic variables, these studies can sometimes be misleading. Generally, larger spherulites segregate more amorphous material and generate larger, thicker interspherulitic zones

which is especially true in poly(ethylene oxide) (PEO) [133] where large grain boundaries are formed that close slowly, eventually reaching impingement. This can lead to grain boundary failure at lower strengths especially at temperatures above T_g; recall the previous example of i-PP [129]. Larger spherulites undergo more local displacement at the boundaries during elongation than smaller ones and cracks are easier to initiate if the temperature is below T_g. When the failure mode is forced to go through the center of a spherulite (by using higher molecular weights and smaller spherulite size so more entanglements in the thinner interspherulitic regions retard grain boundary failure, for example) it can do so as brittle fracture for temperatures below T_g or as ductile extension if $T > T_g$ because in the latter case, the crystallites must deform absorbing energy. This is why commercial i-PP and PE possess exceptional toughness and can extend to draw ratios of 7-8 or higher.

Most investigations have found that increasing spherulite size decreases the strain to fracture and leads to brittleness. This was determined by Way, et.al. [134] for i-PP where 250 μm spherulites were brittle but 90 μm spherulites deformed to > 700% fracture strain. Unfortunately, as in many other cases these investigators controlled spherulite size by changing T_c which alters crystallinity content and crystallite size as well.

In efforts to better independently control spherulite size, Kleiner, et.al. [135] thermally prepared samples via a secondary melt temperature program [136] to obtain equivalent densities (crystallinity content) and long periods (from SAXS) for different spherulite sizes. They found an increase in yield stress and strain to fracture with increasing spheru-

lite size, other sub-spherulitic parameters apparently remaining constant.

According to Starkweather [137], larger spherulites (30-50 μm diameter) in Nylon-6,6 produced a more ductile behavior with a lower yield stress than smaller spherulites (ca. 2-5 μm diameter). Spherulite size was controlled by nucleating agents and data was collected on dry samples (i.e. $T_{def} < T_g$). Unlike these trends, others [132,138,139] believe that spherulite diameter refinement increases toughness much the same as grain size refinement increases the ductility of steel. Supporting this, Hammer et.al. [140] studied compression molded poly(oxymethylene) (POM) and found that smaller spherulites produced by quenching at lower temperatures gave more ductile behavior. Annealing was done to minimize crystallite size variation and give nearly equivalent densities. Additional experiments showed that variations in crystallite size, as determined by the Scherrer equation from X-ray diffraction, had little effect on toughness.

The effect of aging on yield properties was studied by Remaly et.al. [131] with i-PP. They found that spherulite size differences only influenced mechanical properties after aging at room temperature and that tensile strength increased as spherulite size decreased; unaged samples showed no effect of spherulite size with tensile strength.

Clearly, varying trends exist with regards to spherulite size and toughness in the literature mainly because other variables have changed to an unknown degree as the spherulite size was varied. At this point, no universal model or trend between spherulite size and mechanical behavior is evident for the many semicrystalline polymers examined. It

is clear that each polymer responds differently and must be studied independently to ascertain trends of spherulite size (and other variables) on toughness.

Temperature and Rate of Deformation

Temperature and rate effects are inversely related via the time-temperature superposition principle. Deformation at lower temperatures generally is similar to higher rates and vice versa. From the doctoral work of Sandt [141] quoted in [128], lower deformation rates led to grain boundary failure for i-PP versus transspherulitic fracture at higher strain rates. In other work [129], at 25°C an increase in strain rate caused a transition from interspherulitic (along the boundaries) to radial fracture through the spherulites as shown by SEM.

Similarly, low temperatures (which parallel high rates) favor intraspherulitic fracture because the elastic discontinuity effect across the crystallite-amorphous boundary is less, i.e. the moduli are more comparable. Higher temperatures create a greater modulus mismatch, causing increased flow by thermally activated processes and the rubbery amorphous phase yields prior to crystal slip. This process is described mathematically [128] where crack growth rates are related to deformation modes; high strain rates generate much larger stresses which activate many deformation sites resulting in catastrophic relief through the spherulite center whereas low rates create lower stresses and special sites must deform (not enough energy to deform many possible sites) so failure is along easy or specially activated sites around the spherulites.

At temperatures above T_g (or under low strain rates), interspherulitic and interlamellar slip are often the acting deformation mechanisms in tension. At this temperature, the amorphous phase is rubbery and has a low critical shear stress allowing lamellae parallel to the draw direction to slip past each other at low strains. This interlamellar slip has been found to account almost entirely for the elastic part of the deformation in HDPE [142] and is also seen in optical light micrographs of nylon-6 deformed at room temperature obtained in the course of this thesis and shown in Chapter IX.

b. Deformation Models

Analysis of spherulitic deformation can generally be grouped into two categories, either 1) the use of models employing global variables to describe the microstructures, i.e. the macro-to-micro approach or 2) interpretation of structural changes by microscopic observations and generalization to bulk properties, or the micro-to-macro method. Representative works from the former class are the composite theories and micromechanics of Halpin and Kardos [143] who modeled the amorphous-crystalline phase as a two-component material based on earlier attempts at using the crystallites as "crosslinking sites" within an amorphous matrix [144] or series-parallel spring models to describe the crystalline-amorphous interaction [145]. Despite the accuracy achieved by Halpin and Kardos [143] in predicting composite moduli by incorporating the geometry and type of crystallites (lamellar, fibrillar, spherical etc.), quantitative prediction of deformation properties such as the yield and tensile strength and fracture strain were not attempted due to insufficient information on crystallite size and distribution. T.T. Wang

[146] used a multistep model that combined the structural behavior of different scale levels from the lamellar crystals up to aggregated spherulites and determined bulk elastic constants for the material from composite theory. As with other models employing composite theory, no plastic deformation was considered.

An alternate macro-to-micro approach is to measure macroscopic variables such as orientation, yield stress and fracture strain for example, which are simply average properties of the bulk and try and correlate their values to the microstructure using a fracture envelope approach and a generalized model. As an example, Samuels [147] measured the Hermans' orientation function [148] (to be discussed shortly) for polypropylene and related it to the tensile and yield stresses as well as the fracture strain. This approach simply correlates average changes in morphology (orientation) with mechanical properties and then describes effects in terms of a microstructural model. It is pertinent only to samples prepared uniquely by Samuels' group and not generalizable to other i-PP much less other semicrystalline polymers. His combination of all stages of deformation into one model simply can not describe the complex deformation modes of spherulitic polymers beyond the phenomenological level. Both composite models and correlation studies lack the degree of specificity needed to quantify plastic yielding and drawing in semicrystalline polymers. However, it is recognized that these types of studies are just not sufficient but necessary for understanding deformation.

The second approach (micro-to-macro) possess advantages over the former because it utilizes microscopic morphological/analytical observa-

tions (which are not easy to obtain) to predict overall behavior within an acceptable mechanistic framework. The investigators favoring this approach, in general, have realized that spherulitic deformation must be considered in stages, quantified in separate "units" and then reassembled to yield an overall description of plastic deformation.

Within this context, spherulite deformation can be discretized into three stages: 1) elastic/viscoelastic/pre-neck plastic deformation, 2) formation and stabilization of micronecks that transform spherulitic lamellae into microfibrils and finally, 3) plastic extension of the fibrillated and/or microvoided structure until fracture. Yielding can be considered as the delineation between stages 1 and 2. As mentioned earlier, not all semicrystalline polymers undergo "micronecking" in stage 2; rather this specific mechanism could be replaced by some other process that destroys spherulitic microstructure and textures the material. For polymers such as nylon and PET, this process has yet to be fully elucidated but considerable progress has been made with the work of Galeski et.al. [149] and Schaper, et.al. [150] which will be discussed further in Chapter IX. The microstructural information obtained from the observations in the different stages can then be related to distinct mechanical theories and used to piece together a unified picture of spherulite deformation.

Stein and coworkers [151] thoroughly investigated stage 1 using rheo-optics, i.e. dynamic birefringence and x-ray diffraction and found multiple responses of spherulites to the applied stress. In this region, substantial plastic deformation of the spherulitic lamellae occurs via shearing, displacement (along the c-axis which is the chain axis in PE),

stack rotation and chain tilt, the latter occurring primarily in the radial lamellae oriented 45° to the applied stress. These mechanisms do not change the spherulitic texture but simply rearrange the lamellae to provide maximum compliance for transformation into microfibrils by longitudinal chain slip in the next stage of deformation.

Deformation in region 1 (ca. $\epsilon \simeq 0.5$-0.7 for LDPE, $\simeq 0.2$ for HDPE) has been modeled by Sasaguri et.al. [152] and refined by Kawaii, et.al. [153] to include lamellae rotation and untwisting as the c-axis of the orthorombic unit cell aligns with the applied stress. This model is based on affine transformations at constant spherulite density and simply describes the spatially averaged (Hermans') orientation factor, F_α ($=1/2(3\overline{\cos^2}(\alpha)-1)$) as the lamellae are transformed into elongated fibrils; this geometry is similar to Peterlin's microfibrillation discussed below and represents deformation at the limit (or end) of stage 1. The model uses two fitted parameters and gives satisfactory agreement between theory and experiment.

A more realistic model that also incorporates the initial randomness of the lamellae oriented in the spherulite is currently being developed by Argon and Parks [154] to predict deformation in PE and other semicrystalline polymers. This model, to date gives good agreement with experimental data but overpredicts tensile stresses due to the fact that no amorphous material between the lamellae have been introduced as yet. Further developments are in progress.

Region 2 has received a great deal of attention in a theoretical context by Peterlin who advanced the micronecking theory and molecular model [155–159] which describes the destruction of lamellar stacks of

the original spherulites and the creation of bundles of microfibrils. Within the microneck, blocks of folded chains are broken off from the lamellae and incorporated into the microfibril by chain slip along the interface separating amorphous and crystalline regions. The original tie molecules now bridge over several blocks and are more prevalent at smaller draw ratios, λ and higher molecular weights and provide a back-restoring force or retardation of the extension which gives the microfibrils their strength in the longitudinal direction.

The long period of the crystalline blocks within the microfibril depends on the drawing temperature much the same way the mean long period of the spherulite lamellae depends on the crystallization temperature. However, for bulk specimens, the final microfibril long period is independent of the spherulitic lamellar long period and depends solely on the draw temperature, T_d being longer for higher T_d. At a constant $T_d \approx$ 85°C, the microfibril long period is found to be less than the lamellar long period regardless of the lamellae thermal history, being 50% less for samples annealed close to T_m [157]. This indicates large scale reorganization during the micronecking process [159] which persists even in PE drawn at room temperature. This extraordinary chain mobility of blocks of crystals (and not just amorphous, rubbery chains) observed at room temperature in drawn, bulk PE partially can be explained by the conversion of the work of deformation into heat. This raises the local temperature somewhat due to the low thermal conductivity and the low heat dissipation rate. However, this solely can not explain the large temperature rise from room temperature to somewhere close to T_m for all but the highest strain rates. Calculations by Vincent [160] show that at

a stretching rate of 1.5 mm/min with a flow stress of 10 MPa, the temperature rise for PE is only 0.75°C/mm of neck. This calculation however, does not take into account the rate of heat generation which is of paramount importance. Simple extension of Vincent's theory to give the rate of the temperature rise under adiabatic conditions shows that $\Delta T/t = \sigma v^2/k_T = 1.2$ °C/min for the conditions cited above, where σ is the sustained stress, v is the constant velocity of deformation and k_T is the thermal conductivity of the material ($\sim 8 \times 10^{-4}$ cal $cm^{-1} sec^{-1} °C^{-1}$ for PE). Thus, the material would have to deform for over 83 minutes to generate the 100°C temperature rise in the neck to bring the material to the melt under adiabatic conditions. During this length of time, a great deal of heat will dissipate into the atmosphere (the experiment is hardly adiabatic) and prevent the 100°C rise from occurring. Under these conditions, the deformation rate must be increased to $\approx$ 15 mm/min to generate theoretically the "adiabatic" 100°C rise in just a minute or so. In practice, Nakamura and Skinner [161] found that the strain rate had to be O(~ 150 mm/min) in order to produce a ca. 20°C adiabatic temperature rise. The lack of exact agreement between theory and experiment is not important here, rather, only very high rates of deformation will generate sufficient heat to "melt" the polymer and facilitate such large scale rearrangements.

The remaining increase in chain mobility may be accounted for by the production of negative pressure in this pseudo-melt (which lowers T_m) by the application of the tensile stress combined with lateral contraction similar to the reasoning why voids (or less dense regions) are found in deformed nylon-6 [149]. It is not known whether these two factors

alone can account for the necessary ~ 70–100°C temperature difference between ambient and the local temperature actually inside the material where "melt" fibrillation is believed to occur.

Other workers have investigated this region of inhomogeneous spherulitic deformation using experimental conditions to permit large strains. As quoted by Peterlin [162], small loads and low deformation rates do not always guarantee ductile behavior; this will occur only when the viscosity is sufficiently low for shear yielding to compete with crazing or fracture processes. This competition will be covered in the next subsection. As a result, Hay and Keller [163] used plasticizers to promote extensibility of the spherulites and observed that the deformation was highly inhomogeneous and large strains developed in the transverse quadrants (equatorial regions) of the spherulites with respect to the applied tension, σ_∞ and/or at the transverse spherulite boundaries. Micronecking was observed together with longitudinal voiding in spherulitic PE and a schematic model was proposed to explain the observations. No predictive modeling was done. Extension of this model was proposed by McConkey et.al. [164] who proposed block (or lamellar) tilting of equatorial lamellae after chain tilt and slip to explain an increase in the long period and other scattering patterns of hot drawn ($T \doteq 90°C$) LDPE. This increase suggests a different mechanism for spherulite breakup than the microfibrillation where the long period was observed to decrease. Again, no general, predictive modeling was attempted.

Similar observations were made by Predecki and Thornton [165] who found mostly transverse microdrawing between spherulites and substantial necking and deformation at the center of the spherulites at $T = 25\text{-}70°C$

due to transmittance of the lateral stress concentrations onto the centers. A small percentage of microvoids were seen in the polar regions of the spherulites but were not fibrillar, just cracks on the order of 0.1 μm. This is parallel to observations of chevrons or arcs in the polar regions of i-PP made by Atkinson and Way [166]. At very high temperatures (T > 70°C), Predecki and Thornton found that a greater proportion of lamellar boundary slip occurred with intralamellar slip still dominating the reaction of the applied stress. This reinforces Peterlin's views that at sufficiently high temperatures, lamellar boundary slip will facilitate the breakdown and transformation into microfibrils through large-scale mobility; the remaining question (still unanswered) is how this high temperature-like environment is reached in bulk PE at draw temperatures of only 25°C.

Region 3, the drawing of the microfibrils has received a great deal of attention because experiments with oriented and better-defined structures are more amenable to simulation and modeling. This stage of textured deformation is currently being investigated for PE, PET and Nylon-6 at M.I.T. and has received much attention in the literature, (see for example [167]). Detailed discussion is not relevant to this thesis but the striking characteristic of these materials is the alignment of the lamellae normal to the free flow direction and the chain axes parallel to the compression direction when these textures are induced by compression molding. This was found by Young and Bowden [168] for textured PE where the crystallites were oriented normal to the flow direction and within 8° tilt from each other - nearly a perfect crystal. Study of these types of materials should lend insight into the mechan-

ism(s) of fibril drawing that occurs in the final stage of spherulitic deformation.

c. Deformation Mechanisms (Crazing and Shear Yielding)

As seen above, some semicrystalline polymers such as PE and i-PP are able to microneck into fibrillar bundles on cold drawing at room temperature. These microfibrils are similar to the orientation observed in intracraze fibrils [169] and because of this similarity, the intrinsic possibility of crazing in semicrystalline polymers must be regarded.

Low temperature crazing ($T \simeq -30°C$) occurs well below the temperature conducive to micronecking and is most common in i-PP. According to Friedrich [170], three stages occur in craze matter production. First, local slip occurs in the amorphous interlamellar layers oriented 45° to the applied stress which increases the normal stress on the crystallites. Recall that this region of the spherulite selectively deforms in other mechanisms discussed previously. Secondly, when this local stress reaches a critical value, individual blocks approximately 10-30 nm long [171], are pulled out of the chain folded ribbons creating very small (~100x600 $Å^2$) elliptical voids sometimes (inadvertently) referred to as microvoids. These microvoids grow normal to the applied stress with adjacent ones initially defining the craze tufts which contain extended tie chain molecules and small crystallites. Lastly, continued strain further elongates the tufts causing lateral "microvoid" coalescence until mature craze matter is produced. At this time, the alignment of the amorphous material stiffened with crystallites strain hardens and stabilizes the craze.

Morphological evidence [170] shows crazes in i-PP to be similar in scale to those in amorphous polymers; fibril diameter ~ O(15-40) nm and craze thickness ~ O(1-3) μm. They propagate normal to the applied stress and run straight through fine spherulitic structure (20-40 μm diameter). Coarser spherulites (100-200 μm diameter) act as termination sites for surface-initiated crazes and completely coarse (high MW) spherulites initiate and terminate crazes in their secant planes where the lamellae are inclined 45° to the linear craze growth direction. Finer grain spherulites are better suited for supporting craze growth because the lamellae are thinner which gives a greater fraction of lamellae per unit volume favorably oriented oblique to the advancing craze for sustaining growth. Larger spherulites produced at lower supercooling contain thicker crystallites and thus, do not have as many lamellae per unit volume making it is less likely to find favorable lamellar configurations necessary for voiding and drawing into craze tufts. Hornbogen (in ref [151]) has proposed a model to represent the craze-crack tip in semicrystalline polymers based on the aforementioned observations.

The main difference between the development of crazes and microfibrils from Peterlin's micronecking mechanism is that the former fill only a fraction of the sample volume and coexist with the spherulites. Craze and sample failure occur by crack coalescence. Micronecking on the other hand, converts the entire bulk spherulitic structure to microfibrils and occurs at higher temperatures where sufficient chain mobility can be attained for this large-scale micro-reorganization of the entire gauge section.

While low temperatures and high deformation rates favor crazing in some semicrystalline polymers such as PP, higher temperatures and lower strain rates favor shear yielding [173] where shear yielding here represents all other non-dilatational mechanisms. According to these authors, when crazing is not operational, all deformation proceeds by shear yielding which is a very simplistic view but mostly correct. This is because shear yielding is the fundamental mechanism operating in the deformation of most all semicrystalline polymers. To see this, look at the micronecking model of Peterlin where initial shearing of lamellae and chain blocks within the lamellae occurs to orient the chains into the microneck and transform them into the fibrils. Alternately, recall that during crazing, the microscopic voids in the amorphous interlamellar regions are produced by intracrystallite shear (chain slip) and that further drawing and plastic yielding eventually forms mature craze matter. Thus on a molecular level, shear yielding is operative in practically all types of deformation from homogeneous deformation of spherulites in plasticized semicrystalline polymers to highly inhomogeneous deformation such as necking and microfibrillation.

Large scale (i.e. visible in the OLM) shear banding in semicrystalline polymers is much less prominent, being observed primarily in compression where crazing and dilatation are suppressed. The formation of shear bands is controlled by shear stresses which encourage lateral movement without voiding. As in amorphous polymers, shear banding generally occurs at oblique (~ 45°) angles to the compressive axis and can be localized or diffuse. This band type or texture also is temperature/strain rate dependent; higher temperatures (lower rates) producing

more diffuse, finer bands because of greater cooperative movement of amorphous and crystalline regions [170] versus discrete, coarser bands at lower temperatures or higher rates. The bands are seen to pass through fine grain spherulites.

In contrast to general opinion, Yeh et.al. [174] found shear bands and crazes co-existing in i-PS after drawing in tension. The fine grain shear bands ran at ~45° to the applied stress and passed unperturbed through spherulites of ca. 1-2 μm diameter, being controlled by micro-structures much smaller (~O(200-700) Å) than the spherulites themselves, as determined by higher magnification TEM. Morphological evidence was shown for lamellae transformation into craze structures as schematically depicted in the craze model [172]. In a striking micrograph, Yeh et.al. showed after deforming a film biaxially in tension that shear bands actually consisted of fibrils that were drawn apart due to the second drawing in the normal direction to the first stretching. Additional evidence of this is discussed below when shear yielding of amorphous-rubber copolymers is considered suggesting that the internal microstructure of shear bands and crazes are rather similar. Although this work involved exceptional microscopy, no comments based on observation were advanced as to when shear yielding is favored as opposed to crazing; both mechanisms seemed equally operable.

Obviously, the deformation of semicrystalline polymers is complex with an interwoven dependence of mechanical properties on spherulite size, crystallinity and crystallite size, molecular weight and tie chain density. Various micro-mechanisms occur simultaneously in the deformation of the spherulites such as chain slip, rotation, shear etc.

Different micron-scale mechanisms such as micronecking, crazing and/or shear yielding often compete and depend in a complex way on the deformation rate and temperature as well as the morphology (crystallite and spherulite size, etc). Independent control of all morphological parameters is not always possible through thermal treatment for example, but these variables must be defined to yield useful information on deformation mechanisms.

2. Toughening in Multiphase / Multicomponent Systems

The realization that inclusion of rubbery heterogeneities improved the impact strength of glassy polymers was made as early as 1927 [175] with the precursor to high-impact polystyrene (HIPS). Only within the past several decades, however, has the technical understanding of these materials caught up with their commercial exploitation. Presently, the addition of rubber to a matrix can be accomplished by three major pathways:

1) Physical blending ($T > T_g$)

2) Interpenetrating networks (IPN's)

3) Copolymerization

Physical blends are often used initially because of economics or polymer chemistry limitations but usually provide poor adhesion of the rubber or filler to the matrix and marginally improve toughness when rubber content greater than 5-10% or so is required. In many cases the blend has poorer mechanical properties than the pure matrix homopolymer as seen with nylon-6/PDMS from this thesis; see discussion in Chapter IX. Recently however, it has been shown in our laboratories that low amounts

of dispersed butadiene rubber in PS can have a substantial effect on toughening without copolymers or interfacial agents; reasons for this improvement are currently being explored. IPN's are not commercially practical due to molding limitations of the network which leaves graft and block copolymers as the most attractive route to rubber-modified polymers because they provide excellent particle-matrix adhesion (through the covalent bond) and good control and flexibility over domain size and shape. The drawback to the use of copolymers is their (usually) added cost in synthesis.

In order to discuss the specifics of rubber toughening of thermoplastics it is necessary to first introduce the basic principles of particulate effects in the toughening process. Since the experimental data published on the rubber-toughening of amorphous glasses is immense (for a comprehensive review see [176, 177]), only a small sampling of the literature will be presented here to discuss the salient points. This will be followed by a representative discussion of rubber-modified semicrystalline copolymers which is much less extensive than their amorphous counterparts.

a. Particle Mechanics of Toughening

Satisfactory multiphase properties for tough behavior will be attained if the system possesses: i) a high interfacial tension between the rubbery phase and matrix so the former does not wet the latter, (recall $\gamma_{AB} \sim \chi_{AB}^{1/2} \sim [(\delta_A - \delta_B)^2]^{1/2}$, so immiscibility or high χ_{AB} gives high interfacial energy), ii) high interfacial adhesion to ensure good contact between matrix and particle, and iii) an interparticle distance, t less than a critical value, t_c. The first two opposing physical forces

are most readily compromised by a heterogeneous block copolymer where the covalent bond provides the satisfactory adhesion and the difference in solubility parameters creates the high interfacial free energy.

The third requirement, interparticle distance is related to the particle diameter by a simple model developed by Wu [178] to correlate impact strength with morphology for hydrocarbon rubber grafted to nylon-6,6. By assuming a cubic control volume with spherical rubber particles at the corners, the critical particle diameter can be related to the interparticle distance,

$$d_c = \frac{t_c}{\left(\frac{\pi}{6\phi_r}\right)^{1/3} - 1} \qquad (2\text{-}8)$$

where d_c, t_c are the critical particle diameter and surface-surface interparticle distance respectively, and ϕ_r is the volume fraction rubber. At constant temperature, a critical particle diameter marks the tough-brittle transition or the point that delineates between brittle fracture and ductile failure. Materials with interparticle distances less than the critical value, t_c will yield in a ductile fashion because of a strong stress-field interaction between particles that enhances shear yielding [179] whereas particles separated by more than t_c will be brittle.

In an amorphous matrix, the rubber particles, in addition to their elastic modulus mismatch possess a thermal expansion coefficient misfit that combine to create a state of negative pressure within the particle ($-p = -1/3(\sigma_r + \sigma_\phi + \sigma_\theta)$) [180]. This negative pressure is generated from the restraint of the PB particles by the matrix polymer through the

covalent bond as they cool from the melt or other high temperature processing excursion. The PB shrinks faster than the PS matrix ($\alpha_{PB} > \alpha_{PS}$, where $\alpha=1/V(dV/dT)_P$, the volumetric thermal expansion coefficient) developing the triaxial tension within the particle [181]. If a single particle in an infinite matrix is considered, there is no negative pressure in the matrix because $\sigma_r = -\sigma_\theta = -\sigma_\phi$ [181] but substantial deviatoric stresses are present. If multiple particles exist, their interaction as determined by Broutman and Panizza [182] creates positive pressure in the matrix while keeping the deviatoric stress approximately the same [180]. Thus, when a distant tensile stress is applied, which generates a state of triaxial tension at the equator of the particle as shown in Figure 2-12 [183, 184], the stress needed for crazing is lowered due to the existing positive stress field set up in the matrix from particle-particle interactions. The combination of these two stresses (the thermal stresses and the applied stress) generates significant Mises equivalent stress (deviatoric stress) at the surface of the particles to increase the free volume of the matrix and develop micropores that can lead to dilatation. Thus, dilatation, when profuse, consumes a large amount of deformation energy leading to tough materials. This same particle-induced stress field in the matrix can also lead to shear banding as seen in ABS materials [126] and in some cases simultaneous shear and craze yielding in PS-PPO blends [185].

High interfacial adhesion is important in these systems for transmittance of tractions to the matrix or else the applied stress would simply cavitate and tear apart the rubber creating premature voiding and crack initiation. Although voids possess the largest modulus mismatch

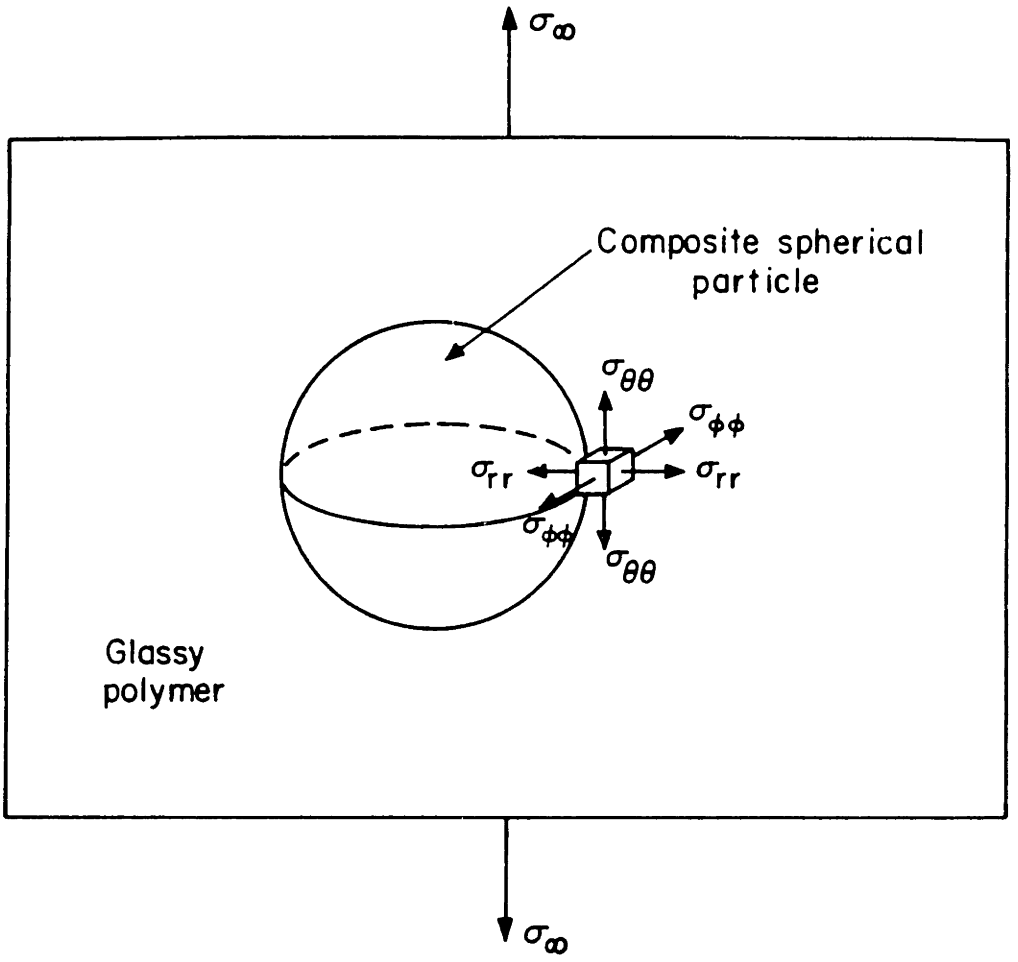

Figure 2-12. Generation of triaxial stress state in glassy matrix at the equator of a rubbery particle where craze initiation is most likely.

and potential for craze dilatation, their existence generates supercritical size cracks within the craze structure leading to catastrophic failure. Due to the small mean particle diameter (≈1-3 μm), and relatively high volume fraction of rubber (10-20%) commonly used, an extremely large number of rubber particles exist which can create many deformation paths through crazes, matrix yielding and/or shear bands substantially increasing the energy required for deformation and improving toughness.

b. Glass-Rubber Copolymers and Blends

Most of the past work in the rubber toughening of plastics has dealt with trying to improve the impact resistance and energy absorbed during deformation of glassy polymers; (see for example several reviews [186–188]). Many of these glasses such as poly(styrene) (PS) and poly(methyl methacrylate) (PMMA) are brittle when deformed in tension at room temperature far below their glass transition temperature. Although high energy absorbing mechanisms such as crazing and to a lesser extent shear yielding [174] occur in these types of polymers, they are localized in a volume representing only a small fraction of the total sample volume and thus, the total amount of energy absorbed during deformation is very low. Hence brittle behavior is obtained.

On the other hand, glassy polymers such as polycarbonate, (PC) poly(ethylene terephthalate) (PET) and poly(phenylene oxide) (PPO) are inherently ductile under identical conditions because of bulk, diffuse shear yielding [189] which occurs throughout the majority of the sample. This principle of increasing the number of sites so that a greater

fraction of the sample is involved in energy absorption during deformation is how rubber toughening of glassy polymers is accomplished.

Crazing and Shear Yielding in Rubber-Amorphous Copolymers

The large difference in thermal expansion coefficients between the rubbery particles and the matrix is mainly responsible for initiation of crazes in rubber-modified glassy copolymers [190], but this can occur by different mechanisms depending on the copolymer. One type of cavitation-induced crazing was demonstrated by Schwier et.al. [192] for PB/PS diblock copolymers of rod and spherical morphologies where the small rubber particles (~$O(10^3)$Å or less) were put in a state of negative pressure due to a greater thermal expansion coefficient (α) for PB than PS as mentioned earlier. When the sum of the thermal mismatch stress, the applied stress and the differential between the maximum stress at the tip of the craze front and the applied stress exceeded the cavitation stress (related to the bulk modulus of PS) the particles cavitated releasing the negative pressure. This caused distortional plasticity of the surrounding matrix polymer drawing it into fibrils and absorbing the energy of deformation which gave the material enhanced toughness.

In other cases, the particles do not cavitate but merely create favorable stress interactions (due to the negative pressure) near the particle surface within the matrix which initiates massive crazing. This behavior has been obtained for more complicated morphologies of HIPS-like, composite particles comprised of alternating concentric shells of PB and PS as found by Gebizlioglu et.al. [192]. These morphologies were obtained by blending homopolymer PB into the KRO-1 copolymer (commercial star polymer of PB-PS arms manufactured by

Phillips) and dispersing it in a high molecular weight PS matrix. Excellent craze density was achieved that decreased the flow stress from ca. 35 MPa to 8–10 MPa and increased the strain to fracture to ~ 0.8 as compared to 0.08 for unmodified, copolymer / PS matrix samples. Thus, transformation of the morphology into "onion-like" particles with alternating concentric layers or shells of PB and PS produced nearly twice the thermal stresses (negative pressure) as compared to HIPS or KRO-1 particles and markedly improved the toughness through creation of a multiplicity of craze sites. This efficiency at nucleating crazes may come from the rippled concentric shell effect of these particles and as yet, some lesser understood interfacial phenomena or from an unexplained, unusually low plastic flow resistance in the craze tufts [180].

Shear yielding also occurs in rubber-modified thermoplastics such as ABS (acrylonitrile-butadiene-styrene copolymers) with shear bands sometimes competing with crazes in the deformation. For small, close-packed particles, shear bands propagate through the particles causing cavitation and some fibril drawing although the structure is not as fully fibrillated as a craze in SAN. This was similar to the observations by Yeh et.al. with PS (both amorphous and isotactic). Since the particles are closely packed, the meniscus instability model of Argon and Salama [122] becomes inoperative and crazes do not propagate; the distance through the matrix between rubber particles is too small to sustain the normal wavelength of the meniscus craze mechanism. For widely separated particles (obtained by diluting the ABS with SAN) which are still small, deformation zones are initiated as much by dust and other heterogeneities in the film as by the rubber particles. These poor-initiator particles

are engulfed by the shear zones which cause them to cavitate and do not act as craze terminators. Rubber-initiated crazing is not operative with these smaller particles because the stresses in the matrix scale with the R^3 (R=radius) and thus is not sufficient to nucleate a craze. Larger size particles (~ 1.5 μm) also cavitated but initiated crazes normal to the applied stress similar to Schwier's PB-PS diblock copolymers. However, here the particles contain matrix polymer within them (composite particles) and are able to withstand the cavitation forces and retain their shape in contrast to Schwier's particles which completely ruptured and coated the surface of the fibrils. With the larger ABS particles the natural wavelength of the meniscus instability mechanism can be established because of the greater interparticle distance and crazing is preferred. Thus, to gain the most in toughness, both large and small particles are used; the smaller ones cavitating and concomitantly sustaining shear yielding while the larger particles effectively initiating crazes.

c. Semicrystalline-Rubber Copolymers and Blends

Impact modification of semicrystalline polymers can be achieved by either blending elastomeric components into the homopolymer or through copolymerization as pointed out earlier. Because of synthesis difficulties, the former is more often used which reflects back on the interaction of a non-crystalline component in the crystalline melt in regards to segregation and/or inclusion as discussed initially in §II.B.3 (this chapter). This blending approach is not the subject of this thesis and an excellent review of its current status can be found in the

literature by Paul and Newman [193], Manson and Sperling [194] and Robeson [195].

A model amorphous-crystalline copolymer of polyethylene-polystyrene, although the PS is a glass at room temperature, often is used in the study of compatibilization on an otherwise mechanically poor physical blend of the homopolymers. Radiation grafted PS to PE [196] and Friedel-Crafts alkylation of PS to LDPE [197] represent less characterized graft copolymers while more recently a block copolymer of PE-copoly(1-butene)--b-PS produced by hydrogenation of mainly 1,4-polybutadiene was studied by Heikens, et.al. [198]. This last investigation found that an increase in copolymer content increased the number of crazes so that a definite yield point was observed as compared to the brittle crazing and fracture of homo-PS. This experimentally demonstrates that more profuse crazing is not detrimental but rather, when controlled can be advantageous and enhance yielding. In addition, a greater percentage of shear yielding was observed as the copolymer content and particulate phase was increased so two mechanisms were working together to improve mechanical performance.

Rubber-modified poly(vinyl chloride) prepared by mixing acrylonitrile-butadiene-styrene (ABS) or methacrylate-butadiene-styrene- (MBS) graft copolymers with homo-PVC was found to have improved impact strength due to the particulate heterogeneities [199]. Rubber particle voiding and excessive stress whitening were found at high strain rates in contrast to little voiding but definite elongation and homogeneous deformation of the particles at low strain rates. Low graft content permitted the formation of a "network" of heterogeneities which gave more

stress-whitening and superior impact strength as opposed to uniformly dispersed, spherical particles where much less whitening was observed. From low angle light scattering (LALS), the cavitated particles were found to be grouped in shear bands oriented 55°-64° from the applied uniaxial tensile stress direction. Since homo-PVC is known to deform primarily by shear yielding, it is believed that the rubber particles cavitate at the tip of the growing shear band which can relieve the hydrostatic tension built up by the inhomogeneous shear band thereby releasing the plastic constraint and permitting a larger volume of material to be deformed plastically [126]. The deviation of the band angle from the theoretical 45° as in homo-PVC deformation was unexplained.

Within the nylon family, rubber-modified nylon-6,6 (Zytel ST-801^{R}, DuPont) showed increased shear banding and higher yield strengths as the content of impact modifier increased. Both types of failure, shear yielding and crazing occurred when a greater amount of impact modifier (composition and content unknown) was added although specific test conditions were not given [200]. This demonstrates that in semicrystalline-rubber systems (similar to amorphous-rubber systems with ABS [126]) both mechanisms can be operative depending on many experimental parameters.

Blends of 10-20% hydrocarbon rubber containing 1% reactive polar groups with nylon-6,6 were prepared by melt extrusion at 265°C [201]. The reactive rubber was grafted to the polyamide to give high (interphase) adhesion strengths as determined by measuring the interfacial tension based on interfacial thickness ($\gamma_{12} = 55\lambda^{-0.86}$ [202] where λ is

the interfacial thickness (Å)) or by conducting peel tests in a laminate geometry. For a given composition, only rubber particle size was varied by different extruder conditions while nylon matrix properties remained approximately constant.

Notched Izod impact tests clearly demonstrated increased toughness for smaller diameter particles and a sharp tough-brittle transition at a critical rubber particle diameter (ca. 0.8 μm for 15 %w rubber). For lesser rubber fractions, the critical size was lower or, in other words, larger particles required more rubber for toughening. Scanning electron microscopy (SEM) photomicrographs showed that the fracture surface of the tough blends had no exposed rubber which was confirmed by etching. This ductile fracture surface indicates extensive shear yielding deformation without crack interaction of the rubber particles. Thus, early theories of rubber particles blunting advancing cracks are not applicable [177]. In contrast, fracture surfaces of larger particle diameter blends (which gave brittle behavior) showed intact, exposed rubber particles. Deformation was at room temperature with dry samples.

The stress whitened zone of the tough specimen (smaller rubber diameter), which is ca. 50X larger than for the brittle blend, showed both extensive shear yielding and crazing according to TEM observations (no micrographs published). By using differential scanning calorimetry, Wu [201] determined that ~25% of the impact energy was dissipated by crazing, the remainder via matrix yielding. The difference in endothermic heat flow in scanning an undeformed sample versus a sample of the stress whitened zone was attributed to the contribution of surface energy stored in the craze matter. (Craze matter exotherm reduces melting

endotherm.) This assumes that no crystal transformation or change in crystallinity content has occurred during deformation so that the matrix heat requirements are the same in both samples. Realizing this, Wu performed wide angle x-ray diffraction (WAXD) analysis of the deformed matrix and found a ~12% crystal structure transformation (triclinic to pseudohexagonal). This martensitic-type transformation, however, is reversed upon slow heating around 200°C [203] so that matrix crystal structure is presumed to be the same through the melting region.

The other term of the craze dissipation energy, the fibril yielding component, is calculated from an intensive energy balance around the deformation zone. The impact energy dissipation density, G (cal/g) was determined experimentally and is constant for both tough and brittle blends. It is the sum of all specific impact energies.

$$G = G_c + G_s + G_{my} \tag{2-9}$$

where G_c is the craze dissipation energy and consists of two terms, the craze fibril yielding energy G_{cy} and the craze fibril surface energy G_{cs}, G_s is the fracture surface energy of formation and G_{my} the matrix yielding energy. Since $G_y = G_{cy} + G_{my}$ or the yielding energy consists of craze and matrix yielding and $G_c = G_{cs} + G_{cy}$ or the craze dissipation energy consists of the craze yielding energy and the craze fibril surface energy (to form the new surface), equation (2-9) can be rewritten as

$$G = G_{cs} + G_s + G_y \tag{2-10}$$

By surface tension analysis, G_s or the fracture surface energy of formation is negligible (~ 10^{-4} cal./g). Since the craze fibril yield energy, G_{cy} is simply the product of the total yield energy and the weight fraction of craze matter as calculated by density measurements ($G_{cy} = w_c G_y$), the total contributions of craze energy dissipation (25%) and matrix yield energy (75%) can be calculated. Wu verified this independently by measuring the temperature rise at impact assuming adiabatic conditions.

Melt blending of an ethylene-vinyl acetate copolymer (Elvax^R, DuPont) and nylon-6 by extrusion showed a phase inversion phenomenon with the EVA spherically dispersed at low shear rates and elongated PA-6 fibrils dispersed in the EVA at high γ_w, despite PA-6 compositions of 70 - 90% wt. [204]. With Izod impact, the observed stress whitening in the induction region of the low shear rate blends was attributed to simultaneous diffuse shear yielding and multicraze formation (although as discussed above for PVC/rubber blends, this may be an incorrect conclusion). No stress whitening of homopolyamide-6 at room temperature was found. Optimum copolymer content of 10% wt. EVA gave a 50% increase in impact strength, but hemispherical holes in the fracture surface of SEM micrographs suggest poor EVA-matrix adhesion and possibly a fortuitous improvement.

Alternating block copolymers from carboxyl telechelic aromatic polyamides and bis(3-aminopropyl)polydimethylsiloxanes were prepared by direct polycondensation using pyridine and triphenylphosphite as the proton acceptors. Films were cast from N,N-dimethylacetamide and strained at a rate of 3.3×10^{-4} sec^{-1} in uniaxial tension to give tensile

strengths of ca. 25 - 30 MPa and strains to fracture of ca. 25% for siloxane content of 25 %w with a presumed triblock structure; core PDMS block $\bar{M}_n \approx 1.7$ kg/mole with the outer two aramid blocks each with a $\bar{M}_n \approx$ 5 kg/mole. No evidence/indication of the resulting morphology was given. These lower molecular weights are obviously the reason for the poorer mechanical performance of these siloxane-polyamide films as compared to the strengths and elongations of the much higher molecular weight copolymers prepared in this thesis work and detailed in Chapters VI (synthesis) and IX (mechanical properties).

Summary

As demonstrated in these few examples, understanding of the deformation mechanisms in semicrystalline-amorphous copolymer systems is semi-quantitative at best. This is due to the complexities in analyzing the morphology of the semicrystalline phase and its interaction with the rubber; these difficulties have slowed microscopic exploration of the deformation behavior. To date, these systems have been characterized mostly in a phenomenological way. Thus, it is hoped that the information presented in Chapters VIII and IX will help reveal in a small way some of the intricacies of semicrystalline-rubber deformation as a result of the morphology.

On the other hand, considerable progress has been achieved in understanding the physics of rubber-toughening of glassy polymers and their particle mechanics of deformation. Quantitative models referred to in this section (§C) have been advanced to explain the state of stresses in the matrix and how these are influenced by a dispersed rubbery phase.

Extension of this understanding to the phenomena of crazing and shear yielding has been made.

In addition, much has been learned about the deformation of semicrystalline homopolymers due to excellent microscopy work that has revealed the misfit of stresses that exist in spherulites during deformation. Although this is more qualitative information then what has been gained through the modeling and microscopy work of amorphous-rubber polymers, it has established the foundation for a better quantitative understanding of semicrystalline polymer deformation in the future.

Much still needs to be understood in the partitioning of the multiple phases in the rubber-modified semicrystalline materials, the preference of crystallization versus phase separation and the interaction of the stress field in a semicrystalline matrix due to rubbery heterogeneities. Answers to these questions will contribute significantly towards a greater understanding in the deformation of rubber-toughened semicrystalline polymers.

II. D. SCOPE OF RESEARCH

1. Objective/Rationale

There is high demand for rubber-modified nylon-6 in the automobile, chemical, recreational and small-molded-parts industries. To fully understand the complicated interactions of the rubber phase with the semicrystalline matrix, a simple reproducible morphology is required amenable to analysis of mechanical deformation and phase equilibria. This "simplest" morphology can best be generated by a diblock copolymer as compared to a more complicated morphology with coexisting lamellae and spheres of a commercially available alternating polyether-nylon-6 block copolymer, for example [205]. Because of this simpler structure, a diblock copolymer can facilitate more controlled variation of the morphology by altering the length of the two blocks, the casting solvent or the cast temperature. In addition, this copolymer is easier to model theoretically for phase behavior or crystallization simulations. As a result of these benefits, the primary objective of this thesis work was to synthesize a diblock copolymer of a substituted alkylsiloxane and nylon-6.

Initially, a fluorinated alkylsiloxane (FS) was chosen as the desired rubber block because it best satisfied certain criteria which will be discussed in the next section. However, it was later discovered that this silicone was unstable to the basic ϵ-caprolactam (CPL) monomer at elevated temperatures of ca. 170°C which prohibited copolymerization. Alternatively, a dimethylsiloxane (MS) was utilized for two reasons: 1) it was stable to the monomer and 2) it could be synthesized via the same mechanism as the fluoroalkylsiloxane; thus, complete redesign of the

synthesis was not required. As will be discussed thoroughly in Chapter VI, the MS was not totally stable to the conventional alkali metal caprolactamate salts (i.e., common catalysts which instantaneously depolymerized the FS). This necessitated invention of chemically modified coordinating catalysts in order to accomplish the first objective, the synthesis of an intact siloxane-nylon-6 diblock copolymer.

Once the copolymer was synthesized, the second and third main objectives of this work were to study the morphology and mechanical behavior of the copolymer with blends of the two homopolymers. This involved TEM, SEM and OLM work to characterize the materials combined with uniaxial tensile measurements to quantify the mechanical performance, specifically the area under the stress-strain curve or the toughness. Considerable understanding of the interrelation of the two competing phenomena, crystallization and phase separation when films were cast from solvent or the melt, was more easily ascertained via the diblock structure. The mechanical performance of cast, melt annealed films was determined and showed substantial improvement over those of homopolyamide-6 which indicated that the goal of rubber-toughening nylon-6 had been accomplished. Thus, this siloxane-nylon-6 rubber system anchored by the role of the emulsifier (diblock), has created a window through which continued study of the rubber-toughening of nylon-6 can be pursued.

2. Candidate Rubber-Nylon-6 Copolymers

Extensive scouting of rubber block components was undertaken before the siloxane rubbers were chosen as shown in Table 2-1. The candidate rubber ideally should satisfy these five major criteria:

a) large ($\delta_A - \delta_B$), (δ_i = solubility parameter)
b) low T_g (<-10°C)
c) high thermal stability (at ≈ 250°C)
d) solubility in 2,2,2-trifluoroethanol
e) anionic polymerizability

Fortunately, very few crystalline polymers are miscible with other polymers (polycaprolactone/poly(vinyl chloride) comes to mind as an counter-example) so the immiscibility criterion in a) between rubber and matrix blocks, is fairly easily satisfied. This immiscibility creates a dispersed phase which must be rubbery at the test temperature to increase toughness and the rubbery block must be thermally stable in an inert atmosphere at 250°C so that nylon-6 can be melt annealed to the desired crystalline morphology. "Melt annealing" implies heating nylon-6 to the melt (ca. 250°C) to destroy previous crystallinity and then cooling at a controlled rate to establish the desired morphology. Of these requirements, the solubility in 2,2,2-trifluoroethanol (TFEtOH) is probably the least restrictive because only very dilute concentrations are needed for size exclusion chromatography and NMR and these are usually below the critical concentration for microphase separation or CMC. This even holds for highly disparate block solubility parameters such as those for nylon-6 ($\delta \approx 13.2$ (cal $cm^{-3})^{1/2}$) and PDMS ($\delta \approx 7.5$ (cal $cm^{-3})^{1/2}$) used in this thesis. And lastly, the rubber should be anionically polymerizable so that functionalization for crossover to the anionic polymerization of ϵ-caprolactam is feasible. This would be preferred over homopolymerization and coupling of the two preformed blocks which is nearly impossible here because 1) the bulk polymer and solvent solubilities are highly disparate precluding melt condensation and 2) the proton(s) of the polar

Table 2-1

Rubber Block Candidates

Rubber	T_g (°C)	T_{deg} (°C)	Anionic Polym	Solubility
Poly(1-butene)	-24	≈ 300	YES	*NO
Chloroprene	cis -20 trans -40	377	YES	NO
Butyl Acrylate	-54	160	YES	YES
Decyl Methacrylate	-70	240	YES	YES
Vinyl Butyl Sulfone	127	–	YES	–
Propylene Sulfide	-47	<265	YES	YES
Propylene Oxide	-65	265	YES	YES
Vinyl Methyl Ether	-31	≈250	NO	YES
Fluorinated Butadiene	OK	OK	YES	NO
Fluorinated Elastomers	OK	OK	NO	NO
Epoxidized Rubber	-60 to -20	<200	YES	YES
Methyl Siloxane	-120	400	YES	NO
Fluorinated Siloxane	-80	300	YES	YES

* via 1,2-polymerization of 1,4-butadiene and hydrogenation

solvent needed to dissolve the polyamide for solution coupling will interfere with the coupling reaction which was demonstrated in §A.2.

Referring to Table 2-1, the solubility criteria eliminates hydrocarbon rubbers such as poly(1-butene) and chloroprene. Epoxidized rubbers enhance solubility but the epoxy ring, like the conjugated dienes, would not be thermally stable and would oxidize/crosslink at the annealing temperatures. Acrylates and methacrylates satisfy the rubbery criteria provided the alkyl group is sufficiently large but contain reactive ester groups which could lead to undefined graft copolymers as the ester group is known to initiate caprolactam polymerization albeit with a larger induction time than initiators used in this thesis. Polyoxymethylene and polyoxyethylene crystallize and polyoxypropylene (or PPO), although anionically polymerizable, thermally degrades to some extent when held at 250°C for 1 hr under N_2 as shown by size exclusion chromatography from this laboratory of a polypropylene oxide-nylon-6 alternating block copolymer ($\bar{M}_w|_o$ = 38.8 kg/mole versus $\bar{M}_w|_{1hr}$ = 27.0 kg/mole).

Poly(vinylmethyl ether) has the desired solubility criteria as well as an all-hydrocarbon backbone (slightly higher degradation temperature than PPO) but cannot be anionically polymerized. At the early stages of this thesis, methods of eliminating chain transfer and termination reactions in cationic polymerizations were not yet fully developed (see for example ref [206] for recent innovations in cationic synthesis) and this method was not considered feasible. Fluorinated elastomers such as Viton^R, Kel-F^R or Tefzel^R as well as fluorinated butadiene do not have an available monomer supply and in the case of the former group, poly-

merize by a free radical mechanism which does not lead to well defined block copolymers as discussed in section II.A.

The silicones and phosphazines are thermally stable but for PDMS, the symmetry of the molecule precludes dissolution in polar solvents. Thus, the fluorinated silicone, poly(3,3,3-trifluoropropylmethylsiloxane) (or PTFPMS), which is commercially used as a gas chromatography (GC) support phase, initially was selected as the rubber of choice. Commercially available PTFPMS dissolves readily in TFEtOH, is used routinely to 250°C in GC columns and can be polymerized anionically by ring opening of the cyclic monomers. This permits terminal functionalization of the siloxane with an ω-N-acyllactam group capable of initiating caprolactam polymerization. This siloxane has a low T_g and is immiscible with the nylon-6 matrix leading to a multiphase material suitable for toughening. Extensive kinetic modeling of its ring-opening polymerization was done and is presented in Chapter IV, section B. Unfortunately, as will be explained in detail in Chapter VI, this siloxane is chemically unstable in caprolactam at high temperatures (>100°C) and could not be utilized as the rubbery block. As a result, methylsiloxane or PDMS was tested for stability in caprolactam and subsequently functionalized in a similar manner and used in the copolymerization with ϵ-caprolactam. Complete details of these polymerizations and the catalytic stability of PDMS will be discussed in Chapters IV and VI.

3. Methodology

The block diagram of Figure 2-13 indicates the process steps required to accomplish this thesis which utilized many experimental techniques within polymer science. The experimental methodology of each

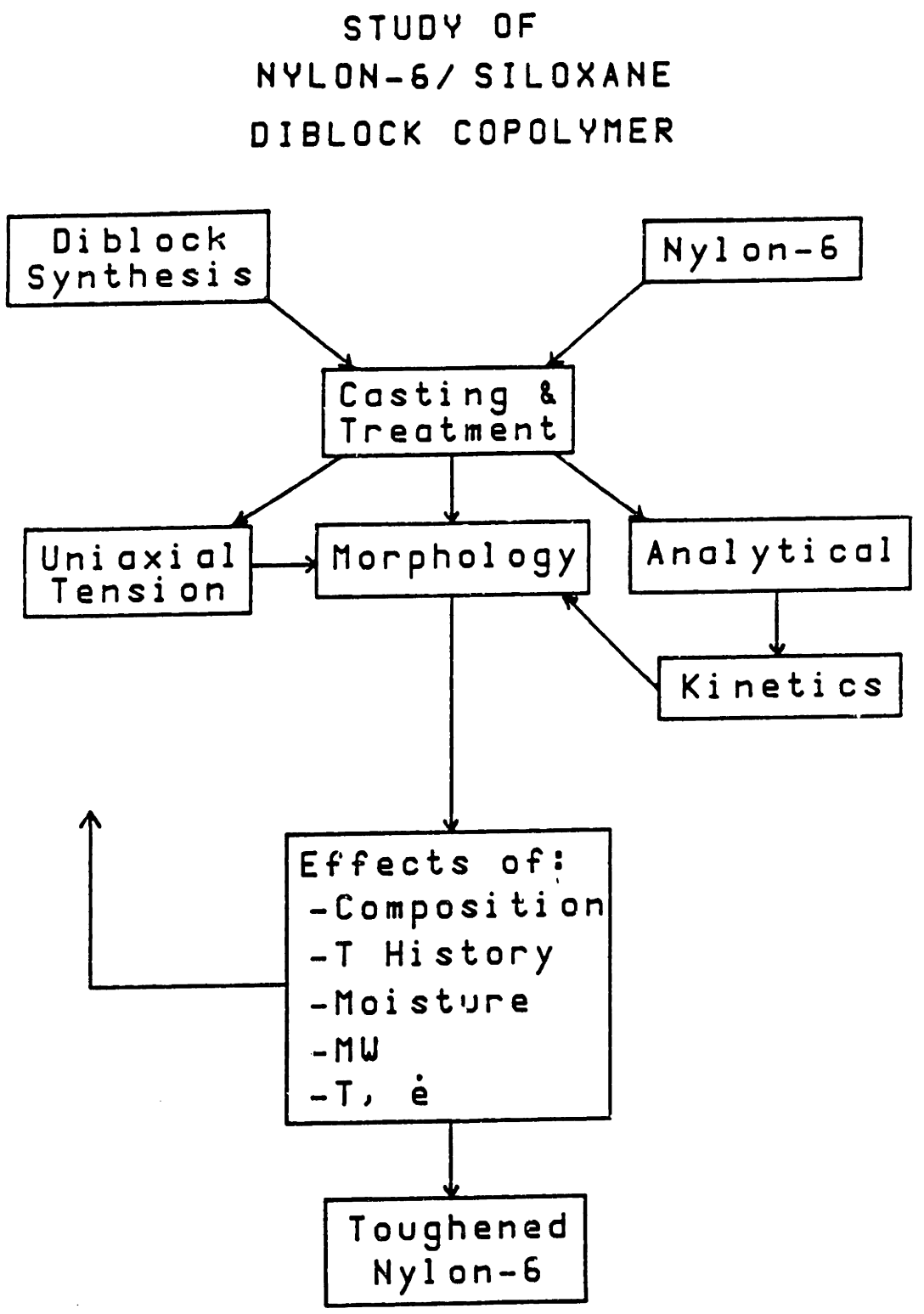

Figure 2-13. The polymer processing block diagram for preparation, testing and characterization of siloxane-nylon-6 diblock copolymers and blends.

block will be discussed in general terms with specifics (including references) being presented in the various chapters where the results are discussed in context. This section is meant to provide an overview of the work to orient the reader for the remaining chapters which deal mostly with experimental results.

Synthesis

The first major step was the synthesis of the new diblock copolymers PTFPMS-nylon-6 and PDMS-nylon-6. Both siloxanes were synthesized via anionic, ring-opening techniques either in bulk or in solution. It was discovered early that the fluoroalkylsiloxane had to polymerized in bulk due to cyclization reactions that drastically reduced the (linear) polymer yield. This was quantified via kinetic modeling which enabled prediction of optimum termination times to maximize the polymer yield at ca. 85%. The PDMS polymerization was done in THF solvent which acted as a promoter as well as a solvent, enhancing the solvation of the Li^+ (n-BuLi was the initiator) counterion away from the siloxanolate to increase reactivity while maintaining high polymer yields. Both growing siloxanolates were terminated with a specially synthesized 11-(dimethylchlorosilyl)-undecanoyl-1-caprolactam coupling/terminating agent that capped the siloxane with an ω-N-acyllactam ring which was capable of initiating anionic polymerization of ϵ-caprolactam. Polydispersities were relatively narrow for PTFPMS ca. 1.2-1.4 versus ca. 1.1-1.2 for PDMS; block molecular weights were ca. 15 kg/mole before copolymerization.

After workup and characterization, the ω-functionalized siloxanes were dispersed in caprolactam and copolymerized using various catalysts

such as caprolactamate salts or substituted lithium aluminum hydrides at temperatures between 150°C and 185°C. Lower temperatures can be employed but will lead to shorter nylon-6 chain lengths due to limited solubility of the polyamide in its monomer. Polyamide-6 molecular weight varied from 45 kg/mole to 100 kg/mole depending on stoichiometry and reaction temperature. The solidified mass was then removed from the reactor and dispersed in TFEtOH and dropwise precipitated/extracted into a large excess of THF. The THF solubilized the unreacted siloxane and monomer, any depolymerized cyclic siloxanes and catalyst as well as oligomeric polyamide-6 leaving only the diblock as the precipitated phase. Filtration and drying followed by a second precipitation/extraction step yielded the final copolymer. In addition, homopolyamide-6 also was synthesized anionically using acetylcaprolactam initiator for use in either blending or mechanical comparison tests.

Casting and Treatment

Films of the copolymer, homopolyamide-6 and binary and/or ternary blends with homopolyamide-6 or PDMS were formed by spin casting or static casting. The latter used teflon-coated aluminum foil dishes in specially-modified dessicators to form the films with an argon purge at room temperature so the rate of solvent removal easily could be controlled. The spin casting used slightly elevated temperatures of 40°C, N_2 flow rates of 0.5 SCFH and the cast took ca. 90 hours to complete for a film thickness of 0.6 – 0.8 mm. After forming the films, they were annealed to remove residual solvent (T_{annl} = 100 – 185°C) and then some of the samples, depending on the desired morphology and degree of crystallinity, were melt annealed to reform the morphology upon cooling from the melt

($T_m|_{ny6}$ ≐ 215-220°C). Films were then conditioned to the desired moisture content by placing them in the vapor space of dessicators containing various aqueous salt solutions and letting them equilibrate. Moisture content was determined via a Mitsubishi moisture analyzer based on conductometric titration of Fisher's reagent. "Dry" test samples were oven dried at 100°C, full vacuum for 24 hours prior to testing and then immediately transported to the testing room in purged, dry, argon-filled stoppered tubes. Moisture analysis showed them to contain ca. 2000 ppm water.

Uniaxial Testing

Mechanical properties were determined in uniaxial tension at constant strain rates on an Instron^R Model 1122 at room temperature under various humidity levels inside an environmental chamber. Humidity in the chamber was maintained by the saturated salt solutions or a stream of dry N_2 for the dry sample tests and monitored by a hygrometer. Various strain rates from $1.3x10^{-4}$ s^{-1} to $1.3x10^{-2}$ s^{-1} were employed.

Morphology

Morphological characterization utilized transmission and scanning electron microscopy (TEM & SEM) and optical light microscopy (OLM). Cryotomed thin film sections contrasted with OsO_4 and phosphotungstic acid (PTA) solutions as well as cast thin-film samples were viewed in the TEM. Thicker sections (ca. 1 μm) also were cryotomed and viewed in the optical microscope under crossed polars to determine spherulitic structure and size, nucleation density, etc. Fracture surfaces of copolymer Instron^R samples were photographed with the SEM. Attempts to reveal the

microstructure via etching with dilute ortho-phosphoric acid (7.8 %w aq) and $KMnO_4$ proved unsuccessful; concentrated acid etches simply swelled or even dissolved the nylon sample.

Analytical

Crystallinity was characterized by differential scanning calorimetry (DSC) and/or a density gradient column with CCl_4/toluene. In addition, wide angle x-ray scattering or WAXS was used semi-quantitatively to characterize the fraction of the crystal lattice as either the α-form (monoclinic) or γ-form (monoclinic, shortened b-axis) although no attempts were made to subtract an estimate of the amorphous scattering and calculate an absolute crystallinity from the WAXS data. Molecular weight analysis of nylon-6 and copolymers was done using DuPont Zorbax^R bimodal (60Å, 1000Å) silanized silica columns with TFEtOH solvent at room temperature and the universal calibration concept with poly(methyl methacrylate) standards. The siloxane molecular weights were analyzed on Waters μ-Styragel^R columns (10^2-10^4Å pore size) in tetrahydrofuran for PTFPMS and in toluene for PDMS at room temperature calibrated by universal values for K', a (the Mark-Houwink constants) for PS and PDMS in toluene. Dynamic mechanical analysis determined the temperatures of the various relaxation processes and the associated effects of microstructure in nylon-6. SAXS analysis of lamellar thickness (or alternately long period) and particulate properties such as interparticle distance and equivalent radius was conducted on films crystallized from the melt and from solution. Using the differential scanning calorimeter (DSC), the crystallization kinetics of homopolyamide-6 versus the diblock

copolymers were studied to compare the various materials' nucleation and growth behavior.

These tools will help reveal the effects of moisture, temperature, strain rate, microstructure and composition on deformation behavior and toughness of homopolymer nylon-6, the diblock copolymers and blends. The correlation of these data and comparison to relevant existing theories are made in the subsequent chapters beginning with the coupling agent synthesis in chapter III. It is hoped that this new, simpler class of siloxane-nylon-6 diblock copolymers will help uncover and define the complex physical responses as a function of material properties for rubber-toughened nylon-6 and other semicrystalline copolymers as well.

E. REFERENCES FOR CHAPTER II

1. Cheng, Pao-Lao, ScD. Thesis, Massachusetts Institute of Technology, June, 1987; F.S. Bates, ScD. Thesis, Massachusetts Institute of Technology, 1982; C.E. Schwier, ScD. Thesis, Massachusetts Institute of Technology, 1984.

2. E.B. Bradford and E. Vanzo, J. Polym. Sci., Polym. Chem. Ed., **6**, 1661 (1968).

3. J.C. Saam, D.J. Gordon and S. Lindsey, Macromolecules, **3**(1), 1 (1970).

4. M.J. Owen and T.C. Kendrick, Macromolecules, **3**(4), 458 (1970).

5. G.L Gaines, Jr. and G.W. Bender, Macromolecules, **5**, 82 (1972).

6. M. Gervais and B. Gallot, Makromol. Chem., **171**, 157 (1973); **178**, 2071 (1977).

7. M. Gervais, B. Gallot, R. Jerome and P. Teyssie, Makromol. Chem., **180**, 2041 (1981).

8. M. Gervais and B. Gallot, Polymer, **22**, 1129 (1981).

9. L.G. Lundsted and I.R. Schmolka, in Block and Graft Copolymerization, R.J. Ceresa, ed., Wiley-Interscience, London, 1976, Ch. 1.

10. M. Morton, Anionic Polymerization: Principles and Practice, Academic Press, New York, 1983, Ch. 9.

11. R.K. Graham, D.L. Dunkelberger and W.E. Goode, J. Am. Chem. Soc., **82**, 400 (1960).

12. P. Rempp and E.W. Merrill, Polymer Synthesis, Huthig & Wepf Verlag Basel, Heidelberg, 1986, p. 216.

13. A. Noshay and J.E. McGrath, Block Copolymers: Overview and Critical Survey, Academic Press, New York, 1977, p. 26.

14. B. Kanner, W.G. Reid and I.H. Peterson, Ind. Eng. Chem., Pdt. Res. Dev., **6**(2), 88 (1967).

15. L.K. Bi and L.J. Fetters, Macromolecules, **8**, 90 (1975); **9**, 732 (1976). check

16. G. Berger, M. Levy and D. Vofsi, Polym. Letters, **4**, 183 (1966).

17. Vandenberg, Preprints IUPAC Symposium on Macromolecular Chemistry, Tokyo, p. N4, (1966).

18. C.H. Bamford and A.D. Jenkins, Nature, **176**, 78 (1955)., C.H. Bamford, A.D. Jenkins and R.P. Wayne, Trans. Faraday Soc., **56**, 932 (1960).

19. Imperial Chemical Industries, Brit. Pat. 1,096,912

20. K. Riches and R.N. Haward, Polymer, **9(2)**, 103 (1968).

21. Commercial product of the Dutch State Mines Co., formerly Nyrim of the Monsanto Co.

22. L.M. Robeson, A. Noshay, M. Matzner and C.N. Merriam, Die Angew. Makromol. Chem., **29/30**, 47 (1973).

23. N. Yui, K. Kataoka, Y. Sakurai, H. Katono, K. Sanui and N. Ogata, J. Bioact. Compat. Polym., **3**, 106 (1988).

24. Y. Gnanou and P. Rempp, Makromol. Chem., **188**, 2111 (1987).

25. G. Greber and E. Reese, Makromol. Chem. **55**, 96 (1962). Y. Chujo, T. Shishino, Y. Tsukahara and Y. Yamashita, Polym. Jnl., **17**, 133 (1985).

26. D.R. Paul and S. Newman, eds., Polymer Blends, Academic Press, London, 1978., Vols. 1,2.

27. R.E. Cohen and D.E. Wilfong, Macromolecules, **15**, 370 (1982).

28 J.H. Hildebrand and R.L. Scott, Regular Solutions, Prentice Hall, Englewood Cliffs, N.J., 1962.

29. P.J. Flory, J. Chem. Phys., **9**, 660 (1941), **10**, 51 (1942).

30. M.L. Huggins, J. Chem. Phys., **9**, 440 (1941); Ann. N.Y. Acad. Sci., **43**, 1 (1942).

31. R.L. Scott, J. Chem. Phys., **17**, 279 (1949).

32. H. Tompa, Trans. Faraday Soc., **45**, 1142 (1949).

33. J.S. Noland, N.N. Hsu, R. Saxon and J.M. Schmitt, Polym. Prepr. Amer. Chem. Soc., Div. Polym. Chem., **11**, 355 (1970).

34. A.E. Van Arkel and S.E. Vles, Trans. Faraday Soc., **42B**, 81 (1946).

35. C.M. Hansen, J. Paint Technol., **39**, 104 (1967); Ind. Eng. Chem., Prod. Res. Dev., **8**, 2 (1969).

36. D.W. Van Krevelen, Properties of Polymers, Elsevier, Amsterdam, 2nd ed., 1976, p.134

37. K.L. Hoy, J. Paint Technol., **42**, 76 (1970).

38. I. Prigogine, The Molecular Theory of Solutions, North Holland Pub., Amsterdam, 1957.

39. P.J. Flory, J. Am. Chem. Soc.,**86**, 1833 (1965).

40. Japanese Patent, 75,006,873, (February 19, 1972).

41. W.K. Fisher, U.S. Patent, 3,806,558 (April 23, 1974).

42. J. Karger-Kocsis, A. Kallo, A. Szafner, G. Bodor and Zs. Senyei, Polymer, **20**, 37 (1979).

43. J. Karger-Kocsis, L. Kiss and V.N. Kuleznev, Polymer Comm., **25**, 122 (1984).

44. J.R. Falender, S.E. Lindsey and J.C. Saam, Polym. Eng. & Sci., **16(1)**, 54 (1976).

45. A.G. Veith, Rubber Chem. Technol., **44**, 962 (1971).

46. R.R. Durst, R.M. Griffith, A.J. Urbanic and W.J. van Essen, Am. Chem. Soc., Adv. Chem. Ser., **154**, 239 (1976).

47. C.B. Bucknall, Toughened Plastics, Applied Science Pub., London, 1977.

48. J. Csernica, R.F. Baddour and R.E. Cohen, Macromolecules, **20**, 2468 (1987).

49. H. Hashimoto, M. Fujimara, T. Hashimoto and H. Kawaii, Macromolecules, **14**, 844 (1981);
T. Hashimoto, M. Fujimara and H. Kawaii, Macromolecules, **13**, 1660 (1980).

50. R.J. Spontak, M.C. Williams and D. A. Agard, Macromolecules, **21**, 1377 (1988).

51. D. Leary and M. Williams, J. Polym. Sci., Pt. B, **8**, 335 (1970);
J. Polym. Sci., Polym. Phys. Ed., **11**, 345 (1973); **12**, 265 (1974).

52. E. Helfand and Z Wasserman in Developments in Block Copolymers, I. Goodman, ed.,Elsevier, London, v.1, 1985, ch 4.

53. T. Inoue, T. Soen, T. Hashimoto and H. Kawaii, J. Polym. Sci., Pt A-2, 7, 1283 (1969).

54. D.J. Meier, J. Polym. Sci., Pt C., **26**, 81 (1969); Am. Chem. Soc., Polym. Prepr., **11**, 400 (1970).

55. M.D. Whitmore and J. Noolandi, Macromolecules, **21**, 1482 (1988).

56. E. Helfand and Z.R. Wasserman, Macromolecules, **9**(6), 879 (1976); **8**, 552 (1975).

57. E. Helfand and Z.R. Wasserman, Macromolecules, **11**(5), 960 (1978).

58. J. Noolandi and K.M. Hong, Macromolecules, **17**, 1531 (1984).

59. J. Noolandi and K.M. Hong, Macromolecules, **15**, 482 (1982).

60. K.M. Hong and J. Noolandi, **16**, 1083 (1983).

61. S. Krause, J. Polym. Sci., Polym. Phys. Ed., **23**, 129 (1985); Macromolecules, **3**, 84 (1970).

62. U. Bianchi, E. Pedemonte and A. Turturro, J. Polym. Sci., Pt B, **7**, 785 (1969).

63. O. Olabisi, L.M. Robeson and M.T. Shaw, Polymer-Polymer Miscibility, Academic Press, New York, 1979, p.38.

64. L. Leibler, Macromolecules, **13**, 1602 (1980).

65. J. Noolandi, Ber. Bunsenges. Phys. Chem.,**89**, 1147 (1985).

66. D.J. Meier, Am. Chem. Soc., Polym. Prepr., Div. Polym. Chem., **18**, 340, 837 (1977).

67. H. Xie, Y. Liu, M. Jiang and T. Yu, Polymer, **27**,1928 (1986); H. Xie and Y. Liu, Makromol. Chem. Rapid Commun., **9**, 79 (1988).

68a. L. Liebler, Macromolecules, **15**, 1283 (1982);
b. Makromol. Chem. Rapid Commun., **2**, 393 (1981).

69. R.-J. Roe and W.-C. Zin, Macromolecules, **13**, 1221 (1980).

70. P.G. deGennes, Scaling Concepts in Polymer Physics, Cornell University Press, Ithaca, N.Y., 1979, ch.10.

71. G.E. Molau, J. Polym. Sci., Pt A, **3**, 1267, 4235 (1965).

72. G. Riess, J. Kohler, C. Tournet and A. Banderet, Makromol. Chem., **101**, 58 (1967);
J. Kohler, G. Riess and A. Banderet, Eur. Polym. J., **4**, 173, 187 (1969).

73. G. Riess and Y. Jolivet, in Copolymers, Polyblends and Composites, Am. Chem. Soc., Adv. in Chem. Series, N.A.J. Platzer, ed., Washington, D.C., 1975, p.243;

74. T. Inoue, T. Soen, T. Hashimoto and H. Kawaii, J. Polym. Sci., Pt A-2, **7**, 1283 (1969); Macromolecules, **3**, 87 (1970).

75. T. Hashimoto, K. Nagatoski, A. Todo, H. Hasegawa and H. Kawaii, Macromolecules, 7(3), 364 (1974).

76. H. Hashimoto, M. Fujimara, T. Hashimoto and H. Kawaii, Macromolecules, 14, 844 (1981).

77. G. Porod, Kolloid Z.Z. Polym., 124(2), 83 (1951); 125(1), 51 (1952); 125(2), 108 (1952).

78. A.R. Ramos and R.E. Cohen, Polym. Eng. & Sci., 17(8), 639 (1977); Am. Chem. Soc., Polym. Prepr., Div. Polym. Chem., 18(1), 335 (1977); 19(1), 87 (1978).

79. R.E. Cohen and A.R. Ramos, Macromolecules, 12, 131 (1979).

80. R.E. Cohen, ACS Symposium Ser., #193, Elastomers and Rubbe Elasticity, J.E. Mark, ed., 1982, p. 489.

81. F.S. Bates, C.V. Berney and R.E. Cohen, Macromolecules, 16, 1101 (1983).
C.V. Berney, F.S. Bates and R.E. Cohen, Polymer, 23, 1222 (1982).

82. R.-J. Roe, M. Fishkis and J.C. Chang, Macromolecules, 14, 1091 (1981).

83. R.-J. Roe and W.-C. Zin, Macromolecules, 17, 183, (1984);

84. R.-J. Roe and W.-C. Zin, Macromolecules, 17, 189 (1984).

85. T. Hashimoto, Y. Tsukahara and H. Kawaii, Macromolecules, 14, 708 (1981).

86. T. Hashimoto, K. Kowsaka, M. Shibayama and H. Kawaii, Macromolecules, 19, 750 (1986).

87. S. Krause, Macromolecules, 10(4), 870 (1977).

88. R.-J. Roe and S. Nojima, Macromolecules, 20, 1866 (1987).

89. T. Hashimoto, M. Shibayama, H. Kawaii, H. Watanabe and T. Kotaka Macromolecules, 16, 361 (1983).

90. L. Leibler, H. Orland and J.C. Wheeler, J. Chem. Phys., 79(7), 3550 (1983).

91. R.-J. Roe, Macromolecules, 19(3), 728 (1986).

92. D. Rigby and R.-J. Roe, Macromolecules, 17, 1778 (1984); 19, 721 (1986).

93. D.J. Kinning, E.L. Thomas and L.J. Fetters, J. Chem. Phys., submitted Dec, 1988.

94. M.D. Whitmore and J. Noolandi, Macromolecules, **18**, 657 (1985).

95. J. Selb, P. Marie, A. Rameau, R Duplessix and Y. Gallot, Polym. Bull., **10**, 444 (1983).

96. C.V. Berney, P.-L. Cheng and R.E. Cohen, Macromolecules, **21**, 2235 (1988).

97. M.R. Munch and A.P. Gast, Macromolecules, **21**, 1360 (1988).

98. E.A. DiMarzio, C.M. Guttman and J.D. Hoffman, Macromolecules, **13**, 1194 (1980); Bull. Am. Phys. Soc., **24**, 382 (1979).

99. B. Lotz, A.J. Kovacs, G.A. Bassett and A. Keller, Kolloid. Z. u Z. Polym., **209**, 97, 115 (1966).

100. B. Wunderlich, Macromolecular Physics, Academic Press, London, volume 1, 1973, ch 3.

101. A. Keller, Jnl. Polym. Sci., **39**, 151 (1959);
B. Wunderlich, Jnl. Polym. Sci., Pt C, **1**, 41 (1963).

102. D.C. Bassett and R.H. Olley, Polymer **25**, 935 (1984).

103. D.C. Bassett, S. Mitsuhashi and A. Keller, Jnl. Polym. Sci., Pt. A, **1**, 73 (1963).

104. D.C. Bassett and A.S. Vaughn, Polymer **26**, 717 (1985).

105. D.R. Norton and A. Keller, Polymer **26**, 704 (1985).

106. B. Wunderlich, Macromolecular Physics, Academic Press, London, volume 2, 1973.

107. J.I. Lauritzen, Jr., Jnl. Appl. Phys.,**44**, 4353 (1973).

108. J.D. Hoffman, G.T. Davis and J.I. Lauritzen, in Treatise on Solid State Chemistry, Crystalline and Noncrystalline Solids, ed. H.B. Hannay, Plenum Press, New York, vol. 3, 1976, Ch 7, p. 497.

109. J.D. Hoffman, SPE Transactions, October, 1964, p.315.

110. F. Gornick, J.D. Hoffman, Ind. Eng. Chem., **58**(2), 41 (1966).

111. J.D. Hoffman, Polymer, **26**, 1763 (1985).

112. J.D. Hoffman, Polymer Communications, **27**, 39 (1986).

113. E. Martuscelli, C. Silvestre and G. Abate, Polymer **23**, 229 (1982).

114. E. Martuscelli, Polym. Eng. Sci., **24**(8), 563 (1984).

115. E. Hirata, T. Ijitsu, T. Soen, T. Hashimoto and H. Kawaii, in Copolymers, Polyblends and Composites, Am. Chem. Soc., Adv. in Chem. Series, N.A.J. Platzer, ed., Washington, D.C., 1975, p.288.

116. T. Kawaii, S. Shiozaki, S. Sonoda, H. Nakagawa, T. Matsumoto and H. Maeda, Makromol. Chem., **128** 252 (1969).

117. P.J. Flory, Principles of Polymer Chemistry, Cornell University Press, Ithaca, N.Y., (1953), p. 574.

118. P.J. Flory and L. Mandelkern, Jnl. Am. Chem. Soc., **73**, 2532 (1951).

119. R.B. Richards, Trans. Far. Soc., **42**, 10 (1946);
H.C. Raine, R.B. Richards and H. Ryder, Trans. Far. Soc., **41**, 56 (1945).

120. J.R. Kastelic and E. Baer, Jnl. Macromol. Sci., Phys., **B7**(4), 679 (1973).

121. A.M. Donald and E.J. Kramer, Jnl. Mat. Sci., **17**, 1871 (1982).

122. A.S. Argon and M.M. Salama, Phil. Mag., **36**, 1217 (1977).

123. G.W. Hawkins, PhD dissertation, Dept. Mechanical Engineering, M.I.T., 1983.

124. C.B. Bucknall and R.R. Smith, Polymer, **6**, 437 (1965).

125. C.B. Bucknall and D. Clayton, Jnl. Mat. Sci., **7**, 202, 1443, (1972).

126. A.M. Donald and E.J. Kramer, Jnl. Mat. Sci., **17**, 1765 (1982).

127. P.B. Bowden and R.J. Young, Jnl. Mat. Sci., **9**, 2043 (1974).

128. J.M. Schultz, Polym. Eng. & Sci., **24**(10), 770 (1984).

129. E. Hornbogen and K. Friedrich, Jnl. Mat. Sci., **15**, 2175 (1980).

130. J. Patel and P.J. Phillips, Jnl. Polym. Sci., Polym. Lttrs. Ed., **11**, 771 (1973).

131. L.S. Remaly and J.M. Schultz, Jnl. Appl. Polym. Sci., **1**, 114 (1970).

132. A.J. Lovinger and M.L. Williams, Jnl. Appl. Polym. Sci., **25**, 1703 (1980).

133. F.P. Price and R.W. Kilb, Jnl. Polym. Sci., **57**, 395 (1962).

134. J.L. Way, J.R. Atkinson and J. Nutting, Jnl. Mat. Sci., **9**, 293 (1974).

135. L.W. Kleiner, M.R. Radloff, J.M. Schultz and T.W. Chou, Jnl. Polym. Sci., Polym. Phys. Ed., **12** 819 (1974).

136. J.M. Schultz, Jnl. Polym. Sci., Pt A-2, **7**, 821 (1969).

137. H.W. Starkweather, Jr., R.E. Brcoks, J. Appl. Polym. Sci., **1**(2), 236 (1959).

138. V.A. Kargin, T.I. Sogolava, N. Ya. Rappaport, I.I. Kurbanova, J. Polym. Sci., **16C**, 1609 (1967).

139. F.J. Padden, Jr., H.D. Keith, J. Appl. Phys., **30**, 1479 (1959).

140. C.F. Hammer, T.A. Koch, J.F. Whitney, J. Appl. Polym. Sci., **1**, 169 (1959).

141. A. Sandt, Doktorarbeit, Ruhr-Universitat Bochum, 1981.

142. R.J. Young, P.B. Bowden, J. Ritchie and J.G. Rider, Jnl. Mat. Sci., **8**, 23 (1973).

143. J.C. Halpin and J.C. Kardos, Jnl. Appl. Phys., **43**(5), 2235 (1972).

144. W.R. Krigbaum, R.T. Roe and K.J. Smith, Polymer, **5**, 533 (1964).

145. M. Takayanagi, Fourth Internatonal Congress on Rheology, ed. E.H. Lee and A.L. Copley, Wiley, New York, 1965.

146. T.T. Wang, Jnl. Appl. Phys., **44**(5), 2218 (1973).

147. R.J. Samuels, Jnl. Macromol. Sci., Phys., **B4**(3), 701 (1970).

148. R.J. Samuels in The Science and Technology of Polymer Films, ed. O.J. Sweeting, Interscience Pub., New York, 1968, v. 1, Ch. 7, p. 255.

149. A. Galeski, A.S. Argon and R.E. Cohen, Macromol., **21**, 2761 (1988).

150. A. Schaper, R. Hirte and C. Ruscher, Coll. Polym. Sci., **264**, 668 (1986).

151. R.S. Stein, Polym. Eng. and Sci., **9**, 320 (1969).

152. K. Sasaguri, S. Hoshino and R.S. Stein, Jnl. Appl. Phys.,**35**, 47 (1964).

153. T. Oda, S. Nomura and H. Kawaii, Jnl. Polym. Sci., **A3**, 1993 (1965).

154. A.S. Argon and D. Parks, M.I.T., private communication, 1989.

155. A. Peterlin, Jnl. Mat. Sci., **6**, 490 (1971).

156. A. Peterlin, Jnl. Polym. Sci., **C18**, 123 (1967).

157. A. Peterlin, Polym. Eng. Sci., **9**(3), 172 (1969).

158. A. Peterlin, Jnl. Phys. Chem., **75**(26), 3921 (1971).

159. F.J. Balta-Calleja and A. Peterlin, Jnl. Macromol. Sci., Phys., **B4**(3), 519 (1970).

160. P. Vincent, Polymer, **1**, 7 (1960).

161. M. Nakamura and S.M. Skinner, Jnl. Polym. Sci., **18**, 423 (1955).
162. A. Peterlin, Jnl. Macromol. Sci., **B19**(3), 401 (1981).

163. I.L. Hay and A. Keller, Kolloid. Z.Z. Polym., **294**, 43 (1965).

164. B.H. McConkey, M.W. Darlington, D.W. Saunders and C.G. Cannon, Jnl. Mat. Sci., **6**. 572 (1971).

165. P. Predecki and A.W. Thornton, Jnl. Appl. Phys., **41**, 4342 (1970).

166. J.L. Way and J.R. Atkinson, **6**, 102 (1971).

167. I.M. Ward, Mechanical Properties of Solid Polymers, Wiley, 2nd ed., Chichester, 1983, Ch. 10.

168. R.J. Young and P.B. Bowden, Jnl. Mat. Sci.,**8**, 1177 (1973).

169. G.J. Sandilands, J.R. White, J. Mat. Sci., **12**, 1496 (1977).

170. K. Friedrich, Adv. in Polym. Sci., **52/53**, ed. H.H. Kausch, Springer Verlag, 1983, p. 225.

171. H.G. Olf, A. Peterlin, J. Polym. Sci.: Polym. Phys. Ed., **12**, 2209 (1974).

172. H.H. Kausch, Kunstoffe, **66**, 538 (1976).

173. B.Z. Jang, D.R. Uhlmann and J.B. Vander Sande, Polym. Eng. & Sci., **25**(2), 98 (1985).

174. T.E. Brady and G.S.Y. Yeh, Jnl. Mat. Sci.,**8**, 1083 (1973).

175. I.I. Ostrominslensky, (Naugatuck Chemical) US Pat 1,613,673, Jan. 11, 1927.

176. E.N. Kresge, in Polymer Blends, ed. D.R. Paul and S. Newman, Academic Press, New York, 1978, ch 20.

177. C.B. Bucknall, Toughened Plastics, Applied Science Publishers, London, 1977.

178. S. Wu, J. Polym. Sci: Polym. Phys. Ed., **21**, 699 (1983).

179. M. Matsuo, T.T. Wang, T.K. Kwei, J. Polym. Sci.: A-2, **10**, 1085 (1972).

180. M.E. Boyce, A.S. Argon and D.M. Parks, Polymer, **28**, 1680 (1987).

181. R.H. Beck, S. Gretch, S. Newman and K.C. Rusch, Polym. Lttrs., **6**, 707 (1968).

182. L.J. Broutman and G. Panizza, Intl. Jnl. Polym. Mat., **1**, 95 (1971).

183. J.N. Goodier, J. Appl. Mech. (Transactions of ASME), **55**, A39, (1933).

184. T. Ricco, A. Pavan, F. Danusso, Polymer Eng. and Sci., **18**(10), 774, 1978.

185. C.B. Bucknall, D. Clayton and W.E. Keast, Jnl. Mat. Sci., **7**, 1443 (1972).

186. A.J. Kinloch and R.J. Young, Fracture Behavior of Polymers, Elsevier Applied Science Publishers, London, 1983, Ch. 11.

187. S. Newman, in Polymer Blends, ed. D.R. Paul and S. Newman, Academic Press, New York, 1978, Ch. 13.

188. C.B. Bucknall in Polymer Blends, ed. D.R. Paul and S. Newman, Academic Press, New York, 1978, Ch. 14.

189. S.T. Wellinghoff and E. Baer, Jnl. Appl. Polym. Sci., **22**, 2025 (1978).

190. A.S. Argon, R.E. Cohen, O.S. Gebizlioglu and C.E. Schwier, Adv. Polym. Sci.; Crazing in Polymers, ed. H.H. Kausch, Springer Verlag, Berlin, **52/53**, 1983, p. 275.

191. C.E. Schwier, A.S. Argon and R.E. Cohen, Philosophical Magazine, **52**(5), 581 (1985).

192. O.S. Gebizlioglu, A.S. Argon and R.E. Cohen, Polymer, **26**, 519, 529 (1985).

193. Polymer Blends, ed. D.R. Paul and S. Newman, Academic Press, New York, 1978.

194. J.A. Manson and L.H. Sperling, eds. Polymer Blends and Composites, New York, Plenum, 1976.

195. L.M. Robeson, Polym. Eng. & Sci., **24**(8), 587 (1984).

196. C.E. Locke and D.R. Paul, Jnl. Appl. Polym. Sci., **17**, 2597, 2791 (1973).

197. W.M. Barentsen and D. Heikens, Polymer, **14**, 579 (1973), **15**, 119 (1974).

198. W.J. Coumans, D. Heikens and S.D. Sjoerdsma, Polymer, **21**, 103 (1980).

199. H. Breuer, F. Haaf and J. Stabenow, Jnl. Macromol. Sci., Phys., **B14**(3), 387 (1977).

200. E.A. Flexman, Polym. Eng. Sci., **19**(8), 564 (1979).

201. S. Wu, Polymer, **26**(11), 1855 (1985).

202. S. Wu, Polymer Interface and Adhesion, Marcel Dekker, N.Y., 1982.

203. R. Pfluger, Polymer Handbook, J. Brandrup and E.H. Immergut, eds, 2nd ed., Interscience Pub., New York, 1975, pp. V79 - V86.

204. L. D'Orazio, C. Mancarella, E. Martuscelli, A. Casale, A. Filippi, F. Speroni, J. Mat. Sci., **21**, 989 (1986).

CHAPTER III. COUPLING AGENT SYNTHESIS

The coupling agent, 11-(dimethylchlorosilyl)-1-oxo-1-(1'-aza-2'--oxocycloheptyl)-n-undecyl is the monomeric compound containing two functional groups for reaction with the growing siloxanolate and initiation of the caprolactam monomer. Alternatively, its common name, 11-(dimethylchlorosilyl)-undecanoyl-1-caprolactam (abbreviated DMCSUCL), will be used throughout the remainder of the thesis. This compound will form the essential linkage between the inorganic silicone polymer and the polyamide-6 block and is necessary because of the hydrolytic instability of the silicic acid ester (>Si–O–CO–) or silazane (–O>Si–NH–) linkages which would be formed from more naive syntheses. These unsuitable bonds would occur if the siloxanolate was used to sequentially attack an bisacyllactam as an example of the former or if a chlorosilyl end group and terminal amine were condensed as representative of the latter. Rather the >Si–C< bond is preferred because of its superior hydrolytic stability [1], especially in strong alcoholic solvents with lower pK_a such as TFEtOH.

However, use of the Si–C bond alone is not sufficient to ensure good hydrolytic stability; juxtapostion between it and the acyl carbonyl is also of paramount importance. It is known that the carbonyl β to the silicon creates the weakest Si–C bond to both electrophiles and nucleophiles [2] due to the alternating relative polarizability ($\delta^{-,+}$) of the bonds as a result of the more electropositive Si versus C as shown in equation (3-1).

$$-\underset{\delta^+}{Si}-\overset{\alpha}{\underset{\delta^-}{C}}-\overset{\beta}{\underset{\delta^+}{C}}-\overset{\gamma}{C}-\qquad \overset{\delta^-}{O} \tag{3-1}$$

This weakness further decreases for the position of the carbonyl to the Si in the order α, γ, δ, etc. (α being next weakest and so on). Thus, a long chain acyl group such as undecanoyl is preferred over an acryloyl group for example because the withdrawing and weakening effects of the carbonyl are far removed from the Si–C bond in the former but are only γ-removed in the latter.

The coupling agent chemistry of this thesis is similar but not identical to that of Owen and Thompson [3]. These investigators started with a carboxylic acid which was converted to an acid chloride via sulfonyl chloride treatment followed by neutralization with two equivalents of caprolactam to give an N-acylcaprolactam. In this thesis work, a commercially available, high purity alkenyl acid chloride was acylated directly to caprolactam using a stoichiometric equivalent of pyridine as the acid acceptor and the hydrosilylation or addition reaction of the dimethylchlorosilyl group was conducted using a new catalyst delivery system. Owen and Thompson went on to solution polymerize PDMS-nylon-6 diblock copolymers of low molecular weight which will be discussed in Chapter VI.

A. N-ACYLLACTAM SYNTHESIS AND CHARACTERIZATION

The synthesis of the coupling agent is accomplished in two steps. First, 10-undecenoyl chloride (98+%, Aldrich) is acylated to ϵ-caprolactam (98%, Alfa) using pyridine base. The caprolactam is dried by

distillation and the middle cut is dissolved in anhydrous diethyl ether (DEE); solubility limit +15°C. The acid chloride is used as received and added dropwise in stoichiometric proportions to both caprolactam (CPL) and pyridine with stirring under argon. The reaction is highly exothermic and reactor temperature is kept at ≈20°C by an ice/water cooling bath. The chemistry is shown below.

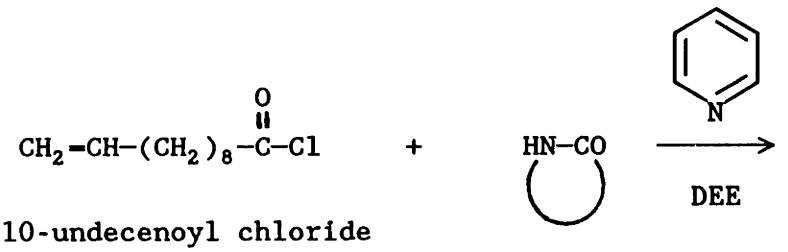

10-undecenoyl chloride

CPL

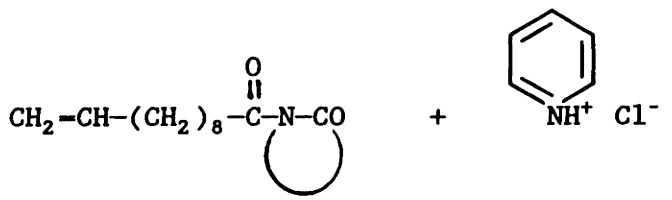

(3-2)

10-undecenoyllactam (UDL)

pyridinium chloride

The by-product pyridinium chloride is mostly insoluble in DEE and the product is separated by filtration followed by extraction with distilled water to remove trace salts. First, the solution of the acylated lactam (UDL)/DEE is cooled to -5°C to precipitate any unreacted caprolactam and cold filtered through a 10 μm filter. The ethereal solution of the acyllactam is then twice washed with 2-4X volume distilled water in a separatory funnel. The wet solution is stirred over anhydrous magnesium sulfate, filtered and the DEE is rotary evaporated to

leave a yellowish-orange oily residue which is stored in the dark under argon. The solids formed from the acylation are water soluble confirming the existence of pyridinium chloride and full progress of the reaction. The yield was quantitative and gas chromatography (3% OV-17 on Supelcoport columns, T_o = 25°C and T_f = 300°C with ramp of 4°C/min, He flow rate at ~ 10 ml/min., FID detector) shows a residue purity of 99.6% (assuming unity response factors). The IR spectrum indicates the olefinic C-H stretch at 3050 and 1640 cm^{-1}, the broad carbonyl stretch at 1700 cm^{-1}, and the C-N stretch between 1300 and 1400 cm^{-1}. No nitrile absorption bands are present, which would indicate an unwanted side reaction.

NMR also confirms the desired product. Summation of the spectra for the caprolactam and acid chloride gives exactly the observed spectrum of the acylated lactam, UDL minus the broad downfield singlet from the amide proton of caprolactam. The spectrum is shown in the top panel of Figure 3-1a. The tall singlet at approximately 1.3 ppm is due to the magnetically equivalent aliphatic methylenes (from the acid chloride), the cyclic CH_2's multiplet (from caprolactam) resonating just further downfield at approximately 1.7 – 1.8 ppm. The first-order splitting of the methylene's alpha to the carbonyls is shown at 2.72 ppm for the aliphatics and at 2.85 for the cyclic protons and at 3.9 for the CH_2's alpha to the imide nitrogen. The characteristic multiplet at 5.8 ppm and the triplet at 5.0 ppm signify the vinylic protons.

B. HYDROSILYLATED ACYLLACTAM SYNTHESIS AND CHARACTERIZATION

Hydrosilylation of the vinyl group in UDL completes the synthesis of the coupling agent. The organosilicon is prepared by adding dimethylchlorosilane (DMCS) to the double bond using hydrated hydrochloroplatinic

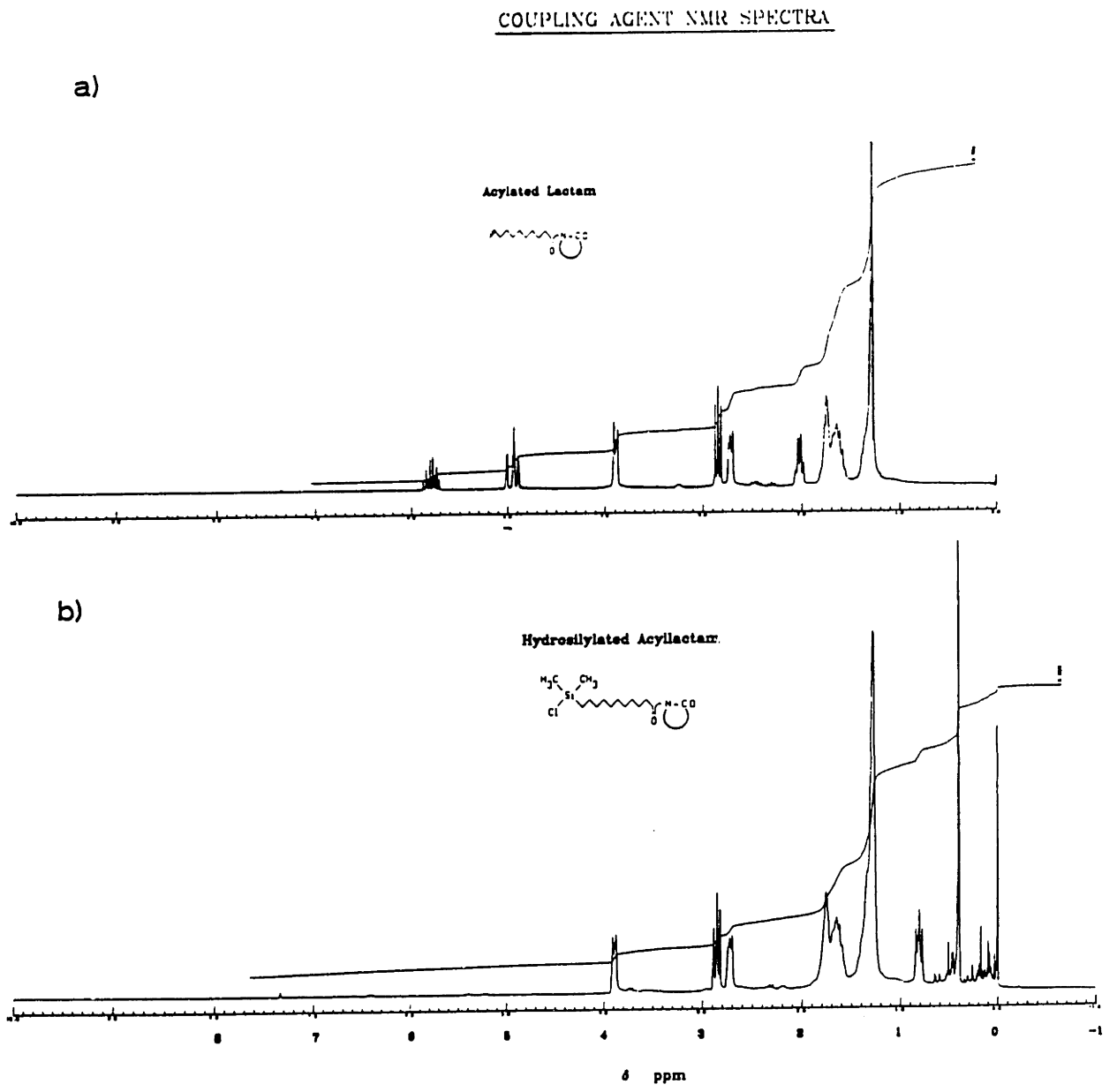

Figure 3-1a ^{1}H NMR spectrum of intermediate 10-undecenoyl-1-caprolactam, (UDL).

3-1b ^{1}H NMR spectrum of the coupling agent, 11-(dimethylchlorosilyl)-n-undecanoyl-1-caprolactam, (DMCSUCL).

acid (CPA) or $H_2PtCl_6 \cdot 6H_2O$ as catalyst via standard synthesis techniques [4]. Many olefins, including halogen-substituted alkenes [5-8], have been successfully hydrosilylated by CPA with yields >90% using various silanes. The reaction has the benefits of leading precisely to the theoretically predicted products with negligible side reactions. The chemistry is shown in equation (3-3).

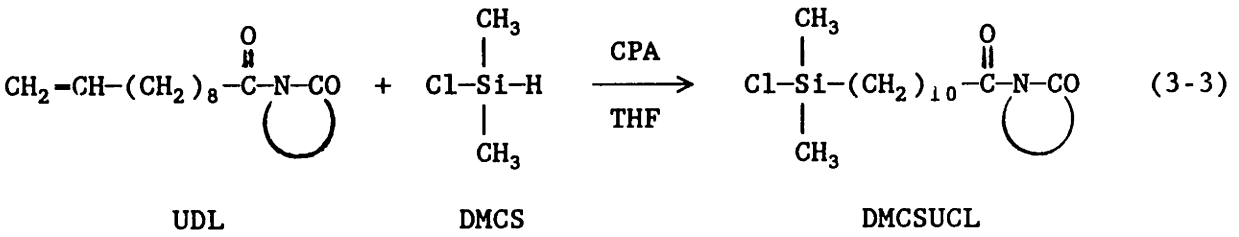

(3-3)

UDL DMCS DMCSUCL

No data in the literature [4,9] have been reported for hydrosilylation of N-alkenylacyllactams except for reference [3] which did not give any details of the reaction. Consequently, various catalyst systems were studied by independently varying the catalyst solvent (such as acetone, diethyl ether and tetrahydrofuran (THF)), concentration of reagents and reaction temperature. It was determined that THF was the best solvent for catalyst delivery because it combined the requisite polarity necessary for solubility of the CPA and is inert because it contains no labile protons. High temperatures (> 100°C) are to be avoided in this reaction due to oligomerization (i.e. production of dimers, trimers, etc.) of the alkene in toluene as confirmed by multiple peaks on the GC chromatogram (not shown). The catalyst is extremely active, efficiently coordinating the incoming silane to the double bond and Pt concentrations of 10^{-4} M (or gmol l^{-1}) were routinely used successfully. The reaction

was run in excess silane or alternatively, THF was used as the reactor solvent combined with just a twofold stoichiometric excess of DMCS. The reaction was allowed to proceed overnight at temperatures of 25 – 50°C (the higher temperatures being required when THF is used as the reactor solvent) which produced a much lighter, paler yellowish solution. Workup consisted of simply removing the excess DMCS and solvent via distillation. The coupling agent is very moisture and light sensitive and must be stored in the dark under argon and is easily transferred via gas tight syringe when needed.

Essentially 100% conversion was obtained as verified by IR spectroscopy and NMR spectrometry. The product (hydrosilylated acyllactam) showed pronounced structural changes as determined by IR where new dimethylsilyl absorptions characteristic of the Si–C stretch are evident at 800 cm^{-1} and 850 cm^{-1} and a broad peak at 1050 – 1100 cm^{-1}. The disappearance of the trans vinyl absorptions at 950cm^{-1} and the olefinic C-H stretch at 3160 cm^{-1} and 1680 cm^{-1} indicated addition across the double bond.

The hydrosilylated structure was confirmed by NMR analysis (250MHz, Bruker), which indicated successful hydrosilylation, bottom panel Figure 3-1b. Here, the dimethylchlorosilyl peak (from DMCS) is deflected downfield to 0.45 ppm from the tetramethylsilane (TMS) internal reference by the electronegative chlorine substituent. The aliphatic methylene proton (1.3 ppm) signal intensified as one additional $-CH_2-$ unit was produced and the cyclic methylene protons (1.3 and 1.75 ppm) remained intact, far removed from the effects of hydrosilylation. The other new $-CH_2-$ protons, α–substituted to the silyl group moved upfield

to 0.9 ppm due to the electropositive effect of Si and represent approximately two protons via integration. The disappearance of the vinyl group multiplet and triplet (δ=5.8 ppm and 5.0 ppm, respectively) is complete (compare top and bottom panels of Figure 3-1) and gas chromatography showed only a single peak confirming the selectivity of the hydrosilylation reaction, i.e. nearly 100% α-addition of the Si to the unsaturation as opposed to the β-addition isomer.

Elemental analysis of the hydrosilylated acyllactam or alternatively DMCSUCL, was performed by Scharwzkopf laboratories (New York) and gave very good agreement between theory and experiment as shown in Table 3-1. Thus, a combined effort consisting of NMR, IR, GC and elemental analysis was used to verify the coupling agent structure. The coupling agent can now be used to terminate the growing siloxane polymers (via the chlorosilyl group) functionalizing them for initiation and polymerization of caprolactam. Next, in Chapter IV, the chemistry of the siloxane polymers will be discussed including an introduction to silicones, experimental polymerization conditions and limited kinetics of the dimethylsiloxane polymerizations as well as kinetic modeling of the trifluoropropylmethylsiloxane polymerization.

Table 3-1

Elemental Analysis of the Coupling Agent

	Mole Percent				
	N	C	H	Si	Cl
Theoretical	3.8	61.0	9.6	7.5	9.5
Experimental	3.7	60.7	9.8	7.8	8.7

C. REFERENCES FOR CHAPTER III

1. W. Noll, Chemistry and Technology of Silicones, Academic Press, New York, N.Y., 1968, p. 642.

2. Ibid., p. 317-324.

3. M.J. Owen and J. Thompson, Br. Polym. Jnl., **4**, 297 (1972).

4. W. Noll, Chemistry and Technology of Silicones, Academic Press, New York, N.Y., 1968.

5. R.W. Bott, C. Eaborn, K. Leyshon, Jnl. Chem. Soc., (London), 1548 (1964).

6. J.L. Speier, J.A. Webster, G.H. Barnes, Jnl. Am. Chem. Soc., **79**, 974 (1957).

7. A.D. Petrov, V.F. Mironov, V.A. Ponomarenko, S.I. Sadykh-Zade, E.A. Chernyshev, Bull. Acad. Sci. USSR, No. **8**, 926 (1958).

8. V.M. Vdovin, A.D. Petrov, Jnl. Gen. Chem. USSR, **30**, 852 (1960).

9. C. Eaborn, Organosilicon Compounds, Butterworth's Pub. Ltd., London, 1960, p.45.

CHAPTER IV. SILOXANE SYNTHESIS

A. GENERAL INTRODUCTION TO SILICONE POLYMERS

Silicone polymers are extremely versatile possessing a range of attractive material properties that include high oxygen permeability, low surface tension, good weathering resistance, moderate thrombogenicity, very low glass transition temperature and chemical versatility which permits network formation, grafting reactions and other chemical modifications to be conducted. High molecular weight siloxanes can be prepared by either hydrolysis and condensation of chlorosilanes or ring opening, re-equilibration polymerization of cyclic siloxanes catalyzed by both acids and bases. The two processes are closely interrelated because cyclic oligomers are by-products of the condensation reactions and also are used as monomers for the catalyzed ring opening polymerizations. It is not completely understood but both of these reaction pathways (condensation and ring-opening) may be operative simultaneously as in the H_2SO_4 catalyzed redistribution of octamethylcyclotetrasiloxane, for example [1]. Thus, the polymerization of silanols/siloxanes with traditional acid and alkali catalysts (e.g. H_2SO_4 and KOH) involves molecular equilibrium or the redistribution of an initial mixture of silanes/siloxanes into a Gaussian molecular weight distribution of siloxanes including linear polymer and cyclic oligomers.

In comparing organosilicon chemistry to organic carbon chemistry, two properties are of fundamental importance. First, silicon has a lower electronegativity than carbon imparting a more pronounced ionic character to siloxane linkages [2]. Thus, $\equiv Si\text{-}O:^-$ is a slightly stronger nucleophile than the corresponding alkoxide, $\equiv C\text{-}O:^-$. Increased electronega-

tivity of the substituent groups to Si, like the 3,3,3-trifluoropropyl group, decreases the positive induction effect and strengthens the Si–X bond where X = halogen (i.e. more resistance to acid hydrolysis). This reduces the rate of hydrolysis and condensation versus methyl or propyl substituents. Electronegative substituents facilitate easier cleavage by base of the Si–O bond because the relative positive character of the Si is enhanced by the electron withdrawing groups. Thus anionic polymerization is more facile with electronegative substituents whereas cationic polymerization rates are enhanced with electron-donating groups. In addition, bulky substituents behave similarly to electronegative groups which is why octamethylcyclotetrasiloxane is much more readily polymerized by acid catalysts versus octaphenylcyclotetrasiloxane which is polymerized almost wholly by basic catalysts such as KOH [3].

Secondly, silicon, unlike carbon, has the ability to use 3-d orbitals in bond formation extending its valence sphere to the pentavalent state [2]. This is important in understanding the reaction mechanism of nucleophilic attack on silicon as in base catalyzed ring opening polymerization (ROP) which will be demonstrated in §A.2.

1. Hydrolysis and Condensation

To produce high molecular weight siloxane polymers, bifunctional chlorosilanes are required. These are catalytically hydrolyzed under acidic or basic conditions [4,5] to the disilanols which subsequently condense to yield macromolecules. A typical acid catalyst is 50% H_2SO_4 where protonation of the silanol oxygen forms the oxonium ion which cleaves via nucleophilic attack from another silanol molecule.

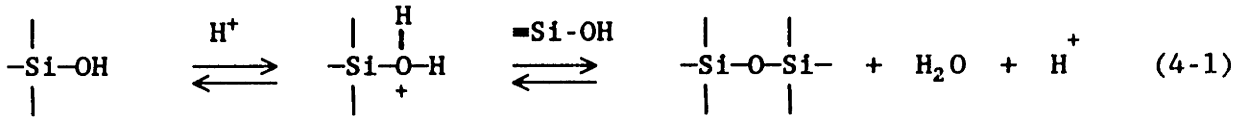

(4-1)

As mentioned previously, this condensation can occur intramolecularly generating cyclic siloxanes which may be able to subsequently ring open concurrently with condensation as discussed in §A.2. The electronegativity of the trifluoropropyl group severely reduces the condensability of 3,3,3-trifluoropropylmethylsilanol catalyzed by mineral acids. Consequently, stronger specialized catalysts are used, namely perfluorinated alkyl sulfonic acids [6] if these electronegatively substituted silanes need to be condensed.

Potassium hydroxide frequently is used as the basic catalyst which abstracts a silanol proton followed by nucleophilic attack of the oxanion on another silanol establishing the pentavalent silicon transition complex.

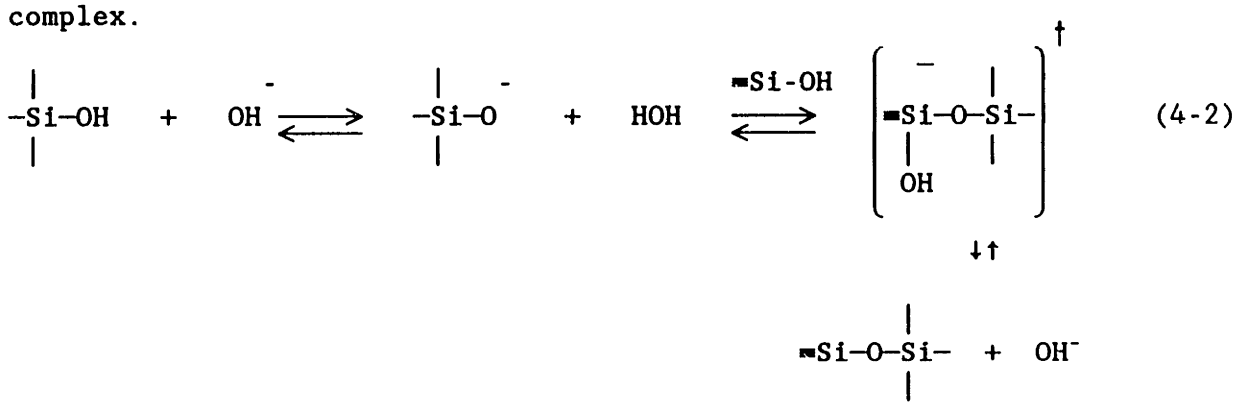

(4-2)

Cleavage of the silanol bond liberates the catalyst and forms the siloxane.

Typical polymer condensation yields are low, ca. 20-40% depending on the monomer with the remainder being cyclic oligomers. Although the

above reagents will yield linear polymeric siloxanes, the true nature of the reaction is simply re-equilibration of the cyclic oligomers with straight-chain polymer by the acid and base catalysts; these catalysts simply drive a greater fraction of the cyclics towards polymer by shifting the equilibrium. An alternate, more controllable and practical route to higher molecular weight siloxanes (MW > 8-10 kg/mole) is achieved by ring opening polymerization using the lithium counterion which sufficiently suppresses the cyclization and redistribution reactions giving much higher polymer yields.

2. Ring Opening Polymerization

The distinction between ring opening polymerization and condensation polymerization is in the starting material and the reactor medium/operating conditions. In ROP, the cyclic oligomer by-products of condensation polymerization are used as the monomer and initiated by acid or base catalysts which results in cationic or anionic propagation, respectively. Cationic catalysts can be mineral acids, such as H_2SO_4 [5] or HNO_3 [6], organic acids, e.g. trifluoromethyl sulfonic acid [7,8] and Lewis acids such as BF_3 [9] and $SnCl_4$ [10] which are largely proprietary. Most commercial production of octamethylcyclotetrasiloxane is still accomplished via acid-catalyzed ring opening polymerization. Again, with bulky and electronegative Si substituents, condensation reactions in cationic polymerization become more difficult and sluggish. This mechanism was not used in this thesis because of the propensity for transfer reactions and cyclization and will not be discussed further; the interested reader is referred to [7,8] for some of the latest developments concerning this mechanism.

Anionic polymerization offers the best and most efficient route to functionalized polymeric siloxanes because the termination reactions can be suppressed and chain transfer can be minimized. It is used extensively in this thesis work and the details of these anionic ROP's will be covered in the following sections. First, the polymerization of the trifluoropropylmethylsiloxane and end-functionalization with the N-acyllactam will be covered followed by the development of a kinetic model designed to predict maximum yields of linear polymer. Unfortunately, due to the instability of this fluoroalkylsiloxane in hot caprolactam, synthesis of dimethylsiloxane polymers was necessitated; results of the hexamethylcyclotrisiloxane (D_3) and tetramethyltetravinylcyclotetrasiloxane ($D_{4_{II}}$) copolymerization and end-functionalization are covered in §C.

IV. B. TRIFLUOROPROPYLMETHYLSILOXANE POLYMERIZATION

The ring-opening polymerization of 1,3,5-tris-(3',3',3'-trifluoropropyl)-1,3,5-trimethylcyclotrisiloxane at 40°C utilized promoter dimethylsulfoxide (DMSO) in conjunction with initiator normal butyllithium resulting in rapid and controllable reaction rates; monomer consumption rate was varied by at least four orders of magnitude depending on the ratio of promoter to initiator concentrations. Compared to experiments with the sodium counterion (also studied in this work), the lithium initiator slowed the backbiting reactions which caused depolymerization of linear polymer to cyclics containing four or more fluoroalkylsiloxy units. This previously uninvestigated polymerization methodology offers greater opportunity for capturing high, nonequilibrium polymer yield of this fluoroalkylsiloxane through appropriately timed termination of the reaction. To facilitate this optimization, a kinetic model of the polymerization was developed by solving the isothermal, constant density rate expressions for a two-step, series mechanism. The solution to the coupled system of nonhomogeneous ordinary differential equations was obtained by matrix variation of parameters. The rate constants were determined by appropriate kinetic analysis of the experimental data obtained for polymer and cyclics concentrations as a function of time under various conditions. This resulted in a quantitative model capable of predicting optimum polymerization time to maximize the yield of poly(3,3,3-trifluoropropylmethylsiloxane) at ca. 85 - 90%.

1. Previous Work

The fluoroalkylcyclosiloxanes, like their methylcyclosiloxane counterparts, are capable of anionic, ring opening polymerization to produce high molecular weight, thermally stable and solvent resistant polymers. Despite these material advantages, only limited data [11-14] have been published on the preparation of high molecular weight fluoroalkylsilicones largely due to the unfavorable polymer-cyclic equilibrium which is shifted heavily in favor of the cyclics (only ~18% wt polymer) [15]. As this work has shown, proper reaction conditions can avoid this low conversion and with careful monitoring of the polymerization, an 85% polymer yield can be obtained comparable to equilibrium polydimethylsiloxane yield.

Yuzhelevskii, et.al. [12] have studied the first order consumption of the fluoroalkylcyclosiloxanes, i.e. dimethylcyclosiloxanes with the $-Si(CH_3)_2O-$ or (D) units of the dimethylsiloxanes replaced by 3,3,3-trifluoropropylmethylsiloxy ($-Si(CH_2CH_2CF_3)(CH_3)O-$) or (F) units. For the 1,3,5-tris-(3',3',3'-trifluoropropyl)-1,3,5-trimethylcyclotrisiloxane (F_3) and 1,3,5,7-tetrakis(3',3',3'-trifluoropropyl)-1,3,5,7-tetramethylcyclotetrasiloxane (F_4) monomers initiated by NaOH or KOH, they found similar kinetic behavior to the D_4/KOH system; namely, first order monomer disappearance and square root dependence on initiator concentration. With KOH at 120°C, the monomer consumption rate for F_4 is approximately 3-4 times greater than D_4 due to the increased electronegativity of the trifluoropropyl substituent and the enhanced negative induction effect on the electropositive ring silicon.

Yuzhelevskii and co-workers also have studied the effect of many promoters on F_3 polymerization [13,14]. Analogous to the methylcyclosiloxanes, activators or aprotic, polar compounds containing carbonyl or thionyl groups, such as dimethylsulfoxide (DMSO), dimethylformamide (DMF) or the organic phosphates, rapidly accelerated polymerization of the fluoroalkylcyclosiloxanes at least two orders of magnitude. Their results show a logarithmic dependence on rate versus activator concentration which will be discussed more thoroughly in the Kinetic Theory section.

With these studies in mind, the study of the fluoroalkylsiloxane polymerization has two objectives. First, since it has been readily established by several investigators that the siloxane polymerizations (both methyl [16-19] and fluoropropylmethyl [13,14]) can be accelerated by various promoters, the effect of one of the best activators, dimethyl sulfoxide (DMSO), on the consumption of F_3 monomer has ben studied. Although F_3 consumption has been previously studied quite thoroughly [13,14], this DMSO/BuLi activator-initiator combination is new for the fluoroalkylsiloxanes and it will be shown that it leads to a much greater variation in the rate of F_3 disappearance than ever observed in these earlier studies.

Secondly, the experimental results were used to develop a comprehensive kinetic model of the F_3 polymerization, attempting to incorporate the equilibration between polymer and large cyclics F_n, $n \geq 4$, at all reaction times. As will be shown, the development of a predictive kinetic model permits high, nonequilibrium yields of polymer or nearly

any desired composition of polymer, unreacted monomer and/or large cyclics to be obtained.

2. Experimental Results

Materials

Fluorinated trimer, F_3 was obtained from Petrarch, checked by infrared spectroscopy and gas-liquid chromatography (99+% pure), dried over 3Å molecular sieves and distilled under vacuum (bp 80-85°C/<1 mm Hg). Middle cuts were directed into round bottom flasks equipped with air-driven paddle stirrers and stoppered injection ports.

Initiators n-BuLi (1.6M in hexane, Aldrich) and sodium trimethyl silanolate (STMS, Petrarch) were used as received and transferred via gas-tight syringes and preweighed ampoules respectively. The concentration of the n-BuLi was ascertained from good molecular weight agreement by size exclusion chromatography (SEC) with target chain length. The STMS was added directly to the reactor or dissolved in DMSO at 50-70°C which remained in solution upon cooling to room temperature. Promoter DMSO (Aldrich, HPLC grade), solvent tetrahydrofuran (THF) and terminating agent, trimethylchlorosilane (TMCS, Petrarch) were used as received.

Analytical

The majority of the kinetic data analysis was done by size exclusion chromatography; the equipment is described in Chapter VII, section C.2. In order to relate polymer and cyclics peak areas to weight fraction, several calibration samples were prepared of known polymer, cyclics (F_n, $n \geq 4$) and monomer compositions. The resulting chromatographs were

integrated and the ratio of the cyclics peak area to the total area was plotted against cyclics weight fraction generating a calibration curve. Polymer weight fraction was determined by difference. See Veith and Cohen for details of the calibration [20].

Procedure

Polymerization was done in bulk, under argon at 40°C ±0.2 maintained by an external oil bath. Temperature rise during BuLi initiation varied by 0.2-0.6°C per gram F_3 charge depending on the amount of activator used; negligible temperature rise occurred during the propagation indicating a nearly athermal reaction. The progress of the polymerization was followed by removing small (0.01–0.05 ml) aliquots which were quenched in THF/TMCS solutions, filtered and analyzed by SEC. In some cases, the reaction rate was too fast for on-line sampling and the entire reaction mixture (4-6g) would be quenched by injecting TMCS. This necessitated repetitive trials for accurate kinetic data at higher activatior concentrations.

Sodium Initiators

The trials using sodium trimethyl silanolate were done at [I] = 0.052M with activator/initiator ratios of 1:1 and 6:1. No polymerization occurred with pure $Na^{+-}OSi(CH_3)_3$ (STMS) despite its dissolution in F_3 in 2-4 min. at 40°C. The 6:1 DMSO/STMS case instantaneously produced broad molecular weight polymer at only 22% yield even though termination with TMCS was carried out in just 6 seconds. At 1:1 A/I, the reaction proceeded more slowly in similar fashion to the lithium-initiated polymerizations with an observed F_3 rate constant of 1.8 $min.^{-1}$. This

reaction was terminated at a polymer yield of 86% analogous to the Li^+ reactions. However, under identical conditions, the Na^+ rate of F_3 consumption was 130 times the Li^+ rate which indicates the stronger basicity with the larger cation due to greater ionization potential. This trend has been observed by Yuzhelevskii [12] for unpromoted polymerization of F_3 at 110°C (20X factor, Na^+ over Li^+) and applies generally in most cases of metallated ion dissociation.

Greater control over the polymerization was obtained with the lithium initiator which permitted collection of polymer-cyclic equilibrium data over greater range of activator/initiator ratios. This A/I combination also gave good correlation between initiator concentration and molecular weight. For Li^+, the MW distributions were Gaussian with polydispersities of 1.2–1.4. A typical SEC chromatogram from this kinetic work is shown in Figure 4-1, curve #1 where this particular polymerization was terminated at ca. 90 % conversion. The unreacted trimer, F_3, and larger cyclics peaks, F_4, F_5 are seen in addition to the polymer which has a $\bar{M}_w/\bar{M}_n = 1.26$. The other curves, #2 and #3 will be discussed in the section on end-functionalization of the FS, §B.4. Since the BuLi in hexane was insoluble in F_3, no polymerization occurred until the DMSO was added which solubilized and solvated the initiator. Stirring speed was ca. 70-90 rpm.

a. Polymerization Chemistry, Mechanism, Kinetics

It is well known that the cyclic trimer has a much greater entropy of polymerization due to ring strain than the tetramer [21]. This higher reactivity favors ring opening propagation over the chain transfer (transsiloxanolization) and/or backbiting reactions at low to moderate

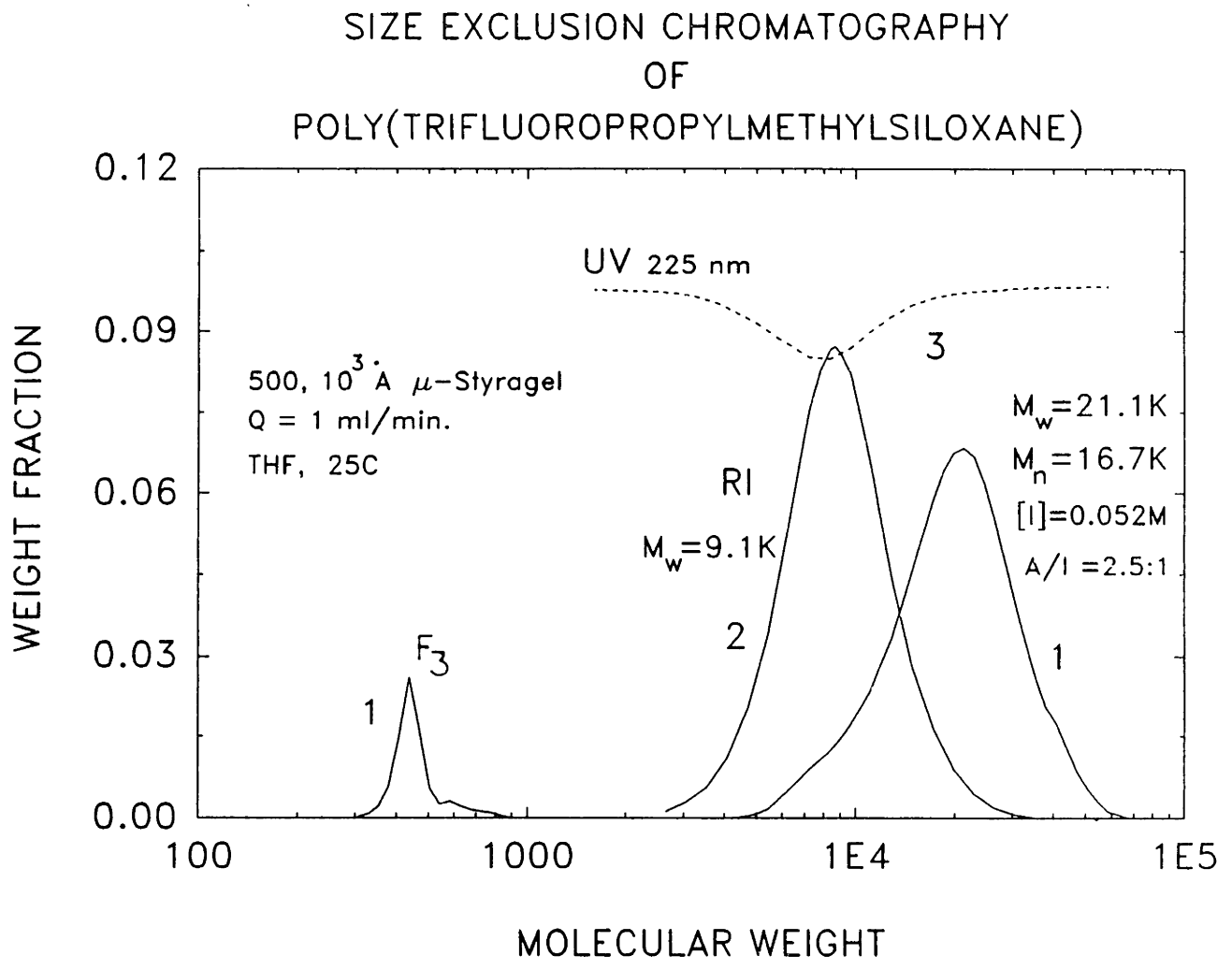

Figure 4-1 Size exclusion chromatography of curve #1 - PTFPMS at ca. 90 % conversion synthesized with the DMSO/BuLi A/I system, 40°C; note the cyclics peaks which consist predominantly of trimer, F_3; Curve #2 - refractive index signal of ω-N-acyllactam-PTFPMS and #3 - ultraviolet detector response of same end functionalized PTFPMS at λ = 225 nm. All chromatograms in THF.

conversions. Pierce, et.al. [11] first recognized this fact for fluoroalkylsilicone polymerization with a NaOH initiator and proposed the two-step mechanism used in this model. Lee, et.al. [22] used Li^+ initiators in the polymerization of hexamethylcyclotrisiloxane (D_3) to suppress the redistribution reactions and give conversion to high polymer of narrow polydispersity. These findings are reinforced in view of the experimental results of this thesis with lithium based initiators where the viscosity is observed to increase fairly rapidly, reach a maximum and then gradually decline with reaction time as the polymer degrades to cyclic oligomers.

After initiation (assumed to be rapid compared to propagation), the trimer is presumed to be converted irreversibly to linear polymer in the first reaction followed by equilibration with larger cyclics F_n, $n \geq 4$.

$$F_3 \xrightarrow{k_1} P \underset{k_3}{\overset{k_2}{\rightleftharpoons}} F_n \qquad n \geq 4 \qquad (4\text{-}3)$$

Rigorously, k_3 must be summed over all back-reacting cyclics but for mathematical simplicity, it will be considered as an average rate constant for all the cyclics ($n \geq 4$).

The ring opening of F_3 involves nucleophilic attack of a partially solvated siloxanolate on the electropositive Si of the trimer. See the forward, propagation reaction in equation (4-4).

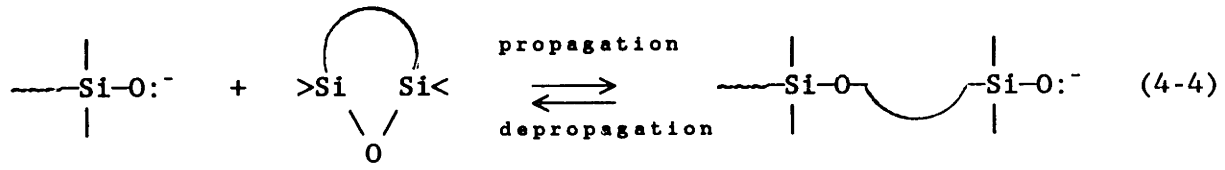

siloxanolate cyclic (F_3 or F_n) (adduct)

This ring opening propagation mechanism also holds with the larger cyclics as reactants as characterized by the reverse reaction with rate constant k_3 in equation (4-3).

With an anionic propagation mechanism and evidence of a continuous cyclic distribution [23], the conversion of polymer to cyclics is assumed to occur via a backbiting mechanism. This is in contrast to cationic ring opening polymerization where the cyclic equilibrium distribution for D_3 favors integral multiples of three, the number of siloxy units in the monomer, due to silanol condensation [24]. Although this backbiting or depropagation in equation (4-4) is a unimolecular reaction, two reactant concentrations, the siloxanolate and intramolecular polymeric siloxy group, enter into the kinetic expression, equation (4-6). These reactions lead to the kinetic expressions below assuming negligible concentration gradients within the reactor or no mass transfer limitations. The kinetic expressions are written for isothermal, constant volume conditions and F_i, $i \geq 3$, and P correspond to the concentrations of repeat units or equivalently, weight fractions of cyclics and polymer, respectively.

$$\frac{dF_3}{dt} = -k_1[SiO^-]F_3 \qquad (4\text{-}5)$$

$$\frac{dP}{dt} = -k_2[SiO^-]\,P + k_3[SiO^-]\,F_n + k_1[SiO^-]\,F_3 \qquad (4\text{-}6)$$

$$\frac{dF_n}{dt} = k_2[SiO^-]\,P - k_3[SiO^-]\,F_n \qquad n\geq 4 \qquad (4\text{-}7)$$

The k_i's correspond to the inherent rate constants which are a function of temperature only and the $[SiO^-]$ represents the concentration of the solvated siloxanolate or "living end".

Since the "living end" equilibrium is established rapidly ahead of the propagating siloxanolate, the $[\sim\!\!>SiO^-]$ is independent of time and the monomer disappearance equation (4-5) can be integrated directly. Substitution of this first order expression into equation (4-6) results in a coupled, two-dimensional system of nonhomogeneous ordinary differential equations which is easily solved by variation of parameters. Briefly, this method requires looking for a particular solution which is the product of the matrix formed from the eigenvectors of the homogeneous solution and an unknown time dependent column vector. The procedure is straightforward and detailed in any advanced mathematics text, e.g. [25]. In vector notation, equations (4-6,4-7) are,

$$\underset{\sim}{X} = \underset{\approx}{K}\underset{\sim}{X} + \underset{\sim}{Y} \qquad (4\text{-}8)$$

where $\underset{\sim}{X} = (P, F_n)^T$ and represents the concentration vector, $\underset{\approx}{K}$ is the rate constant coefficient matrix $\begin{pmatrix} -k_2^* & k_3^* \\ k_2^* & -k_3^* \end{pmatrix}$, and $\underset{\sim}{Y}$ the nonhomogeneous vector $(k_1^* F_{3_o} \exp[-k_1^* t], 0)^T$. Note the abbreviated notation for the rate

constants, $k_i^* = k_i[SiO^-]$, i = 1, 2, 3. The resulting solution is,

$$\underset{\sim}{X} = \begin{bmatrix} 0.000 \\ 0.183 \\ 0.817 \end{bmatrix} - \beta \begin{bmatrix} 0 \\ 1 \\ -1 \end{bmatrix} e^{-(k_2^*+k_3^*)t} - F_{3_o} e^{-k_1^* t} \begin{bmatrix} 1 \\ 0.183-\beta \\ 0.817+\beta \end{bmatrix} \qquad (4\text{-}9)$$

where now $\underset{\sim}{X} = (F_3, P, F_n)^T$ and $\beta = 0.817k_1^*/(k_2^*+k_3^*-k_1^*)$. The first two terms correspond to the homogeneous solution and the third term represents the particular solution. At equilibrium, t=∞ the exponentials decay to give the equilibrium composition and a check at t=0 shows that only trimer is present in the reactor.

b. Kinetic Theory

The expression for the concentration of the solvated siloxanolate, [~>SiO^-], depends on i) whether an activator is used, ii) the activator's chemical structure, iii) the activator's concentration and iv) the type of cation the activator solvates. For nonpromoted anionic polymerizations in nonpolar media, it is generally accepted that the siloxanolate and cation are associated as twins [26,13] as in styrene polymerizations studied by Szwarc [27,28]. These twinned ion pairs are in equilibrium with contact ion pairs which, without activator, are only very slightly dissociated into free ions. This low amount of dissociation leads to the square root dependence of the observed monomer rate constant on initiator concentration ($k_1^* \propto I^{1/2}$) as determined by Grubb and Osthoff [29] for bulk D_4 polymerization and Yuzhevelskii, et.al. [12] for bulk F_4 polymerization. See equations (4-10,11) written for a lithium counterion where the subscript "f" designates the free siloxanolate.

$$1/2 \begin{matrix} \sim\!\!>SiO^-Li^+ \\ Li^+{}^-OSi <\!\!\sim \end{matrix} \underset{\text{twins}}{\overset{K_t}{\rightleftharpoons}} \underset{\text{contact}}{\sim\!\!>Si\text{-}O^-\ Li^+} \overset{K_f}{\rightleftharpoons} \underset{\text{free ions}}{\sim\!\!>SiO^- + Li^+} \qquad (4\text{-}10)$$

$$K_f = \frac{[SiO^-]_f[Li^+]}{[\ SiO^-Li^+]} = \frac{[SiO^-]_f^2}{[I]} \qquad (4\text{-}11)$$

Despite the fact that most of the anion-cation pairs are twinned, the rates of association and dissociation are very high so that all active sites participate in propagation, although not all at the same time. This rapid "shuffling" of active centers keeps the degree of polymerization narrow assuming no transfer reactions.

The addition of an activator in small amounts has been shown by several investigators to dramatically accelerate the polymerization rate. Cooper and Elliot [18] attributed the activator effect to increasing the dissociation towards free ion pairs, i.e. equation (4-10) shifts to the right. But as Yuzhelevskii, et.al. [13] have shown by electrical conductivity measurements, the relative increase in conductivity is not commensurate with the rate increase and the conductivity is still low by absolute standards (from 10^{-11} to 10^{-7} $ohm^{-1}cm^{-1}$). This suggests that the activator does not significantly increase dissociation towards free ions.

A different approach was advanced by Ostrozynski [19] who proposed the dissociation of the metallated, contact ion pairs to solvent separated ions for various phosphine oxide activators in the polymerization of octamethylcyclotetrasiloxane (D_4) by potassium silanolate. This is shown

in equation (4-12) written for a lithium counterion and any arbitrary activator, ACT. This stoichiometry implies an activator

$$1/2\ \begin{matrix} \sim\!\sim\!>SiO^-Li^+ \\ Li^+{}^-OSi<\!\sim\!\sim \\ \text{twins} \end{matrix} \quad \underset{}{\overset{K_t}{\rightleftharpoons}} \quad \begin{matrix} \sim\!\sim\!>Si\text{-}O^-\ Li^+ \\ \text{contact} \end{matrix} \quad \underset{}{\overset{K_f}{\rightleftharpoons}} \quad \begin{matrix} \sim\!\sim\!>SiO^-\ ,Li^+\bullet\bullet\bullet(nACT) \\ \text{solvent separated} \end{matrix} \tag{4-12}$$

concentration dependence in the expression for the equilibrium dissociation constant, viz.

$$K_e = \frac{[SiO^-]_{ss}[Li^+...nA]}{[\ SiO^-Li^+]\ \ [A]^n} \overset{?}{=} \frac{[SiO^-]^2_{ss}}{[I]\ [A]^n} \tag{4-13}$$

The second equality, which was written by Ostrozynski, is not universally valid for all activator concentrations as will be discussed thoroughly below. Here, n is the average number of activator molecules associated with each active site and the subscript "ss" corresponds to the solvent separated siloxanolate (as opposed to the free anion of equations (4-10,11)).

Ostrozynski solved the second equality in equation (4-13) for $[SiO^-]_{ss}$, which implies a linear relation between log k_1^*, the observed monomer rate constant ($k_1^*=k_1[SiO^-]_{ss}$) and the logarithm of the activator concentration, log [A]. The intercept then gives the $k_1K_e^{1/2}$ product for a specific initiator or $[SiO^-M^+]$ concentration. This linearity was found at low activator concentrations (<0.1M) by both Ostrozynski for the D_4-/$K^+{}^-OSi\equiv$/HMPA system and Yuzhelevskii, et.al. for the

$F_3/Na^+{}^-OSi-SiO^-Na^+/DMF$ system over approximately one and two orders of magnitude, respectively, for the observed monomer rate constant.

However, this observed linearity at low [ACT] may be fortuitous and is not likely to persist into the region of higher [ACT] examined in this work. In the second equality of equation (4-13), Ostrozynski set the initiator concentration, [I], equal to the metallated ion pair concentration, $[SiO^-Li^+]$; this holds (see equation (4-12)) only at very low dissociation, i.e. $K_e \ll 1$ so that the concentration of solvated ion pairs, $[SiO^-]_{ss} \ll$ contact pairs, $[SiO^-Li^+]$. According to Ostrozynskii's own data, the K_e of the solvated ion pairs is 10^9 times the K_f of the free ions in the unpromoted case. Order of magnitude analysis (data from ref [26]) shows that K_f values range down to 10^{-7}, which still leaves the solvated ion pair dissociation constant, K_e, much greater than unity ($\simeq 10^2$). Under these conditions, the contact ion pair concentration, $[SiO^-Li^+]$, should be expressed as the <u>difference</u> between the initiator concentration and the solvated siloxanolate, $[I] - [SiO^-]_{ss}$ because the solvent separated siloxanolate concentration is appreciable, or at least not negligible compared to the contact ion concentration. This implies a much more complicated, quadratic relationship between the observed rate constant for monomer consumption, k_1^* and the activator concentration than found by Ostrozynski. This more complex dependence is shown in equations (4-14), (4-15).

$$K_e = \frac{[SiO^-]_{ss}[Li^+\cdots nA]}{[SiO^-Li^+]\ [A]^n} = \frac{[SiO^-]_{ss}^2}{([I]-[SiO^-]_{ss})\ [A]^n} \qquad (4\text{-}14)$$

$$k_1^* = k_1 [SiO^-]_{ss} = (1/2)k_1 K_e A^n \left(\left[1 + \frac{4I}{K_e A^n} \right]^{1/2} - 1 \right) \quad (4\text{-}15)$$

For ease of notation in equation (4-15), the brackets denoting concentration have been dropped on I and A. Note that if $4I/K_eA^n \gg 1$, the bracketed term reduces to $2I^{1/2}K_e^{-1/2}A^{-n/2}$ which recovers Ostrozynski's original relationship of $k_1^* = k_1 K_e^{1/2} I^{1/2} A^{n/2}$. This $4I/K_eA^n$ term can be large compared to unity if $K_e \ll 1$ or if $A^n \ll 1$. The former is probably not the case because the rate is enhanced four to six orders of magnitude over unpromoted polymerizations as indicated by the large ratio of K_e to K_f. The magnitude of the latter, the A^n term, where $n \approx 2.5$ and up, can dominate a large K_e when the activator/initiator ratio is approximately $\geq 1.75:1$ which corresponds to an [ACT] of less than 0.05 to 0.1M or so. Inspection of both Ostrozynski's and Yuzhelevskii's data show linearity below this activator concentration range. Thus, at low activator concentration, the simple linear relationship of log k_1^* vs log [A] is obeyed but higher [ACT] causes negative deviation from linearity due to the contribution of the bracketed term in equation (4-15). This interpretation agrees well with the results obtained in this work which are presented in the next section.

c. Predictive Kinetic Model

Determination of Rate Constants

To use this model, the observed kinetic rate constants, k_i^*, i=1,2,3 must be determined experimentally. First order consumption of F_3 for the lithium initiator is verified in agreement with other researchers [12,13] as shown in Figures 4-2a, 4-2b for several trials; these are just plots of weight fraction trimer versus time because only trimer was present initially which give the observed monomer consumption rate constant (k_1^*) from the negative of the slopes.

Unlike previous work, a greater range of the observed monomer rate constant, k_1^* as a function of activator concentration was studied as shown in Figure 4-3. Three different initiator concentrations that produced 8 kg/mole, 24 kg/mole and 72 kg/mole molecular weight polymers were used with various activator/initiator (A/I) ratios ranging from 0.5 to 9:1. Constant A/I ratios are represented by the dashed lines in Figure 4-3. Thus, traversing a dashed line at constant A/I, the activator concentration varies as indicated on the abcissa and the initiator concentration changes so as the keep the A/I constant. The observed F_3 rate constants (as determined by plots similar to those of Figs. 4-2a, b for each data point in Fig. 4-3) indeed show curvature over four orders of magnitude when plotted against activator concentration; the curvature becomes more pronounced at higher activator concentrations for a given initiator concentration, or at lower [I] for a constant [ACT] in agreement with the magnitude of the $4I/K_eA^n$ term compared to unity in equation (4-15); (note that the activator concentrations used in this work are less than unity).

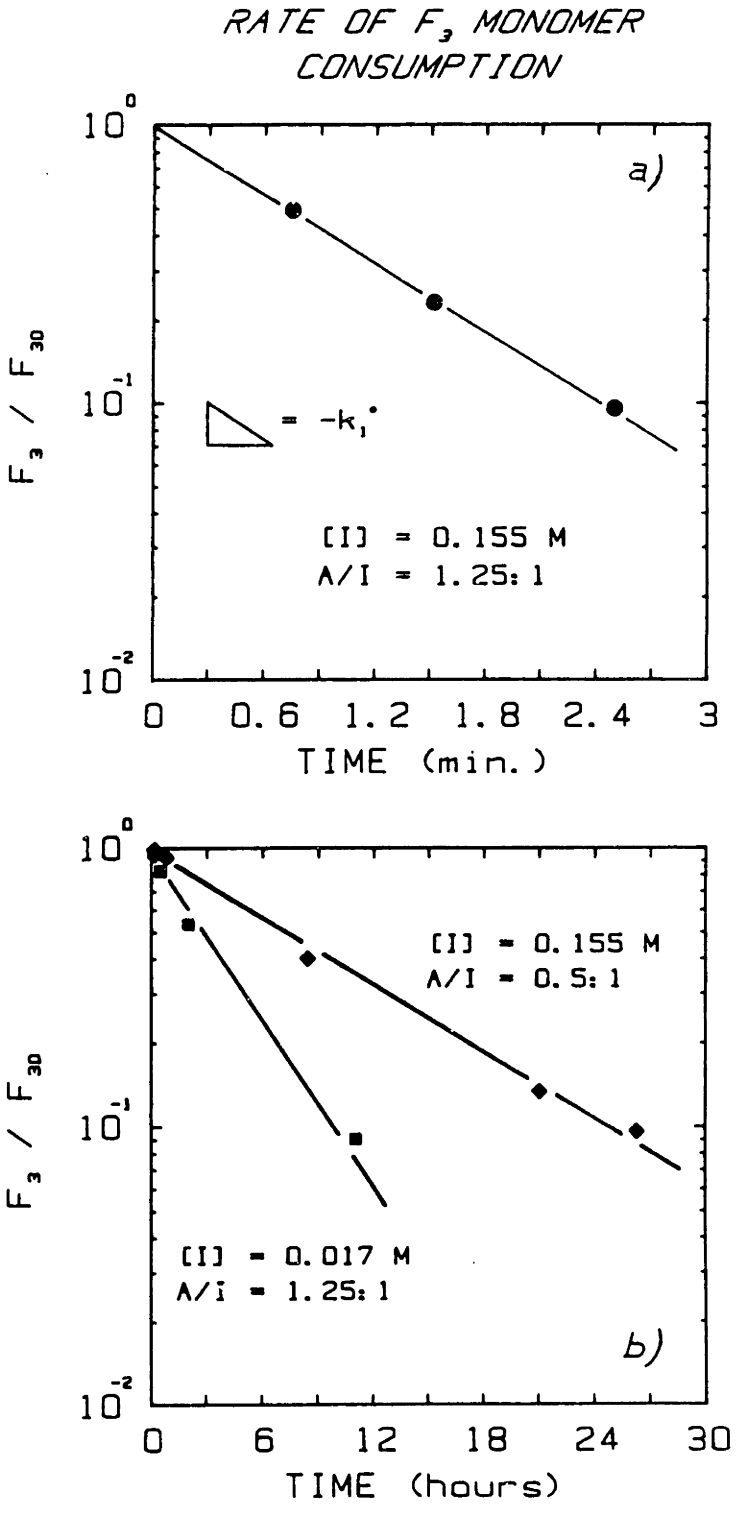

Figure 4-2a,b First order kinetic dependence of monomer (F_3) consumption for several cases of initiator [I] and activator [ACT] concentrations

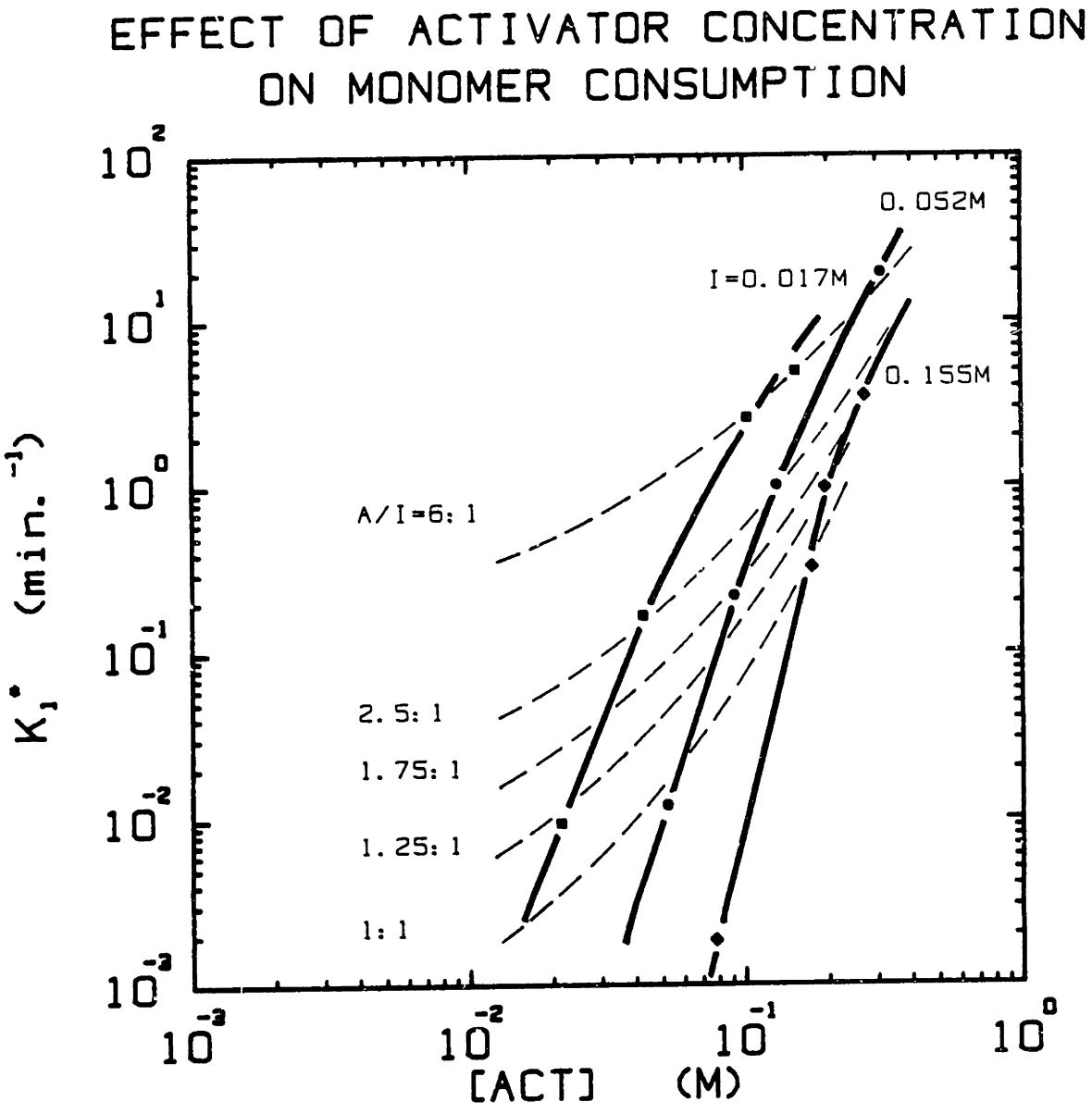

Figure 4-3 Effect of DMSO activator concentration, [ACT] on monomer rate constant, k_1^*; dashed lines represent contours of constant activator/initiator or A/I ratio.

The polymer-cyclic equilibrium constants k_2^*, k_3^* were determined from a simple first order, reversible reaction analysis starting at a point in time when the F_3 concentration had dropped to essentially zero and following the change in polymer-cyclic composition. These data are plotted in Figures 4-4a,b for two different initiator and activator concentrations. The slopes of the linear regression fit give the sum of the rate constants for the two cases from the kinetics,

$$\ln\left[\frac{P - P_e}{P_o - P_e}\right] = -(k_2^* + k_3^*)t \qquad (4\text{-}16)$$

Here, P_o and P_e represent the initial (at the start of the equilibration analysis) and equilibrium polymer concentrations, respectively and are plotted as the ordinate in Figures 4-4a, b according to equation (4-16).

The second relation between k_2^* and k_3^* comes from the thermodynamic equilibrium relation between polymer and cyclics assuming unity activity coefficients as

$$K_{23} = \frac{k_2^*}{k_3^*} = \left.\frac{F_n}{P}\right|_{eq} = 4.46. \qquad (4\text{-}17)$$

Since equilibrium has been shown to be independent of activator or activator concentration for the methylsiloxanes [17] and fluoropropylmethylsiloxanes [15], this ratio holds for all A/I ratios. Thus, for [ACT]=0.27M, k_2^*=0.0065 min^{-1}, k_3^*=0.0015 min^{-1} and for [ACT]=0.045M, k_2^*=5.8x10^{-5} min^{-1} and k_3^* = 1.3x10^{-5} min^{-1}.

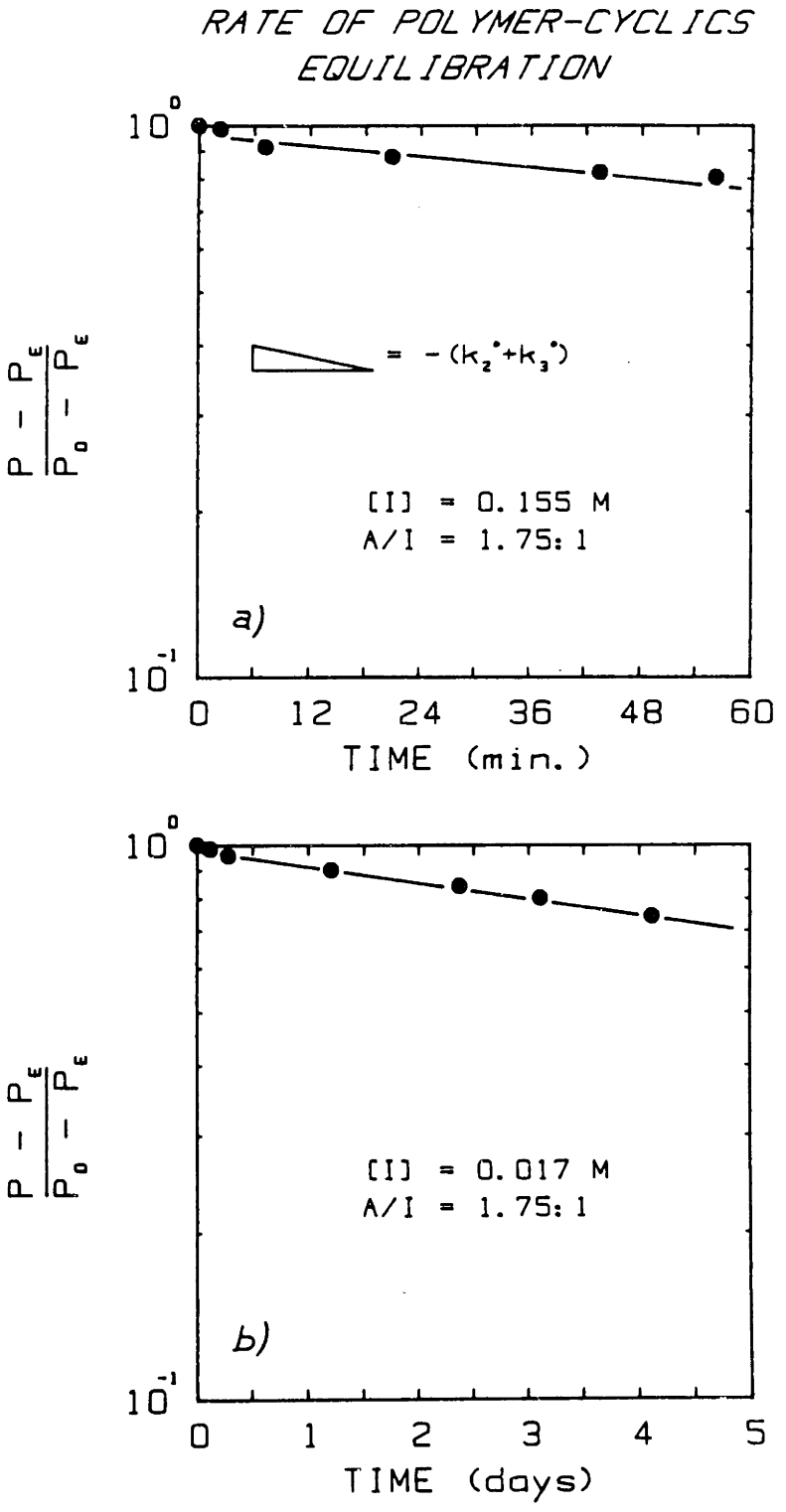

Figure 4-4 Determination of sum of propagation-depropagation rate constants ($k_2^*+k_3^*$) between polymer and larger cyclics, F_n according to reversible first order reaction analysis, (eq. 4-16).

3. Discussion of Model

With the three rate constants determined, the model can be used quantitatively to follow the polymerization in time at a given degree of ion dissociation. This is shown in Figures 4-5a and 4-5b for two sets of conditions. The data points represent the experimentally determined polymer and cyclics concentrations and the curves correspond to model calculations. Note the broad maximum in polymer conversion obtained with the DMSO activator/n-BuLi initiator system. The rise in polymer concentration is accelerated by the additional DMSO in the higher [ACT] case, Figure 4-5a, and this 85-90% conversion can be made permanent by termination of the polymerization after approximately 3 minutes. At $t=\infty$, the polymer trajectory will decrease and the larger cyclics, F_n curve will rise to their equilibrium values of 0.183 and 0.817 wt fraction, respectively.

With less DMSO ([ACT]= 0.045M) depicted in Figure 4-5b, the consumption of monomer is slightly slower yielding a broader polymer maximum in time. Note the difference in scale. The decreased solvation of the $[SiO^-]$ at lower [ACT] not only decreases the monomer consumption rate but also offers a greater optimum "termination window" for capturing high polymer yield because the equilibration reactions between polymer and large cyclics (i.e. reactions 2 and 3 in equation (4-3)) are also slowed by the lower activator concentration. The use of Li^+ effectively reduced these redistribution and depolymerization reactions as compared to Na^+; polydispersities were ca. 1.2-1.4 for the former versus 2.0 for the latter. This is similar to the findings of Lee et.al. [22] for Li^+ counterion propagation with the methylcyclosiloxanes and will be

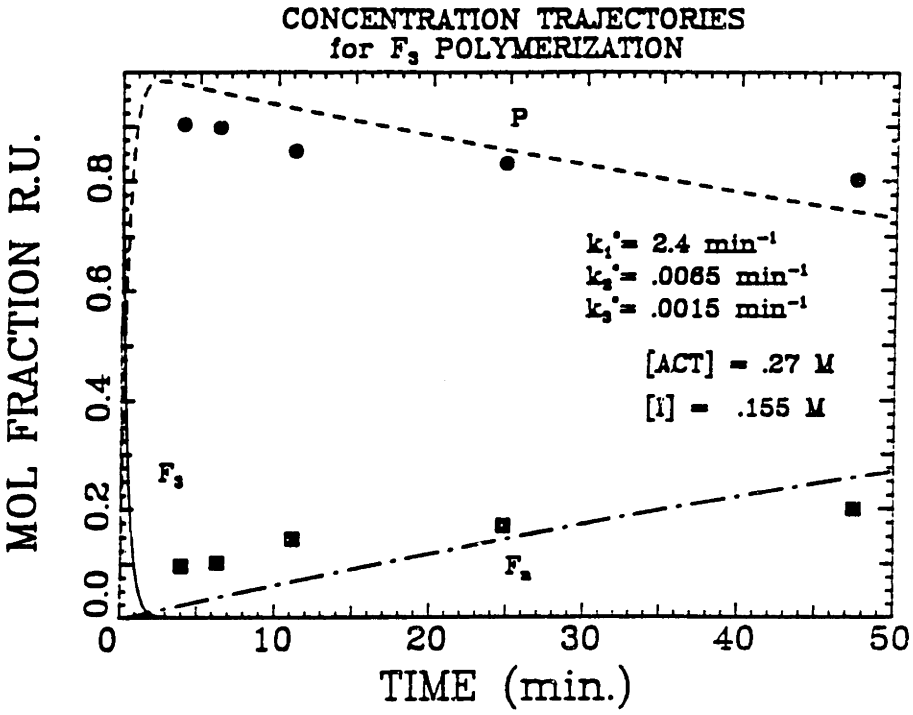

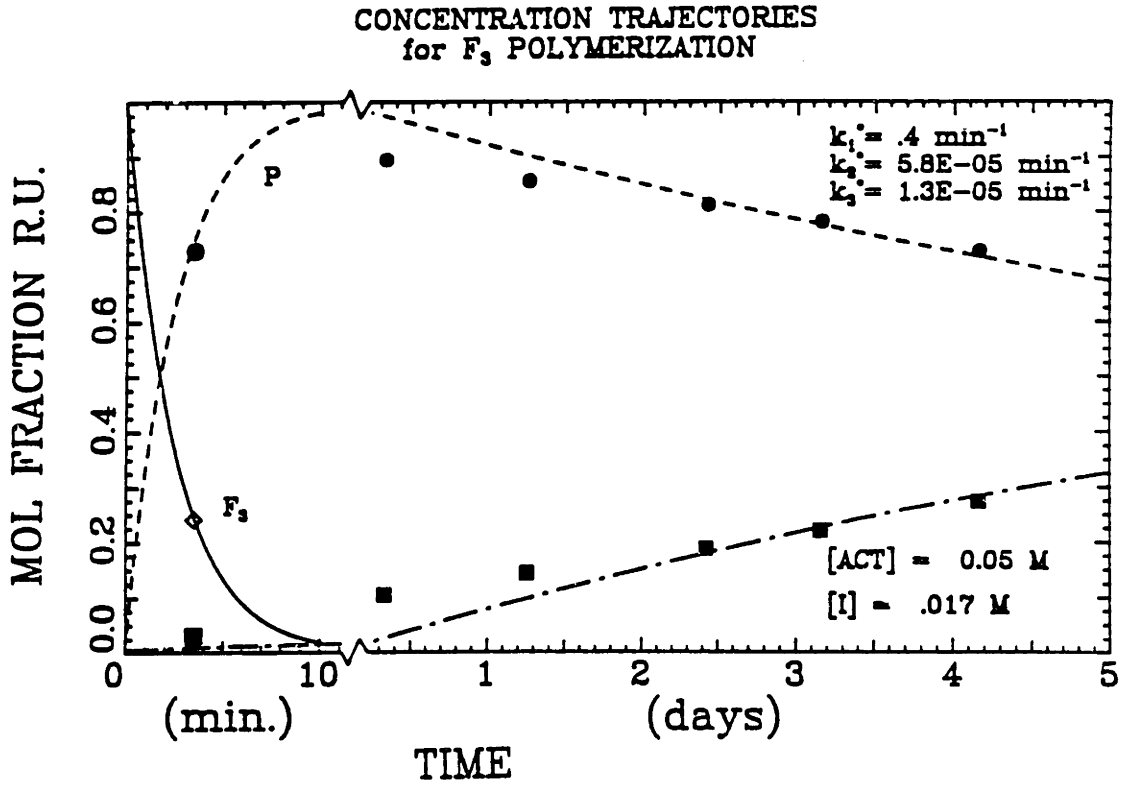

Figure 4-5 Concentration trajectories of monomer, F_3 (——), polymer, P (---) and larger cyclics, F_n (—•—•—) for two different activator and initiator concentrations; rate constants determined as explained in text.

discussed below. This difference in concentration trajectories further emphasizes the flexibility and control of fluoroalkylsiloxane polymerization with the DMSO/BuLi system and by no means represents the limits of operation.

a. Model Predictive Capability

Ideally, this model should be extended to include any, arbitrary DMSO:BuLi ratio and initiator concentration. To do this, the variation of the observed rate constants must be correlated to DMSO concentration. Note that in Figure 4-3 the rate constant data points corresponding to the three lower activator concentrations for each initiator concentration are very nearly collinear. Thus, the relation $k_1^* \simeq k_1 K_e^{1/2} I^{1/2} A^{n/2}$ asymptotically can be used to fit a straight line through the lower three data points at each initiator concentration and thereby determine a common value (at [A]=1.0 M) for $k_1 K_e^{1/2}$ of $9.6 \times 10^4 \pm 1.5 \times 10^4$ $(1/mol)^{(n+1)/2} min^{-1}$ as shown in Figure 4-6. Note that the intercepts are not equal, but after correction for the square root of the initiator concentration in each of the three trials, the common value for $k_1 K_e^{1/2}$ is obtained.

The $k_1 K_e^{1/2}$ product is a function of temperature and the type of activator-cation only and cannot be directly compared to Yuzhevelskii's 1800 $(1/mol)^{0.87} min^{-1}$ for DMF promoted $F_3/Na^{+-}OSi\equiv$ polymerization. This is because the promoter-cation systems are different; (the rate constants have been corrected to 40°C). However, two points should be made. First, the slopes for the three initiator concentrations of this study are 6.7, 4.8 and 3.2 which are 2-5 times the 1.37 value for the F_3/DMF system, (see Figure 4-6 where Δ = slope). Despite the fact that

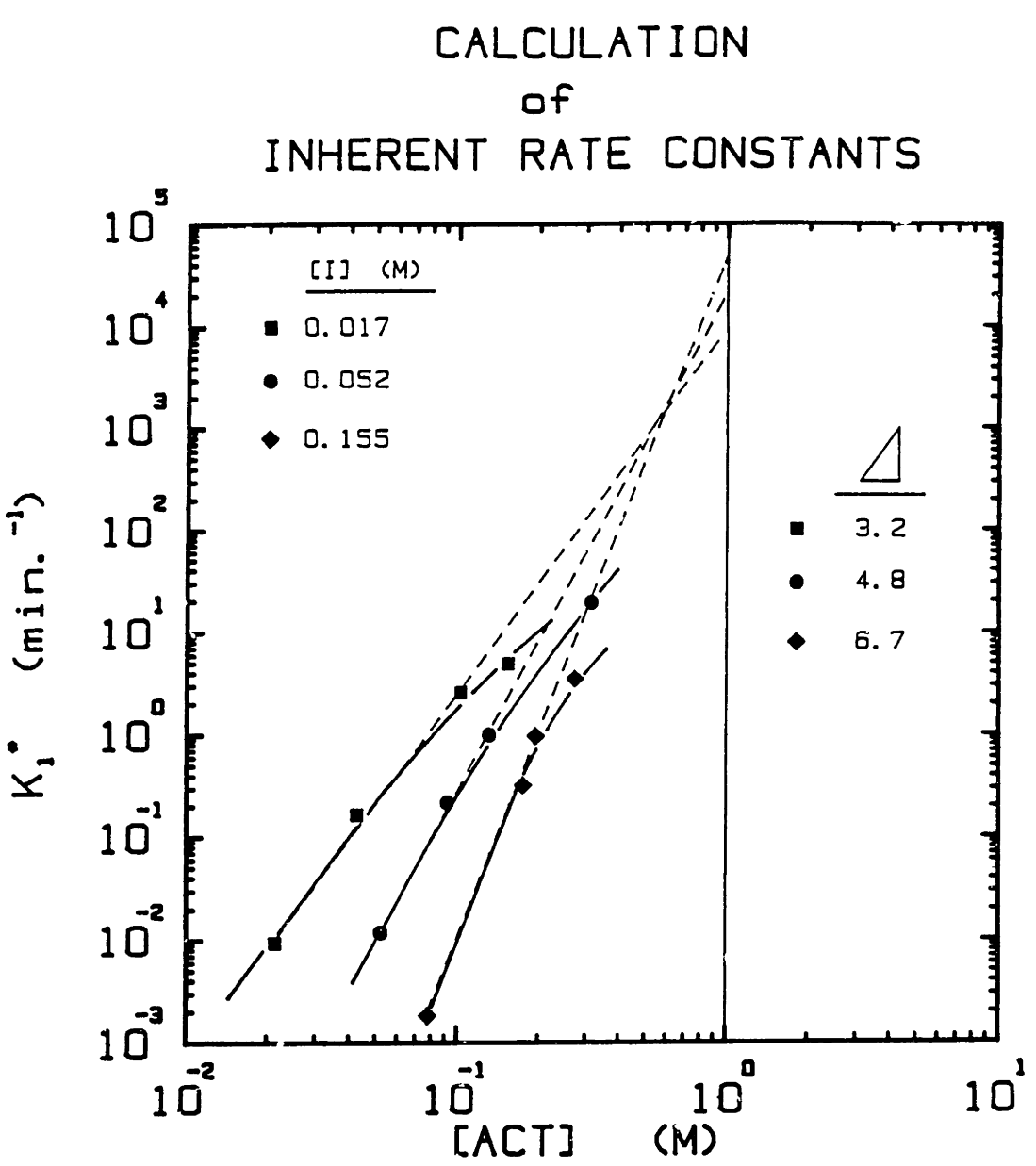

Figure 4-6 Regression of the "asymptotic" observed monomer rate constants, k_1^* for various initiator concentrations to calculate the inherent monomer rate constant product, $k_1 K_e^{1/2} \approx 10^5$ (1/mol)$^{(n+1)/2}$min^{-1}.

Yuzhelevskii's [I] ≈ 0.004M and the slope decreases with [I], the high number of DMSO molecules complexed with the $Li^+ \cdots {}^-OSi\equiv$ here means that the dissociation from contact to solvent separated ion pairs with the Li^+ cation is much more sensitive to DMSO than Na^+ is to DMF. This superior solvation may be attributed to the fact that DMSO contains highly electropositive and electronegative regions at either end of the thionyl group which can solvate either the cation with the electronegative oxygen or the terminal silanolate via the more electropositive sulfur. This "bisolvation" from one promoter molecule combined with the smaller ionic radius of Li^+ versus Na^+ would explain the high slope values of this work where considerably more DMSO molecules are involved in the dissociation of <u>both</u> the cation and siloxanolate.

Secondly, at the x-intercept of the log k_i^*-log [A] plot, the [ACT] is equal to 1.0M and is not dependent on the power of the activator concentration (i.e. the value of n) so that a direct ratio of y-intercepts (corrected for the respective initiator concentrations) yields the ratio of the equilibrium dissociation constants ($K_e|^{Li^+}_{DMSO}$ / $K_e|^{Na^+}_{DMF}$). This shows the K_e in the F_3/DMSO/BuLi system of this thesis is 10^3 times that in the F_3/DMF/Na^+ system of Yuzhelevskii, et.al. and numerically demonstrates the enhanced solvation of Li^+ with DMSO.

If it is assumed that at [ACT]=0.045M the asymptotic form of the observed rate constants, $k_i^* \simeq k_i K_e^{1/2} I^{1/2} A^{n/2}$, (i=1,2,3) is approximately correct, then $k_2 K_e^{1/2}$ = 14.5 $(l/mol)^{(n+1)/2} min^{-1}$ and $k_3 K_e^{1/2}$ = 3.25 $(l/mol)^{(n+1)/2} min^{-1}$. The arbitrary units with respect to the activator power dependence (i.e the value of n) result from the variation in slope

of k_1^* versus [ACT] for the three different initiator concentrations in Figure 4-6.

Now that the inherent rate constant products ($k_i K_e^{1/2}$, i=1,2,3) have been determined the model can be truly extended to arbitrary experimental conditions. Working backwards, for any initiator concentration and DMSO:BuLi ratio, the value of the observed monomer rate constant, k_1^*, can be read from Figure 4-7 and using $k_1 K_e^{1/2} \approx 10^5$ $(l/mol)^{(n+1)/2} min^{-1}$, the power dependence of the activator concentration (i.e. the value of n) can be calculated. Then, the observed rate constants k_2^*, k_3^* can be computed from the asymptotic relation above, combined with k_1^* and substituted into the model, equation (4-9), to estimate the concentration trajectories of monomer, polymer and cyclics. Optimum termination occurs when the derivative of the polymer concentration trajectory with respect to time, dP/dt, vanishes and is given by,

$$t_{max} = \frac{\ln\left[\dfrac{F_{3o}(k_1^*/(k_2^*+k_3^*) - 0.183)}{0.817}\right]}{k_1^* - k_2^* - k_3^*} , \qquad (4\text{-}18)$$

which will maximize polymer yield. Alternately, the reaction can be allowed to proceed to some other chosen time to yield a specific composition of polymer and cyclics for the desired formulation of viscosity in fluoroalkylsilicone oils as an example.

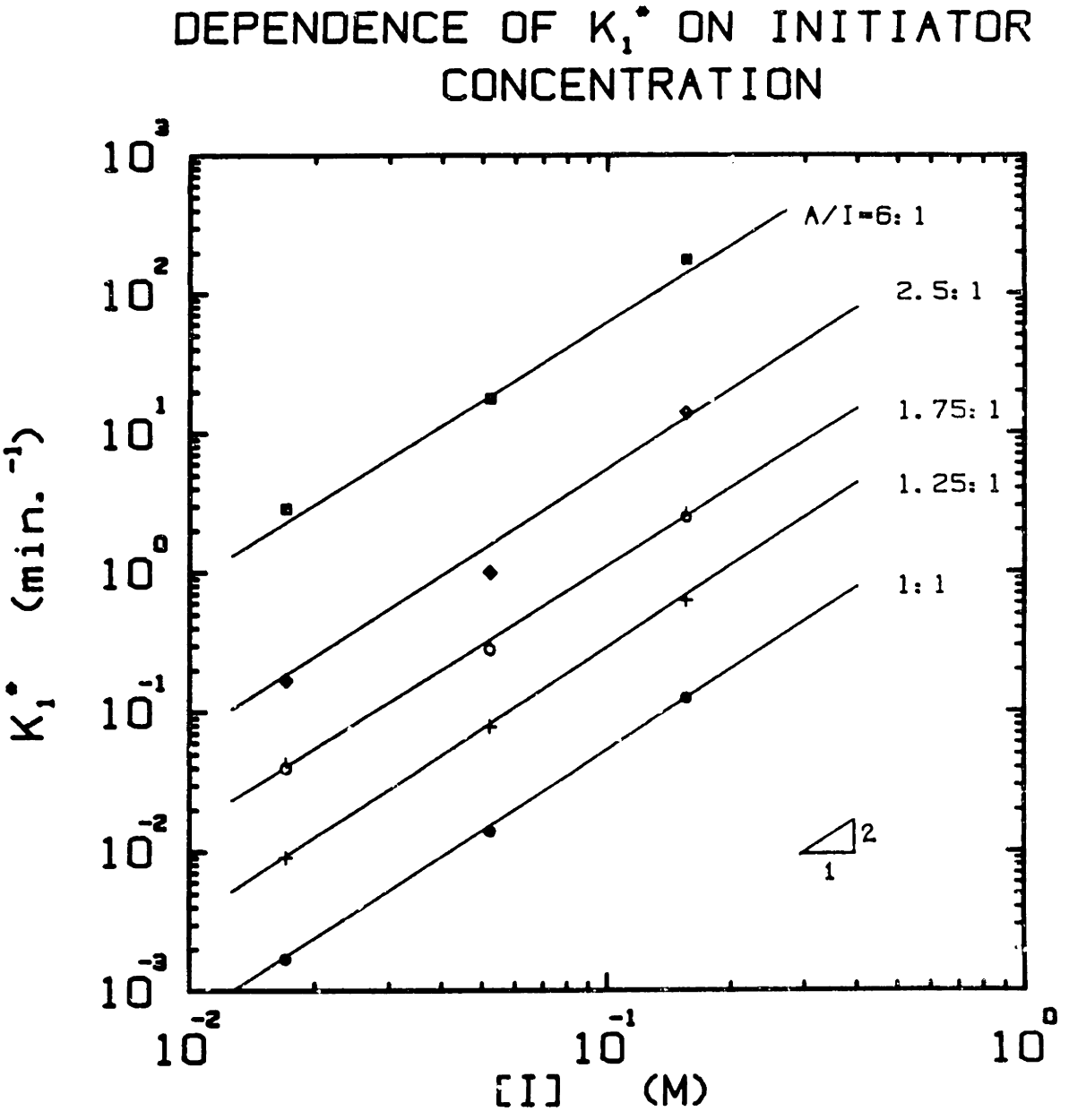

Figure 4-7 Cross-plot of monomer consumption rate constant, k_1^*, versus initiator concentration at constant activator-initiator (A/I) ratio; Δ = slope.

b. Conclusions

The use of initiator n-BuLi in conjunction with activator DMSO at 40°C has converted 1,3,5-tris[(3',3',3'-trifluoropropyl)methyl]cyclotrisiloxane (F_3) to linear polymer with high nonequilibrium yields of 85-90%. This activator/initiator system permitted extraordinary variation in reaction rates to tailor the polymerization to individual requirements. A high concentration of living polymer (85%) was maintained in this laboratory for over one week with 0.5 A/I using the Li^+ counterion which reduced the detrimental transsiloxanolization and backbiting reactions and resulted in a near-Poisson molecular weight distribution with a polydispersity of 1.2-1.4. Good correlation between chain length and initiator concentration was observed with both Li^+ and Na^+ initiators.

The anionic, ring opening of F_3 has been approximately modeled by a two-step, series reaction mechanism which predicts a nonequilibrium maximum in polymer concentration. This maximum undoubtedly exists for all polymerizations promoted or unpromoted, but is not realizable on the time scale of some reaction conditions such as 6:1 DMSO:STMS because the large ionic radius of the Na^+ increases its dissociation and hence its reaction rate towards the instantaneous limit. With Li^+ however, the maximum can be quite broad because the depolymerization reactions are slowed and its use easily permitted termination with high polymer conversion. The model has been extended to any, arbitrary activator and initiator concentrations to predict optimum polymerization time to maximize the yield of poly(trifluoropropylmethylsiloxane) at 85-90%.

4. Acyllactam End-Functionalization

With a working model to predict the optimum termination time of the fluoroalkylsiloxane, it can be suitably end-functionalized via the coupling agent (DMCSUCL) to give the macromonomer for caprolactam polymerization. Initiation occurs by nucleophilic attack of the butyl anion on the more electropositive Si of the trimer ring to give the monoadduct in equation (4-19). Propagation proceeds via the same mechanism except for a siloxanolate nucleophile in lieu of the Bu^- with the polymer attaining equilibrium with larger cyclics, F_n as in equation (4-20). Termination is accomplished by quenching the growing lithium siloxanolate with ca. 15% stoichiometric excess DMCSUCL as shown in the equation (4-21).

Initiation

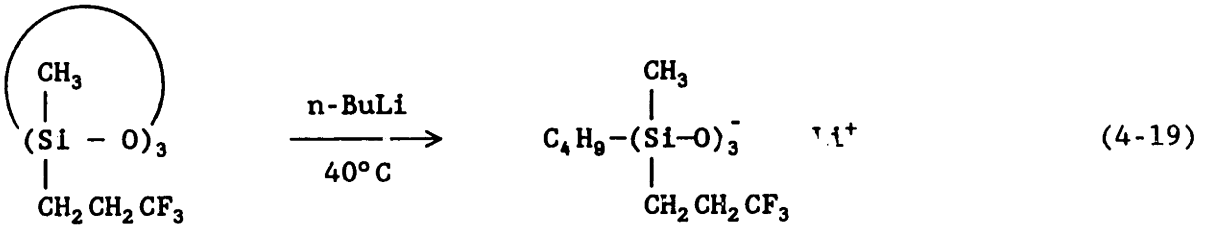

(4-19)

trimer monoadduct

Propagation

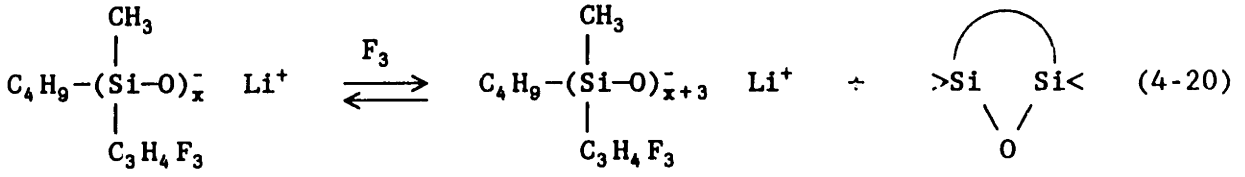

(4-20)

mixed cyclics, F_n

$n \geq 4$

Termination

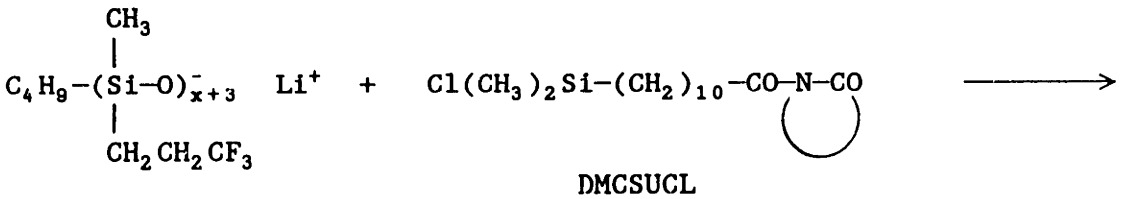

growing siloxanolate

DMCSUCL

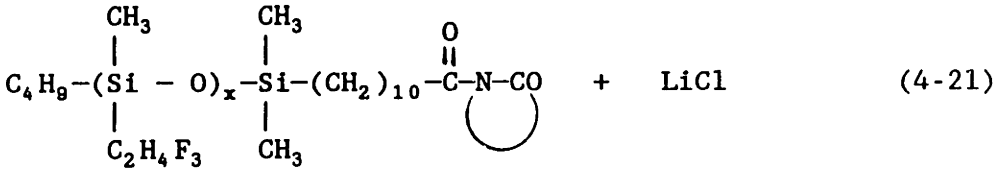

(4-21)

Fluorinated Siloxane-Lactam Macromonomer

(FSLM)

Upon termination, the reactor medium turns milky white with solid LiCl so the polymer is separated by suspending the reactor contents in THF, filtering the suspension through 10 μm and 0.5 μm filters successively and precipitating the polymer from the residual salts and depolymerized cyclics or unreacted trimer with nonsolvent toluene. After settling, the precipitated phase is decanted and its remaining solvent (mostly toluene and some THF) is distilled from the polymer under vacuum. This FSLM polymer was then used in the stability trials with caprolactam which are detailed in chapter VI.§C.

The efficiency of the functionalization reaction was ascertained by three experimental observations. First, the formation of the whitish salts is indicative of the condensation between the living siloxanolate and the chlorosilyl group. The fact that the polymer is stable over long periods of time (months) without depolymerization and generation of

additional cyclics as determined by SEC suggests that the fluoroalkylsiloxane is end-capped with the acyllactam. Otherwise, the known depolymerization reactions would have reduced most of the linear polymer to cyclics.

Secondly, the fractionated, functionalized polymer was chromatographed on the SEC system described in Chapter VII, §C.2 using the UV spectrophotometer and RI detectors to look at different parts of the polymer molecule. The chromatogram of one of the functionalized fluoroalkylsiloxanes is shown in Figure 4-1 where the bottom curve #2 represents the RI detector response (which measures total polymer-solvent differential refractive index) and curve #3 represents the signal from the UV spectrophotometer (of the same polymer simultaneouly obtained) set at 225 nm. Since the homo-PTFPMS is transparent to UV in this wavelength range, the strong absorption of UV indicates presence of the acyllactam chromaphore on the worked-up polymer. Curve #1 (discussed previously, §B.2) represents a PTFPMS with a terminal trimethylsilyl group and shows no UV absorption. Thus, comparing these two chromatographs of the same type of polymer with different end functionality strongly suggests the presence of the ω-N-acyllactam on the fluoralkylsiloxane.

And thirdly, ^{1}H NMR confirmed the existence of the coupling agent in the fluoroalkylsiloxane structure as shown in Figure 4-8. This spectrum shows the the peaks characteristic of the trifluoropropyl methylenes at ca. 0.88 and 2.1–2.3 ppm and the silyl methyl protons at ca. 0.27 ppm which are more downfield than in dimethylsiloxanes due to the electronegative fluoroalkyl substituent. The decyl alkyl protons of the coupling agent are clearly seen (on the same scale as the polymeric

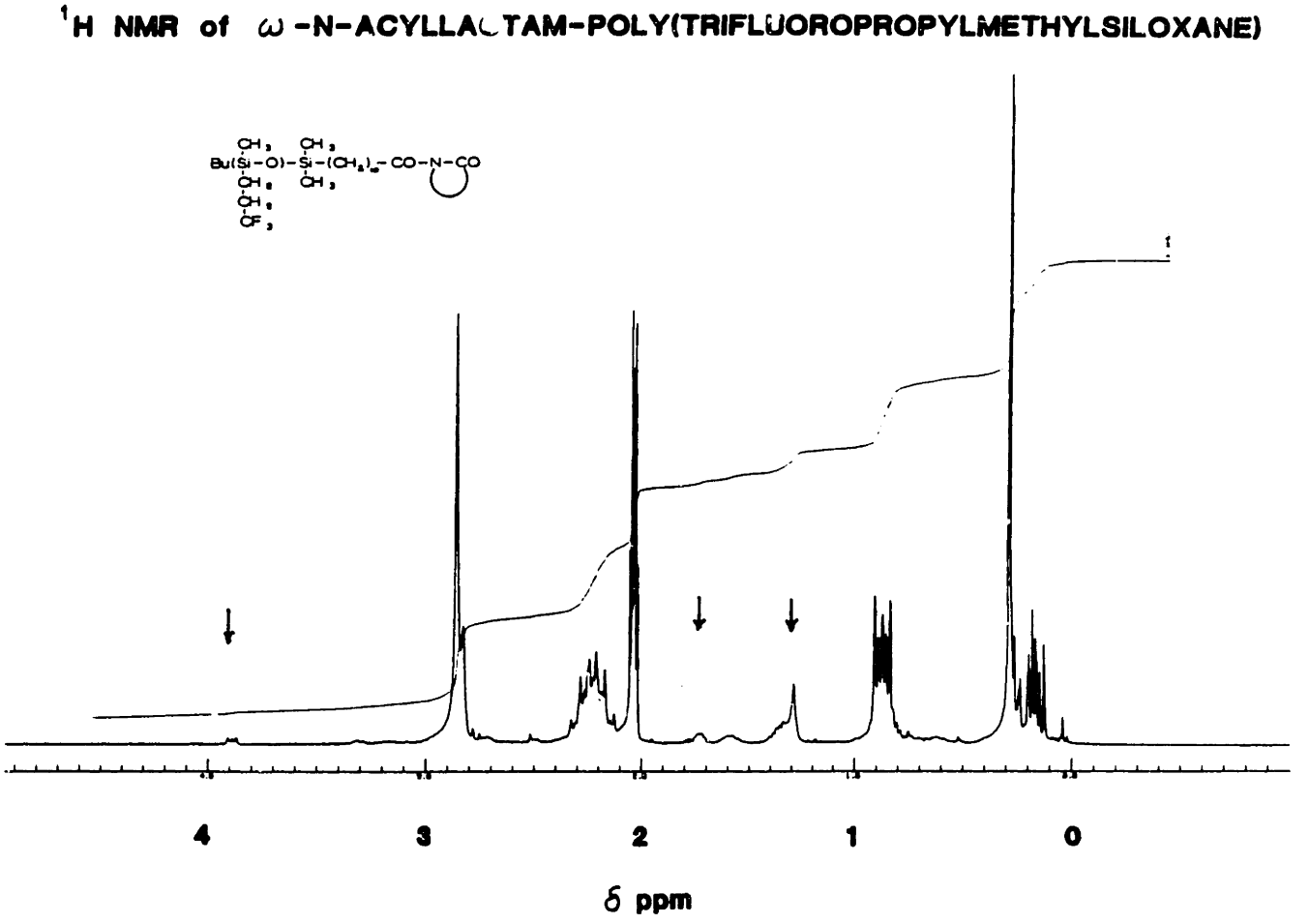

Figure 4-8 ^{1}H NMR of ω-N-acylactam-poly(trifluoropropylmethylsiloxane) showing end group functionality.(↓)

protons) at 1.3 ppm and the methylenes α to the imide nitrogen are evident at 3.9 ppm just as in the coupling agent ^{1}H NMR spectrum in Figure 3-1b, Chapter III. Presence of the signature protons of the ω-N-acyllactam group, in combination with the other experimental evidence, confirms successful end-functionalization.

Conclusions

The polymerization and end-functionalization of poly(trifluoropropylmethylsiloxane) has been accomplished with high efficiency by combining anionic polymerization and the kinetic model developed in §B to give a well defined linear fluoroalkylsiloxane macromonomer capable of initiating caprolactam polymerization. This has been confirmed by several methods including visual observations, size exclusion chromatography with site specific detectors and ^{1}H NMR. Unfortunately, as will be seen in chapter VI, this polymer is incapable of withstanding the harsh, basic environment of the nylon-6 copolymerization reactor. Fortunately, however, this chemistry is easily adapted to the synthesis of poly(dimethylsiloxane) macromonomers for copolymerization with caprolactam which will be discssed next.

C. DIMETHYLSILOXANE POLYMERIZATION

1. Previous Work

The synthesis of polydimethylsiloxane has received considerable attention [30-33], with specific focus on the model octamethylcyclotetrasiloxane (D_4) - KOH system [29,16,17,19,34,35]. This system was studied intensively by Grubb and Osthoff [29] who measured the polymerization kinetics by monitoring reactor vapor pressure and advanced the anionic two-step mechanism for anhydrous systems. First, the base (R = H, $-Si(CH_3)_3$, or $-Si(CH_3)_2O$----) coordinates with Si extending it to the pentavalent state which is followed by ring opening of the siloxane bond to give the adduct.

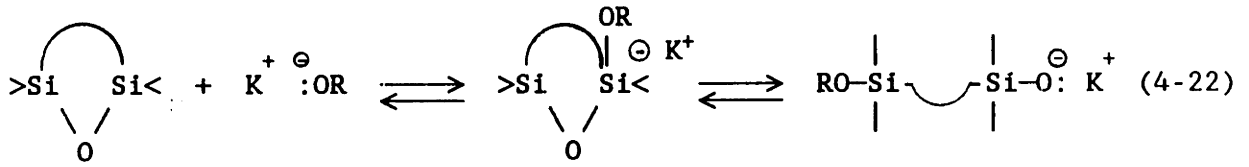

monomer, D_4 pencavalent state adduct (4-22)

They found first order kinetic dependence on monomer consumption and proposed the partially dissociated siloxanolate as the active specie for chain initiation and propagation. The dissociation equilibrium implies square root dependence on catalyst concentration which has been discussed thoroughly in the previous section on trifluoropropylmethylsiloxane polymerization (see equations 4-11 and 4-13) and observed in practice by Grubb and Osthoff [29] and others [16,17,34-36]. It is also observed

that catalytic activity increases with ionization potential of the base, i.e. with the size of the counterion or,

$$k_{Cs^+} > k_{K^+} > k_{Na^+} > k_{Li^+} \qquad (4\text{-}23)$$

for D_4 polymerization as in other anionic polymerizations such as propylene oxide ring opening [37]. This results in a stronger equilibrium shift to the right or greater solvation/ionization and increased reactivity.

Other investigators examined a wider temperature range with [16-19] and without [29,34,35] activators and found similar results. As Carmichael and Winger [38] have shown, the equilibrium composition of poly(dimethylsiloxane) (PDMS) with its corresponding cyclics (as prepared from D_4-KOH) lies in favor of the polymer, $K_e \simeq 0.15$. This favorable thermodynamic state with an equilibrium conversion of ~87% polymer makes PDMS attractive for commercial production and theoretical study and obviates any extensive kinetic modeling in order to maximize the yield as with the fluoroalkylsiloxanes.

The equilibrium of dimethylsiloxanes was first studied semitheoretically by Scott [31] who showed the existence of depolymerization reactions to yield D_4 and larger cyclics. He determined that a minimum concentration of $-(CH_3)_2SiO-$ units (2.2M or ~17% vol) must be present <u>as cyclics</u> before chain formation can occur. Surprisingly, experimental <u>equilibrium</u> data from Grubb and Osthoff (87 %v polymer including cyclics up to D_{14}) confirm this value. Morton et.al. [17] experimentally verified that a minimum concentration of 18 %v D_4 must be present in THF before an appreciable viscosity increase occurred. In fact, in the

D_4/KOH polymerization system, a continuous distribution of macrocyclics up to D_{400} has been experimentally verified by Brown and Slusarczuk [23] who used vapor phase chromatography to determine a maximum concentration of the D_4 cyclic and a local maximum concentration for the D_{15} cyclic. For cyclics of D_{40} to D_{200}, the data confirmed the cyclization theory of Stockmayer and Jacobson [39].

Unexpectedly, this system does not show a ceiling temperature effect whereby equilibrium monomer concentration would correlate with the inverse exponential of temperature, viz.

$$\ln \frac{M_e}{M_s} = \frac{\Delta H_p}{RT_c} - \frac{\Delta S^\circ}{R} \qquad (4\text{-}24)$$

Morton investigated temperatures from 25-140°C for polymerization of D_4 by KOH and found no effect of temperature on equilibrium concentrations [16,17]. According to Morton et.al. [17] the statistical analysis of Scott predicted this independence for all cyclics except the trimer, D_3, where M_e increases with temperature.

Reaction Kinetics of Polydimethylsiloxanes

Kinetic studies [16,29,34,38] have verified the first order dependence of the rate of polymerization of D_4 on monomer concentration and half order dependence on catalyst concentration (catalysts: NaOH, KOH, $K^+ \ ^-OSi(CH_3)_3$ or $Na^+ \ ^-OSi(CH_3)_3$). Since the dissociation equilibrium for the methylsiloxanes parallels that of the fluoroalkylsiloxanes and is established rapidly (see equations 4-11 and 4-13), the ring opening reaction is rate limiting with an activation energy of 19.6 kcal/mol [29]. Thus, to increase the rate, a greater number of more active anions

must be produced by more fully solvating the ion twins, separating the cation from its siloxanolate and other chains and driving the equilibrium towards contact ions. This is exactly the theory of the polar promoters discussed in detail in the previous section on fluoroalkylsiloxane polymerization.

Morton and Bostick [17] found that the presence of THF (20-30% vol; ϵ (dielectric constant) = 7.58) increased the polymerization rate by a factor of 2-3 so that a comparable rate at 60°C was observed versus bulk polymerization (no THF) at 140°C. It was determined that the THF did not enter the reaction as an initiator or electron transfer complex but only "promoted" the reaction by increasing the dielectric constant of the reaction medium.

Another common promoter that has been used [18,22] is dimethyl sulfoxide (DMSO) in small quantities. Approximately 0.5-1.0% wt accelerates the reaction at 95°C by a factor of 100X as measured roughly by viscosity increase. Apparently, no detrimental effect on equilibrium is observed and conversion to polymer remains ~80%. Since the amount of DMSO is small, the dielectric constant of the mixture does not change appreciably [18] so the increase in rate must be due to a solvation effect of the cation by the relatively negatively charged oxygen from the DMSO as well as some solvation of the siloxanolate ion by the electropositive Si of the abundant siloxane monomer units. This juxtaposition is exactly what enhances the displacement reactions in siloxane equilibrations; the promoter is used to solvate away the cation which permits the Si atoms from the monomer to solvate the oxanion.

Other powerful promoters for D_4 polymerization are the trialkyl phosphine oxides and phosphoric triamides such as hexamethylphosphoramide (HMPA). As with DMSO, it is believed that coordination of the gegenion with the nucleophilic portion of the promoter is responsible for increased solvation and concentration of solvent separated ions. This leads to an increase rate much the same as Szwarc found when studying styrene polymerization by twinned and solvent separated ion pairs [27,28].

Ostrozynski [19] extensively studied the kinetics of the promoter-enhanced methylcyclosiloxane polymerization as discussed in the previous section on fluoroalkylsiloxanes and found that (on the average) 2.5 hexamethylphophoramide (HMPA) molecules are complexed with each catalytic ion pair at 50°C. The activation energy was found to be 18.0 kcal/mol over the range of 40-65°C and agrees well with the earlier value at higher temperatures of 120-160°C of 19.6 kcal/mol, unpromoted. This agreement implies that the propagation reaction is rate controlling in both cases only at higher velocities in the "promoted" case due to the increased concentration of active centers.

A narrow molecular weight distribution (MWD) was achieved by Lee et.al. [22] using the more reactive trimer, D_3 to enhance the ring-opening propagation step and a less active catalyst (i.e. with a Li^+) and a promoter. Addition of n-butyllithium to the cyclic trimer at 85°C with ~1% DMSO catalyzed polymerization via the lithium butylsiloxanolate giving narrow MWD polymer (no values quoted, only SEC spectrum published) and no cyclics other than unreacted D_3. This is in contrast to the other equilibration products containing a large fraction of cyclics up to 20%

produced by acids or bases with larger cations such as KOH or NaOH. Reasonable correlation between molecular weight and initiator concentration was quoted if the system was anhydrous implying that the Li siloxanolate catalyst is too weak to initiate the ordinary base-catalyzed redistribution reactions. Thus, the effect of moisture can be detrimental not only in creating hydroxy end-capped chains but in catalyzing the redistribution reactions and randomizing molecular weight. These same trends were found in this thesis work and discussed previously for the fluoroalkylsiloxanes; experimental results for the methylsiloxanes will be covered next.

2. Experimental Results and Discussion

Test of Scott's Theory

An experiment was conducted to test the theory of Scott [31] (and Morton [17]) as to whether a critical concentration of trimer (or cyclics in general) had to be present in the reactor in order to form linear polymer. A master batch of 17.8 %w D_3 in xylene was prepared in the usual manner (solvent was distilled from Na and subsequently from BuLi, trimer was distilled from CaH_2) and initiated with n-BuLi with a 10:1 ratio of DMSO:BuLi at 45°C. In a second run, pure D_3 was added to an aliquot of the 17.8 %w master batch to give a 70.0 %w D_3 in xylene solution which was initiated with n-BuLi and promoted with DMSO:BuLi = 2.25:1 at 45°C. The lower A/I in the latter case compensated for the higher concentration of trimer and an increased rate via the mass action law; activator concentrations were approximately equal. In the former trial, the polymerization reached ca. only 10 % conversion in as little as 20 minutes and remained there for up to 4 days. Based on rough

calculations, the observed monomer consumption rate constant, k_1^* is ca. 0.1 min^{-1}. On the other hand, the latter run reached 90% conversion in just 7 minutes and 99% conversion in 15 minutes (to give a k_1^*=0.32 min^{-1}). Clearly, these results support Scott's theory that linear polymer would be formed only at monomer concentrations roughly above 17 %v cyclics because the low conversion is not due to kinetic limitations but rather to the very low equilibrium attainable with only a minimal amount of cyclics present in the reactor (i.e. ca. 17 %). These results coupled with similar previous literature findings [17] suggest that the equilibrium in methylsiloxane polymerizations is strongly governed by the starting concentration of cycles. However, this does not necessarily mean that bulk or extremely high D_3 concentrations always are preferred due to viscosity effects on the MWD. As has been observed in this thesis work, concentrations around 35 - 50 %w siloxane provide satisfactory rate and conversion and give narrow polydispersity siloxane because the chain transfer reactions are reduced in solution as compared to bulk reactions.

a. Polymerization Chemistry and Kinetics

As discussed previously, n-BuLi was used as the initiator in all trials to take advantage of the reduced nucleophilicity of the siloxanolate-Li^+ as compared to larger counterions. It was found that bulk polymerization at 65-70°C (D_3 m.p.= 64°C [40]) promoted with DMSO as in the fluoroalkylsiloxanes (A/I = 1.125:1 - 3:1) always generated a high molecular weight shoulder peak that ranged in molecular weight from 2 - 3 times the target molecular weight. The source of this high molecular weight peak is unknown but it was believed to result from wetness in the

DMSO (ca. 500 ppm H_2O via the Mitsubishi moisture analyzer) which neutralized the butyl anion producing LiOH. This subsequently formed the lithium hexamethylsiloxanolate-3-ol or (HO-(Si(Me)$_2$-O-)$_3^-Li^+$) which was capable of propagation at either end of the oligomer to give twice the molecular weight for a given kinetic chain length. This shoulder peak was found for target molecular weights ranging from 6 kg/mole to 60 kg/mole and was usually 2-3 times the molecular weight of the main peak.

As a result of the poor performance of DMSO with the methylsiloxanes (from a molecular weight standpoint and not a kinetic one), tetrahydrofuran (THF) was used as the promoter in several different succeeding trials. The THF was purified by stirring over sodium dispersion followed by rapid stirring with BuLi/hexane for only 15 minutes and immediate distillation into a clean, flamed, purged flask capable of isolation from the vacuum system. Both xylene and benzene solvents were used with D_3 concentrations between 25 and 45 %w, initiated by n-BuLi and polymerized at 25°C. The solvents were purified over sodium and then distilled from BuLi in the case of the former and distilled from living polystyryllithium for the latter. The benzene was washed with H_2SO_4, dried over anhydrous $MgSO_4$ and dried over sodium dispersion before distillation into the living polystyryllithium.

The two trials with xylene and benzene gave indistinguishable results as far as solvent effects were concerned. No chain transfer was evident in xylene which is consistent with the known decreased basicity of the siloxanolate as compared to a carbanion, the latter being able to chain transfer with substituted benzene solvents. The polymerization

rates were inexorably slow; D_3 polymerization in xylene with 1.0 %w THF and target MW = 8 kg/mole reached only ~ 30% conversion in a little over 40 hours to give a first order monomer rate constant of 10^{-4} min^{-1}. With added THF at the 43 hour mark to give 2.5 %w total THF, conversion reached 74% after 72 total hours yielding a monomer consumption rate constant of $6x10^{-4}$ min^{-1}. See data in Table 4-1. Polymerization in benzene with THF:BuLi = 6:1 (1 %w THF), increased to 13:1 (2.2 %w THF) gave a $k_1^* = 5x10^{-5}$ min^{-1} as determined from the data in Table 4-1 for reaction times up to 190 hours. Additional THF did not seem to give marked increases as the polymerization took a total of two weeks to complete. The length of these polymerizations is not only prohibitive but also yields slightly broader MWD as determined by SEC due to greater contamination from adventitious moisture which would facilitate more transsiloxanolization (chain transfer) reactions. Note in Figure 4-9 the slightly broader distribution of the PDMS produced in benzene (2 weeks, dashed curve) with a polydispersity of 1.24 versus the PDMS produced by THF solution polymerization in 2 hours, solid curve, $\bar{M}_w/\bar{M}_n = 1.17$. No cyclics larger than the trimer (which would result from depolymerization of the linear PDMS) were observed in either of these systems, i.e. only linear polymer and monomer were present except at very early stages of the polymerization where it is impossible to distinguish via SEC between linear and cyclic oligomers of ca. 300-500 molecular weight.

Much more efficient results were obtained when THF was used as both the solvent and promoter. Here, consumption of D_3 reached 97% conversion in just 2 hours giving a narrow MWD as shown in Figure 4-9 with no depolymerization to large cyclics. This is in sharp contrast with

Table 4-1

Polydimethylsiloxane Synthesis with THF Promoter : Experimental Data

(Initiator = n-BuLi)

Solvent	%w D_3	THF % w	[I] (M)	Peak† MW	Temp	Sample Time (h)	Wt Fract* P / M
Run 5H:				target=8			
Xylene	45	1.0	.05	0.8	25°	4	9 / 91
				2.2		42.5	31 / 69
		2.5		4.7		72	74 / 26
calc D_3 rate const, $k_1^* = 1 \times 10^{-4}$ min^{-1} @ 1% THF; 6×10^{-4} min^{-1} @ 2.5% THF							
Run 5I:				target=10			
Benzene	25	1.0	~.014	0.4	25°	17	5 / 95
		2.2		2.3		38	20 / 80
				5.0		68	– / –
				9.0		136	36 / 64
				10.4		190	48 / 52
		11.9		12.9		232	56 / 44
		22.2		13.9		256	61 / 39
		36		14.2		301	76 / 24
				15.9		346	94 / 6
calc D_3 rate constant, $k_1^* = 5 \times 10^{-5}$ min^{-1} @ 2.2 % THF							
Run 5J:				target=12			
THF	38	62	.036	12.9	25°	90 min	90 / 10
				14.0		120 min	97 / 3
calculated D_3 consumption rate constant, $k_1^* = 2.8 \times 10^{-2}$ min^{-1}							

† Molecular weight in kg/mole

* Weight Fraction of polymer (P) and cyclic monomer D_3, (M)

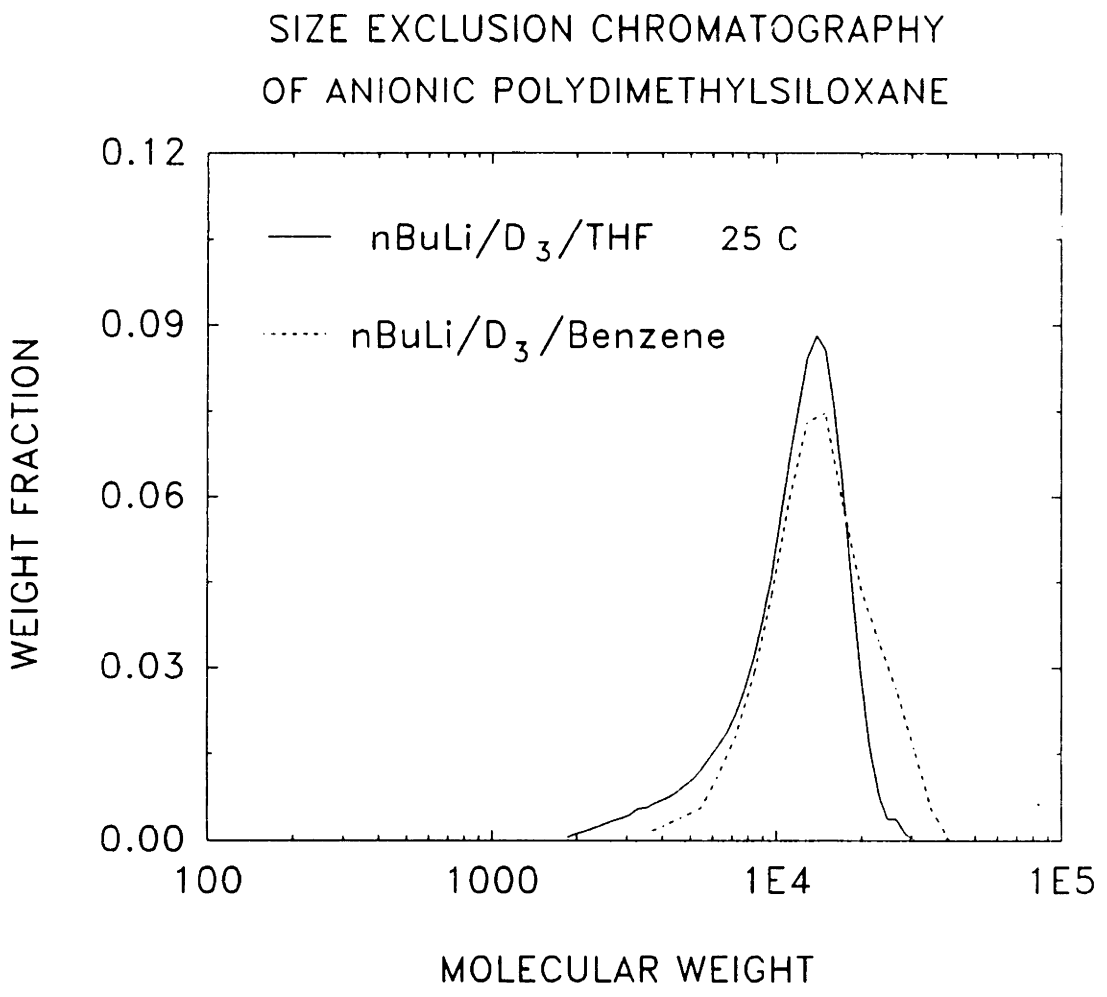

Figure 4-9 Size exclusion chromatographs of ω-N-acyllactam-PDMS in toluene / μ-Styragel[R] at 25°C. Both polymers from trimer initiated with n-BuLi in either THF (———) or benzene (- - -), polymerized at 25°C.

the fluoroalkylsiloxane studied earlier where solution polymerization in THF yielded only larger cyclics (mainly F_4) and no linear polymer. The living PDMS could be held in THF solution for several days with only a slight broadening of the MWD which is quite remarkable considering the strong depolymerizing tendency of the fluoroalkylsiloxane under similar conditions. These results demonstrate that the anionic polymerization of PDMS in THF proceeds nearly without transfer and termination reactions and can be accomplished by a variety of combinations of solvent, initiator and promoter.

During the polymerization of D_3 in THF a large aliquot (~ 2 ml) was removed from the reactor at the 120 minute mark and transferred to another clean, flamed reactor where several equivalents of tetramethyltetravinylcyclotetrasiloxane ($D_{4\pi}$) were added creating a sequential siloxane diblock copolymer of dimethylsiloxane end-capped with methylvinylsiloxane. The dimethylsiloxane block contained ca. 200 repeat units versus only 8 to 12 for the methylvinylsiloxane block. The vinyl groups were incorporated to provide crosslinking sites via peroxides or irradiation if desired and also to permit staining with OsO_4, a heavy atom stain which reacts with unsaturation as determined by Kato [41] for contrast enhancement in the transmission electron microscope (TEM). As it has turned out, the silicone has provided satisfactory contrast in the TEM due to its greater electron density than the other elements of the polyamide block copolymer; the morphology will be covered in chapter VIII.

The chemistry of these reactions is outlined below.

Initiation

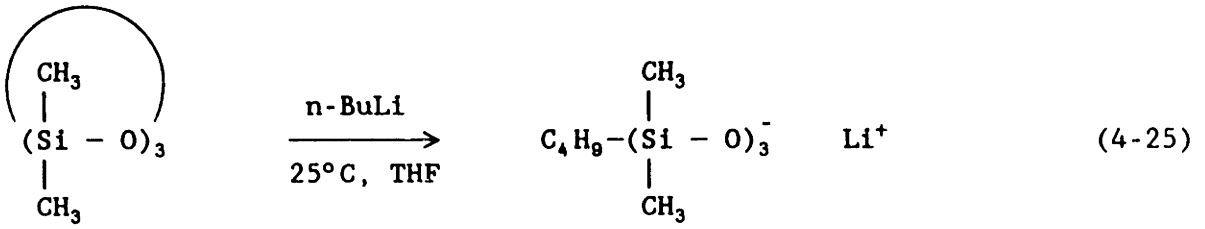

(4-25)

trimer monoadduct

Propagation

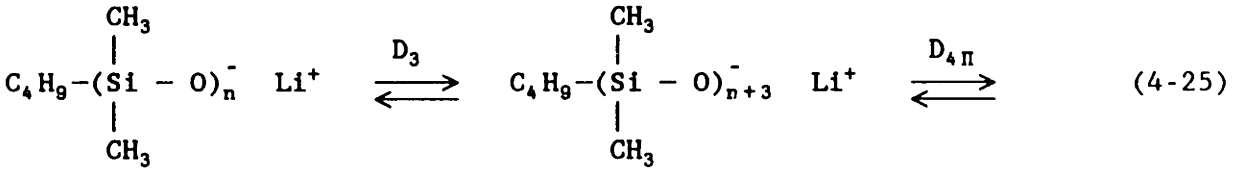

(4-25)

lithium dimethylsiloxanolate

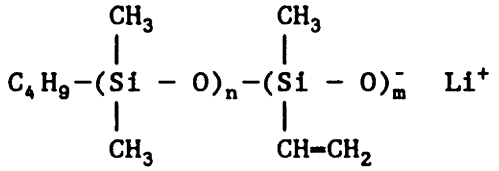

n ≈ 200
m ≈ 12

lithium dimethylsiloxane-b-methylvinylsiloxanolate

Termination

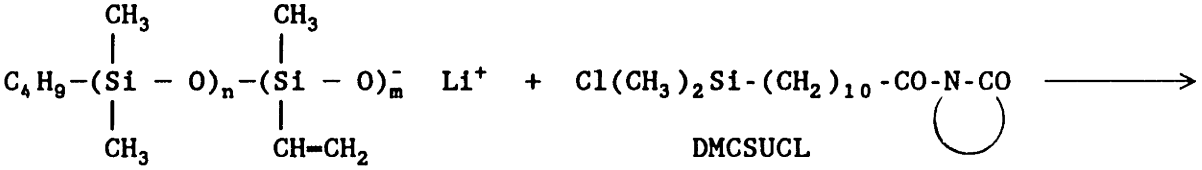

living siloxanolate

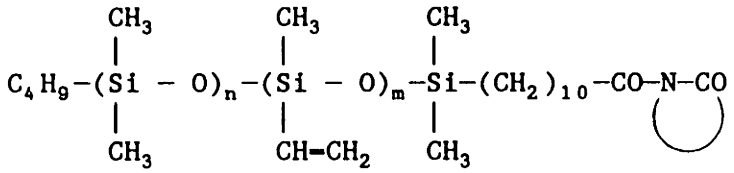

(4-26)

Poly(dimethylsiloxane-b-methylvinylsiloxane)-Lactam Macromonomer

(MSLM)

The reaction steps were the same as for the fluoroalkylsiloxane polymerization where initiation was accomplished by nucleophilic attack of the butyl anion on the electropositive ring silicon opening the ring to give the monoadduct. Successive additions of the trimer, D_3 to the growing siloxanolate consumed the monomer in about 120 minutes which yielded the living dimethylsiloxanolate. Sequential block copolymerization via addition of $D_{4\pi}$ to the living end was followed 20 minutes later by termination with the coupling agent (DMCSUCL) which gave the dimethylsiloxane-b-methylvinylsiloxane-lactam terminated macromonomer (MSLM).

Since virtually no large cyclics are formed with this PDMS polymerization and consumption of D_3 is nearly complete, sequential block copolymerization was possible and represents new possibilities for innovative syntheses. This concept was explored by combining a trifluoropropylmethylsilxoane block with a methylsiloxane block in attempts to improve the chemical stability of the former to caprolactam. Unfortunately, as will be outlined in § VI.C.2, this did not improve the chemical stability of the fluoroalkylsiloxane.

b. Characterization of End-Functionalized Methylsiloxane

Workup of the MSLM parallels that with the FSLM but since the solubilities of the two polymers are different, another nonsolvent-solvent system had to be used. The quenched reactor contents were dissolved in THF, filtered, and then precipitated with acetonitrile, CH_3CN. After vacuum drying, the polymer was chromatographed as shown in Figure 4-9, solid curve, but since the SEC system for PDMS was operated in toluene no UV absorption could be done. However, for one run the system was switched over to THF and the UV absorption was obtained showing the successful end-functionalization. THF is not normally the solvent of choice because it has a $\tilde{n}_d^{20} \approx 1.407$ [42] which is very close to that of the monomer, D_3, $\tilde{n}_d^{20} \approx 1.395$ [41]. This caused polarity reversal during elution of the monomer and subsequent garbage peaks which made integration difficult. In addition, the reaction mixture, at termination of the PDMS polymerization, appeared very similar to that of the end-functionalized PTFPMS giving confidence to the applicability of the coupling agent with any anionically polymerized siloxane.

Additional confirmation of the same type of end-functionalization as obtained with the fluoroalkylsiloxane was obtained by NMR. Shown in Figure 4-10 is the ^1H spectrum for a functionalized PDMS with excellent resolution of the individual coupling agent peaks on the expanded scale which belong to the aliphatic and cyclic methylenes at 1.3 ppm and 1.6–1.7 ppm respectively, the methylenes alpha to the carbonyls at 2.7 and 2.9 ppm respectively and the two methylenes alpha to the Si which are more shielded and hence resonate slightly upfield at about 0.85 ppm. The fact that both lactam-terminated silicone polymers are extensively

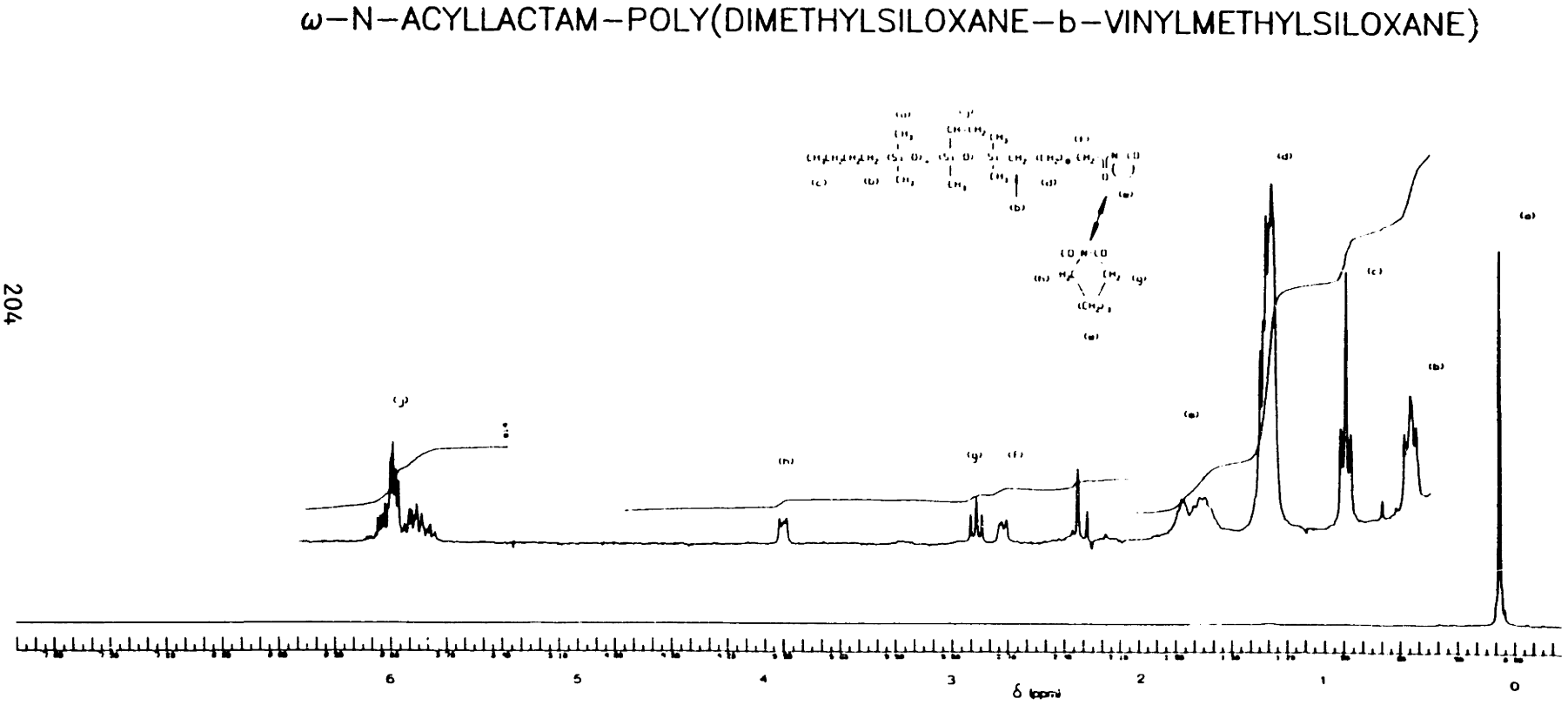

Figure 4-10 ^{1}H NMR spectrum of ω-N-acyllactam-PDMS with expanded scale confirming existence of signature protons from coupling agent in the siloxane.

precipitated which would dissolve away any unbonded acyllactam before characterization and the fact that they both initiate caprolactam polymerization further proves their viability and the success of producing lactam-terminated siloxane macromonomers.

D. REFERENCES FOR CHAPTER IV

1. W. Noll, Chemistry and Technology of Silicones, Academic Press, New York, N.Y., 1968, Ch. 5, §4, p. 209+.

2. V. Bazant and V. Chvalosky, Chemistry of Organosilicon Compounds, Academic Press, New York, N.Y. 1965, p.15.

3. W. Noll, Chemistry and Technology of Silicones, Academic Press, New York, N.Y., 1968, p. 224, 312.

4. Rhone-Poulenc, French Pat. 950582 (1947).

5. F.C. Schmidt and D.F. Wilcock, Jnl. Am. Chem. Soc., **68**, 358 (1946).

6. D.T. Hurd, Jnl. Am. Chem. Soc., **77**, 2998 (1955).

7. L. Wilczek, S. Rubinsztajn, Jnl. Chojnowski, Makromol. Chem, **187**, 39 (1986).

8. P. Siegwalt, Polymer Jnl., **19**(5), 567 (1987).

9. S. Nitzsche, Wacker-Chemie, W. German Pat. 831098 (1949).

10. J.G.E. Wright and J. Marsden, Gen. Elect. US Pat 2389477 (1942).

11. O.R. Pierce, G.W. Holbrook, O.K. Johannson, J.C. Saylor, E.D. Brown, Ind. Eng. Chem. **52**(9), 783 (1960).

12. Y.A. Yuzhelevskii, Y.G. Kagan, E.V. Kogan, A.L. Klebanskii, N.N. Nikiforova, Polym. Sci. USSR, **11**, 1745 (1969).

13. Y.A. Yuzhelevskii, Y.G. Kagan, N.N. Fedoseyeva, Polym. Sci. USSR, **12**(1), 1800 (1970).

14. Y.A. Yuzhelevskii, V.V. Pchelintsev, Y.G. Kagan, Polym. Sci. USSR, **15**, 1795 (1973).

15. J.B. Carmichael, E.D. Brown, Jnl. Polym. Sci: Polym. Lttrs., **3**, 473 (1965).

16. M. Morton, M.A. Deisz & E.E. Bostick, Jnl. Polym. Sci. , **A2**, 513 (1964).

17. M. Morton, E.E. Bostick, Jnl. Polym. Sci., A, **2**, 523 (1964).

18. G.D. Cooper, J.R. Elliott, Jnl. Polym. Sci.: Part A1, **4**, 603 (1966).

19. R.L. Ostrozynski, ACS Polym.Preprts., **8**(1), 474 (1967).

20. C.A. Veith and R.E. Cohen, Am. Chem. Soc., Polym. Mat. Sci. Eng. Div., Polym. Prepts., **57**, 661 (1987);
C.A. Veith and R.E. Cohen, Jnl. Polym. Sci., Polym. Chem. Ed., **27**, 1241 (1989).

21. D.W. Scott, Jnl. Am. Chem. Soc., **68**, 2294 (1946).

22. C.L. Lee, C.L. Frye, O.K. Johannson, ACS Polymer Prpts, Polym. Chem Div., **10(2)**, 1361 (1969).

23. J.F. Brown, G.M.J. Slusarczuk, Jnl. Am. Chem. Soc., **87**, 931 (1965).

24. L. Wilczek, S. Rubinsztajn, J. Chojnowski, Makromol. Chem., **187**, 39 (1986).

25. C.M. Bender, S.A. Orszag, Advanced Mathematical Methods for Scientists and Engineers, McGraw-Hill, New York (1978).

26. P. Rempp, E.W. Merrill, Polymer Synthesis, Huethig & Wepf Verlag Basel, New York, (1986) p.130.

27. M. Szwarc, Die Makromol. Chem., **89**, 44 (1965).

28. D.N. Bhattacharga, C.L. Lee, J. Smid, M. Szwarc, Jnl. Phys. Chem., **69**, 612 (1965).

29. W.T. Grubb and R.C. Osthoff, Jnl. Am. Chem. Soc., **77**, 1405 (1955).

30. W. Patnode, D.F. Wilcock, Jnl. Am. Chem. Soc., **68**, 358 (1946).

31. D.W. Scott, Jnl. Am. Chem. Soc., **68**, 2294 (1946).

32. V.M. Kopylov, P.L. Prikhod'ko, V.A. Kovyazin, I.L. Dubchak, Jnl. Polym. Sci., USSR, **26(9)**, 2104 (1984).

33. R.L. Merker, M.J. Scott, Jnl. Polym. Sci., **43**, 297 (1960).

34. M. Kucera, Jnl. Polym. Sci., **58**, 1263 (1962).

35. M. Kucera, M. Jelinek, Coll. Czech. Chem. Commun., **25**, 536 (1960).

36. M. Morton, A. Rembaum & E.E. Bostick, Jnl. Polym. Sci., **32**, 350 (1958).

37. N.N. Lebedev, Y.I. Baranov, Jnl. Polym. Sci., USSR, **8**, 211 (1966).

38. J.B. Carmichael, R. Winger, Jnl. Polym. Sci., **A3**, 971 (1965).

39. H. Jacobson, W.H. Stockmayer, Jnl. Chem. Phys., **18**, 1600 (1950).

40. C. Eaborn, Organosilicon Compounds, Butterworths Scientific Pub., London, 1960, p.277.

41. K. Kato, Polym. Eng. Sci., 7, 38 (1967).

42. W.W. Yau, J.J. Kirkland and D.D. Bly, Modern Size-Exclusion Liquid Chromatography, Wiley, New York, 1979, p 258.

CHAPTER V. NYLON-6 CHEMISTRY

The polymerization of ϵ-caprolactam can proceed by either a hydrolytic or an anionic mechanism. The distinction between these involves the type of nucleophilic attack on the lactam ring and the presence or absence of large amounts of water deliberately added to the monomer. Hydrolytic polymerization is reserved for water initiated reactions with a primary amine nucleophile whereas the base for the anionic polymerization is the lactam anion attacking an acylated lactam. The polymers will also differ in chain end structure. Hydrolytic nylon-6 will have amine and carboxylic acid end groups and can be titrated to determine molecular weight. Anionic polyamide-6 contains the initiator functional group at one end and an unopened lactam ring at the other (excluding transfer reactions). Although these two nylon-6's are produced via greatly different processes, ultimate mechanical properties are very similar with slightly higher molecular weights and conversions achieved by anionic polymerization. Accordingly, further explanation is grouped into two sections, hydrolytic and anionic.

A. HYDROLYTIC POLYMERIZATION

In 1948, Hanford and Joyce [1] from the DuPont Co. hydrolyzed ϵ-caprolactam at high temperatures of 220+°C and elevated pressures and produced ~ 75 % polyamide-6. Their explanation of the hydrolytic mechanism followed initial observations by Carothers and Berchet [2] who assumed self-condensation of ϵ-aminocaproic acid produced by reaction of water and ϵ-caprolactam as shown on the top of the next page.

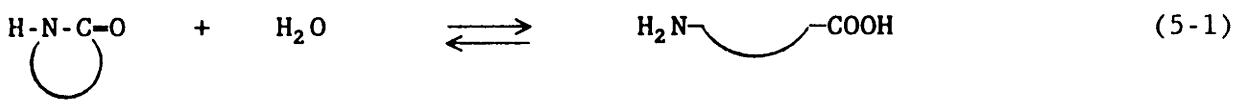

(5-1)

where H-N-C=O =

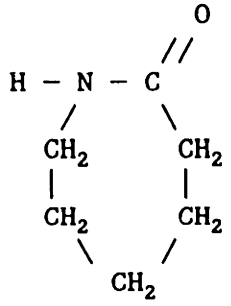

.

And subsequently,

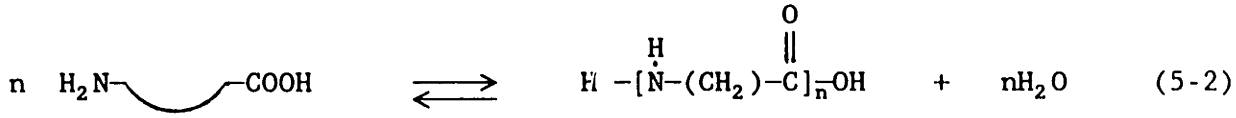

(5-2)

However, kinetic and chemical evidence [3,4] proves that the predominating propagation reaction consists of acid catalyzed addition of the amine group. Experimental observations indicate that the maximum rate coincides with the maximum end-group concentration and that the rate constant based on propagation by aminocaproic acid is three orders of magnitude too low to account for the observed rate. Experiments with additions of hexamethylene diamine and adipic acid showed rapid consumption of the diamine but stable existence of the diacid implying the catalytic role of the -COOH and the nucleophilic attack by the primary amine.

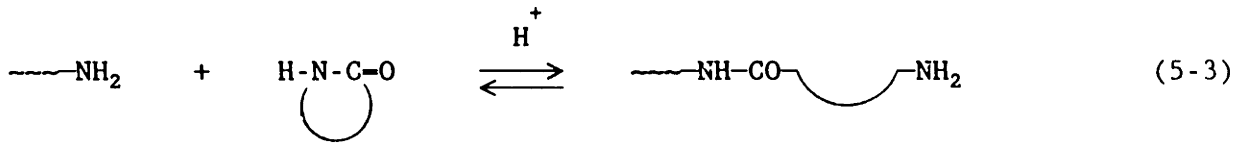

(5-3)

Further details on this mechanism can be found in Appendix 2.

B. ANIONIC POLYMERIZATION

Strong bases such as metal hydrides, amides and organometallic compounds are capable of catalyzing anionic polymerization via generation of the caprolactam anion, viz.,

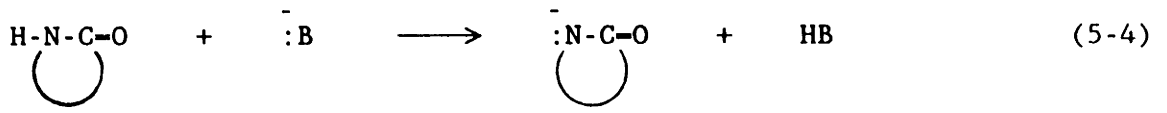

(5-4)

Due to the strong nucleophilicity of the lactam anion, several types of propagation reactions may occur as well as transfer and disproportionation which cause branching and randomization of molecular weight. These side reactions are prevalent at higher temperatures (200+°C) and higher catalyst (base) concentrations [5,6,7]. The accepted mechanism for anionic nylon-6 polymerization is detailed in a comprehensive review by Sebenda [8] and the important reactions are reiterated below.

Initiation

The initiation reaction involves the reversible ring-opening transamidation of the acylated lactam initiator (R can be either monomeric or polymeric) through nucleophilic attack of the lactam anion (or caprolactamate) catalyst at the ring carbonyl(*).

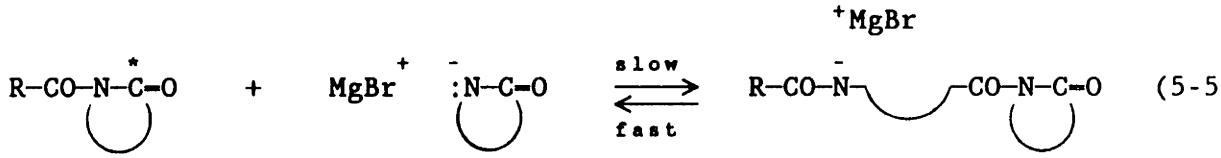

(5-5)

initiator catalyst amide anion

Acylation of the original caprolactam nitrogen to produce the initiator increases the electron deficiency of the imide linkage and increases the susceptibility for nucleophilic attack at the ring carbonyl(*). The amide anion is rapidly neutralized by a lactam proton to regenerate the catalyst and form the monoadduct acyllactam due to the greater acidity of the caprolactam versus the amide anion.

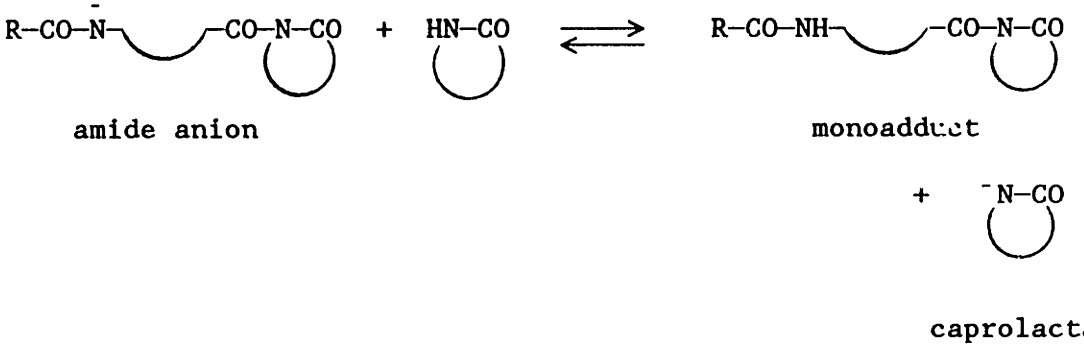

(5-6)

amide anion

monoadduct

caprolactamate

Propagation

The active propagation site is the terminal cyclic amide linkage and more specifically the ring carbonyl where identical nucleophilic attack by caprolactamate adds one more monomer unit as shown in equation (5-7).

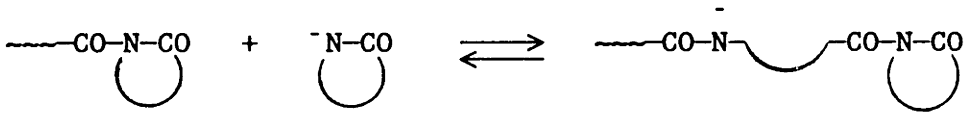

(5-7)

This lactam addition is followed by the fast proton exchange reaction leading to equilibrium between polymer and its amide anion [9] as shown in equation (5-8) and above in equation (5-6) for monoadduct formation. Equilibration in equation (5-8) is fairly rapid especially at earlier stages of the polymerization where the concentration of caprolactam (CPL) is high. These equations demonstrate why this type of propagation is

referred to as an "activated monomer" mechanism because the nucleophile resides on the incoming monomer that has been activated or formed due to the proton exchange reaction (5-6) or (5-8). This is in contrast to typical anionic polymerizations where the charge resides on the polymer chain.

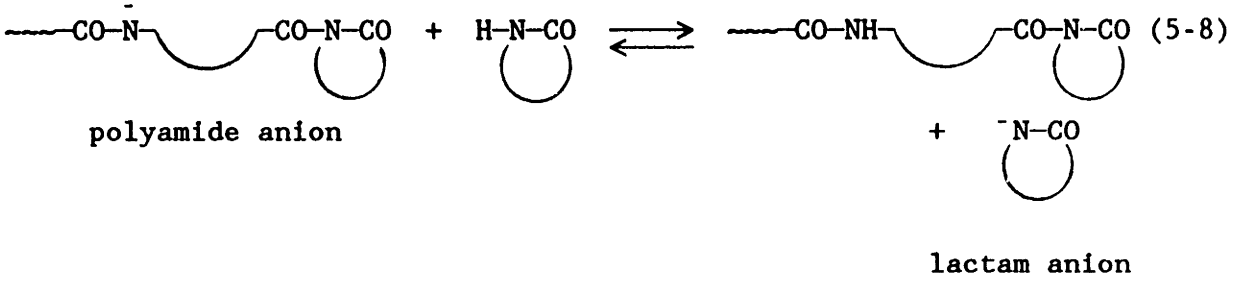

(5-8)

However, a second type of propagation can occur via polymeric amide anion attack on a lactam carbonyl (*) with ring opening, equation (5-9).

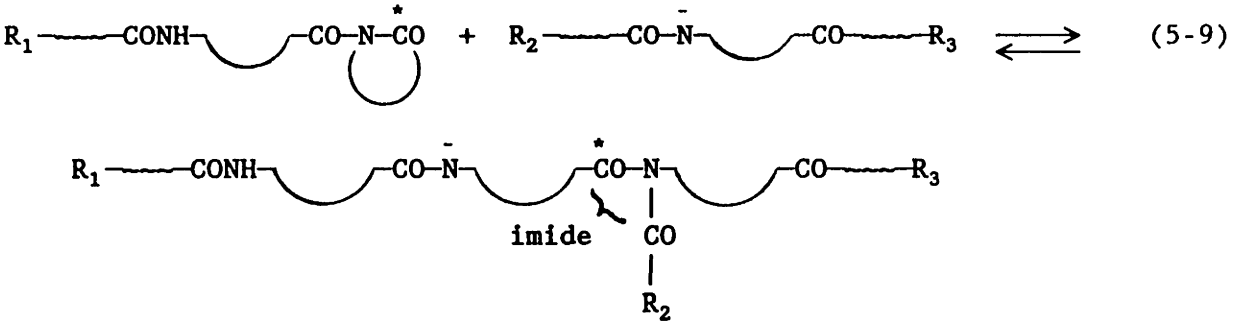

(5-9)

After proton exchange, the newly formed imide group can react with the lactam anion and is a site for continued propagation.

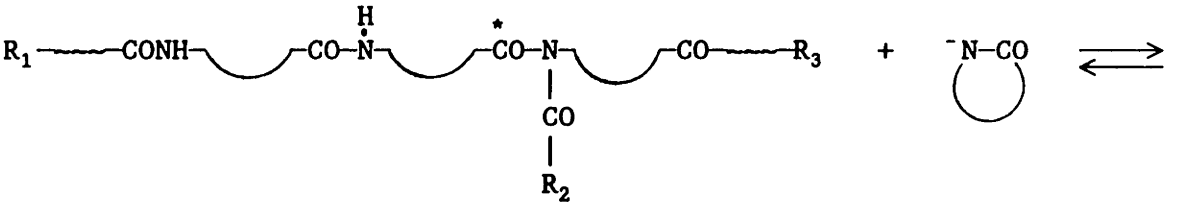

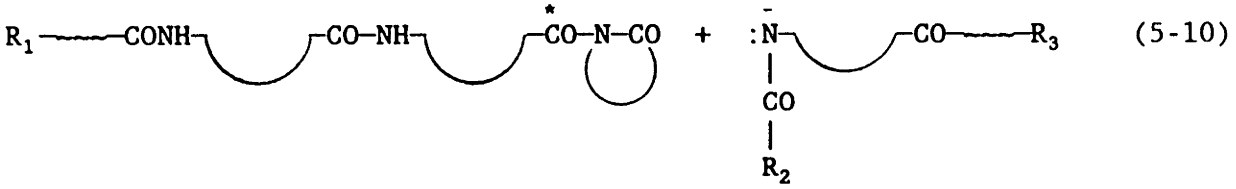

(5-10)

Note that there has been incorporation of a lactam unit in the sum of reactions (5-9) and (5-10) which are prevalent at higher degrees of conversion. These reactions alternatively could have been written for an amide anion attacking a polymeric amide carbonyl instead of the ring carbonyl in which case an amine anion and an imide group are formed. Thus, in addition to the imide and lactam anion, amine anion and carboxyl anions are also generated throughout the reaction. Due to the varying basicity among the anions, the growth rate and chain architecture change throughout the polymerization which makes it difficult to model the reaction scheme. In addition, consumption of imide groups by intermolecular condensation changes the concentration of "initiator" groups in contrast to other, more conventional anionic polymerization mechanisms. For reference, a schematic of the interrelation of many of these reactions is presented in Appendix 2 and some of these additional side reactions will be discussed in more detail in Chapter VI.

Reaction Kinetics

From just the few reactions already discussed, it is apparent that several species are involved in propagation. The rate of reaction obviously depends on the concentrations of the acyllactam initiator, monomer and catalyst but also depends on how these entities interact with the other groups such as main chain imides and their anions as well as

amine and carboxylic acid anions. Unlike conventional, living anionic polymerization, these concentrations are not necessarily constant throughout the reaction. In polymerizations above the melting temperature with a high initiator/catalyst ratio (ca. 2 – 3), most of the base is consumed quickly through Claisen condensation reactions (see Chapter VI) so that chain length equilibration (equation 5-8) is slowed down. This decreases the final polymerization rate and yields a lower polydispersity because of decreased basicity. With high concentrations of base, numerous side reactions such as disproportionation and transfer occur [5] increasing the number of polymer molecules [13] and will be discussed below.

At temperatures below the melt, crystallization can occur simultaneously with polymerization if the supercooling is sufficient. Bessell and Shortall [10] observed an increase in induction time (measured by viscosity rise) with decreasing base concentration at 180°C and attributed this to precipitation/crystallization of the polymer from the reaction mixture. Moore and Pahls [11] observed a local maximum in polymer viscosity as catalyst concentration was reduced from 4% mole to 1% mole for initiator concentrations of 1-2% mole. Maximum molecular weight occurred at ~ 2 mole % catalyst. Thus, low catalyst concentrations yielded a lower rate of polymerization and large amounts of catalyst generated unwanted side reactions, both extremes leading to lower molecular weights.

Tessyie, et.al. [13] extensively studied the effects of the base catalyst/initiator (C/I) ratio. Using N-phenylcarbamoylcaprolactam, Ph-NH-CO-N-$(CH_2)_5$-CO as a model N-acyllactam initiator, the ratio of conversion to number average molecular weight, $x/\bar{M}_n$ remained unchanged as a function of conversion (within experimental error) for a C/I = 1. This meant that the polymerization proceeded essentially via a "living anionic" mechanism void of transfer reactions. With a C/I = 4, the $x/\bar{M}_n$ increased monotonically as $\bar{M}_n$ decreased due to transfer and disproportionation. With the C/I = 1, the $\bar{M}_n$ at total conversion was nearly twice the calculated value indicating that half of the initiator molecules disappeared at the beginning of the reaction possibly due to a Claisen condensation reaction. (See Chapter VI, §B.2 for more details on these side reactions.) The measured polydispersity index, or $\bar{M}_w/\bar{M}_n$ however, increased with conversion as measured by gel permeation chromatography with Waters Styragel^R columns in hexamethylphosphoramide at 105°C. Molecular weight accuracy was uncertain because the only calibration was done with polystyrene standards in THF and no attempt was made to relate this to actual nylon-6 molecular weight. More accurate polydispersities of nylon-6 have been obtained in the course of this work which are presented in Chapter VII, §C. The general trend in the literature including industrial experience from the Monsanto Co. is that catalyst concentrations should be ca. 1-2 mole % and an initiator/catalyst ratio between 0.5 minimum – 2.0 maximum. Initiator/catalyst ratios as high as 2.5 have been used at elevated temperature while still retaining fairly narrow polydispersity [7] but this gives lower reaction rates.

An alternative approach to studying the kinetics of lactam polymerization by chemical experiments is to develop kinetic models and numerically solve the set of reaction equations by comparison with experimental data. Several models and their rate forms have been reviewed by Lin et.al. [12], but one of the major difficulties with this approach is the nature of the polymerization. Due to nearly adiabatic bulk conditions, heat and mass balances are coupled through the rate constant and must be solved simultaneously unless a thin film reactor is used to maintain isothermal conditions. Consequently, simplifications in the mechanism and rate form have to be made to keep the problem tractable.

With reasonable simplifications, Lin et.al. found that an autocatalytic rate form gave the best agreement with experimental data yielding an apparent activation energy of 22-27 kcal/mole. The spread in E_a is due to the nonuniqueness of the autocatalytic rate function and to the simplifications involved. Unfortunately since the polymerizations were carried out from 135-150°C, the heat of crystallization and phase heterogeneity should have been accounted for in the model as well. Nonetheless, despite the real deficiencies, the work reinforces the autocatalytic mechanism presented above and averages out the previous literature variance in apparent activation energies.

Thermodynamics of Caprolactam Polymerization

There is reasonable agreement among the quoted values in the literature for the enthalpy of polymerization [14,15], the value of − 3.2 kcal/mole from Wichterle [16] being roughly the mean of the data. However, poorer agreement is seen for the standard entropy of polymeri-

zation; some positive values of 1.2 cal $gmol^{-1}$ K^{-1} [14] versus other negative values of − 7 cal $gmol^{-1}$ K^{-1} [15] are found which are due mostly, to different reference states for the calculation and/or different mechanisms used for polymerization (i.e. hydrolytic versus anionic). If the absolute entropy at 298°K from reference [14] is used, the equilibrium monomer content (M_e) as calculated by equation (4-24) is low by a factor of about 3 in comparison to Wichterle's data [16]. If the ΔS° is determined from Wichterle's equilibrium monomer content versus temperature data above the melting point, a value of − 3 cal $gmol^{-1}$ K^{-1} is calculated. This agrees approximately with an independent calculation of − 2 $gmol^{-1}$ K^{-1} from the Polymer Handbook [17] based on a quoted equilibrium monomer content at a given temperature.

No definitive (M_e-T) measurements were made in this thesis due to nonequilibrium polymerization conditions achieved during copolymerization of ω-N-acyllactam-siloxanes as a result of complete loss of alkalinity and subsequent cessation of the reaction. During workup of several homopolymerizations about 3 %w CPL monomer was found in equilibrium with the polymerizate which closely agrees with Wichterle's data. As the latter has pointed out [16], the amount of unpolymerized CPL will be in equilibrium with only the amorphous phase and will necessarily be excluded by the crystal. Thus, the equilibrium monomer concentration and hence ΔS°, will depend on the degree of crystallinity achieved during polymerization.

D. EXPERIMENTAL RESULTS AND DISCUSSION

Only one homopolymerization of nylon-6 was intentionally conducted during this thesis work; several such homopolymerizations resulted from over-aggressive catalysts on the fluoroalkylsiloxane macromonomer which depolymerized it completely, thus yielding a homopolyamide-6 without the initial fluoroalkylsiloxane block coupled to it. This depolymerization will be discussed in detail in Chapter VI, §C.1.

Anionic homopolymerization of ϵ-caprolactam was conducted using magnesium bromide caprolactam catalyst (0.5M in CPL) and acetylcaprolactam initiator at an initial temperature of 135°C maintained by an external oil bath with proportional temperature controller. Polymerization was completed in 35-40 minutes using a catalyst/initiator ratio of 1.0 with a catalyst concentration in the polymerization reactor of 0.4 % mole. The resulting $\bar{M}_n$ = 19.7 kg/mole with a PDI = 2.38; this chromatogram is shown in Chapter VII, Figure 7-11. Target molecular weight was 40 kg/mole which is approximately half of the actual number average molecular weight which supports Tessyie's observations [13] that roughly half of the initiator molecules underwent a Claisen condensation (or similar imide-consuming reaction) at or near the beginning of the reaction.

E. REFERENCES FOR CHAPTER V.

1. W.E. Hanford, and R.M. Joyce, J. Polym. Sci., 3(2), 167 (1948)

2. W.H. Carothers, and G.J. Berchet, J. Am. Chem. Soc., 52, 5289 (1930)

3. P.H. Hermans, D. Heikens, P.F. van Velden, J. Polym. Sci., **30**, 81 (1958)

4. D. Heikens, P.H. Hermans, G.M. van der Want, J. Polym. Sci., **44**, 437 (1960).

5. J. Sebenda and V. Kouril, Eur. Polym. Jnl., 7, 1637 (1971).

6. J. Sebenda and V. Kouril, Eur. Polym. Jnl., **8**, 437 (1972).

7. M. Kapuscinska, E. Sittler, J. Sebenda, Coll. Czech. Chem. Commun., **38**, 2281 (1973)

8. J. Sebenda, J. Macromol. Sci., Chem A 6(6), 1145 (1972).

9. S. Barzakay, M. Levy, D. Vofsi, J. Polym. Sci., **B3**, 601 (1965).

10. T. Bessell and J.B. Shortall, Eur. Polym. Jnl., **8**, 991 (1972).

11. J.A. Moore and T.J. Pahls, Die. Ange. Makromol. Chem. **55**, 141 (1976).

12. D.J. Lin, J.M. Ottino, E.L. Thomas, Polym. Engr. & Sci., 25(18), 1155 (1985).

13. D. Petit, R. Jerome, Ph. Teyssie, J. Polym. Sci.: Polym. Chem. Ed., **17**, 2903 (1979).

14. V.P. Kolesov, I.E. Paukov and S.M. Skuratov, Russ. Jnl. Phys. Chem., **36**(4), 400 (1962).

15. A.V. Tobolsky and A. Eisenberg, Jnl. Am. Chem. Soc., **81**, 2302 (1959).

16. O. Wichterle, Makromol. Chem., **35**, 174 (1960).

17. Polymer Handbook, 2nd ed., J. Brandrup, E.H. Immergut, ed., Wiley, N.Y. 1975.

CHAPTER VI. RUBBER - NYLON-6 COPOLYMER SYNTHESIS

A. EXISTING RUBBER-NYLON-6 COPOLYMERS

Lactam-based block copolymers have appeared largely within the last decade or so for numerous reasons. The polyamides have high melting points (ca.215 - 220°C for nylon-6) and when rubber-modified with suitable, thermally stable materials (like the siloxanes), the service temperature limits can be improved substantially over conventional impact plastics such as styrene-butadiene (HIPS), acrylonitrile-butadiene-styrene (ABS) or vinyl chloride-cis isoprene (PVC-NR) for example. The crystallinity of the nylons due to very strong hydrogen bonding among the chains, improves the solvent resistance toward a variety of common organic solvents. Rubber-nylon copolymers can be used as interfacial agents for emulsifying polymer blends which affect mechanical properties through morphological changes as has been done in this thesis. The often hydrophobic rubber segments can reduce the sometimes detrimental hydrophilicity of the polyamides or alter their surface frictional properties [1]. A comprehensive review of nylon copolymers including their synthesis as well as some elaboration on end-uses is given by McGrath and Noshay [2]. The following sections discuss some current nylon - rubber copolymers and are organized by copolymer structure starting with graft copolymers and preceding up to diblock copolymers, the structurally simplest type of copolymer.

1. Graft Copolymers

Undoubtedly, the most important benefit of rubber modified nylon copolymers is the increase in toughness and resistance to impact. Wu [3,4] studied toughening effects (which will be discussed separately in Chapter IX) by blending a reactive and nonreactive version of a hydrocarbon rubber (T_g = -52°C; assumed to be polyisoprene) with nylon-6,6 at 300-325°C through a melt extruder. The reactive rubber contained ~ 1% of polar groups which grafted the rubber to the nylon chain (presumably at the terminal amine hydrogens or possibly at the amide protons) significantly increasing adhesive strength as measured by a peel test. Izod impact energy was greater for the reactive rubber blends partly due to increased adhesion but also due to the smaller rubber microdomains (ca. 0.1-2.0 μm vs 25 μm in the blends) characteristically formed from copolymer emulsification of the two phases. This supports the theoretical predictions of copolymer interfacial activity [5] and demonstrates that emulsification of the rubber via the copolymer produces superior impact strength over pure blends as has been found for other semicrystalline-rubber copolymers [6].

Another type of nylon-6/rubber graft copolymer has been studied by Martuscelli, et.al. [7]. Blends of nylon-6 and EPM (random copolymer, 60% mol C_2) were compared with ternary blends of nylon-6/EPM/(EPM-g-SA)-g-nylon-6. The third component was a graft copolymer of succinic anhydride groups along an ethylene-propylene (EP) random copolymer backbone which subsequently was grafted to hydrolytic nylon-6 chains by condensing with terminal amine groups or the amide protons. The graft EPM precursor was prepared by free radical initiation of maleic anhydride

(MAH) to backbone methylene groups in the EPM [8]. The grafting of up to 3 %w of MAH was a random process controlled only by stoichiometry and some degradation of the EPM occurred during this solution reaction. This demonstrates that graft copolymers, in general, are not as well defined from a molecular viewpoint (as compared to diblock copolymers for example), due to the statistical nature of the grafts.

2. Alternating Block Copolymers

The Dutch State Mines Company currently markets one of the major commercial alternating block copolymers of nylon-6/polypropylene oxide based on technology developed by the workers at Monsanto [9,10]. The nylon-6/polyol copolymer consists of an $(AB)_x$-A structure where A = polyamide and B = polyol and is prepared from polypropylene glycol (M_w=2000) and terephthaloyl biscaprolactam initiator with magnesium bromide caprolactam catalyst. The polymer is reaction injection molded at ~ 135°C (initial temperature) by mixing the lactam/initiator/polyol stream with the lactam/catalyst stream simultaneously inside the mold. Reaction is rapid, solidifying in just several minutes. But as was discussed in Chapter II, §D.2, the PPO block does not posses sufficient thermal stability for prolonged heating at 250°C, even in an inert atmosphere and was not considered satisfactory for use in this thesis work.

Another proprietary alternating block copolymer is comprised of nylon-6 and polybutadiene blocks [11]. This is synthesized via hydrolytic condensation of hydroxy- or amine-terminated PB blocks with ϵ-caprolactam using adipic acid as the chain extender in the melt at 270°C. It is not clear from the patent examination whether significant PB degrada-

tion occurs due to 4-6 hours total reaction time at these high reaction temperatures.

Other alternating block copolymers of nylon-6 using poly(phenylene ether) (PPE) [12] have been synthesized by modifying the PPE hydroxyl end groups with cyanuric chloride after conversion to the metal alkoxide. The cyanuric-end capped PPE's were found to be excellent initiators polymerizing ϵ-caprolactam at 180°C in just 1 – 2 minutes. Depending on the ratio of cyanuric chloride to PPE and the reactivity change as each successive chloride group is consumed, network structures are possible with this system.

3. Triblock Copolymers

The majority of nylon-6-rubber copolymers in the literature are triblocks with the rubber as the central block. These have been prepared from difunctional hydroxyl terminated polytetrahydrofuran (PTHF) and polypropylene glycol (PPG) [13] and polybutadiene [14]. Other non-rubber blocks have also been used such as polycaprolactone (PCL), and polyadipates. In all these cases, the hydroxyl groups have been converted to isocyanate functionality by treatment with tolylene diisocyanate (TDI). The remaining, pendant -NCO group then forms an N-acyllactam by condensing with caprolactam (CPL) but in the process generates a carbamate group. This is depicted in equation (6-1) using poly-THF as the rubber diol block.

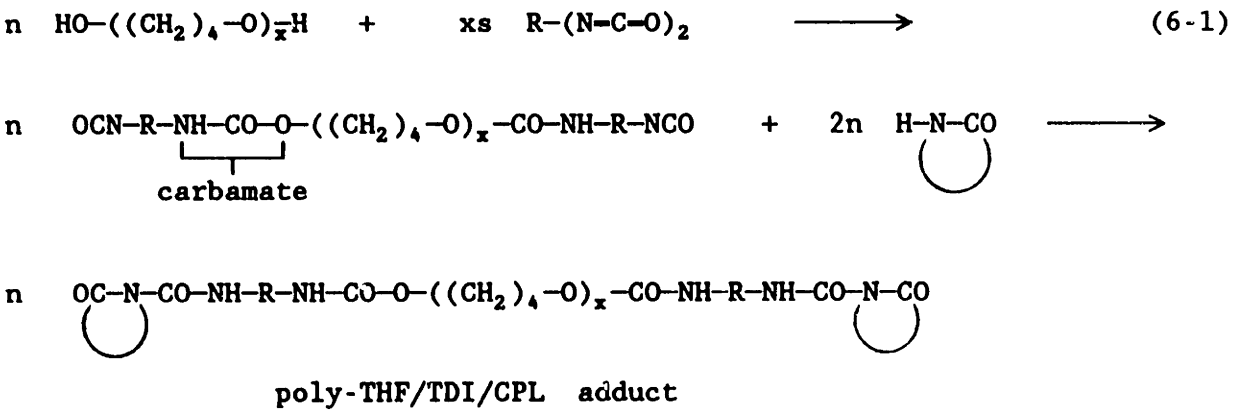

The carbamate functionality is detrimental because it is susceptible to attack (at *) at elevated temperatures by the lactam anion (i.e. the catalyst) during propagation of the nylon-6 block. This forms a diblock with a terminal alkoxide and initiates growth of a homopolyamide chain, viz.,

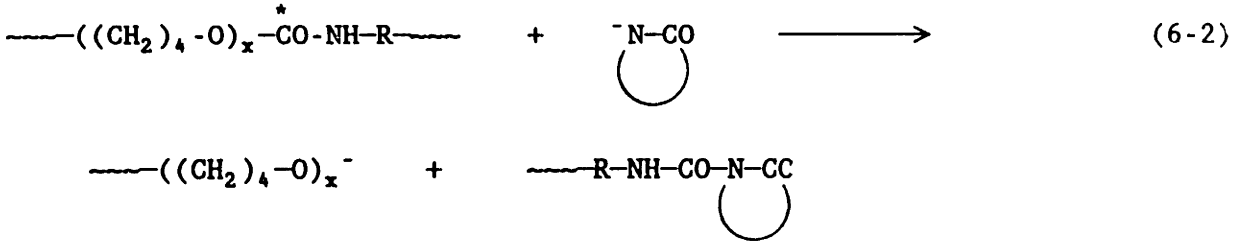

Lower than expected $\bar{M}_n$ values have been attributed to this cleavage reaction in copolymerization of a polybutadiene diol and ϵ-caprolactam with TDI [14]. However, it is possible for the rubber alkoxide to reenter the growing chain by nucleophilic attack at a terminal lactam ring carbonyl forming an ester linkage and creating a multiblock copolymer. This would be a "pentablock" (A-B-A-B-A, A = polyamide-6, B = rubber) copolymer if the terminal carbonyl belonged to a growing triblock. Other block combinations are possible leading to a distribution of structures centered around a triblock copolymer but ranging from

homopolyamide-6 to an alternating block copolymer of many blocks. Granted, the concentration of these multiblock copolymers (i.e. greater than triblock) necessarily will be less than the di- and triblocks due to the weaker basicity of the alkoxide and its corresponding lower reaction rate towards the lactam carbonyl as compared to the caprolactam anion. These side reactions coupled with the normal chain transfer reactions of anionic nylon-6 polymerization (discussed in Chapter V) increase the polydispersity of the block structure (in addition to the polydispersity in molecular weight) as well as creating a significant amount of homopolymer, up to ca. 20 %w as seen by two different investigators [14,15].

Furthermore, it has been shown that the TDI/CPL adduct in equation (6-1), thermally decomposes at temperatures between 108 - 125°C [16]. Realizing this, Tessyie et.al. [14] polymerized nylon-6 at 105°C with model initiators N-ethylphenylcarbamate (Ph-NH-COOEt) which gave only 10% conversion of CPL, versus N-phenylcarbamoylcaprolactam (Ph-NH-CO-N-CO) which showed 86% conversion (at presumed equivalent reaction times). This indicated that the cleavage reaction (6-2) did not compete significantly with propagation at this temperature; otherwise, the N-ethylphenylcarbamate would have been transformed to the acyllactam (which gave 86% conversion) by the action of the catalyst and the polymerization rates would have been more nearly equivalent. This is because the esters are known to have significantly longer induction times than N-acyllactam initiators due to slow transformation of the former to the latter.

Although Tessyie, et.al. avoided the cleavage reaction during synthesis, the carbamate group in the copolymer precludes melt annealing as indicated by a drastic reduction in mechanical properties due to a

decrease in molecular weight from thermal degradation. Thus, this linkage, although relatively convenient from a synthesis standpoint, has the very serious drawback of thermal and chemical instability. This disadvantage has been obviated in this thesis work where an ω-N-acyl-lactam macromonomer was used to initiate caprolactam joined to the siloxane through the Si–C bond which imparted the necessary thermal and hydrolytic stability to permit melt annealing and dissolution in mildly acidic solvents such as TFEtOH.

Considering the aforementioned triblock rubber components, the polyadipates did not copolymerize with caprolactam and the polypropylene glycol gave poor mechanical properties [13]. Poly-THF/nylon-6 triblock demonstrated much better mechanical performance with an elongation at break of ~ 300% and 40MPa tensile strength quite similar to spin casted Nyrim^{R} 2000 (Dutch State Mines Co., formerly Monsanto). The poly(caprolactone-caprolactam) triblocks had desirable physical properties; 400% elongation at break, 50MPa tensile strength but had an extremely low Young modulus of only 11 MPa (@ 5% strain). No physical properties were reported for the PA-PB-PA copolymer [14].

Similar work [17] has been conducted using α,ω-hydroxy-poly(isobutylene) (PIB-$(OH)_2$) prepared by the inifer method [18] as the precursor rubber block. The diol was converted to isocyanates by the conventional TDI and hexamethylene diisocyanate (HMDI), which gave poor blocking efficiencies or by N-chlorocarbonyl-isocyanate (NCCI) or oxalyl chloride which were more efficient. The best blocking efficiency was obtained by NCCI but this polymerization again suffered the generation of homo-PIB as evidenced by only 40 – 60 % conversion of the rubber into block

copolymer; the large amount of homo-PIB was thought not to be uninitiated PIB but rather, PIB-nylon-6 block copolymer that cleaved at the carbamate linkage producing significant quantities of the pure rubber which then is extracted out to give the poor conversion values.

An alternate approach to diisocyanate terminal functionality is to react α,ω-hydroxy rubber with phosgene under high vacuum to produce bischloroformate end-groups as shown in equation (6-3). This is similar to the use of oxalyl chloride (ClOC—COCl) by Wondraczek and Kennedy mentioned above.

$$HO-((CH_2)_4-O)_x-H \;+\; 2\ COCl_2 \longrightarrow ClOC-O-((CH_2)_4-O)_x-COCl \;+\; 2\ HCl \qquad (6\text{-}3)$$

The chloroformate group readily acylates the lactam anion initiating caprolactam polymerization as in equation (6-4) which can be done in situ or as a preformed macromonomer.

$$\sim\!\sim\!\sim((CH_2)_4-O)_x-COCl \;+\; Na^{+-}N-CO \longrightarrow \sim\!\sim\!\sim((CH_2)_4-O)_x-CO-N-CO \;+\; NaCl \qquad (6\text{-}4)$$

In this way, Yamashita, et.al. [19] produced triblocks with poly-THF and polystyrene as the central block. In both cases, the reaction mass was dissolved in formic acid and precipitated. Selective extraction of the "B" (rubber or PST) component was done and in both cases around 3-5% homopolymer was obtained. NMR spectrometry was used to ascertain block molecular weights and IR spectroscopy verified both block sequences in the copolymer after extraction.

4. Diblock Copolymers

By using only monofunctional rubbers, the same chemical pathways used for triblocks can be utilized to prepare diblocks. Allen and Eaves [13] used α-hydroxy SBR converted to an isocyanate functionality by TDI to initiate nylon-6 polymerization. As mentioned before, cleavage of the carbamate linkage is significant and the observed macroscopic (naked-eye) phase separation definitely indicated contamination by significant amounts of homopolymer constituting a poorly emulsified blend and not pure copolymer.

Teyssie, et.al. [14] synthesized PST-PA-6 diblock by using ethyl-chloroformate to terminate the living carbanion producing the ester functionality which subsequently was used to initiate CPL albeit with a significant induction time. This procedure could easily be used on any anionically polymerized hydrocarbon rubber. The drawback to this scheme, however, is the coupling of PST (or rubber) via the ethyl ester. Even in solvent, with an excess of chloroformate, 20% homo-PST was formed due to the strong nucleophilicity of the polystyryl anion. See equation (6-5).

$$\text{PST}^- \text{Li}^+ \xrightarrow{\text{Cl–COOEt}} \text{PST–COOEt} + \text{LiCl} \xrightarrow{\text{PST}^- \text{Li}^+} \begin{matrix}\text{PST}\\ \diagdown\\ \text{C=O}\\ \diagup\\ \text{PST}\end{matrix} + \text{LiOEt} \qquad (6\text{-}5)$$

This chemistry could have been improved if the nucleophilicity of the polystyryl anion had been reduced by reaction with 1,1-diphenylethylene, for example, prior to introduction of the chloroformate ester. Then the

coupling reaction would have been suppressed because the second reaction in equation (6-5) would not occur.

In addition to monofunctional hydroxy and chloroformate end-capped polymers, living carbanion polymers can be coupled to nylon via diisocyanates. Using the isocyanate functionality, Hergenrother and Ambrose [15] synthesized PB-Nylon-6 and PST-Nylon-6 diblocks. The diene block was synthesized per standard anionic polymerization techniques. N-butyllithium initiator was used in n-C_7 solvent at -20°C with ~ 4.6×10^{-2} M N,N,N,N-tetramethylethylenediamine (TMEDA) to give 93% 1,2 diene addition. An equimolar amount of TDI functionalized the 5 kg/mole rubber. Caprolactam polymerization followed at 160°C as shown.

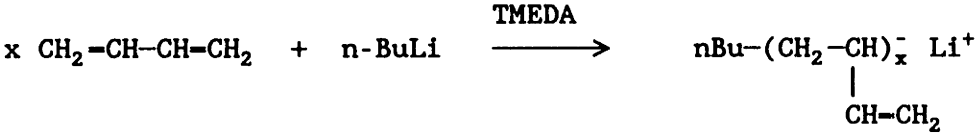

(6-6)

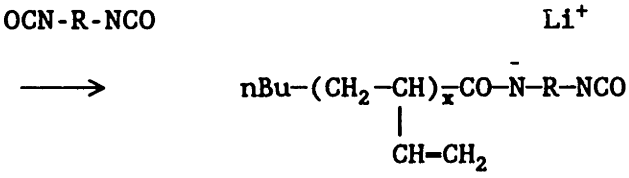

(6-7)

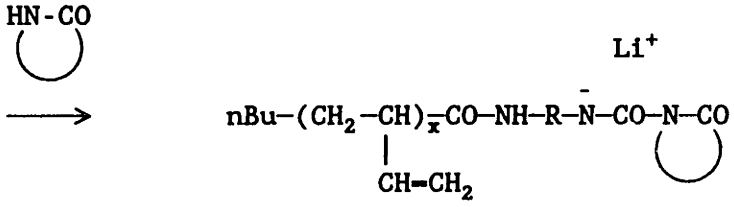

(6-8)

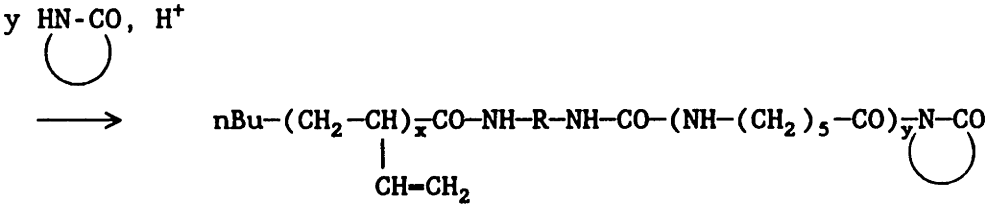

(6-9)

As can be seen, use of a carbanion with a diisocyanate functionalizes the rubber with an amide alkyl carbamoylcaprolactam which does not produce the detrimental carbamate linkage.

The unique feature of this PB-PA-6 diblock is its high pliability at ambient temperature. Despite 70-80% CPL in the diblock, the PB forms the continuous phase as a result of the suspension polymerization of CPL in heptane. This was necessitated by the in situ addition of CPL to the amide anion of reaction (6-8). Phase inversion can be obtained by dissolution and precipitation in a good solvent for nylon-6, such as 1/1 v/v phenol/tetrachloroethane. Upon fractionation, 24% homo-PB was extracted with tetramethylsilane and 26% homo-PA with trifluoroethanol. The homo-PB probably occurred as a result of the incomplete functionalization of the polybutadienyl anion with equimolar TDI.

Previous siloxane-nylon-6 diblock copolymers were synthesized by Owen and Thompson [1] via the macromonomer technique used in this thesis. The differences between their preparation of the coupling agent and the procedures used herein were described in Chapter V. Owen and Thompson utilized the siloxane-nylon-6 diblocks to improve surface properties, such as contact angle, surface tension and coefficient of friction of compression molded nylon-6.

These copolymers were claimed to be synthesized from temperatures of 110°C to 180°C via melt or solution (toluene) polymerization using NaH or $LiAlH_4$ catalysts; however work from this thesis has shown that at temperatures of ca. 170 – 180°C, substantial depolymerization of the dimethylsiloxane in the melt occurs with either catalyst despite contrary claims [1]. Because the copolymer compositions prepared by Owen and

Thompson [1] were at least 40 %w siloxane, toluene solution polymerizations at 110°C was preferred but this necessarily yielded short polyamide-6 blocks due to solubility limitations as discussed by Wichterle [20]; polyamide-6 block molecular weights of Owen and Thompson ranged from 5 to 10 kg/mole maximum, as determined by elemental analysis.

B. SILOXANE-NYLON-6 DIBLOCK REACTION CHEMISTRY

As was seen in the previous review of existing nylon-6 copolymer syntheses, no one pathway was clearly superior. The isocyanate route, although convenient due to an available supply of diisocyanates, leads to copolymer instability during both synthesis and melt recrystallization. Functionalization to yield bischloroformates uses phosgene which requires substantial safety precautions and the ethylchloroformate end-capping method results in significant coupling of the precursor as well as the slow polymerization rate of the macromonomer with caprolactam due to the ester initiator. The only attempt at synthesis of previous nylon-6-siloxane diblock copolymers utilized solution polymerization which necessarily limited the growth of the polyamide block to ca. 10 kg/mole maximum.

In this thesis, the aforementioned chemistry limitations are overcome by end-capping the growing siloxane directly with the N-acyllactam initiator for the nylon-6 block copolymerization which does not yield any unstable linkages (e.g. the carbamate group). Nucleophilic attack on the ω-N-acyllactam-PDMS by the caprolactamate catalyst at the terminal ring carbonyl of the macromonomer will yield the desired ring opening and incorporation of one CPL monomer unit. Attack by the

catalyst on the acyl carbonyl will not cause cleavage into a homopolymer PDMS and an initiator fragment because the leaving group is identical. Thus, no internal cleavage of the bond between rubber and polyamide can occur with this reaction chemistry in contrast to most of the nylon-6 copolymer chemistry previously used. Unfortunately, another type of chemistry shortcoming was encountered in this work, the depolymerization of the siloxane by the anionic catalyst which necessitated further organoaluminum catalyst developments to overcome this deficiency. These will be discussed after the chemistry of diblock copolymerization is introduced.

1. Catalyst Preparation

A variety of catalysts were used in this thesis work as detailed in §C.3.a of this chapter. Most of the initial work was done with the lithium caprolactamate catalyst, but other alkali earth metals or monovalent cations were used such as sodium and magnesium bromide ($MgBr^+$) in addition to the substituted lithium aluminum hydrides which will be described in §C.3.a,b. The lithium caprolactamate catalyst was prepared by reacting n-BuLi with liquid caprolactam at 100°C under slight vacuum (2 – 3 cm Hg vacuum) as shown in equation (6-10); NaH or the Grignard reagent, ethyl magnesium bromide, C_2H_5MgBr were used in lieu of BuLi to prepare the other catalysts in similar fashion.

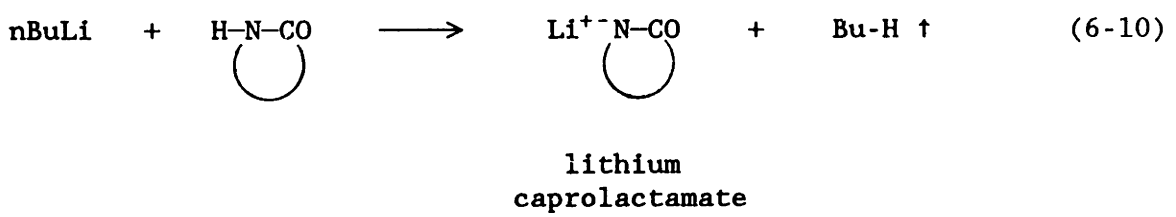

(6-10)

lithium
caprolactamate

The CPL was charged to the catalyst reactor and then dried by distilling over ca. 5 – 10 % of the charge. After slow addition of the n-BuLi in hexane to the caprolactam via syringe with vigorous stirring, the catalyst was degassed two times and used promptly. Catalyst remaining after the polymerization was neutralized (with MeOH) and discarded.

2. Copolymerization with Siloxane Macromonomer

The nylon-6 block copolymerization was accomplished by the nucleophilic attack of the catalyst lactam anion on the lactam carbonyl (*) of the macromonomer, (MSLM) opening the ring and forming the monoadduct as shown in equation (6-11). Note that if attack occurred at the other carbonyl (the acyl carbonyl) then no disproportionation producing homopolymer rubber would occur as in the carbamate-linked copolymers, because the leaving group is identical to the nucleophile. Since the reaction is performed in bulk, the monomer acts as the solvent and its greater acidity plus availability accounts for the rapid proton exchange between CPL and the amide anion as shown in the equilibrium of equation (6-12) which lies far to the right especially at the earlier stages of the reaction.

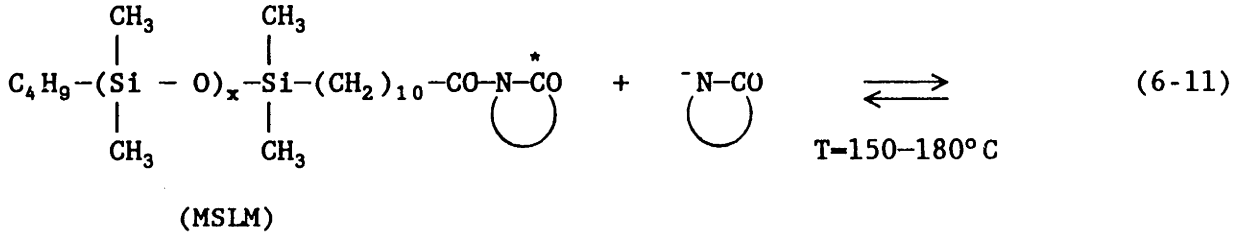

(MSLM) (6-11)

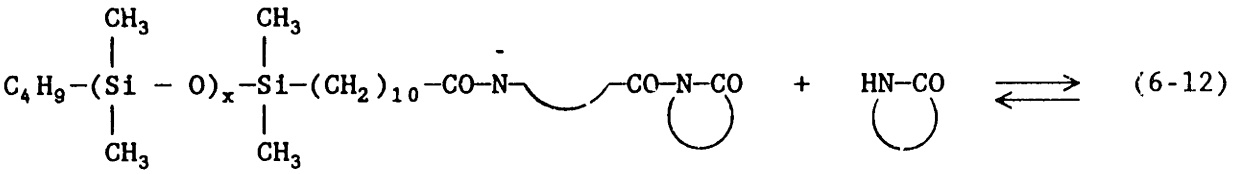

(6-12)

(monoadduct anion)

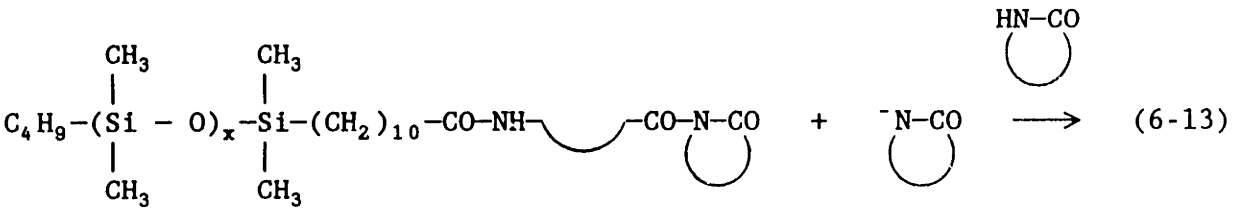

(6-13)

(monoadduct)

In addition to protonating the main chain as in reaction (6-12), the caprolactam anion is also regenerated and can undergo another nucleophilic substitution on the newly inserted, terminal caprolactam ring. Repetition of this process as shown in equation (6-13) gives the diblock copolymer in equilibrium with monomer as shown below.

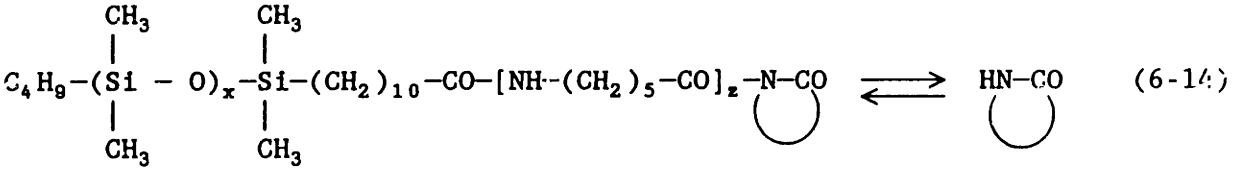

(6-14)

(PDMS-Nylon-6 Diblock Copolymer) $x \doteq 10\text{-}200$, $z \doteq 400\text{-}900$

In contrast to most other anionic polymerizations, the negative charge is carried on the incoming monomer and not on the main chain so no formal termination reaction is needed. The amount of caprolactam remaining in equilibrium with the polymer is a strong function of the polymerization temperature. Approximately 2% wt of the CPL remains in the hardened

polymerized mass for reaction temperatures of 150 – 180°C, but rises sharply for temperatures in excess of 180°C [20]. Thus, for adiabatic or very fast reactions, the exothermicity can cause a temperature rise of 40 – 50°C which can significantly affect the equilibrium composition. Note that this equilibrium is established between the monomer and the amorphous nylon-6 "phase" only, because the crystalline fraction excludes monomer.

The copolymerization is heterogeneous due to the immiscibility of the MSLM in CPL even at elevated temperatures of 210°C. Depending on the degree of dispersion, a substantial fraction of functionalized siloxane does not get incorporated into the copolymer because it is phase separated and its acyllactam end group is inaccessible to the catalyst which is distributed throughout the continuous phase. Efforts to increase the dispersion efficiency and reduce the droplet size via higher agitation speeds with the air-driven, high speed stirrers did little to improve siloxane conversion into copolymer. Eventually, a high energy, ultrasonic dispersion horn was used to increase the fraction of MSLM participating in the copolymerization. These details are described below in the Procedure section and the results are presented in §C.

The reaction temperature is deliberately kept below 180°C not only to minimize the equilibrium monomer concentration but also to avoid the rapid and extensive transamidation reactions that give branching as well as consume caprolactam anions which are more prevalent at higher temperatures. These branching reactions were described in detail in Chapter V, §B and hold for the block copolymerization as well. Consumption of caprolactam anion is believed to proceed via the formation of

keto imides and their subsequent intramolecular cyclization splitting out H_2O which destroys the alkalinity of the reaction mixture. This is manifested by a slow decrease in the rate at which transamidation (and hence, propagation) reactions occur [20]. This type of reaction is shown below where the keto imide is formed by the action of caprolactam anion on a methylene group alpha to the imide group, viz.,

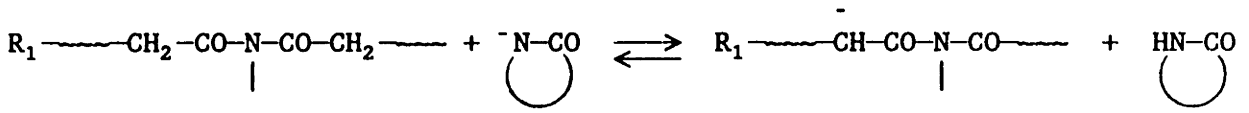

(imide)

(6-15)

The highly reactive carbanion then attacks another imide forming the keto imide.

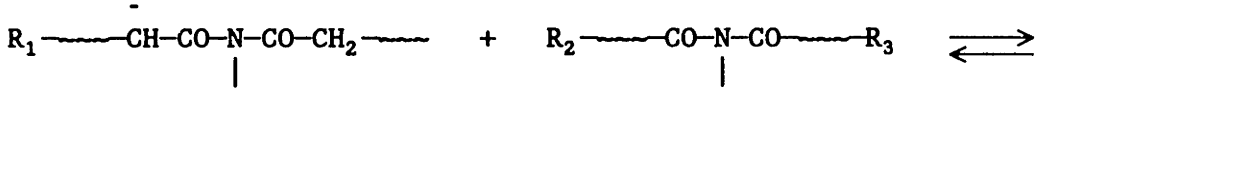

(keto imide)

(6-16)

The keto imide is capable of rearrangement to a keto amide (not shown) by further attack of a lactam anion on the keto imide carbonyl designated with a (*) followed by proton exchange with CPL. This leads to a very reactive group that can generate a variety of compounds including H_2O, CO_2, isocyanates, uracils, etc. which destroy the basicity of the

reaction medium. This is depicted schematically in Appendix 2.

Alternatively, the keto imide can undergo intramolecular condensation with the evolution of H_2O as shown below.

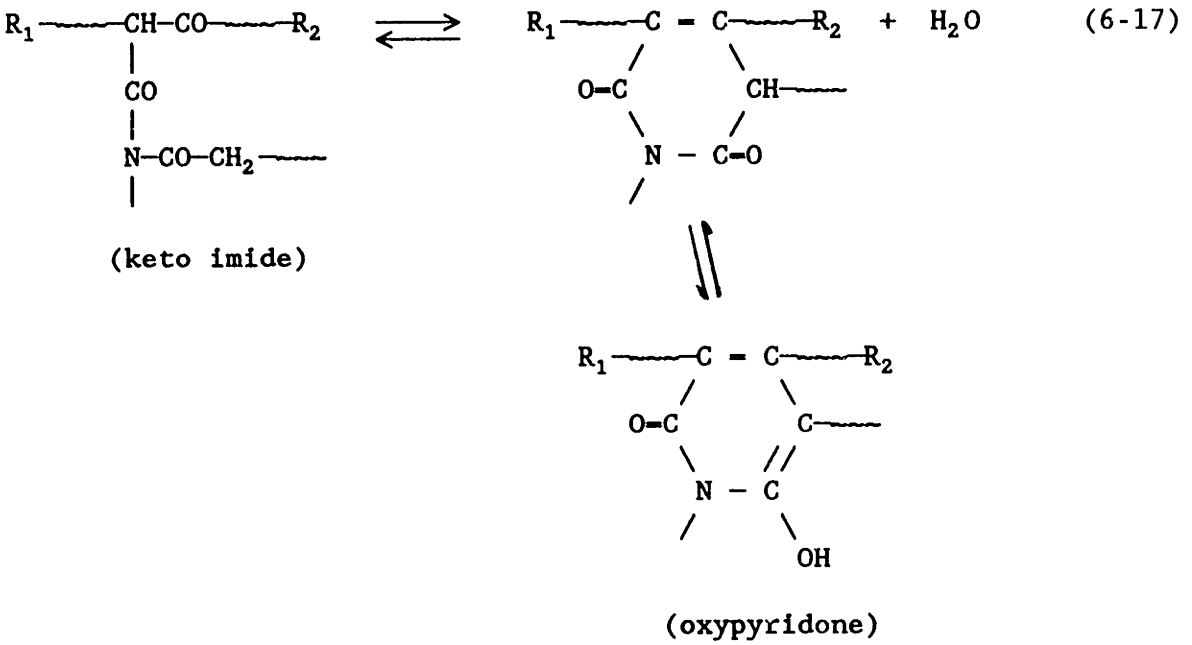

(keto imide) (6-17)

(oxypyridone)

Additional rearrangement leads to the oxypyridone, a stronger acid than the keto imide which can effectively neutralize the alkalinity via the acidic hydroxyl group. These reactions are known to be more operative at higher temperatures, especially above 200°C as reviewed by Sebenda [21]. Regardless of the polymerization temperature, they account for the slow loss of alkalinity during the polymerization and the gradual decrease in rate of reaction.

Procedure

All synthesis procedures used Schlenk inert atmosphere techniques. A vacuum/argon Ace-Burlitch^R manifold was utilized coupled to a manometer and several ports for the catalyst and polymerization reactors. A

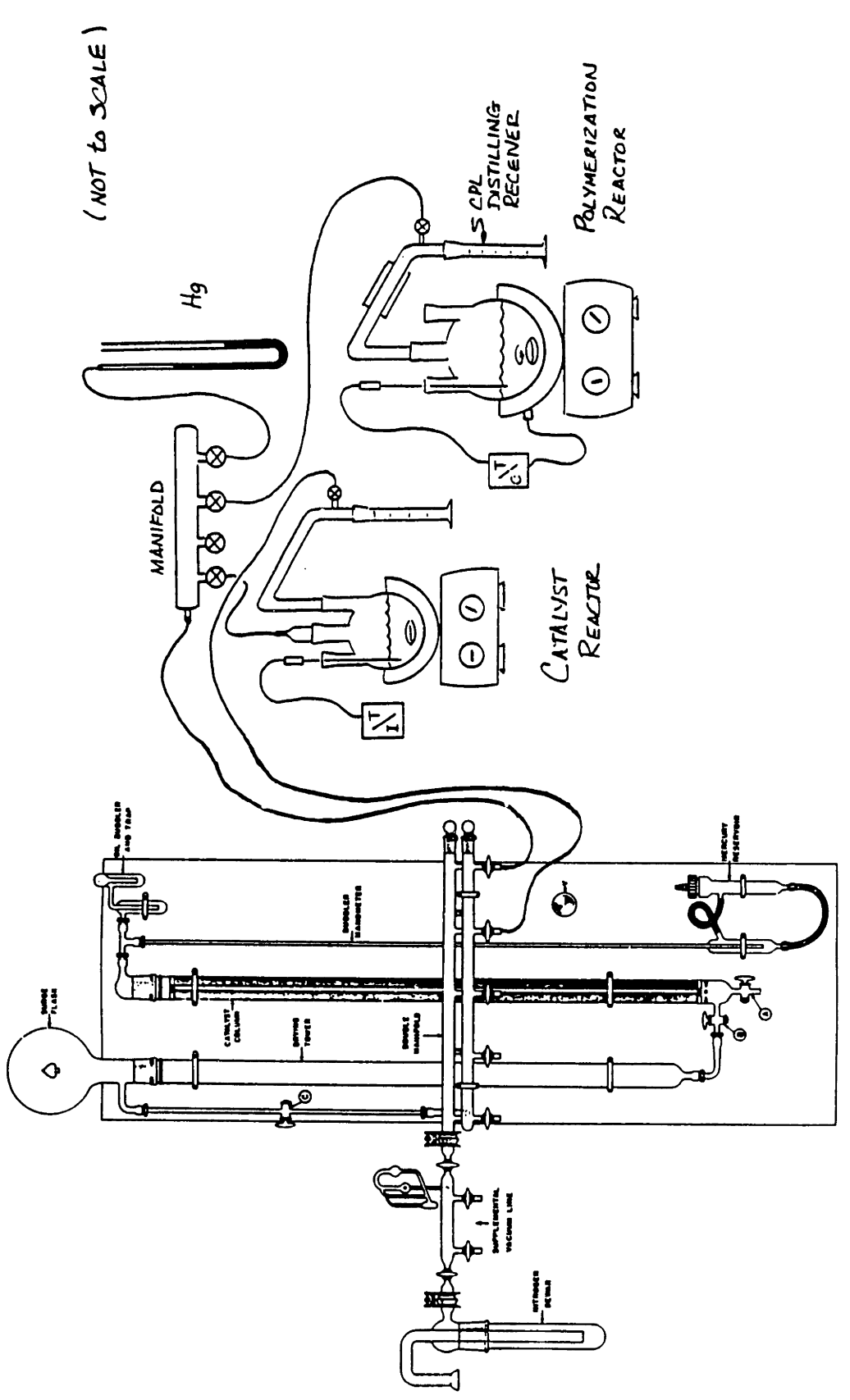

Figure 6-1 Schematic of synthesis equipment showing the inert atmosphere/vacuum manifold and the catalyst/polymerization reactor setup.

schematic of the setup is shown in Figure 6-1. The procedure consisted of drying the caprolactam in the polymerization reactor flask to remove moisture (CPL is very hygroscopic) by distilling over ca. 5 – 10% of the charge at 110 – 135°C under full vacuum. The catalyst was prepared simultaneously in a separate flask as the CPL in the reactor was dried by distillation, (see above for catalyst preparation details). Either 100 ml round-bottom flasks or large, 6" test tubes fitted with rubber septa were used as the reactors; for the latter, CPL was dried in a separate flask and transferred hot via gas-tight syringe when needed. Agitation was provided by a magnetic stir bar/motor or by an air-motor paddle stirrer securely fitted to the reactor through a gas-tight bushing. The macromonomer (MSLM) was then added to the polymerization reactor via syringe and the catalyst solution was syringed hot into the reactor flask such that a catalyst/initiator mole ratio of 1.0 was achieved; i.e. the number of moles of acyllactam groups should be approximately equal to the number of moles of catalyst. Higher ratios (C/I > 2) were avoided so side reactions such as the formation of keto imides (see previous subsection) were minimized. Clean, flushed syringes were kept hot in an adjacent oven until immediate use.

The total CPL/MSLM ratio approximately determined the molecular weight of the nylon-6 block unless low temperatures (T < 150°C) were used which caused premature precipitation of the polyamide from its monomer and cessation of the reaction. The target nylon-6 block length was not precisely controllable due to fluctuation and ultimate depletion of base and imide groups that normally occurs throughout the polymerization as discussed above. Unlike carbanion-site propagation, as in styrene or

butadiene polymerizations, the concentration of reactive groups does not remain constant (even in the absence of impurities) throughout the course of the reaction. This, combined with the chain transfer serves to broaden the molecular weight distribution and to lead to semi-quantitative control of chain length.

Polymerizations were completed usually within 15 – 120 minutes depending on the concentration of imide groups (initiator) and catalyst (caprolactamate), temperature, etc; homopolymerizations were finished in ca. 15 – 20 minutes while diblock reactions took much longer, ca. 90 – 120 minutes. This was due to the lower concentration of imide groups which resulted from the immiscibility of the siloxane in the CPL (i.e., some imide groups were inaccessible to the catalyst due to phase separation). Consequently, additional ultrasonic mixing was used to improve the dispersion of the MSLM in CPL. The ultrasonic horn was borrowed from Rush Enterprises, Inc. (Nashua, N.H.) and fitted to a special commercial Suslick cell (Heat Systems, Inc.) via two O-ring seals and the Suslick collar (Heat Systems, Inc.). See schematic in Figure 6-2. The Suslick cell was fitted with three 6 mm side arm ports for gas-tight syringe transfer of monomer, catalyst and MSLM to the reactor. Ultrasonic energy was limited to 75 watts with a standard 1/2" tip and continuous waveform input. This power input did not induce ultrasonic depolymerization of the functionalized siloxane as the molecular weight distribution (measured by SEC) did not change after one hour of exposure. This was encouraging as the ultrasonic dispersion provided visibly better agitation.

ULTRASONIC COPOLYMERIZATION of METHYLSILOXANE and CAPROLACTAM

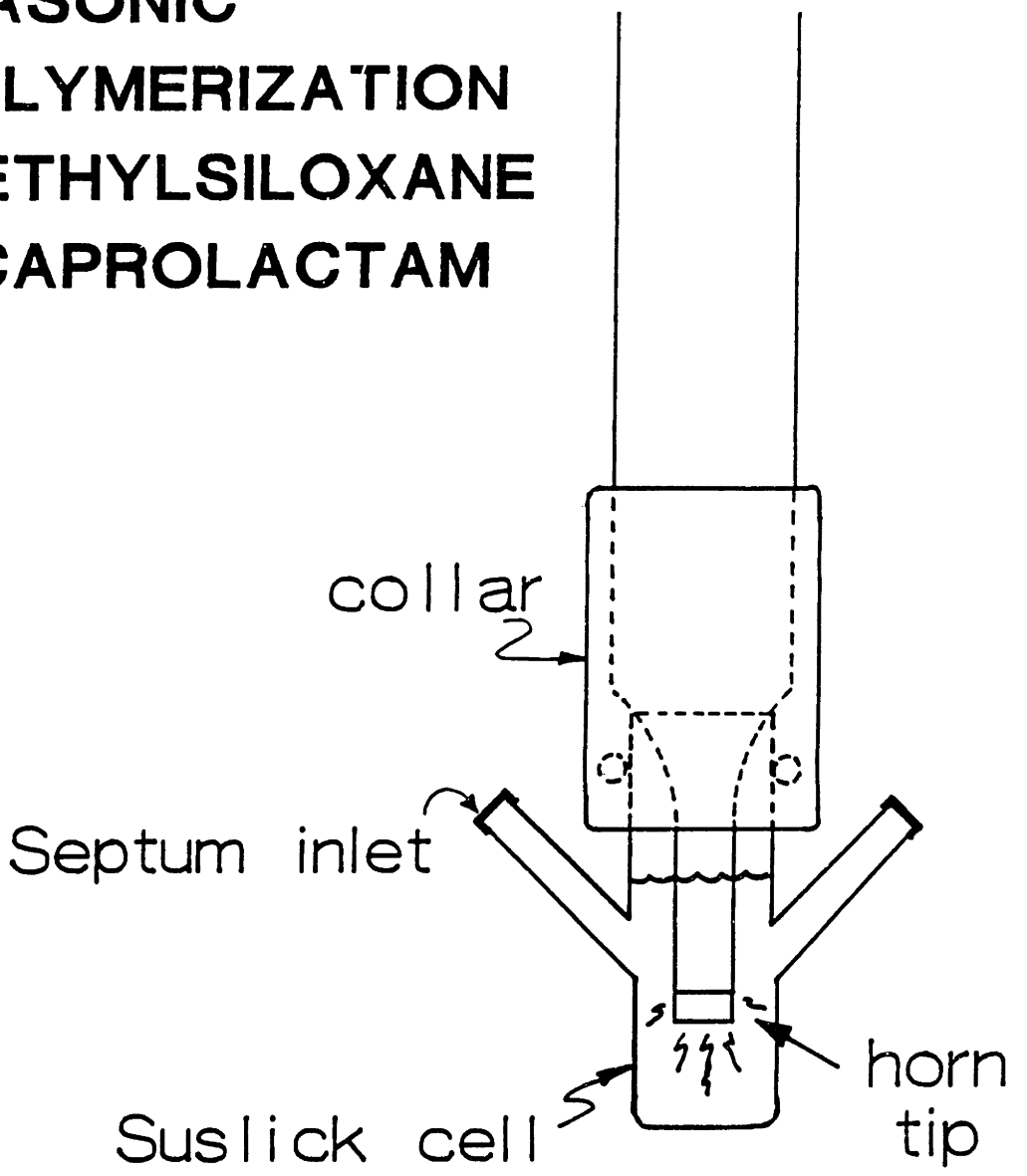

Figure 6-2 Schematic of ultrasonic horn and Suslick cell/collar assembly used to prepare USMSN(15/44).

After copolymerization at 150 – 155°C, the hardened reactor contents were dispersed in trifluoroethanol (TFEtOH) and slowly added dropwise into an excess of THF with stirring for an additional 12 hours or so, filtered through 10 μm PTFE filters in a Millipore^{R} holder and vacuum dried. A second extraction was performed, identical to the first to remove additional, trace amounts of catalyst, caprolactam and unreacted and/or depolymerized siloxane. No extraction for homopolyamide-6 was done with TFEtOH for example, because this was found to remove substantial amounts of copolymer due to the shorter siloxane block lengths coupled with high nylon-6 block molecular weights. Copolymer molecular weight was determined by SEC in TFEtOH (the apparatus is described in Chapter VII, §C.1,3) and composition determined by both ^{1}H solution and ^{13}C solid state NMR. Results of these characterization experiments are detailed in the next section following the discussion of the chemical stability of PTFPMS in CPL.

VI. C. EXPERIMENTAL RESULTS AND DISCUSSION

1. Chemical Stability of Poly(trifluoropropylmethylsiloxane) to Caprolactam and Catalyst

Because of its attractive solubility in TFEtOH combined with its other rubbery properties, poly(trifluoropropylmethylsiloxane) or PTFPMS initially was used as the rubber block in the copolymer. However, as was mentioned in Chapter II, §D, this polymer was soon found to be unsatisfactory due to its chemical instability in moderately basic, molten caprolactam at 170°C. It is postulated that this depolymerization was caused by nucleophilic attack of the caprolactam on the electropositive Si enhanced by the electron withdrawing trifluoropropyl group as shown below.

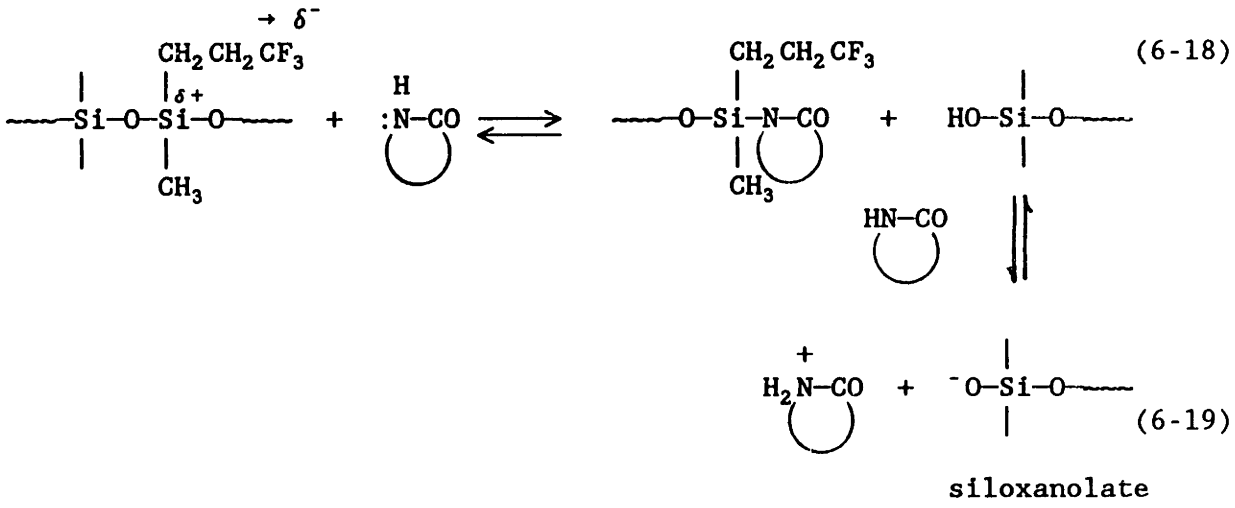

(6-18)

(6-19)

The acidic silanol formed from attack of caprolactam, equation (6-18), is capable of proton exchange with the abundant caprolactam monomer at the interface between the continuous and dispersed phases as in equation (6-19). This produces a siloxanolate which, at the elevated temperatures of 170°C, depolymerizes the PTFPMS. Note that once the siloxano-

late is formed, it not only can depolymerize its own chain to cyclic oligomers but also can chain transfer the siloxanolate to another chain and continue the depolymerization of that macromolecule as well. This is because the depolymerization occurs by a backbiting mechanism which was detailed in Chapter IV, §B.

It is theorized that since the caprolactam was located in a separate phase, acylation (equation (6-19)) to give the lactamonium ion selectively depleted the siloxane phase of silanol protons, increasing its basicity which led to the depolymerization of the PTFPMS to cyclic oligomers by the reactive siloxanolate. This source of protons simultaneously neutralized the alkalinity of the CPL polymerization which reduced the reaction rate. This was observed during the several attempts at copolymerizing PTFPMS and CPL; the reaction slowly decreased and eventually stopped even though there was an abundance of CPL and the reactor was still liquid which was due to the depolymerization and transfer of protons into the continuous CPL phase neutralizing the catalyst.

Details of these depolymerization reactions such as the quantity of cyclics and polymer at a given time under certain reaction conditions are shown in Table 6-1. The first experiment (row 1) indicates that the functionalized fluoroalkylsiloxane was thermally stable in its melt at 170°C so that no depolymerization occurred due to thermal effects. However, upon exposure to wet caprolactam (CPL) at 170°C, approximately one fourth of the polymer was converted to cyclics in 60 minutes and that dilution with dodecane slightly slowed this depolymerization due to mass-action and a lower test temperature of only 110°C. The effect of the end functionalization was tested by exposing fluoroalkylsiloxane

Table 6-1

Chemical Stability of Poly(trifluoropropylmethylsiloxane)

Polymer*	T (°C)	Exposure Time (min)	Nucleophile*	Composition (%w) Polymer	Cyclics
FS–N–CO	170	60	none	100	0
FS–N–CO	170	60	wet CPL	74	26
FS–N–CO	110	70	wet CPL / C_{12}	84	16
FS–$(Si–Me_3)_2$	170	45	wet CPL	94	6
		90		87	13
		16 hr		0	100
FS–MS–N–CO	170	20	dry CPL	88	12
		45		20	80
	170	< 0.1	Li^{+-}N–CO	0	100

* FS = poly(trifluoropropylmethylsiloxane)
MS = poly(dimethylsiloxane)
CPL = caprolactam

---

end-capped with trimethylsilyl groups to CPL; only slightly better retardation of the depolymerization reactions was seen and overnight exposure of this material to the CPL at 170°C, caused complete depolymerization of linear polymer to cyclics.

In efforts to combat the susceptibility to depolymerization in CPL, methylsiloxane was copolymerized with the fluoroalkylsiloxane in both random and sequential block copolymers. Unfortunately, this did little to improve the resistance to nucleophilic attack as seen in Table 6-1

because the weaker trifluoropropyl group is still in the chain. The reaction sequence in equations (6-18,19) is supported by the observation of a strong UV absorbtion during elution of the partially depolymerized fluoroalkylsiloxane in the SEC analysis of the products represented by the second-to-last row in Table 6-1. As the RI detector responded to the presence of the linear, shortened fluorosiloxane chains, the UV spectrophotometer indicated an absorbance at 225 nm which corresponded to the lactam carbonyl as the unfunctionalized fluoroalkylsiloxane does not absorb UV radiation at that wavelength. This suggested that the remaining linear fluoroalkylsiloxane chains at 45 minutes exposure time to dry CPL at 170°C contained a substantial number of lactam carbonyls supporting the reaction path described in equation (6-18).

But in order to be able to withstand the much harsher alkaline environment during caprolactam polymerization, the stability of the fluorosiloxane was tested with lithium caprolactamate catalyst at 170°C. Upon introduction via syringe of the catalyst, the initially turbid dispersion of fluoroalkylsiloxane in CPL became clear, almost instantaneously. SEC showed that the polymer had been cleanly converted to nearly 100% cyclic tetramer with no traces of even linear oligomeric chains. These data are represented by the last row of Table 6-1.

From the data in Table 6-1, it is evident that the alkalinity in the anionic polymerization of caprolactam is too severe for the poly(trifluoromethylsiloxane). Despite being phase separated, slow but steady depolymerization is seen at elevated temperatures of 170°C in caprolactam. If the lithium caprolactamate catalyst is added, instantaneous depolymerization occurs which is clearly unacceptable for producing block

copolymers. As a result of this impasse with PTFPMS, attention was focused on poly(dimethylsiloxane) which is known to have stronger alkali resistance due to the mildly electron donating CH_3 groups that reduce the electropositivity of the silicon to some degree. As will be seen in the following sections, PDMS is resistant to exposure in CPL at a temperature of 170°C but undergoes some catalytic depolymerization although at a much slower rate and not as completely as does PTFPMS.

2. Characterization of Methylsiloxane-Nylon-6 Block Structure

a. Confirmation of Copolymer Structure

Proof of diblock copolymer structure is not easy because of subtle differences between diblocks and other types of copolymers or physical blends. Often, only one type of molecular linkage differentiates between a diblock copolymer and its corresponding blend. The presence of this bond must be ascertained through a concerted effort involving a variety of characterization experiments each contributing evidence that in summation, will undoubtedly confirm a diblock copolymer structure.

The first of these is well-defined chemical synthesis that minimizes the probability of side reactions which produce homopolymers or random copolymers. This is one of the attractive features of the reaction scheme of this thesis. As mentioned earlier, the synthesis of the special coupling agent, 11-(dimethylchlorosilyl)-n-undecanoyl-1-caprolactam or DMCSUCL, provides the chorosilane and acyllactam end-group functionality which specify connection of one polysiloxane chain to one polyamide-6 chain. The polymerization of the siloxane proceeds first followed by addition of DMCSUCL whereby the highly reactive chlorosilane condenses rapidly with the siloxanolate leaving the lactam ring intact.

Subsequently, macromonomer MSLM is used as the one and only initiator for nylon-6 block polymerization. No other source of imide groups is introduced. Misdirected attack by the caprolactamate at the acyl carbonyl is not detrimental in the sense of destroying the linkage between the blocks as with the carbamate-linked copolymers for example. Although transamidation reactions do occur to some extent, the moderate polymerization temperatures, low heat of polymerization of only -3.2 kcal/mole [20] and the low reaction rates maintain temperatures well below 200°C (usually only 10 - 15°C rise, maximum) which helps keep a linear chain architecture.

Secondly, solubility differences between the siloxane polymer and the copolymer/homopolyamide-6 were exploited to selectively extract homo-PDMS and monomeric impurities (e.g. catalyst, oligomers, caprolactam) from the reaction product. Details were given above in the Procedure subsection of §B. The material recovered from the dissolution and workup was considered to be mostly diblock copolymer possibly blended with homopolyamide-6. It was then subjected to a variety of experiments which are discussed separately below; quantitative verification of the presence of siloxane after the extraction/precipitation workup was interpreted as strongly suggesting diblock integrity. As will be shown below, the combination of the results of these characterization experiments leads to the unanimous conclusion that a diblock copolymer has been produced.

Size Exclusion Chromatography

Size exclusion chromatography was conducted on the extracted copolymer product from the various experiments shown in Table 6-2. The diblocks are designated by their experiment number (e.g. 4R-A) and by

their composition (e.g. MSN(3/100)) if NMR analysis was done on the specific copolymer. The NMR results will be discussed separately below. Characterization results of the ultrasonic polymer USMSN(15/44) are discussed later in a separate section (§3.b) after presentation of the catalysis work in section 3.a. The final results of USMSN(15/44) will be presented here though, for completeness and for an explanation of the acronyms (e.g. 'MSN'), see the footnote in Table 6-2.

As can be seen from the table, a wide range of copolymer block lengths and molecular weights were synthesized although not always intentionally. The siloxane blocks were ca. 10 kg/mole and the target polyamide-6 block length for polymerization 4K was only 15 kg/mole whereas for reactions 4R-A and for USP, target polyamide-6 block molecular weights were ca. 60 kg/mole and 75 kg/mole, respectively. Thus, for polymerizations 4K and USP, reasonable agreement between target block length and experimental polyamide-6 block molecular weight was achieved. However, for reaction 4R-A, the block length of the polyamide was much greater than expected which is attributed to the long (4 hours) post-solidification hold time given this polymer as compared to the reaction product 4R which was removed shortly after solidification at 110 minutes and 170°C. This long, high-temperature hold period permitted attainment of equilibrium of the CPL monomer with the polymer in run 4R-A but also exposed the siloxane to the highly basic environment for extended periods of time. This resulted in substantial depolymerization of the PDMS block which will be discussed in the next section.

Table 6-2

Equivalent Molecular Weight of Methylsiloxane-Nylon-6

Diblock Copolymers from Size Exclusion Chromatography[†]

Experiment Number	Copolymer Designation[#]	Initial PDMS $\bar{M}_w$	Initial PDMS $\bar{M}_n$	Initial PDMS PDI[*]	Diblock $\bar{M}_w$	Diblock $\bar{M}_n$	Diblock PDI	T_{pzn} (°C)
4K	MSN(.5/15)	11.0	8.7	1.26	27.6	15.3	1.80	170
4R-A[a)]	MSN(3/100)	12.3	10.5	1.17	133.0	99.0	1.34	170
4R	–	12.3	10.5	1.17	23.4	9.1	2.57	170
4Q	–	~2.3	~1.9	~1.2	45.0	22.3	2.02	170
USP	USMSN(15/44)	17.6	14.6	1.21	96.0	57.7	1.66	155

[#] Nomenclature: MSN = methylsiloxane-nylon-6 diblock copolymer; US = ultrasound polymer; the numbers in parentheses signify the number average block molecular weight for the MS and N blocks, respectively, in kg/mole.

[†] Equivalent molecular weight was calculated for the diblocks by using the same calibration as for homopolyamide-6.
See Chapter VII, §C.1 for nylon-6 SEC details.
All molecular weights in kg/mole.

[*] PDI = polydispersity index, = $\bar{M}_w/\bar{M}_n$

[a)] This methylsiloxane contained approximately 0.7 % mole methylvinylsiloxy repeat units.

The reaction rates and thus, attainment of equilibrium were much slower for these copolymerizations than the corresponding homopolymerizations due to the lower concentration of imide groups. This is attributed to the fact that: 1) some of the imide groups are buried within the phase separated siloxane for some fraction of the reaction time and not

always available for transamidation with the catalyst to initiate a growing polyamide chain, 2) the volume fraction of imide groups is low because they are diluted through connection to the high molecular weight siloxane (i.e. mass action) and 3) some of the side reactions mentioned above may consume the macromonomer's imide groups and reduce an already low concentration of propagating centers. To illustrate the very low rates, at 155°C the USP (ultrasonic) polymerization which undoubtedly possessed superior mixing of the reagents due to the ultrasonic dispersion energy, still took 130 minutes to convert only 1/3 of the reactor from a liquid consisting of monomer, oligomers and siloxane to a whitish solid indicative of precipitating/crystallizing nylon-6 polymer.

The SEC chromatographs of diblocks MSN(.5/15), MSN(3/100) and USMSN(15/44) are shown in Figure 6-3 along with their polydispersity index or $\bar{M}_w/\bar{M}_n$ values. Indicative of most anionic polyamides, these polydispersities are less than those from condensation (normally $\approx$ 2.0) due to the fact that at moderate polymerization temperatures, the transfer and disproportionation reactions are suppressed. In addition, when the polyamide reaches its solubility limit as a function of block length at a given polymerization temperature, it precipitates from the melt and essentially stops growing [20]. This can lead to rather narrow polydispersities due to solubility effects rather than a specific mechanism void of transfer reactions such as carbanion solution polymerization of dienes for example.

In the case of MSN(.5/15), a catalyst/initiator ratio of 2.0 - 2.5 was used and the reaction was completed in approximately two minutes. In this reaction, however, the block length of the polyamide-6 was

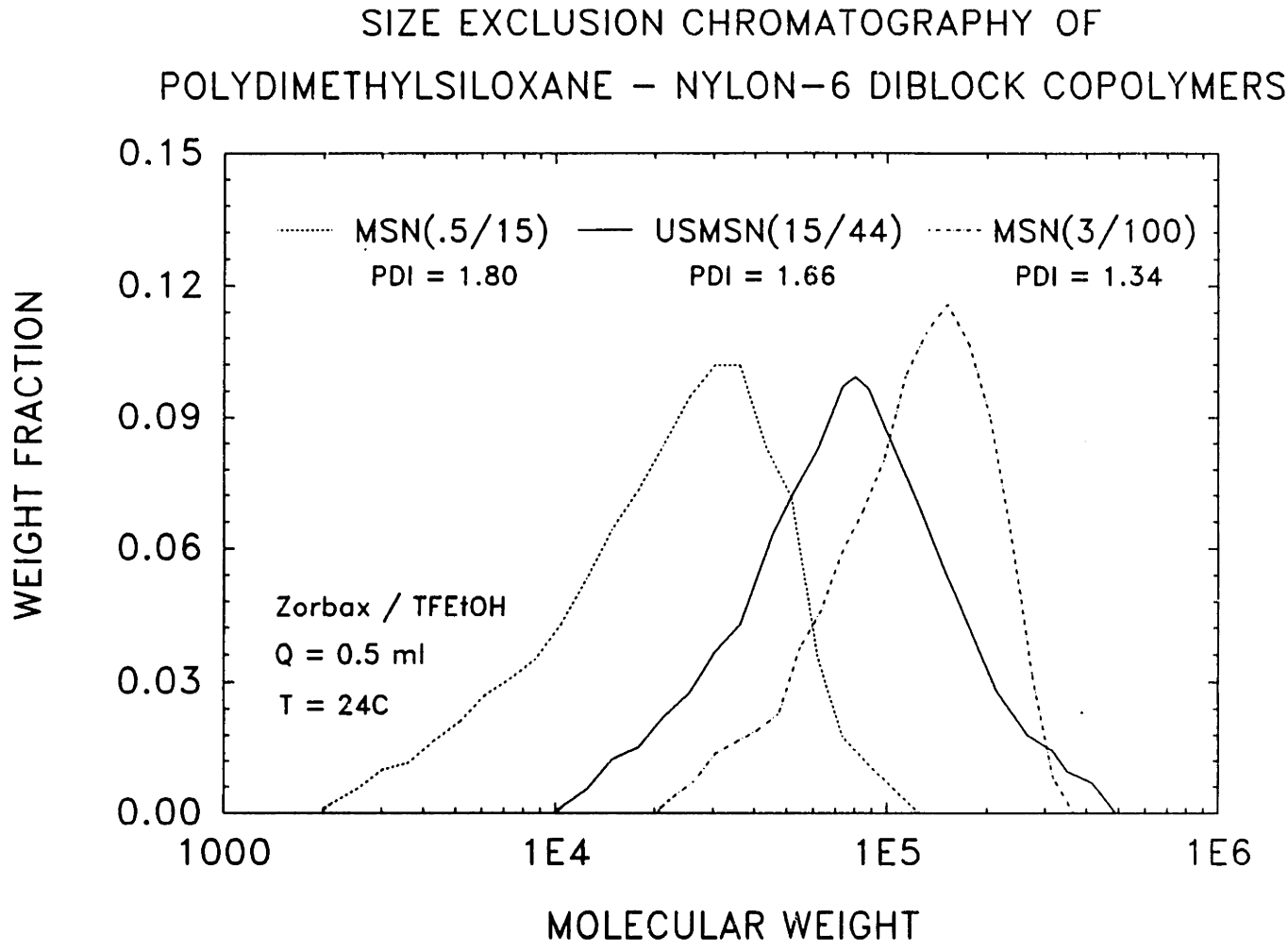

Figure 6-3 Size exclusion chromatograms of the PDMS-nylon-6 diblock copolymers in TFEtOH/Zorbax^{R} columns, 25°C.

deliberately made smaller (ca. 15 kg/mole) which did not dilute the imide groups as much as when the ratio of CPL/PDMS macromonomer is 4/1 to 5/1 as in the MSN(3/100) or USMSN(15/44) polymerizations. The higher catalyst concentration accelerated the reaction rate as indicated by the kinetics of anionic polymerization of caprolactam [22] where the rate is proportional to the instantaneous concentration to the first power of catalyst.

Infrared Spectroscopy

Infrared spectroscopy was conducted on the copolymers initially synthesized (4K, 4R-A) and after workup, showed a weak absorbance at ca. 1000 – 1100 cm^{-1} indicative of the Si-O stretch. However, in these two polymers, it is now known that the siloxane content was very low and that the insensitivity initially attributed to the technique was really due to the composition of the copolymers. Fortunately, since ^{1}H NMR corroborated the IR spectra in these two cases, the latter was discontinued in preference to the former although for incorrect reasons.

Nuclear Magnetic Resonance

Proton NMR using d_3-TFEtOH or d_2-HFIP (hexafluoroisopropanol) was conducted on the major copolymer products (4K, 4R-A, USP runs) and the extracted phase of polymer MSN(3/100) or 4R-A. Prior to solution NMR analysis, ^{13}C NMR was done on the MSN(3/100) polymer because it was anticipated that the siloxane block would be insoluble in the deuterated fluoroalcohol NMR solvents. The solid state spectrum of MSN(3/100) is shown in Figure 6-4a and was obtained on the Bruker, 200 MHz (^{1}H)/50 MHz (^{13}C) spectrometer in the CMSE facility using magic angle spinning and an

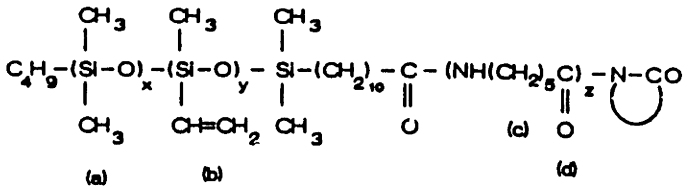

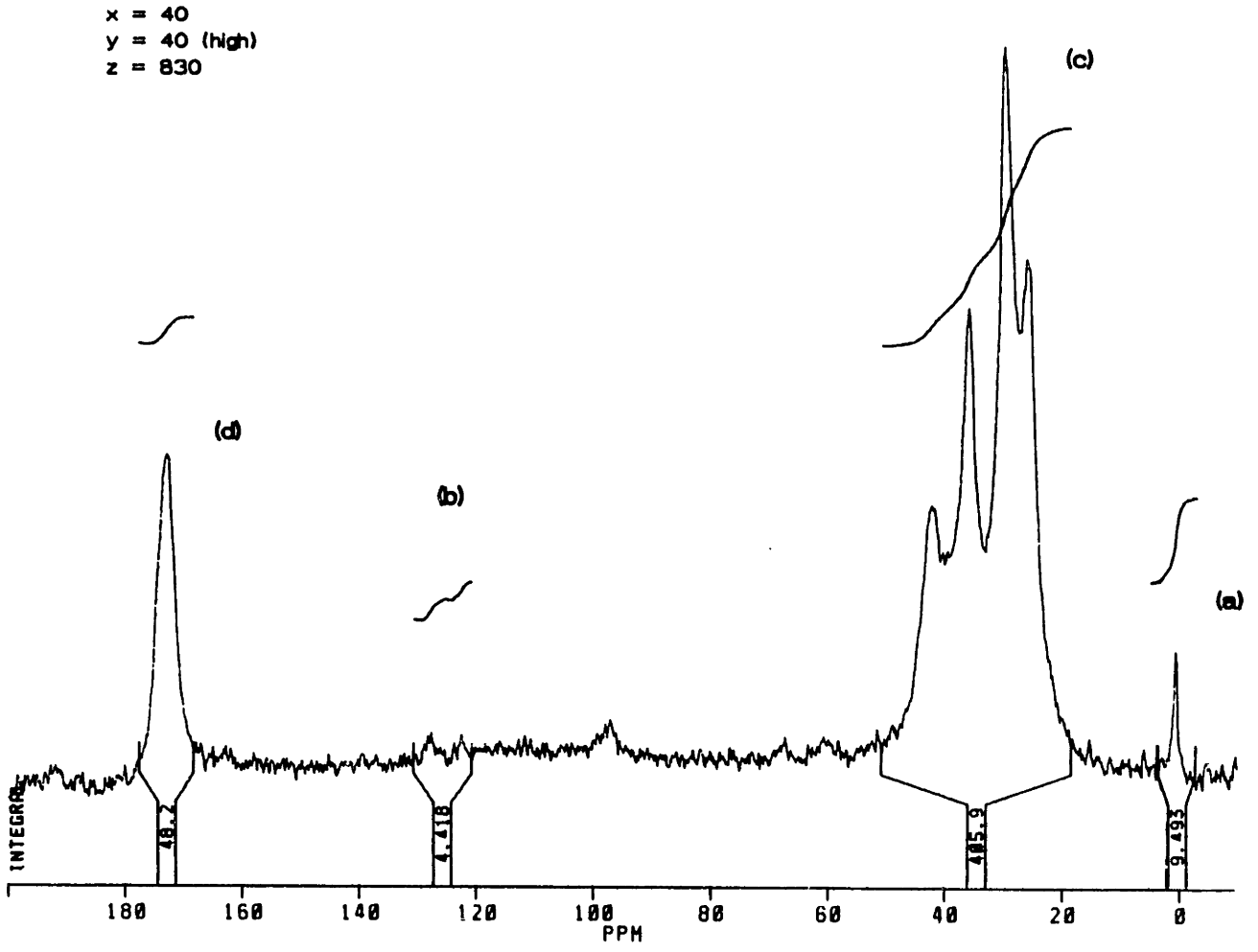

Figure 6-4a DD/MAS/DP ^{13}C NMR spectrum for MSN(3/100) after workup.

inverse gated decoupling direct polarization pulse sequence. A long delay time of 5 minutes was used between pulses to allow for sufficient nuclei decay and suppression of the nuclear Overhauser effect (NOE) which permitted near-quantitative compositional acquisition of the spectrum. The long delay times permitted relaxation of all nuclei (including the crystalline methylenes) approximately back to their Boltzmann distribution before the next pulse was applied. Integration of this spectrum gave approximately 40 repeat units of methylsiloxane, 40 units for the methylvinylsiloxane and roughly 830 repeat units for the polyamide-6 block. The vinyl siloxane peak integrations were arbitrarily high due to the uncertainty of the baseline position in the integration, but the presence of the vinylsiloxane protons is unmistakable at ca. 122 – 129 ppm in Figure 6-4a. It is evident that the molecular weight of the siloxane block has been drastically reduced during the polymerization of the caprolactam from its original length of 10 kg/mole to only 3 kg/mole.

Solution ^{1}H NMR of MSN(3/100) shown in Figure 6-4b indicates a similar composition as that determined by solid state NMR. Since the siloxane block length was very short, this polymer dissolved easily in d_2-HFIP and permitted solution NMR analysis. The values for the length of the two blocks (x=40, z=880) were calculated from the assumption that the SEC number-average molecular weight was approximately the same as the polyamide-6 block due to the extremely small amount of siloxane present in the copolymer. Thus, with a polyamide-6 block $\bar{M}_n$ = 99 kg/mole, the ratio of peak areas in the ^{1}H spectrum corrected for the number of protons per repeat unit of the siloxane (6) versus the polyamide (2), gave the number of repeat units for each respective block. Note that

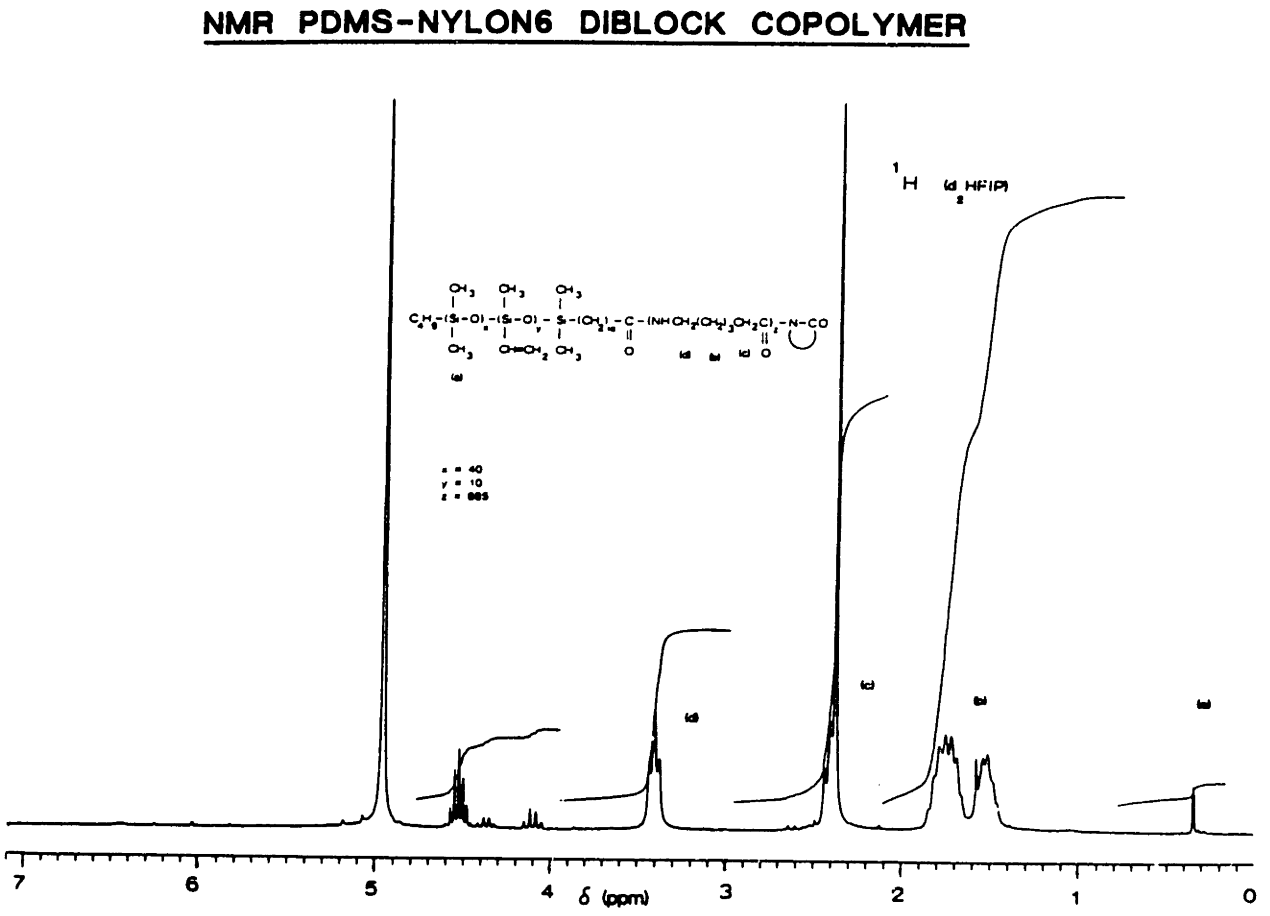

Figure 6-4b ^{1}H NMR spectrum for MSN(3/100) in d_2-HFIP, 25°C

only one methylene group from the polyamide was used in the integration and thus, only 2 protons contribute to its ratio. Also note the excellent agreement between the peak area ratios from the ^{13}C solid state and ^{1}H solution NMR analyses. This implies that in the ^{13}C experiment, the delay time of 5 minutes was satisfactorily greater than roughly $5T_1$ (i.e. five times greater than T_1, the spin-lattice relaxation time) so that sufficient nuclei decay occurred between pulses and a quantitative spectrum was obtained. Thus, the ratio of block molecular weights was determined conclusively to be ~ 3/100 which is represented in the nomenclature MSN(3/100).

Similar calculations led to the designations 15/44 and 0.5/15 for ratio of PDMS/PA-6 block molecular weights (in kg/mole) in the ultrasonic polymer, USMSN(15/44) and 4K polymer, MSN(.5/15). However, in the calculation for USMSN(15/44), the calculation procedure was reversed and the siloxane was assumed to stay intact during caprolactam copolymerization due to catalyst improvements which will be discussed shortly. Actually, the only requirement for molecular weight determination from NMR is that no depolymerization of linear siloxane to cyclics occurred which would decrease the number of linear siloxane repeat units present in the final copolymer and lead to high false molecular weights for the polyamide block. The NMR instrument simply sees a number average of siloxy repeat units and not their molecular weight distribution (MWD). Despite transfer reactions that might have rearranged the siloxane and changed its MWD, the integral of the Si-CH_3 groups can be used accurately to ratio the number of polyamide repeat units and calculate a number average polyamide-6 block molecular weight if none of the siloxane repeat

units were lost to cyclization. If the integrals from the ^1H NMR of USMSN(15/44) are calculated, the molecular weight of the polyamide-6 block is determined to be 44 kg/mole. Checking with the SEC chromatogram in Figure 6-3, the calculated $\bar{M}_n$ = 57.7 kg/mole gives excellent agreement with the ^1H NMR data if the 14.6 kg/mole initial number average molecular weight for the siloxane block is subtracted from this to yield a 43.1 kg/mole polyamide-6 block molecular weight. This compares favorably with the 44 kg/mole as calculated by NMR. Realistically, some correction factor must be applied to the SEC molecular weights because they were determined from a homopolyamide-6 calibration and not a diblock calibration; the hydrodynamic volumes of the homopolyamide-6 and the diblock probably are different. This implies that the diblock molecular weight is slightly greater than 57.7 kg/mole because the siloxane block undoubtedly is compressed in the unfavorable TFEtOH solvent during chromatography. Nonetheless, the experimental agreement is very reasonable and cooperatively demonstrates the drastic reduction in siloxane block molecular weight that occurred during the copolymerization. Details of block structure are shown in Table 6-3 with respect to mole fraction and number of repeat units; the USMSN(15/44) copolymer will be discussed later in §3.b of this chapter.

The filtrate of polymerization 4R-A was analyzed by ^1H NMR to ascertain how much siloxane was either depolymerized or unreacted. Recall that the filtrate is the THF-soluble fraction from the extraction/precipitation/filtration of the copolymer. The filtrate was then further extracted two times with distilled H_2O to remove the caprolactam, catalytic components, etc. and obtain a cleaner spectrum of the remaining

Table 6-3

Compositions of PDMS-Nylon-6 Diblock Copolymers

as Determined from NMR and SEC

Run No.; Abbrev.	Polymer Structure	No. Repeat Units MeSx	MVSx	PA-6	Composition (mol %)† MeSx	MVSx	PA-6
4K[a] MSN(.5/15)	PDMS-PA6	7	–	135	4.9	–	95.1
4R-A[a] MSN(3/100)	PDMS-MVSx-PA6	40	10	885	4.3	1.1	94.6
USP[b] USMSN(15/44)	PDMS-PA6	202	–	389	34.1	–	65.9

† MeSx = Methylsiloxane, MVSx = Methylvinylsiloxane, PA-6 = polyamide-6

a) Determined by SEC to estimate total MW; NMR to estimate composition. Little error due to very short MeSx block lengths as explained in text.

b) Calculated assuming the PDMS block did not depolymerize to cyclics as indicated by SEC and that original $\bar{M}_n$ is still valid; i.e. original siloxane MW from separate chromatogram used in calculation with ^1H NMR and overall MW from diblock SEC. See text above for full discussion.

---

siloxane which is insoluble in water. Some evidence of the coupling agent located at the end of the PDMS macromonomer could be ascertained although its concentration was far less than the proportional amount of siloxane that would be present if only unreacted siloxane was in the filtrate. In other words, most (but not quite all) of the siloxane successfully initiated copolymerization but subsequently was depoly-

merized to cyclic oligomers creating a large excess of unfunctionalized, depolymerized siloxane (i.e. over and above the amount corresponding to the number of moles of N-acyllactam groups). Both unreacted ω-N-acyllactam-PDMS and depolymerized PDMS were extracted by THF into the filtrate and remained insoluble (raffinate phase) in the second, aqueous extraction. The ratio of the silyl methyls to methylenes from CPL combined with a material balance was used to calculate the yield of siloxane incorporated into the copolymer which will be discussed in §2.d.

Transmission Electron Microscopy

In addition to the solubility/molecular characterization experiments discussed above, strong supporting evidence of diblock structure came from electron microscopy. As mentioned in Chapter II, §B.1, when a diblock copolymer undergoes microphase separation, the domain size is usually very small (~ (0)10^2–10^4 Å) and fairly regular owing to the molecular dimensions of the coiled chains. This is in contrast to a blend where phase separation is manifested by domain sizes ca. 1 μm or more and often of very irregular shape. In all three cases, MSN(3/100), USMSN(15/44) and MSN(.5/15), very small (< 10^3 Å) domain sizes were observed as detailed in transmission electron micrographs presented in Chapter VIII. See Figure 8-9 for an example of the morphology of USMSN(15/44) which clearly shows the well defined, fairly uniform spherical domains of PDMS within a nylon-6 matrix. This type of domain structure is only possible via diblock (or possibly triblock) structures and certainly is impossible to attain through simple physical blending of the two homopolymers.

When these materials are observed in the transmission electron microscope (TEM), there rarely was seen any regions of homopolyamide-6, i.e. regions where no dark phase contrast was present. These homopolymer regions were rare in MSN(3/100) which was prepared at 170°C and were nonexistent in the USMSN(15/44) prepared at 155°C. This agrees with the known increase of chain transfer reactions at higher temperatures to give homopolyamide-6 during the nylon-6 block polymerization for the MSN(3/100) polymer. Although not quantitative, this observation helps substantiate earlier statements that moderate polymerization temperatures minimize chain transfer and branching reactions leading to negligible homopolyamide-6 production.

Mechanical Properties

Finally, mechanical behavior can be used in an indirect fashion to support copolymer structure. In most cases, simple blends of two polymers produce poorer mechanical properties than either homopolymer alone. This was seen for a 3 %w blend of low molecular weight PDMS with nylon-6 as discussed in Chapter IX, §C where its tensile strength did not even reach 20 MPa. In contrast, the diblock copolymers (MSN(3/100) and USMSN(15/44)) both performed in uniaxial tension as would be expected of rubber-toughened materials deforming to strains of nearly 200 % with flow stresses ca. 45 – 50 MPa, representing properties far superior to the blended material. Although this does not confirm diblock structure, it supports the conclusion along with results from the other experiments described above, that this synthesis scheme has lead to the successful coupling of a siloxane polymer to nylon-6 via the macromonomer technique. As was seen, significant depolymerization of the siloxane occurs

in the presence of the lithium caprolactamate catalyst which detracts from the viability of this reaction scheme. To circumvent this unwanted depolymerization, extensive catalyst experimentation and scouting was undertaken which is discussed in the following sections.

3. Chemical Stability of Methylsiloxane to Caprolactam & Catalyst

a. Chemical Stability of PDMS to Polymerization Catalysts

Initial trials of copolymerizing the functionalized fluoroalkylsiloxane with magnesium bromide caprolactamate catalyst clearly indicated that a much lower degree of catalytic nucleophilicity was required to maintain siloxane block integrity. The first step towards achieving this was to reduce the cationic radius and hence, the ionization potential through use of lithium caprolactamate instead. This catalyst was prepared by methods described earlier in this chapter and used to copolymerize ω-N-acyllactam-poly(dimethylsiloxane) in experiments 4K, 4R and 4R-A. However, upon analysis of the copolymers (only 4R-A was thoroughly characterized as discussed above because 4K was an initial trial), it was discovered that significant depolymerization still had occurred and that a systematic investigation into the effects of the nylon-6 catalyst(s) was required.

The top panel of Figure 6-5 shows the effect of caprolactam monomer on PDMS at 170°C. Here the PDMS is stirred in the presence of only CPL monomer for a maximum of 24 hours, sampled and analyzed via SEC. This shows that after prolonged exposure to molten CPL, the chromatogram approximately coincides with that of the untreated or starting PDMS represented by the dashed line indicating that the PDMS is stable to the monomer for all practical purposes. Note that completely opposite

A)

B)

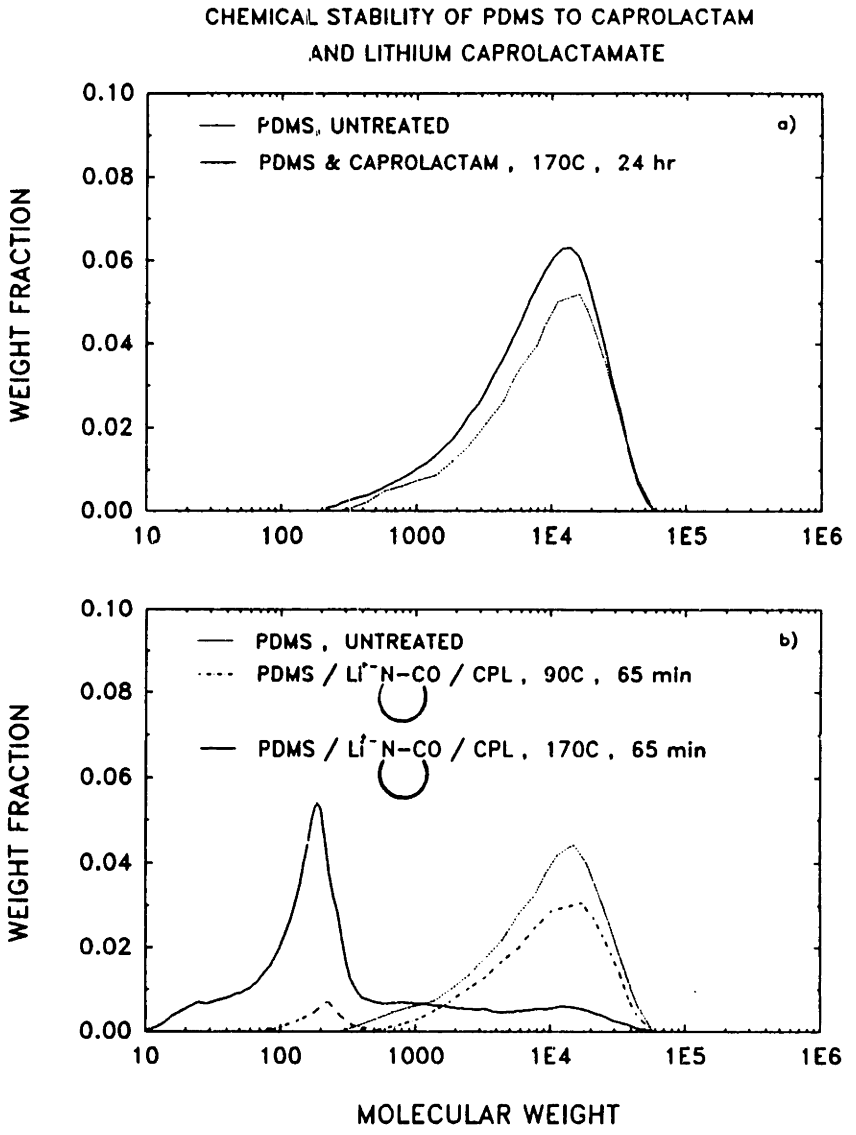

Figure 6-5 a) SEC of unfunctionalized PDMS in CPL at 170°C before and after exposure; b) SEC of unfunctionalized PDMS before and after exposure in CPL and lithium caprolactamate at 90°C and 170°C.

behavior was observed in the total depolymerization suffered by the PTFPMS after overnight exposure. Thus, the initial assumption about the chemical stability of the PDMS in CPL was justified.

Since analysis of the chemical integrity of the PDMS block after copolymerization of the caprolactam was extremely time consuming and difficult (not to mention less accurate), "simulation" reactions were devised to mimic the copolymerization without actually solidifying the reactor with a volume-filling polyamide-6-rubber copolymer. This permitted the use of on-line sampling and SEC analyses to give information on the MWD of the PDMS in various alkaline environments and at different temperatures. The "simulation" reactions consisted of stirring unfunctionalized PDMS in caprolactam at the desired temperature and adding the appropriate catalyst and solvent if desired, followed by periodic sampling and SEC analysis to track changes in the linear siloxane length and MWD.

The first such reaction produced the SEC curves shown in Figure 6-5b (bottom panel) which shows the effect of lithium caprolactamate on PDMS at two different temperatures of 90°C and 170°C both obtained after a 65 minute exposure time. This length of time closely approximates the duration before solidification begins in real block copolymerizations. The untreated polymer again is represented by the short dashed curve. The polymer at 90°C, designated by the dash-dot curve, was only mildly depolymerized to cyclic oligomers (ca. 7-10 %w cyclics) and the peak molecular weight essentially remained constant. After 20 hours (data not shown), only about 75 % of the polymer remained, the remaining 25% having been converted to cyclic oligomers.

In stark contrast, the solid curve represents exposure of PDMS to the catalyst at an elevated temperature of 170°C (i.e. the T_{pzn} of reaction 4R-A) where most all of the methylsiloxane is converted to monomer, D_3 and D_4 with only a fraction remaining as linear polymer. This generated a continuous MWD of siloxane from molecular weights comparable to the starting material all the way down to monomer. The depolymerization chemistry is believed to be very similar to that in equations (6-18,19) where nucleophilic attack by the caprolactam anion directly forms the siloxanolate which, at the high temperature, rapidly depolymerizes to a much higher concentration of monomer due to the ceiling temperature effect (i.e. $\ln(M_e/M_s) = \Delta H/RT - \Delta S°/R$ increases as T increases for an exothermic reaction). Now it is clear why the siloxane signal in the NMR analyses (both ^{13}C and ^{1}H) was so weak; the extended polymerization time of nearly 6 hours at 170°C severely depolymerized the PDMS and drastically randomized its molecular weight distribution. Thus, the effects of the lithium caprolactamate catalyst are clear from this "simulation" experiment and subsequent efforts were focused on developing alternate catalysts that reduced the nucleophilicity towards the methylsiloxane.

In the past, alkali metal aluminum alkyls [23] and hydrides [1,21] have been used as polymerization catalysts with reasonable success; they have produced high molecular weight materials but usually at lower reaction rates. As a result, $LiAlH_4$ was tested in a "simulation" experiment using toluene solvent at mild temperatures of 110°C to check literature claims [1]. This produced no change in the exposed PDMS as compared to the untreated material for up to 130 minutes at a PDMS:CPL

ratio of 1:2.5, 20 % solids and C/I (i.e. catalyst-to-initiator ratio) of 2.0. After 48 hours of exposure, a slight amount of cyclic oligomers had formed but it was only several percent with a shift in peak molecular weight from 15.5 kg/mole to 11.5 kg/mole in the 48-hour sample. Similar results were found for the same "simulation" experiment in the absence of toluene solvent (i.e. bulk) for up to 110 minutes exposure also at 110°C.

If the temperature was raised, however, to ca. 155°C and the same bulk "simulation" experiment conducted using a C/I ratio of 2.0 (which represents the maximum recommended for actual copolymerization), then very different results were obtained. The SEC curves of the untreated narrow polydispersity PDMS (short dash) versus exposure times of 65 and 125 minutes (solid and dash-dot, respectively) are shown in the upper left panel a of Figure 6-6. Here, the $LiAlH_4$ after just one hour has broadened the original PDMS polydispersity with the generation of ca. 10 % cyclic oligomers and after two hours, the molecular weight distribution spanned from a value greater than any chain length present initially all the way down to the cyclic oligomers including D_3 monomer. Thus, the increase in "simulation" or polymerization temperature from 110° to 155°C has introduced a significant amount of depolymerization/rearrangement of the PDMS by $LiAlH_4$ (or its modified form). This higher temperature is desirous from a material properties viewpoint because lower temperatures (< 150°C) will necessarily result in lower molecular weight polyamide-6 blocks which will exhibit decreased toughness. Almost identical results were observed if poly(diethylsiloxane) was exposed to $LiAlH_4$ in a "simulation" experiment implying no retardation effect as the length of alkyl substituent was doubled. Additional efforts in catalyst develop-

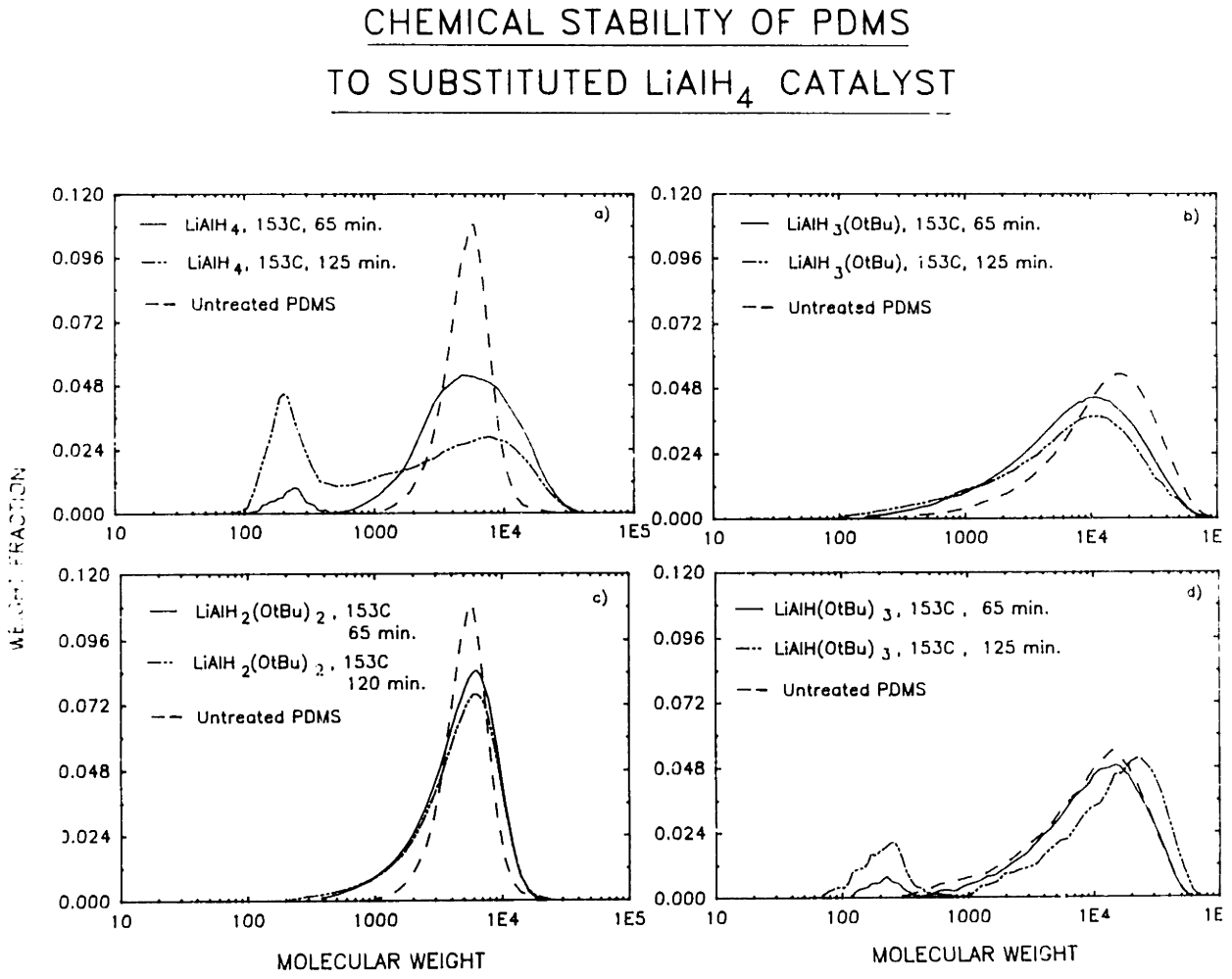

Figure 6-6 "Simulation" experiments of unfunctionalized PDMS in CPL with various derivatized $LiAlH_4$ catalysts at 153°C: a) $LiAlH_4$; b) $LiAlH_3(OtBu)$; c) $LiAlH_2(OtBu)_2$; d) $LiAlH(OtBu)_3$ Curves represent MWD of untreated PDMS (---), PDMS with ca. 1 hour exposure (——), and PDMS after ca. 2 hour exposure (—•••—).

ment obviously were needed if this macromonomer technique was to be conducted successfully to yield high molecular weight polyamide-6 blocks attached to intact poly(dimethylsiloxane) blocks.

Catalyst Development

Since the first two steps in reducing the nucleophilicity of the catalyst (i.e. the decrease in size of the counterion and the use of previously tried $LiAlH_4$) were not sufficient, additional organometallic chemistry modifications were implemented after careful consideration. Realizing that substitution of electron donating groups on the alumino-hydride should decrease its basicity and hopefully retard the siloxane depolymerization, a series of novel lithium tert-butoxyaluminum hydride catalysts were synthesized in diethyl ether according to the reaction scheme of equation (6-20),

$$LiAlH_4 + n\ t\text{-}BuOH \xrightarrow{DEE} LiAlH_{4-n}(Ot\text{-}Bu)_n + n\ H_2\uparrow \qquad (6\text{-}20)$$

where n ranged integrally from 1 to 3. These catalysts were then added to liquid CPL at 100°C under 1 – 2 cm Hg vacuum via either gas-tight syringe or cannula transfer from the catalyst/DEE flask to give catalyst molar concentrations of 1 – 1.5 % in the "simulation" reactor. After degassing the CPL twice, the unfunctionalized PDMS was added and stirred vigorously under the action of the magnetic stir bar for the desired amount of time and sampled for SEC analysis. These results are shown in panels b, c, d of Figure 6-6.

Panel b shows the effect on the MWD of the PDMS by replacing one hydride with a tert-butoxy group in the catalyst after 65 minutes of

exposure (solid curve) and 125 minutes of exposure (dash-dot curve) in molten CPL at 153°C. The original PDMS had a $\bar{M}_w$ = 16.6 kg/mole and an $\bar{M}_n$ = 6.5 kg/mole but after roughly one hour of exposure, the $\bar{M}_w$ had dropped to 11.6 kg/mole ($\bar{M}_{n,65\ min}$ = 3.3 kg/mole). Further changes for this catalyst composition and the others are detailed in Table 6-4. As can be seen by comparison of panels a and b in Figure 6-6, replacement of one hydride by a tert-butoxy group resulted in a marked improvement in the stability of the PDMS and in the successful suppression of cyclic oligomer formation.

Replacement of two hydrides by corresponding tert-butyl alkoxide groups gives the stability behavior shown in panel c, Figure 6-6. Here the initially narrow polydispersity is broadened somewhat but the peak molecular weight remained approximately constant. Again, as in the case of $LiAlH_3(OtBu)$, no cyclics are formed upon the action of this catalyst with PDMS in CPL at 153°C. A tertiary substituted aluminum hydride results in the catalytic activity shown in panel d of Figure 6-6. This catalyst is not as effective in suppressing cyclic oligomer formation as the two former compounds which is seen by formation of 5 %w cyclics concentration at the 65 minute mark and roughly 23 %w after two hours of exposure. Reasons for the decrease in stability of this trisubstituted lithium aluminohydride catalyst towards PDMS is presented below.

Discussion

These novel catalysts for the polymerization of caprolactam are a marked improvement over currently used caprolactam salts with regards to the depolymerization of the siloxane. Without their development, this copolymerization methodology would be almost useless due to the harsh

Table 6-4

Activity of Various Substituted $LiAlH_4$ Catalysts Towards PDMS

At 153°C

Catalyst	Exposure Time (min)	Initial PDMS MW* $\bar{M}_w$	Initial PDMS MW* $\bar{M}_n$	Exposed PDMS MW $\bar{M}_w$	Exposed PDMS MW $\bar{M}_n$	Composition (%w) Polymer	Composition (%w) Cyclics
$LiAlH_4$	0	5.5	4.6				
	65			7.0	4.0	94.1	5.9
	125			6.6	2.7	71.8	28.2
$LiAlH_3(OtBu)$	0	16.6	6.5				
	65			11.6	3.3	100	–
	125			10.8	2.2	100	–
$LiAlH_2(OtBu)_2$	0	5.5	4.6				
	65			5.4	3.4	100	–
	125			5.5	3.4	100	–
$LiAlH(OtBu)_3$	0	13.9	5.6				
	65			12.9	5.7	95.0	5.0
	125			17.0	7.9	77.4	22.6

* Molecular weights in kg/mole

chemical environment and the susceptibility of the siloxanes to depolymerization by base at the elevated temperatures where high molecular weight polyamide-6 must be synthesized. It is believed that the catalysts are successful because of their ability to complex with the lactam

anion and reduce its nucleophilicity by resonating electrons from the more electrophilic tert-butoxy groups into the caprolactam carbonyl-aluminum coordination bond. Thus, upon addition to CPL the catalysts form a complex as shown in equation (6-21) where the disubstituted lithium aluminum hydride is used as an example.

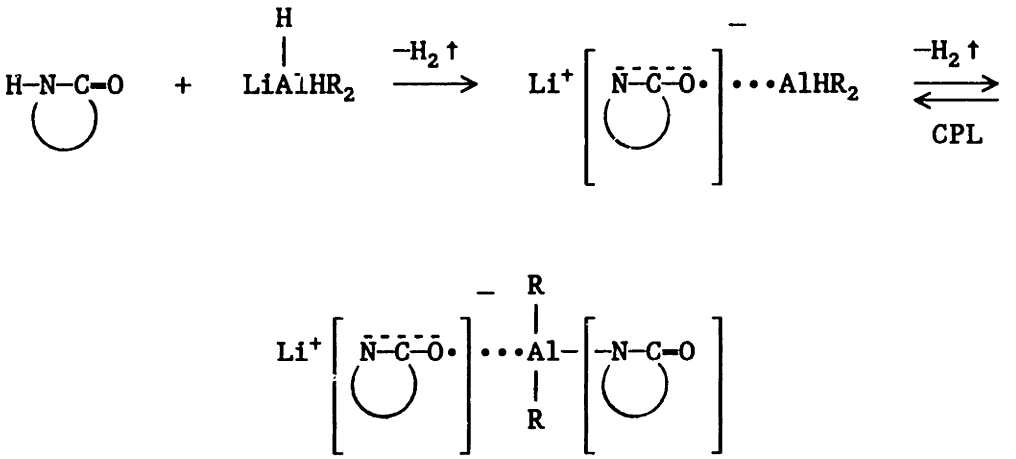

(6-21)

Normally, the electron density around the nitrogen anion is high due to the electron withdrawing ability of the amide carbonyl group. Here, this high, local electron density is decreased due to the resonance provided by the coordinating aluminum-oxygen bond and the electron donating character of the aluminum substituents, the tert-butoxy groups. These groups push electrons into the complex to delocalize the charge as depicted above much the same way a carbanion is delocalized by alkoxy group substituents. In this latter analogy, a polystyryl anion is highly nucleophilic due to the electron resonating (and withdrawing) ability of the phenyl substituent but an alkoxy (or ether) substituent weakens the carbanion so much that it is unstable which is why monomers like vinyl

methyl ether can not polymerize anionically, but rather polymerize cationically. This resonance and charge delocalization explains why the tert-butoxy substituted aluminohydride is far less devastating towards the siloxane than the parent compound, $LiAlH_4$ both of which are able to complex the carbonyl in the same manner; the latter simply has no electron donating groups to aid in charge delocalization. In addition, the hydrides of $LiAlH_4$ are much more reactive and can form only aluminum-lactam complexes (as in the far right structure of equation (6-21)), which are slightly electron withdrawing and do not sufficiently delocalize the charge to be effective.

In addition, the catalyst prepared by addition of $LiAlH_4$ to CPL contained dark, metallic precipitate which was not present in the other catalyst "solutions" and may have been lithium aluminum hydride oxide (AlR_2OLi, where R = H or $\overline{\text{N—CO}}$). This would be produced by at least two transfers of hydride ion to reduce the lactam carbonyl to the homopiperidine. If the remaining hydride(s) reacted with the lactam proton(s) of CPL to evolve H_2 gas, then the Al would be alternatively substituted as such by the lactam ring(s) as indicated above in the nomenclature for R. These reactions are known to occur in solution reductions of CPL [24] by $LiAlH_4$ to give 60 – 95 % yield of the cyclic imine. Other substituted alkoxy aluminum hydrides such as sodium bis(2-methoxyethoxy)aluminum hydride have been reported to reduce imides and lactams to the corresponding cyclic imines [25] at comparable efficiencies but only when 50 – 200 % excess reducing agent is used. In this thesis work, the tert-butoxy substituted aluminohydride catalysts, due to their decreased reactivity and large deficiency in concentration with respect to CPL,

probably did not attain such high yields of cyclic imine production and the corresponding concentration of aluminum oxide salt probably was much less than with $LiAlH_4$. However, no experiments were done to verify the structure of the precipitate and this is merely a cohesive hypothetical explanation of some experimental observations.

The size exclusion chromatograms of the exposed PDMS in Figure 6-6 show an expected trend except for the PDMS stirred with the trisubstituted aluminohydride, panel d. While the first two substituted catalysts in the series successfully eliminated the formation of cyclic siloxanes (i.e. panels b and c), the $LiAlH(OtBu)_3$ produced a significant amount of these oligomers. This can be interpreted as a modification of the complex established in equation (6-21) due to a fully satisfied aluminum valence shell with electrons from covalently bonded oxygen. The affinity of aluminum for oxygen is well known and in $LiAlH(OtBu)_3$, the Al after giving up its hydride, has its $3s^2$, $3p^1$ subshells satisfactorily filled with the electrons from the covalent –OR bonds and thus does not coordinate as fully with the lactam carbonyl to reduce the nucleophilicity of the lactam anion as in equation (6-21). This different electronic structure is shown below in equation (6-22).

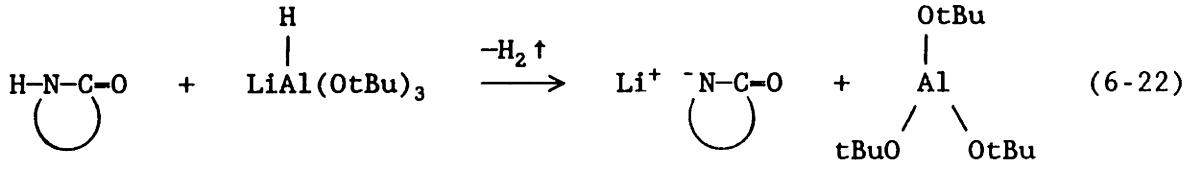

(6-22)

Although there may be some degree of coordination between the aluminum of the $Al(OtBu)_3$ and the carbonyl oxygen, it certainly is much less than with the other mono- and di-substituted aluminum hydrides. Hence, the

lactam anion acts more like the caprolactamate and is able to depolymerize the PDMS to a greater extent producing the cyclics in panel d, Figure 6-6 in similar proportion to the $LiAlH_4$ "simulation" experiment, panel a.

b. Ultrasonic Diblock Synthesis with $LiAlH_2(OtBu)_2$ Catalyst

Due to the heterogeneous nature of the copolymerization, an ultrasonic dispersion horn was used to improve the mixing of the functionalized PDMS in the CPL. As compared to the polymerization to produce MSN(3/100) which gave ca. 0.1–1.0 millimeter size droplets of the siloxane in CPL via magnetic stir bar agitation, the use of the ultrasonic horn reduced the scale of the inhomogeneity to that equivalent in dairy milk for example, (maybe 0.1 – 10 μm). This polymerization, run #USP to produce USMSN(15/44), was conducted at 155°C with the disubstituted catalyst $LiAlH_2(OtBu)_2$ with a continuous (no pulse sequence employed) ultrasonic input energy of 75 watts.

At the outset of the polymerization, the ω-N-acyllactam-PDMS was inhomogeneous in the CPL monomer, but within 5 minutes of addition of the catalyst to give a 1.0 C/I ratio, the reaction mixture turned nearly transparent. An aliquot was withdrawn at the 30 minute interval and showed oligomeric nylon-6-PDMS diblock copolymer of equivalent $\bar{M}_w$ = 3.6 kg/mole with a polydispersity nearly identical to the final product as determined by SEC and shown previously in Figure 6-3. The reaction "solution" remained nearly transparent until the 60 minute mark when a whitish solid was observed precipitating around the tip of the ultrasonic horn. This polymerizate expanded to eventually fill the entire volume of

the reactor in about 4 hours. The reaction was continued for 3 additional hours and then cooled to room temperature and worked up in the same manner as previously described.

The filtrate from the extraction/filtration step, which contains the monomer, unreacted or depolymerized siloxane, catalyst and nylon-6 oligomers was analyzed by SEC and ^{1}H NMR. The size exclusion chromatogram in toluene is shown as the dash-dot curve in Figure 6-7 and although it shows some broadening of the MWD from the original macromonomer (dashed curve), no cyclic oligomers are seen in the filtrate. This implies that the catalyst has satisfactorily eliminated the depolymerization of PDMS to cyclics but has not prevented transsiloxanolization reactions from occurring. This broadening in MWD is necessarily greater than in the "simulation" experiment because the copolymerization generates amide anions and other basic species not present in the "simulation" tests. Despite some chain transfer, this is still a significant improvement over the substantial conversion of PDMS to cyclic oligomers seen with lithium caprolactamate or lithium aluminum hydride catalysts.

In addition, the unreacted siloxanolate from the filtrate probably is more severely rearranged by chain transfer as compared to the siloxane incorporated into the diblock and so the chromatogram represents a worst-case alteration in siloxane MWD. This would occur because the active site for propagation of the nylon block, the imide group, resides at the end of the chain which would grow away from the siloxane micelles after initiation. Thus, the siloxane would be "sequestered" from the harmful basic species and attack by the basic lactam anion would be reduced thus abetting redistribution and depolymerization reactions.

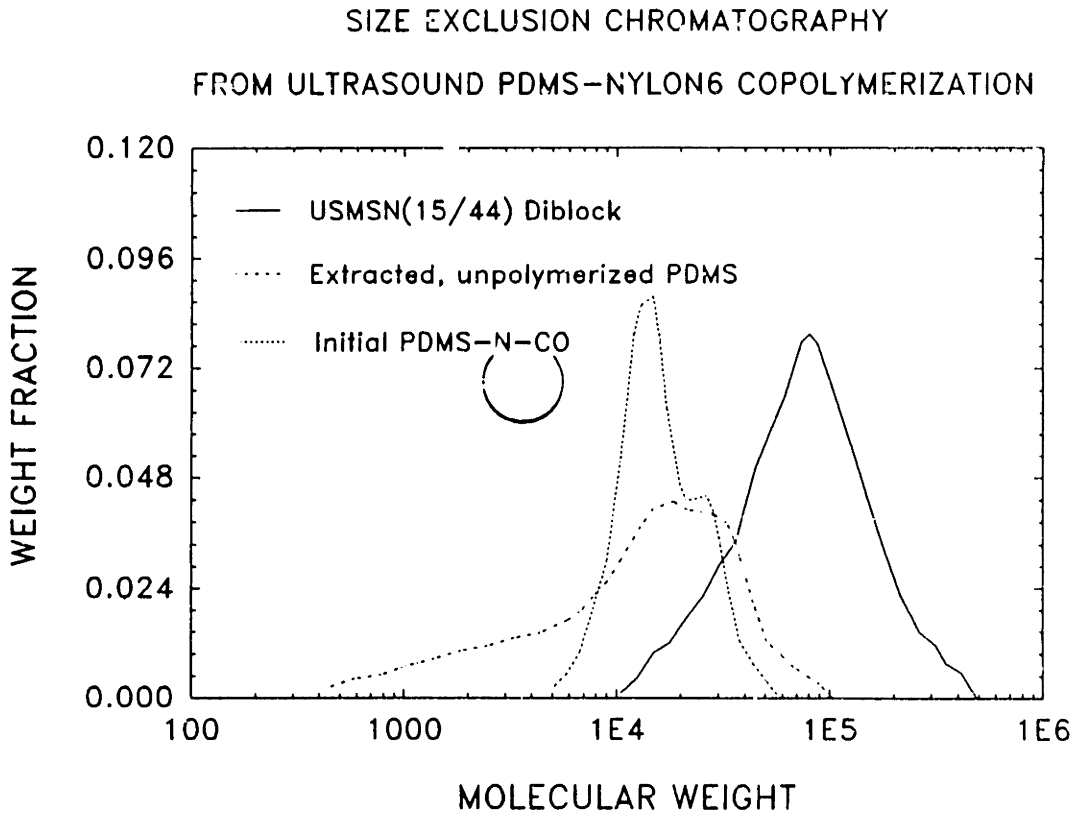

Figure 6-7 Size exclusion chromatography of ω-N-acyllactam-PDMS before (---) and unincorporated PDMS after copolymerization (–•••–); Chromatogram of USMSN(15/44) given for reference.

This may be the reason why the domains are fairly regular in the TEM micrographs of diblock USMSN(15/44) shown in Chapter VIII. The siloxane in the copolymer is pretty much intact and retains its narrow polydispersity as synthesized in THF from D_3 because it was not exposed to as harmful an environment as the siloxane that did not get incorporated into copolymer.

The filtrate contained some siloxane in a 1:7.8 ratio of siloxane:hydrocarbon (mainly CPL) as determined by NMR which will be used to ascertain yield and the amount of unreacted siloxane discussed next. This spectrum was much cleaner than the filtrate spectrum from the polymerization of MSN(3/100) (run 4R-A) and contained mostly CPL and siloxane which supports the conclusion that the new catalyst is much less harsh than lithium caprolactamate.

The ^1H NMR spectrum of the copolymer after workup is shown in Figure 6-8. The large singlet indicative of a much higher concentration of dimethylsiloxane as compared to the spectrum of MSN(3/100) in Figure 6-4b is evident at ca. 0.15 ppm along with the triplets at 3.15 ppm and 2.15 from the methylenes adjacent to the amide nitrogen and carbonyl, respectively. Note the methine impurity peak from the d_2-HFIP solvent which interferes with the triplet peak at the letter 'c'; the fluoroalcohol NMR solvents typically are only 97 – 98 % deuterated. Intergration of this spectrum gives the values presented in Table 6-3 for the number of repeat units per block based on the conclusion from the SEC of the filtrate that the siloxane block did not depolymerize to cyclic oligomers.

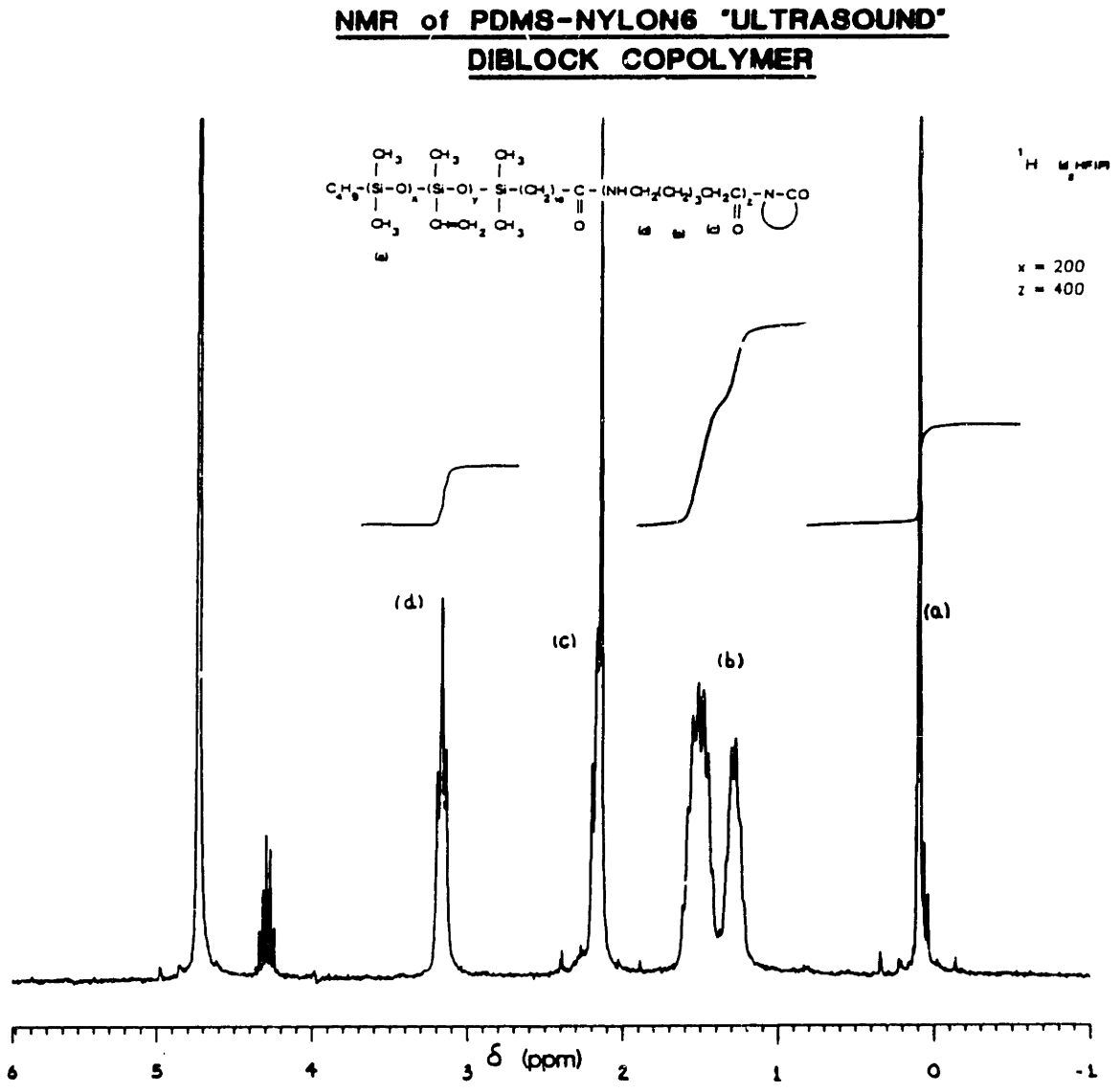

Figure 6-8 ^{1}H NMR spectrum of USMSN(15/44) after workup; in d_2-HFIP at 25°C. Integration yields $N_{NY} \doteq 2N_{MS}$.

The SEC of the diblock copolymer was shown in Figure 6-3 and has a fairly narrow polydispersity for polyamide-6. The determination of block molecular weights was done in §2.a of this chapter; basically this involved calculation of the block number average molecular weights via NMR which were corroborated with good agreement by SEC data. The primary conclusion from these data of the copolymer after workup is that the new catalyst, $LiAlH_2(OtBu)_2$ coupled with the ultrasonic dispersion effectively eliminates the depolymerization reactions and increases the conversion of PDMS incorporated into the copolymer as discussed next.

c. Performance Data of PDMS-Nylon-6 Copolymerizations

The aforementioned NMR data of the two major polymerizations, run #4R-A and #USP were used in conjunction with material balances to calculate the yield and conversion data as summarized in Table 6-5. These data show that MSN(3/100) had a very poor conversion of methylsiloxane into copolymer mainly due to the extensive depolymerization from the strongly basic caprolactamate catalyst but had a good conversion of CPL because of the long hold time at elevated reaction temperature to drive the nylon-6 block polymerization towards equilibrium.

The ultrasound polymer, USMSN(15/44) had a much better conversion of siloxane into copolymer (57.4 % versus 13.6 % for MSN(3/100)) due to the improved mixing and reduced catalyst depolymerization effects. However, the potencial exists for conversion of some of the imide groups of the ω-N-acyllactam-PDMS in the USMSN(15/44) copolymerization to cyclic imines by the aluminum hydride catalyst which essentially deactivates the macromonomer. Thus, quantitative improvement in acyllactam reactivity as interpreted from the filtrate NMR spectra is not absolutely certain due

Table 6-5

Performance Data for the Methylsiloxane-Nylon-6 Copolymerizations

Polymer	T_{pzn} (°C)	Initial Charge (g) PDMS	Initial Charge (g) CPL[a)]	Extract Phase (g) Total	Extract Phase (g) Oil Sol.	Extract Phase (g) H_2O Sol.[b)]	Copoly (g)	Yield (%)†	Conversion (%) MeSx	Conversion (%) CPL
MSN (3/100)	170	1.91	8.51	4.08	2.56	1.52	6.28	60.3	9.6	71.6
USMSN (15/44)	155	2.00	10.52	8.01	–	–	4.42	35.3	55.3	31.3

a) Includes catalyst charge

b) Oil and water solubilities; i.e. the extract phase was further extracted into an aqueous soluble and aqueous insoluble phases. Amounts of each phase determined by NMR (composition) and material balance (weight).

† Yield based on grams copolymer ÷ total grams into reactor.

---

to these other potential reactions. That is to say, the presence of siloxane in the filtrate may not be simply depolymerized or unreacted siloxane; rather there could be some deactivated siloxane present (through carbonyl reduction or imide condensation) that is unavoidable by virtue of the anionic polymerization mechanism.

While the siloxane conversion increased markedly in the USMSN(15/44) polymerization, the caprolactam conversion decreased because of the weaker basicity and lower polymerization temperature which slowed the propagation rate. Longer reaction times and higher polymerization temperatures would probably improve CPL conversion. Undoubtedly, the

$LiAlH_2(OtBu)_2$ catalyst partially is responsible for the reduced rate because it can be converted to the inert lithium di-tbutoxyaluminum oxide ($LiAlO(OtBu)_2$) from the reduction of the lactam carbonyl. This further lowers the alkalinity in the reactor (in addition to all the other side reactions detailed in this and the preceding chapter) and subsequently causes premature cessation of the polymerization. This may be partially remedied by going to higher polymerization temperatures or by using higher catalyst/initiator ratios but at the expense of increased depolymerization of the PDMS.

Conclusions

The anionic copolymerization of PDMS and nylon-6 has been accomplished via use of a ω-N-acyllactam-PDMS to initiate ϵ-caprolactam with a newly developed catalyst, $LiAlH_2(OtBu)_2$. It is believed that these catalysts decrease the nucleophilicity of the lactam anion by coordinating the aluminum with the lactam carbonyl to effectively delocalize the negative charge reducing its detrimental reactivity with the siloxane. As a result of reduced basicity, these new catalysts increase the time needed to attain polymer-monomer equilibrium but offer increased protection of the siloxane macromonomer; long polymerization times are also seen in patent examinations of PB-nylon-6 copolymers using much stronger catalysts [11].

To date, the copolymerization has been optimized mainly by the "simulation" experiments which provided a first order estimate of the ability of the various catalysts to avoid PDMS rearrangement and depolymerization. As was discussed in §C.1, these depolymerization reactions also contribute to the reduction in alkalinity which decreases the

propagation rate and halts attainment of equilibrium CPL conversion. The improvement in mixing provided by the ultrasonic dispersion helped to achieve a higher conversion of macromonomer acyllactam (imide) groups into the copolymer as seen from the filtrate ^{1}H NMR spectra of MSN(3/100) versus USMSN(15/44) and the yield data of Table 6-5. Combining the new catalyst, the ultrasonic reactor and a slightly lower polymerization temperature has increased the productivity of the copolymerization significantly and hopefully has provided a solid foundation to pursue additional improvements in the anionic copolymerization of lactams.

D. REFERENCES FOR CHAPTER VI.

1. M.J. Owen, J. Thompson, Br. Polym. Jnl., 4, 297 (1972).

2. J. McGrath, A. Noshay, Block Copolymers, Overview and Critical Survey, Academic Press, NY, 1977.

3. S. Wu, J. Polym. Sci: Polym. Phys. Ed., **21**, 699 (1983).

4. S. Wu, Polymer, **26**(11), 1855 (1985).

5. J. Noolandi, Ber. Bunsenges. Phys. Chem., **89**, 1147 (1985)

6. M.A. Drzewinski, MIT Doctoral Thesis, Dept. of Mat. Sci. & Eng., 1986, p. 227

7. E. Martuscelli, F. Riva, C. Selliti, C. Silvestre, Polymer, **26**(2), 270 (1985)

8. S. Cimmino, L. D'Orazio, R. Greco, G. Maglio, M. Malinconico, M. Mancarella, E. Martuscelli, R. Palumbo, G. Ragosta, Polym. Eng. Sci., **24**, 48 (1984)

9. U.S. Patent No. 4,031,164, R.M. Hedrick, J.D. Gabbert, to Monsanto Co., June 21, 1977

10. R.M. Hedrick, J.D. Gabbert, Papers Presented at AIChE National Summer Meeting, Detroit, Michigan, August 17, 1981

11. U.S. Patent No. 4,473, 686, U. Grigio et. al., to Bayer, Sept 25, 1984

12. H.S.-I. Chao and T.W. Hovatter, Polym. Bull., **17**, 423 (1987).

13. W.T. Allen and D.E. Eaves, Die. Angew. Makromol. Chemie, **58/59**, 321 (1977).

14. D. Petit, R. Jerome and Ph. Teyssie, Jnl. Polym. Sci., Polym. Chem. Ed., **17**, 2903 (1979).

15. W.L. Hergenrother and R.J. Ambrose, Jnl. Polym. Sci., Polym. Chem. Ed., **12**, 2613 (1974).

16. Z. W. Wicks, Prog. Org. Coat. **3**, 73 (1975).

17. B.H. Wondraczek and J.P. Kennedy, Jnl. Polym. Sci., Polym. Chem. Ed., **20**, 173 (1982).

18. J.P. Kennedy, L.R. Ross, J.E. Lackey and O. Nuyken, Polym. Bull., 4, 67 (1981).

19. Y. Yamashita, H. Matsui and K. Ito, Jnl. Polym. Sci., Polym. Chem. Ed., **10**, 3577 (1972).

20. O. Wichterle, Makromol. Chem., 35, 174 (1960).

21. J. Sebenda, J. Macromol. Sci., Chem A 6(6), 1145 (1972).

22. J. Sebenda and V. Kouril, Eur. Polym. Jnl., **8**, 437 (1972).

23. H. Tani and T. Konomi, Jnl. Polym. Sci., Pt. A-1, 4, 301 (1966).

24. L. Ruzicka, M. Kobelt, O. Hafliger and V. Prelog, Helv. Chim. Acta., **32**, 544 (1949).

25. M. Cerny, J. Malek, M. Capka and V. Chvalovsky, Coll. Czech. Chem. Comm. , 34, 1033 (1969).

CHAPTER VII. MOLECULAR CHARACTERIZATION

A. CRYSTALLIZATION PROPERTIES OF MULTIPHASE SYSTEMS

1. Introduction to Crystallization in Block Copolymers and Blends

A second amorphous component in the melt with a semicrystalline copolymer exerts a strong influence on the crystallization depending on many physical properties of the diluent such as its glass transition temperature, miscibility with the crystalline component and surface free energy. These factors will markedly influence many crystallization properties such as growth rate, work of chain folding, nucleation density, lamellar thickness, etc. Generally, the second component can be subdivided into two groups depending on its solubility characteristics, those that are miscible with the crystalline component in the melt and those that phase separate into distinct amorphous domains.

Miscible components exert a strong influence on both the nucleation free energy barrier, ΔF^* and the transport free energy barrier, ΔF_η as a function of the glass transition of the diluent [1]. If the T_g of the diluent is less than the T_g of the crystalline component, than the growth rate contribution from the transport term for the blend will be greater than for the crystalline component alone as a result of a decrease in the free energy barrier for transporting the crystallizable material to the interface; it is essentially plasticized by the diluent. Opposite trends are to be expected for $T_g^a > T_g^c$. However, in addition to the ΔF_η barrier, the nucleation term must account for the fraction of the interface occupied by noncrystalline material and thus, the ΔF^* barrier will be greater. As in homopolymer crystallization, the actual growth rate will be determined as the best compromise of the two competing forces,

nucleation and transport. Omitted in this very general discussion are the local changes in the interface concentration (as compared to bulk) and the depression of T_m at the interface due to these differences in concentration which affects the supercooling ($T_m - T_c$) and hence the growth rate. But since the nylon-6-PDMS system is believed to be heterogeneous in the melt (because of a large solubility parameter difference), additional discussion of miscible systems is deferred to the literature [2-4].

The second class of materials are those that form an immiscible phase in the melt and these will be discussed in this thesis. Here, energy must be spent not only in nucleation and transport of crystallizable chains, but also in rejection, occlusion and deformation of the droplet phase. This will be discussed in conjunction with morphological observations of the poly(dimethylsiloxane)-b-polyamide-6 diblocks in Chapter VIII. These additional factors serve to increase the free energy barrier as shown in equation (7-1) and hence, slow the growth rate as is observed experimentally [1,5,6].

$$\dot{G} = \dot{G}_o \exp \left[- \Delta F^*/kT - \Delta F_\eta/kT - [(E_r + E_v + E_o + E_d)/kT] \right] \qquad (7\text{-}1)$$

Here, the ΔF^* and ΔF_η represent the nucleation and transport barriers as usual, and the additional term represents the free energy expense for:

E_r ~ free energy of rejection of droplet phase,

E_v ~ kinetic energy potential to overcome droplet inertia,

E_o ~ free energy of occlusion and formation of new interface,

and E_d ~ energy expended to deform the droplets from their equilibrium spherical shape.

Normally, E_v is very small and can be neglected. The rejection term, E_r is usually the largest being ca. (0) ~$10-10^4$ J/mole as determined for i-PP [1] versus E_o, E_d ~ (0) $1\text{-}10^{-2}$ J/mole. The rejection energy barrier which scales with the melt viscosity obviously will decrease at higher crystallization temperatures, T_c, so that it may become comparable to the other two terms, E_o and E_d for nylon-rubber systems. The melting temperature of nylon-6 is some 50 – 70°C above the T_m for i-PP. The work expended by the crystallizing system is greater for finer dispersion of the amorphous phase within the melt as E_o and E_d scale as r^{-1} and E_r ~ r^{-2}.

For blends of i-PP and EPR rubber, rejection was dominant and occlusion (or coalescence and then occlusion) occurred only at longer crystallization times and higher rubber concentrations. Growth rates were decreased only slightly. For i-PP/EPDM blends, more occlusion and deformation of the droplets was seen in the optical light microscope [1] and the growth rate dropped more quickly as rubber was added to the i-PP. The fold surface free energy for these two different rubbers showed opposite trends as a function of the amount of rubber added to the blend; a monotonic increase in σ_e with rubber content was observed for EPR where primarily rejection occurs, whereas with EPDM, the σ_e dropped to a minimum at ca. 10 – 12 %w rubber and then slowly increased but always remained below σ_e of pure i-PP for all rubber concentrations up 40 %w EPDM. Although there probably are other intangible variables, the data from these systems suggest that a blend possesses a lower σ_e than

the corresponding homopolymer if occlusion is prevalent versus a larger σ_e than the homopolymer if rejection is dominant.

For blends of PIB with i-PP, both low and high molar mass PIB were preferentially rejected to interspherulitic regions at lower rubber concentrations (ca. 10 %w). At higher concentrations, the high molar mass PIB was occluded on the scale of 5 – 10 μm which was slightly larger than the regions for the EPR due to the higher molecular weight. The low and high molar mass materials showed a sharp drop in growth rate from the homopolymer to the blend with 10 %w rubber followed by a much slower decrease for higher PIB concentrations (>10%w). The medium molar mass material suffered a less drastic decrease in growth rate from 0 – 10 %w rubber. Fold surface free energy effects were generally lower than for pure i-PP except for one isolated case at 20 %w low molecular mass PIB. No explanation was given for this deviation from the trend established by the other data.

Modification of the model of Martuscelli et.al. [1,6] for rejection, occlusion and deformation has not been done in the literature (to the author's knowledge) for block copolymers containing an amorphous block that phase separates prior to crystallization. With these types of materials, the original terms need to be modified because of the connectivity between the rubbery and crystalline blocks which will affect the ability to reject the amorphous domains especially over large distances to interspherulitic regions, for example. No mathematical forms for the terms have been given in this thesis but these differences are discussed qualitatively in view of the morphology of the diblocks as detailed in Chapter VIII.

Contrary to the findings of Martuscelli, et.al. [1] are those presented by Drzewinski [7] who observed slightly higher linear growth rates as a function of supercooling for blends of PB and i-PP versus either the corresponding diblock and/or the same homo-i-PP used in preparing the blends. However, closer inspection of his data shows that the $\dot{G}$ of the experimentally prepared i-PP actually is greater than either the blend or the block (over most of the higher supercooling range) which is consistent with the findings of Martuscelli et.al. in references [1-3] discussed above. Rather, it is the commercial i-PP growth rates quoted by Drzewinski which are less than the blend or the block but this i-PP is not prepared in the same manner and can differ in tacticity, molecular weight, nuclei content etc. which are known to strongly affect growth rates leading to the difference in findings.

The presence of a second component in the melt not only affects the growth rate, but other physical parameters of crystallization as well. Melting points of the blend of i-PP/EPR increased due to the "scrubbing" out of low molecular weight i-PP material by the EPR; this low molecular weight material creates more imperfections in the crystal and hence lowers the melting point. The T_m of the i-PP/PIB blends decreased according to the diluent effect. Spherulite size is seen to decrease and nucleation density is observed to increase for diblock copolymer crystallization as compared to a pure blend as demonstrated by Drzewinski with PB/i-PP [7]. This nucleating ability of the copolymer is quite plausible because of the already formed "nucleus" (although much larger than normal heterogeneities) of the amorphous, phase-separated domains in addition to the random heterogeneous nuclei ("dirt") distributed through-

out the sample. Thus, additional nucleation points result from phase separation and can lead to higher nucleation densities as seen in this thesis work.

This greater nucleation density causes an increase in the bulk crystallization rate constant, K, for the diblock versus the blend at a given crystallization temperature [4]. Note that K is proportional to the product of the cube of the growth rate and the nucleation density or $K \propto \dot{G}^3 N$. This increase in K for the diblock occurred in [4] despite a slightly larger growth rate for the blend versus the diblock. This can be understood by considering the constraints of the crystalline copolymer blocks which are anchored at the domain interface whereas no such restraint is present in the blend. Due to this lower conformational entropy as compared to a crystalline homopolymer, the diblock chains are not as free to orient themselves for incorporation into the growing crystal. Thus, the growth rate of a diblock is less than homopolymer, all else being equal. In contrast, the free energy penalty for the immiscible phase in the blend is the higher energy for rejection, occlusion and deformation of the particles. Depending on which process consumes more free energy, the loss in conformational entropy of the diblock chains versus the greater interfacial free energy of interaction of the immiscible blend components, that growth rate necessarily will be lower.

Opposite behavior in the value of K was observed [8] for the kinetics of the nylon-6/EPM system, a pure blend compared to a graft copolymer, EPM-g-SA-g-nylon6. Here, the crystallization of the graft copolymer prepared by random grafting of EPM to nylon-6 through anhydride

groups slowed quadratically proportional to the amount of rubber added. Despite the perceived benefit of increased nucleation from the graft copolymer, the increased viscosity of the transport term was assumed to dominate and slow the overall rate. The pure blend of nylon-6 and EPM, on the other hand, had a higher kinetic constant, K (lower crystallization half-time, $\tau_{1/2}$) than either the graft copolymer or homopolyamide-6. This was attributed [5] to a slight increase in nucleation density as was seen above over pure homopolymer (Drzewinski, ref [7]) and to a decrease in melt viscosity (lowers the transport barrier) of the two-phase system. However, no further details were given as to how the decreased viscosity versus homopolyamide-6 affects an immiscible system; i.e., how the viscosity of the nylon-6 phase is dependent on the phase-separated EPM.

The Avrami exponent (see Appendix 1) in Martuscelli's study indicated athermal, heterogeneous, spherulitic crystallization for homopolymer and Ny-6/EPM blends (n=3 ± experimental error) [5]. For the EPM-g-SA-g-nylon-6 graft copolymer, n was 3.1-3.8 depending on the isothermal crystallization temperature. No explanation was given (in ref [5]) for this shift towards thermal, truncated spherulitic nucleation for the copolymer but this is quite plausible because copolymers are known to have different nucleation/growth characteristics than their corresponding homopolymers. The dispersed rubber within the crystalline matrix could have truncated the spherulitic growth because it could not be rejected at the growing front due to the connectivity which was then manifested as an increase in the Avrami exponent.

For the nylon-6-g-SA-g-EPM graft copolymer, Martuscelli, et.al. [5] found a larger σ_e than either the σ_e from the blend or the pure polyamide-6 similar to the results of Hay, et.al. [6], for short block length PE-PB diblock copolymers. In contrast, Drzewinski [7] observed a decrease in σ_e for i-PP-PB diblock copolymer versus the blend or pure i-PP. Calculations of σ_e by Drzewinski were supported by a lower melting point indicative of thinner crystals with more chain folding; (recall that the work of chain folding, $q = 2A_o\sigma_e$, and thus, for lower σ_e, chain folding is easier and more prevalent). Thus, comparing the results of just these few studies, no universal tendency in the change of σ_e, T_m or growth rate is evident for the crystallization of a block copolymer containing a noncrystalline block as compared with its homopolymer or simple blend. This is because too little is known about the effects of chain architecture (tacticity, branching, etc.), compatibility and heterogeneities on crystallization at the molecular level to facilitate a complete understanding of the phenomena.

2. Experimental Results

a. Crystallinity Content in Nylon Polymers

Crystallinity content in nylon-6 polymers was determined by three methods: 1) differential scanning calorimetry (DSC), 2) gradient density column and 3) wide angle x-ray scattering, although the last method was not used quantitatively for absolute crystallinity values; only relative amounts of the α and γ forms were determined (see Chapter VIII). Thermal analysis was done on a Perkin-Elmer DSC 4 with TADS Data Station suitable for cryogenic studies. The gradient density column was constructed by

A. Galeski using toluene/carbon tetrachloride solutions and the WAXS data will be discussed in Chapter VIII, §C.

1. Differential Scanning Calorimetry

Crystallinity levels, melting and glass transition temperatures were determined for homopolyamide-6 and the copolymers via DSC. Weight fraction crystallinity, w_c was determined by the ratio of specific enthalpy of fusion for a given sample to that of a perfect nylon crystal. Since nylon-6 is polymorphic, the heat of fusion for the perfect crystal is arbitrary unless independent assessment of the fraction of the various crystalline forms can be made (via WAXS for example). Although the content of the two crystalline forms frequently was determined by WAXS analyses discussed in Chapter VIII, crystallinity contents are not quoted based on these fractions multiplied by the corresponding pure crystalline heats of fusion. This can lead to obscure interpretation if not done carefully and so only heats of fusion generally are reported. Sometimes, for ease of comparison, percent crystallinities are quoted based on the assumption (although not rigorously correct) of 100% α nylon-6 crystals which puts all values on a common basis using the value from the work of Wunderlich, et.al. [9] which is ΔH_u = 45.4 cal/g. Then, w_c can be calculated from the ratio of the observed heat of fusion to that of a perfect crystal, viz.,

$$w_c = \frac{\Delta H_f}{\Delta H_u} = \frac{\Delta H_f}{45.4} \qquad (7\text{-}2)$$

For diblocks or blends, the divisor must account only for the potentially crystalline component, i.e. 45.4 x W, where W is the weight fraction semicrystalline material.

The volume fraction crystallinity, v_c is easily calculated from w_c using values of crystalline and amorphous densities (1.23 and 1.09 g/cc, respectively) [10,11],

$$v_c = \frac{1}{\frac{\rho_c}{\rho_a}\left(\frac{1}{w_c} - 1\right) + 1} \qquad (7\text{-}3)$$

or can be determined directly via density measurements.

Table 7-1 shows an extensive list of heats of fusion and calculated crystallinity content assuming perfect α-form for the various types of nylon-6 used in this study. Note the high degree of crystallinity in the fibrillar spin cast film versus the spherulitic microstructure obtained after melt annealing at temperatures of ~ 240 – 250°C. All samples were analyzed with ca. 3 %w moisture content. The morphologies of these materials are shown in Chapter IX where the mechanical behavior of these films is analyzed.

Melting curves of isothermally crystallized nylon-6 and the copolymers often show multiple peaks as seen in Figure 7-1 which indicates either rearrangement on melting (crystal perfection) or multiple crystal phases. Both of these, however, may occur together. While it is known nylon-6 prefers the monoclinic, α-form crystal structure with hydrogen bonding between antiparallel chains [12], as in the (001) crystal plane (b-axis parallel to chain axis), some molecules "trapped" in a parallel alignment (γ phase) complete only roughly 50% of the possible hydrogen bonding. The γ-form has chains that are twisted 90° to make hydrogen bonds in the (100) crystallographic plane which may become sufficiently mobile at temperatures just below T_m (melting temperature) to transform

Table 7-1

Crystallinity of Nylon-6 by
Differential Scanning Calorimetry

Sample	Annealing	ΔH_f (cal/g)	$w_c^{\#}$	$v_c^{\$}$	T_g † (°C)
Monsanto	as rcvd	19.2	0.423	0.396	31.2
Allied	as rcvd	20.4	0.450	0.423	–
Monsanto Spin Cast	unannealed	19.0	0.419	0.392	–
Monsanto Spin Cast	60°C/24 h	24.8	0.546	0.518	91.8
Allied Spin Cast	100°C/24 h	25.8	0.568	0.540	–
Allied Spin Cast	250°C/2 h slow cool	9.4	0.207	0.192	–
Monsanto Spin Cast	240°C/15 min slow cool	15.8	0.349	0.324	50.3
Monsanto Nyrim[R a)]	250°C/1 min slow cool	13.5	0.374	0.345	34.3 Ny6 -66.0 PPO

Weight fraction crystallinity calculated assuming 100% α phase crystals with a ΔH_u = 45.4 cal/g.

$ Volume fraction crystallinity calculated from w_c assuming ρ_a=1.09 g/cc and ρ_c=1.23 g/cc.

† As determined by cryogenic DSC

a) Formerly Monsanto Nyrim[R] product, now technology belongs to the Dutch State Mines Co.

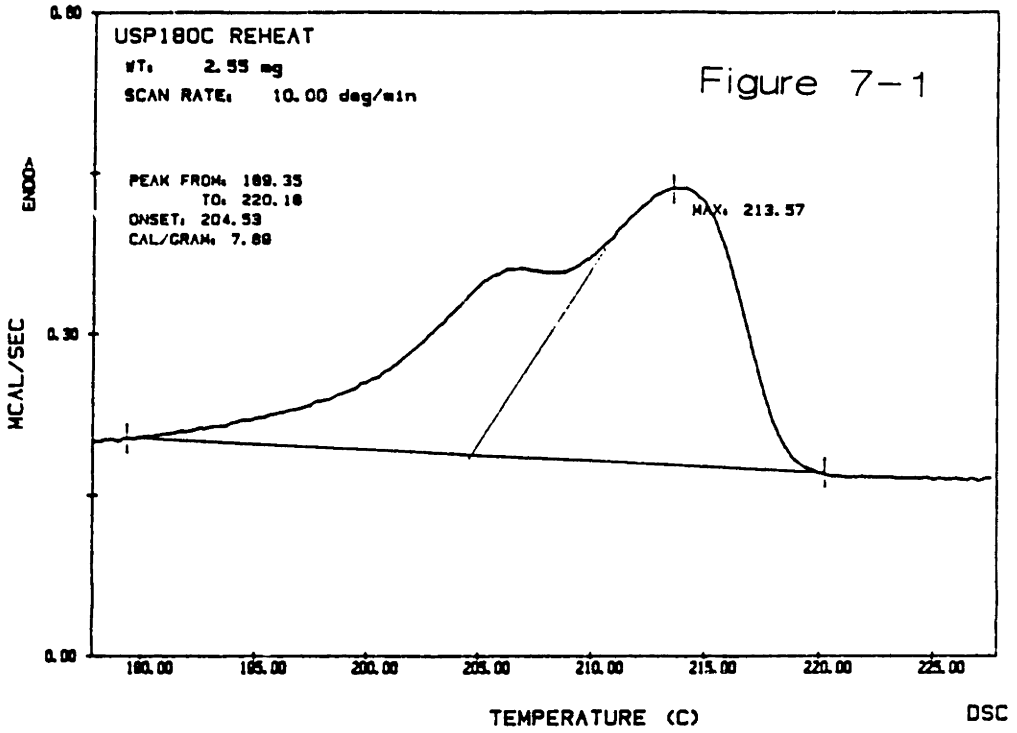

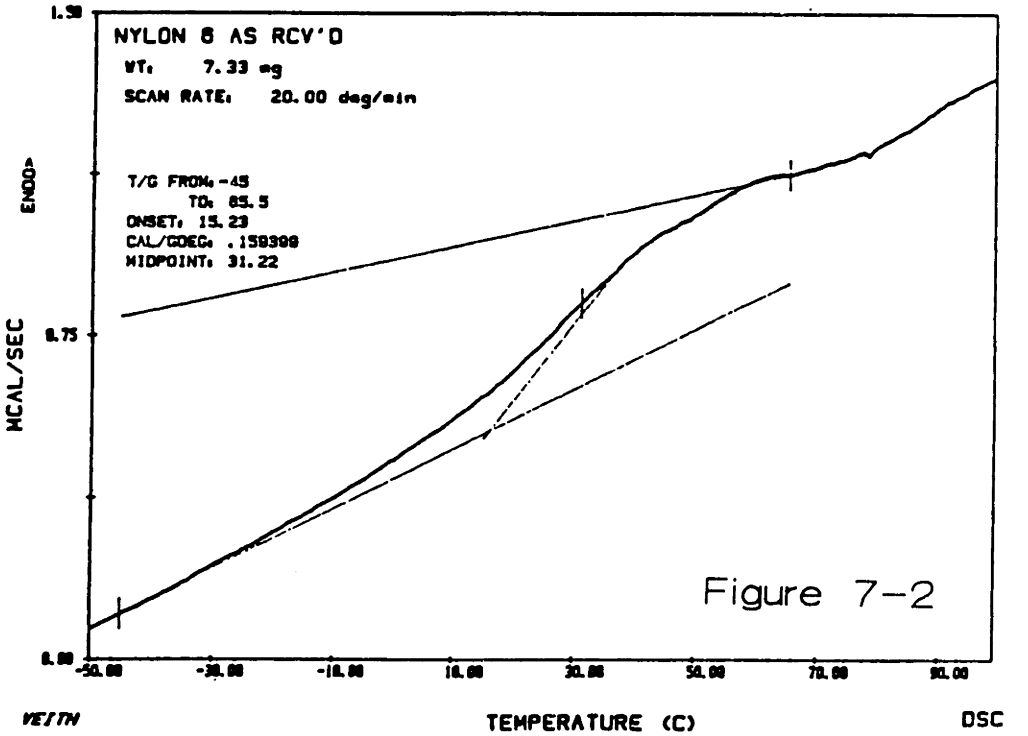

Figure 7-1 Differential scanning calorimetry of isothermally crystallized (180°C) USMSN(15/44) with multiple peak endotherm.

Figure 7-2 Glass transition analysis by cryogenic DSC of RIM Monsanto nylon-6 containing ca. 3.3 %w moisture.

the γ to the α phase, liberate moderate enthalpy (sometimes seen as a drop in curve between peaks) and perfect the crystal structure to some degree, before final melting. This is the interpretation for the observed melting curves like that for the ultrasound diblock USMSN(15/44) shown in Figure 7-1 which indicates multiple peaks; here, the highest peak melting temperature is approximately 213.5°C. It is known that this material contains roughly 17.2% γ structure (from WAXS) which is represented by the lower peak endotherm. More separation between peaks has been observed with homopolyamide-6 samples both isothermally crystallized as well as cast from solution. Melt annealed homopolyamide-6 cooled at a moderate rate which crystallizes through a temperature range occasionally shows evidence of a slight shoulder but no peak separation is usually seen. These materials contain much less γ-form crystals due to crystallization temperatures above ca. 180°C as will be discussed in the next chapter, §C.2.

The glass transition of homopolyamide-6 was determined by DSC using the cryogenic kit attachment. Representative results are shown in Figure 7-2 for anionic, RIM nylon-6 as received from the Monsanto Co. and equilibrated in a ~ 60% R.H. environment (sample contains ~ 3.3% moisture). This material has a T_g of approximately 30°C; if analyzed dry, the T_g would rise to ca. 85 – 90°C, values which are corroborated by dynamic mechanical analysis of nylon-6 described in §B.

Similar heat of fusion determinations were carried out on the various diblock copolymers and their corresponding blends. The morphologies of these materials and their mechanical behavior will be discussed in Chapters VIII and IX, respectively. Table 7-2 shows that like

Table 7-2

Crystallinity Data for PDMS-Nylon-6 Diblock Copolymers and Blends via DSC and Density Measurements

Polymer[a)]	Annealing (°C)	T_m[b)] (°C)	ΔH_f (cal/g)[c)]	χ_C[d)]	ρ_N[c)]	ψ_C[e)]
MSN(3/100)	100	220.6	27.65	0.609	1.1635	0.525
	m annl, 250	215.3	9.61	0.212	1.1517	0.441
MSN(3/100)/NY6	100	219.9	28.26	0.623	–	–
43/57	m annl 250	217.6	11.79	0.260	–	–
MSN(3/100)/NY6/PDMS	100	211.4[f)]	22.64	0.499	–	–
42/56/2	m annl 250[g)]	213.5	14.22	0.313	–	–
	m annl 250	216.1	13.08	0.288	–	–
MSN(3/100)/NY6/PDMS	180	217.9	38.05	0.838	1.1773	0.623
38/51/11	m annl 250	216.8	21.96	0.484	<1.00 => voids	
NY6/PDMS blend	180	218.4	22.15	0.488	–	–
0/97/3	m annl 250	219.1	10.79	0.238	–	–
USMSN(15/44)	100	–	–	–	1.1949	0.749
	180	–	–	–		
	m annl 250	212.8[f)]	12.85	0.283	1.1631	0.522

a) Nomenclature: MSN = methylsiloxane-nylon-6 diblock; US = ultrasound polymerization; numbers in parentheses signify $\bar{M}_n$ values of respective blocks; numbers below polymer name for each entry signify weight percent composition in blend in order of Diblock/Nylon-6/PDMS.

b) Peak melting temperature

c) Corrected for rubber content: $\Delta H_f = \Delta H_{obs}/W_N$; $\rho_N = (1-W_S)/(1/\rho_{obs} - W_S/\rho_S)$; N=nylon-6, S=siloxane, W_i=weight fraction i, $_{obs}$ = observed values

d) Weight fraction crystallinity via DSC: $\chi_C = \Delta H_f/\Delta H_u$; ΔH_u=45.4 cal/g. [34]

e) Crystallinity content (volume fraction) via density col. measurements: ρ_c = 1.23 g cm^{-3} [35]; ρ_a = 1.09 g cm^{-3} [36]; $\psi_C = (\rho_N - \rho_a)/(\rho_c - \rho_a)$

f) Multiple peaks on DSC thermogram

g) Compression molded in Carver lab press between two quartz glass plates with teflon spacers

homopolyamide-6, the solution cast copolymers possessed very high crystallinity regardless of the exact annealing temperature as compared to the melt annealed material. All of the melt annealed films were cooled at a moderate rate (i.e. ca. 30–40 minutes cool time from 250°C to room temperature) and probably crystallized over a range of temperatures. The higher viscosity and moderate cooling rate account for the lower heat of fusion of these copolymers/blends which are seen to be very tough materials as discussed in Chapter IX. All samples contained ca. 3 %w moisture when analyzed.

2. Density Measurements

Density measurements were made in a gradient column of carbon tetrachloride (CCl_4) and toluene which spanned densities from 1.0 – 1.2 g cm^{-3}. Density measurements are shown in the last two columns of Table 7-2 for a select few samples. Consistent trends are seen in that the melt annealed copolymers have lower densities than the same material cast from TFEtOH as corroborated by DSC. The calculation of volume percent crystallinity, ψ_c is also just as ambiguous as the calculation of the weight fraction crystallinity from a single heat of fusion because the value for the crystal density, ρ_c depends on what crystal forms are present and their composition. Nonetheless, the calculation is straightforward assuming all α-form and included in the last column for completeness but not for rigorous comparison; i.e. direct comparison between columns headed by ψ_c and χ_c is not rigorous whereas intra-column comparison can be valuable.

It is rather interesting to note the exceptionally high density of the USMSN(15/44) cast and annealed at 100°C as compared to the other

copolymers or homopolyamide-6. This is unexpected because this material, as will be explained in the next chapter, undoubtedly phase separates prior to crystallization when cast from solution and yet is still able to attain a very high degree of crystallinity. This must occur in the interstitial regions occupied by the nylon-6 "corona" chains where the additional constraints due to joint and block localization, perturbations beyond random coil conformation, etc. (all as compared to a homogeneous solution) would be expected to cause a more nonequilibrium crystal structure with more crystal imperfection. Yet clearly, this is not the case in light of the very high density of this material. The nylon-6 block chains evidently are able to fold into well organized domains which possess higher crystallinity than any other material studied in this research. This is a very striking conclusion and will be discussed further in Chapter VIII when the WAXS diffractograms of these materials are studied.

b. Crystallization Kinetics of Nylon-6 and Copolymers

1. Homopolyamide-6

Crystallization kinetics of nylon-6 have been studied by many investigators with varied results which undoubtedly is due to the variance in experimental techniques, polymer molecular weight and structure (degree of branching, etc), moisture content and estimated parameters used in the data analyses. These various experiments will be described briefly followed by discussion of kinetic results obtained on the crystallization of nylon-6 from this thesis work via DSC.

Different nucleation models have been proposed in addition to the classical theory detailed in Appendix 1. A two-dimensional disk-shaped

nucleus by Burnett and McDevit [13] yielded only one surface free energy (actually this would be an end interfacial energy for the known chain folded morphology). Koutsky et.al. [14] conducted droplet experiments to measure athermal homogeneous nucleation but this study had serious drawbacks because isothermal crystallization equations were used in conjunction with slow cooling experiments. It was tacitly assumed by Koutsky, et.al. that homogeneous and isothermal catastrophic nucleation occurred upon cooling. Existing evidence shows that their experimental cover slip oil can heterogeneously initiate nucleation and that nylon-6 crystal growth studies in bulk at T_c = 77°C do not show the onset of myriad crystallization indicative of homogeneous nucleation.

The variety of crystallization results in the literature for nylon-6 is summarized in Table 7-3 which gives the various parameters used or determined by the different investigators. Several of the studies used optical birefringence for growth rate determination in constant temperature baths. As Inoue [15] showed, this can lead to gradients in the sample of 2-3°C which can significantly alter the results. Several investigators [15,16] showed that the crystallization rate was independent of melt temperature when the latter exceeded 250 – 255°C. Consequently, the growth data of Burnett and McDevit [13] may be overestimated due to self-nucleation since they melted nylon-6 at 300°C for only 30 seconds before cooling to T_c.

Magill [16-18] has done the most intensive investigation into crystallization behavior of nylon-6 via hot stage optical microscopy. Using thin film techniques, Magill concluded that below 190°C, nylon-6 nucleated athermally and heterogeneously with linear fit to the Avrami

Table 7-3

Literature/Experimental Summary on Nylon-6

Crystallization Kinetics

Author(s)	T_m^o(C)	n	$G\|_{186°C}$ (μm/min)	b_o(Å)	$\sigma\sigma_e$(ergs^2/cm^4)
Magill (1962)	226-27	3<190°C 4>190°C	~10-20	4.2	480 (465-520)
Inoue (1961)	-	2.5<210°C 4>210°C	-	-	-
Burnett & McDevit (1957)	232	-	~30	4.5	σ_s = 18.1; no σ_e
Martuscelli (1985)	233	2.8-3.1 (191-203°C)	-	4.25	σ_e = 54 ergs/cm^2
Veith (1989)	230	3<190°C 4>190°C		4.2	600 σ_e = 60 ergs/cm^2
(USMSN diblock		2→3			850)

isotherms and that the material obeyed the proper $1/T_c\Delta T$ dependence. Presumably, extrapolation to three-dimensional, bulk systems is applicable although not certain. This is an advantage of studying crystallization kinetics via DSC; the thickness of the sample is ca. ~(0) 0.1 mm which is greater than the tens of microns normally employed in hot stage microscopy and more closely approximates bulk conditions.

Experimental

Each trial used fresh, dry, extracted hydrolytic polymer and was melted at 250°C for 30 minutes to destroy previous crystallites. The samples were cooled rapidly at 320°C/min in the DSC furnace to the desired isothermal crystallization temperature, T_c. Due to the finite instrument adjustment time, the lowest temperature that could be reached by the instrument before appreciable crystallization had occurred was 180°C. Temperatures below this caused rapid crystallization and the exotherm was not able to be satisfactorily recorded in full. Five different temperatures were used from 180°C to 192°C as shown in Figure 7-3 for extracted, dry (~0.1% H_2O) Allied nylon-6 as received. The isotherms from 180°C to 192°C in three degree intervals follow Avrami kinetics rather well and give slopes and intercepts by linear regression as shown below in Table 7-4. These data suggest athermal, heterogeneous nucleation with an Avrami exponent approximately 3.0 for temperatures below ~190°C. Near this temperature, a rather striking change in transition of the Avrami exponent from ca. 3 to slightly greater than 4 which suggests (but is not wholly conclusive) a change from athermal heterogeneous to thermal homogeneous nucleation. This duplicates Magill's [17] results exactly as he also observed a change in Avrami slope from n=3 to n=4 at 190°C.

From these data, the plot according to equation (7-4) yields the surface free energy product as proportional to the slope and the nucleation density as proportional to the intercept assuming the primary nucleation density, which equals $(4\pi/3)(\rho_c/\rho_a\omega_c^{\infty})NG_o$ where $G_o = n_s b_o(kT/h)$, is constant in time and varies weakly as a function of

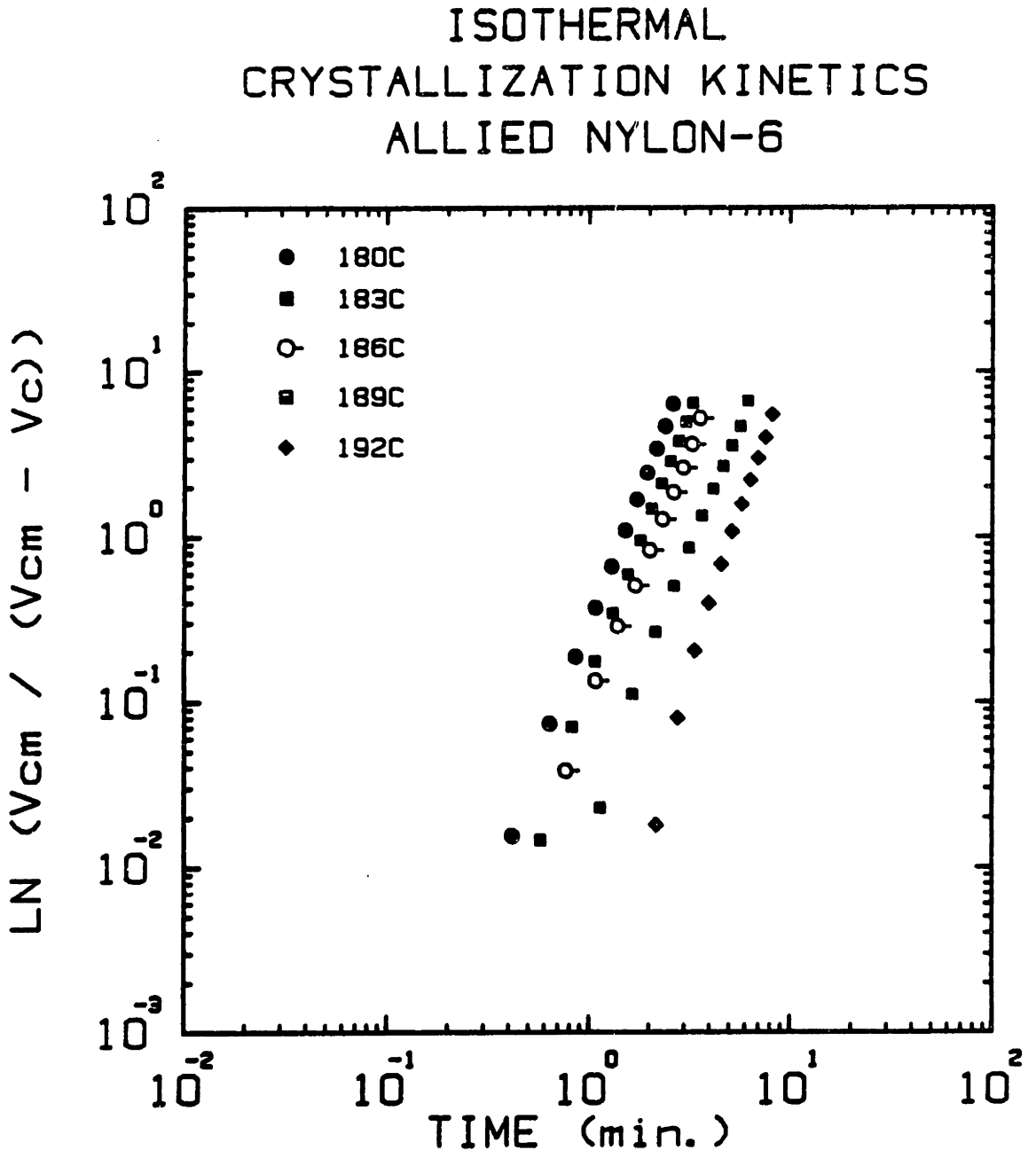

Figure 7-3 Avrami kinetics for hydrolytic, dry nylon-6 melted at 250°C for 30 minutes followed by isothermal crystallization at T_c = 180–192°C.

Table 7-4

Isothermal Crystallization Results for Nylon-6

T_c (°C)	$n \pm \sigma_n$	$K \pm \sigma_K$ $(min)^{-n}$
180	3.2±0.03	$2.827 \times 10^{-1} \pm 5.15 \times 10^{-3}$
183	3.4±0.06	$1.213 \times 10^{-1} \pm 5.49 \times 10^{-3}$
186	3.1±0.04	$9.489 \times 10^{-2} \pm 3.34 \times 10^{-3}$
189	3.2±0.08	$1.930 \times 10^{-2} \pm 1.92 \times 10^{-3}$
192	4.1±0.15	$1.080 \times 10^{-3} \pm 2.56 \times 10^{-4}$

Isothermal Crystallization Results for USMSN(15/44)

180	2.1	6.1024
183	2.2	2.5328
186	2.5	0.4379
189	3.1	0.1183

temperature. Note that ρ_c = the crystal density, ρ_a = the amorphous density, ω_c^∞ = the maximum crystalline weight fraction, N = the nuclei density, n_S = number of substrate steps and b_o = the thickness of the nucleus on the substrate at each growth step.

$$n^{-1} \ln K + \frac{\Delta F_\eta}{kT} = \ln \left[[(4\pi/3)(\rho_c/\rho_a \omega_c^\infty) n_S N]^{-n} G_o \right] - \frac{4 b_o \sigma \sigma_e}{\Delta H_f \rho_c k} \frac{T_m^o}{T_c \Delta T} \quad (7\text{-}4)$$

Note that this equation is written for the actual value of the slope of the Avrami plots shown in Figure 7-3 as suggested by Mandelkern [19] instead of the exact value of 3 for heterogeneous, athermal nucleation. Using the most common value in the literature for T_m^o of 230°C, these data yield the free energy product of 600 ergs^2 cm^{-4} which is also listed in the last row of Table 7-3, from the slope of the plot in Figure 7-4 Efforts to calculate T_m^o by extrapolation of the melting points for the various isothermal crystallization trials was not successful because the range of T_c was not sufficient to cause a significant variation in the observed T_m obtained immediately after crystallization. In addition, the multiple peaks made it difficult to assign one particular melting temperature to the sample due to its polymorphism.

Figure 7-4 expresses the temperature dependence of the bulk crystallization rate constant. Use of the Thomas-Staveley [20] relationship (σ=0.1$\Delta H_f \rho_c b_o$) gives the side surface free energy of 10 ergs cm^{-2} which then yields an end surface free energy of 60 ergs cm^{-2}. The transport term was calculated using the conventional WLF equation with constants derived by Boon, et.al. [21] instead of the universal constants; Boon, et.al. showed these new constants to give a much better fit to OLM growth data for nylon-6. See Appendix 1 for details. Note that the free energy product and end surface free energy agree nicely with the results of Martuscelli and Magill and provide a good basis of comparison for the data from copolymer crystallization kinetics. Results of the second curve of the diblock will be discussed next.

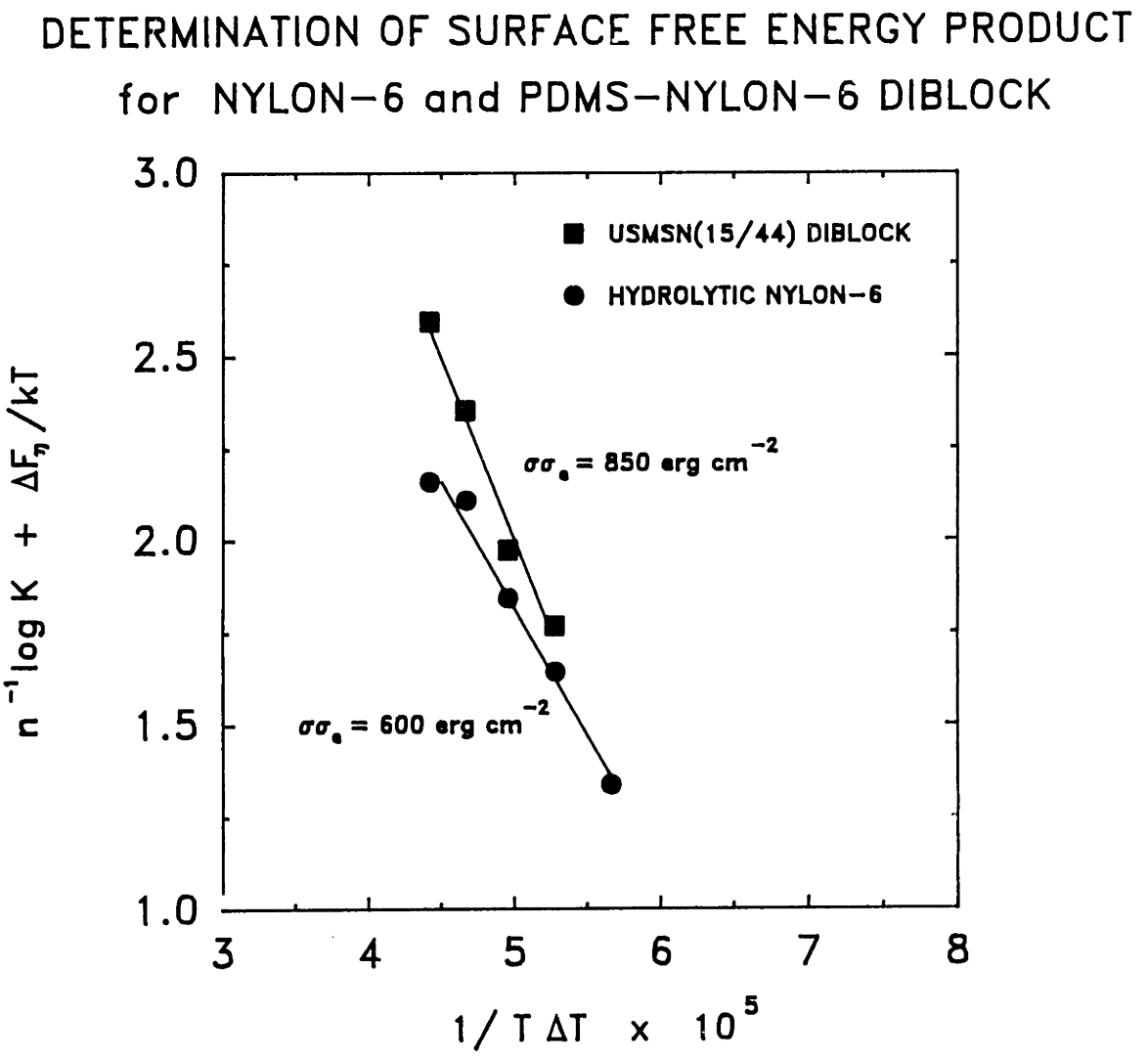

Figure 7-4 Determination of the surface free energy product for heterogeneous nucleation following Avrami kinetics for hydrolytic homopolyamide-6 and diblock copolymer USMSN(15/44)

2. PDMS-Nylon-6 Copolymer Crystallization Data

Similar trials were conducted for diblock copolymer USMSN(15/44) at the same temperatures 180° – 189°C; unfortunately the trial at T_c = 192°C had to be discarded. The results of the Avrami kinetics for the block copolymer are shown in Figure 7-5 for the four temperatures. Less linearity is evident as compared to the homopolymer; this could be due to nonisothermal conditions at the lower temperatures (180 and 183°C) because the higher nucleation density (ca. 10^5 times greater for the diblock versus the homopolymer) initiated crystallization before the temperature had truly reached the desired T_c. At the higher two temperatures (186° and 189°C), nucleation and growth begin essentially after the crystallization temperature is reached and true isothermal conditions are achieved; hence the data are more linear (regression coefficients r= 0.98, 0.99, respectively).

Alternatively, the change in slope may be mechanistic and has been seen in other block copolymer systems [8]. The data from this thesis, displayed in the bottom panel of Table 7-4, show that the Avrami exponent is lower for the diblock than the homopolymer as would be expected. This decrease is manifested by the curvature towards lower slope at longer crystallization times which indicates either a retardation in the crystallization rate possibly due to the constraints of the copolymer chains anchored into the mesophase structure or due to crystal perfection which is known to decrease n [22]. The former results because phase separation preceded crystallization and "fixed" the crystalline blocks in space prior to nucleation and growth of the polyamide-6. As the isothermal crystallization temperature is raised, the Avrami exponent

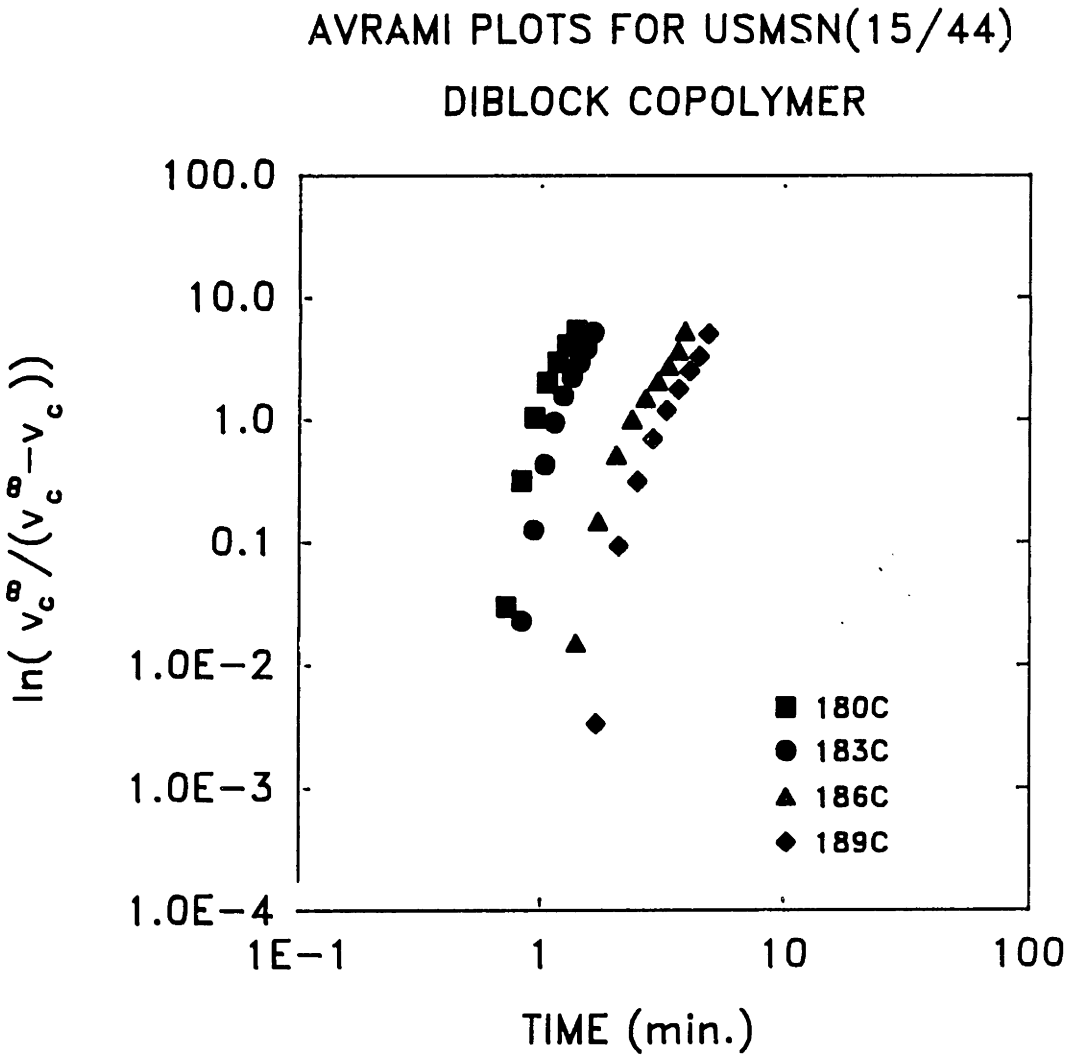

Figure 7-5 Avrami crystallization kinetics for the USMSN(15/44) diblock copolymer; abscissa represents real time but analyses for K, n use effective time for crystallization, i.e. $(t-\tau)$.

increases from a value of ca. 2 at T_c = 180, 183°C to 2.5 at 186°C up to a value of ca. 3 at 189°C in similar fashion to the rise seen for homopolyamide-6 although at lower absolute values.

Also shown in Figure 7-4 is the plot of the rate constant and transport barrier height versus the reciprocal product of supercooling and isothermal crystallization temperature for the USMSN(15/44) diblock. This gives a higher surface free energy product, $\sigma\sigma_e$ of 850 ergs^2 cm^{-4} which yields a σ_e of ca. 85 ergs cm^{-2}, substantially higher than the σ_e of homopolyamide-6. Thus, the work of chain folding is greater for the diblock than the homopolymer in contrast to the findings of Drzewinski [7] for i-PP-PB diblock copolymers.

Upon examination of the intercepts of the plots in Figure 7-4, it is seen that the nucleation rate is ca. $5x10^4$ greater for the diblock versus the homopolymer which supports hypotheses that the phase separated domains act as nucleation sites. However, the growth rates for the diblock are necessarily less than those of the homopolymer due to the higher $\sigma\sigma_e$. The growth rate and the nucleation density combine to yield a kinetic constant, K for the diblock which is larger than for the homopolymer at all temperatures studied. Thus, despite a slower growth rate for the diblock, its greater nucleation density compensates to cause a decrease in the crystallization half times versus homopolymer and a faster overall completion of crystallization at a given T_c.

B. VISCOELASTIC PROPERTIES

All polymers exhibit molecular relaxations in the anelastic spectrum at certain temperatures and frequencies. The Rheovibron^R viscoelastometer studies these relaxations by applying a sinusoidally varying strain to a small strip of material and measures the resultant force with a tensiometer. The strain wave lags the stress wave response by the ratio known as tan δ. This can be represented mathematically as the phase angle between the two wavefront vectors and the ratio of the loss modulus to storage modulus is equivalent to the tangent of the phase angle or tan δ.

The usual grip corrections were made for the Rheovibron DDV-II-C and the loss and storage moduli and tan δ were calculated by computer. The temperature range was from -150 to 210°C at 11 Hz with a manual heating rate of 1°C/min. The sample chamber was purged with dry nitrogen to avoid condensation and moisture absorption.

Transitions or "lossy" relaxations occur at local maxima of tan δ as a function of temperature at constant frequency. The relaxations of spin cast, melt annealed hydrolytic nylon-6 conditioned to ca. 60% R.H. versus the dry sample are shown in Figure 7-6. These samples have heats of fusion of 9.4 cal/g and 8.1 cal/g for the wet and dry Allied nylon-6, respectively. For the wet (~3.3% H_2O) melt annealed, spin cast nylon-6, the α-relaxation or glass transition is reduced to approximately 26°C due to plasticization by moisture. Recall that this is the same nylon-6 sample that gave a midpoint T_g by DSC of 30°C. Samples with this moisture content deformed at room temperature are highly viscoelastic and sensitive to small fluctuations in temperature which can cause signifi-

cant changes in modulus, yield stress, etc. Compare the dry Allied nylon-6 melt annealed spectrum in Figure 7-6 (upper curve) to the spectrum of the same material conditioned to 3.3% H_2O. The dry nylon-6 T_g has now risen to 85°C with only 0.02% wt. H_2O as determined by Karl Fisher titrometry. See Table 7-5 for moisture content determination of several nylon-6 samples. The α transition in the dry sample has narrowed considerably which correlates with decreased hydrogen bonding because fewer water molecules are available to plasticize the polymer and facilitate additional hydrogen bond formation. This is analogous to the observation of a narrower T_g peak for nylon-12 versus nylon-6 where the latter has twice the number of hydrogen bonds [23].

Table 7-5

Moisture Content in Nylon-6†*

Annealing Temp (C)	Moisture Condition	% H_2O# Content
250	Dry	0.02
100	Dry	0.19
100	42 % R.H.	1.68
100	62 % R.H.	3.33

† Spin cast, hydrolytic nylon-6.

* All wet samples conditioned over saturated salt solutions at T = 23°C.

\# Absolute moisture content (wt %) determined via Karl Fisher titrometry.

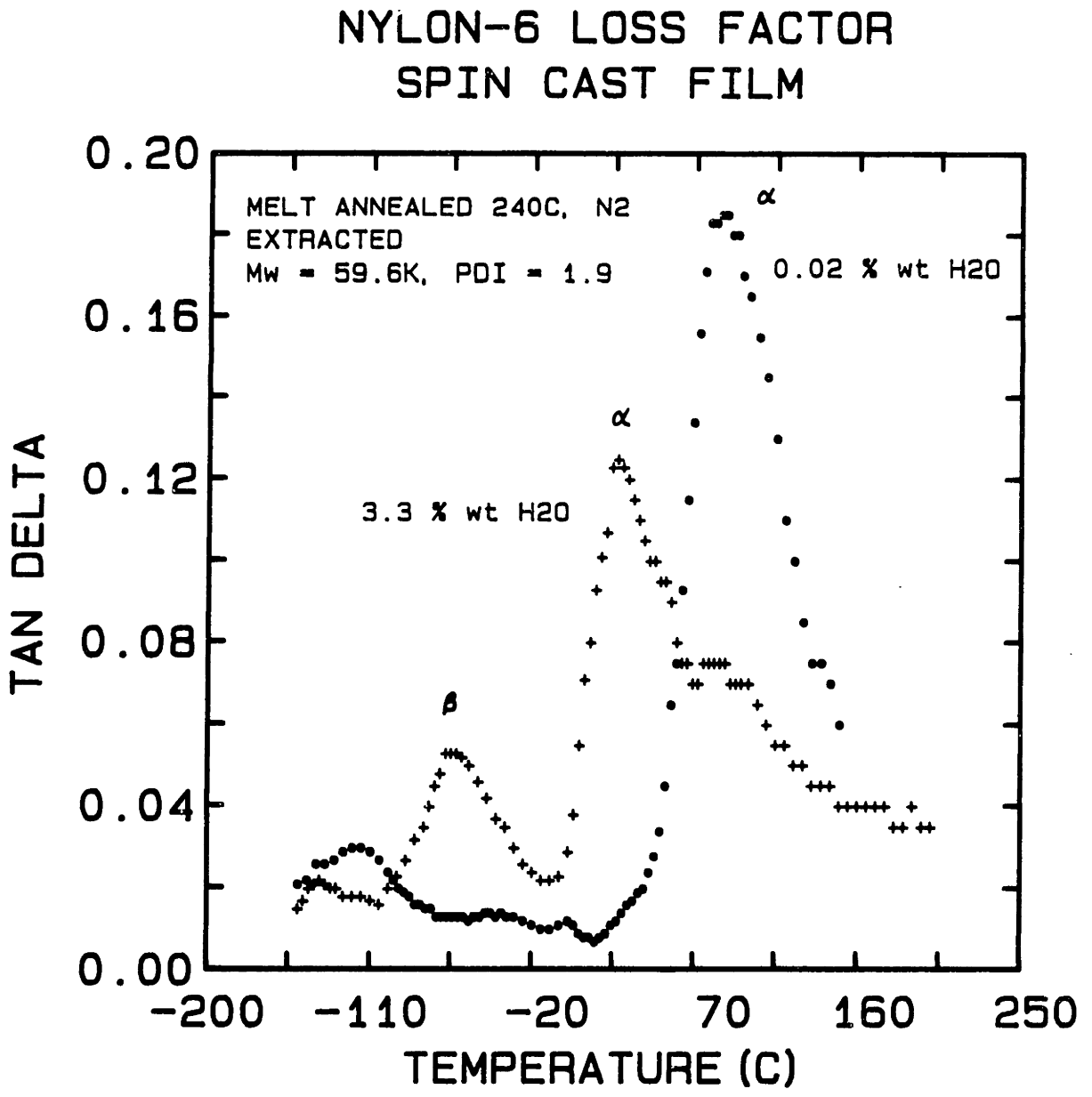

Figure 7-6 Comparison of anelastic relaxations between wet and dry hydrolytic nylon-6.

The secondary or β-relaxation at -65°C usually is characteristic of side group motion as in ester mobility of PMMA [24] for example. In the case of nylon-6, however, Illers [25] believes the origin of this relaxation to be the motion of hydrosolubles hydrogen-bonded to the main chain. Comparison of melt annealed, spin cast Allied nylon-6 spectrum in Figure 7-6, dry versus wet in the range of -100 to +10°C, shows the disappearance of the β-relaxation for the dried sample in agreement with Iller's postulate. This result is not obtained by Garbuglio, et al. [26] who found only a slight shifting of equal intensity β peaks for supposedly dry and wet moldings. This disparity in findings is not real because Garbuglio et.al. "dried" their moldings to a hydrosoluble content of only 1.5 %w which is not significantly different from their "wet" sample at 8.8 %w. This is because the α-relaxation (T_g) is not directly proportional to water content over the entire range; it drops drastically from 95°C to 71°C with the addition of only 1.2% w H_2O [27] and asymptotically levels off above ~ 2.0 %w moisture. Thus, a "dry" state of 1.5 %w H_2O is not anhydrous enough to suppress the β peak.

A great deal of controversy has surrounded the β relaxation and its relation to toughness. Some authors [28-31] have tried to correlate the strength of this secondary relaxation with the room temperature impact strength in such polymers as impact polystyrene, poly(trifluorochloroethylene), polypropylene (PP) and polycarbonate (PC). Others, such as Vincent [32] have cautioned against such broad generalizations despite some cause-effect data.

Boyer [33] has summarized the existing literature and surveyed some eight polymers including PVC, PE and PTFE semicrystalline polymers. Of

those that craze, a general speculative trend was that the β-process provided the molecular motion responsible for cold drawing and tuft formation. The semicrystalline polymers are considerably more complex due to multiple interactions of the various phases and PE and PTFE remain tough below any secondary or lower transition. Poly(vinyl chloride) shows a distinct positive correlation between impact strength and height (or area) of the β-peak which was decreased by addition of plasticizer [34]. It is unknown whether the plasticizer decreased the hydrostatic tension required to initiate crazing or suppressed the accepted crankshaft motion for the low temperature transition but this semicrystalline polymer demonstrates the correlation between intensity of the β peak in the dynamic mechanical spectrum and prediction of mechanical properties. Unfortunately, this does not confirm that the cause for decreased toughness is the drop in the β peak. Some materials, especially those that show crazing under deformation at room temperature, show better correlation of impact strength with β-relaxation. Despite the possibly fortuitous successes of PVC and PMMA for example, not enough molecular information can be obtained through only dynamic mechanical measurements to unquestionably claim a one-to-one correlation between β-relaxation intensity and impact strength for all polymers.

The low temperature relaxation or γ-transition is more pronounced for the dry (0.02% wt H_2O) material and occurs at ~ -115°C as compared to a more flattened maximum at ~ -140°C for the wet (3.3% wt H_2O) sample. This low-temperature transition is attributed to in-chain motion of four or more methylene groups [35]. This idea lead to the crankshaft mechanisms of Shatzki [36] (rotation about every 7^{th} bond) and Boyer [37]

(rotation about every 5th bond) which have been proposed [38,39] for the γ-transition in polyamides.

A surprising result of the dynamic mechanical experiments on spin cast, melt annealed nylon-6 is shown in Figure 7-7. Two Monsanto RIM, moisture conditioned samples are represented, one undeformed and the other from the gauge section of a deformed tensile specimen. The second sample was deformed, wet (3.3% H_2O) at a $\dot{\varepsilon} = 1.3 \times 10^{-4}$ s^{-1}, 23°C and showed a load drop and yield point at ~ 66 MPa with a final strain to fracture of 550%. Its stress-strain curve will be discussed in Chapter IX. The lower temperature relaxations remain unchanged as there is no difference in moisture content. The α transition for the deformed sample has risen to approximately 55°C which possibly can be interpreted as an orientation within the amorphous phase increasing the amount of H-bonding and decreasing the plasticization effect of the water.

A second well defined α'-transition occurs for this deformed material at ca. 118°C versus a "shoulder" transition for the undeformed material. The origin of this α' peak is probably associated with the orientation of the lamellae with respect to the direction of applied stress. Takayanagi [40] studied crystal mats of polyethylene (grown from dilute solution with the chain axes folded normal to the mat plane) and found an absence of an α'-transition for the mats because the normal chain axes oriented the applied stress within the lamellae. Apparently, this prevented the α' relaxation from occurring.

McCrum and Morris [41] also studied PE and similarly concluded that the α' relaxation corresponded to slip at the lamellae boundary. As a result of the deformation, the second nylon-6 sample must have a

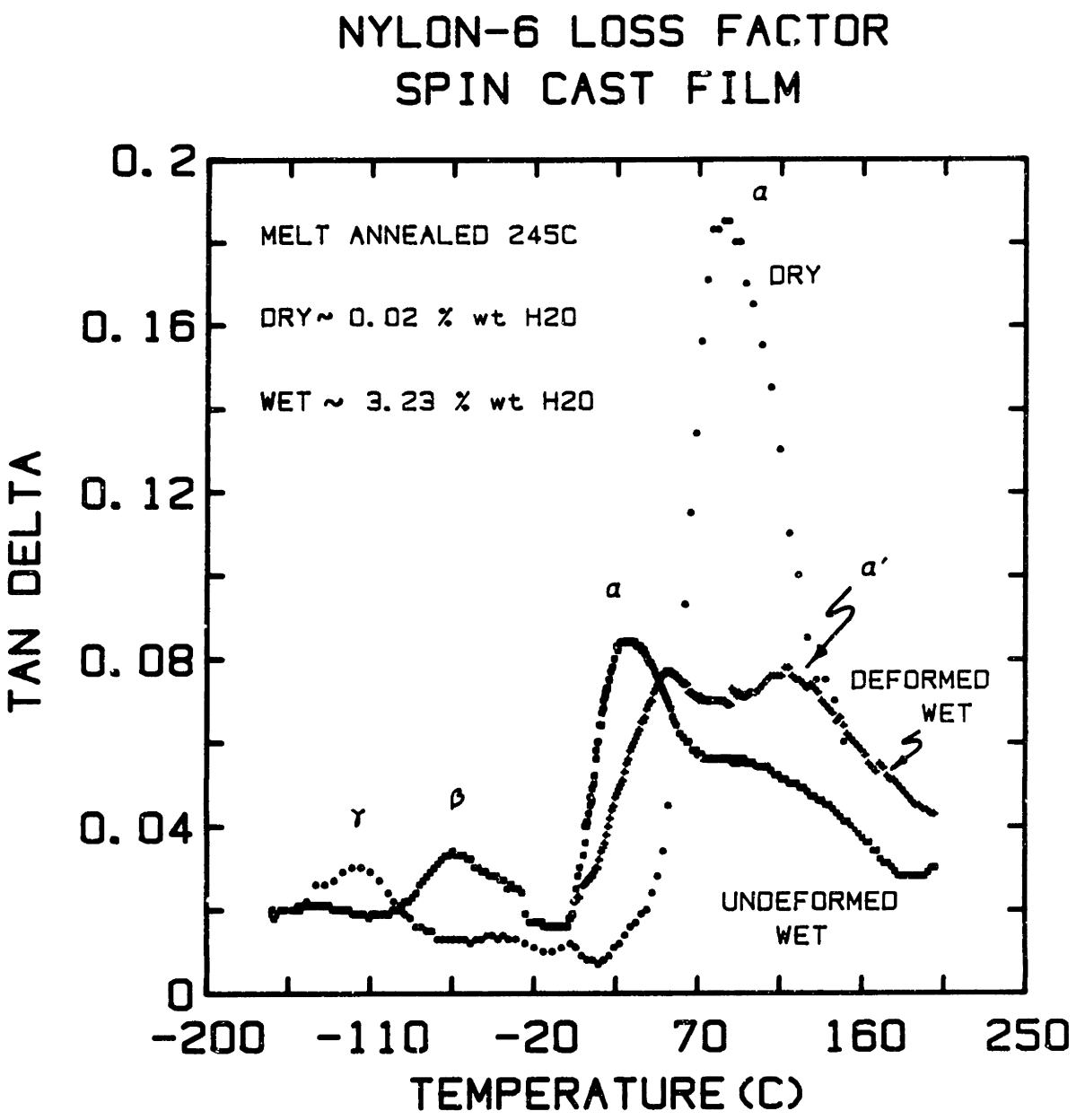

Figure 7-7 Dynamic mechanical spectroscopy on the gauge section of tensile specimen of anionic nylon-6 as compared to undeformed material.

preferred orientation (possibly fibrillated lamellae or a microfibril texture) which is more conducive to interlamellar shear than bulk samples. These oriented structures may have a greater fraction of slip planes oriented parallel to the oscillatory axis in the Rheovibron where interlamellar shear is more pronounced giving rise to the additional α' relaxation.

C. MOLECULAR WEIGHT ANALYSIS

It is desirous to have a molecular weight analysis that is accurate, reliable and rapid. This expedites routine analysis and facilitates on-line sampling during synthesis for good molecular weight control as was necessary with the siloxane polymerizations, particularly PTFPMS. Although membrane osmometry, light scattering (LS) and intrinsic viscosity (IV) are accurate techniques, they are considerably more time-consuming and give only one molecular weight average each. The advantage of high performance size exclusion chromatography (HPSEC) in addition to the aforementioned characteristics, is its ability to provide not only the three molecular weight averages (number, weight and viscosity) but information on the entire molecular weight distribution, if calibrated properly. Consequently, investigation into a functional HPSEC system for the siloxanes and nylon-6 was undertaken.

1. Nylon-6

During the course of this thesis work, a new size exclusion chromatography (SEC) system for nylon-6 was developed which utilized the universal calibration peak retention of narrow dispersity poly(methyl methacrylate) (PMMA) in 2,2,2-trifluoroethanol (TFEtOH). The SEC system,

operated at room temperature with silanized silica columns, obviated the solvent incompatibility of TFEtOH with styrene-gel packings and gave simple and reproducible chromatograms of polyamide-6. The method provided molecular weight accuracy within ±10% without correction for dispersion.

To support the universal calibration for nylon-6, it was necessary to investigate the macromolecular hydrodynamics of PMMA in TFEtOH; results are represented well by the Stockmayer-Fixman viscosity-molecular weight theory. Poly(methylmethacrylate) in TFEtOH exhibits a Mark--Houwink exponent of 0.88 and a polymer-solvent interaction parameter, χ_{12}, equal to 0.38. The details of these polymer-solvent characterization experiments are presented in Appendix 3.

a. Review of Existing Nylon-6 SEC Systems

The same physico-chemical properties that give nylon-6 its exceptional strength, toughness and solvent resistance complicate the analysis of its molecular weight distribution via size exclusion chromatography (SEC). The limited number of suitable solvents for the mobile phase in the SEC of polyamides in general, has slowed the development of this analytical tool for these polymers. The current state of solvent selection for the chromatography of polyamide-6 can be divided into three main categories:

1) High temperature solvents, e.g. m-cresol,

2) Common solvents (e.g. THF, CH_2Cl_2, etc) with polyamides modified by trifluoroacetylation

3) Room temperature specialty solvents such as the fluorinated

alcohols; e.g. 2,2,2-trifluoroethanol (TFEtOH) and hexafluoro-2-isopropanol (HFIP).

These solvents present a wide range of compatibility differences with the two major types of column packing currently used (styrene-gels and modified silicas) as well as calibration difficulties since the commonly used polystyrene standards are not soluble in the fluorinated alcohols. This work utilizes the availability of narrow dispersity poly(methyl methacrylate) (PMMA) standards which are soluble in TFEtOH and the universal calibration concept [42] to develop an accurate, reproducible SEC system for determining the molecular weight distribution (MWD) of nylon-6.

High Temperature Solvents

Size exclusion chromatography of polyamides generally has been accomplished using m-cresol at temperatures of 100-130°C with μ-Styragel^R columns [43-45]. Despite the elevated temperature, column dispersion resulting in broadened chromatograms was still significant and distillation of the m-cresol to remove water and acid contaminants did not inhibit its tendency to degrade in the chromatograph [43]. This acidity at 130°C causes transamidation and a slow degradation of the MW as measured by viscosity [46] similar to known reactions with the polyesters [47]. In addition, high temperature increases the risk of oxidative degradation of the polymer as well as risk and inconvenience to the SEC operators. Despite these disadvantages, the m-cresol/polyamide-6 system is still in use for lack of a better solvent (e.g. [48]).

Benzyl alcohol (BzOH) has not shown much promise either. Pastuska and Just used BzOH with silica columns [49] but observed strong solvent-

packing (hydrogen-bonding) interactions and Marot and Lesec developed calibration problems with polystyrene (PS) standards and μ-Styragel^R columns in BzOH at 130°C [50]. Other solvents such as hexamethylphosphoramide (HMPA) have been used in the SEC of polyamides at 105°C [51] and at 85°C [52]. In the former case, no details of molecular weight accuracy were given; the latter case used PS standards and a Q correction factor to determine polyamide MW but no comparison with independent MW measurements was mentioned. Goedhart et. al. [53] suffered frequent gelation of polyamides in HMPA causing plugged columns and fouled tubing. These operating problems in addition to the suspected carcinogenicity [50] of HMPA are major disadvantages in its use. As with any of these high temperature solvents, the possibility of polymer degradation due to oxidation must not be overlooked.

Mixed solvent systems such as equivolume chlorobenzene and m-cresol [46] were tried to reduce viscosity and temperature but still showed solute adsorption effects which required the addition of benzoic acid (0.25% w/w). Other diluents to m-cresol such as chloroform or dichloromethane have been proposed [53] but these like other mixed solvent systems, suffer from the main drawback of compositional changes affecting the hydrodynamic volume of the solute, the baseline stability in the refractometer and/or solvent gradients from the main flow field to the inside of the pores. These disadvantages along with the maintenance concerns make mixed solvents less desirable over single solvent systems.

Common Solvents with Acetylated Polyamide-6

An alternate method to the use of polar, high temperature solvents is to acetylate the amide group with trifluoroacetic anhydride which

destroys the crystallinity of the polyamide and facilitates dissolution in common solvents. This technique was developed originally by Schuttenberg and Schulz [54,55] and later extended by Biagini et.al. [56] and Weisskopf [57,58]. All investigators of N-trifluoroacetylated polyamides claim nearly quantitative conversion with no polymer degradation as determined by IR, viscometry and titration. However, Biagini et.al. [56] cite significant differences in the MWD of polyamide-6 depending upon the degree of acetylation. Also, if the modified polyamide absorbs moisture via contact with a high humidity environment or wet solvents, hydrolysis occurs leading to an incorrect MWD via SEC. This necessitates rigorous drying of solvents and exclusion of atmospheric moisture from the polymer.

In some cases, the acetylated polyamides did not seem to follow the universal calibration (UC) concept; e.g. PS standards in $CHCl_3$ [56]. Weisskopf [58] achieved better MW accuracy from broad dispersity acetylated polyamides standardized by light scattering and osmometry via the method of Weiss and Cohn-Ginsberg [59]. Here, the experimental chromatogram was fitted to the Schulz-Zimm [60,61] distribution and peak retention volume was equated to the known $\bar{M}_w$ of the broad standard [62]. Weisskopf attributed the decrease in accuracy of the universal calibration to polar interactions of the $-COCF_3$ side groups and consequently used his "effective" calibration curve from the polydisperse samples. However, it is generally accepted that calibration with broad standards is useful only when the polydispersity of the sample approximates that of the standards due to the "effective" nature of the calibration [63].

Fluorinated Alcohols

The fluoroalcohols are attractive SEC solvents because of their ability to dissolve most polyamides at room temperature, their low to moderate viscosity and good spectral properties (low UV cutoff and low refractive index increment). Costa and Russo [64] have discussed several fluoroalcohols including trifluoroethanol, HFIP and 2,2,3,4,4,4-hexafluorobutanol (HFB) as potential solvents for polyamides. The HFB was synthesized and characterized with nylon-6 with respect to the Mark-Houwink constants which show it to be a good solvent ($K'=4.2x10^{-4}$ dl/g, a=0.76). It has a lower volatility than the other two fluoroalcohols but no data as a SEC solvent were presented.

Hexafluoroisopropanol has been used as a SEC solvent [65,53] but required the addition of sodium trifluoroacetate to obtain a unimodal, Gaussian shaped peak for nylon-6,6. Without this salt, the chromatogram was bimodal which was attributed by Drott [65] to the polyelectrolyte effect. This phenomenon occurs in low pK_a solutions where protonation of the amide nitrogen yields polymeric ammonium ions causing intramolecular repulsion and expansion of the chain. The additive salt increases the ionic strength of the solution electrically balancing the charged chain by replenishing the anions near the backbone. These additional ions suppress and counteract the osmotic forces which drive counterions away from the charged chain. This results in a return to normal chain conformation which leads to predictable and reproducible fractionation and elimination of the bimodality.

However, HFIP is expensive (>$1000/l) which requires solvent reclamation and it should not be used with μ-Styragel^R because it does

not swell the polystyrene-gel packing sufficiently as evidenced by a column efficiency of only 1400 plates/(4)-column set [65]. The high cost of this solvent and poor performance with μ-Styragel^R columns are the main reasons why we consider TFEtOH a better SEC mobile phase for polyamide-6.

Since it was recognized early that PMMA is soluble in TFEtOH, Provder et. al. [66] developed a hydrodynamic volume calibration technique based on broad dispersity PMMA. This involved a series of transformations from PS standards in THF to broad MWD PMMA in TFEtOH based on the concept of equivalent hydrodynamic volumes (PS/THF to PMMA/THF to PMMA/TFEtOH). This procedure required clarification [67] because of its complexity, the need for more than one set of (K', a) values to describe the hydrodynamics of the various PMMA fractions and the fact that TFEtOH was used with Styragel^R columns which results in false peaks and broadened chromatograms as reported by Dudley [43].

Matzner, et. al. [68] also have used μ-Styragel^R columns (10^5 - 250 Å) with TFEtOH but reported no "false-peak" chromatograms. They did not show any calibration and their results via light scattering in TFEtOH for the molecular weights of both hydrolytic and anionic nylon-6 did not agree with their chromatogram peak retention volumes. Matzner's single peak chromatograms are contrary to Dudley's work and results obtained in our laboratory where multimodal, false peaks are seen for nylon-6 with μ-Styragel^R columns (10^4, 10^3, 500 Å) in TFEtOH.

In this thesis work, the aforementioned complications of calibration in TFEtOH have been obviated by using narrow MWD PMMA standards with the universal calibration to develop a new, simple and reproducible SEC

system for nylon-6. The solution hydrodynamics of the PMMA fractions in TFEtOH at 30°C have been measured and are used to construct the nylon-6 calibration using literature values for the Mark-Houwink parameters of hydrolytic nylon-6 in TFEtOH. See Appendix 3 for details. When combined with silanized silica columns which eliminate the false, multimodal peaks and show much better resolution than Styragel^{R} in TFEtOH, simple and reproducible analysis of nylon-6 with molecular weight accuracy within 10% (i.e. less than 10% error) is achieved.

b. Experimental Results and Dioscussion

Size Exclusion Chromatography

The nylon-6 HPSEC system was a homemade unit consisting of the following equipment:

- Altec 100A dual action positive displacement metering pump
- (2) DuPont Zorbax bimodal (60 Å, 1000 Å) silanized silica columns
- Waters Lambda Max 480 Variable Wavelength UV Spectrophotometer
- Waters R401 differential refractometer
- Rheodyne Injector, Model #7125

The mobile phase was 2,2,2-trifluoroethanol (Aldrich, gold label 99+%) operated at a flow rate of 1.0 ml/min. at room temperature. Injection volume was 100 μl with concentrations 0.3-0.4% w/v. the solvent was dried over molecular sieves to remove traces of moisture and then degassed and filtered through 0.5 μm filters. This gave good reproducibility and baseline stability.

Narrow MWD PMMA standards were purchased from the Pressure Chemical Co. ($M \doteq 27$ kg/mole) and Polymer Standards Service, West Germany (low molecular weights, $M = 9$ kg/mole and 17 kg/mole). Polymer polydispersity

varied from 1.06 to 1.15 as reported by the manufacturer (from supplemental data such as $\bar{M}_n$, $\bar{M}_w$ and $\bar{M}_v$ as well as chromatograms supplied by Polymer Standards Service). Peak retention volumes were used and correlated to the reported peak molecular weight, M_p, which always fell between $\bar{M}_n$ and $\bar{M}_w$. The chromatography system has a theoretical plate count of ~ 13,000 and chromatograms were integrated by in-house software programs.

Viscometry

The Mark-Houwink parameters for PMMA standards in TFEtOH were determined in a Ubbelohde No. 1 viscometer immersed in an oil bath maintained at 30°C±0.1°C. With dilute solutions, the kinetic energy correction (second term) in the Newtonian fluid mechanics analysis was neglected and the ratio of flow times (t>100 sec) was used to calculate the relative viscosity. A check for excessive wall shear rates was performed by calculating the β parameter, which shows positive deviation from unity for shear thinning conditions [69]. Its low value as shown in equation (7-5) for M = 60 kg/mole, implies first Newtonian regime confirming the accuracy of flow time ratios, where $[\eta]$ = intrinsic viscosity, η_0 = solvent viscosity, M = molecular weight, γ_w = wall shear rate (sec^{-1}), T = temperature (K) and the factor of 100 converts the cgs units to dl/g.

$$\beta = \frac{100[\eta]M\eta_0|\gamma_w|}{RT} = 1.5 \times 10^{-3} \qquad (7\text{-}5)$$

Four PMMA fractions ranging in nominal molecular weight of 525 kg/mole to 27 kg/mole were prepared at concentrations of ~0.8 g/dl and slowly filtered through 0.5 μm filters. The polymer concentration after

filtration was rechecked. A minimum of three timings was recorded for each concentration followed by successive dilution with filtered solvent to extend the measurements towards infinite dilution. Intrinsic viscosity was determined by least squares regression of both the inherent and reduced viscosities as function of concentration for each fraction. Agreement of the intercepts for each regression was within ±0.5-1.0%.

The Mark-Houwink parameters for nylon-6 in TFEtOH are available from several sources in the literature [70,71,72] and are shown in Table 7-6. The agreement between these K' and a values in the first two sources is quite good considering: 1) the known variability of molecular architecture in hydrolytic polyamides as a function of polymerization temperature and concentration of chain regulator and 2) the varying extents of polymer fractionation and monomer extraction. The last sample obviously differs from the first two due to the lower molecular weight range which causes a shift towards the "free draining" molecule and a Mark-Houwink exponent of 1.0 to 1.1. The molecular weights used in our work are in the range of 18 kg/mole to 40 kg/mole and the best agreement of SEC molecular weight with other independent measurements (such as end group analysis or viscosity) is obtained with the K',a values from Mattiussi, et. al. [71].

1. Viscometry

The inherent viscosity ($\ln \eta_r/c$) and reduced viscosity (η_{sp}/c) were plotted versus concentration for each PMMA fraction as shown in Figure 7-8. The difference between the Huggins [73] and Kraemer [74] constants in each of the trials is very close to the expected value of 0.50 [75].

Table 7-6

Summary of Mark-Houwink Constants for Nylon-6/TFEtOH at 25° C

M-H Parameters				
K' (x10⁴ dl/g)	a	Type Nylon-6/T_{pzn} (C)/MW*	Technique†	Ref
4.58	0.742	H / NA / 20-100K	IV	70
5.36	0.75	H / 180-280 / 13-100K	IV,LS	71
0.97	1.0	H / 230 / 1-4K	EG	72

* H = hydrolytic nylon-6; T_{pzn} = polymerization temperature; MW = molecular weight range (in thousands); NA = not available.

† Independent technique of measuring MW: LS = light scattering; IV = intrinsic viscosity; EG = end group analysis.

The Mark-Houwink parameters for PMMA in TFEtOH are determined by the relation

$$[\eta] = K' M^a \qquad (7\text{-}6)$$

as shown in the log-log plot of Figure 7-9. The Mark-Houwink parameters from the slope and the intercept are $K' = 2.81 \times 10^{-5}$ dl/g and $a = 0.88 \pm 0.03$.

2. Universal Calibration

The universal calibration, introduced by Benoit, et al. [42] is based on separation by the macromolecular hydrodynamic radius (or volume) in size exclusion chromatography. At a given retention volume, V_R, the hydrodynamic size of a PMMA and a nylon-6 molecule is the same since this volume is proportional to the product of molecular weight and intrinsic

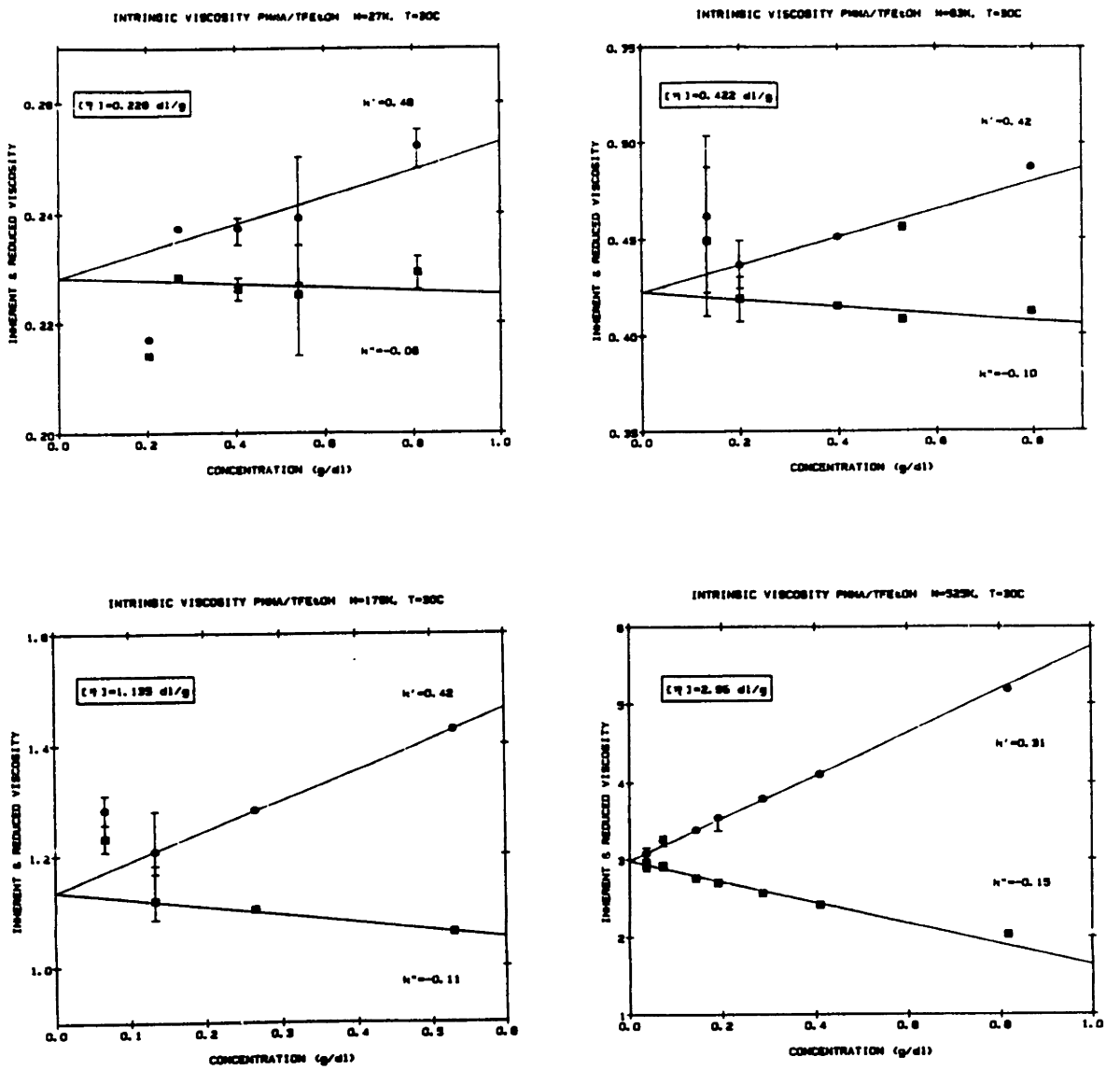

Figure 7-8 Determination of intrinsic viscosity for PMMA fractions in 2,2,2-trifluoroethanol at 30°C in a Ubbelohde No. 1 viscometer.

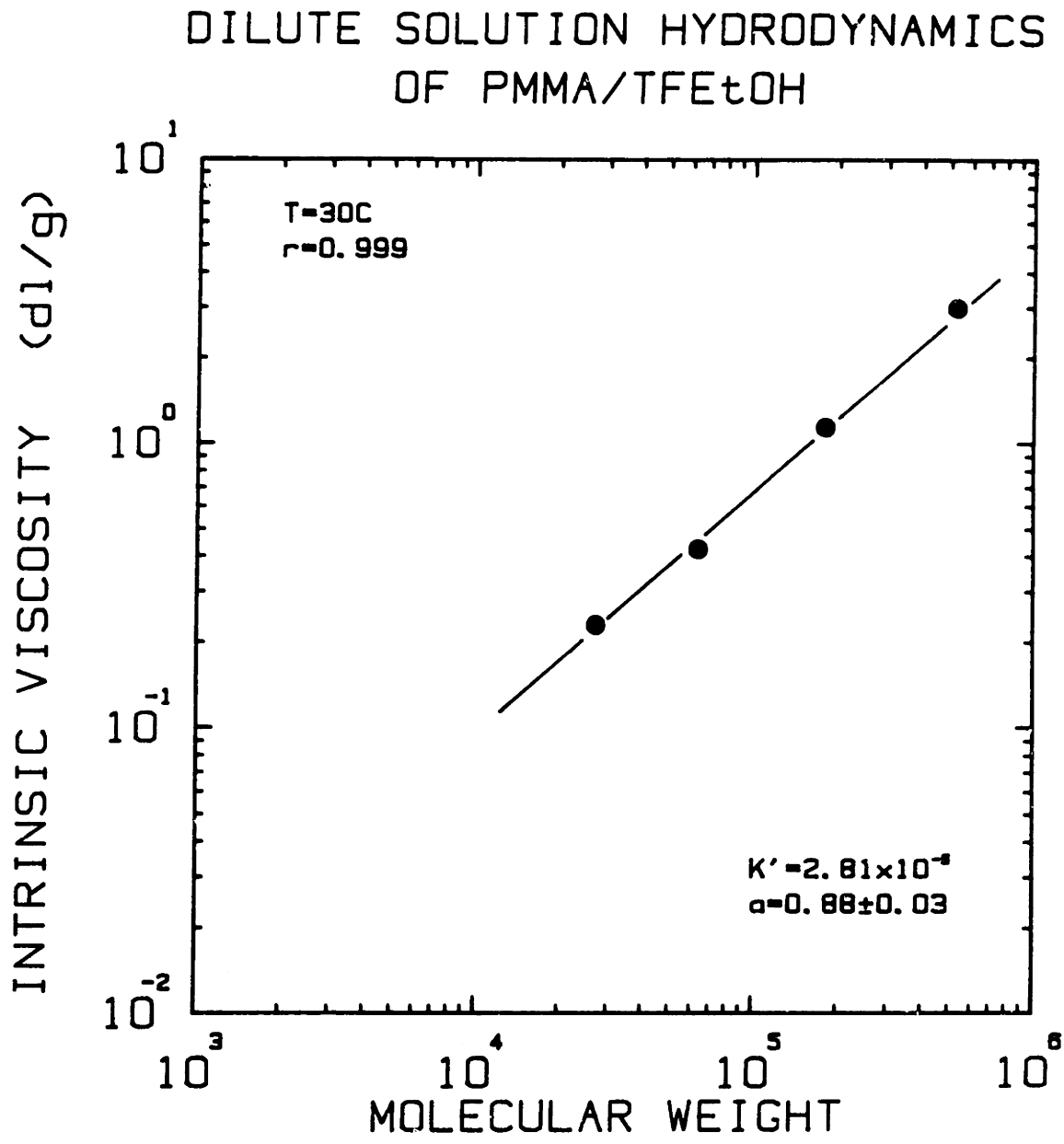

Figure 7-9 Calculation of the Mark-Houwink parameters for PMMA in 2,2,2-trifluoroethanol at 30°C; $K' = 2.81 \times 10^{-5}$, $a = 0.88 \pm 0.03$.

viscosity [76,77] or

$$[\eta]_1 M_1 = [\eta]_2 M_2 \qquad V_R = \text{const.}, \qquad (7\text{-}7)$$

where 1 ~ PMMA and 2 ~ Nylon-6. Substituting the Mark-Houwink expressions (equation (7-6)) for the intrinsic viscosities of both polymers and the peak molecular weight as a function of retention volume for PMMA (obtained from the PMMA calibration using the standards) into equation (7-7) yields the relation of nylon-6 molecular weight as a function of retention volume,

$$M_2 = D_1 \exp[-D_2 V_R] \qquad (7\text{-}8)$$

where $D_1=(K_1'/K_2')^{1/(1+a_2)} D_1'^{,(1+a_1)/(1+a_2)} = 5.4006\text{x}10^9$ and $D_2=D_2'(1+a_1)/(1+a_2) = 1.4602$. The parameters D_1' and D_2' are the intercept and absolute value of the slope of the PMMA calibration curve. This method gave a very linear calibration curve (regression coefficient = 0.999) from 2 kg/mole to 250 kg/mole nylon-6 molecular weight.

3. Size Exclusion Chromatography

Three different types of nylon-6 were analyzed: 1) commercial hydrolytic nylon-6, Allied Chemical's Capron^R which contains carboxyl and amine end groups and 2) Monsanto's RIM (reaction injection molded) nylon-6 containing an acetyllactam (initiator) moiety and a terminal lactam ring and 3) anionic nylon-6 synthesized in this laboratory with end group structure identical to that of 2). Chromatograms of the Allied and Monsanto nylon-6 are shown in Figure 7-10 uncorrected for any dispersive behavior.

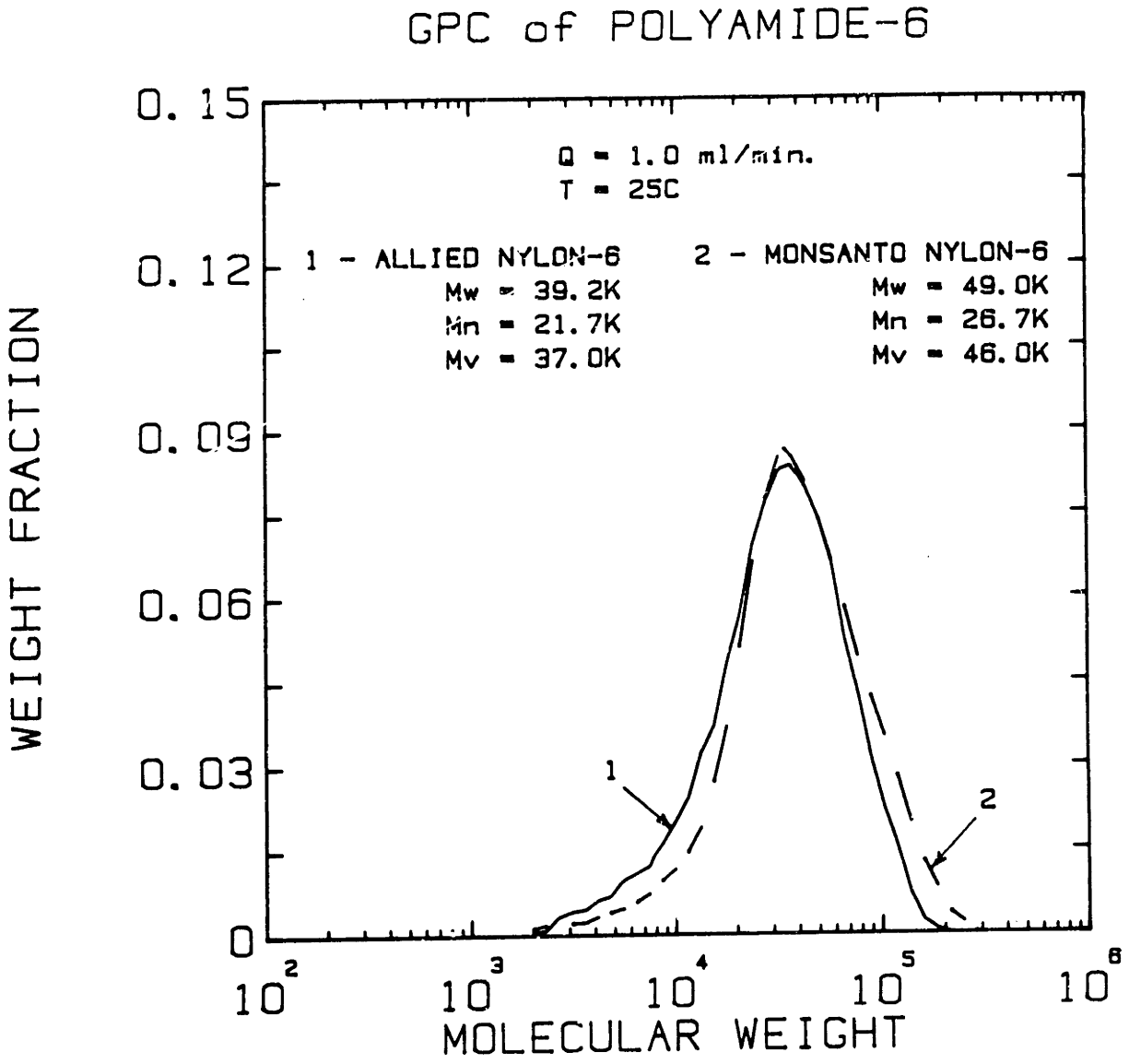

Figure 7-10 Size exclusion chromatography of commercial nylon-6 with Zorbax^R columns in TFEtOH; (——) = Allied hydrolytic PA-6; (---) = Monsanto RIM nylon-6.

To check the accuracy of the calculated nylon-6 molecular weights, independent MW determinations via end-group analysis and intrinsic viscosity were performed on Allied's hydrolytic nylon-6. The end group analysis gave an average (3 trials) $\bar{M}_n$ of 20.2 ± 0.36 kg/mole versus 21.7 kg/mole via the SEC. The inherent and reduced viscosities were measured in the Ubbelohde No. 1 viscometer mentioned previously at 30°C and used to determine the intrinsic viscosity of Allied nylon-6 in TFEtOH as shown in Figure 7-11. From this, the viscosity average molecular weight, $\bar{M}_v$, was calculated to be 40.3 kg/mole using the (K',a) values of Mattiussi, et. al. as compared to the SEC $\bar{M}_v$ of 37.0 kg/mole. These results are accurate to within ±10% using the SEC system described here and offer, in our view, the best combination of simplicity and accuracy of any system available in the literature for the determination of nylon-6 molecular weight.

To illustrate the inaccuracies that can develop when μ-Styragel^R columns are used with TFEtOH, anionic nylon-6 synthesized in our laboratory was chromatographed on both 10^3, 10^4 Å μ-Styragel^R and DuPont ZSM Zorbax^R columns with TFEtOH at room temperature and a flow rate of 1.0 ml/min. Figure 7-12, curve 1 shows the molecular weight distribution of the anionic nylon-6 as eluted from the Zorbax columns (the normal columns used in this work) which gives a $\bar{M}_w$ of 46.9 kg/mole and a $\bar{M}_n$ of 19.7 kg/mole. In contrast, the same sample chromatographed with μ-Styragel^R columns produced the dashed curve 2 of Figure 7-12 which shows the incorrect bimodal peak with highly inaccurate molecular weights due to an abnormal MW distribution. This result agrees with the comments of Dudley [43] and demonstrates that μ-Styragel^R should not be used with TFEtOH

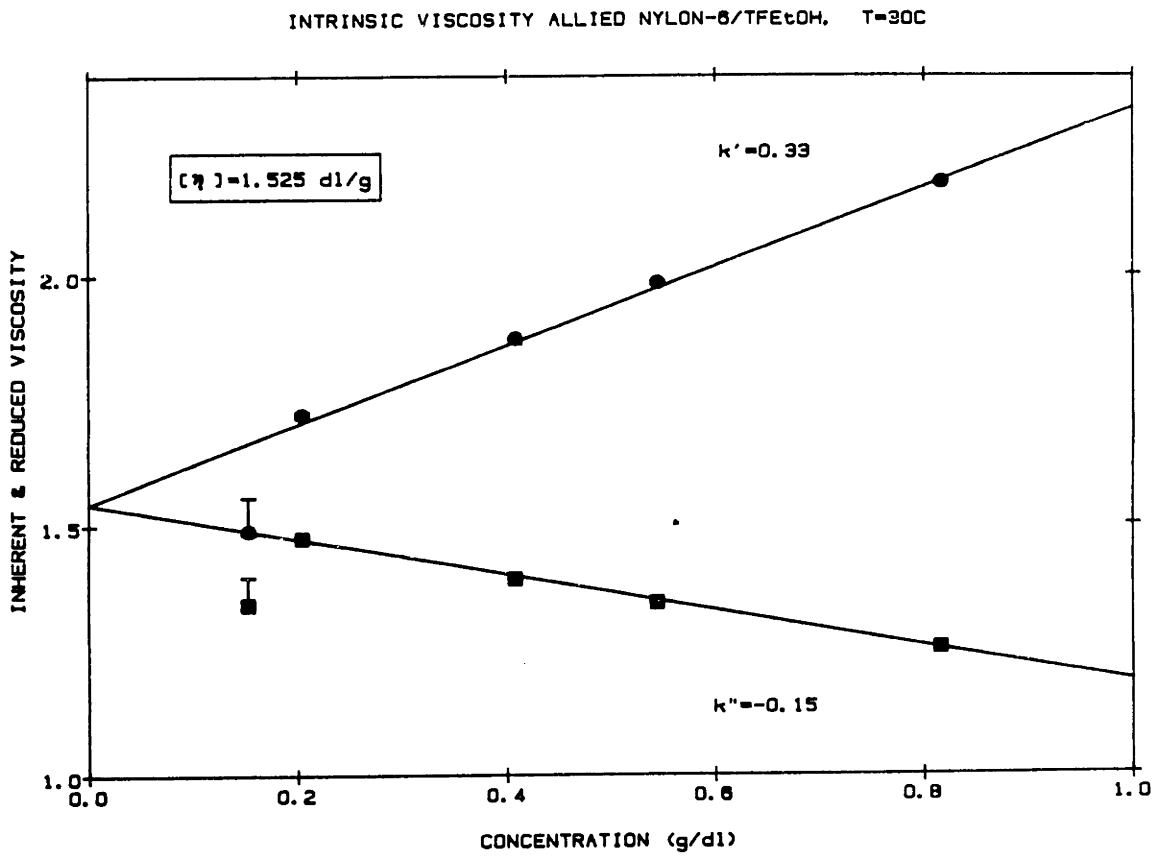

Figure 7-11 Intrinsic viscometry of hydrolytic nylon-6 in TFEtOH at 30°C; k' = Huggins constant, k" = Kraemer constant.

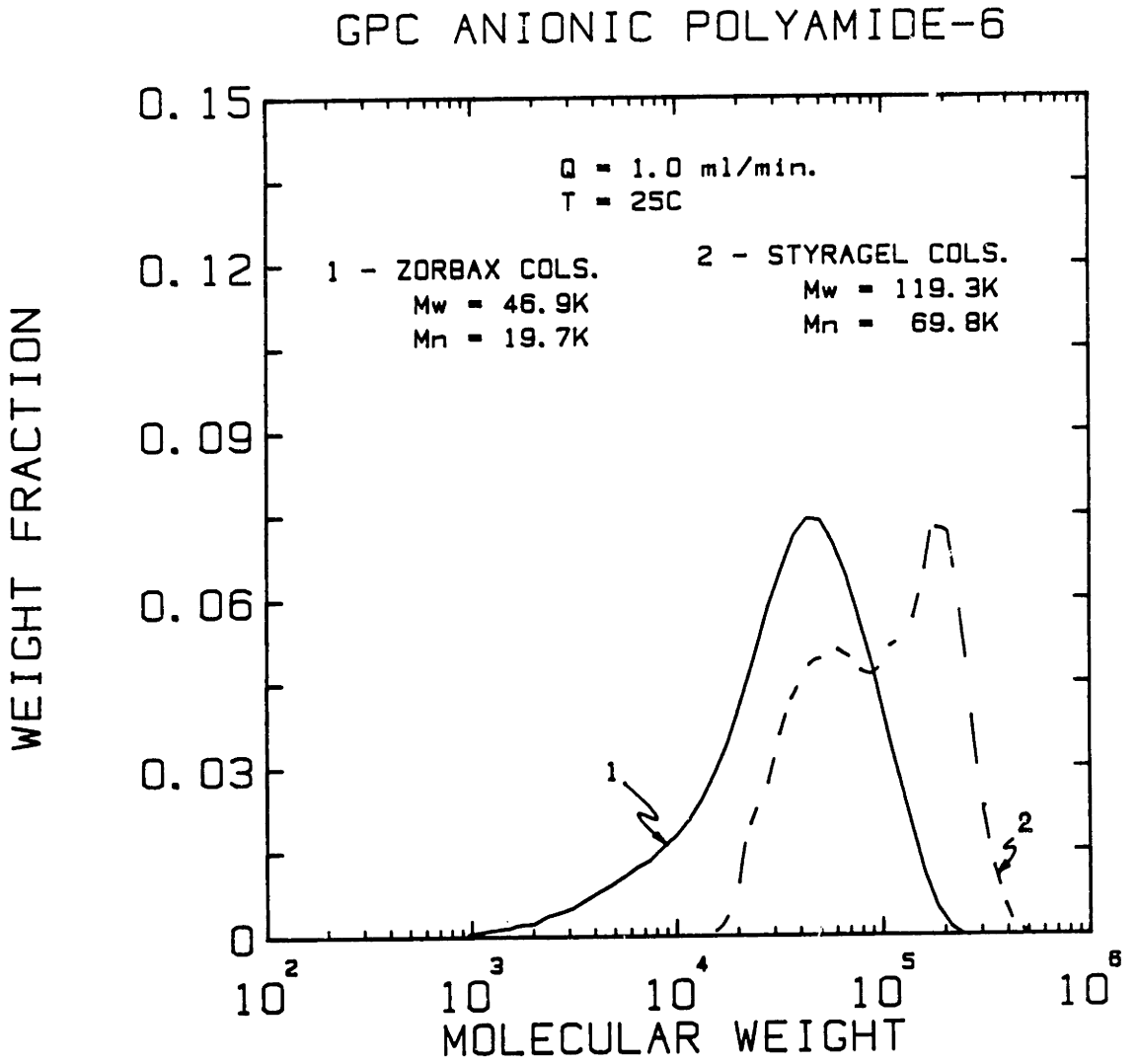

Figure 7-12 Size exclusion chromatography of anionically synthesized nylon-6 on Zorbax^R columns (———) and on μ-Styragel^R (10^4, 10^3, 500 Å) columns (---), both in TFEtOH, 25°C.

because of insufficient swelling of the styrene-gel packing which can minimize operational pore volume and cause channelling leading to artificially high molecular weights and poor column performance.

The SEC results in Figure 7-10 also indicate that the polydispersity of Monsanto's RIM nylon-6 (anionically synthesized) is comparable to Allied's hydrolytically produced nylon-6, both with a $\bar{M}_w/\bar{M}_n \approx 1.8$. The applicability of the same SEC accuracy achieved with the hydrolytic nylon-6 to anionically synthesized nylon-6 can be substantiated by Tuzar, et. al. [78] who showed that the (K', a) parameters for the two types of nylon-6 are the same in tetrafluoropropanol (TFP). Thus, if moderate synthesis temperatures are used to keep the anionic nylon-6 essentially linear, the two types of nylon-6 seem to be indistinguishable and to adopt essentially the same conformation in solution.

Although the polyelectrolyte effect has been demonstrated in 2,2,3,3-tetrafluoropropanol [79], its presence in TFEtOH has not been confirmed. Matzner, et. al. [68] performed light scattering in TFEtOH without observation of this effect and Mattiussi et. al. [71] attributed the larger unperturbed dimension of nylon-6 in TFEtOH versus HCOOH or m-cresol to strong polymer-solvent (1-2) interactions rather than the polyelectrolyte effect; (see the Appendix 3 for a further discussion of nylon-6 hydrodynamics in TFEtOH). Observations from this thesis work substantiate these viewpoints as well. The acidity of TFEtOH is simply not sufficient to substantially protonate the amide group causing widespread polarization and expansion of the polyamide chain; the K_a of TFEtOH is ~ $(0)10^{-13}$ [68] versus the K_a of strong acids such as HCOOH or H_2SO_4 of ~ $(0)10^{-2}$ to 10^{-5}. In addition, the deviation from linearity of

the reduced viscosity at low concentrations in the presence of the polyelectrolyte effect is positive [79] (i.e. the η_{sp}/c increases with decreasing concentration) whereas our observed nonlinear effect with Allied nylon-6 is negative as seen in Figure 7-11 below concentrations of ~ 0.2 g/dl. This implies that the bimodality of the nylon-6 in TFEtOH with μ-Styragel^R columns is caused simply by the poor resolution due to the solvent-packing incompatibility and not by a change in the true hydrodynamic volume of the polyamide-6 in TFEtOH due to the polyelectrolyte effect.

Conclusions

A new, accurate and simple SEC system was developed for the analysis of the MWD of nylon-6 based on proven and accepted principles of polymeric hydrodynamics. The method combined the utility of silanized silica columns and the solubility of PMMA standards in TFEtOH mobile phase to yield molecular weight accuracy within 10% via the universal calibration. Although the molecular weight accuracy was proven with hydrolytic nylon-6, the system will give accurate molecular weight values of anionic nylon-6 as well, provided the polymer is essentially linear (synthesized at moderate polymerization temperatures). The system was convenient and easy to operate, calibrate and maintain and offers the best combination of advantages over any other current SEC system for nylon-6.

The hydrodynamics of PMMA in TFEtOH were determined (see Appendix 3) via viscosity relationships which showed a much more compact conformation for PMMA versus nylon-6 in TFEtOH for equivalent molecular weights. The universal calibration satisfactorily related the sizes of the two polymers in solution to give a very linear calibration over two-and-

-a-half decades of nylon-6 molecular weight. This calibration gave accurate molecular weights without the need for the dispersive corrections which are necessary for other systems used in the SEC of polyamides. It is this advantage that made this SEC system particularly useful for both routine analyses as well as on-line molecular weight analysis during synthesis.

2. Siloxanes

The SEC system for analysis of the siloxanes (both methyl and trifluoropropylmethyl) was the same hardware as in the nylon-6 SEC system except that 500, 10^3, 10^4 Å μ-Styragel^R columns were used with THF solvent for PTFPMS and toluene for PDMS. Similar degassing and filtering procedures were followed with the hydrocarbon solvents as for TFEtOH. For most of the siloxane analysis, only the two smaller Styragel columns were used to minimize retention volume (and hence, run time). These columns were calibrated with poly(styrene) standards which yielded a linear calibration curve from 40 kg/mole to 200 g/mole molecular weight.

PTFPMS Molecular Weight Analysis in THF

The calibration generated by PS in THF was used without modification for MW analysis of PTFPMS and its oligomers with satisfactory accuracy. Agreement of the calibration curve with target molecular weight during synthesis was good and if the calibration curve of PS in THF was extrapolated to oligomeric molecular weight (F_3, F_4 molecular weights = 468.3, 624.4 g/mole, respectively), it predicted the exact peak elution volumes observed for the trimer and tetramer on the SEC chromatogram. This combined with the fact that the correction of the hydrodynamic volume of

PDMS in toluene versus PS in toluene via the Mark-Houwink parameters was minor (see below), indicated that no further work was necessary in establishing SEC accuracy for PTFPMS in THF. This calibration yielded the equation shown in equation (7-9) which was used to calculate PTFPMS molecular weights reported in Chapter IV of this thesis via

$$M = 1.608 \times 10^8 \exp[-0.72V_R] \quad . \tag{7-9}$$

PDMS Molecular Weight Analysis in Toluene

Since the Mark-Houwink constants were available in the literature for PDMS in toluene [80] and for PS in toluene [81], the same type of conversion of retention volume to absolute siloxane molecular weight was made as explained above for PMMA and nylon-6 in TFEtOH. See equations (7-6) through (7-8). This gave $M_{Sx} = 1.5\ M_{PS}^{0.98}$ which was used to calculate absolute siloxane molecular weight.

3. PDMS-Nylon-6 Diblock Copolymer

As explained in Chapter VI during characterization of the nylon-6--PDMS diblock copolymers, the nylon-6 calibration was used for analysis of diblock molecular weight. No attempt was made to construct a calibration based on real diblock molecular weights. Nonetheless, reasonable internal agreement was achieved with relative molecular weights based on equivalent nylon-6 chain size. For copolymers with very short siloxane blocks, negligible perturbation in the hydrodynamic volume as compared to nylon-6 occurred so that accurate, absolute molecular weights could be ascertained. See Chapter VI for details and interpretation.

D. REFERENCES FOR CHAPTER VII

1. E. Martuscelli, Polym. Eng. Sci., 24(8), 563 (1984).

2. C.J. Ong and F.P. Price, Jnl. Polym. Sci., Pt. C, 63, 59 (1978).

3. R.S. Stein, F.B. Khambatta, F.P. Warner, T. Russell, A. Escala and E. Balizer, Jnl. Polym. Sci., Pt. C, 63, 313 (1978).

4. L.M. Robeson, Polym. Eng. & Sci., 24(8), 587 (1984).

5. E. Martuscelli, C. Silvestre, G.C. Abate, Polymer 23, 229 (1982)

6. Z. Bartczak, A. Galeski and E. Martuscelli, Polym. Eng. Sci., 24(15), 1155 (1984).

7. M.A. Drzewinski, Ph.D. Thesis, Dept. Materials Science, MIT, (1986), Ch 4.

8. E. Martuscelli, F. Riva, C. Sellitti and C. Silvestre, Polymer, 26, 269 (1985).

9. M. Dole and B. Wunderlich, Makromol. Chem., 34, 29 (1959).

10. L.G. Roldan and H.S. Kaufman, Polym. Letters, 1, 603 (1963).

11. A. Verma, B.L. Deopura, A.K. Sengupta, Jnl. Appl. Polym. Sci., 31, 747 (1968).

12. R.H. Boyd, Polymer, 26(8), 1123 (1985).

13. B.B. Burnett, W.F. McDevit, Jnl. Appl. Phys., 28(10), 1101 (1957).

14. J.A. Koutsky, A.G. Walton, E. Baer, Jnl. Appl. Phys., 38(4), 1832 (1967).

15. M. Inoue, Jnl. Polym. Sci., 55, 753 (1961).

16. J.H. Magill, Polymer, 6, 367 (1965).

17. J.H. Magill, Polymer, 3, 655 (1962).

18. J.H. Magill, Polymer (London), 3, 43 (1963).

19. L. Mandelkern, Crystallization of Polymers, McGraw Hill, New York, 1964.

20. D.G. Thomas and L.A.K. Staveley, Jnl. Chem. Soc., 4569 (1952).

21. J. Boon, G. Challa, D.W. vanKrevelen, J. Polym. Sci.: A-2, 6, 1791 (1968).

22. B. Wunderlich, Macromolecular Physics, Academic Press, 1976, Vol 2, p. 147, 168.

23. E.S. Ong, Y. Kim, H.L. Williams, Jnl. Appl. Polym. Sci., 31, 367 (1986).

24. N.G. McCrum, B.E. Read, G. Williams, Anelastic and Dielectric Effects in Polymer Solids, Wiley, London, 1967.

25. K.H. Illers, Makromol. Chem., 38, 168 (1960).

26. C. Garbuglio, G. Ajroldi, T. Casiraglu, G. Vittadini, Jnl. Appl. Polym. Sci., 15, 2487 (1971).

27. G.J. Kettle, Polymer, 18, 742 (1977).

28. L. Bohn, H. Oberst, Acustica, 9, 431 (1959).

29. A.J. Staverman, J. Heijboer, Kunststoffe, 50, 23 (1960).

30. L.E. Nielsen, Mechanical Properties of Polymers, Reinhold Pub. Co., N.Y., 1962, p. 180.

31. E.G. Bobalek, R.M. Evans, Trans. Soc. Plastics Eng. J., 1, 93 (1961).

32. P.I. Vincent, Polymer, 1, 425 (1960).

33. R.F. Boyer, Polym. Eng. & Sci., (SPE Award Paper), 8(3), 161 (1968).

34. L. Bohn, Kunststoffe, 53, 826 (1963).

35. A.H. Willbourn, Trans. Faraday Soc., 54, 717 (1958).

36. T.F. Shatzki, Jnl. Polym. Sci., 57, 496 (1962).

37. R.F. Boyer, Rubber Rev., 34, 1303 (1963).

38. I.M. Ward, Mechanical Properties of Solid Polymers, Wiley, N.Y., 2nd ed., 1983, p. 176.

39. K. Schmieder, K. Wolf, Kolloid Z.Z. Polym., 134, 157 (1953).

40. M. Takayanagi, in Proceedings of the Fourth International Congress of Rheology, Pt 1, Interscience Pub., N.Y., 1965, p. 161.

41. N.G. McCrum, E.L. Morris, Proc. Royal Soc. A, 292, 506 (1966).

42. H. Benoit, P. Rempp, Z. Grubisic, Jnl. Polym. Sci., Polym. Lttrs., 5, 753 (1967).

43. M.A. Dudley, Jnl. Appl. Polym. Sci., **16**, 493 (1972).

44. Z. Tuzar, P. Kratochvil and M. Bohdanecky, Adv. Polym. Sci., **30**, 117 (1979).

45. W.W. Yau, J.J. Kirkland and D.D. Bly Modern Size Exclusion Liquid Chromatography, Wiley Interscience, New York (1979) p. 390.

46. P.S. Ede, Jnl. Chromatog. Sci., **9**, 275 (1971).

47. E.E. Paschke, B.A. Bidlingmeyer and J.G. Bergmann, Polym. Prepts., **17**, 440 (1976).

48. W.A. Dark, Proc. Int'l GPC Symposium, May 11-13, 1987, p.18.

49. G. Pastuska and U. Just, Die Ang. Makromol. Chem., **81**, 11 (1979).

50. G. Marot and J. Lesec, Proc. Int'l GPC Symposium, May 11-13, 1987, p. 113.

51. D. Petit, R. Jerome and Ph. Teyssie, Jnl. Polym. Sci., Polym. Chem. Ed., **17**, 2903 (1979).

52. R. Panaris and G. Pallas, Jnl. Polym. Sci., Pt. B. Polym. Lttrs., **8**, 441 (1970).

53. D.J. Goedhart, J.B. Hussem and B.P.M. Smeets, Liquid Chromatography of Polymers and Related Materials, in Chromatographic Science Series, vol 13, (ed. J. Cazes, X. Delaware), Marcel Dekker, New York, 1977, p. 203.

54. H. Schuttenberg and R.C. Schulz, Angew. Chem., **88**, 848 (1976).

55. E. Jacobi, H. Schuttenberg, R.C. Schulz, Makromol. Chem., Rapid Comm., **1**, 397 (1980).

56. E. Biagini, E. Gattiglia, E. Pedemonte, S. Russo, Makromol. Chem., **184**, 1213 (1983).

57. K. Weisskopf and G. Meyerhoff, Polymer, **24**, 72 (1983).

58. K. Weisskopf, Polymer, **26**, 1187 (1985).

59. A.R. Weiss and E. Cohn-Ginsberg, Jnl. Polym. Sci. A2, **8**, 148 (1970).

60. G.V. Schulz, Z. Physik. Chem., **B43**, 25 (1939)

61. B.H. Zimm, Jnl. Chem. Phys., **16**, 1099 (1948).

62. G. Meyerhoff, Jnl. Polym. Sci., Pt. C., **21**, 31 (1968).

63. W.W. Yau, J.J. Kirkland and D.D. Bly Modern Size Exclusion Liquid Chromatography, Wiley Interscience, New York (1979) p. 299.

64. G. Costa and S. Russo, Jnl. Macromol. Sci., Chem. Ed., **A18(2)**, 2 9 9 (1982).

65. E.E. Drott, Liquid Chromatography of Polymers and Related Materials, in Chromatographic Science Series, vol 8, (ed. J. Cazes), Marcel Dekker, New York, 1977, p 41.

66. T. Provder, J.C. Woodbrey and J.H. Clark, Sep. Sci., **6(1)**, 101 (1971).

67. T. Provder, J.C. Woodbrey, J.H. Clark and E.E. Drott, Adv. Chem. Ser., **125**, 117 (1973).

68. M. Matzner, L.M. Robeson, R.J. Greff and J.E. McGrath, Angew. Makromol. Chemie, **26**, 137 (1972).

69. J.D. Ferry, Viscoelastic Properties of Polymers, J.W. Wiley and Sons, Third Edition, (1980), p. 219.

70. S.M. Aharoni, F.G. Cilurso, J.M. Hanrahan, J. Appl. Polym. Sci., **30**, 2505 (1985).

71. A. Mattiussi, G.B. Gechele, R. Francesconi, J. Polym. Sci., Pt A-2, **7**, 411 (1969).

72. G.M. Burnett, A.J. MacArthur and J.N. Hay, Eur. Polym. Jnl., **3**, 321 (1967).

73. M.L. Huggins, Jnl. Am. Chem. Soc., **64**, 2716 (1942).

74. E.O. Kraemer, Ind. Eng. Chem., **30**, 1200 (1938).

75. E.A. Collins, J. Bares and F.W. Billmeyer, Jr., Experimerts in Polymer Science, Wiley-Interscience, N.Y., 1973), p.149.

76. P.J. Flory, Jnl. Chem. Phys., **17(3)**, 303 (1949).

77. P.J. Flory and T.G. Fox, Jr., Jnl. Polym. Sci., **5**, 745 (1950).

78. Z. Tuzar, P. Kratochvil and M. Bohdanecky, Jnl. Polym. Sci., Part C, **16**, 633 (1968).

79. H.C. Beachell and D.W. Carlson, Jnl. Polym. Sci., **40**, 543 (1959).

80. A. Haug and G. Meyerhoff, Makromol. Chem., **53**, 91 (1962).

81. Polymer Handbook, 2nd ed., J. Brandrup, E.H. Immergut, ed., Wiley, N.Y. 1975.

CHAPTER VIII. MORPHOLOGICAL CHARACTERIZATION

A. MORPHOLOGY OF NYLON-6 HOMOPOLYMER

Electron Microscopy

The supermolecular structure of nylon-6 has been investigated by electron microscopy in thin films by a number of investigators [1–5] who deduced chain folded structures from photomicrographs of edge-on lamellae. Phosphotungstic acid (PTA = $H_3[P(W_3O_{10})_4]$ @ 2 %w aqueous) staining agent as introduced by Spit [3] was used to provide the necessary contrast by complexing with the amorphous amide groups. Diffusion of this stain into the amorphous regions in the nylon sample has been enhanced by 2 %w benzoyl alcohol [1].

In an early work, Geil [7] studied nylon-6 single crystals grown from glycerine suspension at 100°C under vacuum. He found a rhombohedral habit composed of flat platelets or lamellae growing in a spiral from screw dislocations in the basal plane of the lamellae. Platelet thickness was ca. 50–100 Å which indicated chain folding within the crystals. Selected area electron diffraction of the monocrystal indicated characteristic spacings of 4.0–4.1 Å corresponding to the distance between hydrogen bonded sheets and 2.4 Å (~ 2θ=37.5°) indicative of half the distance between hydrogen bonded chains within the sheets. The reason for the γ-form (see below and §C.2 for further explanation of the various crystalline forms) monocrystals with parallel chains is not altogether clear since the chain folding into the platelets should have produced antiparallel chains by its very nature. On the other hand, spherulitic nylon-6 crystallized from solution gave diffraction spacings of 3.7 and 4.4 Å which are known today to represent the α-form (antiparallel chain

packing in a monoclinic crystal, (002) and (200) reflections, respectively [8]). Lamellar thickness was also found to be the same, ca. 50-100 Å as the single crystals. These values are all seen in the wide-angle x-ray scattering (WAXS) and transmission electron microscopy (TEM) obtained on nylon-6 and copolymers from this thesis and are discussed in §C.2.

Only recently, however, have the details of the bulk spherulitic structure of nylon-6 been revealed. In sample preparation for transmission electron microscopy, Galeski, et.al. [9] utilized embedding of thin nylon-6 filaments in an epoxy matrix and cryo-ultramicrotomy (T = −30°C) while Schaper, et.al. [10] employed staining, some swelling with dilute aqueous HCl and γ-irradiation followed by room-temperature microtomy to satisfactorily prepare ultra-thin sections. These two studies concurred remarkably well revealing lamellar thicknesses in bulk materials of approximately 35–60 Å, lamellar widths varying from 50–400 Å and in diametrical sections, lamellar lengths of many microns, some starting at the origin, gently curving and running continuously the entire radius of the spherulite. This generically continuous, fanning lamellar growth is also observed in spherulitic nylon-6 and copolymers from this work. As pointed out in [10], this is in contrast to other spherulitic polymers such as PE and i-PP where the lamellae periodically alter their orientation in a branched fashion from either tangential growth or nucleation of other crystallites from existing lamellar surfaces [11], which can lead to banded spherulites as seen in the optical light microscope (OLM).

Both Galeski et.al. and Schaper, et.al. conclude that the packing of the lamellae within the spherulite is random and as growth proceeds,

non-crystallographic branching (or secondary nucleation) is responsible for the appearance of new, volume-filling lamellae. Galeski, et.al. advanced a simple geometrical model to illustrate this point showing the grouping of 3-4 lamellae into bundles and the appearance of additional lamellae within the same group at greater radial position. Schaper, et.al. also studied the nucleation and embryonic growth of lamellae in samples quenched to room temperature from the melt. They found that the initial lamellar clusters which eventually grew into sheaf-like domains appeared to nucleate from unmelted aggregates resembling dendrites rather than heterogeneities. Unfortunately, no details of the melt history were published to estimate how this "melt memory" persists in typical melt-crystallized nylon-6.

The striking conclusion that can be drawn from both Galeski's and Schaper's work is that the morphology of bulk nylon-6 is very similar to that of thin films (see references [1–5]). Lamellar dimensions and an "axialite" shape of the spherulites with generically continuous lamellae are the same in both cases. Axialites are a special class of spherulites that do not possess the spherical symmetry of the latter, rather they have an axis or plane of symmetry, generically continuous lamellae that span the entire radius and "eyes" or circular regions on either side of the axis of symmetry that contain tightly curved lamellae and less perfect crystals. Refer to Figure 2-5 of this thesis for an example. The similarity between thin film and bulk morphology is further supported by small angle x-ray scattering (SAXS) results which give bulk long period spacings similar to lamellar dimensions measured by TEM on thin films [10]. Thus, these experiments suggest that the thin-film studies

from this thesis work in addition to their own merit, may have some relevance to actual morphology in bulk nylon-6 copolymers. This rather fortuitous but nonetheless real similarity between bulk and thin-film morphology is somewhat surprising because thin-film samples can be influenced strongly by substrate and atmospheric effects. Evidently, these do not strongly perturb the lamellar growth process in nylon-6 much the same way that chain defects do not significantly inhibit the growth of lamellae to such large radial dimensions as reported by Galeski, et.al. [9]. In the study of thin film properties in this thesis, any deleterious substrate effects were eliminated by the development of a new casting technique and atmospheric effects were minimized by casting the thin films in the same solvent-rich atmosphere that bulk samples were cast. Hopefully these safeguards can be used as a first step in relating thin-film observations to bulk material behavior in siloxane-nylon-6 systems.

Unit Cell

The crystallography of nylon-6 initially was investigated by Brill [12] who determined the crystal lattice to be monoclinic with the chains oriented along the b-axis. This essentially was confirmed by Holmes, et.al. [13] for the α-form who determined cell dimensions of a = 9.56 Å, b (chain axis) = 17.24 Å and c = 8.01 Å with β = 67.5°. This gives theoretically 8 mers per cell with a crystalline density of 1.23 g cm^{-3}. From these spacings, Holmes, et.al. determined that a doubling of chains occurs along the a-axis because adjacent chains are inverted and that the doubling along the c-axis is due to a staggering of hydrogen bond

planes. The chains are inclined approximately 7° from the hydrogen bond planes or (001) planes.

The second form of nylon-6, γ-monoclinic has been characterized initially by Kinoshita [14] and later by Arimoto [15] based on an aqueous I_2/KI treatment to convert the α-form to the γ-form devised by Ueda and Kimura [16]. This γ-form has a slightly shorter b-axis due to a parallel arrangement between hydrogen-bonded chains where the amide groups are twisted normal to the (001) plane and complete their bonding in the (100) plane. They can also establish a pleated plane along the (010) direction giving rise to the comments that it appears as a network in the γ-form [9]. Unit cell dimensions are a = 9.33 Å, b = 16.88 Å and c = 4.78 Å, β = 59°. Note that the c-axis distance has been roughly halved due to straight stacking of the hydrogen bond planes instead of the offset stacking (i.e., sheared by ~ 3/14 b) in the α-form. Note that the a axis can not be halved as well because the chains in that direction still are antiparallel. An extensive tabulation of the various reflections of the α- and γ-forms is given by Gurato [8] in addition to the δ or amorphous peak. The major reflections are reproduced in Table 8-1 which will be discussed thoroughly in § C.2 and C.3.

This γ-form also was studied by Murthy et.al. [17] using treatment with aqueous I_2-KI solution followed by removal of the iodide by aqueous sodium thiosulfate. They found that in an initially unoriented film, the penetrating iodine caused the chains to be oriented normal to the surface of the film with the hydrogen bond plane (001) also normal to the film surface. This occurred presumably as a result of the unidirectional

Table 8-1

Theoretical X-ray Diffraction Data for Nylon-6
(from reference [8])

Crystal Form	Label	hkl	Calculated* d_{hkl}(Å)	Calculated* 2θ	Best fit Range 2θ
γ-monoclinic	γ_1	020	8.44	10.5	10.7–11.3
α-monoclinic	α_1	200	4.42	20.1	19.8–20.1
δ-amorphous	δ	100#	4.40	20.2	20.2–21.8
γ-monoclinic	γ_2	200	4.16	22.2	20.5–21.5
α-monoclinic	α_2	002	3.70	24.05	22.6–24.0
		202	3.59	24.8	

* 2θ measured in degrees

Two-dimensional pseudo-hexagonal close packed structure approximation

diffusion and orientation by the iodide ions. This orientation is lost when the $\gamma \rightarrow \alpha$ transition occurs which rearranges the chains so they and the hydrogen bond planes are parallel to the surface of the film (again in the 001 planes). This finding is different than Arimoto's work [15] for two reasons: 1) the chains here are normal to the surface versus a parallel orientation to the surface due to rolling in reference [15], and 2) the hydrogen bond plane is the same as the α-form for Murthy's iodinated nylon-6 whereas the hydrogen bond planes from Arimoto are primarily in the (100) planes with a pseudo-planar organization in the (010) plane. Closer inspection of Murthy's schematic indeed shows

antiparallel chain configuration which is in conflict with the work of Arimoto and others.

Transition between the two phases is easily accomplished with known techniques. The α-form is obtained by high temperature annealing (ca.200°C) or treatment in boiling water for 6 hours [18] whereas higher content γ-form films are obtained by crystallization at lower temperatures (ca. < 130°C [19,22]) or by the iodine treatment reported by Arimoto [15]. Infrared spectroscopy has been used by D'Alo [18] and by Hirami [19] for discerning the presence of the two phases; the former used IR only qualitatively whereas the latter quantified measurements by correlating IR intensities with wide-angle x-ray scattering (WAXS) data although only intensities and not peak areas were used to estimate fractional content of the two phases. Kyotani et.al. [22] reported that a higher percentage of γ-form crystals were obtained when crystallized from solution (e.g. glycerine as the solvent) below temperatures of ca. 130°C in analogy to the melt, but unlike samples crystallized from the melt, the γ-form of samples crystallized from solution above 100°C was stable and did not transform to the α-form upon annealing at 200°C, for as long as 10 hours. This indicates that: i) the γ-form crystallization rate surpasses the α-form rate at temperatures below $\approx$ 130°C, ii) the γ-form is present in both solution and melt crystallized samples and iii) the γ-form from solution is stable whereas the γ-form from the melt is readily transformed to the α-form upon high temperature (200°C) annealing. Reasons for this stability of the γ phase from solution are not fully understood.

However, as Ruland pointed out [23] by way of his disorder parameter, D (= $\exp[-ks^2]$, where $s = 2/\lambda \sin\theta$), polyamide-6 produced by precipitation has much more disorder as determined by the value of the lattice imperfection exponent, k which = 4.4 versus bulk material with a k = 3.3. Upon annealing both materials at temperatures of ≈ 195–200°C, the k values fell to 3.7 for the solution precipitated versus 3.0 for the bulk, quenched and annealed material. Original crystallinity levels of essentially zero and ~ 35% were calculated for the bulk, quenched material and the solution precipitated polymer, respectively. The values after annealing were approximately the same, the bulk material reaching 33% crystallinity and the solution precipitated material decreasing to 32%. This higher imperfection in the solution-crystallized polyamide-6 might be consistent with more γ-form material but both crystalline forms were not considered stable by Ruland and thus only the antiparallel α-form was incorporated into the model as an ordered phase, the γ-form being considered paracrystalline. In this thesis work, much greater heats of fusion are achieved from solution-casted films as compared to melt crystallized ones. However, no lattice imperfection calculations were made and it is unknown if the higher crystallinity achieved by solution casting is associated with a larger degree of perfection. Intuitively, this seems quite plausible throwing some inconclusiveness on Ruland's results with respect to observations of Kyotani [22] and results from this thesis.

In general, the work on the unit cell of nylon-6 still has not given consistent conclusions as illustrated by the previous discussion. Different opinions on chain orientation, degree of crystal perfection and

why some forms of nylon-6 are formed by certain treatments still exist. Future work with sophisticated x-ray analysis combined with proven microscopic techniques discussed at the beginning of this chapter is the only way to resolve these issues and answer existing questions.

Crystallite Dimensions

Small angle x-ray scattering (SAXS) has been done on nylon-6 to investigate lamellar thicknesses as a function of crystallization temperature from the melt by several workers [19,20,21]. As expected, it was determined that larger thicknesses (here lamellar thickness is equated to maximum scattering intensity angle via Bragg's law, which is only an approximate relationship in this context) were obtained for crystallization at lower supercooling. Values from Hirami [19] ranged from 177 Å at T_c = 210°C to 134 Å at T_c = 180°C to 68 Å at T_c = 20°C. He concluded that the deviation from linearity of the average lamellar thickness, $\langle \ell \rangle$ versus $T_m \Delta T$ was due to the temperature dependence of the end surface free energy, σ_e. Rather, this may have been due to the misuse of T_m (instead of T_m^o) in the equation relating lamellar thickness to temperature as given by Hoffmann's theory [25,26] as shown in equation (8-1) and discussed in Chapter II, §B.2.

$$\langle \ell \rangle = \frac{2\sigma_e T_m^o}{\Delta H_u \Delta T} + \delta \ell \qquad (8\text{-}1)$$

If his data are plotted as $(d\langle \ell \rangle / dT)^{-1/2}$ versus ΔT, the intercept gives a T_m^o of 260°C in exact agreement with the value from Wunderlich [24] which assumes a constant σ_e, but Hirami considered this value too high and unreal. The fact that he considered crystallization over nearly a 200°C range may have some merit for his analysis of a temperature-dependent σ_e

which he found to vary inversely with T_c, but proper use of the equilibrium melting temperature may have led to different conclusions.

Crist et.al. [27] also measured lamellar thickness (Lorentz corrected) for isotropic, cast nylon-6 film as a function of annealing temperature and found a small change for temperatures up to ca. 150°C; these values were ca. 75 Å but above 150°C, the lamellar thickness rose rapidly to a value of 102 Å at 210°C. These values are smaller than the lamellar thicknesses found by Hirami at comparable annealing temperatures. As pointed out by Crist et.al., the estimation of the long period, ℓ from the dimension associated with the maximum intensity from Bragg's law overestimates ℓ due to unrealisitic representation of the two-dimensional scattering from a one-dimensional model. According to Crist, et.al., the finite lateral coherence length of the lamellar stacks causes distortion in the radial intensity distribution leading to the misinterpretation.

B. MORPHOLOGY OF PREVIOUS NYLON-6 / RUBBER SYSTEMS

The numerous morphological studies on homopolymer polyamide-6 have produced valuable insights into the supermolecular structure of this polymer; however the same can not be said about nylon-6/rubber systems for various reasons. First, there are few well-defined nylon-6-rubber copolymers amenable to detailed morphological examination. The random, multiple morphologies of many nylon-6-rubber copolymers discussed in Chapter VI, §A preclude accurate interpretation of the effects of composition, molecular weight and thermal history (to name just several variables). Second, many investigators of nylon-6/rubber systems have focused on blends of the two homopolymers because they are (much) easier

to prepare and the characteristic sizes of the microdomains are large enough for good characterization via OLM. Often, thin-films of pure blends are unsuitable for TEM examination because of the immiscibility and accompanying difficulty in preparing samples; most blends have to be specially dispersed via high shear, high temperature processes. And third, many researchers do not study all aspects of block copolymers, ranging from synthesis and characterization to morphological examination and mechanical property testing. As seen in Chapter VI, §A, some investigators primarily interested in synthesis do not examine the resulting morphology and mechanical properties of their materials as has been done in this thesis. All three of these reasons have combined to slow the morphological development of nylon-6-rubber copolymers and blends.

Nylon-6/Rubber Blends

General morphological features as the result of phase separation competing with kinetics of crystallization of various blends has been discussed, albeit briefly, in Chapter II, §B.3. For nylon-6/rubber blends, morphological characterization in the literature has been confined mainly to blends of nylon-6 with EPM [28,29] or the dienes [30]. The latter showed nearly contiguous PB particles (~O(0.5) μm diameter) in the matrix with no discernible spherulitic structure of the polyamide-6. The studies with EPM blends revealed via SEM ca. 1 μm rubber particles in the polyamide-6 matrix and their relation to the type of fracture (ductile or brittle). However, none of these studies have employed high-resolution TEM to discern the molecular structure on the sub-micron scale. Small angle x-ray scattering [31] showed a decrease in

the long period as EPM concentration was increased from 0 to 20 %w and an increase for higher isothermal crystallization temperatures.

Nylon-6-Rubber Copolymers

There is also a scarcity of morphological studies conducted on nylon-6-rubber copolymers as well. With one notable exception [32] most of the morphological investigations have been limited to super-micron SEM analysis on random graft copolymers of EPR [33], EPM [29] and EPDM [28] with nylon-6. All of these studies have observed (via etching/SEM) large scale rubber particles (> 1 μm) with large size disparity due to randomness of the grafting reaction. Additional studies [31] using WAXS showed that the fraction of γ-form crystallization was independent of rubber concentration from 10-30 %w for a blend of nylon-6/EPM and nylon-6-EPM graft copolymer. This was determined by the ratio of peak intensities (α_1, α_2, γ) for samples isothermally crystallized at temperatures of 191°C and 203°C. Long periods from SAXS analysis could only be calculated for pure blends of nylon-6 and EPM because the graft copolymers possessed a polydispersity that was greater than the packing density which lead to a monotonically continuous decay of the intensity function without an inflection point [34].

Some TEM micrographs of nylon-6-poly(isobutylene) (PIB) diblock, triblock and radial tristar block copolymers have been published by Wondraczek and Kennedy [32]. Unfortunately, only limited details of their work are given; presumably they used PTA staining to contrast the nylon-6 regions from the lighter PIB domains. In a triblock PIB-nylon-6 copolymer, spherulites of ca. 6-10 μm were seen in ultra-thin cast films with excellent contrast of the lamellae similar to some of the figures of

this chapter but no observation of discrete rubber domains was possible, maybe due to the low magnification images. Additional micrographs of a diblock copolymer showed only light and dark regions with no real spherulitic or other crystalline structure. Thus, rigorous interpretation of these morphologies is not possible.

C. EXPERIMENTAL RESULTS

1. Methodology

Among the many variables outlined in Chapter II, §D.3 that affect nylon-6-rubber copolymer/blend properties, composition of the components is one of the most influential. To study this compositional dependence, a ternary diagram is convenient to illustrate how the three components, the nylon-6-rubber copolymer and the two homopolymers, combine to alter morphology and eventually mechanical properties, the latter being discussed in the following chapter. This ternary diagram with the various blend compositions studied in this work is shown in Figure 8-1. Note that this diagram does not represent phase boundaries, for the siloxane and nylon-6 are completely immiscible at room temperature, rather only depiction of the compositions of the various blends. At the top of the diagram is the pure copolymer, being either MSN(3/100) or USMSN(15/44), borrowing the nomenclature from the synthesis chapter, VI. Only the MSN(3/100) has been extensively studied throughout the diagram while the ultrasonic polymer has been evaluated just as pure copolymer. The bottom two apexes represent pure homopolymer nylon-6 of $\bar{M}_w$ = 39.2 kg/mole and $\bar{M}_n$ = 21.7 kg/mole and poly(dimethylsiloxane) of peak molecular weight 1000 g/mole. Note that both homopolymers have molecular

TERNARY COMPOSITION DIAGRAM

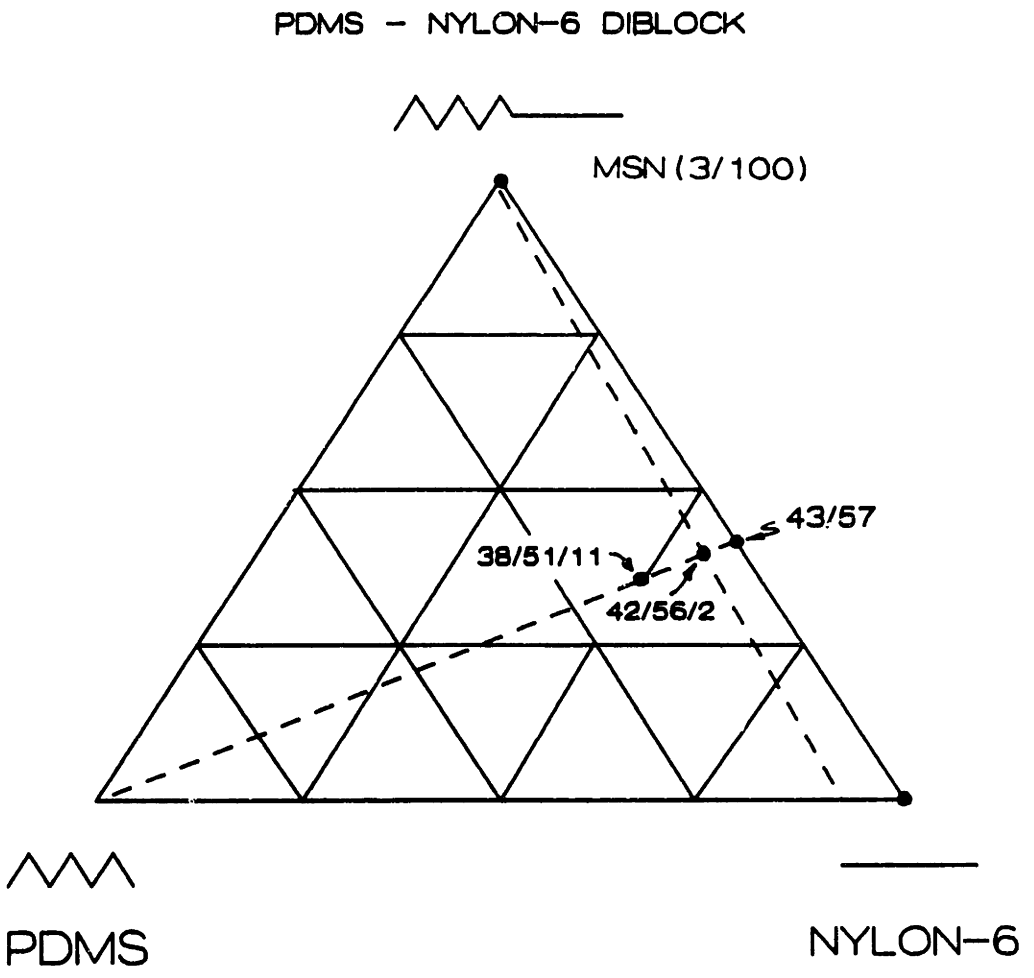

Figure 8-1 Ternary composition diagram showing the makeup of the various blends with the three components, diblock MSN(3/100), nylon-6 and PDMS in that order. Values given represent weight percent composition.

weights less than the corresponding blocks of the copolymer MSN(3/100) as discussed in Chapter II, §B. Compositions are determined by the inverse lever rule for segments drawn from the point of interest to the respective apexes. See any introductory mass transfer chemical engineering text for an explanation, e.g. [35].

Most of the morphological investigation was conducted by transmission electron microscopy (TEM) because of the ultra-small domain structures present in the copolymer and its respective blends. Since the PDMS has a $T_g \approx -125°C$, ultracryomicrotomy was extremely difficult (only thicker sections, ca. 5 μm, for the OLM could be produced) due to the natural toughness of the material. Consequently, a thin-film casting technique was developed that permitted ultra-thin films of ca. 1000 Å to be formed directly on the copper TEM grid. These films were formed over many square grid sections which permitted low magnification as well as high magnification work. The technique consisted of preparing a container saturated with solvent vapor and depositing two drops (with intermittent evaporation) of filtered, ca. 0.3 – 0.5 %w/v solution onto the grids. The first drop served to coat the grid surface without coverage of the squares while the second apparently bonded to the initial coating and spread across the grid with good uniformity.

Subsequent thermal treatments such as annealing and melt recrystallization could then be conducted on the grid samples. This was performed in either the high temperature chamber of the Mitsubishi moisture analyzer under nitrogen or vacuum, which provided more accurate temperature control and means for quick removal of the samples if desired or in the high temperature vacuum oven under either N_2 or vacuum. Slow and

moderate cooling rates were achieved, the "moderate" program moving from the melt at ~ 250°C to room temperature in about 35 minutes whereas the "slow" cooling took about 80 minutes. All ternary compositions except for some homopolymer nylon-6 samples had the 35 minute cooling history.

Since the copolymers contain silicon, atomic weight of 28.1 a.m.u., no additional heavy metal staining was required because the silicon provided the necessary phase contrast in the TEM. In addition to its convenience, the fact that the samples did not have to be stained extended their lifetime because strong oxidative staining agents have been seen to destroy samples in a period of days. In the course of this work, however, several samples such as the binary blend of nylon-6 and MSN(3/100) were stained to enhance contrast of the nylon-6-rich regions where little or no siloxane polymer was present. The following sections are arranged into discussion of the morphology as interpreted from WAXS and SAXS and visualized from microscopy for the homopolyamide-6 followed by discussion of the copolymer morphologies and finally the binary and ternary blend morphologies.

2. Nylon-6 Homopolymer

The nylon-6 homopolymer used extensively in this work was Allied Chemical Co. Capron which had molecular weights given above. It was used as received since Allied had extracted the polymer before shipment. After dissolution in TFEtOH, the polymer was cast into film via spin casting at 40°C, 0.5 SCFH N_2 for ca. 90 hours from a 2.5 % w/v solution or static casted in Teflon^R-coated aluminum foil "boats" in dessicators with a prescribed solvent flow rate. Most of the copolymer/blend films were prepared via static casting due to the limited supply of copolymer

whereas most of the homopolyamide-6 films were prepared by spin casting. Some homopolyamide-6 also was prepared via static casting for cross-comparison. The casting technique was unimportant if melt annealing was done which reformed the microstructure of these films. About 90 minutes was required with the homopolyamide-6 (Capron) to obtain well defined spherulitic structure in melt annealed, spin cast film as seen in Figure 8-2a. This is an optical light micrograph using transmitted light with crossed polars and shows spherulite diameters of approximately 25 μm which completely filled the volume of the sample. The longer melt annealing times (~ 90 min.) were needed to transform the morphology from the fibrillar material produced by the spin caster to these fully developed spherulites. The static cast films on the other hand, were spherulitic originally and did not have to be held in the melt for such long times. In the OLM micrograph, the dark "cross" regions are where the net polarization of the light caused by the sum of the lamella optical axes coincides with the optical axes of the analyzer/polarizer and complete extinction of the lightwaves occurs. When the material's optic axes are not coincident with the analyzer/polarizer, the phase change of the refracted light induced by the birefringence of the lamellae creates a component of the electric light vector oriented parallel to the analyzer which is then transmitted to the viewer through the lenses. This birefringence produces the familiar Maltese cross

---

Figure 8-2 (see next page) Top panel, a) optical micrograph of bulk hydrolytic nylon-6, melt annealed and cryotomed at −30°C. Contrast enhanced by OsO_4 staining before sectioning.
Bottom panel, b) polarized OLM of melt annealed MSN(3/100) cryotomed at −110°C.

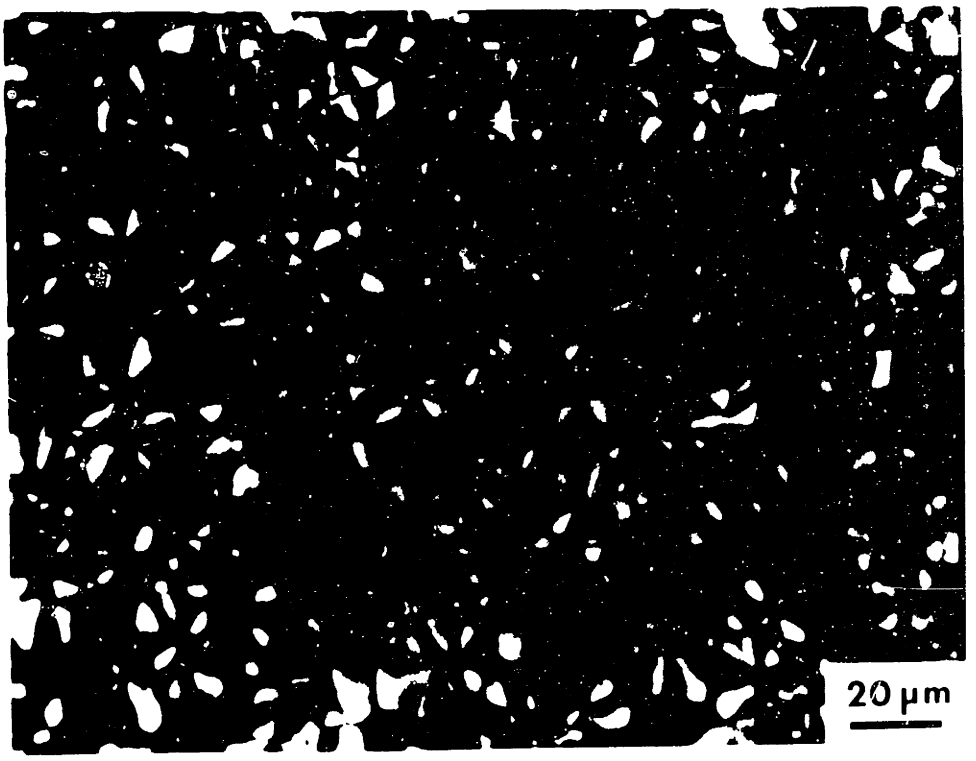

Fig. 8-2a,b
p. 362

pattern for spherulites sectioned diametrically as seen in Figure 8-2a. Note that Figure 8-2b will be discussed shortly.

Wide angle x-ray scattering of the melt annealed (Allied), slow-cooled nylon-6 is shown in Figure 8-3a, curve 1 for a 2θ range from 8° to 42°. The WAXS equipment was a Rigaku Rotaflex with a rotating anode which operated at 50kV and 60mA produced CuKα radiation filtered electronically and with nickel film. Detector to sample distance was 185mm with a powder sample goniometer and the scans were obtained with a 0.2° step program with a collection time of 10 seconds per step. No smoothing of the data was done. The two prominent α-form peaks at 20.43° (200) and 24.00° (002) with a small portion of γ-form at 21.46° (200) are evident in the melt annealed hydrolytic nylon-6. A curve fitting program designed by Dr. A. Galeski of the Centre of Molecular and Macromolecular Studies, Polish Academy of Sciences, Lodz, Poland was used to determine that there was approximately 90 % α-form crystallinity and 10 % γ-form in this nylon-6. A very similar spectrum is obtained for the as-received Monsanto reaction injection molded (RIM) nylon-6 with major α peaks at 20.17° and 23.77° with a γ shoulder at 21.65° which are all slightly lower (in 2θ) than for the Allied, spin cast and melt annealed sample. This difference is attributed to be negligible. Approximately 23 % γ phase is seen in the anionic nylon-6 which crystallizes as it polymerizes; thus, the processing of these two types of nylon-6 is very different and the nylon which crystallizes during polymerization is seen to contain a slightly greater amount of nonequilibrium γ phase. All nylon-6 samples (homopolymer as well as copolymer) exhibited the well known interference peak at ca. 38.5° indicative of the 2.33 Å half-width

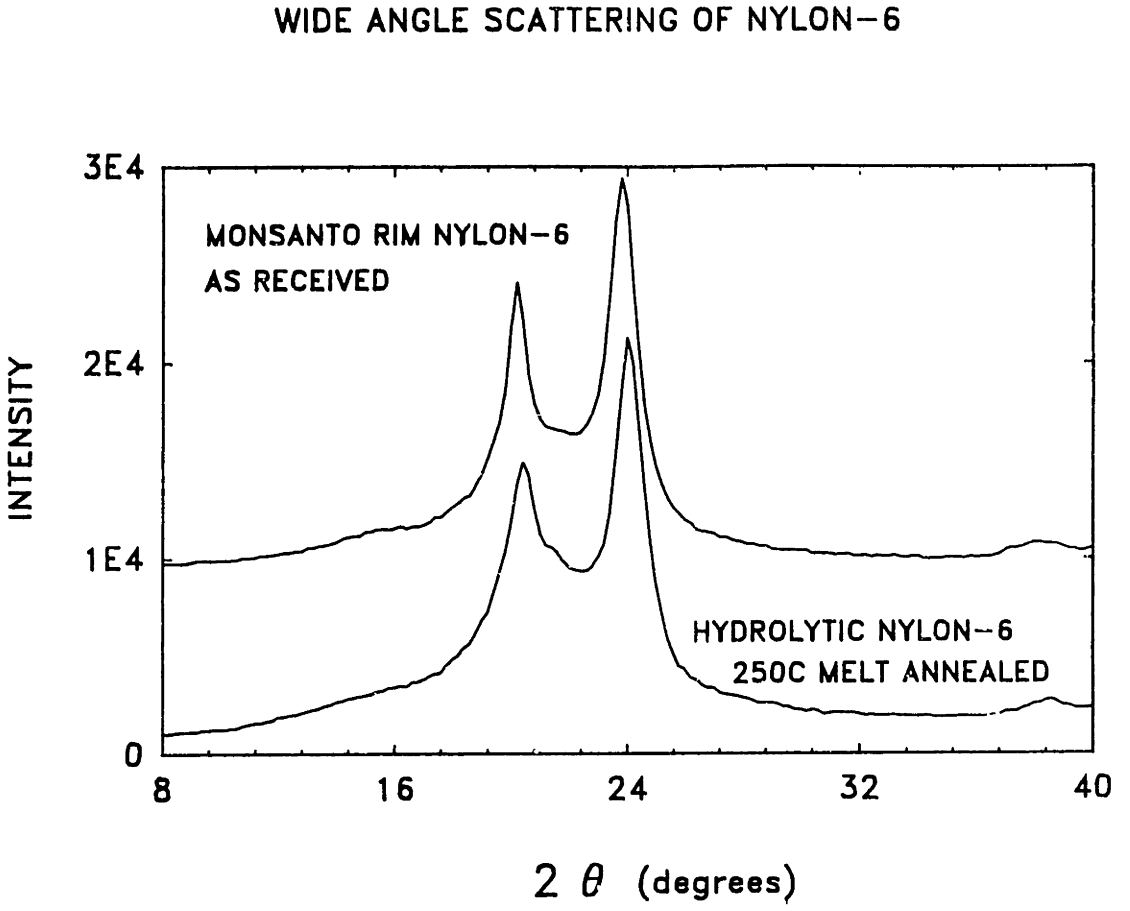

Figure 8-3 Wide angle x-ray scattering of hydrolytic, melt annealed nylon-6 and commercial RIM anionic nylon-6.

between hydrogen bonded chains, as reported by Geil [7]. Details of the WAXS angles for the homopolyamides are given in the first two rows of Table 8-2.

Table 8-2

WAXS Results for Nylon-6 and Copolymers

	Peak Assignments (2θ degrees)				% Crystallinity	
Sample	γ_1 (020)	α_1 (200)	γ_2 (200)	α_2 (002)	α	γ
Allied melt anneal	–	20.43	21.46	24.00	89.6	10.4
Monsanto RIM nylon6 as rcvd	–	20.17	21.65	23.77	77.3	22.7
MSN(3/100) annl 180C	–	20.17	–	24.00	91.0	9.0
MSN(3/100) melt annl	10.88	20.43	21.27	23.39	51.8	48.2
USMSN(15/44) melt annl	–	20.43	21.57	23.77	82.8	17.2

3. Polydimethylsiloxane-Nylon-6 Diblock Copolymers

The three PDMS-nylon-6 copolymers discussed in the synthesis chapter VI, give very different morphologies depending on sample preparation and thermal history. In solvent casting, this variance is due primarily to the differences in solubility of the siloxane and polyamide blocks which affect crystallization rates and phase separation behavior. For melt annealing the already-cast films, the greater melt viscosity (as compared to solution) combined with the immiscibility controls the

morphology by preventing long-range ordering and diffusion of the chains; they are essentially locked into their phase separated morphology. In this section the resulting morphologies of the three diblock copolymers MSN(3/100), USMSN(15/44) and MSN(0.5/15) from both solution casting and melt crystallization will be presented as revealed by TEM and OLM.

Ultra-thin films were formed on TEM grids as described in the previous section, §C.1, annealed at the respective temperatures of either 100°C or 250°C (melt annealed) and examined in a Phillips 300 EM or 400 EM microscope at an accelerating voltage of 100kV or 120kV, respectively. The 300EM was equipped with a high resolution stage whereas the 400 EM used a single tilt specimen stage.

MSN(3/100)

As discussed in Chapter VI, this copolymer has a short, very high polydispersity siloxane block with a number average block molecular weight of 3 kg/mole and a molecular weight of 100 kg/mole for the nylon-6 block. Its morphology as cast from TFEtOH and annealed at 100°C, full vacuum is shown in Figure 8-4a,b revealing spherulitic (more specifically axialitic) morphology with the darker regions, approximately circular (in cross-section) regions of ca. 0.1 μm being the siloxane block of the copolymer due to greater electron density. The spherulites are seen to be only several microns in diameter from Figure 8-4a. No stain was used to achieve the contrast which clearly defines the lamellae as seen

---

Figure 8-4 (see next page) Transmission electron micrograph of MSN(3/100) cast from TFEtOH; a) low magnification top panel, b) medium magnification, bottom panel.

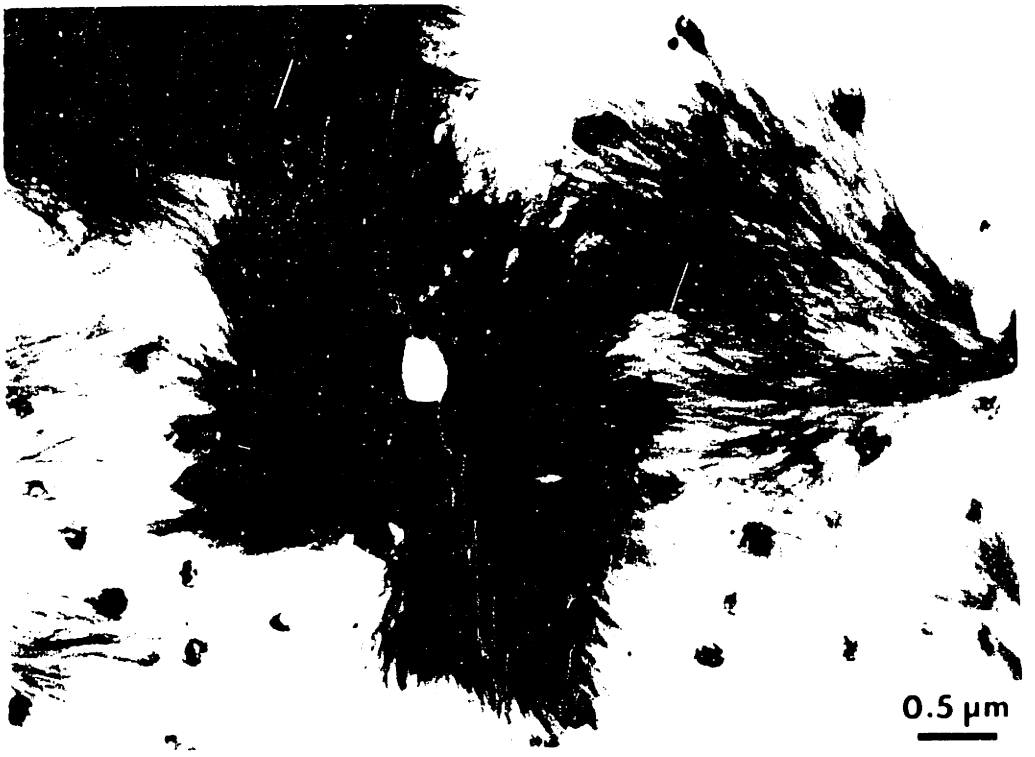

Fig. 8-4a,b
p. 367

at higher magnification in Figures 8-4b and 8-5a,b to emanate from the center of the spherulites and run continuously without interruption all the way to the boundaries. Branching from secondary nucleation creates additional lamellae in the "fan" regions to fill the volume. The excellent contrast is provided by the very short, oligomeric siloxane chains still bonded to the polyamide-6 blocks which are excluded from the chain-folded crystal into the amorphous, interlamellar domains. All four panels, a and b of Figures 8-4 and 8-5 show the randomly distributed spherical-type domains of the longer siloxane blocks phase-separated from the polyamide-6 before crystallization occurred. This was due to the immiscibility of the longer siloxane blocks with the solvent, TFEtOH. Crystallization then proceeded from heterogeneous nuclei around the established domains of rubber to fill the volume with spherulites.

In some areas the siloxane content is higher as evidenced by a greater population density of rubbery inclusions as in Figure 8-5a. This morphology supports the postulate that phase separation of the rubber preceded crystallization, otherwise substantial amounts of the rubber would be rejected and segregated to the interspherulitic regions and not be randomly distributed over the volume of the sample. The large number of rubber domains does not affect noticeably the lamellae that are nucleated near the center of the spherulite (or axialite) and grow along the major axis as shown by arrows from numbers '1' and '2' since these

---

Figure 8-5 (see next page) Transmission electron micrograph of MSN(3/100) cast from TFEtOH at higher magnification showing rubbery domains and different types of lamellar growth. For explanation of the numbers see the text; a) top panel, b) bottom panel.

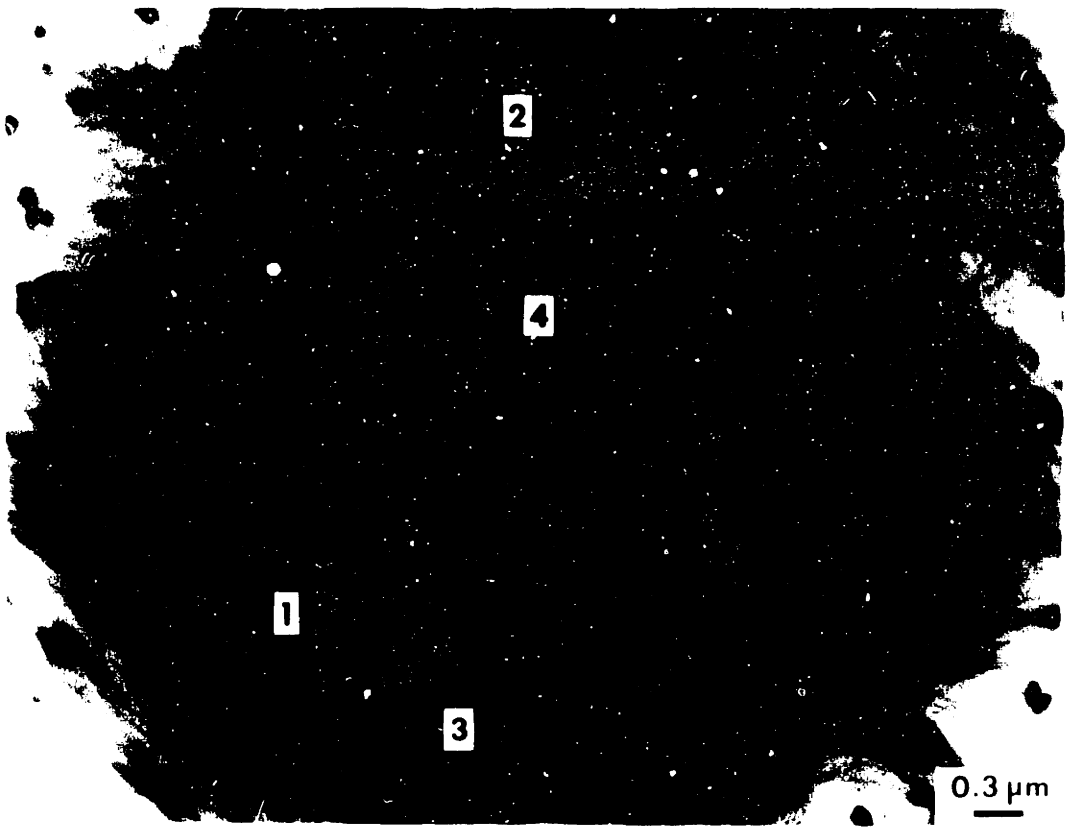

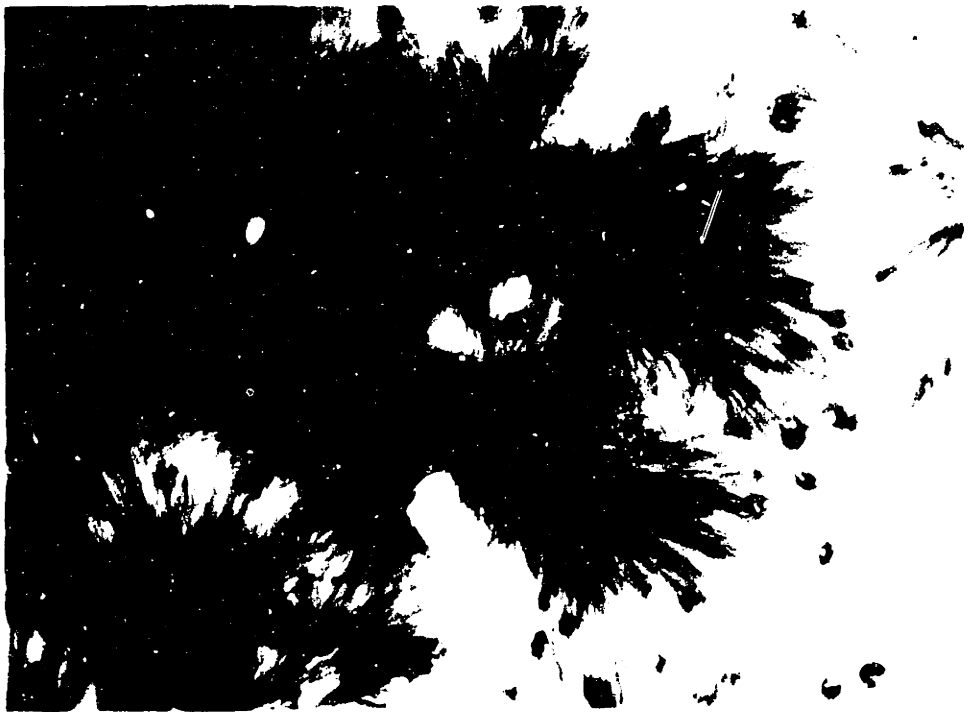

Fig. 8-5a,b
p. 369

lamellae are still smooth, less wavy and seem less perturbed. They do not appear to be strongly influenced by the separate siloxane domains and either push them to the side (due to the lower viscosity created by the solvent) as shown around the radial sheaf at '1' (also notice the other side of the sheaf from the number '1') or simply occlude the domains as seen in the radial sheaf at '2'.

Yet despite this nearly total independent growth of the lamellae along the major axis of the axialite with respect to the presence of the rubber domains, the transverse growth seems more perturbed possibly due to the rubber. The lamellae change from generically smooth structures with low angle noncrystallographic branching to more wavy, zig-zag forms. Branching at much greater angles is occurring (look just to the right of '1' and above '3') and continues throughout the entire transverse (or equatorial) region until impingement and overgrowth occurs. This "zig-zag" growth is not as noticeable in Figure 8-5b where a lower concentration of rubber exists and the lamellae resemble more of the smooth, gently curving, gradual fanning outward structures found in bulk, nylon-6 spherulites by Galeski, et.al. [9] and in binary blends of MSN(3/100) with pure nylon-6 homopolymer as discussed in Chapter II, §B.2. The reason for the development of this sharp, high angle lamellar branching, which is more noticeable in panel a, may be due to density constraints (volume-filling requirement) but is not known for certain,

---

Figure 8-6 (see next page) High magnification TEM of MSN(3/100) cast from TFEtOH showing clear lamellar definition; a) top panel, b) bottom panel; refer to text for description about '1', '2'.

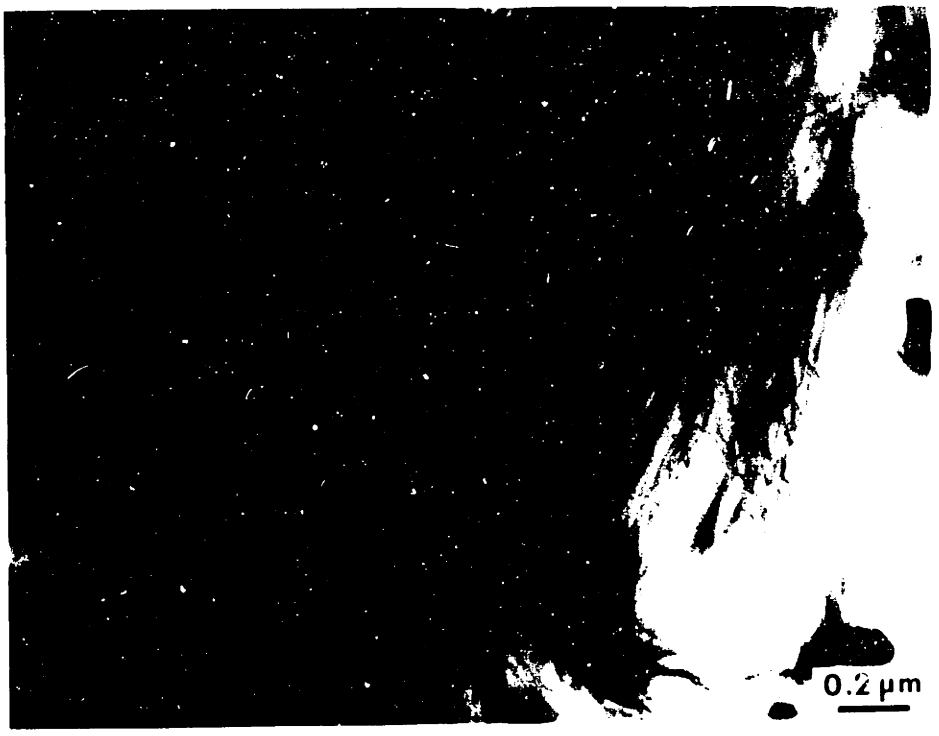

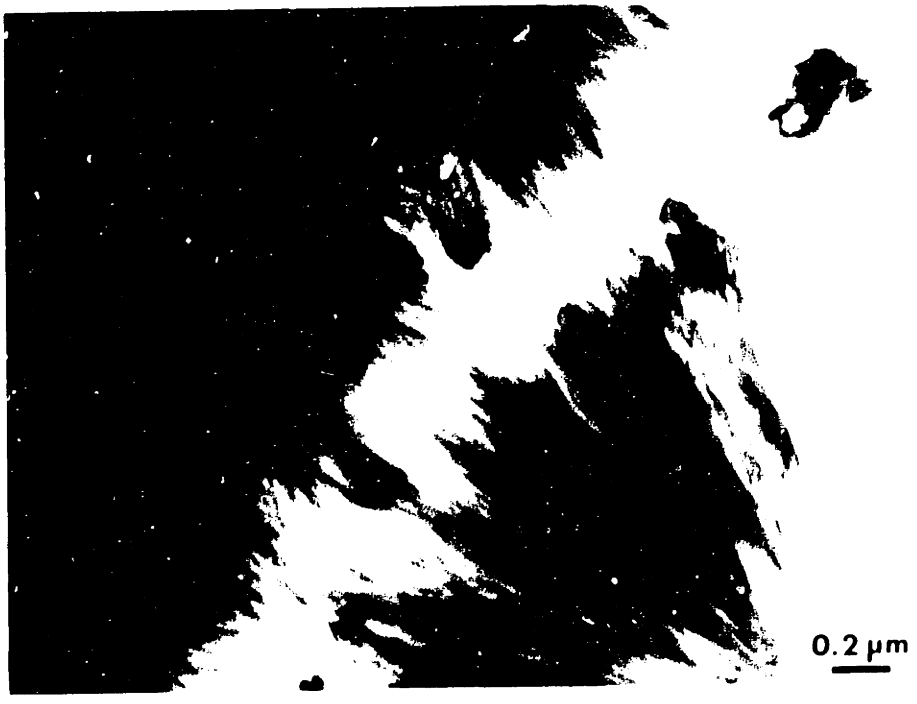

Fig. 8-6a,b
p. 371

nor is it understood why some spherulites possess more of this morphology than others.

Closer inspection of these "rubbery-dotted" spherulites shows that the rather large rubber particles are not completely amorphous, i.e. some appear to be composite particles of nylon-6-PDMS copolymer instead of completely phase separated siloxane rubber. This is shown in Figures 8-6a,b as well as Figure 8-5a where the particles seem to either contain nylon-6 within the particle (lighter regions, point '2', Figure 8-6b) or are aggregates of several smaller particles (near '1', '3' and elsewhere in Figure 8-5a). This aggregation is unusual because the nylon-6 "sheath" or corona around the siloxane should act like a surfactant, sterically shielding the siloxane cores from close proximity of other siloxane particles. Apparently, the crystallization/orientation of these corona polyamide-6 blocks may have perturbed the sheath enough to accommodate the observed aggregation. These corona nylon-6 blocks are free to crystallize either entering the growing lamellae or chain folding into their own independent domains as is observed by the particle at point '1' in Figure 8-6a. This particle seems to be able to fold one half (hemisphere) of its polyamide-6 chains into a passing lamellae (near the number '1') while coordinating chains from the other side of the particle into a different lamellar bundle with similar lamellae from a neighboring particle (located above and to the right of '1'). This "backside" lamellar bundle is much less dense than those generically related to the axialite nucleus as is seen well to the left of '1' which participate in the main growth sheaf. Thus, this micrograph provides direct visual evidence that these phase separated siloxane regions can

act as macro-nucleating agents and initiate crystallization independent of the (presumed) heterogeneous nucleation of the spherulites. This was shown mathematically by the higher crystallization rate constants of the diblock over the homopolymer in Chapter VII. As seen in Figure 8-6a,b, some of these siloxane particles can be rather large due to the presence of very high siloxane block molecular weights caused by the random scission and chain transfer that occurred during catalyst addition in their synthesis.

If this MSN(3/100) copolymer is subsequently melt annealed from the casted state, i.e. heated above the melt temperature and cooled at a moderate rate, the morphology is dramatically altered. This is shown in Figures 8-7a,b, two TEM micrographs of different regions of the same melt annealed film. Notice that all the siloxane has pooled together in a micellar organization with a siloxane core and a nylon-6 corona/matrix due to the strong incompatibility of the two components. The two micrographs of panels a and b reveal different size particles ranging from ca. 50 Å up to 500 Å again indicative of the breadth of molecular weight distribution of the siloxane block. Lack of contrast in the matrix implies the absence of silicon; note that the lighter and darker regions of the film are simply due to film thickness effects and not solubilized siloxane. Since no quenching experiments were done from the melt to ascertain its morphology (freezing the structure upon quenching), it is

---

Figure 8-7 (see next page) Transmission electron micrograph of MSN(3/100) melt annealed at 250°C and moderately cooled. Both panels a) top and b) bottom from same sample.

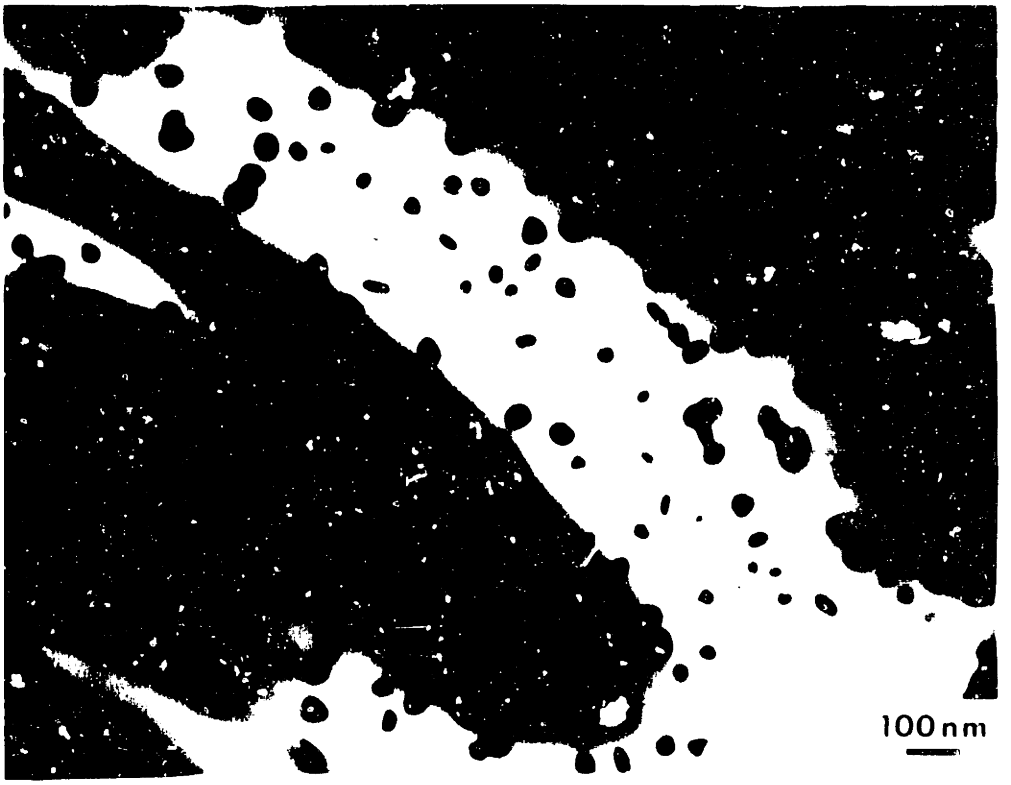

Fig. 8-7a,b
p. 374

difficult to say where the MST (microphase separation temperature) occurs presuming it even exists at temperatures between 25° and 250°C. Estimation of the Flory interaction parameter at 25°C gives $\chi_{AB} \approx 4.3$ which scales inversely with temperature so that $\chi_{AB} \approx 2.8$ at 250°C which is not enough of a reduction to solubilize the PDMS in molten nylon-6 except for possibly oligomeric siloxane blocks. Thus, even in the melt, the micellar structure probably persists which is subsequently frozen-in upon cooling. Due to the high viscosity and incompatibility of the two blocks, sufficient reorganization of the crystallizable nylon-6 chains anchored in the micelle is presumed to be impossible. This hypothesis can easily be tested by using high temperature SAXS when available.

Since no silicone is present in the matrix (except for an imperceptible soluble fraction), the morphology of the nylon-6 matrix is not discernible in the TEM due to a lack of electron density contrast. Previous experience with phosphotungstic acid (PTA) stain revealed artifacts (speckles and grains) at high magnification only (~ $2x10^5$X) in TEM micrographs. Thus, TEM would not be likely to unambiguously reveal the morphology in the matrix of MSN(3/100). As a result, crossed polarization OLM was done on a cryotomed section, ca. 5 μm thickness, of the bulk, cast, melt annealed film to check for the presence or absence of spherulites. The material was sectioned at −120°C in a LKB Cryoultramicrotome V without embedding or fixation. The micrograph is shown in Figure 8-2b and reveals no super-micron spherulitic structure as found by TEM of the solvent cast films of Figures 8-4,5,6. This confirms the hypothesis that organization into mature, chain folded spherulites is not possible from the melt due to the mesophase structure and the high

viscosity. It simply requires too much free energy to reptate even the shortest siloxane blocks through the incompatible polyamide-6 melt into a spherulitic, chain folded habit. This does not preclude the existence of sub-micron spherulitic embryonic structures as found by Schaper et.al. [10] in rapidly quenched samples. Nor does it preclude the possibility that the interstitial regions resemble chain folded, highly birefringent crystal structures as depicted schematically by Kawaii [36] and reproduced in Figure 2-8, Chapter II. Both or either of these two morphological entities are possible in the interstitial regions of this sample. Regardless, this lower degree of crystallinity inferred from the micrographs is confirmed by DSC and density measurements of the cast film versus the melt annealed material as detailed in Chapter VII, §A.2a. The ΔH_f for the solution cast material was 27.65 cal g^{-1} versus 9.61 cal g^{-1} for the melt annealed copolymer corrected for the homopolyamide-6 content. Based on a purely crystalline nylon-6 heat of fusion [37] of 45.4 cal g^{-1}, the crystallinity level dropped from 60.9% to 21.2% as a result of melt recrystallization.

Wide angle x-ray scattering data of this copolymer are shown in Figure 8-8a, curve 1 representing the film cast from TFEtOH solution and annealed 180°C, 16 hours, full vacuum versus melt annealed, moderately cooled, copolymer in curve 2. These data show the presence of the α-form in the solution casted material although the (200) reflection at 20.17° is much suppressed as compared to the (002) reflection from 2θ = 24.00°. This could be due to: 1) orientation from solution where stacking of the hydrogen bond planes normal to the c-axis of the unit cell is preferred or 2) differences in crystal size in the directions

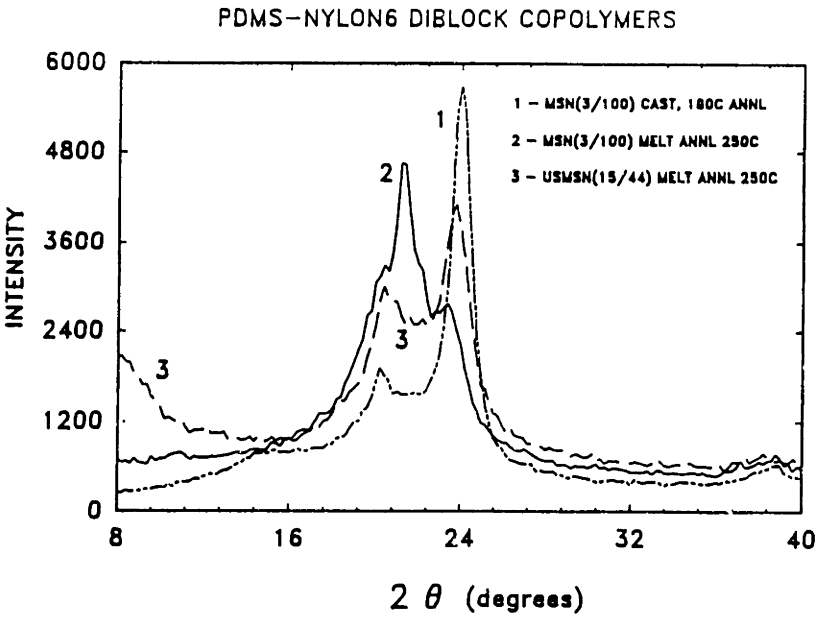

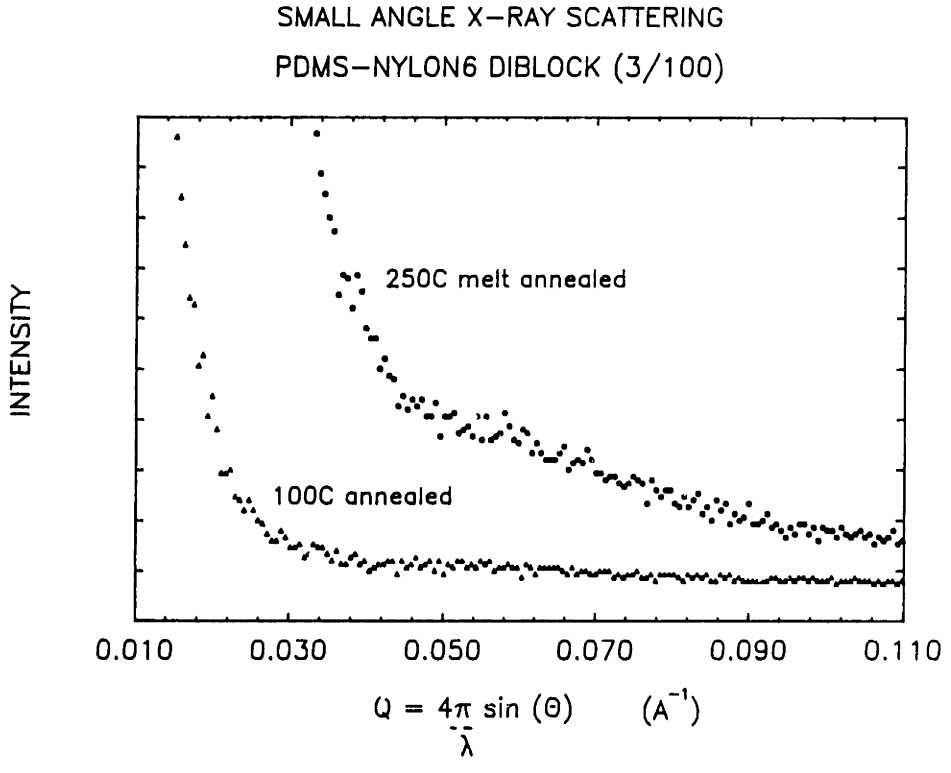

Figure 8-8 a) WAXS of MSN(3/100), curve 1 - solvent cast from TFEtOH and annealed at 180°C, curve 2 - melt annealed 250°C and USMSN(15/44), curve 3 - melt annealed 250°C; top panel. b) SAXS of MSN(3/100) melt annealed and annealed 100°C after casting; bottom panel.

normal to these two sets of reflecting planes. This would occur if reflections from planes along the c-axis are greater than those along the a axis of the unit cell. This situation is possible in lamellar habits provided the lamellae are not randomly oriented in space. Otherwise, the diffraction signal would not be stronger from that particular plane.

The melt annealed material, unexpectedly possesses a much greater proportion of the γ-form crystals as seen in Table 8-2 which shows 48 % γ-form crystallinity versus only 9 % γ-form in the solution cast, 180°C annealed material. The reason for this greater percentage of γ-form crystals is unknown and has not been seen before in material melt crystallized at such high temperatures; normally γ-form is produced at $T_c \leq 130°C$ or so. Based on half-times of crystallization obtained by independent DSC measurements, the crystallization rate is too rapid to have occurred at temperatures much lower than 170° – 180°C ($\tau_{1/2}$ = 10 min for MSN(3/100) versus $\simeq 10^{-2}$ for nylon-6; data not disclosed elsewhere). Note that melt annealed USMSN(15/44) shows a majority of the α-form, curve 3 which was formed under identical conditions and will be discussed in the next section.

Small angle scattering of copolymer MSN(3/100) cast from solution and annealed at 100°C versus melt annealed at 250°C is shown in Figure 8-8b. Essentially no discrete peaks indicative of interparticle scattering are seen. A slight shoulder is seen for the melt annealed material with a broad maximum roughly at 100 Å spacing from the Bragg law. This lack of intense particle or lamellae scattering could be due to a large interparticle distance of ca. 0.5μ which is too small (in Q units) for resolution. Alternately, the lack of a broad maximum for the as-cast,

100°C annealed material and the weak peak for the melt annealed material can be explained by Hosemann's theory [34]. If the polydispersity of the overall system is greater than the packing density, only continuous scattering will result. Since the siloxane block length is known to be extremely polydisperse (see Figure 6-5b), this sample may simply possess these attributes which explains the observed behavior in Figure 8-8b.

USMSN(15/44)

The polymer produced by ultrasonic copolymerization of ω-acyllactam-PDMS and ε-caprolactam has been characterized in Chapters VI and VII. It has a narrower siloxane block polydispersity due to chemical improvements in the synthesis and $\bar{M}_n^s$ = 15 kg/mole with $\bar{M}_n^n$ = 44 kg/mole. The morphology of this copolymer as cast from TFEtOH by the same ultrathin film technique as before is shown in Figure 8-9a. The spherical siloxane domains are clearly evident and possess a very similar radial dimension indicative of a narrow polydispersity rubber block. The domains appear to be largely amorphous, i.e. no composite particles formed with intraparticle nylon-6 chains and they are characteristically 200 – 300 Å in diameter. No real long range order exists in these samples although some regions resemble a hexagonal close packed structure; the irregularity probably coming from the polydispersity of the nylon-6 chains due to transamidation and branching during polymerization

---

Figure 8-9 (see next page) Transmission electron micrographs of USMSN(15/44) as a) cast from TFEtOH solution or b) melt annealed at 250°C with an exceptionally slow cooling rate. See text for details.

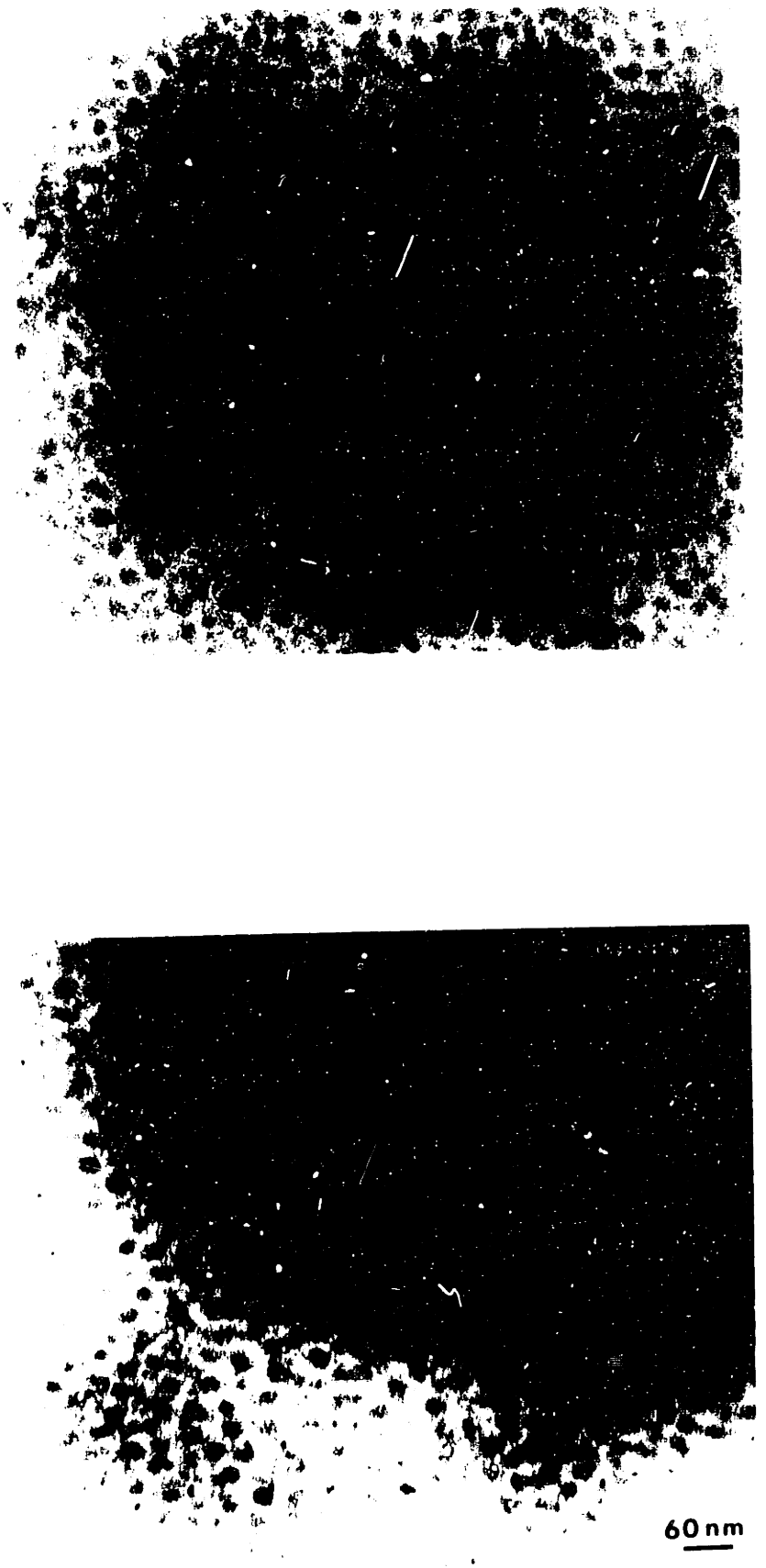

Fig. 8-9a,b
p. 380

as detailed in Chapter V. This type of morphology is indicative of phase separation of the large siloxane rubber chains prior to precipitation and crystallization of the nylon-6 blocks due to the large incompatibility of the siloxane with the TFEtOH solvent.

The melt annealed material, i.e. this same sample heated to 250°C for 10 minutes was cooled from the melt at an extremely slow rate; from 250°C to 220°C in 30 minutes followed by 0.2°C/min reduction until 200°C followed by subsequently cooling to 25°C in ca. 35 minutes. This was done to hopefully a morphology as close to equilibrium as possible through slow cooling. This processing gave the morphology shown in panel b, Figure 8-9 and appears identical to the solvent cast sample in panel a. This is in sharp contrast to the difference in morphologies of MSN(3/100) cast and subsequently melt annealed, Figure 8-4 versus Figure 8-7 for example. The USMSN(15/44) material, in either preparation method undergoes phase separation before crystallization whether the siloxane blocks precipitate from the solvent or phase separate in the melt. This observation is quite reasonable because the solvent TFEtOH, is nearly an athermal solvent for nylon-6 (χ_{AB} = 0.09) and the siloxane blocks see similar environments whether in solution (actually micellar dispersion) or in the melt. Even with the reduced viscosity of the solvent in the cast preparation method, the incompatibility of the siloxane is simply too great to facilitate break-up of the micelles to accommodate chain folding into a spherulitic microstructure. Thus, larger molecular weight amorphous blocks in a poor solvent for them favor phase separation before crystallization, forcing the chain folding to occur in the interstitial regions around the siloxane domains.

This restriction of the crystal blocks to the interstitial region does not necessarily dictate a decrease in crystallinity as compared to more spherulitic microstructures, for example. Nor does this spherical mesophase with interstitial crystallization represent a significant departure from equilibrium (as compared to the morphology shown in Figure 8-10 which will be discussed shortly). On the contrary, exceptionally high crystallinities were found in USMSN(15/44) as cast from solution and were discussed in Chapter VII. Thus, the overall free energy can be minimized to the greatest extent via this morphology because phase separation and crystallinity can both occur to a large degree to give the lowest ΔG_{TOT}. That is, the free energy gained by crystallization plus that gained by phase separation are both large (in the negative sense) and neither one is forced to "give up" free energy at the expense of the other process. This occurs despite the mesophase control of the morphology. Because of a lower total free energy, this block copolymer forms spheres instead of lamellae even though its ratio of crystal:amorphous repeat units is well within the range studied by Gallot, et.al. [46], who obtained only lamellar structures for PEO-PS. This fact may be appreciated by theoreticians such as Noolandi who have published equilibrium thermodynamic theories to predict crystal-amorphous morphological parameters for strictly lamellar habits.

Figure 8-10 (see next page) Transmission electron micrograph of USMSN(15/44) cast from a 2:1 Toluene:TFEtOH v/v solution.

Fig. 8-10
p. 383

Theoretically, if the solvent compatibility for the amorphous block could be enhanced while simultaneously decreasing the affinity for the crystalline block, phase separation could be delayed permitting crystallization to commence first possibly leading to a different morphology. This experiment was attempted by using a 2:1 v/v mixture of toluene/TFEtOH which, at room temperature, still dissolved the US-MSN(15/44) diblock copolymer (precipitation at ca. 73 %v toluene and a polymer concentration of ~ 0.6% w/v). The resulting morphology from ultra-thin film casting from this solvent is shown in Figure 8-10 where substantial orientation of the film is seen despite no imposed strain during film formation. Dozens of grid squares (thousands of microns) were similarly oriented, not only with the same texture but with all the domains aligned in the same direction. To the author's knowledge this macroscopic orientation of a block copolymer cast from solution has not been seen before in unoriented film and represents new possibilities for anisotropic morphologies such as in selective directional permeation. The domains are not perfect lamellae as found by Lotz, et.al. [38] or Gallot, et.al. [46] for PEO-PS as an example, but do possess substantial lamellar appearance which is quite different from the morphology of spherical domains as cast from pure TFEtOH. The effect of the solvent is seen more dramatically when the as-cast morphology in Figure 8-9a is compared to Figure 8-10. It is postulated that the toluene selectively swelled the siloxane blocks in solution causing the polyamide-6 to precipitate out of the toluene-rich solvent and crystallize before or simultaneously with phase separation of the siloxane block from solution. This is plausible because the TFEtOH has a lower boiling point and

would evaporate more quickly further driving the crystallization process before phase separation.

The appearance of the domains in Figure 8-10 typifies a highly nonequilibrium morphology. Perhaps if the casting process could be slowed down or if this sample were to be heated for a prolonged time just under its melting point, the lamellar morphology would become more distinct and well-defined. Alternatively, this may promote transformation back to the morphology seen in Figure 8-9, the spheres of PDMS in a matrix of nylon-6. Regardless, the possibilities of altering the morphology as determined by the compatibility of the respective blocks with selective solvents offers great potential in creating varied, functionalized morphologies for specific end uses.

Wide angle x-ray scattering of the melt annealed USMSN(15/44) is shown as curve 3 in Figure 8-8a. Predominantly α-form crystals are present in this material, again with the (002) peak at 23.78° being more prominent than the (200) reflection at 20.43° although only slightly. The amount of γ-form crystallinity is calculated to be 17.2 % via peak deconvolution as shown in Table 8-2. The large increase in the baseline at low angle is unexplained, but is not attributed to white radiation noise because the other scans made under identical conditions and at the same time had satisfactory electronic filtration to eliminate this.

MSN(0.5/15)

This copolymer morphology represents the first copolymer synthesized and contains a very short siloxane block as well as a short polyamide-6 block. The former is due to the active lithium caprolactam catalyst used which depolymerized the methylsiloxane and the latter is

due to the stoichiometry to intentionally limit the growth of the nylon-6 block for analytical reasons. As a result, this copolymer does not possess sufficient chain length to support a chain-folded spherulitic habit and consequently phase separates into extremely small, fine rubber particles dispersed in a polyamide-6 matrix as shown in Figure 8-11. Unfortunately, not enough material was available for any additional testing.

4. PDMS-Nylon-6 Binary and Ternary Blends

Binary Blend (43/57)

One binary blend consisting of MSN(3/100) and Allied hydrolytic nylon-6 was studied at a composition of 43/57 % w/w MSN/nylon-6. The exact composition in relation to the other components is depicted on the copolymer-homopolyamide-6 binary axis of the ternary diagram in Figure 8-1 and molecular weights of the constituent blocks and homopolymers are given in Tables 6-2, 6-3. This composition cast from TFEtOH gave a mixed morphology probably due to the fact that the nylon-6 homopolymer was able to heterogeneously nucleate and form homopolymer spherulitic domains. Copolymer molecules containing longer siloxane chains were not able to enter the growing homopolymer crystallites due to density considerations of the large, rubbery chain in the interlamellar regions. Instead, these copolymers with the long siloxane blocks were segregated to other regions forming composite particles with some of the nylon-6 homopolymer

---

Figure 8-11 (see next page) Transmission electron micrograph of MSN(.5/15) cast from TFEtOH

Fig. 8-11
p. 387

solubilized within these domains. This gives rise to dual morphologies which will be discussed separately.

The spherulitic morphology of the cast film has already been shown in Figure 2-5 in Chapter II where contrast was enhanced with PTA solution and OsO_4 vapor staining. Higher magnification of the radial lamellae is depicted in Figure 8-12a which shows ca. 50 – 60 Å thickness with the darker, amorphous interlamellar regions clearly visible in contrast to the white crystallites. Other darker, roughly spherical regions within the radial lamellae represent moderate length siloxane blocks of copolymer MSN(3/100) that participated in the lamellar growth via chain folding of the polyamide-6 block and whose noncrystalline siloxane blocks were rejected by the lamellae and occluded by the spherulite growth front. These siloxane regions were stained dark by complexation of the OsO_4 with the vinyl groups in the siloxane backbone from copolymerization with D_{4H} as described in Chapter IV, §C.

In the transverse regions of some of these spherulites, a wavy lamellar growth is seen as discussed in §C.3 above. Shown in Figure 8-12b is a higher magnification TEM micrograph where the larger angle noncrystallographic branching is easily discernible. No heavy metal stain has been applied to this sample. Note the composite particles of the copolymer in the upper right which were segregated and then occluded by the growing lamellae.

Figure 8-12 (see next page) TEM of binary blend of MSN(3/100) / Nylon-6, 43/57 %w/w cast from TFEtOH; top panel, a) high magnification of lamellae of spherulitic structure shown in Fig. 2-5, b) wavy transverse lamellae, no stain; shows occluded particles

Fig. C-12a,b
p. 389

As mentioned earlier, the other type of morphology seen in this sample was the composite particles found in the intraspherulitic regions (Figure 8-12b) as well as outside the spherulites in the matrix. This morphology was not as prevalent as the spherulitic morphology described above. An example of the composite particles found outside the spherulites is shown in the TEM micrograph of Figure 8-13a. This is a cast sample annealed at 100°C and stained with OsO_4 vapor only and shows the copolymer/homopolyamide-6 composite structure. These particles contain not only copolymer MSN(3/100) but solubilized homopolyamide-6 which mixes with the copolymer because of the lower molecular weight of the homopolymer as compared to the block polyamide-6 molecular weight.

Melt annealing of this material gave the microstructure shown in Figure 8-13b, the expected micellar organized spheres of rubber dispersed in a nylon-6 matrix. Again, since all the siloxane has been scrubbed out of the polyamide-6, no contrast is available for enhancement of the matrix morphology which is probably partially spherulitic where the copolymer concentration is lower and mesophasic where copolymer exists at greater concentration as in Figure 8-13b. Undoubtedly, there is some homopolyamide-6 solubilized within the nylon-6 corona of the copolymer increasing the mean interparticle distance as would be measured by SAXS.

Figure 8-13 (see next page) TEM of binary blend, MSN(3/100)/Nylon-6 43/57 %w/w cast from TFEtOH showing less prevalent, alternate morphology. a) top panel, as cast; b) bottom panel, melt annealed, 250°C.

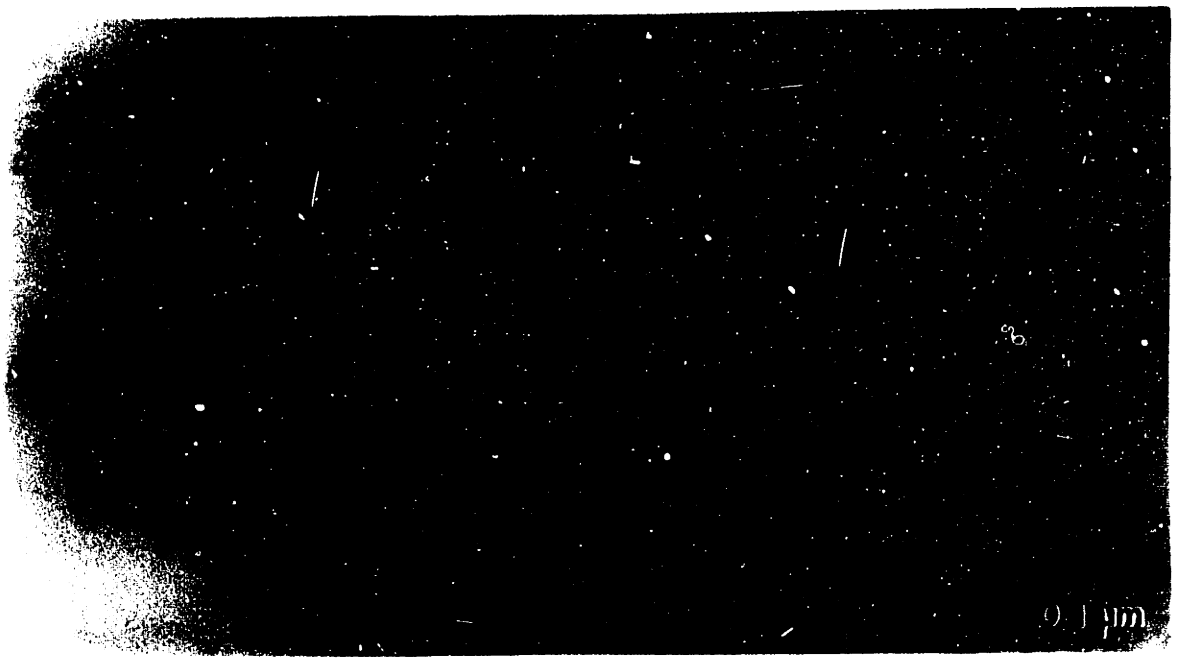

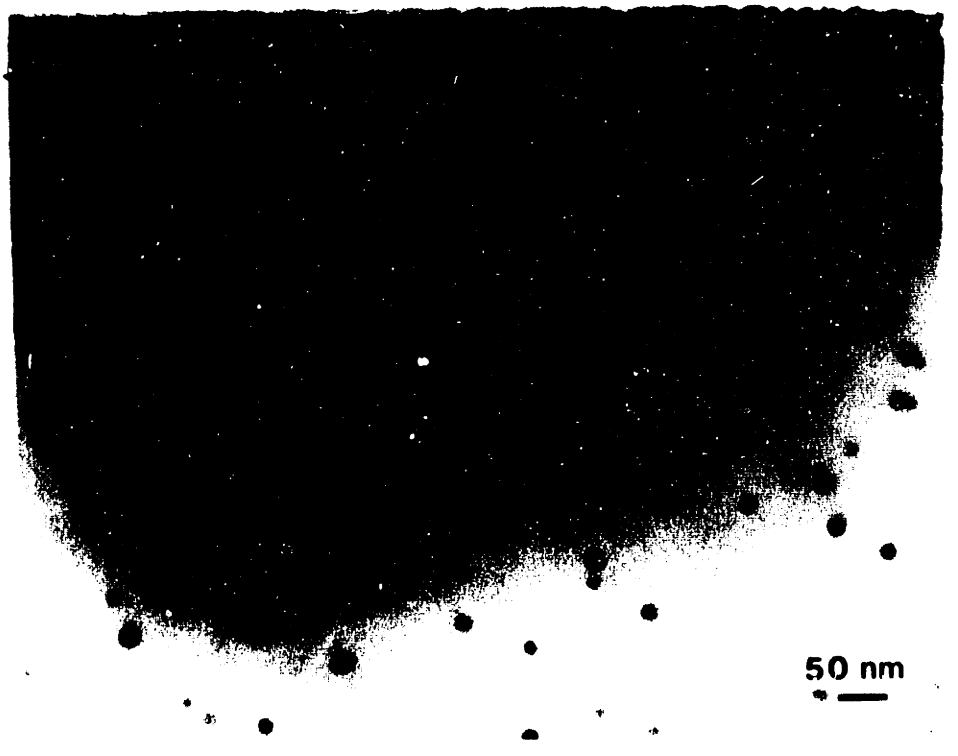

Fig. 8-13a,b
p. 391

Ternary Blends

Two ternary blend compositions were explored to examine the emulsification ability of the copolymer with respect to homopolyamide-6 and homopoly(dimethylsiloxane). These are depicted in the ternary diagram (Figure 8-1) and denoted as the 42/56/2 % w/w/w MSN(3/100)/nylon-6/homo-PDMS (1K) and the 38/51/11 % w/w/w blends. The numbers represent the weight percent of the three components, in order, the block copolymer or MSN(3/100), Allied nylon-6 and 1 kg/mole low molecular weight PDMS. Both solution cast and melt annealed samples were examined in ultra-thin films with the TEM.

Ternary Blend (42/56/2)

The cast film of sample 42/56/2 contained ~ 3.2 %w total rubber and the micrographs are shown in Figures 8-14a,b. The lower magnification micrograph, panel a, depicts the spherulitic structure with occluded homo-PDMS and siloxane blocks of the copolymer that were engulfed by the growing spherulite. The addition of the homo-PDMS decreased the crystallinity to ca. 50% (from ca. 62% in the binary blend solution cast sample) probably by disrupting well-defined lamellar growth similar to results seen with i-PP/EPM [39] or i-PP/EPDM [40] blends. In these latter two examples of i-PP blends, the growth rates and sizes of the lamellae are affected by the presence of a second, immiscible phase. More energy is

---

Figure 8-14 (see next page) TEM of ternary blend MSN(3/100)/Nylon-6/PDMS 42/56/2 %w as cast from solution for both a), b).

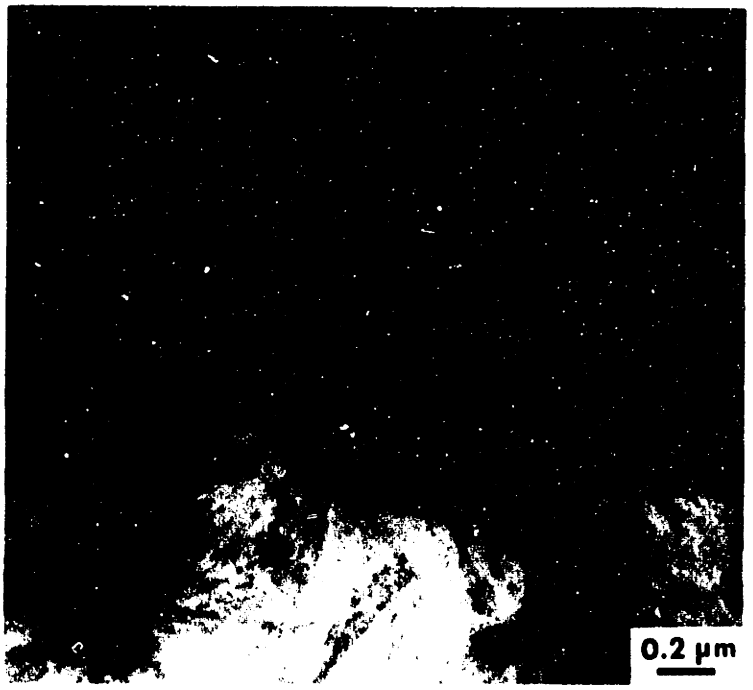

Fig. 8-14a,b
p. 393

required to engulf, reject or deform these rubber particles thus decreasing the spherulitic growth rate. Figure 8-14b, with higher magnification shows a spherulite with occluded and deformed siloxane domains and lamellae which are not as well defined as in crystallization of the pure copolymer in Figure 8-4a,b for example. Although there was some rejected rubber "pools", they were minimal and most of the rubber appeared occluded as in Figure 8-14b. The decrease in growth rates in rubber-crystalline systems will be examined more thoroughly in the Discussion section, §C.5.

The micellar dispersions of the ternary blends are stable in time and do not settle or precipitate homo-PDMS. This is true even if they are quiescent (not stirred) because the copolymer surfactant satisfactorily stabilizes the suspension. However, precipitation of the homo-PDMS during crystallization may occur as seen from the micron-long "rod" aligned along the spherulite radius in Figure 8-14a. This may be due to the precipitation of the homo-PDMS from the micelles as soon as crystallization commences. This is envisioned to occur as a sequence of events beginning with the incorporation of dissolved (in the background solution) copolymer with very short siloxane blocks into the crystallites. This perturbs the micelle equilibrium and causes a shift in the number of copolymer chains from the micelle into the solution to replenish those that crystallized. This in turn results in a decrease of micellized copolymer able to stabilize the pure rubber and thus, some of the micellized homo-PDMS is eventually released from the micelle core. It immediately precipitates from solution due to its incompatibility with TFEtOH solvent and disrupts the growing lamellae to a large degree as

seen in Figure 8-14a. Thus, as copolymer or surfactant is removed from the micellar system by disruption of the equilibrium through crystallization, the once-emulsified PDMS precipitates from solution and interferes with lamellar growth and perfection similarly to that in pure blends.

Melt annealing of this film drastically reforms the morphology as shown in Figure 8-15a,b. The large, supermicron size spherulites have disappeared and are replaced by spherical rubbery inclusions ca. 0.1 μm that contain the emulsified homo-PDMS. There exists no evidence of supermicron size (rubber) particles indicative of two purely immiscible phases such as rubber and nylon-6 dispersed one within another. Thus, the majority of the rubber is believed to be emulsified by the siloxane block of the copolymer and prevented from self-coalescence by the corona of nylon-6 block of the copolymer and from the homopolyamide-6 of the matrix dissolved within the corona.

The matrix itself appears to contain some crystallinity from the weakly defined fibrillar or lamellar spherulitic morphology seen in both Figures 8-15a,b. Differential scanning calorimetry shows that the level of crystallinity has dropped from 50% (solution cast) to roughly 29% in this melt annealed sample which parallels results obtained with the binary copolymer/homopolyamide-6 blend (26%) and the pure MSN(3/100) copolymer (22%) as detailed in Table 7-2. This lower degree of

---

Figure 8-15 (see next page) TEM of ternary blend MSN(3/100)/Nylon-6/PDMS 42/56/2 %w melt annealed; Weak spherulitic structure is seen for both panels.

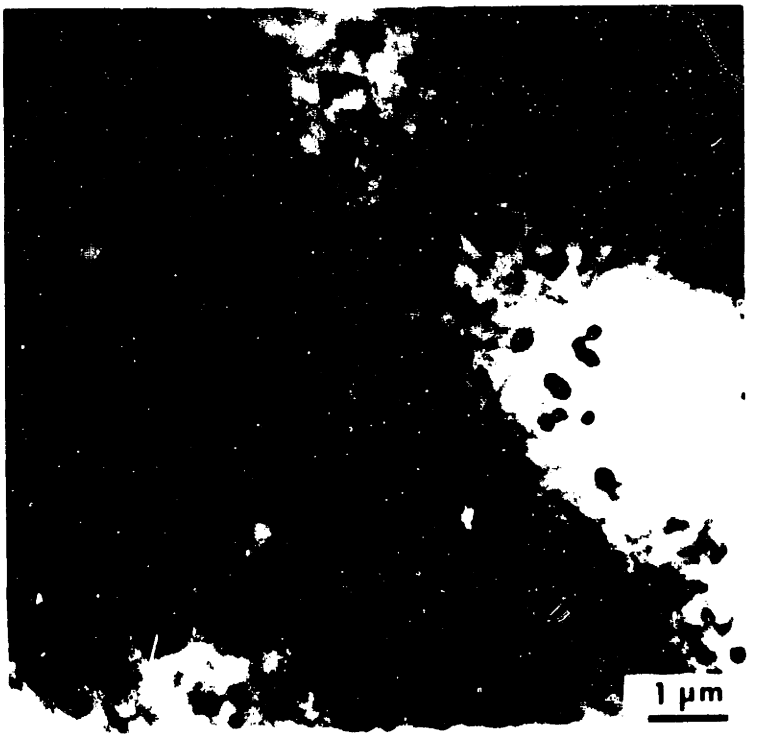

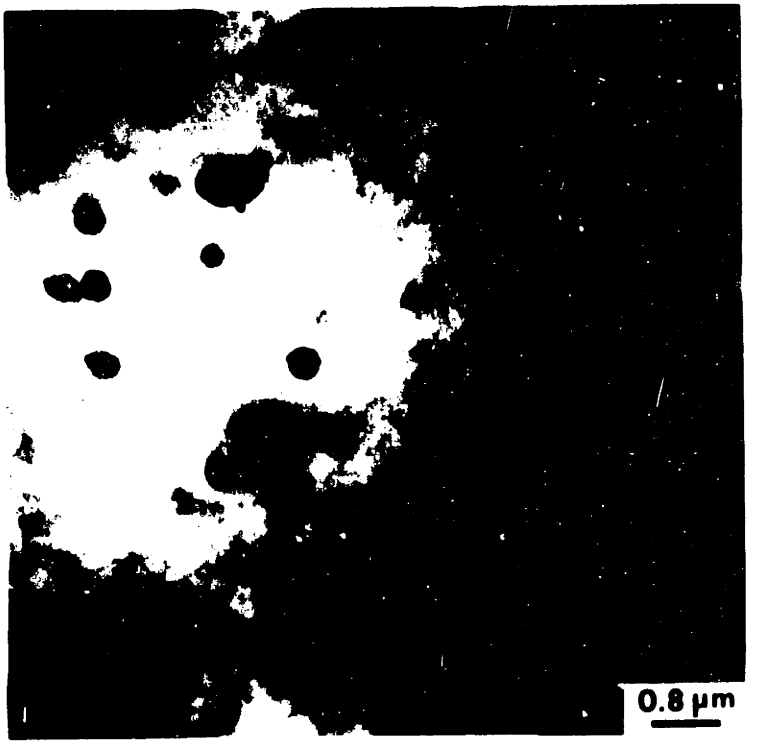

Fig. 8-15a,b
p. 396

crystallinity indicates that the small spherulites which are roughly discernible, are not well developed and contain an appreciable volume fraction of amorphous material as well as large interspherulitic and/or interstitial amorphous fractions.

Ternary Blend (38/51/11)

The solution cast (from TFEtOH) morphology of the 38/51/11 ternary blend is shown in Figures 8-16a,b. The 1–3 μm diameter spherulites are readily seen in Figure 8-16a with good contrast as a result of ~ 12.1 %w total rubber in this sample. This morphology looks like a logical extension of the MSN(3/100) copolymer morphology shown in Figures 8-4 through 8-6 inclusive; approximately spherical domains of siloxane block/homopolymer randomly distributed throughout the lamellar sheafs of the spherulites, only in this ternary blend case, the population of rubbery domains is much greater. This is a very unique morphology with so much free rubber emulsified into extremely small, well dispersed domains within the spherulitic superstructure. Similar results were observed previously by Hirata et.al. for PEO-PI di- and triblock copolymers [36] where they observed the rubber randomly distributed throughout a less well defined spherulitic structure than the one in Figure 8-16a, but no evidence of this type of morphology for ternary blends has been reported previously in the literature.

Figure 8-16 (see next page) TEM of ternary blend MSN(3/100)/Nylon-6/PDMS 38/51/11 %w as cast from solution. Emulsification is evident by the finely distributed rubbery domains throughout the spherulites

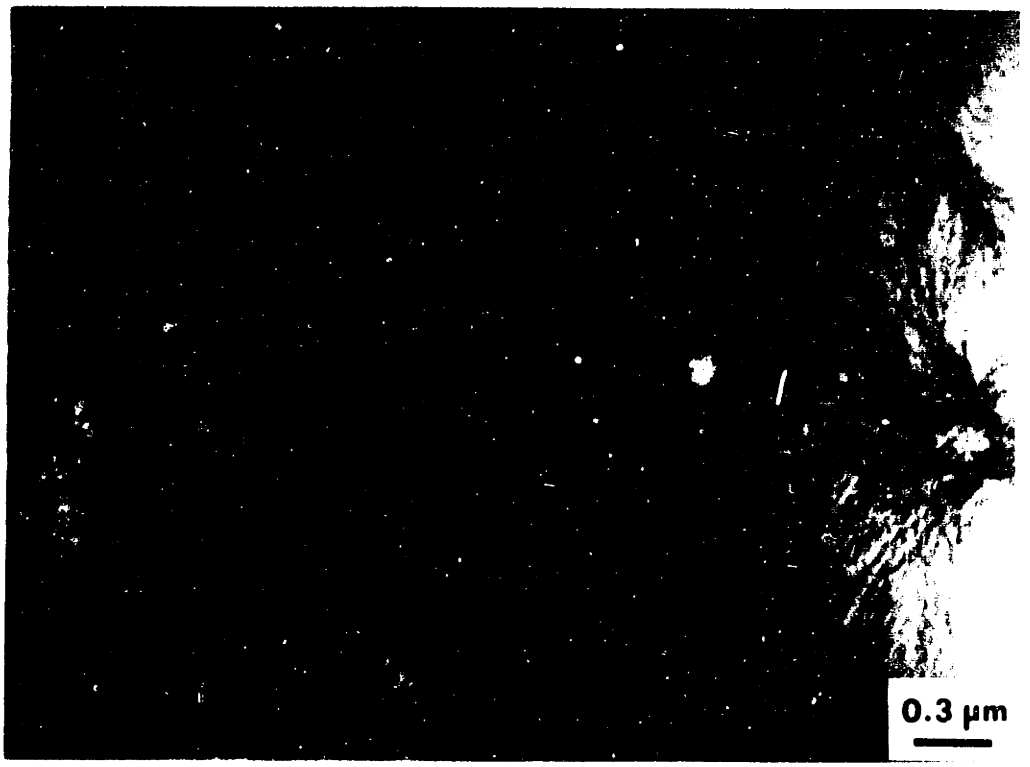

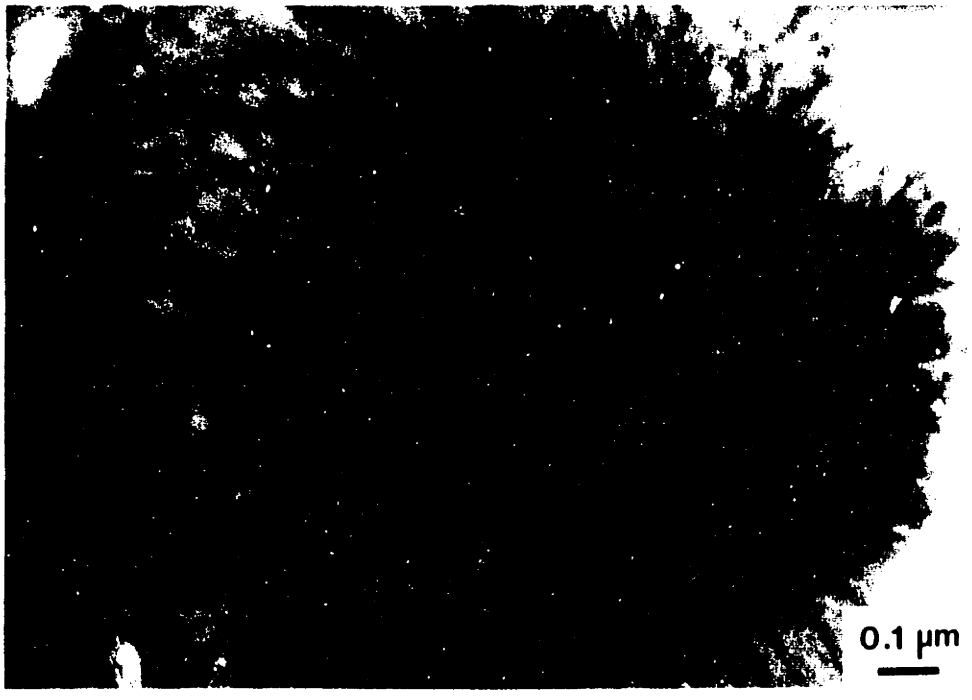

Fig. 3-16a,b
p. 398

The emulsification ability of the MSN(3/100) copolymer is evident in the higher magnification micrograph of Figure 8-16b. Here, the profuse number of rather uniform, ca. 300–500 Å siloxane domains found in all regions of the spherulite(s) is proof of the emulsification ability of the block copolymer in solution. In addition, after several months of sitting on the shelf, the ternary blend solution in TFEtOH remains cloudy, indicative of sufficient stability to keep the microdispersion from coalescing. If the surfactant effect of the copolymer was insufficient, the siloxane domains would have coalesced in solution and formed large pools of homo-PDMS in the beaker but this was not observed. Very few large domain sizes were seen in the copolymer/blend samples examined in this work and were considered isolated instances where local perturbations in the crystal-micelle equilibrium occurred as discussed above.

Differential scanning calorimetry measurements showed an exceptionally large 84% crystallinity for the 38/51/11 ternary blend as compared to 60% for the MSN(3/100) copolymer. Thus it seems that these rubber domains enhance rather than inhibit crystallinity in this sample. A plausible hypothesis often used in the literature to explain enhanced crystallization effects is that heterogeneous nucleating agents from the rubber were washed into solution upon dispersion in TFEtOH and then were able to nucleate a higher density of spherulites. However, this is not supported by the micrographs in Figures 8-16a,b where spherulite size is seen to be roughly the same as in solution cast MSN(3/100) in Figure 8-4. Thus, the higher crystallinity must result from greater perfection within these spherulites and not from a greater number of them.

In addition, the lamellae appear to be much coarser in Figure 8-16a,b than in Figure 8-4a,b probably as the result of larger bundles of lamellae organized together and/or lamellae coated on all sides with primarily homo-PDMS. The PDMS, which was squeezed out of the growing crystallites, would be dispersed around the lamellar bundle thus coarsening the appearance. The higher concentration of rubber contributes significantly to this "overstaining" effect and decreases contrast.

The melt annealed ternary blend 38/51/11 shows different behavior from the melt annealed 42/56/2 blend. The morphology of the former is shown in Figures 8-17a,b where spherulitic behavior is seen even though no stain has been utilized. These spherulites are much larger than those in the 42/56/2 blend, ranging from 2 – 6 μm in diameter, larger than even the solution cast copolymer samples, Figure 8-4. In addition, there is a large number of very small rubber domains (ca. 500–1000 Å) dispersed throughout the spherulites which demonstrate the emulsification ability of the MSN(3/100) copolymer. Thus, the rubber domains are finely distributed for this melt annealed material as well as for its solution cast counterpart. As it appears, this morphology would seem to be very promising as a tough material but due to volatilization of the low molecular weight component of the homo-PDMS during melt annealing, these materials did not extend to strains commensurate with their rubber

---

Figure 8-17 (see next page) TEM of ternary blend, MSN(3/100)/Nylon-6/PDMS, 38/51/11, %w as obtained from the melt. Emulsification ability is demonstrated.

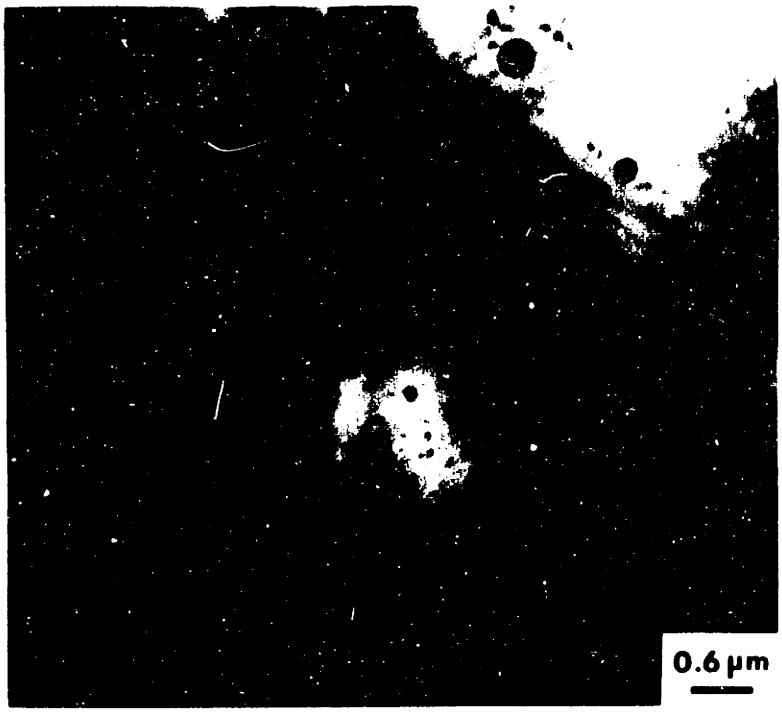

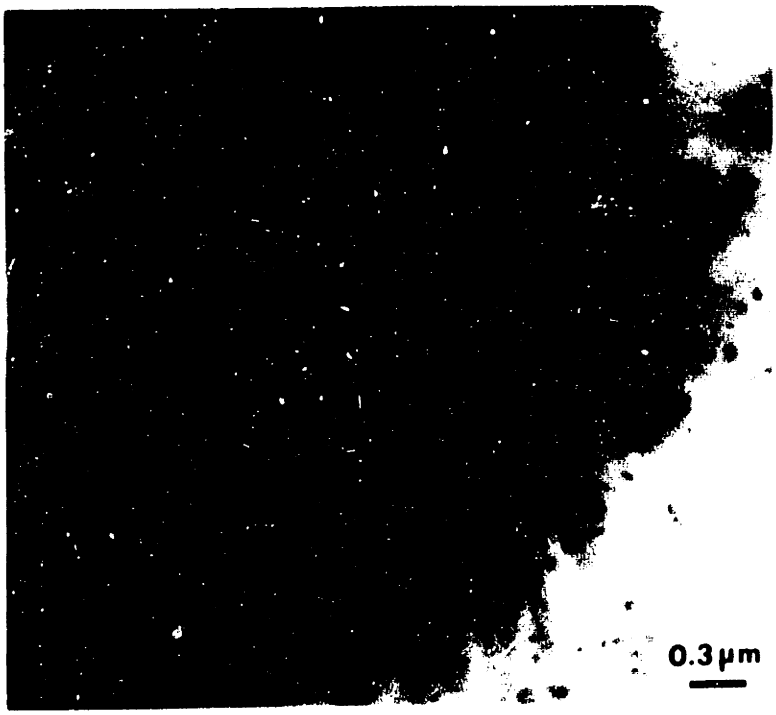

Fig. 8-17a,b
p. 401

loading. This will be discussed in detail in Chapter IX. For both the solvent cast and melt annealed films, higher rubber concentrations have resulted in greater degrees of crystallinity. This may result because the less viscous rubber decreases the kinetic resistance to transport facilitating more chain mobility to accommodate crystal perfection. Hence, an increase in the degree of crystallinity is observed.

5. Discussion

The morphology of the copolymers, binary and ternary blends have been presented and show a diversity of microstructures. These range from spherulites with occluded siloxane particles to melt annealed morphologies that are weakly spherulitic (embryonic) as in the case of the melt annealed MSN(3/100) copolymer with no discernible matrix morphology in the TEM and only sub-micron spherulitic development if any, as seen by the OLM. Other melt annealed morphologies, with greater amounts of rubber, show more developed spherulitic structure culminating in large, super-micron size spherulites in the melt annealed 38/51/11 ternary blend.

The solution cast samples were all highly crystalline, highly spherulitic (except for USMSN(15/44)) with unique morphologies that indicate a competition between phase separation and crystallization phenomena. This competition is manifested by the two processes occurring simultaneously as the MSN(3/100) copolymer is cast from solution. Here, as discussed in Chapter VI, §C.2, the siloxane block lengths range from oligomeric to somewhere around 30 kg/mole with a number average of about 3 kg/mole. Thus, the copolymer chains with the high molecular weight siloxane blocks phase separate from solution at very low concentrations

(~ (O) 0.6 %w/v as observed visually in solution) well before any crystallization has taken place. This micellar transition of the high siloxane block molecular weights from homogeneous solution (H) to a mesophase (M) as a function of composition is represented in Figure 8-18 by the curve designated 'CMC' and '2', where 2 ~ a CMC locus for a higher molecular weight siloxane block in the copolymer. As mentioned in Chapter II, §B, this phase change is not first-order because the entropy does not change discontinuously at the given T_c and P_c but rather smoothly and continuously as more copolymer is added to the system. Recall that the first derivative of the chemical potential $(\partial\mu/\partial T)_P$ = −S and is discontinuous for a first-order phase transition for a pure component. Thus, the curve labeled 'CMC' is a locus of CMC transitions as a function of temperature obtained by minimizing the free energy of the system with respect to composition at a given T.

This CMC transition occurs at a given composition of polymer, Φ_2 when the T and P are fixed and can be seen to occur as solvent is removed (i.e. move left to right along the dashed line parallel to the abscissa). For the longer siloxane blocks, these molecules reach the CMC (at point 'b') before the crystal-liquidus (c-ℓ) curve at 'c' and phase separate prior to crystallization. This produces the spherical particles seen in Figure 8-4a which were formed from the solution first in real time and then subsequently are occluded by the growing lamellae.

For the lower molecular weight siloxane block fraction of MSN (3/100), the CMC will be shifted to higher copolymer volume fractions, Φ_2 as illustrated by the curve labeled '1' which indicates a lower

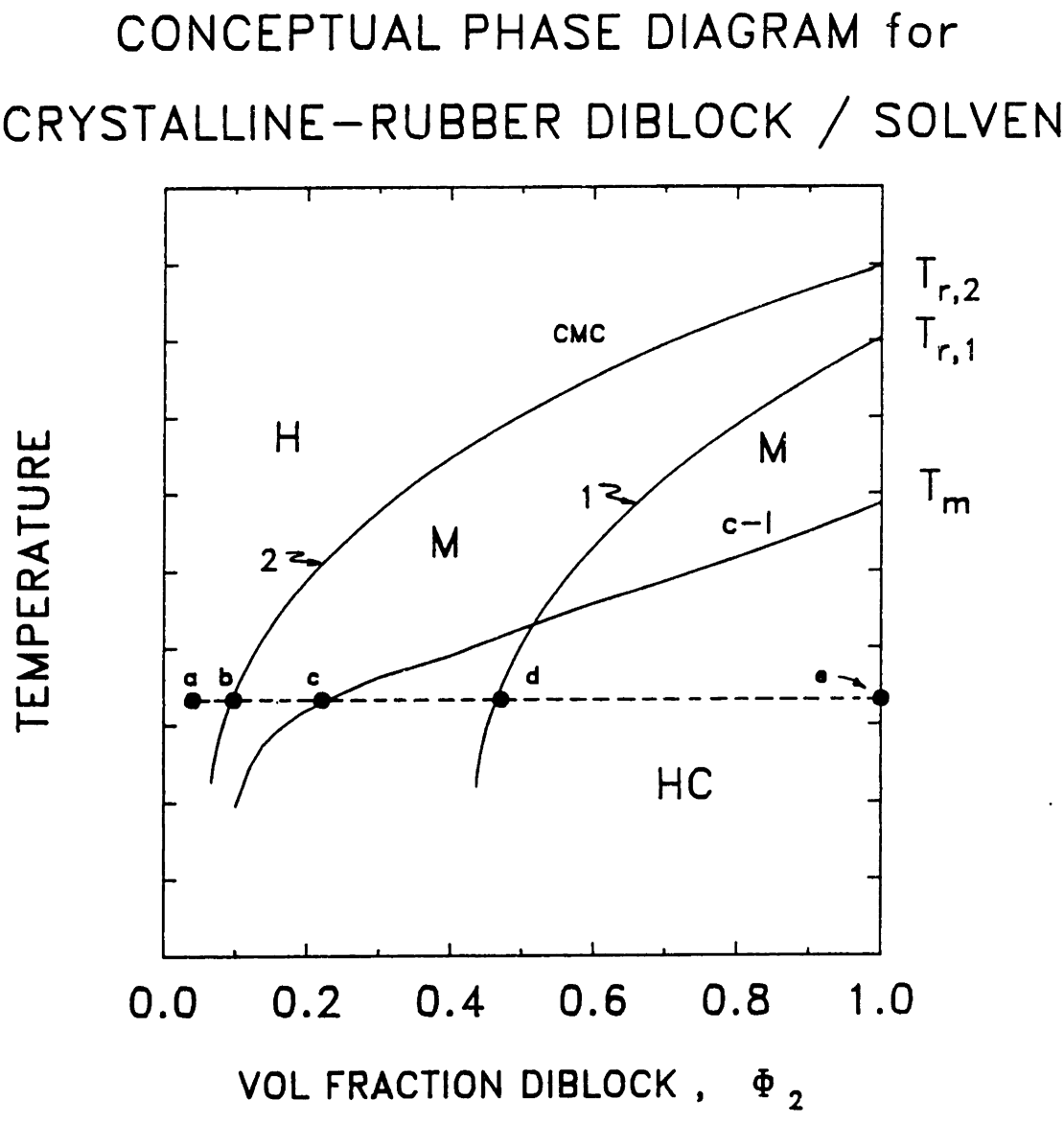

Figure 8-18 Conceptual phase diagram depicting crystallization versus micellization (CMC) phenomenon as function of volume fraction diblock, Φ_2 and temperature; H = homogeneous fluid, M = mesophase; '2' = higher block MW siloxane; '1' = lower (more soluble) siloxane block MW.

molecular weight. Now upon evaporation of solvent at a given temperature below the melting point, T_m, the crystal-liquid binodal ('c') is reached prior to the corresponding CMC at 'd' and the copolymer crystallizes out of solution before phase separation occurs. This creates microcrystallites in equilibrium with the solution although the two "phases" (crystal and solution) are mechanically inseparable at 'c'. In contrast to monomeric binary phase transitions, tie lines across the c-ℓ region (c-e) can not be drawn due to polydispersity effects as was discussed in detail by Richards [31]. Further solvent evaporation drives the crystallization till volume filling spherulites are produced which grow around the larger, phase-separated siloxane blocks to give the morphology of Figure 8-4a. Alternatively, the preference for crystallization over phase separation can be accomplished by using a solvent selective to the amorphous block. This is illustrated for larger siloxane blocks in the copolymer, by the highly oriented, lamellar-like morphology of the USMSN(15/44) cast from a solvent more favorable to the siloxane block than the polyamide-6 block. It is felt that here, in Figure 8-10, crystallization preceded phase separation but not because of short PDMS block lengths, but rather because of preferential solvation of the amorphous block by the toluene-rich solvent.

In addition to predicting the CMC, accurate description of the c-ℓ curve is required to understand the competing processes. Flory [43] has derived the melting point depression as function of diluent concentration (binodal) for an ordered, copolymer with miscible blocks as shown below.

$$\frac{1}{T_m} - \frac{1}{T_m^o} = \frac{R\, Z_A/Z_S}{\Delta H_u} \left[1 - \phi_2 + \frac{1}{y\text{-}\zeta+1} - \chi_{CS}(1-\phi_2 X_A)^2 \right] \qquad (8\text{-}2)$$

where Z_A/Z_S = ratio of segmental volumes, X_A = mol fraction crystallizable sequences, y = number of consecutive crystallizable sequences, ζ = crystallite length, ϕ_2 = the copolymer volume fraction and T_m^o = equilibrium melting point for copolymer of ∞ molecular weight. This equation assumes that: i) high molecular weights were used, ii) equilibrium crystallization occurs to give an crystallite length, ζ_e and iii) chain end effects are neglected. However, if the amorphous and crystalline blocks are immiscible then the normal melting point depression equation should be used to calculate the crystal-liquidus curve as in equation (8-3),

$$\frac{1}{T_m} - \frac{1}{T_m^o} = \frac{R\ Z_A/Z_S}{\Delta H_u} \left[1 - \phi_2 - \chi_{CS}(1-\phi_2)^2 \right] \qquad (8\text{-}3)$$

where A = nylon-6, S = solvent and the other nomenclature applies as above. This particular equation was used to calculate the c-ℓ border curve in Figure 8-18 using χ_{AS} = 0.09 [47].

The MSN(3/100) copolymer cast from solution is unique because depending on the molecular weight of the siloxane block, both crystallization and phase separation are occurring simultaneously but preferentially for the different rubber block length copolymers. The shorter siloxane block copolymers are undergoing crystallization in chain-folded lamellae organized into spherulites while the longer siloxane block copolymers are phase separating into mesophase domains. Thus, both phenomena are occurring simultaneously (or nearly so accounting for the induction times of both processes) but for copolymers with different block lengths. This produces the unique morphology of well defined

spherulites nucleating heterogeneously and then crystallizing around the already established longer siloxane block copolymer molecules of the mesophase. The longer siloxane block copolymers of MSN(3/100) behave similarly to all the chains from USMSN(15/44) where phase separation dominates the entire morphology and no crystallization into a spherulitic structure is observed; the nylon-6 blocks simply crystallize around the mesophase domains.

Application of existing micelle theory to calculate the locus of CMC's necessitates accurate values for the polymer-polymer interaction parameter χ_{AB} as function of temperature. These data are not experimentally available for the PDMS-nylon-6 system so an estimate was made at room temperature where a χ_{AB} value was ascertained from solubility parameter data to be ≈ 4.3 and used in the micelle theory of Munch and Gast [41] for MSN(3/100). Unfortunately, this high χ_{AB} yielded a CMC volume fraction ~(0) 10^{-20} which is essentially zero indicating the strong incompatibility of the siloxane and the nylon-6 blocks as surmised. Working backwards in the theory of Munch and Gast, a CMC or ϕ_c of 0.006 which corresponds to the visually observed "cloud" point of the copolymer in TFEtOH yields a $\chi_{AB} \approx 1.22$ which is fairly physically realistic. This implies that the theoretical framework is approximately correct and that a better understanding of the functionality of χ_{AB} in polymer-solvent interactions is needed. Systems that are more nearly compatible and void of polar interactions are probably better described by the current use of the solubility parameter interpretation of χ_{AB}.

Returning to the phase diagram, Figure 8-18, it is interesting to explore the transitions of pure copolymer at $\phi_2 = 1$. If the copolymer is

heated without degradation, the first transition would be the melting of the crystallites at T_m of the crystalline phase. The sharpness of this transition would depend on the molecular perfection of the crystals, the molecular weight of the crystalline block and the rate of heating through the transition. If done slowly to ensure equilibrium, the last trace of crystallinity should occur within a few degrees of the melting onset [42] at the binodal. After the melting of the crystallites, a mesophase would exist for both block lengths given the order-disorder transition temperatures, T_r on the phase diagram. This order-disorder transition should be an inverse function of molecular weight of the blocks implying $T_{r,2} > T_{r,1}$. Continued heating transforms the low molecular weight block copolymer from a mesophase to a homogeneous fluid at $T_{r,1}$ while the higher molecular weight material is still in the mesophase. Further heating finally converts all the high molecular weight copolymer/solution into a single homogeneous fluid. Thus, as a result of the polydispersity, a range of MST or mesophase transition temperatures would be observed for MSN(3/100). Whether the mesophase domain structure of the lower rubber block length copolymer will be different from the high molecular weight rubber block copolymer is hard to predict from the qualitative arguments presented here. Certain theories that predict the domain morphology of amorphous block copolymers (Helfand's theories) based on block size may be applicable if temperature dependent physical parameters are available. This area is receiving current interest via the use of SAXS to determine phase transitions here at M.I.T. as elsewhere.

In addition to the thermodynamics of phase equilibria, the kinetics of crystallization of a copolymer in the presence of a non-crystallizable phase is important in these systems. The crystallizing block copolymers in this work have shown evidence of occlusion and deformation of the rubbery domains in many micrographs. Since the crystallization of a copolymer in situ around an existing mesophase has not been discussed in the literature, the principles and observations of crystallization with an immiscible blend component as mentioned briefly in §C.4, will be presented with some exceptions/modifications where relevant to the copolymers of this thesis.

First, it is known [40] that more energy is required to occlude smaller particles because $E_{occl} \sim r^{-1}$ (see equation 8-4). In these systems, the presence of the copolymer stabilizes particles with dimensions that are much smaller than those of a physical blend of siloxane and nylon-6 and thus, if the equations of Bartczak, et.al. [40] are applicable, more energy is spent in occluding these particles reducing the energy available for crystal growth and perfection. The smaller particles in the MSN/nylon6/homo-PDMS systems are seen in the higher magnification micrograph in panel b of Figure 8-14 cast from solution or in Figure 8-17a,b when crystallized from the melt. In either of these samples, ca. 0.1 μm or less regions of siloxane have been engulfed as compared to i-PP/EPDM blends of Bartczak, et.al. [40] where occlusion of large (~ (0) 1 μm), coalesced particles occurred. Although the particles are smaller than in the blends, the energy spent in the engulfing process should be less than in a pure blend because the particles are micellar consisting of a nylon-6 corona which is much less incompatible

with the growing crystal front and can crystallize within the lamellae. This should reduce the energy spent in engulfing the rubber domains because the growing crystal has only to interact with "like" corona chains. These possess a much lower interfacial energy difference, ΔF than that between the crystal and rubber particles as in the case of the blends of i-PP for example. This is illustrated in equation (8-4) from [40],

$$E_{occl} = \frac{3\phi_r M_o \Delta F}{\rho_c R_r} \tag{8-4}$$

where $\Delta F_b = \gamma_{cr} - \gamma_{mr}$ for the blends [40] and here in this work $\Delta F_c = \gamma_{co} - \gamma^0_{mo}$ for the micellized copolymer. Note that ϕ_r is the volume fraction rubber, M_o is the repeat unit molecular weight in the crystallizing polymer, ΔF is the interfacial energy difference defined previously, ρ_c is the crystal density, R_r is the rubber particle radius and for the subscripts: 'c' denotes crystal, 'm' ~ melt, 'r' ~ rubber, 'b' ~ blend and 'o' stands for the corona chains of the copolymer. Thus, γ_{cr} is the crystal-rubber interfacial energy, γ_{co} is the solid crystal-melt corona interfacial energy (same as for homopolymer crystallization), etc. Since the corona chains are in an identical environment as the melt in the absence of solvent, the melt-corona interfacial energy, γ_{mo} is zero. Thus, it is evident that the crystal only has to interact with the corona chains during occlusion of a copolymer micelle with a phase separated non-crystallizable block and since $\gamma_{co} \ll \gamma_{cr} - \gamma_{mr}$, the corresponding energy, E_{occl}, is much less. This could be verified by crystallization kinetic experiments of diblock versus blend but unfortunately, this was not accomplished during the course of this work.

However, there is more than just the occlusion term to consider as mentioned in Chapter II, §B.3, during the crystallization in the presence of an immiscible, noncrystalline component. These particles in Figure 8-14b also appear to be deformed to some extent by the crystallizing lamellae which also absorbs energy (E_{def} again scales as r^{-1}) resulting in disturbances in crystallization. Thus, it requires more energy to deform smaller particles as in this case versus larger particles in a blend, for example. In addition, rejection of the immiscible, non-crystalline particles ahead of the growing front also consumes energy which scales as r^{-2}. Thus, more energy is spent in rejection of finely dispersed particles as compared to larger ones which are more easily occluded. However, in this micellized copolymer/homcpolymer ternary blend, rejection is made more difficult due to the entangled corona chains which increase the viscous drag contribution. More difficult rejection combined with the tendency for the corona chains to enter the crystal via chain folding, reduce the interfacial energy difference for the copolymer versus the blend and hence make occlusion more favorable. This is seen in Figure 8-14b or Figure 8-17 a,b where there are high concentrations of siloxane domains scattered throughout the sheaf of the spherulite indicative of occlusion.

In summary, the same forces of occlusion, rejection and deformation exist in the crystallization in these copolymer/homopolymer blends as in pure blends studied by Galeski [44] and Martuscelli [45] among others. In the copolymer systems examined here, slightly less disturbance in the lamellar structures probably occurs than for corresponding blends due to the qualitative trends in less rejection and easier

engulfment just discussed. These factors in the crystallization of the copolymers and blends are largely determined by their phase equilibria which depends heavily on temperature, molecular weight of the blocks and the casting solvent. Although attempts have been made to relate these observations to existing theories of micellization, unsatisfactory results have occurred due mainly to the difficulty in determining an accurate representation for the interaction parameter for the two blocks as a function of temperature. Despite this, a consistent explanation of the observed morphology from solvent casting of both diblock copolymers has led to a conceptual phase diagram. Having made a first attempt at predicting the thermodynamic behavior of such a system, it now remains the goal of future endeavors to develop the experimental techniques with which to measure the CMC loci and crystal-liquidus as a function of temperature and verify our theoretical predictions.

D. REFERENCES FOR CHAPTER VIII

1. J. Martinez-Salazar and C.G. Cannon, Jnl. Mat. Sci. Lttrs., **3**, 693 (1984).

2. E. Schultz, Faserforsch. Textiltech., **26**, 309 (1975).

3. B.J. Spit, Faserforsch. Textiltech., **18**, 161 (1967).

4. K. Masuzawa, Chem. High Polym., **15**, 14 (1958).

5. H.A. Stuart and B. Kahle, Jnl. Polym. Sci., **18**, 143 (1955).

7. P.H. Geil, Jnl. Polym. Sci., **44**, 449 (1960).

8. G. Gurato, A. Fichera, F.Z. Grandi, R. Zannetti and P. Canal, Die. Makromol. Chem., **175**, 953 (1974).

9. A. Galeski, A.S. Argon and R.E. Cohen, Makromol. Chem., **188**, 1195 (1987).

10. A. Schaper, R. Hirte, C. Ruscher, R. Hillebrand and E. Walenta, Coll. Polym. Sci., **264**, 649 (1986).

11. F.J. Padden and H.D. Keith, Jnl. Appl. Phys., **44**(3), 1217 (1973).

12. R. Brill, Z. Physik. Chem., **B53**, 61 (1943).

13. D.R. Holmes, C.W. Bunn, D.J. Smith, J. Polym. Sci., **17**, 159 (1955).

14. Y. Kinoshita, Makromol. Chem., **33**, 1 (1959).

15. H. Arimoto, Jnl. Polym. Sci., Pt. A., **2**, 2283 (1964).

16. S. Ueda and T. Kimura, Kobunshi Kagaku, **15**, 243 (1958).

17. N.S. Murthy, A.B. Szollosi and J.P. Sibilia, Jnl. Polym. Sci., Polym. Phys. Ed., **23** 2369 (1985).

18. B. D'Alo, G. Coppola B. Pallesi, Polymer, **15**, 130 (1974).

19. M. Hirami, Jnl. Macromol. Sci., Phys., **B23**(4-6), 397 (1984-85).

20. R.J. Matyi and B. Crist, Jr., Jnl. Polym. Sci., Polym. Phys. Ed., **16**, 1329 (1978).

21. P. Dreyfuss and A. Keller, Jnl. Polym. Sci., Polym. Phys. Ed., **11**, 193 (1973).

22. M. Kyotani and S. Mitsuhashi, Jnl. Polym. Sci., Pt A-2, **10**, 1497 (1972).

23. W. Ruland, Polymer, 5, 89 (1964).

24. B. Wunderlich, Macromolecular Physics, Academic Press, New York, Vol. 3, 1980, p.73.

25. J.I. Lauritzen and J.D. Hoffman, Jnl. Res. Nat. Bur. Std., 64A, 73 (1960).

26. J.D. Hoffman, J.J. Weeks, J. Res. Nat. Bur. Stds., A-66, 13 (1962).

27. R.J. Matyi and W.R. Crist, Jr., Jnl. Polym. Sci., Polym. Phys. Ed., 16, 1329 (1978).

28. R.J.M. Borggreve, R.J. Gaymans, J. Schuijer and J.F. Ingen Housz, Polymer, 28, 1489 (1987).

29. S. Cimmino, L. D'Orazio, R. Greco, G. Maglio, M. Malinconico, M. Mancarella, E. Martuscelli, R. Palumbo, G. Ragosta, Polym. Eng. Sci., 24, 48 (1984).

30. F. Ramsteiner, W. Heckman, Polym. Commun., 26, 199 (1985).

31. E. Martuscelli, F. Riva, C. Sellitti and C. Silvestre, Polymer, 26, 270 (1985).

32. R.H. Wondraczek and J.P. Kennedy, Jnl. Polym. Sci., Polym. Chem. Ed., 20, 173 (1982).

33. R. Greco, N. Lanzetta, G. Maglio, M. Malinconico, E. Matruscelli, R. Palumbo, G. Ragosta and G. Scarinzi, Polymer, 27, 299 (1986).

34. R. Hosemann and S.N. Bagchi, Direct Analysis of Diffraction by Matter, North Holland Publishing Co., Amsterdam, 1962, Ch. XI.

35. E. Treybal, Mass Transfer Operations, McGraw Hill, New York, 2nd Ed., 1968.

36. E. Hirata, T. Ijitsu, T. Soen, T. Hashimoto and H. Kawaii, in Copolymers, Polyblends and Composites, Am. Chem. Soc., Adv. in Chem. Series, N.A.J. Platzer, ed., Washington, D.C., 1975, p.288.

37. Polymer Handbook, 2nd ed., J. Brandrup, E.H. Immergut, ed., Wiley, N.Y. 1975.

38. B. Lotz, A.J. Kovacs, G.A. Bassett and A. Keller, Kolloid. Z. u Z. Polym., 209, 97, 115 (1966).

39. E. Martuscelli, C. Silvestre and G. Abate, Polymer, 23, 229 (1982).

40. Z. Bartczak, A. Galeski and E. Martuscelli, Polym. Eng. Sci., 24(15), 1155 (1984).

41. M.R. Munch and A.P. Gast, Macromolecules, **21**, 1360 (1988).

42. L. Mandelkern, Crystallization of Polymers, McGraw Hill, N.Y., 1964, Ch. 4.

43. P.J. Flory, Jnl. Chem. Phys., **17**(3), 223 (1949).

44. A. Galeski, M. Pracella and E. Martuscelli, Jnl. Polym. Sci., Polym. Phys. Ed., **22**, 739 (1984).

45. E. Martuscelli, Polym. Eng. Sci., **24**(8), 563 (1984).

46. M. Gervais and B. Gallot, Makromol. Chem., **171**, 157 (1973); **178**, 2071 (1977);
M. Gervais, B. Gallot, R. Jerome and P. Teyssie, Makromol. Chem., **180**, 2041 (1981);
M. Gervais and B. Gallot, Polymer, **22**, 1129 (1981).

47. A. Mattiussi, G.B. Gechele, R. Francesconi, J. Polym. Sci., Pt A-2, **7**, 411 (1969).

CHAPTER IX. MECHANICS OF DEFORMATION

The deformation processes of semicrystalline polymers possessing spherulitic structure were detailed in Chapter II, §C.1 focusing on the more conventional and often-studied semicrystalline polymers such as i-PP, i-PS and PE (both LDPE and HDPE). These polymers alone, exhibit he range of deformation mechanisms from dilatational (crazing) to distortional (shear) plasticity. Both localized and diffuse shear banding has been found in these polymers and shear deformation often was seen to compete with crazing, occasionally the two occurring simultaneously (as in i-PS). Section II.C.2 discussed the mechanisms of deformation for rubber-modified amorphous and crystalline polymers where crazing, shear banding and simple voiding were all seen to be possible means of relieving internal stresses. This chapter focuses primarily on the deformation of nylon-6 homopolymer and rubber-modified copolymer/blends and is organized into three sections. First, the pertinent, existing literature concerning nylon-6 homopolymer deformation will be discussed followed by a similar overview of the rubber-modified material. Finally, in the third section, the experimental results of this thesis with regards to homopolymer and copolymer deformation, including morphology of the deformed materials will be presented.

A. NYLON-6 HOMOPOLYMER DEFORMATION

The existing literature on the deformation of homopolyamide-6 has recently been enhanced by the publications of Galeski, et.al. [1] and Schaper, et.al. [2] who detailed the changes in the morphology as the material deformed. Previous TEM studies on deformed material have been

essentially nonexistent due to difficulties in preparing satisfactory specimens; only recently, these two investigators have refined and improved the fixation and sectioning techniques required to achieve representative, non-sheared sections for TEM observation. However, rather than begin with the latest developments, some of the earlier work will be discussed first, followed by these later studies.

Initial investigation of the possible deformation mechanisms of nylon-6 was done by Geil [3]. As detailed in Chapter VIII, single crystals of nylon-6 were cast from glycerin on a Mylar^{R} substrate at 100°C. The planar crystals were deformed at various angles to the hydrogen bond plane, shadowed with Pt and observed in the TEM. Diffraction patterns showed that the original spacings of 4.0Å and 4.1Å [4] remained unchanged up to strains of ~ 100% indicating the absence of twinning or martensitic transformations during single crystal deformation. In these samples, cracks were formed at elongations as low as 5% and jogged nonlinearly through the planar crystals oriented parallel to the hydrogen bond planes when deformed normal to them. Some plastic deformation occurred, particularly perpendicular and oblique to the hydrogen bond planes and despite lateral contraction, no thinning of the lamellar thickness occurred. These observations indicated that a slip mechanism controlled the deformation at room temperature. No information on moisture content, hence T_g, was published.

Turning to bulk samples, the microstructure as formed from various thermal histories and influenced by molecular parameters such as chain defects and molecular weight, plays a crucial role in crystalline polymer deformation. Simple changes in degree of crystallinity by different

thermal treatments produce complex, interrelated changes in a variety of morphological parameters, such as spherulite and lamellae size, density of tie molecules and crystalline lattice coordination as detailed in Chapter II, §C.1. These, in turn, affect the deformation (and fracture) modes where a variety of different mechanisms may exist, often operating within various regions of the same spherulite.

The easiest morphological variable to control is the crystallinity content. Several authors have examined fracture strength and yield stress of nylon-6 as a function of crystallinity. Russell and Beaumont [5] showed that yield stress increased proportionally to density in the range 1.130 - 1.145 g/cc for injection molded samples (or 32-44% crystallinity assuming ρ_a = 1.080 [6] and ρ_c = 1.230 [7]). Crystallinity was varied by mold temperature and spherulite diameter was ~ 6 μm but no variation in diameter with density was reported. These authors showed that notched fracture toughness, (as measured by the stress intensity factor, K_{Ic}) decreased with crystallinity and dropped drastically as the crystallinity reached 38-40% but quote that the fracture mode (brittle, ductile or semi-brittle) was independent of crystallinity. This seems contradictory because the fracture mode should correlate with the impact strength (brittle ~ low impact strength, ductile ~ high I.S., etc.) but since other morphological parameters were not determined, the cause of the toughness decrease, besides the increase in crystallinity, was unclear.

Spherulite size is usually controlled by the heterogeneous nucleation density as an inverse function of crystallization supercooling which was discussed in Chapter II, §C.1. An alternative method of varying

spherulite size is to change the molecular weight through various polymerization temperatures as in RIM polyamide-6, for example. To maintain a sufficient conversion rate, Bessell, et.al. [8] used higher catalyst and initiator concentrations at lower polymerization temperatures producing lower molecular weight nylon-6. The lower molecular weight material gave smaller spherulites (ca. 10-20 μm diameter.) and failed in a brittle mode. Fracture strains were only 5-10%. Higher molecular weight nylon-6 crystallized into larger spherulites (ca. 40–60 μm diameter) and had greater strain to fracture with comparable yield stresses (~80MPa). Strain rates in all cases were ~ 1.7×10^{-3} sec^{-1} and crystallinity was 40-42% as measured by a density column. Attempts were made to exclude moisture. Thus, reaction injection molded nylon-6 showed a direct correlation between spherulite size and toughness but other variables, such as molecular weight, changed as well.

Bessell et.al. [8] also demonstrated that toughness (area under σ-ϵ curve) dropped drastically above a "critical" crystallinity of ~ 35%. Here, higher molecular weight polymer ($\bar{M}_n$=35 kg/mole) was annealed differently to give crystallinities ranging from 20-45% with constant spherulite size of ~60 μm. The tough materials (crystallinity <32%) showed no yield drop and deformed fibrillarly by coalescence of small voids into a stress whitened zone before failing at strains of ca. 250%. Intermediate crystallinity nylon-6 (35-42%) formed intraspherulitic cracks after the yield drop. These cracks grew normal to the applied stress and widened with strain and finally coalesced into intraspherulitic voids which joined with others forming interspherulitic cavities as

seen in the OLM. Final fracture occurred by interspherulitic crack propagation.

Interestingly, the initial appearance of the fine cracks occurred only in the polar sectors of the spherulite confined to approximately ±30° off the tensile axis. The authors' [8] explanation of the geometrical limitation to crack formation in these sectors is based on X-ray measurements [9] indicating hydrogen bonds in the (010) plane or parallel to the spherulite radius. This suggests a parallel γ-form (or nonequilibrium) crystalline habit which could produce cracking/voiding between the sheared hydrogen-bonded planes in these regions. Although no exact hypothesis was given, this would occur because of misfit in the plastic resistances between interplanar and intraplanar material similar to the explanation of Zaukelies [10] for the formation of kink bands due to slip between hydrogen bond planes. Because only weaker van der Waals' forces are found normal to the planes, these provide a path of least resistance for yielding and cavitation.

In oriented nylon-6, deformation phenomena similar to crazes has been found by Zhurkhov et.al. [11]. Under mechanical load, clusters of disk-shaped "submicrocracks" normal to σ_∞ were detected by SAXS. Their concentration was on the order of 10^{16} cm^{-3} with a mean long axis dimension of 90Å (normal to σ_∞) and a short axis of ~50Å (parallel to σ_∞). These dimensions are an order of magnitude below the microfibril and microcrack sizes reported by Peterlin, c.f. [12] and are similar to the dimensions of very small crazes.

The proposed formation of these disk shaped cavities is by bond rupture due to thermal fluctuations under load. This cleavage forms two

free radicals per rupture which attack bonds of adjacent macromolecules forming additional ruptured chains with a steady state concentration of radicals. The propagation of chain rupture by the "shuffling" free radicals eventually forms the destroyed microzones called submicrocracks. Confirmation is by agreement of the steady state free radical density determined by electron paramagnetic resonance (EPR) with the submicrocrack density as determined by SAXS. This scheme implies that the number of ruptured macromolecules greatly exceeds the concentration of free radicals, i.e. once homolytic scission occurs, heterolytic scission is propagated by the attacking free radicals and is responsible for most of the ruptured bonds.

Evidence of chain rupture during the deformation of unoriented nylon-6 has been supported by the work of Galeski, et.al. [1] who used OsO_4 fixation at 4°C to chemically crosslink the polyamide-6 chains that were damaged by deformation. This was manifested as dark OsO_4-containing regions (ca. 500 Å in diameter) that were visible in TEM and were found to be preferentially oriented along the spherulite radii in the equatorial zones and also in the interspherulitic regions where weak spots are known to exist [13]. These interspherulitic weak spots are formed when trapped melt due to impingement of the growing spherulites finally crystallizes producing negative pressure much the same as with rubbery inclusions in modified amorphous copolymers. Then under additional imposed stress, these regions cavitate due to the deformation misfit from different plastic resistances of the spherulites and the grain boundary material.

It has been previously observed with PE [14–16] that the equatorial (transverse) regions are particularly susceptible to cavitation. It is hypothesized [1] that the compressive radial stresses in the equatorial regions of a deforming spherulite cause kinking of the lamellae and due to the tension applied normal to their radial direction, periodic fracture and subsequent microvoids could easily occur. See Figure 9-1 from reference [1]. This deformation mechanism is supported by Galeski's micrographs where the OsO_4 particles seem to follow the initial equatorial lamellae radii where misfit and cavitation were maximized. Undeformed nylon-6 does not complex OsO_4 because the latter chemically binds with chains that are damaged from deformation, being able to diffuse into those less dense, cavitated regions and react. Whether these damaged zones were formed as the result of chain rupture and free radical generation of microvoids or by stress misfit which exceeded the local cavitation strength of the material is not clear; nonetheless, they represent the first direct evidence of cavitation occurring in the plastic deformation of nylon-6.

However, these cavitation zones are not seen at all levels of strain. Galeski found the less dense zones at draw ratios (λ) between 2 and 2.5 whereas Schaper, et.al. [2] examined material in TEM with a $\lambda \approx 4$ and did not detect any evidence of cavitated zones. This could be due to the fact that no fixation techniques were employed after straining the samples; the lack of fixation is known to permit voids and less dense, partially cavitated regions to "heal" and close up when the strain is released on the sample. This matter aside, Schaper et.al. observed an intermediate structure between the initial lamellar organization and a

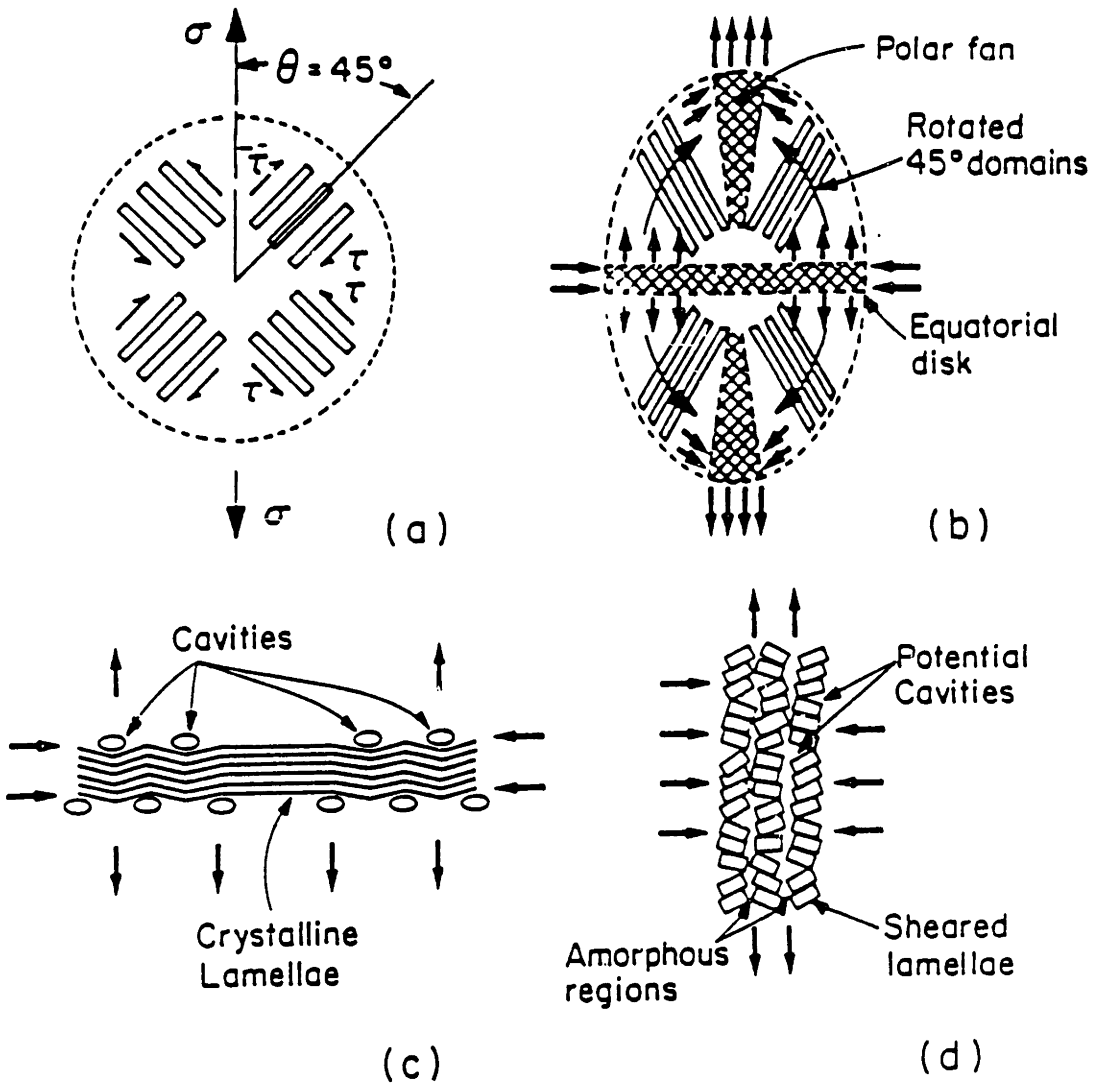

Stages in the formation of cavities in the equatorial regions of spherulites: (a) the 45° domains in an undeformed spherulite, (b) lattice rotations due to simple shear in 45° domains subject equatorial regions to enhanced tension and radial compression, and polar regions to enhanced compression, (c) kinking of non-deforming lamellae due to shear instability in amorphous matrix in equatorial region, and (d) shear instability due to chain slip in lamellae in polar regions.

Figure 9-1 Schematic showing spherulitic morphology under tension; after Galeski, et.al. [1].

fully developed fibrillar structure described by Peterlin's [12] micronecking model which was discussed in Chapter II, §C.1. They interpreted the observed structure as a lateral mosaic crystal model where the individual chain folded blocks which initially comprised the lamellae, were oriented more or less normal to the draw direction but not in complete longitudinal register (alignment) as in fibrillar PE formed by micronecking.

These observations have combined to show that highly crystalline nylon-6 usually exhibits poorer toughness and impact resistance. Decreasing the crystallinity improves these properties because it generates more tie molecules to anchor and "crosslink" the crystallites. Water has been shown to be an excellent plasticizer, suppressing most of the microvoiding found by Galeski, et.al. [1] in samples deformed at room temperature (near or at T_g). And at large draw ratios, well beyond the average extension achieved in the samples of this thesis, a long range mosaic block crystal arrangement has been shown to exist, indicating a tendency towards microfibrillation as described by Peterlin for the polyolefins.

B. NYLON-6 - RUBBER POLYMER DEFORMATION

Both blends and copolymers of nylon-6 with various rubbers have been studied in the past but deformation behavior has not always been found to be enhanced, and sometimes not even reported. This section presents an overview of the relevant literature in regards to nylon-6-rubber systems (both blends and copolymers) with emphasis on mechanical properties. Morphological characterization when mentioned, is related to the descrip-

tion of deformation. This section will set the stage for the discussion of the results found in this thesis work, presented in section C.

Ramsteiner and Heckman [17] studied nylon-6 blended with polybutadiene and found no crazes in the TEM or transmission light micrographs after samples were deformed in tension. Experimental details are limited but significant voiding was observed at a deformation temperature of -20°C as evidenced by ruptured rubber particles which were found on lines inclined ~55° to the applied tensile direction. Thus, it appears that blending with rubber produced only shear yielding with cavitated particles ~ 0.5 μm in diameter similar to the deformation behavior of PVC discussed earlier.

Solution grafted maleic anhydride onto ethylene-propylene monomer (EPM) rubber has been prepared via a free radical process by Martuscelli et.al. [18] and subsequently condensed with the terminal amine of hydrolytic polyamide-6 to yield a graft copolymer through an imide linkage. A similar process was used with dibutyl succinate grafted to EPR rubber which was incorporated during hydrolytic caprolactam polymerization [19]. However, SEM shows isolated regions of very large particles (> 50 μm) in the blends which are indicative of unreacted, unsolubilized EPR lending some confusion as to how much free rubber is actually in the blends and what was the efficiency of the grafting copolymerization. In binary blends of pure polyamide-6 and EPM, no discernible improvement in impact strength was observed. However, upon addition of 10 %w and 20 %w graft copolymer, (the latter concentration being more efficacious) significant reduction in the brittle-ductile transition was observed. For EPR blends, greater impact strength at all

levels of grafting content of succinate to EPR were achieved with binary blends, i.e. the rubber enhancement came solely from the copolymer and additional homopolymer EPR added in lieu of copolymer decreased the impact strength approximately 50% at -10°C and -25°C. This is indicative of insufficient emulsification of the homo-EPR which is supported by the SEM micrographs. In these two systems it is very difficult to separate out all the independent factors because of the random structure of the graft copolymers and the incomplete grafting reaction. Similar studies of PP and a-PS grafted to nylon-6 have been made; the PP was grafted via maleic anhydride and the PS by copolymerizing styrene with methacrylic acid monomer [20].

A very thorough study of these types of olefinic-graft-polyamide-6 copolymer systems was conducted by Borggreve [21] who used EPDM (ethylene-propylene-diene monomer) rubber. He found that regardless of the concentration of maleic anhydride grafts and thus the amount of polyamide-6 at the interface, the impact properties of the binary blends were not changed at given particle size. Although he offered no explanation, the probable cause of this inefficacy was that the grafted nylon-6 chains were estimated to be only 7 - 10 kg/mole and from discussion in II.B.1 of this chapter, these chain lengths are not sufficient to incorporate the 35 kg/mole matrix polyamide-6 into the copolymer morphology. Thus, the graft copolymer may not have acted as a true emulsifying agent locating at the interface because its nylon-6 grafts could not solubilize the matrix homopolyamide-6 and thus the copolymer phase separated into its own respective domains. This rendered the copolymer practically

ineffective and resulted in no change in impact strength with changing amount of grafted nylon-6.

Superimposed on this non-existing trend of no impact strength improvement as a function of number of polyamide-6 grafts is the positive effect particle size had on the brittle-ductile transition, i.e. smaller particles (< 1 μm) gave lower T_{DB} and higher impact strengths; this trend follows previous observations by Wu and those determined by Borggreve on pure nylon-6/EPDM blends discussed next.

Borggreve et.al. [22] also studied pure homopolymer blends of polyamide-6 and EPDM and found the aforementioned trend of particle size on impact strength as well as the fact that lower rubber content resulted in higher T_{DB} and lower strengths. These two variables can be related by the interparticle distance model of Wu [23] for prediction of T_{DB} and this was roughly supported by Borggreve's results. However, these latter investigators also found no evidence of crazing in the deformed blends and feel that the toughening mechanism was due more to voiding of the particles rather than the rubber acting as stress concentrators generating interacting stress fields. This release of negative pressure when under a state of triaxial tension is believed to be the primary mechanism for toughening in polyamides despite only van der Waal's forces of adhesion between the rubber particles and the matrix and the possible delamination that could occur.

A series of diblock, triblock and radial triblock star copolymers of nylon-6 with poly(isobutylene) (PIB) have been synthesized [24] using hydroxy terminated PIB's functionalized by the inifer method [25]. Coupling was via diisocyanates or N-chlorocarbonyl-isocyanates. The

diblock copolymer using the latter coupling agent, contained about 52% molar nylon-6 with block molecular weights of 22 and 10 kg/mole nylon-6 and PIB, respectively. It had a everywhere concave upward stress-strain curve indicative of the tensile response of human skin or a crosslinked rubber with a tensile stress of 18 MPa and strain to fracture of only 15%. A triblock copolymer with (2) 15 kg/mole polyamide-6 blocks joined to a 38 kg/mole rubber block had twice the tensile stress (i.e. ca. 35MPa) and strain (ca. 30%) as the diblock copolymer.

Alternating copolymers of siloxane and various polyamides including nylon-6 were synthesized from melt condensation of bis(3-aminopropyl)-tetramethyldisiloxane and dicarboxylic acids such as adipic acid [26]. These materials were compression molded and deformed at $2x10^{-2}$ sec^{-1} strain rate but gave poor performance with tensile strengths of only 14 – 25 MPa and strains to fracture of 3 – 8%. Superior mechanical performance is attained with silicone polyamide copolymers of this thesis detailed in the next section.

The major commercial rubber-toughened nylon-6 copolymer is a product of the Dutch State Mines Company which recently (within the last several years) acquired the technology from the Monsanto Co. This is an alternating polyether-polyamide-6 block copolymer made by reaction injection molding a polyol or poly(butadiene)diol with a bisacyllactam activator in the presence of a suitable catalyst such magnesium bromide caprolactam. The tensile data [27] for this copolymer showed that at 20% rubber content, the toughness (area under the σ-ϵ curve) increased by a factor of 1.5 - 2.0 over homopolyamide-6 as the flow stress dropped from 65 MPa to 40 MPa. However, it is not known what mechanism was responsible for

this higher elongation and toughening. From microscopy done by A. Galeski while on sabbatical at M.I.T. in 1985-86, this material has been shown to have a mixed morphology consisting of alternating lamellae in some regions while others show a spherical morphology of dispersed rubber. Although this may be an attractive commercial product, it is difficult to study theoretically due to the unknown variance in its morphology.

Other reaction injection molded nylon-6 triblock copolymers with polypropylene glycol using diisocyanates have been reported [28]. This formed the often-used carbamate linkage between the central polyether block and the two outer polyamide-6 blocks. Rubber particle sizes of ca. 100 Å were presumed to be dispersed in the semicrystalline matrix due to no large domains at the resolution limit of the SEM (which is ~ 100 Å). These materials possessed a notched Izod impact strength of 50 – 60 kJ/m^2 comparable to the values given by Wu [23] for rubber-modified nylon-6,6 discussed in Chapter II, §C.2.b.

C. UNIAXIAL TENSILE TESTING: EXPERIMENTAL RESULTS

1. Nylon-6 Homopolymer

To establish a standard of comparison for the mechanical performance of the copolymers and blends, nylon-6 homopolymer was tested in uniaxial tension under a variety of experimental/environmental conditions (see Figure 2-13) such as varying strain rates and moisture content. Water effectively plasticizes the polymer which lowers the glass transition temperature so that the difference between the test temperature and T_g decreases as was reported in Chapter VII. All tests were conducted on an Instron^R model 1122 tester using constant strain rates (for that particu-

lar experiment) at room temperature. An environmental chamber with saturated salt solutions kept the relative humidity constant during the deformation for the "wet" homopolyamide-6 samples. In almost all cases, dry or wet, regardless of fibrillar or spherulitic morphology, nylon-6 showed tough behavior as the ductile-brittle transition is ca. −120°C (1.5%H_2O, $\dot{\varepsilon} = 5.5 \times 10^{-3}$ sec^{-1}) with a critical stress of 186 MPa [29].

The analysis of deformation of polymers is complex owing to the vast effects of a number of molecular, morphological, and environmental parameters as discussed in detail in Chapter II and above. Differences in sample preparation, specimen size and shape and testing conditions make it difficult to directly compare tensile data from various sources. Thickness effects transform the sample from plane stress to plane strain conditions and significantly alter behavior which may account for the solvent cast samples of homopolyamide-6 from this laboratory (ca. 0.2 − 0.6 mm thickness) giving superior mechanical strength compared to industrial nylon-6 (ca. 0.25 in. thickness). The yield stresses for the spin cast, melt annealed nylon-6 (hydrolytic or anionic) exceeded commercial nylon-6 σ_y by as much as 60% [30]. Whether this superior performance is due to the specific thermal processing done in our laboratory or thickness effects is unclear and probably moot. All that is required is consistent, reproducible films that can be compared internally to ascertain performance. Comparison from other sources is beneficial but should not be considered absolutely quantitative.

The effect of crystallinity level on the mechanical behavior of films cast in our laboratory using anionically synthesized RIM nylon-6 from the Monsanto Co. is shown in Figure 9-2. This is a plot of

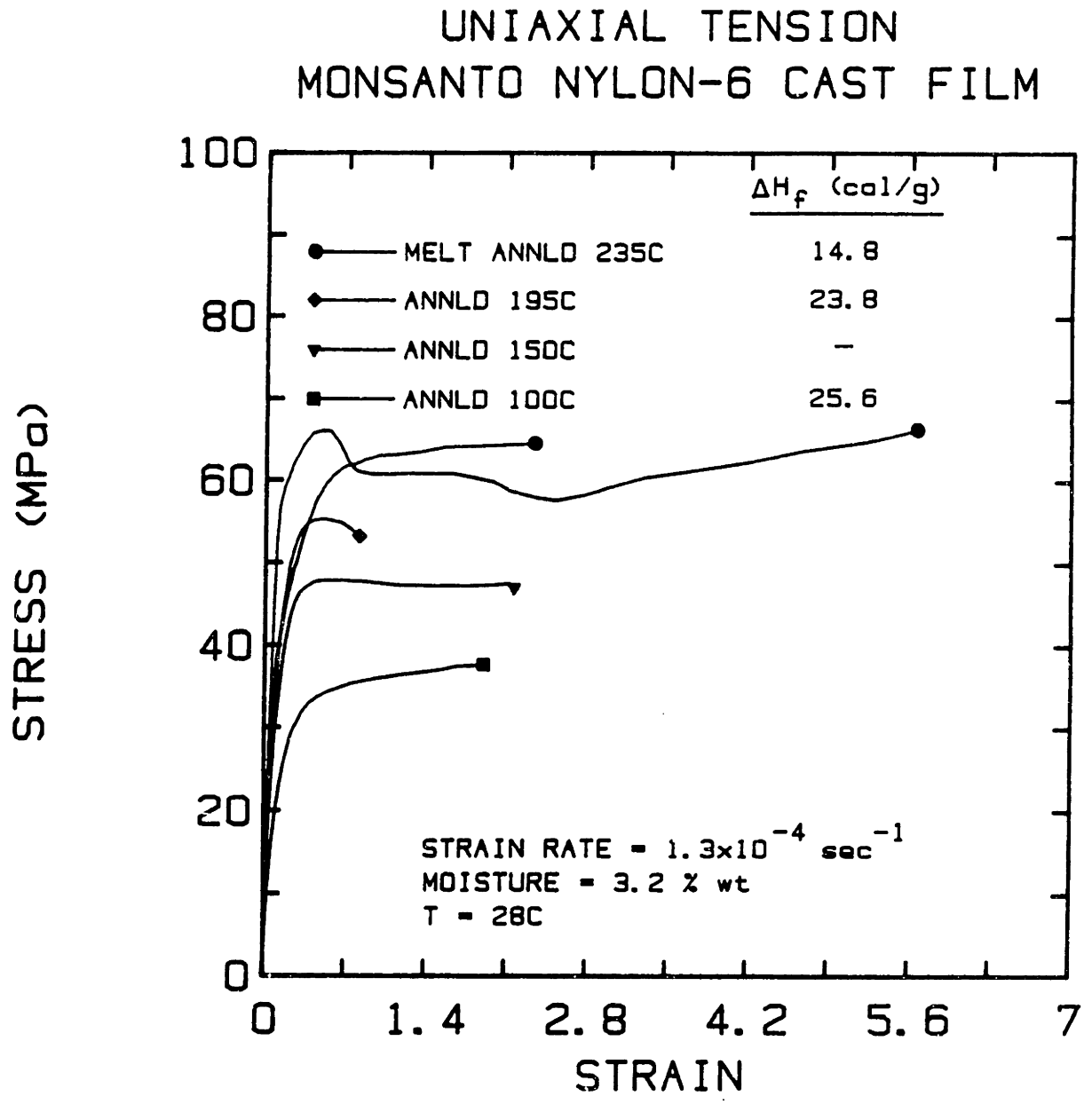

Figure 9-2 Uniaxial tension of spin casted anionic nylon-6 annealed at various temperatures to give the heat of fusion shown. Polymer supplied by Monsanto.

engineering strain versus nominal stress for samples equilibrated in 60 % R.H. environment and deformed at 0.05 mm/min. The films were spin casted from TFEtOH and subsequently annealed at various temperatures. The change in the heat of fusion is not considered significant between 100°C and 195°C despite the steady improvement in yield stress, the exact cause for which is unknown. The morphology of the spin casted material annealed at 100°C is shown in Figure 9-3 courtesy of A. Galeski who performed the cryotoming and electron microscopy. The sample is stained with PTA/BzOH solution which shows imperfect quasi-spherulites. The orientation of the material undoubtedly results from the high gravity field present in the spinning cup which forces the material to more extended chain conformations as in annealing under high pressure [31]. The long axis of the figure is in the azimuthal direction of the casting cup and the long axis of the tensile bar is in that same direction; i.e. tensile specimens were cut so that the longitudinal orientation of Figure 9-3, was parallel to the applied stress, σ_{∞}. No additional morphological information such as lamellar thickness was obtained for the various annealing treatments.

The melt annealed material, on the other hand, has considerably less crystallinity (a decrease from 56% for solution cast to 32% for melt annealed based on pure α-form ΔH_u = 45.4 cal/g) and forms a spherulitic structure as shown by the OLM in Figure 8-2a. It is presumed that the

---

Figure 9-3 (see next page) Transmission electron micrograph of anionic nylon-6 spin cast and annealed at 100°C; stained with phosphotungstic acid (2% aq), courtesy of A. Galeski

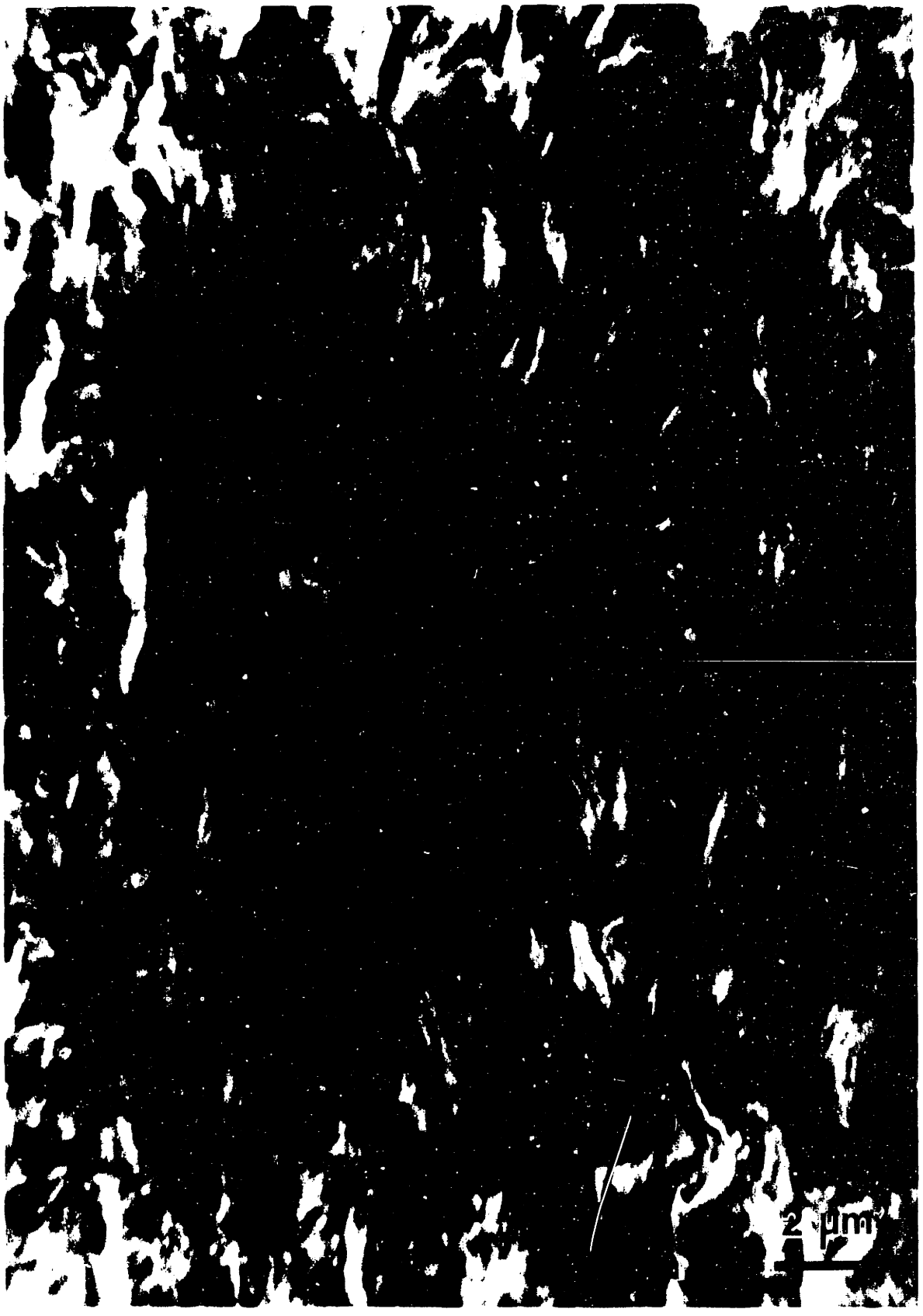

Fig. 9-3
p. 433

crystallization rate and morphology of comparable molecular weight hydrolytic nylon-6 (as in Figure 8-2a) is similar to the anionically polymerized nylon-6 of these samples where no micrographs were taken. This decrease in crystallinity significantly improves the yield stress to 60 – 65 MPa and extends the strain to fracture to 200 – 500+% as found in one extraordinary specimen. Thus, lower crystallinity creates more tie molecules to give tougher materials.

The difference in the σ-ϵ curve for the two melt annealed samples is not fully understood. The 500+ % strain-to-fracture curve exhibits a marked yield drop followed by necking and cold drawing at or very near its T_g whereas the second sample deforms with minimal necking (termed simple necking) and no cold drawing, as would be expected with the 3% H_2O acting as a plasticizer. The only difference is their annealing treatment pressure; the cold drawn sample was annealed under vacuum earlier in the developmental stages of this research, whereas the "simple necking" sample was annealed under ca. 1 psig N_2 to minimize bubble formation. As will be seen in the following paragraph, the σ-ϵ curve of the latter is more realistic for wet nylon-6 at room temperature. Perhaps the vacuum annealing procedure on the 500+% strain sample removed additional monomeric plasticizers before moisture conditioning. Thus, less plasticization occurred which facilitated a pronounced yield drop followed by cold drawing. This parallels the behavior of some dry nylon-6 samples as well as the dry, rubber-modified copolymers of this work. Evidently, the deformation behavior must depend critically on the degree of plasticization at these temperatures and slight changes can cause a dramatic alteration in the competing deformation mechanisms. Vacuum annealing was

discontinued in the preparation of future samples due to profuse foaming and bubble formation which prevented the preparation of high quality films. Despite this, superior mechanical behavior is achieved for films melt annealed under N_2 which show no anisotropy above the spherulite scale (~ 25 μm).

Since the melt annealed material gave superior mechanical performance, the behavior of wet, melt annealed Allied nylon-6 was examined and is shown in Figure 9-4a,b. Here, both engineering stress and true stress are plotted against nominal strain, the latter is calculated assuming negligible dilatation during deformation which will be shown to be approximately correct. This material is slow cooled from the melt (2 hours cool time) and possesses 35% crystallinity (assuming 100% α phase crystals). It has a well developed spherulitic structure as shown in the OLM of Figure 8-2a with a average spherulite diameter of 25 μm. These materials regardless of deformation rate show behavior that is all but equivalent to simple necking as indicated by a Considére construction [32] on the true stress-nominal strain plot, Figure 9-4b. This graphical procedure gives the maximum true stress of the yield point as the largest slope of the tangent line from $\epsilon = -1$ to the true stress-strain curve. If two points of tangency can be drawn, then yielding has occurred followed by strain softening and some degree of cold drawing of a stabilized neck. But in these samples, really only one tangent can be drawn (if two could be drawn they would be nearly indistinguishable and lie practically on top of one another) indicating that very little, if any, strain softening occurred after yielding and that negligible cold drawing was present. This correlates with what was observed; the neck

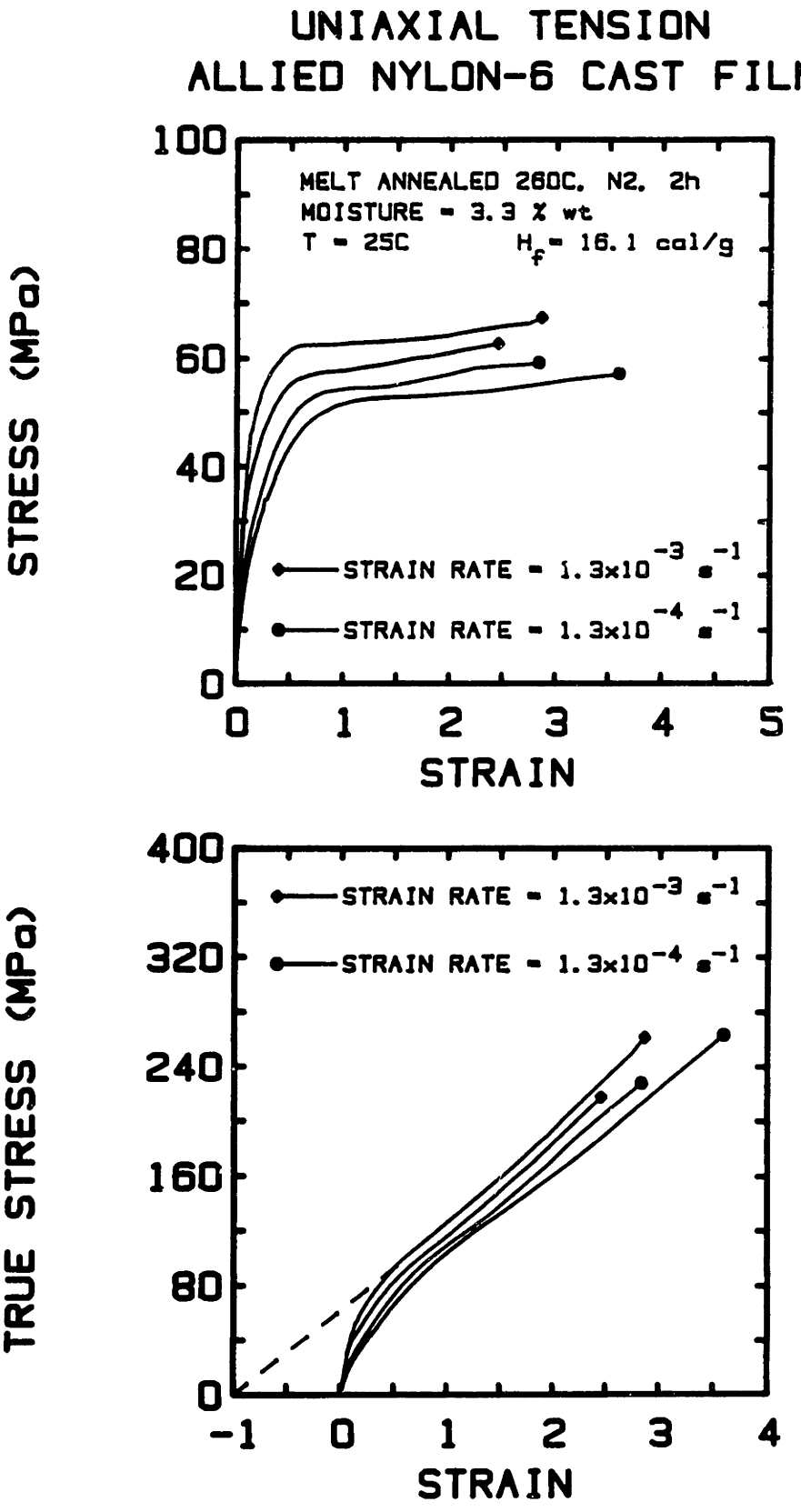

Figure 9-4 Deformation of spin cast, melt annealed hydrolytic nylon-6, equilibrated with ca. 3 %w H_2O; a) plot of engineering stress-strain and b) true stress-nominal strain.

simply thinned until fracture. Otherwise, if strain softening and cold drawing had occurred, the slope of the second tangent would be significantly less than the yield tangent because yielding produces the maximum true stress in the sample (except for strain hardening near fracture). The materials simply yielded, strain hardened and extended via reduction in the cross sectional area of the neck region. The rate of increase of the true stress as a function of strain never diminished as seen by the almost linear rise in σ_T versus ϵ. In most of the samples a second upturn, although barely detectable, of the curve signified final strain hardening of the neck. Thus, with essentially only one tangent to the curves, the materials fall into the simple necking category. As mentioned above, the stress-strain properties of these materials deformed very near or at T_g are very sensitive to the environmental conditions such as moisture content and small changes in moisture, hence T_g, can produce large changes in behavior.

This thinning of the neck without cold drawing in one of the higher strain rate samples is seen in the optical light micrograph in Figure 9-5a,b. The micrographs in both panels were obtained from ~ 1 μm thick cryotomed sections, stained and fixed via OsO_4 and cut from the gauge section after fracture in the Instron^R for one of the samples in Figure 9-4 deformed at 1.3×10^{-3} sec^{-1}. No efforts were taken for fixation

---

Figure 9-5 (see next page) Optical micrograph of hydrolytic, wet, deformed nylon-6, stained with OsO_4 and viewed between crossed polars; a) sectioned normal to σ_∞, b) sectioned parallel to σ_∞

Fig. 9-5
p. 438

because only OLM was done. Panel a represents a section normal to the applied tensile stress and shows essentially an "end-on" view of the deformed spherulites. Undoubtedly, the elastic component has caused some recovery which is why the material retains much of its undeformed character in this projection. This clearly shows that the spherulites are still intact at a natural draw ratio or $\lambda \doteq 2.6$.

The micrograph of the same sample cut parallel to the deformation direction with the knife direction 45-50° to the σ_∞ is shown in panel b. This shows the deformed spherulites with their heavily sheared oblique lamellae (those initially inclined ca. 45° to σ_∞) which have rotated significantly towards the draw direction. A much more grainy, fibrillated and highly distorted microstructure is seen within the spherulites. Panel b also indicates that deformation occurred primarily by interspherulitic (grain boundary) and some interlamellar slip as the test temperature was at or very near T_g. Note that substantial birefringence still remains which indicates that blocks of chain folds are still intact although probably not within their original lamellae. An additional observation, although not shown, is that spherulites near the surface edge of the tensile specimen were compressed to a much smaller fraction of their original diameter in contrast to less lateral contraction of centrally located spherulites which are shown in panel b. This further supports the conclusion that the neck simply thinned after formation without actually cold drawing and that the majority of the contraction was sustained by surface spherulites.

Similar observations were made by Crystal and Hansen [33] on nylon-6,6 deformed wet with 8% H_2O at identical strain rate and tempera-

ture. They saw a similar "brickwork-like" organization of the deformed spherulites viewed parallel to the draw direction at a draw ratio of 4:1 (higher than the observed $\lambda \approx 2.6$ of Figure 9-5a,b due to greater moisture content) where substantial fibrillation was observed. Optical micrographs of sections normal to the draw direction showed a "rosebud" type of spherulitic structure due to this fibrillation. TEM revealed large oblate, dilated regions at the grain boundaries of the spherulites which were ca. 0.5 μm by 2-3 μm in size. These were confirmed by density measurements and an analogy was made to crazes although the data is inconclusive.

An electron micrograph of wet, deformed Allied nylon-6 from this thesis work is shown in Figure 9-6 prepared by cryoultramicrotomy at −30°C. The gauge section of the tensile specimen deformed at 1.3×10^{-4} s^{-1} was immediately immersed in dry ice-heptane after fracture and stained by OsO_4 at 4°C followed by embedding in Ladd epoxy. Details of the embedding procedure are given elsewhere [34]. The sample was sectioned parallel to the applied draw direction (as indicated by the two-headed arrow) and revealed regions of lower density within the core of the spherulites as stained by OsO_4. Although there appears to be some OsO_4 deposited on the surface of the section that was not rinsed away after treatment, there are some dark "spots" (see arrows) that follow the lamellae radii in identical fashion to that found by Galeski,

---

Figure 9-6 (see next page) Transmission electron micrograph of deformed hydrolytic nylon-6; specimen fixed with OsO_4, embedded, cryotomed at −30°C, stained with PTA solution, 10 minutes. Tensile direction is horizontal.

Fig. 9-6
p. 441

et.al. [1]. Since the sample was deformed with 3.2 %w H_2O, the density of these OsO_4 spots is less than seen in the dry deformed samples of commercial compression and injection molded nylon-6. Nonetheless, their presence is unequivocal and implies that the deformation mechanism in melt annealed nylon-6 cast film is similar to commercially available material which was discussed above in section A.

In Figure 9-6, the impression of the spherulite complete with nucleating center and radiating "lamellae" (or remnants thereof) indicates that the section represents a diametral slice of the spherulite which is precisely the region found by Galeski to undergo extensive cavitation. As discussed previously, the OsO_4 regions could result from damaged chains or reaction with free radicals generated by bond rupture upon loading. It is well known that free radicals detected by ESR are produced when nylon is deformed up to fracture [35,36] and additional studies show that these radicals achieve a steady-state concentration with time despite load removal [37,38]. This suggests that the radical concentration is a function of strain. It is also known that an inert atmosphere and low temperature maximize radical lifetime. Evidently, if the dark spots represent OsO_4 complexed with polymeric radicals, these species must have survived the immersion in dry ice-heptane and were able to react with the OsO_4 solution in the refrigerator. The location of the dark spots along the radius of the spherulite is probably due to slip between lamellae or bundles of lamellae followed by cavitation which results from the misfit of stresses between the amorphous and crystalline regions. Because the "shell" or form of the spherulite is still intact, largescale reorganization, such as microfibrillation has not occurred

here although the individual lamellae probably have lost their discrete identity. These dark regions representing cavitated or less dense regions were never seen i undeformed material.

The tensile behavior of dry Allied nylon-6, melt annealed is shown in Figure 9-7. This is the same molecular weight material as in Figure 9-4 but now a yield stress of 75-80 MPa dry, as compared to 60 MPa wet is observed. This temperature of deformation (also 25°C) is now some 60°C below the glass transition and shows strains to fracture on the order of 100% regardless of strain rate. These yield stresses and strains to fracture are comparable to commercial nylon-6 compression molded as reported in the work of Galeski [1,34].

The one sample deformed at $\dot{\epsilon} = 1.3 \times 10^{-3}$ s^{-1} showed very unique behavior with two different necks forming within the same sample. This specimen showed typical neck formation followed by cold drawing to a nominal strain of ~ 1.6 as the neck propagated from the tensile dumbbell shoulder towards the center of the gauge length. Then, instead of continuing to draw material from the undeformed gauge section, the material under went strain softening across the center of the gauge section, formed a second neck which then propagated towards the opposite dumbbell shoulder. Note that the cold drawn extension ratios for the two necks are approximately equal since the second neck started at the center of the gauge length. It is unknown why the neck of this sample stabilized to facilitate cold drawing when other samples prepared in identical fashion fractured just after yield and strain softening.

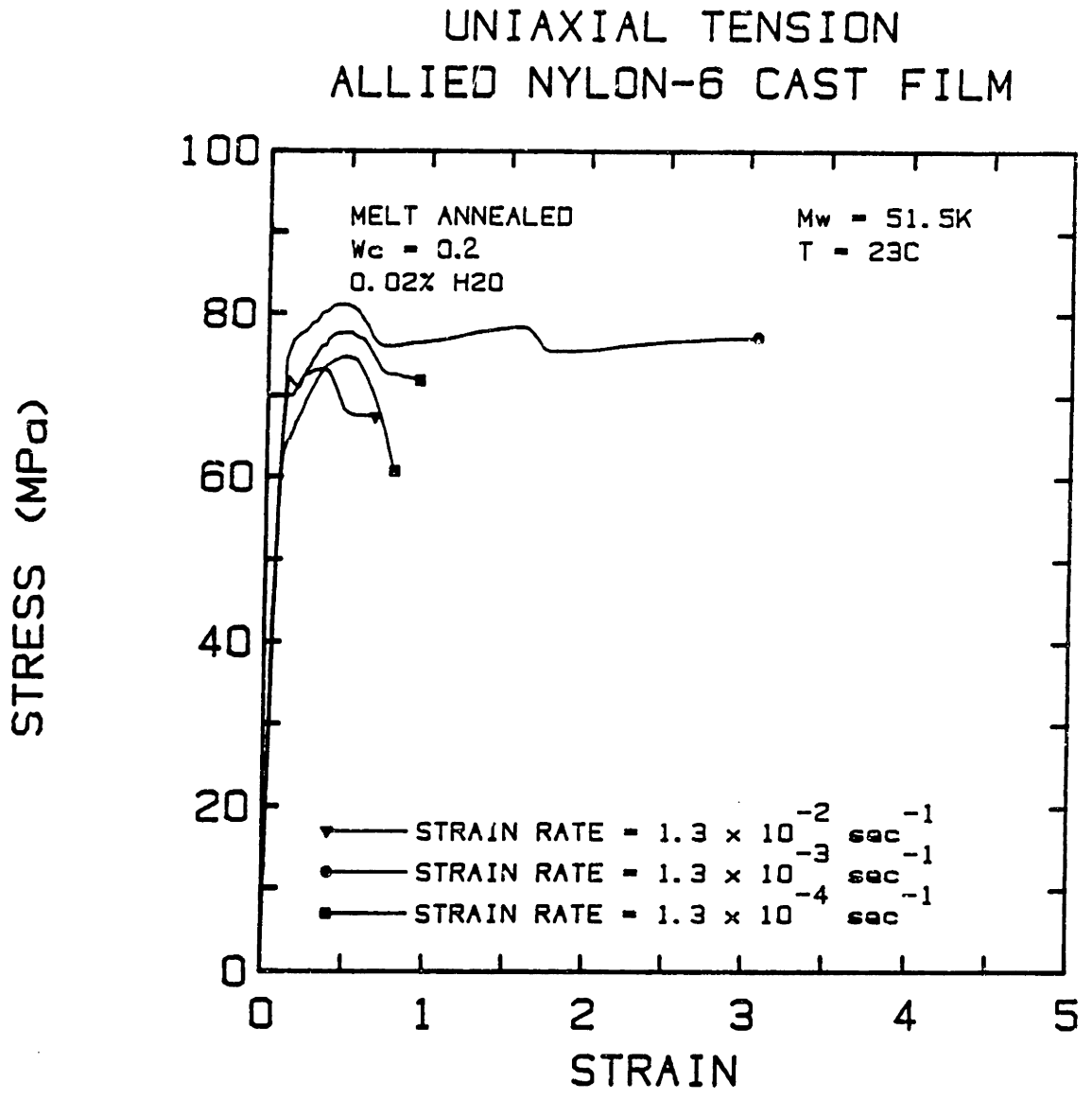

Figure 9-7 Uniaxial tension of spin cast, melt annealed, dry hydrolytic nylon-6 at three different strain rates. Crystallinity content ca. 20 % (based on 100% α form).

The necking and cold drawing may be interpreted from a tensile stress activation theory by Pakula and Fischer [39] which was modified from Argon and Bessenov's [40] viscous flow theory. Pakula and Fischer's theory uses the spinodal tensile stress instability as the thermodynamic activation barrier height in the Eyring transition rate equation (ignoring competitive shear processes of Argon's model). If the deformation stress is less than a critical spinodal (metastable) stress, the volume element can pass from the undeformed to the deformed state only through a series of thermally activated processes where the free energy contour changes due to orientation and alignment. Deformation is finally halted when the strain resistance increases the $\Delta G^{\dagger}$ barrier between successive metastable states so that it can not be overcome by thermal fluctuations. Apparently, the first neck could not continue drawing because it could not produce sufficient strain softening due to increased plastic resistance. Evidently, material on the other side of the central strain hardened region could produce sufficient stress localization, possibly due to geometric instabilities to bring the material to yield, strain soften and neck.

2. Nylon-6-PDMS Diblock Copolymers and Blends

The uniaxial tensile behavior of the PDMS-nylon-6 diblock copolymers and their binary and ternary blends with the respective homopolymers is discussed in this section. The morphology of these materials has been presented in Chapter VIII, §C which shows spherulitic structure with phase separated and occluded rubbery regions for the solution cast films versus emulsified, micellar organization for the melt annealed films. Early experiments focused on discerning any difference in solution cast

versus melt annealed films as was done with homopolyamide-6. As will be shown, the solution cast films were brittle and possessed very little toughness whereas the melt annealed films demonstrated significant enhancement in strain to fracture while maintaining substantial flow stresses. The first subsection will cover the deformation behavior of cast films followed by the melt annealed diblock copolymers and one binary blend with homopolyamide-6. This section will conclude with the performance of the ternary blends consisting of Allied hydrolytic nylon-6 and homo(polydimethylsiloxane) (1 kg/mole) blended with MSN(3/100).

Solution Cast Film Tensile Behavior

The diblock copolymer MSN(3/100) was dispersed in TFEtOH or in one case, blended with some homopolyamide-6 to give a 43/57 % w/w copolymer/nylon-6 binary blend and cast onto teflon-coated aluminum foil dishes or "boats" under slow, controlled solvent evaporation rates. The films formed in about 3-5 days depending on the purge rate and were annealed at 100°C in a vacuum oven (full vacuum) for 16 – 24 hours to remove absorbed solvent. Then, they were cut from the standard dogbone template (gauge section 6.35 mm) and redried at 100°C overnight before testing in the Instron. Moisture was excluded intentionally, so that the toughening effect of the rubber could be ascertained from the σ-ϵ behavior without interference from moisture plasticization. The strain rate for all copolymer tests was 1.3×10^{-3} sec^{-1} (0.5 mm/min). The brittle behavior of these materials is shown in Figure 9-8 for MSN(3/100) and the 43/57 blend plus two nylon-6 cast, 100°C annealed samples (one static casted, the other spin casted) for comparison. The MSN(3/100) diblock was extremely brittle not even reaching a yield point. Additional nylon-6 homopolymer

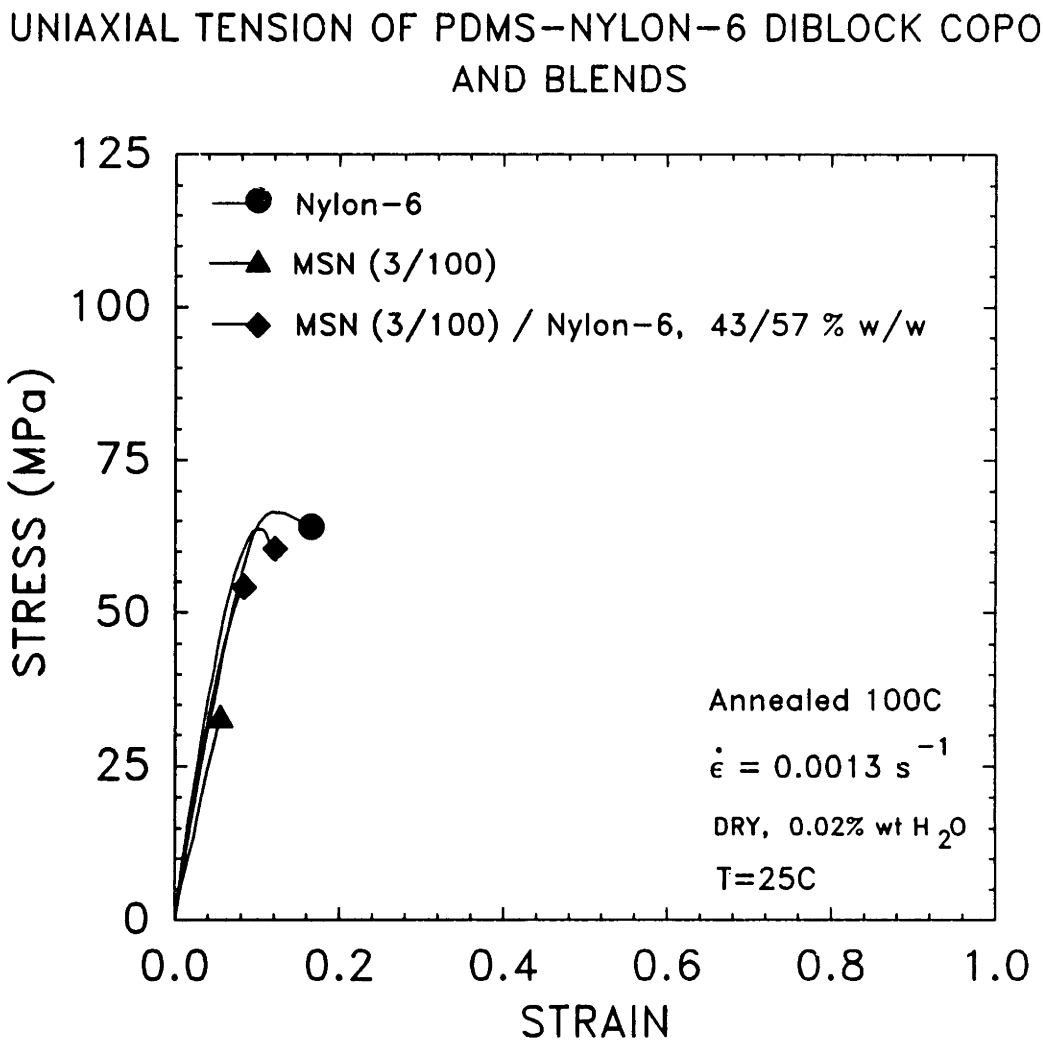

Figure 9-8 Uniaxial tension of diblock copolymer MSN(3/100) and binary blend 43/57 %w MSN/Nylon-6 as compared to nylon-6; all films static cast, annealed 100°C, 24h.

improved the performance increasing the yield stress to ca. 60 MPa with strains to fracture of 12-15 % as compared to homopolyamide-6 with a yield point of ~ 65 MPa. The modulus, yield and tensile stress, toughness (obtained by integration), strain to fracture and natural draw ratio of these materials varied as detailed in Table 9-1.

The reason for the brittle failure of these materials probably is due to several variables. First they have extremely high levels of crystallinity as detailed in Chapter VII reaching over 60 % based on a pure α-form. As was shown in section A of this chapter, this abundance of crystallinity has led to brittle behavior of homopolyamide-6. Apparently, 3 %w rubber distributed in a spherulitic morphology is not sufficient to offset the ease of fracture of these cast materials. Note that much less than 3 %w rubber is actually phase separated into pure rubber microdomains because some portion of the siloxane blocks are chain folded into the interlamellar regions of the spherulitic lamellae and are not available for interaction with the matrix as a separate domain, (see Figures 8-4 to 8-6). Thus, the brittleness may simply be due to the high crystallinity coupled with an insufficient amount of rubber (<3 %w) within the spherulitic morphology to enhance yielding and drawing. Pure nylon-6, being an inherently tough polymer, is able to recover some of the poor performance as its concentration is increased for the binary blend 43/57 %w.

In addition, scanning electron micrographs of cryogenically fractured surfaces (not shown) revealed the presence of micron-size voids that are not due to the fracture process, but rather, were formed during the casting operation when solvent became trapped in the matrix. These

Table 9-1

Mechanical Behavior of Nylon-5 Homopolymer, PDMS-Nylon-6 Copolymer and Blends†

($\dot{\epsilon} = 1.3 \times 10^{-3}$ sec $^{-1}$)
Dry Samples, ca. 2000 ppm Water (unless noted)

Material, T_{annl} (°C)	Young's Modulus* E (GPa)	Yield Stress σ_Y (MPa)	Tensile Stress σ_B (MPa)	Fracture Strain ϵ_f	Toughness (kJ m^{-2}) $\int\sigma d\epsilon$	(λ)
Nylon-6,100†						
Dry Allied	1.55	0.0	59.5	0.15	32	
Wet Monsanto[b)c)]	.82	38.0	38.0	1.7	408	
Nylon-6,250†						
Dry Allied[a)e)]	1.5	62.0	57.6	.60	187	
Allied[c)]	2.25	77.6	72.2	.95	438	2.55
Monsanto[a)]	2.52	80.6	78.1	.57	260	
Wet Allied[a)]	1.15	60.0	65.5	2.67	980	
Monsanto[a)]	1.3	61.2	63.8	1.92	700	
Dry Samples:						
MSN(3/100), 100	1.95	–	33.8	.055	6	
MSN(3/100), 250	1.53	45.6	44.9	1.685	459	
	1.83	68.1	62.3	.51	185	
	2.19	77.5	64.6	.8	314	2.41
	<E>=1.85					
USMSN(15/44), 250	1.52	46.3	46.9	2.07	592	2.13
43/57, 250	1.92	56.7	56.2	1.244	418	1.8
	2.01	57.6	57.0	.66	223	
43/57, 100	2.67	53.5	53.5	.08	–	
	3.09	63.5	61.5	.121	33	
42/56/2, 250						
	1.41	58.3	58.3	.29	88	
Compr Mold[d)]	2.52	73.3	77.6	.49	212	
38/51/11, 250	.99	51.6	47.1	.56	155	
	1.65	58.5	57.6	.54	176	
0/97/3, 250 Binary blend	.67	19.8	19.8	.21	20	

Footnotes for Table 9-1:

† Average values reported for (2) runs; otherwise individual data are shown. All samples static casted unless noted.

* corrected for effective gauge length = 3.0 x actual gauge length; => $E_{corr} = 3.0 \times E_{act}$

a) spin casted film

b) wet samples = 3.2 %w moisture.

c) using $\dot{\varepsilon} = 1.3 \times 10^{-4}$ sec^{-1}

d) compression molded sample, 250°C, 25 min, cool to room temperature in 45 min.

e) Physically aged two years at room temperature

---

voids were also observed by Galeski in the TEM during his sabbatical work here at M.I.T., 1985 in spin casted films of nylon-6. These large voids could also partially be responsible for the brittle behavior and premature fracture of these materials.

The SEM Instron fracture surface of MSN(3/100) annealed at 100°C is shown in Figure 9-9a. The upper left panel resembles a brittle fracture surface without much drawing (plasticity) and contains very smooth upper surfaces of the specimen (highest contour elevation out of the plane of the picture) which were the last interacting surfaces with the other half of the sample. One of these uppermost surfaces is shown at higher

---

Figure 9-9 (see next page) Scanning electron micrographs of fracture surfaces of MSN(3/100) copolymer and 43/57 %w MSN/Nylon-6 binary blend; a) MSN 100°C annealed, deformed in Instron^R; b) MSN/Nylon6 melt annealed, 250°C - Instron^R; c) cryogenically fractured MSN(3/100).

A

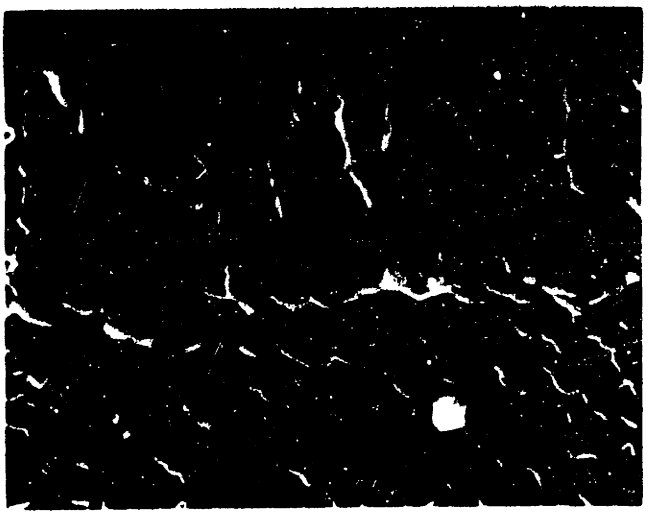

B

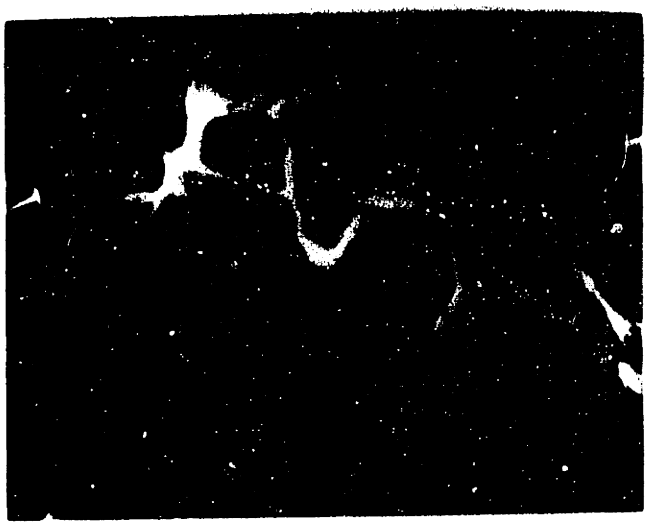

C

Fig. 9-9
p. 451

magnification in the right panel of Figure 9-9a, (with magnification X8 of the left-hand panel 100μm scale bar). The smooth fracture surface is readily seen along with submicron, whitish, spherical regions (on the surface in the upper part of the right-hand panel) that could represent uncavitated rubber domains. If so, this would be analogous to the observations of Wu [41] who observed similarly sized, ca. 0.1 – 1 micron rubbery domains on the fracture surface of brittle samples whereas no rubber particles were seen on the fracture surface of ductile specimens in his nylon-6,6/PI graft copolymer blends. Unfortunately, this can not be confirmed with selective dissolution experiments (using boiling xylene, for example) which normally are done to remove homopolymer rubber from surfaces because the rubber is covalently bonded to the polyamide-6 matrix. Since there is no free rubber in MSN(3/100), this could lead to inconclusive results and was not attempted.

Melt Annealed Copolymer/Binary Blend Tensile Behavior

If these same materials are melt annealed , i.e. heated to 250°C for 10 minutes or so and cooled at a moderate rate, the mechanical behavior is quite different. This is shown in Figure 9-10 where engineering stress is plotted versus nominal strain for the MSN(3/100) copolymer, the 43/57 binary blend, homopolyamide-6 (which represents the best σ-ϵ performance for comparison) and the ultrasonically polymerized polymer USMSN(15/44). The behavior of these materials follows expected trends of yield stress and strain to fracture as a function of rubber content except for the two premature failures in two of the MSN(3/100) samples. These are attributed to flaws in the sample (such as surface imperfections or tiny bubbles created during melt annealing) which limit the

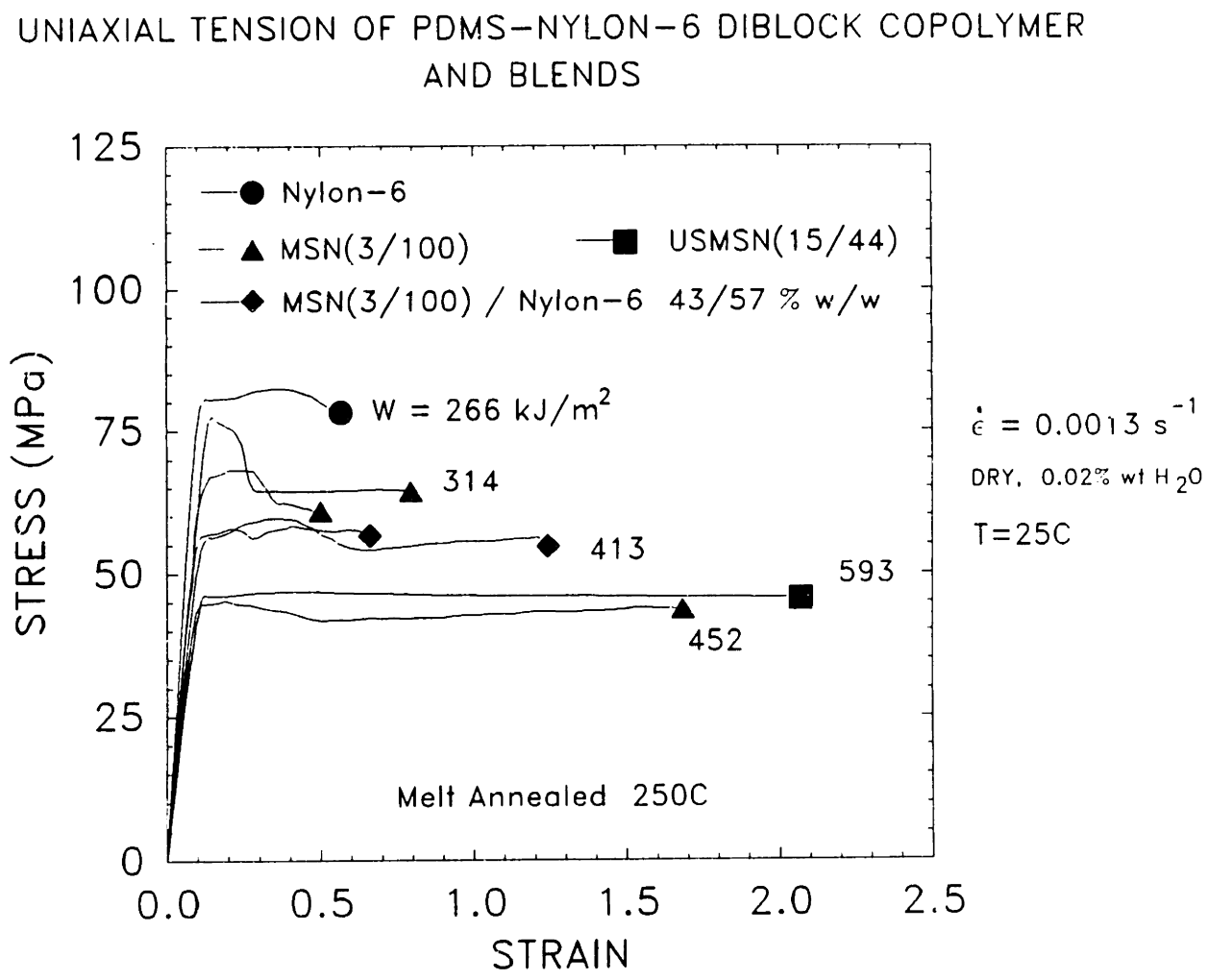

Figure 9-10 Uniaxial tension of dry, melt annealed MSN(3/100), USMSN(15/44), binary blend 43/57 and nylon-6. $W = \int \sigma d\epsilon$ or toughness, [-] kJ/m^2.

inherent ability to reach higher strains to fracture as observed in the third sample of MSN(3/100).

The curves indicate that as the rubber content is increased from 0 % (pure nylon-6) to 1.3 % in the 43/57 blend, the yield stress drops from 75 – 80 MPa to 55 – 60 MPa with a concomitant increase in strain to fracture from approximately 0.6 – 0.8 to 1.0 – 1.2. There is an increase in toughness by about 50 % in the 43/57 blend over pure nylon-6. Performance is compared using the best σ-ϵ curves for each composition. Average behavior for the limited number of samples prepared in this work can be ascertained from Table 9-1 if desired, but the results of the best (i.e. toughest) curves reflect what is inherently possible at each composition.

Continued improvement in toughness is seen at 3.0 %w rubber in MSN(3/100) where the yield stress has been reduced to ca. 45 MPa but with an increase in the strain to fracture to roughly 1.5 – 1.6. This material has increased its toughness by about 70 % over homopolyamide-6 with a moderate decrease in modulus as measured from the σ-ϵ curve, corrected for the elasticity of the dogbone shoulders. The modulus of dry, melt annealed nylon-6 is ca. 2.5 GPa versus 1.85 GPa (mean of all three runs from Table 9-1) for the MSN(3/100) melt annealed sample. This is an approximate 40% decrease comparable to that observed in polybutadiene-polystyrene copolymers [42] for similar rubber loadings. These elastic modulus results should only be considered preliminary, however and probably need to be verified by more sensitive experiments such as dynamic mechanical spectroscopy before they are accepted as absolute.

These materials possess a morphology consisting of spherical rubber domains in a polyamide-6 matrix as determined by TEM in Chapter VIII, §C. The SEM fracture surface of the high strain 43/57 blend is shown in Figure 9-9b indicative of a more ductile failure. Plasticity is evident especially in the bottom half of the figure where a "scallop" structure was produced as a result of greater ductility in the matrix. The "scallop" morphology, however, was present only at the edge of the width of the gauge section where the last contact between the two halves of the specimen existed and the highest distortional plasticity occurred. The upper part of Figure 9-9b is more indicative of the fracture morphology of the major part of the gauge section and shows a similar but less pronounced plastic yielding effect. Unfortunately, this magnification is about one order magnitude too low to conclusively reveal any rubber on the surface; at least at this magnification there does not appear to be any rubber or remnants of cavitated rubber on the fracture surface in agreement with Wu's findings [41] above.

An SEM micrograph of a cryogenically fractured surface of melt annealed MSN(3/100) is shown in Figure 9-9c which reveals two different types of adjacent surfaces. The smooth texture on the left is similar to the fracture surfaces of MSN(3/100) solution cast and annealed at 100°C and then deformed to fracture in the Instron tensile machine at 25°C; see Figure 9-9a, right panel. Both surfaces showed occasional pronounced tufts of highly drawn material but in general were smooth. Note that the sample in panel c is fractured at a much higher (unknown) rate and at liquid N_2 temperature. Evidently the stress distribution is highly non-uniform and creates isolated regions of much higher plasticity whereas

the majority of the material fails in a brittle fashion resulting in the smooth surface.

The right hand portion of Figure 9-9c represents the other type of surface within this cryogenically fractured material and it appears very similar to the fracture surface of melt annealed MSN(3/100) deformed at 25°C in the Instron^{R} (not shown). Both possess a grainy, particle-like surface but the dimensions of the particles or pseudospheres are ca. 1 μm which is larger than the rubbery domains as seen in the TEM micrographs. This type of surface (semi-brittle) is reasonable for the cryogenically deformed sample because the relaxation time of the sample is greater at -196°C. Thus, coordinated movement of chains in response to the applied stress would have been longer than the characteristic time of the fracture process ($\alpha \dot{\epsilon}^{-1}$). This leads to the sort of semi-brittle surface seen in the right hand portion of Figure 9-9c. But why this surface is so similar to that of the high strain to fracture tensile sample deformed at room temperature well above the ductile-brittle transition is not known. Despite a ϵ_f of 1.6, no evidence of highly drawn tufts, cavitated regions or plastically deformed material was present anywhere on the gauge section fracture surface. It is not understood why the fracture surface should consist of spherical particles of apparently homogeneous composition (at least at the 1 μm scale) and largely intact, i.e. no significant distortion in shape or texture. The answer may lie in why the fracture surface of the cryogenically broken sample changed in appearance midway through the thickness of the sample indicative of multiple modes of deformation. This could be related to compositional fluctuations due to the broad distribution of rubber block molecular

weights and accompanying particle sizes. Clearly, more work is required to gain a better understanding of the fracture and deformation processes occurring in these rubber-modified semicrystalline polymers.

The tensile behavior of the USMSN(15/44) melt annealed sample is very attractive from a toughening standpoint. This material contains roughly 25 %w methylsiloxane and possesses a spherical morphology of dispersed rubber in a nylon-6 matrix. Crystallinity of this material is ca. 28 % based on pure α-form (as calculated before). Despite the additional rubber, this material yielded at approximately 46 MPa, similar to the σ_Y of MSN(3/100) and extended to a final strain of over 200%. Profuse stress whitening was found all throughout the gauge section. This gives the largest area under the σ-ϵ curve of the copolymer samples tested. Despite this additional rubber, the modulus of this material is still high at 1.5 GPa, comparable to that of MSN(3/100), $\langle E \rangle$ = 1.8 GPa.

To gain a better understanding of the deformation of this material, and possibly an explanation for the stress whitening, a simple experiment similar to that of Kramer et.al. [43] was performed. The ultra-thin, cast and subsequently melt annealed film was deformed plastically right on the copper TEM grid while gripped in a pair of forceps. Although the deformation is highly nonuniform because different regions of the grid deform proportional to the local tensile and shear stresses which are not homogeneous throughout, some initial understanding can be gained from these types of experiments. Shown in Figure 9-11 is a micrograph of a "micro-craze" from this type of deformation, so named because the thickness of the craze is ca. 100 Å in contrast to the larger dimensions (ca. 1 μm) of more typical crazes in semicrystalline polymers such as in

i-PP [44]. Smaller crazes on the order of 0.1 – 0.5 μm in thickness were observed by Schwier, et.al. [45] in PB-PS diblocks with a dispersed PB phase of ca. 10^3 Å particles. In that study, the craze thickness spanned 1 to 3 particle diameters whereas with this PDMS-nylon-6 diblock material, the craze width is less than the diameter of the particles. Fibrils bridging the thickness of the micro-craze can be seen in both panels of Figure 9-11; unfortunately the fibril structure which was initially much more intact and profuse within the craze cavity was not able to be photographed successfully because of severe beam damage upon first examination. Micrographs taken earlier in the microscopy session were blurred due to movement of the sample probably as a result of charging in the E-beam. Nonetheless, the fibril structure of the craze is evident even though it has been partially destroyed. Only very slight continued growth of the craze occurred during examination in the TEM as a result of beam exposure.

The particles are substantially elongated and although the contrast is low due to the high magnification, can be seen to resemble oblate spheroids (footballs) indicating a strain of ca. 50%. This concurs approximately with the dimensions of the grid square which were photographed before and after exposure. Closer examination of Figure 9-11b indicates that some of the particles seemed to enter the craze, i.e. the plastic deformation of the tufts within the craze drew (or possibly

---

Figure 9-11 (see next page) Transmission electron micrograph of thin-film deformation of dry, melt annealed USMSN(15/44) at ca. 50 % strain. Stress applied in direction indicated by two-headed arrow.

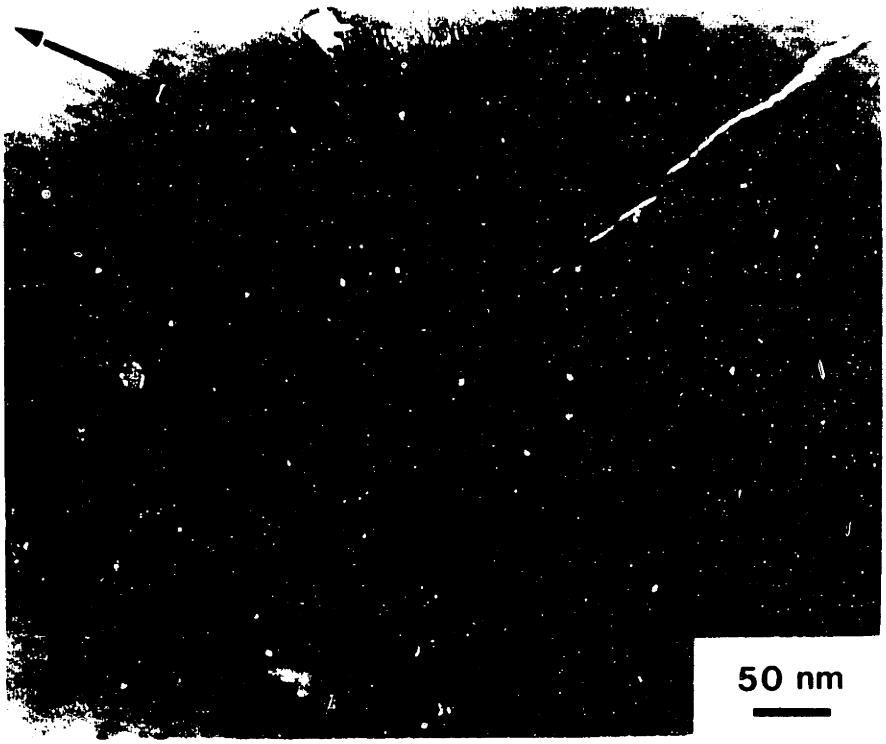

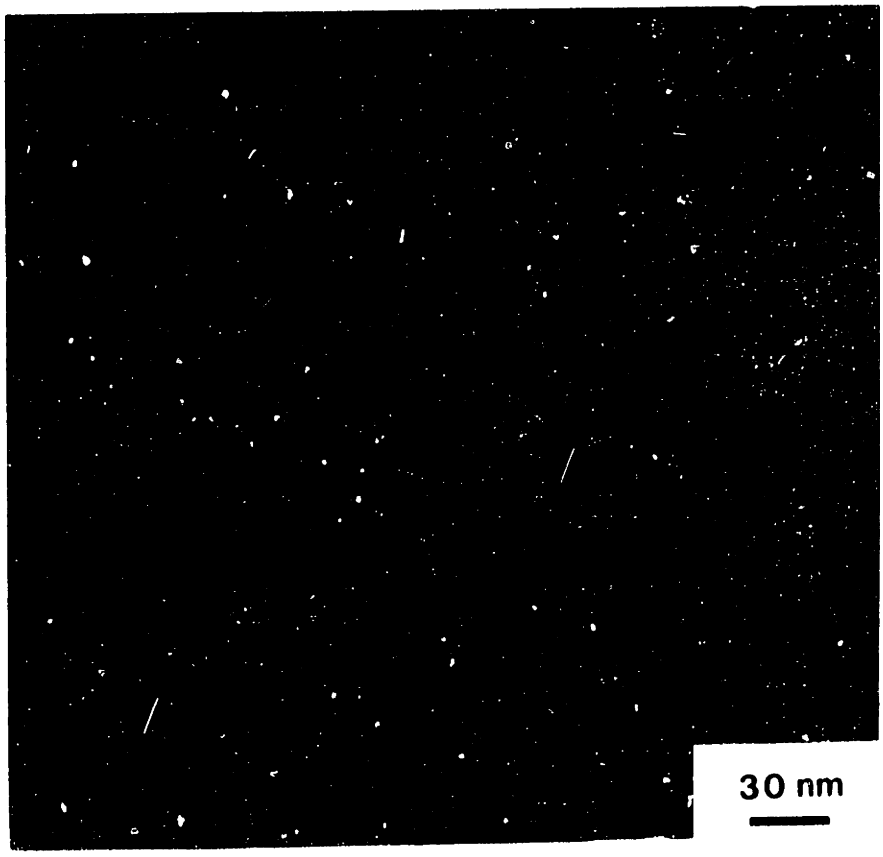

Fig. 9-11
p. 459

sucked via negative pressure) some portion of the siloxane particles into the craze region similar to the cavitation and drawing mechanism found in Schwier's work with amorphous PB-PS diblock copolymers. However, no direct evidence of cavitation of the rubber is observed here, at least not at the ca. 50% strain or so in the thin film. The presence of siloxane in the craze would easily explain the very high beam sensitivity of the craze upon first irradiation in the TEM; siloxane rubber has been seen to literally "boil" in the microscope under the action of the E-beam. The lighter regions in the micrographs which were produced during melt annealing of the film (they were not present in the solution cast material) may be domains of nylon-6 homopolymer or other (electronically) less dense (electronically) regions. They were not produced as a result of the deformation of the sample and do not seem to influence in any way the path of the craze.

The density of the gauge section of USMSN(15/44) after deformation was found be only 1.007 g cm^{-3} as compared to 1.1631 g cm^{-3} initial density. This dramatic decrease supports the observation of stress whitening of the gauge section which has been shown in the literature to be associated with cavitation of rubber domains or dilatational craze plasticity. However, this craze in Figure 9-11 was isolated and no others were seen elsewhere in the film. Most of the other regions underwent simple distortional plasticity with elongation of the rubber particles and did not experience any dilatational plasticity (as in the craze structure). This is probably due to the highly nonuniform stress field developed in deformation of this type. Since the final strain to fracture of the USMSN(15/44) tensile sample was 2.07 with a $\lambda = 2.13$, the

microcraze which occurred in thin film deformation at ca. 50 % strain may have been at the onset of more profuse dilatation. Alternately, other modes such as cavitation may have been operational in the bulk sample. Unfortunately, there was no opportunity to further explore this very important development but it obviously represents an area for continued research.

Melt Annealed Ternary Blend Tensile Behavior

Melt annealed ternary blends of MSN(3/100) copolymer with homopolyamide-6 (Allied) and homo-PDMS (M_p = 1 kg/mole) were evaluated via tensile testing as shown in Figure 9-12. Two of the three σ-ϵ curves for the pure MSN(3/100) which were discussed above are given here for comparison. The 42/56/2 % w MSN(3/100)/Nylon-6/PDMS ternary blend was produced by taking the 43/57 % w MSN(3/100)/Nylon-6 blend and adding 1.7 %w pure PDMS homopolymer to give a total 3.0 %w rubber. This is equivalent of moving along a line in the ternary diagram of Figure 8-1 from the binary composition consisting of 43 %w MSN(3/100) towards the homo-PDMS apex. One sample was static casted and melt annealed under a stream of N_2 (filled square) while the other was compression molded in a Carver lab press at 250°C and ca. 5 psig (open square).

The yield stress of the free surface melt annealed sample (58.3 MPa) is slightly less than the MSN(3/100) curve yielding at 68 MPa but greater than the very tough MSN(3/100) curve which yielded at 45.6 MPa. All of these are below the one MSN(3/100) sample which exhibited a yield stress of ca. 78 MPa comparable to pure nylon-6. The reason for this scatter in yield stress is unknown because all samples contain roughly 3 %w rubber with the 42/56/2 sample containing only 1/3 the amount of di-

block as MSN(3/100). Unfortunately, these results do not facilitate an accurate understanding of how the emulsification affects the mechanical properties. The strain to fracture of the free surface annealed 42/56/2 material is low, reaching only 30% in contrast to the compression molded sample of the same polymer which behaved very similar to nylon-6 homopolymer in both yield stress (σ_Y=73.3 MPa) and strain to fracture (ϵ_f=.49). It is believed the difference in behavior from the two different thermal treatments is due to the suppression of microscopic voids in the compression molded sample which were prevalent in the other 42/56/2 sample. These voids occurred during melt annealing from volatilization of the low molecular weight siloxane in the homo-PDMS. Such low molecular weight homo-PDMS (and its corresponding low molecular weight or oligomeric fraction) was used to ensure miscibility of the homo-PDMS into the rubber block of the copolymer. For the methylcyclosiloxanes, the cyclic hexamer down to the cyclic trimer all have normal boiling points below 250°C, the melt annealing temperature. Since the compression molding operation required larger amounts of copolymer due to the large amount of overflow in the press, additional compression treatments were not done. Although the USMSN(15/44) copolymer would have been an attractive material for ternary blending, similar studies were not undertaken with it due to time constraints and its availability only later in the thesis work.

The other ternary blend, 38/51/11 %w (using the same nomenclature system as above) contained approximately 12 %w total rubber and demonstrated successful emulsification of the homo-PDMS into the block copolymer as discussed in Chapter VIII. This composition is also shown

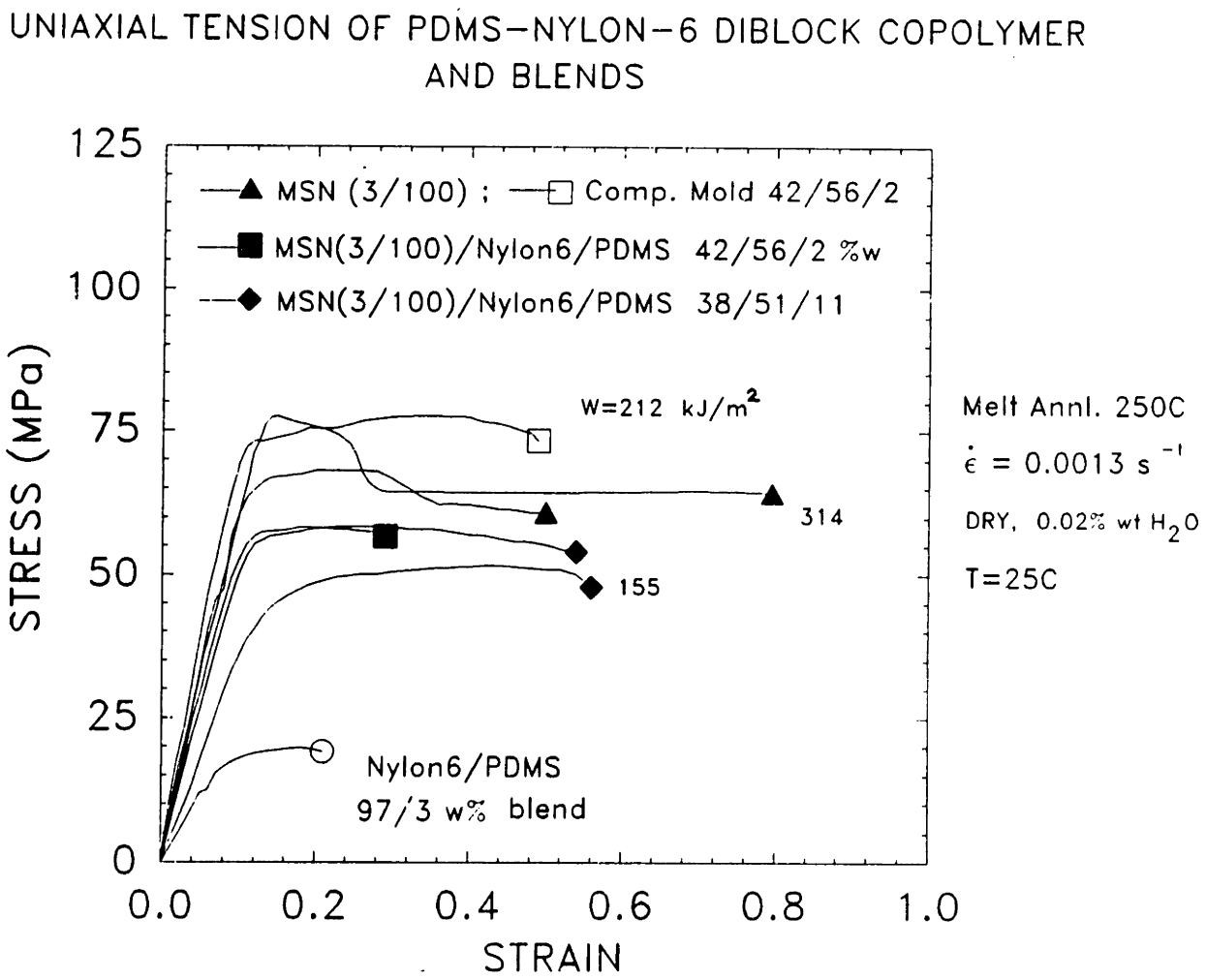

Figure 9-12 Uniaxial tension of dry, melt annealed ternary blends of MSN(3/100) / Nylon-6 / PDMS; Compositions = 42/56/2 %w and 38/51/11 %w; additional curves MSN(3/100) for comparison.

in Figure 8-1 for reference. Unfortunately, the same foaming problem due to oligomeric siloxane prevented a detailed interpretation of its performance which shows a lower average yield stress than the 42/56/2 blend and higher strains to fracture (mean σ_y=54 MPa and ϵ_f=.55). Because of the foaming that developed rapidly upon heating above the melting temperature, these samples were not held above the melt for more than 3 – 5 minutes which may not have been enough time for complete melting of the solution cast spherulitic morphology and re-establishment of the micellar morphology that was found to be very tough with the pure copolymers and binary blend with nylon-6.

As expected, the binary blend of pure homopolymers 0/97/3 consisting of 97 %w homopolyamide-6 with 3 %w of the low molecular weight PDMS gave very poor mechanical performance. Its stress-strain curve is shown in Figure 9-12 and reaches only 20 MPa yield stress. The addition of just 3 % of the immiscible rubber drastically reduced the strength (yield and tensile) and modulus of pure nylon-6. Thus, it is obvious that a copolymer is required to achieve significant improvements in toughness because the immiscibility of the blend simply degrades mechanical performance.

Summary

The mechanical behavior of the rubber-modified nylon-6 materials is encouraging, particularly the copolymers. Very good toughness has been found in USMSN(15/44) as well as the lesser defined MSN(3/100) copolymer and its binary blend with homopolyamide-6. For these materials, expected trends have been observed in increase of strain to fracture, yield stress and energy absorbed during deformation as a function of rubber content.

Unfortunately, the results of the ternary blends have been masked by the unforeseen volatilization of the low molecular weight siloxane. Much better results undoubtedly can be achieved in future blending studies with USMSN(15/44) where the greater molecular weight siloxane block should give more flexibility in blending studies. Alternately, higher molecular weight homo-PDMS could be used directly with MSN(3/100) despite the rule of thumb in regards to block versus homopolymer molecular weights.

From this limited exploration into the mechanical properties of siloxane rubber-modified nylon-6, it is evident that the USMSN(15/44) diblock copolymer has the requisite simplicity in structure that will permit analysis of the mechanics of deformation from a theoretical standpoint. The performance of this particular material has been extremely encouraging; the exceptional toughness of this material holds potential for use as an impact plastic at low service temperatures. The discovery of dilatation, no matter how profuse, coupled with the observations of the stress whitening and density measurements in bulk, has opened the door for investigation into an entirely different and as yet, unexplored area in rubber toughening of semicrystalline polymers. And finally, the emulsification potential of diblock copolymers can be more fully explored with these new materials which giver greater flexibility in tailoring material properties to suit specific mechanical requirements.

D. REFERENCES FOR CHAPTER IX

1. A. Galeski, A.S. Argon and R.E. Cohen, Macromolecules., **21**, 2761 (1988).

2. A. Schaper, R. Hirte and C. Ruscher, Coll. Polym. Sci., **264**, 668 (1986).

3. P.H. Geil, Jnl. Polym. Sci., **A2**, 3857 (1964).

4. P.H. Geil, Jnl. Polym. Sci., **44**, 449 (1960).

5. D.P. Russell and P.W.R. Beaumont, Jnl. Mat. Sci, **15**, 197, 216 (1980).

6. L.G. Roldan and H.S. Kaufman, Polym. Lttrs., **1**, 603 (1963).

7. D.R. Holmes, C.W. Bunn and D.J. Smith, Jnl. Polym. Sci., **17**, 159 (1955).

8. T.J. Bessell, D. Hull and J.B. Shortall, Jnl. Mat. Sci., **10**, 1127 (1975).

9. A. Keller, Jnl. Polym. Sci., **17**, 351 (1955).

10. D.A. Zaukelies, Jnl. Appl. Phys., **33**, 2797 (1962).

11. S.N. Zhurkhov, V.A. Zakrevskyi, V.E. Korsukov, V.S. Kuksenko, Jnl. Polym. Sci., Pt A-2, **10**, 1509 (1972).

12. A. Peterlin, Jnl. Phys. Chem., **75**(26), 3921 (1971); also see additional references in Chapter II.

13. A. Galeski and E. Piorkowska, Jnl. Polym. Sci., **21**, 1299 (1983).

14. I.L. Hay and A. Keller, Kolloid. Z.Z. Polym., **294**, 43 (1965).

15. B.H. McConkey, M.W. Darlington, D.W. Saunders and C.G. Cannon, Jnl. Mat. Sci., **6**, 572 (1971).

16. P. Predecki and A.W. Thornton, Jnl. Appl. Phys., **41**, 4342 (1970).

17. F. Ramsteiner, W. Heckman, Polym. Commun., **26**, 199 (1985).

18. S. Cimmino, L. D'Orazio, R. Greco, G. Maglio, M. Malinconico, M. Mancarella, E. Martuscelli, R. Palumbo, G. Ragosta, Polym. Eng. Sci., **24**, 48 (1984).

19. R. Greco, N. Lanzetta, G. Maglio, M. Malinconico, E. Matruscelli, R. Palumbo, G. Ragosta and G. Scarinzi, Polymer, **27**, 299 (1986).

20. F. Ida and A. Hasagawa, Jnl. Polym. Sci., **18**, 963 (1974).

21. R.J.M. Borggreve, "Toughening of Polyamide-6", doctoral thesis, Universiteit Twente, Netherlands, 1988, Ch. 5.

22. R.J.M. Borggreve, R.J. Gaymans, J. Schuijer and J.F. Ingen Housz, Polymer, **28**, 1489 (1987).

23. S. Wu, Jnl. Polym. Sci, Polym. Phys. Ed., **21**, 699 (1983).

24. R.H. Wondraczek and J.P. Kennedy, Jnl. Polym. Sci., Polym. Chem. Ed., **20**, 173 (1982).

25. J.P. Kennedy and R.A. Smith, Jnl. Polym. Sci., Polym. Chem. Ed., **18**, 1523 (1980).

26. T. Kiyotsukuri, N. Tsutsumi, K. Ayama and M. Nagata, Jnl. Polym. Sci., Pt. A, Polym. Chem., **25**, 1591 (1987).

27. J.D. Gabbert and R.M. Hedrick, "Properties of RIM Nylon-6 Block Copolymers", paper presented at AIChE meeting, August, 17, 1981, Detroit, MI.

28. J.L.M. Van der Loos and A.A. Van Geenen, Am. Chem. Soc. Symp. Ser., **270**, 181 (1975).

29. C. Garbuglio, G. Ajroldi, T. Casiraghi, G. Vittadini, Jnl. Appl. Polym. Sci., **15**, 2487 (1971).

30. DuPont Design Handbook, Zytel^{R} and Minlon^{R} Module II, p.38.

31. S. Gogolewski and A.J. Pennings, Polymer, **18**, 647, 660 (1977).

32. A. Nadai, Theory of Flow and Fracture of Solids, McGraw-Hill, New York, 1950, p.71.

33. R.G. Crystal and D. Hansen, Jnl. Polym. Sci., PtA-2, **6**, 981 (1968).

34. A. Galeski, A.S. Argon and R.E. Cohen, Makromol. Chem., **188**, 1195 (1987).

35. S.N. Zhurkov, A.Ya. Savostin, E.E. Tomashevskii, Dokl. Akad. Nauk SSSR, **159**, 303 (1964).

36. S.N. Zhurkov, E.E. Tomashevskii, Phys. Basis of Yield and Fracture, Conf. Proc. 1967, 1968, p.200.

37. D.K. Roylance, K.L. DeVries, M.L. Williams, Fracture, Chapman & Hall, London, 1969, p.551.

38. G.S.P. Verma, A. Peterlin, Kolloid-Z. Z. Polym., **236**, 111 (1970).

39. T. Pakula, E.W. Fischer, Jnl. Polym. Sci., Polym. Phys. Ed., 19, 1705 (1981).

40. A.S. Argon, M.I. Bessonov, Polym. Eng. Sci., 17(3), 174 (1977).

41. S. Wu, Polymer, 26(11), 1855 (1985).

42. E.R. Wagner and L.M. Robeson, Rubber Chem. Technol., 43, 1129 (1970).

43. C.S. Henkee and E.J. Kramer, Jnl. Polym. Sci., Polym. Phys. Ed., 22, 721 (1984).

44. K. Friedrich, Adv. in Polym. Sci., 52/53, ed. H.H. Kausch, Springer Verlag, 1983, p. 225.

45. C.E. Schwier, A.S. Argon and R.E. Cohen, Philosophical Magazine, 52(5), 581 (1985).

CHAPTER X. SUMMARY; CONCLUSIONS AND RECOMMENDATIONS

A. CONCLUSIONS

Considerable insight has been gained into the rubber-modification of semicrystalline materials in general, and nylon-6 in particular through this thesis work. A coordinated ternary effort involving synthetic chemistry, morphological characterization and mechanics of deformation has been accomplished which has led to some insightful findings. Although poly(dimethylsiloxane)-nylon-6 diblock copolymers have been previously synthesized, this thesis work developed the first process to do this anionically and attain sufficiently high molecular weights of polyamide to be useful as toughening agents in blends or in pure form. Unique morphologies have been discovered in these materials and have led to a better understanding of the interaction of crystal, rubber and solvent when films are cast from solution. And finally, these materials have shown excellent toughness when deformed in uniaxial tension.

Much has been learned about the polymerization of cyclic siloxanes through kinetic modeling work and the further development of promoter/initiator systems. Quantification of the detrimental backbiting and depolymerization reactions in the synthesis of poly(trifluoropropylmethylsiloxane) has significantly improved the yield of this siloxane over the often accepted equilibrium value. The siloxanes have been successfully end-functionalized with a coupling agent synthesized in-house and used to initiate ϵ-caprolactam ring opening copolymerization. The strong basicity of the conventional caprolactam salt catalysts has been altered by the discovery of coordinating catalysts which have permitted successful copolymerization of PDMS macromonomer at elevated

temperatures in bulk so as to produce high molecular weight polyamide-6 blocks suitable for toughening applications.

The yield of siloxane macronomoner incorporated into the diblock copolymer has been enhanced by utilization of ultrasonic dispersion to provide better mixing of the immiscible siloxane and caprolactam monomer. Diblock copolymer structure has been proved through a concerted effort using various techniques that include solubility\molecular characterization experiments, electron microscopy and "simulation" reactions to ascertain the detrimental effect of nylon-6 polymerization catalysts on siloxane block integrity.

The morphologies of the diblock copolymers and blends have been determined mostly by transmission electron microscopy and shown to be heavily "path dependent"; i.e. dependent on the preparation process. Well defined spherulitic structure with occluded siloxane domains is seen for the copolymer and blends when cast from solution. Melt annealing has been shown to transform the morphology of copolymers with shorter siloxane blocks from the spherulitic to a mesophasic structure; copolymer morphology for those with longer siloxane blocks is seen to be invariant when cast from a good solvent for the crystalline block versus that from melt recrystallization.

Electron microscopy also has been used to support a general theory about the competition between phase separation and crystallization phenomena. A conceptual phase diagram was proposed that combined tenants of general thermodynamic theories with experimental observations to predict a molecular weight dependence on the controlling behavior of micellization versus crystallization. Crystallization studies have been

done which yield expected trends in surface free energy and nucleation density and indicate that the onset of crystallization is more rapid in the copolymers than for homopolyamide-6 under identical conditions.

And finally, improved mechanical performance of the new diblock copolymers over nylon-6 has been found. Substantial increases in toughness (area under the σ-ϵ curve) have been observed for both diblock copolymers and the binary blend with homopolyamide-6. The ability of the copolymers to emulsify and stabilize blends of homopoly(dimethylsiloxane) and homopolyamide-6 has been demonstrated via electron microscopy. This supports existing viewpoints on the emulsifying ability of copolymers in controlling morphologies for specific end uses. The successful synthesis of a high molecular weight poly(dimethylsiloxane)-b-polyamide-6 diblock exhibiting well-defined morphology has provided a solid foundation for continued understanding of the toughening mechanisms in rubber modified semicrystalline copolymers.

B. RECOMMENDATIONS

This research has developed a strong foundation for continued study in the modification of thermoplastics for impact applications. Perhaps the most salient conclusion to be reached in this work is that the use of a siloxane-nylon-6 diblock copolymer can markedly improve the toughness of homopolyamide-6 when deformed below its T_g. More questions currently exist than have been answered as to how the copolymers, particularly USMSN(15/44), achieve the large strains to fracture without sacrificing a great deal of yield and flow stress. The actual mechanism of deformation still remains to be ascertained although evidence of dilatation has been gathered for both bulk and thin film samples. There is a great potential

for exploring the emulsification of the homopolymers into USMSN(15/44) and the resulting changes in morphology. This exists because a well defined structure is available as the starting point (the spheres of PDMS in a nylon-6 matrix) that is more amenable to mechanical modeling and theoretical interpretation.

Much still needs to be learned about the effects of selective solvents, composition, molecular weight and processing on the morphology of semicrystalline-amorphous diblock copolymers. Current theories require assistance in determining molecular parameters with greater precision and accuracy and this can only come from planned, coordinated experiments undertaken with the realization of what is needed and why.

The synthetic implications of this work may be more widespread than just polymerizations of lactams. Other compounds such as oxazolidine diones which are precursors to the polypeptides may be polymerized with siloxanes through similar chemistry. The advent of a nonaggressive catalyst that permits successful copolymerization of siloxane with lactams may have use outside academe in industrial applications. This technology is worth exploring because of the other intrinsic properties (such as hydrophilic oxygen membranes) that are contained within silicone-polyamide copolymers.

APPENDIX 1: SEMICRYSTALLINE HOMOPOLYMER CRYSTALLIZATION KINETICS

Homopolymer crystallization is a complex process due to the interaction of a long chain at a small nucleation surface. This simple fact causes crystallization to deviate from equilibrium thermodynamics and be controlled by metastable kinetics. The field of crystallization has seen many advances in the last 40 years most notably, the theory for classical nucleation and growth from germ nuclei by Avrami [1], Turnbull and Fisher's [2] absolute rate theory for condensed systems and the kinetic theory of chain folding by Lauritzen and Hoffman [3].

In 1837, Poisson determined the probability that m waves emanating from various point sources will reach a given point P simultaneously. This expression is known as the Poisson distribution where E = (wave) expectation value.

$$P_m(t) = \frac{E^m}{m!} \left[\exp - E(t) \right] \qquad \text{(A1-1)}$$

For a given point to remain amorphous, m must equal zero (no waves reach P) which gives

$$1 - \frac{v_c(t)}{v_c^\infty} = \exp[- E(t)] \qquad \text{(A1-2)}$$

where the equation is normalized by v_c^∞, the maximum volume fraction crystallinity and v_c = the time dependent volume fraction crystallinity.

The rate of crystallization depends on the growth rate function $G(r,\theta,\phi,t)$ and the rate of nuclei generation in space and time which is represented by the nucleation density function, $F(r,\ell,\phi,t)$ [4]. Since E

corresponds to the expectation value for any growth rate, it is just the integral of the nucleation density function over the melt volume throughout the time interval of interest.

$$E(t) = \int_0^t \int_V F(r,\theta,\phi,t')\, dV\, dt' \qquad \text{(A1-3)}$$

The exact functional form of the nucleation density function can only be determined analytically for specific nucleation modes. For cases where multiple crystallization mechanisms are present, the nucleation density function must be determined by additional experiments. Fortunately, simplifying assumptions can be made without introducing appreciable error. If the growth is isotropic, then $G \neq G(\theta,\phi)$, $F \neq F(\theta,\phi)$ and if the nucleation events are randomly distributed in space, the nucleation density function is independent of r and depends on t only. The growth rate function can also be considered independent of radial position unless transport conditions (the Stefan problem) dominate as in crystallization from the gas phase [5]. Additionally, for nylon-6 and many other polymers, the radial growth rate is constant in time [6,7,8]. This is because spherulite growth is usually rate limited by secondary (or molecular) nucleation upon the spherulite lamellar substrate. The following theory also assumes true isothermal crystallization which presupposes negligible gradients within the sample; this is realistically met only for very thin samples due to the low to moderate thermal conductivity of the polymer melt/crystals.

Nucleation can be divided into two classes, heterogeneous or homogeneous usually depending on the supercooling. Homogeneous nuclea-

tion usually occurs when all foreign nuclei are removed which permits larger supercoolings (ΔT) to be realized. This is because thermal (density) fluctuations create the nuclei and they have a lower activation barrier at large supercooling. However, for some polymers like nylon-6, evidence of homogeneous nucleation from an Avrami exponent, $n = 4$ exists at low supercooling as found by Magill and in results of this thesis, see Chapter VII. In practice, heterogeneous primary nucleation often dominates due to traces of catalyst, dust or particulate heterogeneities and can be either thermal (spontaneous) or athermal (instantaneous). The time dependence of nucleation can be ascertained by hot stage optical microscopy where the appearance of birefringent sheafs of the spherulites indicates whether nucleation is thermal or athermal.

Athermal Nucleation

The mathematical form of the nucleation density function for athermal nucleation is the Dirac delta function where τ represents the crystallization induction time and N represents the nuclei density [=] nuclei/cm^3.

$$F(t) = \delta (t - \tau) N \qquad \text{(A1-4)}$$

Assuming three-dimensional spherulitic structure, the impulse function is substituted into equation (A1-3) to give the expectation value which subsequently is substituted into equation (A1-2).

$$1 - \frac{v_c}{v_c^\infty} = \exp\left[- \int_0^t \delta(t'-\tau) N \, dt' \int_\tau^t 4\pi\phi_{cs} \; G^3 \; (t'-\tau)^2 \; dt' \right] \tag{A1-5}$$

where $dV = 4\pi r^2 \phi_{cs} \, dr = 4\pi \, \phi_{cs} \, G^2 \, (t-\tau)^2 \, G \, dt$

and ϕ_{cs} = crystalline volume fraction <u>within</u> the spherulite.

Performing the intergration, noting that $\int_{t'}^{t} \delta(t'-\tau) \, N \, dt' = N(\tau) = N =$ constant, gives the kinetic expression for spherulitic, athermal nucleation.

$$1 - \frac{v_c(t)}{v_c^\infty} = \exp\left[- \frac{4}{3} \; \pi \; G^3 \; \phi_{cs} \; N \; (t-\tau)^3 \right] \tag{A1-6}$$

Taking logarithms twice gives,

$$\log \left[\ln \frac{v_c^\infty}{v_c^\infty - v_c} \right] = 3 \log (t-\tau) + \log K_a \tag{A1-7}$$

where $K_a = (4\pi/3)N\phi_{cs}G^3$ for athermal, spherulitic nucleation. This is the well known Avrami equation in traditional double log form.

<u>Thermal Nucleation</u>

For thermal nucleation, the nucleation density function must account for the spontaneous generation of nuclei. Let I^* represent the generation of nuclei per second per cm^3 where the exact functional form will be developed shortly. As the process proceeds, nuclei are randomly generated in space and time and the growing fronts pass through point P in a differential spherical volume element, $4\pi r^2$ dr. Any front reaching P must have been growing for time (t - r/G) where r = the radius of the

spherical shell from the point source and G = the constant growth rate in cm/sec. Thus,

$$F(t)\, dV = (t - r/G)\, I^* \, 4\pi r^2 \phi_{c_s} \, dr \qquad \text{(A1-8)}$$

and subsequent substitution and integration in equation (A1-2) gives the expectation value.

$$E(t) = \pi I^* \phi_{c_s} G^3 t^4/3 \qquad \text{(A1-9)}$$

Substitution into Poisson's distribution for m=0 gives the Avrami equation for spherical, thermal nucleation,

$$\log \left[\ln \frac{v_c^\infty}{v_c^\infty - v_c} \right] = 4 \log t + \log K_t \qquad \text{(A1-10)}$$

where $K_t = \pi \phi_{c_s} G^3 I^*/3$.

As can be seen from the athermal versus thermal developments (compare eqs (A1-7) and (A1-10)), the general form of the Avrami equation can be written

$$\log \left[\ln \frac{v_c^\infty}{v_c^\infty - v_c} \right] = n \log t + \log K \qquad \text{(A1-11)}$$

where the exponent n represents the type of nucleation and growth and K contains the nucleation density function. This general analysis will aid in revealing the type of crystallization from the slope of a log-log plot of the crystallinity quotient as a function of time. Since many types of crystallization exist such as ribbon crystallization in two-dimensional thin films and lamellar, fibrillar or truncated spherical growth in three dimensions, the general form Avrami equation provides a framework for analysis of crystallization data. However, this data analysis should not

take the place of microscopic investigation in determining crystallization mechanisms, nor does the general theory allow for fractional exponents unless two-stage or truncated spherulitic growth occurs or some similar physical change in the growth mechanism.

Several key assumptions are inherent in the Avrami analysis which can be significant. First, the theory assumes no density change upon crystallization which is rarely observed (nylon-6 $\Delta\rho \approx 10\%$). Multiple nucleation and growth modes may be involved or there may be a mechanistic change during crystallization, neither of these being accommodated by the theory. And very importantly, crystal perfection may occur causing a decrease in the Avrami exponent as secondary and tertiary nucleation become dominant. These factors limit the usefulness of the Avrami analysis despite its widespread acceptance and use.

Thermodynamics of Nucleation

Chain folded lamellar structures have been verified in crystal mats grown from dilute solution by various authors using experimental techniques such as electron microscopy and diffraction, SAXS and optical microscopy and a detailed summary is given by Geil [9]. Only recently, [10] has there been conclusive evidence of chain folded structures in the bulk nylon-6 he thermodynamics of nucleation and chain folding onto a substrate are discussed next. Consider a nucleus with sides of dimension a and ℓ and thickness b_o. The crystal has free energy contributions from the bulk crystal nucleus plus interfacial free energy terms.

$$F_c = F_{bc} + \sum \sigma_i A_i \qquad \text{(A1-12)}$$

The free energy change on crystallization is therefore,

$$\Delta F_c = F_c - F_a \tag{A1-13}$$

$$= F_{bc} - F_a + \sum \sigma A \tag{A1-14}$$

$$= -a\ell b_o \Delta g_f + 2\ell b_o \sigma + 2ab_o \sigma_e \tag{A1-15}$$

where Δg_f = free energy of fusion per unit volume and σ and σ_e are the side and chain folded end surface free energies. No contribution comes from the top surface because the surface energy in producing it is compensated by covering equal area on the bottom. This function for ΔF_c represents a three-dimensional surface with a saddle point where the derivatives with respect to the nucleus dimensions ($\partial \Delta F_c / \partial \ell$, $\partial \Delta F_c / \partial a$) vanish. These give the critical nucleus dimensions.

$$a^* = 2\sigma / \Delta g_f \tag{A1-16}$$

$$\ell^* = 2\sigma_e / \Delta g_f \tag{A1-17}$$

Hence, the critical free energy of crystallization is

$$\Delta F_c^* = \Delta F^* = 4b_o \sigma \sigma_e / \Delta g_f \tag{A1-18}$$

and represents the minimum value of ΔF_c for a given nucleus size.

The volumetric free energy of fusion can be expressed as

$$\Delta g_f = \Delta h_f - T \Delta s_f \quad . \tag{A1-19}$$

For moderate to low supercoolings, the entropy of fusion is constant over the temperature range and can be computed from $\Delta s_f = \Delta h_f / T_m^o$ where T_m^o = equilibrium melting temperature. Thus,

$$\Delta g_f = \Delta h_f (1 - T/T_m^o) \tag{A1-20}$$

$$= \Delta H_f \rho_c \Delta T/T_m^o \tag{A1-21}$$

where ΔH_f is the specific heat of fusion of the crystal and ΔT is the supercooling = T_m^o-T. With this expression for Δg_f, the critical nucleus free energy of formation becomes

$$\Delta F^* = (4b_o \sigma\sigma_e/\rho_c \Delta H_f) T_m^o/\Delta T \tag{A1-22}$$

Note that the free energy of crystallization increases indefinitely as T $\rightarrow T_m^o$, i.e. the barrier to nucleation is virtually insurmountable near the equilibrium melting temperature.

The derivation of the critical nucleus size and free energy barrier for homogeneous nucleation is analagous to the development for heterogeneous nucleation except that the top and bottom surfaces must be included in the interfacial free energy term. Thus,

$$\Delta F_c = -a\ell b_o \Delta g_f + (2a\ell + 2b_o \ell)\sigma + 2ab_o \sigma_e \tag{A1-23}$$

and if $a = b_o$, then

$$a^* = 4\sigma/\Delta g_f \tag{A1-24}$$

$$\ell^* = 4\sigma_e/\Delta g_f \tag{A1-25}$$

followed by

$$\Delta F^* = [32\sigma^2 \sigma_e/(\Delta H_f \rho_c)^2]\ T_m^{o\,2}/\Delta T^2 \tag{A1-26}$$

However, there are limitations to the classical thermodynamic approach to nucleation. These expressions for ΔF^* hold only for the lowest free energy shapes, i.e. equilibrium nuclei. Other non-equili-

brium paths are possible, which are not described by the classical thermodynamic approach and may contribute significantly to the development of the crystal. Secondly, intensive thermodynamic properties of a macroscopic system, such as σ_e and ΔH_f, are used in the estimation of the free energy of formation, ΔF^* of a microscopic surface nucleus. In most all cases, the macroscopic crystal does not have the degree of perfection for these substitutions. And finally, the surface and end interfacial free energies are considered isotropic; in reality, especially at large supercooling, a spatial dependence might be necessitated for such small volumes.

Crucial in the development of nucleation theory is the determination of T_m^o, the equilibrium crystal melting temperature. With extrapolation of the well known Thompson-Gibbs [11] equation for small molecules, the melting point, T_m corresponds to the lamellae thicknes, ℓ.

$$T_m = T_m^o[1 - 2\sigma_e/\Delta H_f \rho_c \ell] \qquad \text{(A1-27)}$$

This has been found to apply for PE [12] and PTFCE [9] using SAXS in the former case to measure lamellae thickness.

An alternate method is to use the Hoffman-Weeks [13] equation and extrapolate or find the point where the T_m-T_c curve intersects the T_m=T_c line.

$$T_m = T_c/\beta + T_m^o(1 - 1/\beta) \qquad \text{(A1-28)}$$

Here, the parameter β is a morphological factor. Obviously, this method is easier and obviates the need for analyzing scattering data for the long period which has some variability in its interpretation.

Classical Nucleation Rate Theory

Based on absolute reaction rate theory (see Glasstone et.al. [14]), Turnbull and Fisher [2] derived an expression for the nucleation rate in a condensed phase.

$$R^*(\text{nuclei/sec}) = \frac{NkT}{h} \exp\left[-(\Delta F^* + \Delta F_\eta/kT\right] \qquad \text{(A1-29)}$$

The pre-exponential factor has been derived by Turnbull and Fisher to within an order of magnitude by a Taylor series expansion of the exponentials of nuclei free energy of formation ($\exp[d(\Delta F_i/kT)/di]$ in their paper). The N represents the surface atoms available for nucleation and the argument of the exponential represents the total nucleation barrier. It consists of two terms; the free energy activation barrier to nuclei formation, ΔF^* as described earlier, and the barrier to molecular transport across the crystal-melt interface, ΔF_η.

This transport term has been represented in previous developments as the barrier associated with segmental mobility of the chain suggesting use of a modified WLF equation [15].

$$\Delta F_\eta/kT = 2070 \,/\, [51.6 + T - T_g] \qquad \text{(A1-30)}$$

This equation holds for temperatures up to about T_g + 100°C [16]. However, data for several polymers (PE, PTFCE, and i-PST) collected by Boon [17] showed that a special fit to the data was necessary to accurately account for the transport term. His form uses a single adjustable parameter, C_2,

$$\Delta F_\eta/kT = C_1 \,/\, [C_2 + T - T_g] \qquad \text{(A1-31)}$$

where C_1 = 2070 and C_2 = 75 for i-PST, = 90 for poly(tetramethyl-p--silphenylene siloxane), = 130 for nylon-6 but = 51.6 for PE and PTFCE. The variance is attributed to the bulkiness of the chain substituents and hence chain mobility. This seems reasonable due to the bulky side groups in the first two polymers and the hydrogen bonding interaction in nylon-6. The last two are vinyl polymers with minimum hindrance to mobility and only van der Waal's interaction forces to overcome for reptation and transport.

Since linear growth is rate limited by the nucleation step, the normal growth rate, G is given by [18],

$$G(cm/sec) = b_o R^* n_s / N = G_o \exp\left[-\frac{\Delta F^*}{kT} - \frac{\Delta F_\eta}{kT} \right] \qquad (A1\text{-}32)$$

where n_s is the number of substrate "steps" and is essentially constant during growth. It is usually left out of more conventional developments and its presence as a multiplying factor in G_o should be noted.

The growth rate expression contains the sum of the thermodynamic barrier which is greatest at higher temperatures (low supercooling in denominator of eqn (A1-22)) and the transport barrier which increases sharply as $T \to T_g$. Thus, the growth rate versus T curve appears bell-shaped and has its maximum where the sum of the two terms is minimal.

Homogeneous nucleation is characteristic of the supercooled melt devoid of any wettable heterogeneities. This is difficult to achieve practically except with droplet-type experiments although Inoue [19] claims that nylon-6 undergoes a transition from heterogeneous to homogeneous nucleation above T_c=210°C as a result of a shift in the Avrami

exponent, n = 2.5→4.0. Using the critical nucleus free energy of formation derived in the previous section,

$$I^*(\text{nuclei/cm}^3\text{-sec}) = \frac{NkT}{hV_m} \exp\left[-\frac{\Delta F_\eta}{kT} - \frac{32\sigma^2\sigma_e T_m^{o\,2}}{(\Delta H_f \rho_c \Delta T)^2 T_c}\right] \qquad \text{(A1-33)}$$

where Vm = molar volume associated with the folded chain length. This nulceation rate is exceedingly more temperature dependent than R^* (heterogeneous nucleation) due to the $1/T_c\Delta T^2$ term and is greatest at high ΔT.

The above theories hold whether the growth rate is studied by polarized light microscopy or crystallization kinetics by the DSC. If the latter is pursued, the growth rate can be substituted into the corresponding expression for the kinetic intercept, K (equations A1-7 or A1-10). For heterogeneous, athermal, three-dimensional nucleation, a plot of $\log K + \Delta F_\eta/kT$ versus $T_m^o/T_c\Delta T$ as shown in equation (A1-34), yields the interfacial free energy product $\sigma\sigma_e$ from the slope and the nucleation density from the intercept

$$n^{-1} \log K + \frac{\Delta F_\eta}{2.3\ kT} = \log[(4\pi/3)(\rho_c/\rho_a\omega_c^a N)^{-n} G_o] - \frac{4b_o\sigma\sigma_e T_m^o}{2.3\Delta H_f \rho_c k} \frac{1}{T_c \Delta T} \qquad \text{(A1-34)}$$

This assumes T_m^o can be estimated accurately and independently and that the expression for the transport term is valid; additional terms defined in text, Chapter VII.

REFERENCES FOR APPENDIX 1.

1. M. Avrami, Jnl. Chem. Phys., 7, 1103 (1939); 8, 212 (1940).

2. D. Turnbull, J.C. Fisher, Jnl. Chem. Phys., 17(1), 71 (1949).

3. J.I. Lauritzen, Jr., J.D. Hoffman, Jnl. Chem. Phys., 31, 1680 (1959).

4. A. Galeski, E. Piorkowska, Jnl. Phys. Chem., Oct, 1985.

5. B. Wunderlich, Macromolecular Physics, Academic Press, 1976, Vol 2, p. 130.

6. B.B. Burnett, W.F. McDevit, Jnl. Appl. Phys., 28(10), 1101 (1957).

7. J.A. Koutsky, A.G. Walton, E.Baer, Jnl. Appl. Phys., 38(4), 1832 (1967).

8. J.H. Magill, Polymer, 3, 655 (1962).

9. P.H. Geil, Polymer Single Crystals, Interscience Pub., N.Y., 1963, p. 375.

10. 9. A. Galeski, A.S. Argon and R.E. Cohen, Makromol. Chem., 188, 1195 (1987).

11. B. Wunderlich, Macromolecular Physics, Academic Press, 1976, Vol 3.

12. R.G. Brown, R.K. Eby, Jnl. Appl. Phys., 35, 1156 (1964).

13. J.D. Hoffman, J.J. Weeks, Jnl. Res. Nat. Bur. Stds., A-66, 13 (1962).

14. Glasstone, K.J. Laidler, H. Eyring, The Theory of Rate Processes, McGraw Hill, N.Y. 1941.

15. M.L. Williams, R.F. Landel, J.D. Ferry, Jnl. Am. Chem. Soc., 77, 3701 (1955).

16. A.J. Kinloch, R.J. Young, Fracture Behavior of Polymers, Elsevier, N.Y., 1985, p.373.

17. J. Boon, G. Challa, D.W. vanKrevelen, Jnl. Polym. Sci.: A-2, 6, 1791 (1968).

18. F. Gornick, J.D. Hoffman, Ind. Sci. & Eng. Chem., 58(2), 41 (1966).

19. J.A. Koutsky, A.G. Walton, E. Baer, Jnl. Appl. Phys., 38(4), 1832 (1967).

APPENDIX 2: NYLON CHEMISTRY

1. Hydrolytic Nylon-6

Reaction 1: ϵ-Caprolactam is heated in the presence of H_2O to super--atmospheric pressures and temperatures of ~ 220°C for 2-3 hours.

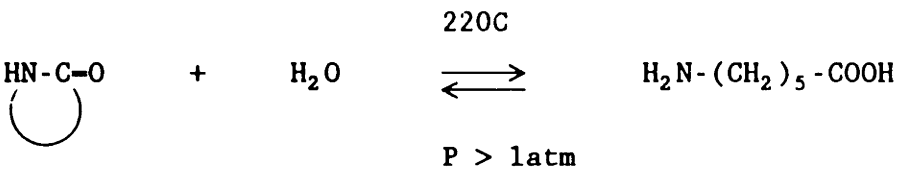

Reaction 2: Self-condensation of ϵ-aminocaproic acid occurs as pressure is dropped allowing water to escape.

Simultaneously, reaction 3 occurs.

Reaction 3: Protonation of lactam by carboxylic acid is followed by nucleophilic attack of neutral amine (N electron pair) on "activated" lactam.

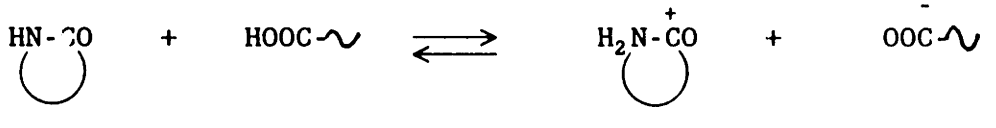

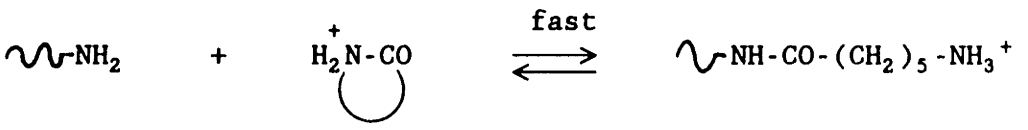

This reaction is rapid because of the strong acylating activity of the protonated lactam to the nucleophilic amine. Neutrality is maintained

and propagation insured by proton transfer to monomer.

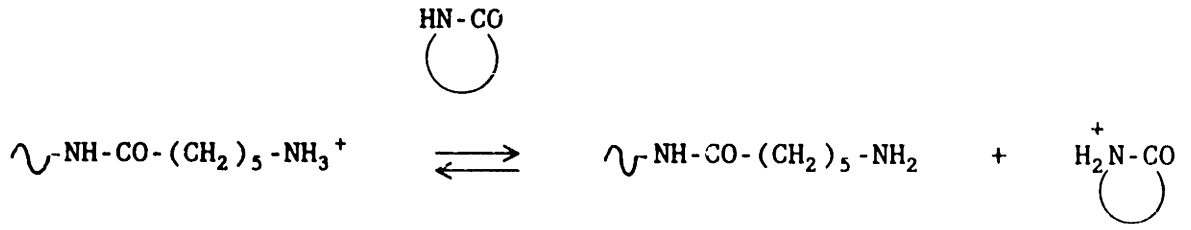

The ring opening reaction #3 proceeds ~100X faster than the self condensation and is mainly responsible for the formation of hydrolytic nylon-6.

2. Anionic Polymerization

The following schematic details the various reactions that occur in the anionic polymerization of ϵ-caprolactam.

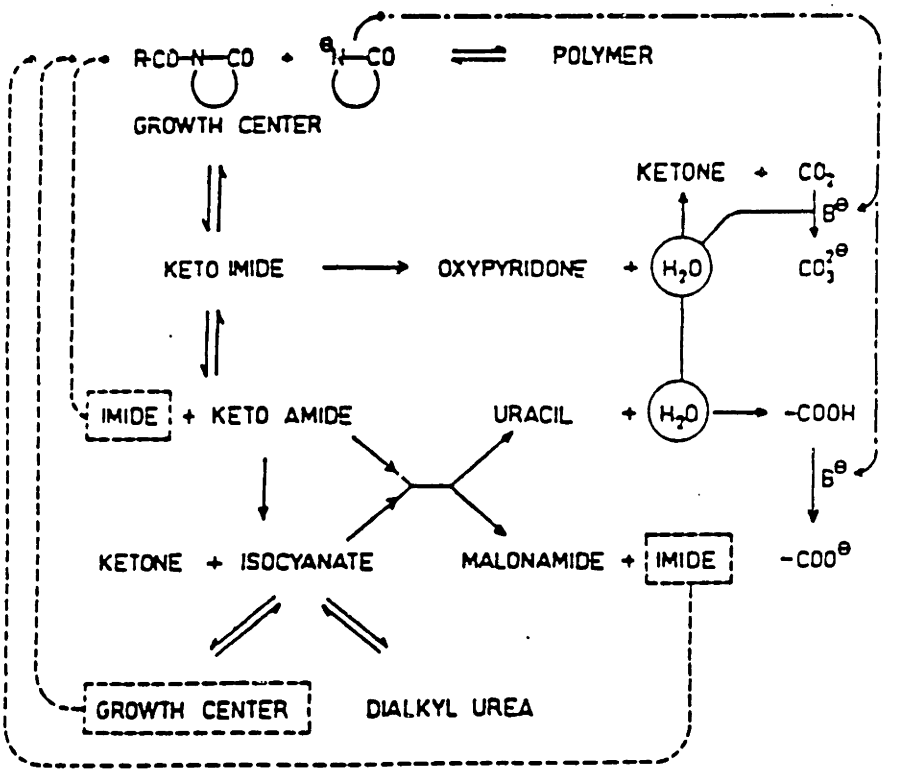

ANIONIC POLYMERIZATION OF 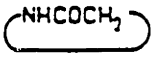

APPENDIX 3: MACROMOLECULAR HYDRODYNAMICS OF NYLON-6 AND PMMA IN TFEtOH

In the course of calculating the hydrodynamic volume of PMMA for the SEC universal calibration, the solution thermodynamics of PMMA and nylon-6 in TFEtOH were investigated with respect to several existing theories.

Solution Thermodynamics

PMMA - TFEtOH

The Flory [1] expression for intrinsic viscosity

$$[\eta] = KM^{1/2}\alpha_\eta^3 \quad , \tag{A3-1}$$

where

$$K = \Phi_0 \left[\frac{\overline{r_0^2}}{M}\right]^{3/2} , \tag{A3-2}$$

M = molecular weight and α_η = the viscosity expansion factor, is valid for all random coil macromolecules of molecular weight greater than ~10 kg/mole. The constant K contains the product of the unperturbed root-mean-square (rms) end-to-end distance divided by the molecular weight, $(\overline{r_o^2}/M)^{3/2}$ and a universal constant, Φ_0, which $\approx 2.5 \times 10^{21}$, [2]). From this relationship, Flory, Fox and Schaefgen [3] predicted the polymer-solvent interaction parameter, χ_{12}, and unperturbed dimension $(\overline{r_o^2}/M)^{1/2}$ from $[\eta]$-M data as shown in equation (A3-3),

$$\frac{[\eta]^{2/3}}{M^{1/3}} = 2C_m(1 - 2\chi_{12})\, K^{5/3}\, \frac{M}{[\eta]} + K^{2/3} \qquad \text{(A3-3)}$$

where

$$C_m = \left(\frac{3}{\sqrt{2\pi}}\right)^3 \frac{v_2^2}{N_A V_1} \left(\frac{r_0^2}{M}\right)^{-3/2} \qquad \text{(A3-4)}$$

with v_2 = specific volume of the polymer, V_1 = molar volume of the solvent and N_A = Avogadro's number, 6.023×10^{23}. However, the $[\eta]$-M data for PMMA/TFEtOH do not follow the mathematical form of the Flory-Fox-Schaefgen equation (A3-3). The fit is poor with a regression coefficient of 0.88 and yields a negative intercept which is physically unrealistic. This result may arise if the unperturbed dimension depends significantly on short range polymer-solvent interactions which has been observed for polar solvent polymer systems such as hexene-1-polysulfone in methyl ethyl ketone/isopropanol mixtures [4]. This polar theta-solvent mixture decreases the "unperturbed" dimension by 20-25% compared to less polar, n-hexylchloride, <u>also a θ solvent</u>.

An alternate viscosity theory that better represents polymer hydrodynamics in good solvents is that by Stockmayer and Fixman [5], equation (A3-5)

$$[\eta] = KM^{1/2} + 0.51\Phi_0 BM \qquad \text{(A3-5)}$$

where $B = v_2^2(1 - 2\chi_{12})/V_1 N_A$ with the same nomenclature previously

defined. The data for the PMMA/TFEtOH system are plotted in accordance with the Stockmayer-Fixman (S-F) theory and are shown in Figure A3-1. Good linear regression is obtained and the unperturbed chain end dimension, $(\overline{r_o^2}/M)^{1/2}$ is equal to 0.595 Å $(g/mole)^{-1/2}$ in excellent agreement with Kriste's [6] and Fox's [7] identical value of 0.61 Å $(g/mole)^{-1/2}$ for PMMA in 50/50 v/v butanone/propanol at 22.5C, a θ-solvent as reported by the former and an average of various θ-solvents ranging in θ-temperatures from 30 to 70°C in the case of the latter investigator. From the slope, the polymer-solvent interaction parameter is calculated to be 0.38.

Nylon-6 - TFEtOH

Workup of the intrinsic viscosity-molecular weight data of Mattiussi, et. al. [8] for nylon-6/TFEtOH gives a slightly larger unperturbed dimension at 25°C in TFEtOH of $(\overline{r_o^2}/M)^{1/2}$ = 1.108 Å $(g/mole)^{-1/2}$ versus 0.971 Å $(g/mole)^{-1/2}$ in 85% formic acid. This expansion of the unperturbed dimension from the S-F theory also has been observed for nylon-6 in other fluorinated alcohols; $(\overline{r_o^2}/M)^{1/2}$ = 1.09 Å $(g/mole)^{-1/2}$ at 25°C in Perfluoroalcohol P-1, (a commercial tradename) which is close to tetrafluoropropanol in material properties [9]. This contrasts with the random-coil unperturbed dimensions of nylon-6 in HCOOH [8], m-cresol [10] or TFP-H_2O-LiCl [11] which are all equivalent and approximately 25% smaller than $(\overline{r_o^2}/M)^{1/2}$ in the two fluoroalcohols. This "stiffening effect" plus the fact that TFEtOH is a better solvent for nylon-6 (χ_{12}=0.09 [8]) versus PMMA (χ_{12}=0.38, this work) explains

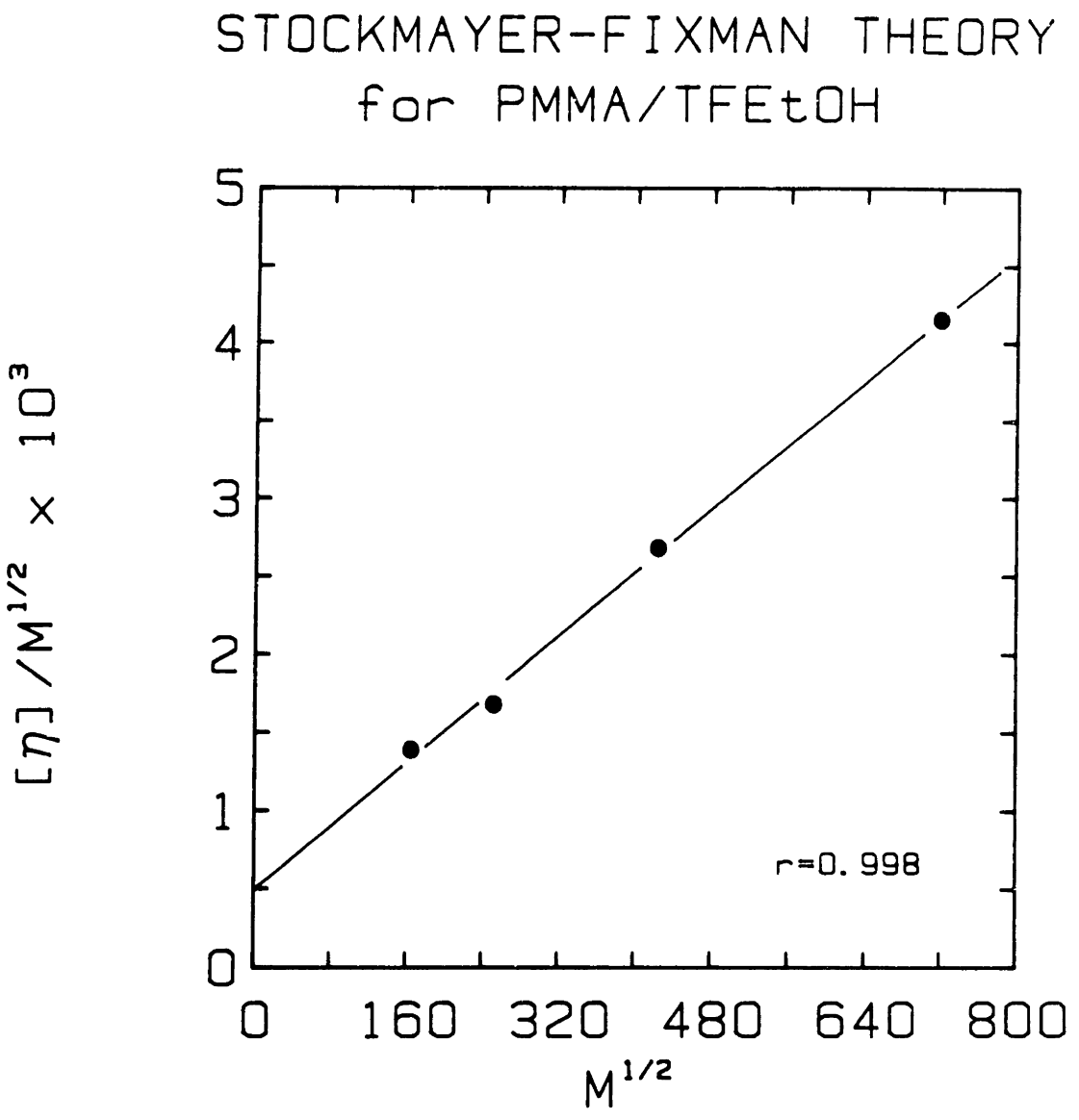

Figure A3-1 Stockmayer-Fixman plot for PMMA in 2,2,2-trifluoroethanol at 30°C. Slope is proportional to χ_{AB} = 0.38 and intercept yields unperturbed dimension, $(\overline{r_o^2}/M)^{1/2}$ = 0.595 Å $(g/mole)^{-1/2}$

why the hydrodynamic volume of nylon-6 is much greater than PMMA in TFEtOH for equivalent molecular weight.

REFERENCES FOR APPENDIX 3

1. P.J. Flory, Principles of Polymer Chemistry, Cornell University Press, Ithaca, N.Y., (1953), p. 612.

2. Ibid., p. 617.

3. P.J. Flory and T.G. Fox, Jnl. Am. Chem. Soc., **73**, 1904 (1951).

4. K.J. Ivin, H.A. Ende and G. Meyerhoff, Polymer, **3**, 129 (1962).

5. W.H. Stockmayer and M. Fixman, Jnl. Polym. Sci., Pt. C., **1**, 137 (1963).

6. R. Kriste, Z. Physik. Chem., **30**, 171 (1961).

7. G. Fox, Polymer, **3**, 111 (1962).

8. A. Mattiussi, G.B. Gechele, R. Francesconi, J. Polym. Sci., Pt A-2, **7**, 411 (1969).

9. A.M. Kulakova and I.K. Nekrasov, Vysolomol. soed. (Polym. Sci., USSR), **A18**, 146 (1976).

10. M. Liquori and A. Mele, Gazz. Chim. Ital., **83**, 941 (1953).

11. M. Kurata and W.H. Stockmayer, Fortschr. Hochpolym.-Forsch., **3**, 196 (1963).